Structure of Nickel-Iron and Nickel-Zinc Electrodeposits

Volume I

Claudia Erdmuthe Lehmberg

A thesis submitted in partial fulfilment of the requirements of Sheffield Hallam University for the degree of Doctor of Philosophy

November 1998

Declaration

I have not been registered for another award of a University during this research programme.

This thesis is submitted in partial fulfilment of the requirements of Sheffield Hallam University for the degree of Doctor of Philosophy. It contains an account of research carried out between November 1993 and November 1998 in the Materials Research Institute, Sheffield Hallam University, under the direction of Dr. G. W. Marshall and supervision of Dr. D. B. Lewis. Except where acknowledge and reference is appropriately made, this work is, to the best of my knowledge, original and has been carried out independently. No part of this thesis has been, or is currently being, submitted for any degree, diploma or any other academic award at this or any other university.

Claudia E. Lehmberg

November 1998

Acknowledgements

I am indebted to the School of Engineering for the provision of laboratory equipment and facilities for the production of the electrodeposits. I would like to thank the Materials Research Institute for the use of the specimen preparation and materials characterization equipment.

I would like to express my sincere gratitude to the director of studies Dr. G. W. Marshall for his encouragement and support during the course of this research and for his invaluable advice. I am grateful to the supervisor Dr. D. B. Lewis for his dedicated help with transmission electron microscopy and for his support and constructive discussions in the interpretation of X-ray diffraction data. I would like to thank Dr. G. W. Marshall and Dr. D. B. Lewis for their supervision and interest they have shown in this work.

I would like to acknowledge the kind technical and practical support from the staff of the School of Engineering particularly Mr. A. Earnshaw, Mr. P. Haythorne, Mr. D. Latimer, Mr. B. Sidebottom, and Mr. T. O'Hara. Furthermore thanks to the staff of the Materials Research Institute, especially Dr. M. Ives for his support with the Glow Discharge Optical Emission Spectrometer. Technical support from staff of the Materials Research Institute, in particular from Mrs. C. Shaw, Mr. P. Slingsby, Mr. G. Gregory, Mr. S. Creasey and Mr. K. Blake are acknowledged with pleasure. A special debt of gratitude is owed to Mr. E. Weik and Miss A. Clark for their encouragement and friendship.

Finally, I wish to thank my family for their unfailing support and encouragement.

Scientific work carried out during the course of this research programme:

To be published: D. B. Lewis, C. E. Lehmberg, G. W. Marshall, "The Structure of High Nickel Content Zinc-Nickel Electrodeposits from Sulphate Baths".

March 1997 M. Ives, D. B. Lewis, C. E. Lehmberg, "Depth Profile Analysis of Multilayer Ni-Fe Alloy Coatings by Glow Discharge Optical Emission Spectroscopy (GDOES) and Energy Dispersive X-ray (EDX) Linescan - a Comparative Study",
Surf. Interface Anal., **25**, 3 (1997).

May 1996 C. E. Lehmberg, D. B. Lewis, G. W. Marshall, "Nickel-Zinc Alloy Electrodeposits from Sulphate Solutions".
Paper presented at the 4th International Conference on Advances in Surface Engineering in Newcastle upon Tyne 14-17 May 1996.

August 1995 G. W. Marshall, C. E. Lehmberg, "Towards Cleaner Wet Surface Finishing".
Paper given at AMPT' 95, Dublin City University, 8-12 August 1995.

October 1994 C. E. Lehmberg, A. Zielonka, "Untersuchungen zur elektrolytischen Abscheidung von Kupfer-Antimon-Mehrlagenschichten".
Proceedings of the DGO Conference, Bad Reichenhall, Germany, 12-14 October 1994.

September 1994 G. W. Marshall, C. E. Lehmberg, D. Clements, B. Perry, "Education and Training in Surface Finishing and Engineering".
Proceedings Engineering Education Conference: Increasing Student Participation, Sheffield Hallam University, 12-14 September 1994, p 442-447. PAVIC Publications, SHU, Sheffield (1994).

Abstract

Electrodeposited nickel-iron and nickel-zinc alloys have been studied using 'direct' methods e.g. XRD, microscopy, EDX and GDOES on coatings having different thicknesses and deposited on different substrates.

The work has confirmed and extended the ideas of Finch et al. [2, 51], Piontelli et al. [3] and Pangarov [49, 120, 121] applicable to alloy deposition. It has shown that a better understanding, particularly of the initial deposition stages, can be obtained by considering crystallographic, energy and electrochemical aspects in combination rather than individually.

Initially alloy is deposited on a 'foreign' substrate but subsequently the growing alloy itself serves as the 'substrate'. Similarly 'old' crystallites have to compete for growth with 'newly' nucleated ones as the deposit develops. The three stages of growth observed in nickel-iron and nickel-zinc are discussed.

Crystallographic strain, resulting from mismatch between substrate and deposit structures and the presence of impurities, along with the energies required to produce different structures are considered to play a major role in determining structure during alloy deposition.

Competition for discharge between hydrogen and metallic ions at the changing deposit surface, including changes in its electrochemical nature are considered. In addition possible effects resulting from adsorbed species, including co-discharged hydrogen as well as other species such as hydroxyl ions or precipitated hydroxides are discussed.

Whereas during initial nucleation the original substrate is the dominating influence, in the later stages the electrolytic parameters determine the structure of the deposit. If the structure of the outer deposit differs markedly from that of the deposit during the initial stages, then a transitional growth stage may be involved. The structures of deposits studied in the present work tended to be fine grained in the initial stages but developed coarser columnar structures due to selected grain growth with favoured grains becoming broader during the intermediate and final stages of growth.

Nomenclature and Abbreviations

ρ	Specific density
η	Current efficiency for metal deposition
λ	Wavelength of X-rays
θ	Angle of incidence
μ/ρ	Mass absorption coefficient
°C	Degree Celcius
Δf	Dispersion correction factor
µm	Micron (10^{-6} m)
A	Ampere
a	Lattice parameter
a_c	Activity
AES	Auger Electron Spectroscopy
APD	Automated Powder Diffraction
B_0	Zero point energy
bcc	Body centred cubic
BF	Bright Field
BSI	Backscattered Image
B_T	Thermal vibration
c	Electrochemical equivalent
d	interplanar lattice spacing
DF	Dark Field
E	Electrode potential
E^0	Standard electrode potential
e^{-2m}	Temperature factor
E. D. M.	Electro-Discharge Machining
EDX	Energy Dispersive X-ray analysis
E_i	Electrode potential when current is flowing
E_{over}	Overpotential

eV	Electron Volt
F	Structure factor
f	Atomic scattering factor
F	Faraday constant
f_{av}	Average atomic scattering factor
fcc	Face centred cubic
Fe	Iron
f_o	Uncorrected value of scattering factor from tables
g	Gram
GDOES	Glow Discharge Optical Emission Spectroscopy
H	Hydrogen
hcp	Hexagonal close packed
I	Current
i	Current density
$I_{\{hkl\}}$	Measured intensity of the textured specimen
i_M	Partial current
I_o	Intensity of the incident beam
K_{edge}	Mass absorption coefficient
kV	Kilo Volt (10^3 V)
l	Litre
LP	Lorentz-polarization factor
m	Metre
mA	Milli Ampere (10^{-3} A)
mass-%	Concentration in mass per cent
m_d	Mass of deposit
n	Valency
Ni	Nickel
nm	Nano meter (10^{-9} m)
P	Multiplicity factor
$P_{\{hkl\}}$	Statistical change of any plane lying in the plane parallel to the surface
QSDPA	Quantitative Surface Depth Profile Analysis

R	Gas constant, molar
$R_{\{hkl\}}$	Calculated intensity corresponding to a random specimen
S	Cross-sectional area of the beam
SADP	Selected Area Diffraction Pattern
SEI	Secondary Electron Image
SEM	Scanning Electron Microscopy
STEM	Scanning Transmission Electron Microscopy
STM	Scanning Tunnelling Microscopy
T	Temperature
t	Time
t_d	Thickness of deposit
TEM	Transmission Electron Microscopy
v	Volume
V	Volt
W	Work
XPS	X-ray Photoelectron Spectroscopy
XRD	X-Ray Diffraction
XRF	X-Ray Fluorescence analysis
ZAF	Z: Atomic number, A: Absorption, F: Fluorescence
Zn	Zinc

Volume I

List of Tables

List of Figures

1 Introduction to Present Work

The electrodeposition of alloys has a history that goes back to brass plating by Jacobi in 1841, and up to 1990 around three hundred binary alloy systems have been deposited from aqueous solutions [1].

In their classical work Finch et al. postulated that electrodeposits grow in three stages, an initial, intermediate and final stage [2]. It was inferred that the substrate structure has a major effect on the deposit orientation during the initial nucleation and growth stage. In this earlier work little consideration was given to either alloy deposition or the difference in potential between the substrate and the metals being deposited.

The present study was undertaken to elucidate the initial nucleation and subsequent development in the cathodic electrocrystallization processes for the alloy systems nickel-iron and nickel-zinc. This appeared interesting since in established literature nickel and iron are classified as 'inert' metals and zinc as an 'intermediate' with respect to their electrochemial behaviour [3]. Thus an 'inert' and an 'intermediate' metal was alloyed with an 'inert' metal nickel, which was common to both systems. The general postulation by Finch et al. stating that the cathodic process of crystal growth involves three stages proved useful as a guideline [2]. In the present work these stages were found, with the characteristics of these stages being unique in each deposit. Particular interest was given to the initial stages where the influence of the original cathode dominates until it becomes covered by deposited alloy, whereas in the subsequent stages the electrodeposition parameters mainly influence the properties of the deposit.

Investigations were intentionally restricted to methods directly on the deposits, for it was inferred that distinct knowledge regarding the deposition process could be gained by direct examination of deposits. The work was directed at obtaining information on the elemental composition, the crystal structure and orientation, as well as the morphology, of the deposits from which a fundamental understanding of the growth mechanisms could be developed.

2 Literature Survey

2. 1 Theoretical Background to Alloy Deposition

2. 1. 1 Thermodynamics and Faraday's Laws

Metals cannot always be deposited singly or as alloys during electrolysis of an electrolyte containing one or more ionic species due to the competitive situation which exists for discharge between the different metallic ionic species and hydrogen ions present. A consideration of the thermodynamics of a system will however give some insight into whether or not a metal or an alloy might be deposited.

A fundamental equation in electrochemistry, which relates the potential of a metal to the activity of its ions in an electrolyte and the prevailing conditions, is the Nernst equation [4].

$$E=E^0-\frac{RT}{nF}\ln a_c \qquad [2.1]$$

where E : Electrode Potential

E^0 : Standard electrode potential

R : Gas constant, molar

T : Temperature

n : Valency

F : Faraday constant

a_c : Activity

In the Nernst equation the values of E and E^0 relate to an equilibrium under reversible conditions. However the electrodeposition of metals and alloys occurs under non-reversible conditions and the potential must be shifted from the equilibrium value for deposition to take place. The change in potential when current is applied is termed the overpotential E_{over}.

If E_i is the electrode potential when current is flowing and E is the normal electrode potential, then the overpotential, E_{over}, is determined by:

$$E_{over} = E_i - E \qquad [2.2]$$

The total overpotential or polarization is caused by inhibiting factors of various kinds and can be defined as activation polarization, concentration polarization and resistance polarization [5].

A basic requirement for alloy deposition is that the electrode potentials of the components are very similar. Lowenheim suggested that the potential difference should not be higher than 200 mV for the co-deposition of the alloy's constituents [6]. If the normal standard potentials of the metals related to the Nernst equation and the electrochemical series are considered, then the feasibility of alloy deposition is severely limited.

Akiyama et al. proposed that the condition that permits alloy deposition of the metals M and N is described by an equation consisting of four terms [1].

$$(E_M^0 - E_N^0) + (\frac{RT}{nF}) \ln (\frac{a_{cM}^{n+}}{a_{cN}^{n+}}) - (\frac{RT}{nF}) \ln (\frac{a_{cM}}{a_{cN}}) - (E_{over\,M} - E_{over\,N}) = 0 \qquad [2.3]$$

The first term describes the difference in standard single electrode potentials of the metals where M is more noble than N. This term is characteristic of the alloy system and cannot be varied. The second and the third term are related to the activities of the metals in the bath and in the deposit, respectively. The difference in deposition overpotentials between the deposited metals is indicated by the fourth term.

When the metals to be co-deposited are specified the first term is fixed. Since M is assumed to be more noble than N the first term is positive. The latter terms in the expression are varied in magnitude when electrolyte composition or operating conditions are altered. The equation satisfies the condition permitting alloy deposition when the variable terms, i.e. the second and the fourth terms, are adjusted to cancel out the first term, which is the difference between the standard electrode potentials of the metals concerned.

The practical application of the Nernst equation is limited since it is a thermodynamic law and therefore only relates to thermodynamic aspects of a reaction under equilibrium conditions [5]. The behaviour of an electrode may alter from that predicted by the Nernst equation, since kinetic processes, reaction inhibitions, catalytic effects and overpotentials influence the electrodeposition process.

Furthermore, in relation to alloy deposition, it should be remembered that even when conditions are such that more than one metal can be discharged simultaneously there will be additional competition for discharge between metallic species and hydrogen ions at the cathode.

Electrodeposition takes place in accordance with Faraday's Laws which may be expressed quantitatively as:

$$m_d = I\,t\,c\,\eta \qquad [2.4]$$

where m_d : Mass of deposit

I : Current

t : Time

c : Electrochemical Equivalent

η : Current efficiency for metal deposition

For the electrodeposition of a binary alloy accompanied only by hydrogen co-discharge the total current, *I*, is the sum of the partial currents i_{M_1} and i_{M_2} respectively and that associated with hydrogen co-discharge i_{H_2}. Thus

$$I = i_{M_1} + i_{M_2} + i_{M_3} \qquad [2.5]$$

The normal percentage cathode current efficiencies of each of the three species involved, η_{M_1}, η_{M_2} and η_{M_3} are then

$$\frac{i_{M_1}}{I} \times 100,\ \frac{i_{M_2}}{I} \times 100, \text{ and } \frac{i_{H_2}}{I} \times 100 \text{ respectively.}$$

2. 1. 2 Electrochemical Classification of Metals and Alloys Deposited

Metals have been classified by Piontelli et al. [3] according to their electrochemical behaviour with respect to polarization effects into inert, normal and intermediate metals. Inert metals strongly absorb hydrogen, and are relatively sluggish in respect to anodic dissolution or cathodic deposition. Inert metals deposit electrochemically with high polarization and low current efficiency irrespective of the cathode substrate. Furthermore hydrogen is discharged at low overpotentials at inert cathodes.

Normal metals have high cathodic current efficiencies when deposited and exhibit low exchange current densities for hydrogen discharge but high exchange current densities for metal deposition. Normal metals are deposited with low overpotential and high current efficiencies irrespective of the cathode metal substrate. A distinction is made if metals are deposited with low overpotential, but the magnitude of polarization is influenced by the cathode material; metals that show such electrochemical behaviour are termed intermediate metals.

There has been some ambiguity in the allocation of individual metals to the different classifications. Thus Piontelli et al. [3] classed zinc as an intermediate metal whilst West [7] placed it in the normal group, and similarly silver has been quoted as an example of both a normal and intermediate metal [8].

In the present work the binary alloys systems investigated were initially chosen with Piontelli's [3] classification in mind. Thus the alloy system nickel-iron is a combination of two inert metals and nickel-zinc one of an inert and intermediate metal, with nickel being common to both alloys.

Clearly the electrochemical nature of different metals present in an electrolyte during electrolysis will affect the outcome as reflected in the thermodynamic situation (see Akiyama's [1] equation [2. 3] above) and both the overall and the partial efficiencies as defined above in relation to Faraday's Laws.

Nevertheless there is strong evidence that the course of the deposition process can change significantly during the early stages of deposition as a substrate consisting of one class of metal is replaced by that of another class, say for example inert becomes covered by a metal of another class [9]. Furthermore the normal electrode potential E, (see equation [2. 1]) is a 'single value' which is an averaged value of the 'local potential' values taken at different points over the electrode's surface. Therefore the deposition potential at a specific point on the cathode may be higher or lower. The phenomenon whereby metals and alloys can deposit at a potential lower than the 'standard' electrode potential has been recognized and is called 'underpotential' deposition [10].

2. 1. 3 Alloy Deposition and Its Classification

The standard electrode potentials of nickel, iron zinc are [11]:

Electrode	E^0 [V]
Zn^{2+}/Zn	-0.763
Fe^{2+}/Fe	-0.44
Ni^{2+}/Ni	-0.23

The differences between standard electrode potentials of nickel and iron is 0.21 Volts and that of nickel and zinc is 0.533 Volts. The difference between the standard electrode potentials of nickel and iron is about the limit which Lowenheim has suggested might allow co-deposition [6]. However the difference in the standard single electrode potentials of nickel and zinc is outside the limit and too large to be cancelled out only by the alteration of the metal ion concentrations in the electrolyte [1].

In his empirical classification of alloy deposition, Brenner classed both alloy systems, nickel-iron and nickel-zinc as so-called 'anomalous co-deposition', since in the electrodeposition of the alloys the less noble species deposits preferentially [12].

The fact that the co-deposition of iron and zinc with nickel does not follow the predictions based upon a consideration of the electrochemical series and the Nernst equation led the author to call these alloy systems as 'anomalous' [12]. Once factors such as polarization, mass transfer, electrode reaction kinetics, precipitate formation and ionic interactions are considered, then their so-called 'anomalous' behaviour can be explained. However, Brenner's terminology in the classification of alloy electrodeposition has become common and frequently cited [12].

2. 1. 4 Electrodeposition Characteristics of the System Ni-Fe

The 'anomaly' in the co-deposition of nickel-iron has been confirmed by several workers and has been explained as resulting from a hydroxide suppression mechanism [1, 13, 14]. Polarization curves for nickel-iron alloy deposition and those of the individual constituent metals indicate that nickel deposition is suppressed as the metal hydroxides are formed at the cathode under conditions corresponding to the limiting current for hydrogen evolution. No suppressed nickel deposition is observed when only nickel is deposited.

Hence it was concluded that the formation and subsequent preferential adsorption of ferrous hydroxide on the cathode causes nickel deposition to be suppressed, although the hydroxides of both nickel and iron are formed above the limiting current for hydrogen discharge. This hydrogen suppression theory [1], used to explain the mechanism for nickel-iron deposition, is supported by other work [15, 16, 17, 18]. It was found that increasing the current density reduces the iron content of deposits and increases the current efficiency for alloy deposition since the rates for both iron and hydrogen deposition are diffusion controlled, whilst the nickel deposition is not [15]. Adsorption of iron compounds on the cathode surface results in polarization during alloy deposition. It has been noted that at low current densities, where the pH rise in the cathode layer is small little iron hydroxide is formed leading to high nickel contents in the deposits [16]. As the current density is raised the iron content is increased due to larger pH rises in the cathodic layer. Further increases in current density eventually lead to a decreased iron content.

The hydroxide suppression mechanism was confirmed by the fact that the highest iron content is found in deposits obtained when the partial current density of iron is well below its diffusion limiting current. The decrease in iron content cannot be explained solely by the mass transport limitation relating to the ferrous ion concentration in solution. The pH rise occurring at the cathode surface is sufficient to result in ferrous hydroxide formation [17]. 'Anomalous co-deposition' in the nickel-iron alloy was found to occur only when the pH near the cathode was raised high enough for ferrous hydroxide to be formed and adsorbed. The preferential deposition of iron was explained as resulting from the depolarization and polarization of iron and nickel respectively, due to adsorbed ferrous hydroxide on the cathode surface. It was concluded that the slow ionic diffusion of ferrous ions through an adsorbed hydroxide layer at the cathode results in the decrease in the iron content of the deposits. Thus the hydroxide suppression hypothesis initially proposed by Dahms and Croll explained how 'anomalous co-deposition' results [13, 14]. Supporters of the hydroxide suppression mechanism believe that the iron is discharged through an iron hydroxide film.

This theory has been revised insofar as it has been suggested that a trace amount of ferric ions in solution accounts for precipitation of ferric hydroxide, rather than ferrous hydroxide, on the cathode surface causing selective discharge [18]. This conclusion was justified by the fact that it was found more difficult to raise the pH-value of the cathodic layer in iron solutions than in nickel electrolytes and that the solubility constant was much higher for $Fe(OH)_2$ and $Ni(OH)_2$ than for $Fe(OH)_3$. Therefore it was suggested that the precipitation of ferric hydroxide plays an important role not only in the buffering action which occurs in the cathodic layer but also in the co-deposition of nickel-iron alloys.

A mathematical model for the 'anomalous co-deposition' of nickel-iron has been developed [19] assuming the existence of $FeOH^+$ and $NiOH^+$ intermediate species, which are reportedly involved in alloy deposition [20, 21]. The metal-hydroxide ion complexes $FeOH^+$ and $NiOH^+$ have much larger dissociation constants than their corresponding solid phase metal hydroxides, $Fe(OH)_2$ and $Ni(OH)_2$, which allow them to be thermodynamically stable at several pH units lower than their hydroxide equivalents. The formation of solid metal hydroxide precipitates requires a much higher pH-value than metal-hydroxide ions. The retardation of the nickel deposition rate was explained by the relative concentrations of the two metal hydroxide ions. $NiOH^+$ has a much larger dissociation constant than $FeOH^+$, therefore the cathode surface is covered preferentially with iron hydroxide ions. The presence of $FeOH^+$ results in competition between $FeOH^+$ and $NiOH^+$ for surface sites. Furthermore the pH rise is buffered leading to lower coverage by $NiOH^+$ compared with that when nickel is deposited on its own. Subsequently the presence of iron results in inhibited nickel deposition.

Pulse and pulse reversed electrodeposition results in lower iron contents, i.e. reduces 'anomalous behaviour' [22]. The preferential deposition of the less noble iron was found to be retarded by pulse reversed current electrodeposition, since the adsorbed hydrogen atoms which are formed during the cathodic period are oxidized during the anodic period and thus preventing the pH rising at the cathode surface [22].

Formation of a layered structure, visible in the cross-sectional views of the nickel-iron electrodeposits, has been found which may be indicative for cyclic catholyte depletion of species [23, 24, 25]. Raising the temperature was reported to hamper compositional modulation of the layers since totally uniform composition was obtained only if the temperature is raised to 70-80 °C, which additionally resulted in nickel-richer deposits[23]. As a result of hydrogen adsorption, nickel-iron deposits are frequently 'pitted' [23]. This can be avoided through the use of wetting agents, a rise in temperature [23] and agitation[24].

'Anomalous behaviour' of the electrodeposition of nickel-iron alloy leads to the characteristic feature of composition gradients in their initial several hundred nanometers [26, 27, 28, 29, 30, 31, 32]. The initially deposited atoms appear to be pure nickel but subsequently the deposit becomes greatly enriched in iron after which the iron content decreases until finally approaching a steady state [28]. The occurrence of composition gradients during the initial stage of nickel-iron deposition was explained [28, 29, 30] using the hydroxide suppression hypothesis [13, 14]: Initially nickel deposits preferentially until the hydrogen ion concentration at the cathode surface is depleted and metal hydroxides are formed. When the adsorption of hydroxides has occurred, ferrous ions from the diffusion layer are discharged preferentially leading to the subsequent enrichment of iron in the nickel-iron electrodeposit. The equilibrium composition of the nickel-iron deposit is approached as the diffusion layer becomes depleted of ferrous ions and steady state diffusion conditions for the ferrous ions are established. Nevertheless, other workers reported that electrodeposited nickel-iron alloys can be prepared with uniform composition throughout their thickness when appropriate conditions are chosen [33, 34]. By superimposing alternating current on direct current, i.e. by the application of stepped pulse current, anomalous co-deposition was reported to have been eliminated and deposits of uniform composition were obtained.

2. 1. 5 Electrodeposition Characteristics of the System Ni-Zn

A number of mechanisms including the hydroxide suppression mechanism have been put forward to explain the 'anomalous deposition' of nickel-zinc alloys. Four types of behaviour are found during deposition of nickel-zinc alloys depending upon cathode current density [1]. These are: (1) normal type alloy deposition with poor current efficiency; (2) preferential deposition of the less noble zinc which proceeds at high current efficiencies with increasing current density giving an alloy of almost constant composition; (3) deposition with increasing nickel content during which a high current efficiency is still maintained; and (4) deposition with further increases in nickel content, until the ratio of nickel and zinc in the deposit corresponds to that of the bath, accompanied by a decreased current efficiency.

The transition current densities associated with the transitions between behaviour types (2) to (3) and (3) to (4) correlate with the limiting current densities of zinc and nickel respectively.

A developed form of the hydrogen suppression mechanisms is now generally used to explain the deposition of nickel-zinc, although it does not explain all the known facts entirely [35]. Brenner pointed out that at elevated temperatures and at low current densities normal deposition behaviour is observed [12]. He reported the sudden transition of the normal to the 'anomalous' type as the current density was increased. These transition current densities were interpreted using a hypothesis referred to as the 'addition agent theory', since the levelling effect of zinc and nickel deposition is similar to that observed in the presence of certain addition agents. The hypothesis suggests that normal co-deposition occurs at low current density whereas 'anomalous co-deposition' is observed at higher current densities because the 'addition agent', i.e. zinc hydroxide or zinc hydroxyl ions, are only produced by the cathodic reaction when the current density is sufficiently high to significantly raise the pH in the cathodic diffusion layer. It was proposed that a certain concentration of 'addition agent' is required in the cathodic diffusion layer for nickel-zinc electrodeposition to change from normal to 'anomalous behaviour'. It was reported that the polarization behaviour for nickel deposition during nickel-zinc co-deposition is similar to that observed in nickel electrolytes containing inhibitors [36, 37, 38].

Thus it was suggested that the inhibition of nickel deposition is due to zinc hydrolysis products adsorbed at the cathode surface. Zinc deposition takes place more readily via the initial formation of $ZnOH^+$ and $Zn(OH)_2$ rather than by the direct discharge of Zn^{2+} ions. 'Anomalous co-deposition' was also found in the cobalt-zinc system, where experiments implied that zinc crystals grew by the reduction of $Zn(OH)_2$ from the solid phase rather than direct metal deposition [9].

The hydroxide suppression mechanism for 'anomalous deposition' is further supported by the fact that the pH-value in the cathodic layer increases to that required for zinc hydroxide precipitation [39, 40]. Thus the deposition of nickel is suppressed by the adsorption of zinc hydroxide at the cathodic surface and zinc deposits at its equilibrium potential. In contrast nickel requires an extra overpotential due to the limited availability of suitable deposition sites at the cathodic surface.

An investigation into the amount of zinc hydroxide incorporated in nickel-zinc electrodeposits showed that the zinc hydroxide content is related to the pH-rise in the cathode layer during deposition [1].

An alternative explanation to the hydroxide suppression theory for 'anomalous' nickel-zinc electrodeposition has been suggested based upon polarization studies. Polarization curves for the separate and simultaneous deposition of nickel and zinc led to the assumption that the polarization of nickel in the presence of zinc is attributable firstly to, the high overpotential of nickel and zinc and secondly, to the structural peculiarities in the double layer when nickel and zinc coexist in the electrolyte [1].

Furthermore other workers suggested that the hydroxide suppression mechanism is valid only under particular plating conditions which yielded unsatisfactory deposits containing hydroxides [41]. 'Anomalous co-deposition' was explained in terms of the extremely low value of the exchange current density for nickel as compared to that for zinc, which means that the kinetics favour zinc deposition to such an extent that the result is the reverse of what one might expect from thermodynamic considerations alone.

A mathematical model for the kinetics of nickel-zinc alloy deposition has been developed [42, 43, 44]. The calculation of the concentration of surface species reveals that 'anomalous co-deposition' may occur even when the current density for hydrogen discharge is not high enough to raise the interfacial pH-value sufficiently high to bring about hydroxide precipitation. It was concluded that 'anomalous co-deposition' should be attributed to the high reactivity of zinc as exemplified by its high exchange current density, which is five orders of magnitude greater than that of nickel.

Other workers ascribed the preferential zinc deposition and the uniform composition of the nickel-zinc alloy to the exchange current density of zinc being five orders of magnitude higher than that of nickel [45]. Thus the preferential deposition of the less noble zinc during the simultaneous discharge of nickel and zinc was explained as activation controlled.

Yet another alternative mechanism has been suggested, which connected 'anomalous co-deposition' of nickel-zinc with 'underpotential' deposition [10]. It has been found that different crystal phases of nickel-zinc electrodeposits exist which indicates the occurrence of 'underpotential' deposition of zinc. The formation of each of the deposited phases is associated with a different local potential. Thus α-, γ- and η-phase have different equilibrium potentials which in the cases of the α-, γ- and η-phases are significantly more positive than that for bulk zinc.

2. 2 Nucleation and Growth of Electrodeposits

Finch et al. postulated, that crystal growth at the cathode consisted of three stages [2]. The 'initial stage', where the structure of electrodeposited crystals are mainly influenced by the substrate surface, a 'transition stage', and a 'final stage', which is only present in thicker deposits and in which the deposit structure is mainly influenced by the electrolyte and deposition conditions. Generally during the electrodeposition process there is a high mobility of deposited atoms over the surface.

2. 2. 1 Initial Nucleation

Continuation of the substrate lattice in the initial stage of deposition was reported to occur if "lattice spacings in parallel directions in the contact plane of the substrate and deposit differ by less than about 15 per cent" [2]. It is interesting to note that a parallel to this '15 per cent rule' can be found in relation to solidification from the molten state. Hume-Rothery stated that a precondition for elements to fit together in a common lattice is that the atomic diameters of the components do not vary by more than 15 per cent [46].

It was reported that on a polycrystalline substrate, the initially deposited nuclei will be random, but that as electrocrystallization proceeds the high mobility of the deposited atoms will tend to cause the development of large crystal faces parallel to the most densely packed planes [2]. In the competition for growth, nuclei orientated with the most densely packed lattice planes parallel to the substrate will grow laterally more rapid than nuclei having other orientations and will predominate in the final deposit. At the same time, outward growth from the projections will lead to increased deposition on crystal nuclei orientated with the most densely packed plane perpendicular to the substrate. Hence, two types of oriented crystal growth are considered possible, 'lateral' and 'outward' growth. The structure of electrodeposits is furthermore influenced by bath constituents of various kinds which are adsorbed from the catholytic layer and which may influence the deposition process in various ways, e.g. reduce the mobility of deposited atoms or the outward growth from projections.

It has been pointed out that from the thermodynamic view point imperfections, particularly screw dislocations, on the cathode surface are favourable sites for nucleation [47, 48]. Screw dislocations exhibit kink sites for growth and it is suggested that atoms or molecules migrate over the surface to the step lines resulting from the presence of screw dislocations, see figure 2-1.

Initial nucleation on a single crystal substrate requires three-dimensional nucleation, as shown in figure 2-2.

Once the initial nuclei have formed then one-, two- or three dimensional growth may take place as the deposit structure develops (see fig. 2-3).

2. 2. 2 Deposit Growth

Pangarov pointed out that there is a strong preferred orientation in cases where the growth habit is neither dominated by 'lateral' or 'outward' growth [49]. On the basis of a mathematical model he determined the work 'W' required for the formation of crystal planes, e.g. the {111}, {100} and {110} in the fcc lattice and the {110}, {100}, {112} and {111} in the bcc crystal structure, and postulated that the orientation of thick deposits depends on this work. In the calculations he distinguished between limiting cases, i.e. (i) low overpotential, (ii) high overpotential, (iii) intermediate levels of overpotential, and (iv) extremely high overpotential.

For the formation of the fcc lattice at low overpotential, $W_{111}<W_{100}<W_{110}$, i.e. nuclei with {111} planes parallel to the substrate will be formed preferentially. Conditions are reversed at high values of overpotential, when $W_{111}>W_{100}>W_{110}$, i.e. the work required for nucleating {110} planes is smallest and thus {110} orientation prevails. At intermediate overpotential levels, $W_{111}\approx W_{100}$ or $W_{100}\approx W_{110}$, i.e. there is a possibility of the simultaneous formation of two types of nuclei. At extremely high overpotential random distribution of crystals is expected.

Similar calculations for the bcc lattice at low overpotential showed $W_{111}>W_{112}>W_{100}>W_{110}$, i.e. preferential formation of nuclei orientated with {110} planes parallel to the substrate results. At high overpotential, $W_{111}<W_{112}<W_{100}<W_{110}$, and thus the work for the formation of nuclei with {111} planes parallel to the substrate is a minimum, i.e. the preferential formation of those nuclei results. At intermediate levels of overpotential there is the possibility of simultaneous formation of two types of nuclei and at extremely high of overpotentials randomly orientated deposits are predicted.

In the classical theory of solidification from the molten state under equilibrium conditions, a spherical nucleus is stable once its radius has exceeded a critical value such that the surface energy is smaller than the volume energy [50]. Consideration of Pangarov's ideas in relation to the classical solidification theory suggests that the {111} and the {110} planes of the fcc and bcc lattice respectively have closest packing and hence involve the least energy to bring about metal deposition. Therefore under conditions close to equilibrium, i.e. low overpotential, fcc {111} and bcc {110} orientations are expected to form.

Pangarov's [49] postulations were confirmed by Finch's early work [51, 52], e.g. nickel deposition which occurs with very high overpotential. The orientation of nickel deposits was normally {110} indicating high overpotential, the {111} orientation was described as being unusual and only found together with the {100} orientation, inferring intermediate levels of overpotential.

The formation of some textures may result from certain adsorbed species at the cathodic surface brought about by the varying electrode potential through pulse plating. Thus Chan et al. postulated a relationship between preferred crystal orientation and the kind of adsorbed species on the cathode during electrodeposition [53]. Nickel deposits produced with pulsed reverse current using different pulse cycles were found to have different crystal orientations. Hydrogen or nickel-hydroxide are adsorbed during the cathodic steps. Different orientation densities of the main [100] fibre texture in the nickel deposits were reported to result from adsorbed inhibiting hydrogen, resulting in {210} and {530}. Similarly formation of {111} and {332} texture was attributed to nickel hydroxide adsorbed at the cathode surface.

The conclusion that adsorbed species in the catholytic layer determine the crystalline structure of nickel electrodeposits was also drawn by other research [54, 55]. Organic additives in specific concentrations at given current density in a Watt's electrolyte were found to result indirectly in characteristic deposit textures. This has been attributed to the inhibiting mechanisms of the organic additives that favour hydrogen adsorption and reduction which leads to alkalization of the catholytic layer and formation of nickel hydroxide. Thus it is the inhibiting effect of atomic hydrogen (H_{ads}), molecular hydrogen and nickel hydroxide that directly determine the orientation of crystal growth in nickel deposits. Due to the high overpotential during nickel electrodeposition the most densely populated plane {111} parallel to the substrate is rather uncommon. It is only found when organic components provoked alkalization and therefore nickel hydroxide adsorption on the cathode.

2. 2. 3 Multilayered Electrodeposits

Multilayered electrodeposits are of increasing interest since they can be regarded as materials with unique properties and designed microstructure. The possibility of electrodeposition of multilayered alloys consisting of layers of different elemental composition was mentioned by Brenner who discussed the co-deposition of copper-bismuth alloys generated via switching between high and low current [12]. The production of silver-palladium multilayered alloys has been attained using triangular and stepped direct current waveforms. Increasing cathodic polarization results in increasing deposition of the less noble metal in the respective solutions [56]. Other workers reported on multilayers consisting of nickel-copper alloys [57, 58, 59, 60, 61]. The properties of these nickel-copper alloys were reported to be superior to those of the corresponding uniform alloyed electrodeposits, e.g. tensile strength of multilayered nickel-copper was found up to 4.5 times higher than that of conventional nickel-copper alloy electrodeposit [57]. Compositionally modulated cobalt-tungsten multilayers have been investigated recently [62]. A method of depositing multilayered cobalt films composed of alternating layers of hcp and fcc phases from one electrolyte by programme-controlled pulsed current has been reported [63].

When a single layered deposit is produced there is only one 'initial' stage of growth involved. However, when a multilayered deposit is formed there is an 'initial' stage associated with each layer. Therefore clearly the factors controlling deposit composition and structure of metals during the early stages of deposition are of prime importance during the formation of multilayered deposits.

2. 3 Investigative Techniques

Two approaches may be taken in the study of electrodeposits: (i) *In situ* measurements during electrodeposition and (ii) examination of deposits after formation (*ex situ*).

(i) *In situ* techniques are mainly electrochemical, e.g. voltammetry where the current between the working electrode and a counter electrode is measured as a function of the potential difference between the working electrode and the reference electrode [64]. Such methods lead to the development of models relating to the electrodeposition and crystallization processes but do not give direct information about bulk structure or composition.

(ii) Direct investigations carried out on deposits provide direct evidence of structure and composition and how they change during the course of deposit formation. Information on variations in structure and composition during the electrodeposition process cannot be readily obtained for deposits from type (i) studies, especially in relation to thick deposits. Direct investigations of deposits once formed has not often been carried out in detail because of its known difficulties and time consuming nature. High spatial resolution is demanded of the techniques for meaningful studies of the early stages of deposition and the development of electrodeposits. The sample preparation is often associated with laborious procedures when using such investigative techniques, e.g. Transmission Electron Microscopy (TEM). Nevertheless in the present work deposits were investigated directly despite the difficulties involved.

In table 2-1 the characteristics of techniques used in the present work are set out. Furthermore for completeness table 2-2 summarizes alternative techniques not applied in the present work.

2. 3. 1 *In Situ* Techniques - Indirect Investigations

Most investigators have studied deposition kinetics *in situ* via voltammograms and from the results obtained conclusions on how the electrodeposits formed. The application of stripping voltammetry has been applied to the study of the electrochemical kinetics of nickel-zinc [45, 69] and nickel-iron [70] alloy deposition. Cyclic voltammograms of lead electrodeposited on silver single crystals were used to investigate nucleation mechanisms on substrates having different orientations [71]. The electrochemical kinetics involved in the electrodeposition of lead on copper single crystal substrates [72] were studied by sweep voltammetry and from the results it was inferred that in the underpotential region a monolayer of lead is laid down as a precursor to three-dimensional growth.

In situ voltammetry complemented with *in situ* STM was reported for the study of initial stage electrodeposition [66, 67, 68]. By *in situ* STM the changing surface topography could be visualized during deposit growth. A method has been reported for *in situ* XRD investigations which enabled phase transitions to become detected during electrodeposition [65].

From the shape of time versus current curves it was possible to interpret whether initial nucleation of a nickel monolayer involved two-dimensional growth of a large number of growth centres or three dimensional growth [73]. Current-time transients were calculated and it was claimed that the initial nucleation habits of the first atomic layer can be calculated. Other workers developed a mathematical model for elucidation of the nucleation and growth habits but the theoretical data calculated using the model only fitted that obtained experimentally for thicknesses up to two atomic layers. It was therefore concluded that the model was inadequate [9]. Thus to date the growth habits of bulk deposits cannot be derived from theoretic mathematical models.

2. 3. 2 *Ex Situ* Techniques - Direct Investigations

These techniques may additionally be classed as either destructive or non-destructive. Of the techniques used in the present work GDOES was a destructive technique and XRD, SEM and TEM are non-destructive in the sense that the area of alloy studies is not destroyed. Further detailed information regarding techniques applied in the present work are given in the experimental section.

3 Experimental Procedures

3. 1 Electrolytes

In this section the electrolytes used for the electrodeposition of the nickel-iron and nickel-zinc alloys are dealt with. All electrolytes were made up using deionized water.

3. 1. 1 Nickel-Iron Electrolytes

Nickel-iron electrodeposits were prepared from a number of Watt's type formulations but based upon mixed nickel- and iron salts. The molar concentration of total metal content was the same in all the nickel-iron baths studied. The concentration of iron in *Nickel-Iron Solution 4* was greater than that in *Nickel-Iron Solution 1*. Details concerning the solution compositions and the conditions under which they were operated are given in table 3-1.

Soluble nickel anodes were employed in all nickel-iron electrolytes and their pH-values were adjusted with ammonia solution to between 3.25 and 3.5 at the start of each experiment, the working temperature of the solutions was 60 °C, and the electrolyte volume was 1500 ml.

3. 1. 2 Nickel-Zinc Electrolytes

A number of acidic electrolytes based upon nickel- and zinc sulphates were prepared. The composition and operating condition relating to individual solutions are given in table 3-2. The molar concentration of total metal content was the same in all the nickel-zinc baths studied. The nickel-zinc electrolytes were operated at 50 °C.

Nickel-Zinc Solutions 1- 6 had the same ratio of nickel to zinc (1:1.2). In contrast the nickel to zinc ratio in solutions *7* and *8* was higher, i.e. 1:0.14 and 1:0.06 respectively, than in solutions *1* to *6* with the total metal ion concentration being the same in all *Nickel-Zinc Solutions* tested.

3. 2 Preparation of the Cathodes

3. 2. 1 Cleaning and stopping off

Copper and brass substrates were cathodically cleaned in *Kleenax*, a cyanide containing solution (see table 3-3).

In contrast mild steel samples were anodically cleaned in *Activax*, an alkaline cyanide free solution (see table 3-4).

Following electrolytic cleaning all substrates were washed in deionized water, immersed for 30 seconds in *Activator No. 2*, an activating solution, and washed again. Immersion in the *Activator No. 2* solution served not only to activate the metal surfaces but also to neutralize any traces of drag-out remaining from the electrolytic treatment (see table 3-5).

Stopping off of cathodes was done using *lacomite* lacquer (AGAR Scientific Ltd., Stansted, UK) either prior to cleaning or following cleaning, washing and drying as appropriate. Two coatings of lacquer were used for stopping-off with the first being allowed to dry for at least 24 hours before the application of the second coating.

Prior to plating the cathodes, now having a 'defined' exposed surface area, were electrolytically degreased, rinsed, activated and re-rinsed again. Cathodes cleaned in this way were generally transferred directly to the plating baths without being allowed to dry.

3. 2. 2 Hull Cell Panels

Sixty/forty brass and mild steel panels, 102 mm × 76 mm and 0.2 mm in thickness, were supplied by W. Canning Ltd., Sheffield, UK. The working faces of the panels had a bright rolled finish protected by a thin plastic sheet which could be peeled off before use.

3. 2. 3 Cathodes for Thick Electrodeposits

Copper cathodes, 30 mm × 40 mm, were cut from 1 mm thick rolled copper sheet, and any oxide present was mechanically removed using a scouring pad. The cathodes were attached to a steel rod by a crocodile clip, which served both to make electrical contact and hold them firmly during subsequent cleaning and plating operations. Prior to cleaning and plating, all but an area of 20 cm^2 on the working face of the cathodes was stopped off as shown in figure 3-1.

Following plating, the bulk of the stop-off lacquer was removed mechanically and the remainder was dissolved off using acetone before the plated cathode was re-weighed.

3. 2. 4 Cathodes for Thin Electrodeposits

Deposits were produced on 32 mm diameter copper cathodes which were 6 mm thick for XRD, GDOES, and EDX analyses. These were machined from a copper rod of 32 mm in diameter. The dimensions of the samples were chosen for convenience, since these fitted in the sample holder of the *BÜHLER* semi-automatic polishing machine.

Each copper disc had a groove machined around its circumference to facilitate wiring up ready for electrolytic cleaning and plating. The copper discs were ground and polished utilizing the *BÜHLER* semi-automatic polishing machine.

The 32 mm diameter discs fitted directly into the sample holder of the polishing machine, which accommodated six samples at a time. *BÜHLER's* recommendations for the surface preparation of copper were followed and the samples were polished to a 1 μm finish [74].

Prior to lacquering and wiring for plating the copper discs were manually polished to a 0.25 μm finish, washed with soap, cathodically degreased, rinsed, activated, rinsed again and then dried before being weighted. Since only the polished faces of the copper discs were to be electroplated, all remaining areas, as well as the electrical connection were stopped off with *lacomite*. To ensure sufficient adhesion of the *lacomite*, the discs together with the suspension wires, were pre-cleaned as for plating, and dried prior to lacquering. Figure 3-2 shows schematically samples stopped off and thus having a defined surface area ready for plating.

3. 2. 5 Cathodes for TEM Investigations

Two different kinds of copper substrates were used to deposit various nickel-iron and nickel-zinc coatings. The copper substrates for TEM investigations of single and double layers of Ni-Fe electrodeposits were cut from rod stock. They were 32 mm in diameter and 2 mm thick. The copper discs had a groove machined around their circumferences. The working faces of the samples were polished manually to a 0.25 μm finish. The grooves kept the copper wire which provided the electrical connection in position. The substrates together with the wires were cathodically degreased, rinsed, activated, rinsed again and then dried. Since only the polished faces of the copper discs were to be electroplated, all remaining areas, as well as the electrical connection had to be stopped off.

Mild steel substrates were also used in the investigation of nickel-zinc electrodeposits which were machined, 6 mm thick, from 32 mm diameter rod material. The face sides had a 0.25 μm finish and were omitted when the remaining areas of the samples were stopped off.

Lacomite lacquer was used as stop off agent. Two layers of *lacomite* were applied, each layer being allowed to dry for at least 24 hours. Prior to electrodeposition the discs were cathodically degreased, activated, rinsed again and whilst still wet immersed in the respective electroplating solutions.

3. 3 Electrodeposition of the Coatings

In this section the electrodeposition procedures are described. Following pre-treatment, i. e. degreasing, rinsing, activation, rinsing again, the still wet stopped-off cathodes were transferred to the plating solutions and coatings electrodeposited under the appropriate conditions. The current had been set previously using a dummy cathode.

As soon as the samples had been electroplated they were taken out of the solution, rinsed above the solutions with deionized water from a squeeze bottle to keep drag-out to a minimum. Samples were then rinsed again in a beaker containing deionized water. Subsequently they were immersed in industrial methylated spirit and blown dry with hot air to avoid drying stains.

3. 3. 1 Electrodeposition of Hull Cell Panels

Preliminary tests were done using a 250 ml Hull Cell [75, 76, 77] having provision for gas agitation. The Hull Cell was maintained at temperature in a water bath. Due to the poor thermal conductivity of the Hull Cell, the test solutions were brought to temperature in a glass beaker before being transferred to the pre-heated cell.

For the electrodeposition of the nickel-iron deposits the Hull Cell was used in conjunction with brass cathodes and soluble nickel anodes. The nickel-zinc electrolytes were investigated using the Hull Cell fitted with mild steel sheet cathodes and inert platinized titanium mesh anodes after preliminary experiments showed that the solutions were unsuitable for use with soluble nickel anodes. The solutions were agitated with nitrogen gas. Figure 3-3 shows schematically the experimental set-up used for electrodeposition in the Hull Cell.

The nickel-iron and nickel-zinc electrodeposits were evaluated visually and their composition investigated as a function of current density. Each point along the central horizontal plane of the Hull Cell panel can be related to a specific current density [75, 76]. The following equation was applied to relate current densities to points on the horizontal plane between x = 0.64 cm and 8.25 cm on the deposited area of the Hull Cell panel [6].

$$i = I(5.101 - 5.240 \log x) \qquad [3.1]$$

Where i: Current density [A dm^{-2}]

I: Total cell current [A]

x: Distance of any point from the edge of the Hull cell cathode nearest to the anode, which has the highest current density [cm]

For the evaluation of the deposits plated on the Hull Cell panels only a one centimetre strip lying one centimetre beneath the solution level was taken into consideration, i.e. the top of the electrodeposited area, as indicated aside.

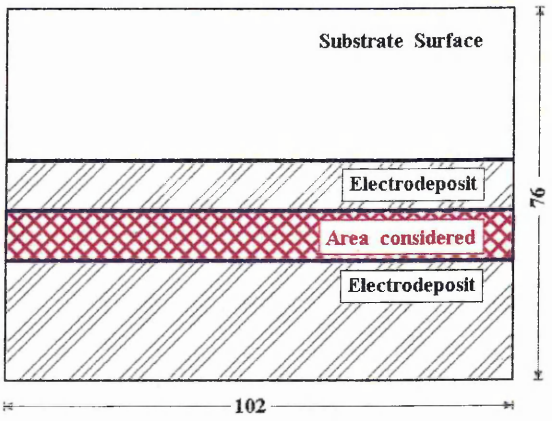

Areas of deposits produced upon Hull Cell panels at different current densities were marked using a steel scriber. The compositions of the alloys in these areas were determined using Energy Dispersive X-ray Spectrometry (EDX), an additional facility of the Scanning Electron Microscope (SEM).

3. 3. 2 Preliminary Electrolyses at Individual Current Densities

Further electrolyses were carried out at specific cathodic current densities using copper cathodes. The current densities used were in the range 10 to 60 mA cm^{-2}. The electrolytes studied in this way were those numbered *1, 3* and *4* in table 1 for nickel-iron deposits, and number *8* in table 2 for nickel-zinc deposits. The electrolyte volume was 1500 ml. Deposits produced in these experiments were approximately 30 μm thick.

Prior to, and during electrodeposition, the electrolytes were de-aerated with nitrogen gas. The flow-rate of the inert nitrogen gas was controlled using a flow-meter (*ROTAMETER 1100*, GEC-Elliot Process Instrument Ltd., Croydon, England).

Generally electroplating solutions containing sodium lauryl sulphate as a wetting agent were not suitable for gas agitation due to excessive foaming. These solutions were therefore agitated by a submersible magnetic stirring unit.

To determine the mass of electrodeposited alloys the samples were weighed before stopping-off and after electrolyses and subsequent removal of the *lacomite* stop-off. The crystal structure of the deposits was determined by X-ray diffraction. The composition of the electrodeposited alloys was determined using Energy Dispersive X-ray analysis (EDX) and Glow Discharge Optical Emission Spectroscopy (GDOES). The cathodic current efficiencies were then calculated by applying Faraday's laws and using the data obtained relating to the mass of alloys deposited and compositional data.

3. 3. 3 Electrodeposition of Thin Alloy Coatings

To investigate nickel-iron and nickel-zinc deposits further, series of deposits were produced ranging in thickness from very thin to bulk deposits. The thinnest of the deposits were 0.05 μm, and the thickest 3 μm. The electrolytes used in this work were the *Nickel-Iron Solution 4* (see table 3-1) and the *Nickel-Zinc Solution 8* (see table 3-2) for nickel-iron and nickel-zinc deposits respectively. The crystal structure of alloy deposits was studied by X-ray diffraction.

Prior to, and during electrodeposition, the solutions were de-aerated with nitrogen gas and filtered continuously. Again the flow rate of the nitrogen gas was controlled using a *ROTAMETER 1100.* The solutions were filtered at a rate of 46 ml min^{-1} through an 8 μm disposable in-line nylon filter (*Whatman®,* Whatman Ltd., Maidstone, England) with the aid of a pump (*302 S/RL* variable speed pump, Watson-Marlow Ltd., Falmouth, Cornwall, England). The plating time to obtain a given thickness was calculated using the current efficiency results of preliminary electrolyses at individual current densities. The plating times were controlled using an automatic timer (*TIMER 814,* Crouzet Ltd., Farnborough, England) connected into the circuit. The current was pre-set using a dummy cathode prior to main experimental electrolyses. Figure 3-4 shows the schematic experimental set-up.

3. 3. 4 Multilayered NiFe Electrodeposits

Compositionally 'modulated' nickel-iron deposits were produced in *Nickel-Iron Solution 4* onto copper cathodes. By alternating the current density, the composition of the electrodeposited alloy could be varied. Increasing the current density at the cathode caused it to become more negative, i.e. polarized, which caused preferential deposition of the less noble ion species, in this case iron. Increasing the current density also resulted in an accelerated deposition rate. In nickel-iron electrodeposition, increasing the current density produced an initial sharp increase in the iron content of the deposits.

Multilayered compositionally 'modulated' nickel-iron electrodeposits were prepared using a step-pulsed current cycle consisting of high and low current densities separated by an off-time. High current density was 60 mA cm^{-2} and low current density was 10 mA cm^{-2}. The application of the higher current density resulted in iron richer deposits, during the off-time the depleted diffusion layer had opportunity to recover. The nickel-iron multilayered deposit consisted of ten individual layers, the first being put down with high current density, i.e. iron rich layer adjacent to copper deposit.

3. 3. 5 Alloy Deposits for TEM Investigations

Electrodeposits investigated by Transmission Electron Microscopy (TEM) were:

1. Single layered nickel-iron and nickel-zinc coatings, approximately 3 μm thick, deposited on copper rod substrates at 10 and 60 mA cm^{-2} from *Nickel-Iron Solution 4* and *Nickel-Zinc Solution 8*, respectively (see tables 3-1 and 3-2).

2. Double layers of nickel-iron deposited on copper rod material using *Nickel-Iron Solution 4*. Double layers were made up of one initial layer of 0.5 μm and 2 μm thickness, respectively, either deposited with a current density of 10 or 60 mA cm^{-2}. The second layer was 2 μm thick and deposited with a current density of 60 or 10 mA cm^{-2}, respectively.

3. Single-layered nickel-zinc coatings having a thickness of 2 μm, deposited on steel rod substrates at 10 and 60 mA cm^{-2}, respectively, using *Nickel-Zinc Solution 8*.

Sample preparation for TEM:

A sample preparation technique was established to obtain electron-transparent cross-sections of electrodeposits. Electron-transparency is the basic requirement for TEM investigations, and cross-sections were needed since the growth of the electrodeposits, and the change of deposit characteristics as it builds up, are of prime interest in this investigation. The sample holder of the TEM is designed to accommodate 3 mm diameter discs. For the cross-sectional view, the area of interest, i. e. the alloy electrodeposit, has to be in the middle of the disc. The electrodeposits to be investigated were deposited on copper or mild steel substrates.

The sample preparation technique established for TEM investigations involved the following steps.

- *Overplating with copper.*

A copper deposit of at least 1.5 mm thickness was overplated onto the alloy coating to be studied using first a cyanide 'strike' and then an acid bath to build up the copper deposit.

The alloy coatings to be investigated were rinsed, cathodically degreased, and rinsed again before being immersed in the cyanide copper bath, with the potential already applied. Any activation procedure was omitted since the alloy coatings, particularly the nickel-zinc alloys, may have dissolved in the acid *Activator No. 2* solution. Details of the cyanide and copper plating baths are given in tables 3-6 and 3-7, respectively.

The cyanide electrolyte was utilized mainly to ensure satisfactory adhesion of the copper deposit to the alloy deposits, which might have had a tendency to passivate due to their nickel content. There may also have been the possibility of forming immersion deposits had an acid copper bath been used, due to the less noble nature of the alloy coatings relative to copper, which might have resulted in unsatisfactory adhesion. The use of a cyanide bath also precluded the possibility of any dissolution of the alloy deposits, which might have taken place during initial plating in an acid bath. Only a thin 'strike' copper deposit of approximately 10 μm was deposited in the cyanide copper electrolyte. Following the application of the copper 'strike' coating the samples were rinsed, cathodically degreased, rinsed again, activated and immersed into the acid copper bath, which was used to build up the thickness of the copper overplate.

- *Spark eroding of a cylinder.*

A three millimetre diameter cylinder was spark eroded from the overplated sample so that the alloy electrodeposit formed the mid-line of the circular cross-section as shown in figure 3-5.

Electro-discharge machining (E. D. M.) provided a gentle method of forming a sample of cylindrical shape required for cross-sectional TEM investigations [78]. Conventional machining on a lathe had the inherent danger that the samples may have cracked along the interfaces. In contrast to conventional methods of machining, where a tool or grinding wheel is rotated at high speed to chip or grind away particles of metal, electro-discharge machining (E. D. M.) is a process where particles of metal are removed by the energy released by repetitive spark discharge. These discharges take place between two conductors placed at suitable distances apart when they are connected to a direct current supply. Generally the erosion of the positive electrode is considerably higher than that of the negative electrode if they are submerged in a suitable dielectric liquid during spark discharge. Therefore the sample being studied is normally made the positive and the counter electrode the negative pole. However, certain material combinations give enhanced wear of the sample if the poles are reversed. If a sufficiently high voltage stress is applied to the dielectric it exhibits the characteristics of a conductor and permits current to flow. When the voltage between the electrodes is sufficiently high the dielectric acts as a conductor since, at a critical voltage, the dielectric ionizes accompanied by spark discharge. The dielectric reverts to its deionized form when the voltage is removed. The ionization of the dielectric associated with a critical voltage ensures that spark discharge between electrode and workpiece occurs at only one point where the voltage stress is maximum, which is at any instant the closest point between electrode and sample. Spark erosion is operated in pulsed d. c. mode.

The spark erosion equipment used in the present work was a SPARCATRON serial No 71/2002/6CW1/6 (Sparcatron Ltd., Glouster, England). The electrode was a rod, having an inner diameter of about 4 mm to account for the spark gap envelope. A copper-tungsten electrode was used after initial work using copper electrodes produced excessive wear of the electrodes. The use of copper-tungsten electrodes proved satisfactory. The principal features of the experimental set-up used are depicted in figure 3-6.

- *Cutting off slices from the cylinder.*

A wire saw (*WELL* Model 3241, series 9407, *WELL*, W. Ebner, Le Locle, Switzerland) fitted with a diamond wire provided a gentle method of cutting off approximately 0.3 mm thick slices from the cylinders previously machined and containing the alloy deposit (see fig. 3-7).

- *Thinning of the cross-sections.*

i) Grinding

The 3 mm diameter discs, cut off using the wire saw, were ground to a thickness of less than 70 μm which is the thickness required for ion beam thinning using a very low angle beam. Samples were mounted for grinding on glass slides with *Crystal Bond* (Gatan Ltd., Corby, Northans, UK). Coarse grinding was done with 1200 and 4000 grid silicon-carbide grinding paper. Samples were washed at regular intervals during grinding to remove any contaminating debris. One side of the coarsely ground specimen was then ground to a 1 μm finish, first using wet 3 μm and then 1 μm diamond grinding paper (3M Imperial™, 661 X Diamond Lapping Film; 3M, St. Paul, MN 55144-1000, USA). A schematic drawing of the sample produced by the above procedure is shown in figure 3-8.

ii) Dimpling

Dimpling was carried out using a *Precision Dimple Grinder Model 656/3* (Gatan Ltd., Corby, Northans, UK). The sample obtained by grinding was mounted on a stub, with the side having the 1 μm finish facing downwards. The dimple was ground in the side with the coarser surface. The mounts with the samples were inserted into a rotating table. With the aid of a microscope, fitted with a hair-cross, the area of interest was moved into the centre of rotation. The dimple grinder was fitted with a dial with which the desired dimple depth could be adjusted [79].

The dimpling process consists of three main steps:

1. The formation of an approximately 40 μm deep dimple using 6 μm diamond paste on a brass wheel.

2. The formation of an approximately 20 μm deep dimple using 1 μm diamond paste on a brass wheel.

3. Polishing the bottom of the dimple using 1 μm paste on a felt wheel.

Figure 3-9 shows schematically the plan view and the side view of a dimpled specimen. At the end of these three stages, the base of the dimple was approximately 5 μm thick. For the sample preparation to be successful, i. e. to obtain an electron-transparent area in the alloy electrodeposit, the area of interest needed to be in the base of the dimple.

iii) Ion Beam Thinning

Electron transparent sections were finally produced in the ground and polished dimpled samples using the ion beam thinner, during which the argon beam sputtered off the surface of the specimen. The instrument used was a *Precision Ion Polishing System Model 691 PIPS™* (Gatan Ltd., Corby, Northans, UK). Initially the dimpled side of specimens were first subjected to the ion beam to clean it before perforating the undimpled side.

The polishing is done by two miniature Penning ion guns aimed at glancing angles of incidence to the specimen during which it is rotated about its axis, while being bombarded by the argon beams [80]. The particle beams consists of both ionic and fast neutral species. The rotation speed of the sample may be varied. The facility of the ion beam modulator enables an individual argon beam to pulse whilst the other is switched off. Thus, specimens within one sample can be thinned at different rates.

In practice, the dimpled side was ion beam polished first, using the normal modus, i. e. constantly bombarding the specimen with two ion guns. This was merely done to clean the dimpled side. The specimen was then turned around and the undimpled side having the 1 μm finish was ion beam polished in the normal mode until it was perforated. In figure 3-10 the ion beam polishing process of the discs is shown.

The side having the 1 μm finish was thus thinned until the specimen became perforated. Electron-transparent areas were present around the edge of the perforation in prepared specimens, which could then be examined by TEM. In practice initial perforation did not always occur in that part of the specimen containing the electrodeposited alloy. It appeared as if different metals had different sputtering rates, i.e. copper was usually perforated prior to areas containing the electrodeposited alloy of interest. The ion beam modulation facility allowed the position of the perforation to be controlled to some extent.

3. 4 Investigative Techniques

Microscopic, compositional and structural studies of the nickel-iron and nickel-zinc alloy electrodeposits made using various investigative techniques are discussed in this section.

3. 4. 1 Electron Microscopy

In electron microscopy an electron beam is utilized as source, generated when electrons produced by thermionic emission from a glowing cathode/filament are accelerated through a perforated anode.

3. 4. 1. 1 Scanning Electron Microscopy (SEM)

Scanning Electron Microscopy (SEM) on a JOEL 840A, incorporating an Oxford Instruments EDX (Energy Dispersive X-ray analysis) system was used to investigate the electrodeposited alloys. An accelerating voltage of 20 kV was applied to examine cross-sections and surfaces of the alloy electrodeposits. Cross-sectioned specimens were mounted in conductive bakelite for investigation. Micrographs were taken as Secondary Electron Images (SEI) and in the Backscattered Images (BSI) mode. Semi-quantitative EDX spot analyses and line-scans were produced.

Principle:

The electrons of the electron beam are focused onto the specimen by a series of magnetic lenses. An electron probe of fine diameter is produced, hence small spot size. The electron beam passes through a pair of deflection coils, distorted by 90° against one another. The scanning generator controls the current of the deflection coils in such a way that the electron beam scans over a rectangular field of the sample surface; synchronous the electron beam of a picture tube are controlled (see figure 3-11).

Thus every spot of the scanned field of the sample is allocated to a spot on the screen picture. The magnification is the ratio of the fixed length of the screen to the variable length of the scanned area.

Primary electrons, i.e. incident electrons from the beam, are elastically and inelastically scattered as they interact with the specimen.

Elastic scattering: An incident primary electron is deflected by the electric field of a nucleus. If the angle of deflection was sufficient, the electron leaves the sample as a backscattered electron.

Inelastic scattering: An incident primary electron knocks out an electron of the atom shell, transmitting part of its energy. Thus a secondary electron is generated. As an electron from an outer shell falls into its vacancy, X-rays of a characteristic energy are released.

Figure 3-12 gives a schematized overview of excitation volumes for major SEM sample emissions.

Secondary Electrons are generated through inelastic scattering of incident electrons which transmit energy and knock electrons out of the atomic shell. Secondary electrons are those with energies less than 50 eV. As they have very little energy, secondary electrons can be detected only when they are created near to the surface see figure 3-12. Thus, the secondary electron signal is largely dependent upon the local surface orientation and hence give rise to topographical, and crystal orientation contrast.

Backscattered electrons are produced through elastic scattering of the incident electrons as they are reflected by the electric field of the nucleus. The stronger the electric field of the nucleus the more primary electrons are reflected, thus detectable as backscattered electrons. Therefore backscattered electrons produce atomic number contrast, i.e. give information about material composition. The higher the atomic number of the specimen, the brighter its image. As shown in figure 3-12, backscattered electrons are emitted from a greater sample depth than secondary electrons.

3. 4. 1. 2 Transmission Electron Microscopy (TEM)

For these investigations a Transmission Electron Microscope type CM 20 (Philips) was used. In the TEM the illumination system consists of an accelerated electron beam, generated by the acceleration of a glowing cathode/filament, and the condenser lens which produces a fine electron beam to illuminate the specimen. The filament material used was LaB_6 and the acceleration voltage was 200 kV. The objective lens forms the diffraction pattern and an initial magnified image of the specimen. The magnification system, consisting of the intermediate and projective lens, yields the final image. The recording system is a fluorescent screen where images are observed. The screen can be removed to allow the image to be recorded photographically. All the investigations were made on electron-transparent cross-sections of the electrodeposits. Bright and dark field images were taken using the TEM imaging mode. Structural investigations on the electrodeposits were made by means of Selected Area Diffraction Patterns (SADP). The TEM can be operated in different modes the standard, conventional imaging mode for bright/dark field image formation, or in its diffraction mode for production of Selected Area Diffraction Patterns (SADP) [83]. In its diffraction mode the TEM is operated without the objective aperture. A bright field image is formed if the direct beam (0-order spot) is used for image formation. Without the objective aperture a diffraction pattern of the specimen is formed by the objective lens in its backfocal plane. A dark field image is formed if only the diffracted beam (other than the 0-order spot in the SADP) is utilized for image formation.

Figures 3-13a and b show schematic representations of a cross-sectional transmission electron micrograph and electron diffraction pattern from a bcc nickel-iron electrodeposit on a copper substrate. The diffraction pattern figure 3-13b of grain 'x' in figure 3-13a shows a [110] zone. Lines A, B and C show the [002], [$1\bar{1}2$], and [$1\bar{1}0$] respectively in the grain. Thus, direction A represents the predominant growth direction of the grains in figure 3-13a. In grain 'x' this corresponds to the [002] growth direction. In practice a bright field image is generated by inserting the objective lens around the 0-order spot, i.e. the 000 position in figure 3-13b. To generate the corresponding dark field image, the objective aperture is removed initially to study the diffraction pattern

and re-inserted around the spot corresponding to the diffracted beam. If for example an objective aperture was inserted around the [002] spot in figure 3-13b, then, in the dark field image, only grains with [002] growth directions would appear bright.

3. 4. 2 Compositional Investigations

The elemental composition of the nickel-iron and nickel-zinc alloy electrodeposits was investigated by Glow Discharge Optical Emission Spectrometry (GDOES) and Energy Dispersive X-ray Analysis (EDX), destructive and non-destructive methods, respectively.

3. 4. 2. 1 Glow Discharge Optical Emission Spectrometry (GDOES)

Depth profile analysis of the electrodeposited alloys were performed using a LECO GDS-750 spectrometer (LECO, Munich, Germany) equipped with a 4 mm diameter anode and operated at -700 V and 30 mA in an argon atmosphere. Quantified compositional results were evaluated automatically utilizing the standard LECO QSDPA (Quantitative Surface Depth Profile Analysis) software. The instrument was calibrated with standards of known composition. Elemental concentrations were obtained by comparison of specimen emission intensities with stored intensities of specimen having known elemental composition. Depths were calculated using relative sputter rates, obtained from the sputter yields of each major element with corrections for composition and discharge conditions.

Depth profiles of thin alloy deposits from the deposits surfaces inwards were produced by Glow Discharge Optical Emission Spectrometry (GDOES). In GDOES resolution degradation occurs with increasing depth caused by non-uniform sputter erosion resulting in a deformed crater shape. To counteract this inherent feature and to obtain optimum resolution, particularly thin, i.e. 0.05 μm thick, deposits were being studied. The surface finish of substrates prior to electrodeposition was 0.25 μm. The interface deposit/substrate could not become clearly resolved, for the surface roughness was five times higher than the deposit thickness.

Principle:

In Glow Discharge Optical Emission Spectroscopy (GDOES) the sample is connected as the cathode in an argon plasma. In the plasma, atoms are dissociated into positive (ions) and negative (electrons) charged particles. Plasma excitation occurs via the transmission of electrical energy. The precondition to maintain the plasma is the presence of a sufficient quantity of electrons. As the electrons move in the electrical field, they transmit their kinetic energy when they collide with other particles in the plasma. As a result of the difference in potential between plasma and cathode/sample, the positive charged ions generated in the argon plasma are accelerated towards the specimen under investigation. On impact, kinetic energy is transferred to the specimen which causes ejection of neutral atoms and secondary electrons. The secondary electron emission accelerates rapidly away from the cathode surface and on collision with working gas atoms, causes further ionization of the working gas thus sustaining the discharge. The sputtered atoms from the specimen surface diffuse across the dark space into the negative glow region and are excited or ionized by collisions with secondary electrons or working gas ions. During relaxation the excited cathode atoms emit characteristic line spectra, i.e. wavelength in visible or ultraviolet region.

The wavelength of light that is given off in the 'glow' is characteristic for each element, whereas a intensity is a measure of elemental composition. This radiation is focused by a lens prior to its transmission towards the concave holographic grating. Depending upon its wavelength the radiation is reflected at different angles. The detectors for each element are precisely arranged around the so-called 'Rowland Circle' opposite the holographic diffraction grating. Each detector, i. e. photomultiplier tube, collects and intensifies the incoming light for one specific element only. Analogue signals are digitized by a converter and optically transmitted for evaluation by a computer.

3. 4. 2. 2 Energy Dispersive X-Ray Analysis (EDX)

During interaction of the scanning electron beam with the sample characteristic X-rays are generated. When an electron is ejected as a photo-electron from the inner atomic

shell by interaction with a high energy electron beam, e.g. 20 kV, the result is an ion in an excited state. Through relaxation processes the excited ion gives up its energy and returns to the normal or ground state. One of the processes of relaxation involves an electron from an outer shell filling the vacancy in an inner shell, which results in the loss of a specific amount of energy, namely the difference in energy between the vacant shell and the shell contributing the electron. This electron is given up in the form of characteristic X-rays and the energy of the radiation uniquely indicates the element which is came, hence characteristic X-rays.

By integrating with respect to time, the total number of X-rays detected with a particular energy is proportional to the number of atoms of the particular element present under the electron beam at a particular position on the sample. For EDX analyses, the SEM was operated at 20 kV. The electron beam was focused to 0.1 μm diameter spot size during analysis but the interaction volume was larger, i.e. 1-2 μm, see figure 3-12. Spot analysis is performed with the electron beam stationary on the sample for typically 100 seconds. For line-scanning the electron beam is stepped across the sample surface and X-rays are collected at each point [84]. Quantification is performed by comparing the magnitudes of the X-ray counts with those from pure element standards and making appropriate corrections for atomic number (Z), absorption (A) and fluorescence (F), collectively known as ZAF correction [85].

3. 4. 2. 3 Scanning Transmission Electron Microscopy (STEM)

For the quantitative EDX analyses the TEM was used in its STEM mode in connection with the PMTHIN software for thin sections of materials [86]. The acceleration voltage was 200 kV. The electron beam was focused to 5 nm diameter spot size during analysis. Spot analysis was performed with the electron beam stationary on the sample for 100 seconds.

Cross-sections of electron transparent nickel-iron and nickel-zinc alloys were analyzed at their nucleating interface. This type of quantitative analysis was utilized primarily to study possibly occurring compositional gradients in the initial stages of deposit formation.

3. 4. 3 X-Ray Diffraction

Structural investigations with X-ray diffraction were made from the specimens surfaces. Thus planes parallel to the substrate, i.e. growing planes, diffracted incident X-rays, see also figures 3-14 and 3-15.

3. 4. 3. 1 Principle

The principle of X-ray spectroscopy is that monochromatic X-rays are diffracted by the lattice planes of a sample, if their wavelengths are of the same order of magnitude as the repeat distance between lattice planes [87].

This requirement follows from Bragg's law:

$$\lambda = 2\ d\ \sin\theta \qquad [3.2]$$

Where λ: wavelength of X-rays

d: interplanar lattice spacing of sample

θ: angle of incidence

In figure 3-14 the interaction between X-rays and diffracting planes of a sample is shown. For structure analysis X-rays of known wavelength, e.g. CuK_{α}-radiation, is used and the angle θ is measured. Thus from Bragg's equation the spacing 'd' of various planes can be determined.

3. 4. 3. 2 X-Ray Diffraction under Bragg-Brentano Conditions

In figure 3-15 an X-ray spectrometer with Bragg-Brentano geometry is shown. X-rays emitted by the X-ray source are incident on a sample rotating about an axis through the centre of the spectrometer circle. The sample is positioned so that its reflecting planes make a particular angle θ with the incident beam. The specimen and detector are inclined at θ and 2θ respectively to the X-ray source. Thus the system is driven such the sample rotates by θ and the detector by 2θ to maintain Bragg-Brentano conditions.

The spectra obtained show the angles 2θ versus count rate, i.e. intensity of diffraction. From the θ-angles the lattice spacing 'd' can be calculated using Bragg's law. These can be compared with standard Bragg angles, e.g. with JCPDS diffraction data [88]. With the appropriate software, e.g. Automated Powder Diffraction (ADP) by PHILIPS spectra can be compared to standards [89].

3. 4. 3. 3 Radiating Source

Selection of target material:

X-ray diffraction analysis was carried out using monochromatic CuK_α radiation. X-ray diffraction traces performed on thin electrodeposited coatings on a copper substrate were characterized by a high background signal resulting in a low peak to background. In figure 3-16 the X-ray diffraction spectra of a nickel-iron electrodeposit on a copper substrate, with and without a nickel β-filter for the CuK_α radiation, are shown. Filtration of monochromatic CuK_α radiation through a nickel foil resulted in lower background noise than was the case without the nickel filter.

The level of the signal also increases with increasing Bragg angle θ. The high background signal was due to fluorescence of the copper substrate by Bremsstrahlung with wavelengths shorter than that of the mass absorption coefficient for copper, i.e. 'K_{edge}' for copper. The copper tube was operated at 20 kV and 50 mA, which gave a short wavelength limit 'λ_{min}' of 0.0615 nm with the maximum intensity, 'I_{max}' of the

Bremsstrahlung at 1.5 x 0.0615 nm, i.e. 0.093 nm, since the relation for the short wavelength limit 'λ_{min}' is equal to $\frac{1243}{V}$ [nm], and the wavelength at which intensity is maximum is 1.5 times the minimum wavelength [90].

Thus, Bremsstrahlung with wavelengths shorter than the mass absorption coefficient 'K_{edge}' for copper but longer than the wavelength limit 'λ_{min}' are capable of fluorescing the copper substrate to produce both CuK_α and CuK_β radiation. The monochromator removes the CuK_β component as it is set to diffract CuK_α radiation only. Other radiation, e.g. CoK_α or MoK_α radiation, are possible alternatives to copper. In these cases the fluorescent characteristic radiation produced from the copper substrate would be removed by the monochromator, which would be set to detect either CoK_α or MoK_α respectively, thus the high background would not be a problem.

Yet, since in Bragg's Law 'sinθ ' cannot exceed unity, hence

$$\frac{\lambda}{2d} = \sin\theta \leq 1.$$

Subsequently

$$\lambda \leq 2d \quad \text{or} \quad \frac{\lambda}{2} \leq d$$

That means that for diffraction to take place, the wavelength of radiation of the source is required to be smaller than twice the value of the d-spacing of the plane to be diffracted. As can be seen in table 3-8, the wavelength of the CoK_α radiation is approximately equal to 0.179 nm. Only planes with d-spacings of equal to or greater than half that value, i.e. > 0.0895 nm, can be diffracted with CoK_α radiation. To diffract the planes of interest in the samples, a source with a shorter wavelength was needed. For example, reflections of the (222) planes of bcc nickel-iron, which has a d-spacing of 0.0828 nm [88], a wavelength shorter than 0.1656 nm is required for diffraction to take place. With molybdenum the problem is more one of peak separation, because of its short wavelength it would be difficult to separate the (111) reflections of the copper substrate from the (111) and (110) reflections in the nickel-iron coating and from the

(330) reflections from the γ-phase in the nickel-zinc coating. Hence, the use of copper as the radiation source appeared to be the only possibility in analyzing the nickel-iron and nickel-zinc electrodeposits. The peak to background ratio was found to be significantly increased by the use of a nickel filter between the X-ray source and the specimen, see figure 3-17.

Beta-Filter:

From table 3-8 and figure 3-17 it can be seen that the mass absorption coefficient 'K_{edge}' for the nickel filter lies between the wavelengths of the CuK_α and CuK_β radiations. In practical terms the mass absorption coefficient for CuK_α radiation is significantly less than that for the Bremsstrahlung, at wavelengths between the maximum intensity 'I_{max}' and the mass absorption coefficient 'K_{edge}' for the nickel filter, produced at an accelerating voltage of 20 kV. Thus, the intensity of the CuK_α radiation is increased relative to the Bremsstrahlung which significantly increases the peak to background ratio.

The spectra obtained using a copper target with an absorbing nickel filter had much less background noise than those where unfiltered copper radiation was used.

In figure 3-17 the effect of filtration is shown. The partial spectra of unfiltered and filtered radiation of a copper target are shown superimposed on a plot of the mass absorption coefficient of the nickel filter.

3. 4. 3. 4 Lattice Parameter Measurements

To find the true lattice parameters 'a' of the substrate materials the dependence of lattice parameter a_{hkl} versus $\cos\theta \cot\theta$ was used [91]. This involved calculating the lattice parameter for each reflection in the substrate materials (6 and 7 reflections were used for the steel and copper substrates respectively) and plotting these against the function $\cos\theta \cot\theta$. The true lattice parameter 'a' was determined from the intercept on the 'y' axis of a least squares fit of the measured values a_{hkl}.

3. 4. 3. 5 Inverse Pole Figures

Inverse Pole Figures, also termed Harris texture indices [92], offer a convenient method of depicting the proportions of grains with various orientations referred to a unique axis. The unique axis is taken as being the normal to the deposit.

Theory:

In X-Ray Diffraction under Bragg-Brentano conditions, specimen diffraction takes place only from planes parallel to the surface, when surface and the counter are inclined at angles θ and 2θ respectively to the X-ray beam. Thus, if the intensities are recorded at Bragg angles corresponding to particular diffracting planes, (hkl), a quantitative measurement of the percentage of planes of a particular orientation, with respect to the normal of the electrodeposit can be evaluated.

Inverse Pole Figures are represented in terms of 'P' values which are a measure of the statistical chance of any plane, (hkl), lying in the plane parallel to the surface. For a particular plane, (hkl), '$P_{(hkl)}$' is evaluated as follows [93]:

$$P_{hkl} = \frac{\frac{I_{(hkl)}}{R_{(hkl)}}}{\frac{1}{n}\sum_{0}^{n}\frac{I_{(hkl)}}{R_{(hkl)}}} \qquad [3.3]$$

Where '$I_{(hkl)}$' is the intensity of the (hkl) reflection from the textured specimen, '$R_{(hkl)}$' is the intensity corresponding to a random sample, and 'n' is the number of reflections considered. Thus a 'P' value of one signifies a random orientation, while for values greater than one, the plane is considered to have preferred orientation.

The value of '$R_{(hkl)}$' may be determined by two different methods: From a randomly orientated powder of the same material, or by calculation. The intensity of X-rays diffracted from a particular plane in a pure metal specimen in a diffractometer may be expressed as [94]:

$$R_{hkl} = Q\, I_o \operatorname{cosec}\theta \left(\frac{1}{2\frac{\mu}{\rho}\rho \operatorname{cosec}\theta} \right) \left[1 - e^{-2\frac{\mu}{\rho}\rho t_d \operatorname{cosec}\theta} \right]$$

and simplified to:

$$R_{hkl} = \left(\frac{Q\, I_o\, S\, \rho}{2\mu\rho} \right) \cdot \left[1 - e^{-\frac{2\mu\rho t_d}{\sin\theta\rho}} \right] \qquad [3.4]$$

where 'S' is the cross-sectional area of the beam, 't' is the thickness of the electrodeposit, 'I_o' is the intensity of the incident beam, 'μ/ρ' is the mass absorption coefficient, 'ρ' is the specific density, and 'Q' is given by the following expression:

$$Q = \frac{1}{v^2} \left[F^2\, P(LP) \right] \left(e^{-2m} \right) \qquad [3.5]$$

where 'F' is the structure factor and 'P' is the multiplicity factor, which allows for the contribution of equivalent planes to the reflection. Multiplicity factors for respective {hkl}-planes are compiled in the following manner.

Planes {hkl}	Multiplicity Factors
{hkl}	48
{hhl}	24
{0kl}	24
{0kk}	12
{hhh}	8
{001}	6

In the diffraction of X-rays, (i) the zero point energy as well as (ii) the thermal vibration are to be taken into consideration. The temperature factor 'e^{-2m}' is given by:

$$e^{-2m} = e^{-B\sin^2(\theta/\lambda)} \qquad [3.6]$$

with $B = B_{total} = B_T + B_0$ [3.7]

Where 'B_T' is the thermal vibration and 'B_0' is the zero point energy. The 'B_T'- and 'B_0'-values were taken from the literature [95]. The 'B'-value calculated in equation [3. 7] is substituted in equation [3. 6]. The temperature factor 'e^{-2m}' obtained from equation [3. 6] is substituted in equation [3. 5]. In equation [3. 5], 'v' is the volume of the unit cell, which for cubic materials is given by:

$$v = a^3 \qquad [3.\ 8],$$

where 'a' is the lattice parameter, which is calculated from

$$a = d\sqrt{\left(h^2 + k^2 + l^2\right)} \qquad [3.\ 9]$$

The interplanar spacing 'd' was determined from the Bragg angle for each reflection. 'LP' is the Lorentz-polarization factor which without a monochromator is given by [94]:

$$LP = \frac{1 + \cos^2 2\theta}{\sin^2 \theta \cos\theta} \qquad [3.\ 10]$$

In the presence of a monochromator equation [3. 10] becomes

$$LP_{monochr.} = \frac{1 + \cos^2 2\alpha \cos^2 2\theta}{\sin^2 \theta \cos\theta} \qquad [3.\ 11]$$

where 'α' is the Bragg angle of the monochromating crystal which equals in this case, i.e. CuK_α radiation in connection with a single crystal graphite monochromator, 13.2° [96]. The '$LP_{monochr.}$' term computed from equation [3. 11] is substituted in equation [3. 5].

Calculation of the structure factor F

For fcc $F = 4f$ [3. 12a]

For bcc $F = 2f,$ [3. 12b]

where 'f' is the atomic scattering factor.

The atomic scatting factor 'f ' for each element was determined from the literature [97], where tables give plots of 'sin θ/λ' versus 'f ' (where 'λ' is the wavelength of the CuK_α radiation). Since the radiation used was close to the adsorption edges of the elements present in the alloys, corrections had to be made to the atomic scattering factor 'f ' for each element to allow for dispersion [98]. The following correction is used:

$$f = f_o + \Delta f \qquad [3.\ 13]$$

where 'f_o' is the uncorrected value of the atomic scattering factor from the tables [97] and 'Δf ' is the dispersion correction factor [98]. For an alloy assuming a random solid solution the average atomic scattering factor 'f_{av}' is given by:

$$f_{av} = \sum_{a=1}^{a=n}\left(AtFrac._a \cdot f_a\right) \qquad [3.\ 14]$$

where 'a' is the element and 'n' is the number of elements considered. The value obtained for 'f_{av}' is substituted in equations [3. 12a] and [3. 12b] respectively, which are substituted into the 'F' term in equation [3. 5].

For alloy deposits the mass absorption can be calculated from the following relationship:

$$\left(\frac{\mu}{\rho}\right)_{av} = \sum_{a=1}^{a=n}\left(MassFrac_a\left(\frac{\mu}{\rho}\right)_a\right) \qquad [3.\ 15]$$

where 'μ' is the mass absorption coefficient and 'ρ' is the density. The average density of the alloy is calculated by

$$\rho_{av} = \sum_{a=1}^{a=n}\left(MassFrac.\rho_a\right) \qquad [3.\ 16]$$

The 'μ/ρ' and 'ρ' values for the alloy obtained from equation [3. 15] and [3. 16] respectively are substituted for 'μ/ρ' and 'ρ' values for the pure metal in equation [3. 4].

Experimental Methodology to determine Inverse Pole Figures:

◊ Texture data were obtained using the Philips PW 1820 powder goniometer with Bragg-Brentano geometry, supplied by the Philips PW 1830 generator.

◊ Intensity measurements '$I_{(hkl)}$' were obtained by de-convolution of the diffraction peaks using the Philips' APD 3.6 software [89].

◊ 'P' values were subsequently calculated using equation [3. 3].

3. 4. 3. 6 Rocking Angle X-Ray Diffraction

In the case of a strong preferred orientation, as is the (111) in the fcc nickel-iron electrodeposits, the Harris texture index [92] or inverse pole figure may differ from the texture function. The 'Ω-scan', also termed rocking angle X-ray diffraction, is a more appropriate method to determine to what extent a strongly preferred orientation deviates from the fibre texture [99].

In contrast to conventional structural analysis by X-ray diffraction under Bragg-Brentano conditions, where the specimen and detector are inclined at θ and 2θ respectively to the X-ray source, in rocking angle X-ray diffraction the angle 2θ between X-ray source and detector is fixed to the 2θ value for the reflection of interest. The specimen is driven about the angle Ω (sample rotating about goniometer axis), see figure 3-18.

The spectra show one single peak, plotted as number of counts versus angle Ω, see figure 4-78. Strong fibre textures can be characterized by the width of the Ω-scan which are related to the distribution of the corresponding crystallographic planes. Strong fibre textures are characterized by narrow peak width, the broader the peak the weaker the fibre texture.

Rocking angle X-ray diffraction was used to investigate into the very sharp (111) reflections found in the nickel-iron electrodeposits with face centred cubic structure.

3. 4. 3. 7 Diffractometer and Conditions

The X-ray measurements were undertaken with the Philips PW 1820 powder goniometer coupled with 2θ. The goniometer was fitted with a graphite single crystal monochromator. The power was supplied by the Philips PW 1830 generator. Monochromatic CuK_{α} radiation was used for all X-ray diffraction analyses carried out. Intensity measurements '$I_{(hkl)}$' were obtained by de-convolution of the diffraction peaks using the Philips APD version 3.6 software [89]. The sample was rotated about its axis at a speed of one revolution per second. Further operating conditions varied depending on the samples.

Thick deposits, i.e. > 30 μm, had been plated on copper sheet material, of approximately 1 mm thickness. The margins of these specimen was cut off, leaving a square (2 mm × 2 mm), which could conveniently be placed into the XRD sample holder where it was supported with plasticine. To ensure reproducible experimental conditions, i.e. sample height, a special specimen holder was designed for the thin coatings deposited on disc substrates. In the XRD specimen holder assembly, depicted in figure 3-19, the specimen was fitted into the holder and fastened with the holder clip. With the groove being machined around its circumference the sample holder could be conveniently inserted into the goniometer with a device.

Since the electrodeposits were relatively thin compared to the substrates they were deposited on, conditions had to be adjusted to the substrate material as well as to the actual electrodeposits investigated. The difficulty in analyzing thin samples in general was the relatively low intensity and the high background noise. As a rule only those reflections were considered, whose intensity was higher than three times the square root of the background, i.e.

$$I_{hkl} > 3\sqrt{Background}$$

Nickel-Iron Electrodeposits:

Bremsstrahlung with wavelengths shorter than 'K_{edge}' for copper excited the copper substrate to give off fluorescent radiation, which resulted in high background noise. A nickel filter was used for the examination of electrodeposits plated on a copper substrate, i.e. nickel-iron, which significantly increased the peak to background ratio. For maximum peak to background ratio, the slowest possible scan rate was applied, which was 20 seconds for every 0.02° angle continuously scanned. Once the Bragg angles of the reflections were established through continuous scans, only an appropriate angular range for each reflection was scanned. Angular ranges of 2θ Bragg angles that were covered and the appropriate reflections for the fcc and bcc crystal structure, are set out in table 3-9 and 3-10, respectively. Operating conditions of the generator were 20 kV and 50 mA for nickel-iron deposits on copper substrates.

Nickel-Zinc Electrodeposits:

Reflections of the bcc γ- phase in nickel-zinc were found to overlap with those of the copper in the substrate. No such problems existed when the nickel-zinc samples were deposited on steel substrates. In the latter case the reflections for bcc γ nickel-zinc were well separated from those of the bcc steel. The generator was operated at 40 kV and 40 mA for nickel-zinc deposits on mild steel substrates. The scan speed was chosen at 10 seconds for every 0.02° angle continuously covered. An angular range of between 20° and 100° was covered. No filter was needed for the X-ray analysis of nickel-zinc electrodeposits since they were on mild steel. In contrast to copper substrates, where CuK_{α} radiation excited the copper substrate to fluorescence, resulting in spectra with high background noise, mild steel substrates were not excited to fluorescence, thus the background noise was low in the spectra.

3. 4. 4 Electron Diffraction

Selected Area Diffraction Patterns (SADP) are produced in the lattice imaging mode of the Philips CM 20 Transmission Electron Microscope (TEM). In contrast to the conventional imaging mode of the TEM, in its diffraction mode the objective aperture is removed, which results in the generation of a diffraction pattern in the backfocal plane of the objective lens. This diffraction pattern is magnified by the intermediate and projective lens. The Selected Area Diffraction Pattern is finally projected onto a fluorescent screen for observation. The images can be recorded photographically.

Since specimens were studied in their cross-sectional view only, individual spots in the Selected Area Diffraction Patterns represented crystal directions. Selected Area Diffraction Patterns were indexed, zone axis determined and individual lattice types determined (fcc/bcc) in accordance with the method outlined in Andrews et al. [100].

4 Results

4. 1 Preliminary Results

In this section the solutions studied and the development of those compositions used in the more detailed latter studies are summarized. The nickel-iron and nickel-zinc electrolytes are described in the experimental section, formulations and working parameters are compiled in tables 3-1 and 3-2. Results obtained in these preliminary studies and thinking/logistics behind the studies are set out below.

4. 1. 1 Hull Cell

The Hull Cell was used to obtain preliminary information about the performance of the electrolytes, since it allowed a quick and convenient way of assessing the characteristics of the deposits obtained from the different solutions as a function of current density. Following visual examination of alloy deposits on Hull Cell panels further information, including compositional trends as a function of current density, was obtained by applying Energy Dispersive X-ray (EDX) analysis and Scanning Electron Microscopy (SEM) to specific areas of the deposit. However, these data were by no means regarded as absolute, only as a rough guide in the decision as to which solutions were worthwhile further examination or modification.

4. 1. 1. 1 Nickel-Iron Electrodeposits

The results of experiments using the solutions listed in table 3-1 are set out in this section. The concentration of iron in *Nickel-Iron Solution 4* was greater than that in *Nickel-Iron Solution 1*. Consequently deposits obtained from bath *4* were richer in iron than corresponding deposits obtained from bath *1*. The colour of the deposits obtained appeared to be dependant upon their nickel content. Thus deposits obtained from electrolyte *4* having nickel contents higher than 60 to 70 mass per cent were brownish-

grey, whereas those obtained from solution *1* and having nickel contents lower than 60 mass per cent were silverish-grey in colour.

Although the composition of alloys obtained from solutions *1* and *4* were different, the deposits obtained from both had some common features. Thus the incidence of pitting associated with hydrogen co-deposition generally increased with increasing current density. Use of both high current densities or agitation favoured the production of brighter deposits in both cases in contrast to the use of low current densities and quiescent solution which favoured the production of dull deposits.

Increasing current density up to a point led to higher iron contents which then decreased with further increases in current density. Agitation generally increased the iron content of deposits and lowered the current density at which the maximum iron content was obtained in both *Nickel-Iron Solution 1* and *4*.

These general observations were interpreted by the fact that iron was the less concentrated species in solution. The cathode layer therefore was sooner depleted of iron- than of nickel ions. When the solutions were agitated, the diffusion layer was decreased and hence more ions from the bulk electrolyte could diffuse to the cathode where they were discharged. Increasing the current density initially led to increased iron content in the deposits, since increasing the current density increases the polarization which generally results in deposits with a higher content of the less noble species. The iron content of the nickel-iron deposits decreased with a further increase of current density after the limiting current density for the iron species was reached.

Nickel-Iron Solution 1

Initially *Nickel-Iron Solution 1* (table 3-1) was tested. Its formulation was taken from the literature [101]. In the Hull Cell total cell currents of 1, 3 and 7 Amperes were applied, the electrolytes either left quiescent or agitated with nitrogen gas having a flow rate of one litre per minute. The results of the Hull Cell tests on *Nickel-Iron Solution 1* without agitation at overall cell current of 1, 3 and 7 Amperes are set out in tables 4-1, 4-2 and 4-3, respectively.

In tables 4-1, 4-2 and 4-3 the elemental composition and the visual observations made on deposits are related to specific current density areas on the panels. In table 4-1 the results are set out using an overall cell current of 1 Ampere which gave a current density range from 4 to 50 mA cm^{-2}. The deposit was found to be nickel-rich in the area of lowest current density with a approximate composition of 73 mass per cent nickel and 27 mass per cent iron. The iron content of deposits rose from about 27 to 30 mass per cent as the current density increased from 4 to 10 mA cm^{-2} and then decreased to about 17 per cent with increasing current densities up to 50 mA cm^{-2}. The deposit's appearance was generally found to be dull over the whole deposit, at areas of low current density it was smooth but showed an increase in the degree of pitting with increasing current density. In table 4-2 elemental compositions and deposit appearance is related to current densities between 12 and 150 mA cm^{-2}, which were obtained by applying an overall cell current of 3 Amperes. The highest iron content, i.e. approximately 28 mass per cent, was found at the point corresponding to the lowest current density on the panel, which then decreased with increasing current density until at the point corresponding to the highest current density it was approximately 13 mass per cent. The deposit was dull and brownish-grey in colour with an increasing degree in pitting with increasing current density. In table 4-3 the Hull Cell panel, obtained using an overall cell current of 7 Amperes is described, giving a current density range of 52.5 to 350 mA cm^{-2}. Here the point corresponding to 52.5 mA cm^{-2} had a nickel content of approximately 84 mass per cent nickel, 16 mass per cent iron. With increasing current density the iron content decreased and was approximately 10 mass per cent at the point corresponding to the highest current density on the panel, i.e. 350 mA cm^{-2}. The appearance of the deposit obtained using an overall cell current of 7 Amperes in *Nickel-Iron Solution 1* without agitation was dull and brownish grey, with an increase in the degree in pitting with increasing current density.

To reduce the degree of pitting in the deposits and to counteract the depletion of ferrous/ferric ions in the diffusion layer which was assumed to be responsible for the decrease of iron content in the deposits with increasing current density, *Nickel-Iron Solution 1* was agitated with nitrogen gas at a flow-rate of one litre per minute. Again overall currents of 1, 3 and 7 Amperes were applied. Data relating points of assumed

current density to elemental composition, determined by EDX, as well as visually evaluated deposit appearance are stated in tables 4-4, 4-5 and 4-6 respectively.

In table 4-4 compositional data and deposit appearance are related to points on the Hull Cell panel representing current density values. The results of Hull Cell tests on solution *1* with and without agitation, but with all the other conditions remaining equal, are given in tables 4-1 and 4-4 respectively.

As can be deduced by comparing the two tables electrolyte agitation causes the iron content to increase over the whole current density range investigated and this effect was more prominent the higher the current density. At the point assumed to represent the lowest current density, i.e. 4 mA cm^{-2}, the iron content of deposits from the agitated solution was approximately 30 mass per cent. It then increased steadily with increased current density up to 50 mA cm^{-2} when it reached 40 mass per cent. This indicates, that agitation of the solution decreased the depletion of iron cations near the cathode surface. It was furthermore observed, that the overall deposit appearance was improved by agitation and although pitting was still observed its occurrence was shifted towards higher current densities (cf. tables 4-1 and 4-4).

Comparison of the results of Hull Cell tests carried out on solution *1* (table 3-1) using cell currents of 1, 3 and 7 Amperes in the quiescent (tables 4-1 to 4-3) and agitated states (tables 4-4 to 4-6) confirm and extend the observations based upon a comparison of tables 4-1 and 4-4 alone. Namely that:

1. The iron content of deposits initially increases to a maximum value then decreases in both cases with increasing current densities between 4 and 350 mA cm^{-2} in the approximate ranges 27 - maximum 30 - to 10, and 30 - maximum 50 - to 28 mass per cent for quiescent and agitated solution respectively.

2. Agitation decreases the degree of pitting in deposits and suppresses its occurrence to higher current densities.

3. Agitation improves the quality and appearance of the nickel-iron deposits.

Nickel-Iron Solution 2

As a remedial measure against the occurrence of pitting in the deposits, sodium lauryl sulphate was added to the formulation of the previously tested *Nickel-Iron Solution 1*. To increase the iron content in the deposits, the amount of ferrous sulphate was increased in solution *2* but the total molar metal concentration was kept the same as that in the previously tested *Nickel-Iron Solution 1*. However *Nickel-Iron Solution 2* was not tested in the Hull Cell for it soon became obvious that the addition of sodium lauryl sulphate made the application of nitrogen agitation unfeasible. Therefore only specimen at individual current densities with were produced with the electrolyte being agitated via a magnetic stirrer unit.

Nickel-Iron Solution 3

Freshly prepared nickel-iron electrolytes turned cloudy over a period of time and, if left standing, a brownish precipitate was formed, a small amount of which floated on the bath surface as a scum with the bulk settling to the bottom of the solution. Deposits formed from these solutions (*Nickel-Iron Solutions 1* and *2* in table 3-1) were of variable and suspect quality presumably due to adsorption of precipitated solid during deposition.

Nickel-Iron Solution 4

Since operating nickel-iron solutions with nitrogen gas agitation was found not only to generally improve the surface appearance, but also serves to de-oxygenate the solution, solution *3* was modified insofar that the addition of sodium lauryl sulphate was omitted which allowed the solution to be purged with nitrogen gas. Test results on this solution with cell currents of 1, 3, and 7 Amperes, with and without nitrogen agitation, are given in tables 4-7 to 4-9 and 4-10 to 4-12, respectively.

In table 4-7 the visual observation and elemental composition of the deposit formed at a cell current of one Ampere without nitrogen agitation are summarized. Deposits were produced in the current density range from 4 to 50 mA cm^{-2}. The deposit was smooth at lower current densities with pitting at higher current density. At the lowest current density considered the mass percentage of iron in the deposit was about 47. The iron content of the deposit increased with increasing current density until it reached its maximum of about 55 mass per cent at 15 mA cm^{-2}. Further increases in current density resulted in a decrease in iron content to an approximate value of 47 mass per cent at 50 mA cm^{-2}. Table 4-8 records the visual appearance and elemental compositions measured in the Hull Cell deposit produced at a cell current of 3 Amperes in the non-agitated *Nickel-Iron Solution 4*. Using a cell current of 3 Amperes gave a current density range between 12 and 150 mA cm^{-2}. The deposit's colour was silverish-grey throughout but its appearance was only shiny and smooth in lower current density areas, i.e. up to 30 mA cm^{-2}. Higher current density areas were found to become slightly pitted, and at current densities above 60 mA cm^{-2} the deposit's appearance altered from shiny to dull. The iron content was about 50 mass per cent at the lower current density end of the panel, increased to 51 mass per cent at the area corresponding to a current density of 22 mA cm^{-2} before falling to a value of 32 mass per cent at the high current density end (150 mA cm^{-2}) of the panel. Tests using a cell current of 7 Amperes produced deposits in the range of 28 to 350 mA cm^{-2}, see table 4-9. The deposit's appearance was shiny, smooth and silverish-grey in colour in regions of low current density, i.e. up to 70 mA cm^{-2}, areas of higher current densities showed a dull finish with pits, and in areas where the current density was higher than 280 mA cm^{-2} the deposit was powdery, burnt and consequently non-adherent. The iron content of the deposit was found to decrease in areas with increasing current density until the minimum concentration of about 30 mass per cent iron was reached at approximately 210 mA cm^{-2}. The iron content then increased in areas with current densities higher than 280 mA cm^{-2}. The results of the Hull Cell tests with nitrogen agitation of *Nickel-Iron Solution 4* using cell currents of 1, 3, and 7 Amperes are shown in tables 4-10, 4-11 and 4-12, respectively.

With the working parameters of the overall cell current being one Ampere with nitrogen gas agitation (table 4-10), the deposit's appearance was observed to be shiny, silverish grey and smooth over the entire panel. The iron content was found to increase with increasing current density, the lowest iron concentration of around 45 mass per cent occurred at 4 mA cm^{-2} and the highest, of approximately 68 mass per cent, at 50 mA cm^{-2}. Table 4-11 gives the visual observations and compositional results obtained for the nickel-iron deposit produced with nitrogen gas agitation from *Nickel-Iron Solution 4* using a cell current of 3 Amperes. The deposit was found to be shiny, silverish-grey and smooth in the current density range between approximately 12 and 90 mA cm^{-2}, but had fine cracks and slight pits at higher current densities. The iron content in the deposit increased with increasing current density, from approximately 57 to 67 mass per cent at current densities of 12 and 150 mA cm^{-2} respectively. Operating the Hull Cell with nitrogen gas agitation at a cell current of 7 Amperes produced shiny, silverish-grey, smooth deposits in areas of low current density from about 28 to 105 mA cm^{-2}, but cracks and pits were found in areas of deposits formed at higher current densities which became more prominent the higher the current density, when the deposits became less shiny. The iron content increased with increasing the current density between 28 and 350 mA cm^{-2} from approximately 52 to 60 mass per cent.

Comparison of the relationship between alloy composition and current density for *Nickel-Iron Solution 4* operated with (tables 4-7 to 4-9) and without (tables 4-10 to 4-12) agitation indicates that nitrogen gas agitation counteracts the diffusion control of the less concentrated iron species in the electrolytes: In agitated electrolytes the iron content increased with increasing current densities, whereas in solutions that were left quiescent the iron content was decreased from a critical current density onwards.

As soluble nickel anodes were used during the investigation of nickel-iron electrolytes and no attempt was made to replace any preferential removal of metal from solution, it can be expected that a limited change in the ratio of nickel to iron occurred in the course of these preliminary experiments.

4. 1. 1. 2 Nickel-Zinc Electrodeposits

Nickel-Zinc Solutions 1 to *3* (table 3-2) became cloudy after short periods of electrolysis. Initially this was interpreted as being due to hydrolysis. However it was found that lowering the pH (i. e. *Nickel-Zinc Solutions 4*, *5* and *6* in table 3-2) did not prevent the nickel-zinc solutions from turning cloudy but caused the deposits to become more pitted as a consequence of the increased hydrogen reduction and subsequent hydrogen gas adsorption on the cathode surface. A decrease of pH was found to occur during electrolysis using both inert and nickel anodes (*Nickel-Zinc Solutions 1* to *6*).

Further work was carried out on reformulated nickel-zinc electrolytes (numbers *7* and *8* in table 3-2) using inert platinized titanium anodes. These solutions were filtered continuously during and before electrodeposition to counteract excessive precipitate formation. The pH-value decreased as the baths were worked.

To counteract these changes in pH during use, the acidity of all solutions was adjusted to the 'correct' value using sodium hydroxide at the start of each experiment. This change in pH during electrolysis indicated that oxygen evolution was taking place at not only inert but also at 'soluble' nickel anodes according to the equation:

$$4OH^- - 4e^- \rightarrow 2H_2O + O_2 \qquad [4.1]$$

Thus the nickel dissolution reaction,

$$Ni - 2e^- \rightarrow Ni^{2+} \qquad [4.2]$$

could not have been occurring at 100 per cent efficiency when nickel anodes were used.

Nickel-Zinc Solutions 1 to 6

In the Hull Cell a cell current of one Ampere was applied, thus the current density range from 5 to 50 mA cm^{-2} was covered on the test panels which produced deposits of 80 to 90 mass per cent zinc. As the current density increased the zinc content in the deposited alloys showed a tendency to increase. The deposits were poor, powdery, burnt and had poor adhesion. Therefore no further work was done on *Nickel-Zinc Solutions 1* to *6*. Since a higher nickel content of the deposits was aimed for, the solution was modified.

Nickel-Zinc Solution 7

To obtain a higher nickel content in the deposits, in *Nickel-Zinc Solution 7* the nickel to zinc ratio was increased, i.e. 1:0.14, compared to *Nickel-Zinc Solutions 1* to *6* (Ni:Zn=1:1.2). The compositional results and visual observations from the deposit produced in the Hull Cell using *Nickel-Zinc Solution 7* with nitrogen gas agitation and a cell current of one Ampere are shown in table 4-13. The zinc content of the deposit initially increases with increasing current density, i.e. in areas corresponding to current densities of 5 and 40 mA cm^{-2} the zinc content was approximately 61 and 81 mass per cent, respectively. At higher current densities, i.e. > 50 mA cm^{-2}, the zinc content decreased. Increasing the current density led to higher zinc contents in the deposits until the limiting current density for zinc deposition was reached. The zinc content then decreased as the current density increased further. Deposits formed at low current densities were brownish grey but those formed at higher current densities were silverish-grey in colour due to decreasing nickel content. The deposit formed in the current density range 10 to 20 mA cm^{-2} was dull but that formed at higher current densities up to 50 mA cm^{-2} was shiny.

Nickel-Zinc Solution 8

Subsequently *Nickel-Zinc Solution 8* was tested in the Hull Cell in more detail. The results using this electrolyte operated without agitation and cell currents of 1, 3 and 5 Amperes are given in tables 4-14, 4-15 and 4-16 respectively. A cell current of 1 Ampere covered a current density range of 4 to 50 mA cm^{-2}. The resulting deposit was shiny and brownish grey in colour at low current densities but turned dull and silver-grey at higher current densities. The zinc content increased from about 36 to 66 mass per cent in areas of increasing current density from 4 to 30 mA cm^{-2} before decreasing to 59 mass per cent in higher current density areas up to 50 mA cm^{-2}.

In table 4-15 compositional data and visual observations relating to the deposit produced from *Nickel-Zinc Solution 8* without agitation using a cell current of 3 Amperes are compiled. The deposit was dull and patchy in the current density range 12 to 60 mA cm^{-2} but burnt and powdery at higher current densities. The zinc content was approximately 12 mass per cent at 12 mA cm^{-2} and increased as the current density was increased until it reached about 37 mass per cent at 30 mA cm^{-2}. Further increases in current density between 30 and 150 mA cm^{-2} corresponded to a decrease in the zinc content although the compositions measured in the burnt areas at high current densities are possibly not reliable.

The results relating to the current density range of 20 to 250 mA cm^{-2} are compiled in table 4-16. The deposit appearance was dull and brownish grey at lower current densities, cracked in intermediate current density areas (50 mA cm^{-2} and higher) and burnt in the high current density areas (120-150 mA cm^{-2}). The zinc content was highest at the lowest current density, i.e. 20 mA cm^{-2}, and decreased as the current density was increased. The compositional results measured in the burnt regions are possibly not reliable but are stated for completeness.

The compositional results as well as the visual observations relating to the deposits obtained from the Hull Cell tests using *Nickel-Zinc Solution 8* with nitrogen gas agitation are compiled in tables 4-17, 4-18 and 4-19. Conclusions drawn from the application of a cell current of one Ampere corresponding to a current density range from 4 to 50 mA cm^{-2} are shown in table 4-17. The deposit was shiny and brownish-grey at low current densities but became dull and silverish-grey in areas of increasing current density. The zinc content was low at low current densities, i.e. about 37 mass per cent at 4 mA cm^{-2}, and initially increased with increasing current density reaching its maximum, i.e. approximately 74 mass per cent, at 40 mA cm^{-2}. A further increase in current density led to a decreasing zinc content, as indicated by the composition of approximately 55 mass per cent in an area corresponding to the current density value of 50 mA cm^{-2}.

In table 4-18 the deposit appearance and compositional results obtained with nitrogen gas agitation using 3 Amperes cell current for *Nickel-Zinc Solution 8* are given. The Hull Cell test panel covers a current density range from 12 to 150 mA cm^{-2}, with the deposit appearance being shiny and silverish grey at lower current densities, but changing with increasing current density through a dull finish at intermediate current densities until the deposit appeared burnt, black and powdery at the highest current density on this test panel. The zinc content of the deposit initially increased with increasing current density, reaching its maximum concentration of about 67 mass per cent in an area corresponding to a current density of 15 mA cm^{-2}, and then decreased as the current density was increased further. As in previous experiments, the analysis obtained from the burnt deposit is merely stated for completeness with little claim in regard to reliability.

Table 4-19 shows the conclusions drawn from the test panel prepared with a 5 Amperes cell current in *Nickel-Zinc Solution 8* using nitrogen gas agitation. The deposit finish was observed to be dull, brownish-grey interspersed with silver patches at low current densities. At higher current density values the brownish-grey finish was associated with a silverish-grey deposit, until at even higher current densities the deposit

was burnt, black and powdery. As a function of increasing current density the zinc content initially increased from about 11 to 29 mass per cent in the current density range from 20 to 75 mA cm^{-2} before decreasing to 28 mass per cent with further increases in current density to 100 mA cm^{-2}. As noted previously the compositional data associated with burnt deposits is probably unreliable.

Generally it was observed from the individual panels that as the current densities were increased the zinc content was increased until a maximum was reached. Further increases in current density resulted in a decreasing zinc content. The initial increase can be explained as resulting from increasing polarization which leads to the deposition of the less noble zinc. Once the limiting current density for zinc is reached, more nickel is deposited. Deposits that were produced with nitrogen gas agitation exhibited greater zinc contents compared to those that were prepared without electrolyte agitation.

4. 1. 2 Individual Current Densities

Nickel-iron and nickel-zinc solutions, described in detail in tables 3-1 and 3-2 respectively, had been tested for their suitability in the Hull Cell. Where solutions tested in the Hull Cell were considered worthy of further examination deposits at individual current densities were produced. From these deposits further information, such as compositional data, partial current efficiencies, as well as structural information were derived. Deposits of approximately 30 μm thickness produced at current densities in the range of 10 and 60 mA cm^{-2} were investigated.

The surface morphology of the nickel-iron electrodeposits was generally dull and cracked with occasional nodules. Figures 4-1 and 4-2 show Secondary Electron Images (SEI) representing the typical surface morphology found in nickel-iron electrodeposits.

Micrographs (SEI) showing the surface morphology of the deposit, produced in *Nickel-Zinc Solution 8* at 10 mA cm^{-2}, are given in figures 4-3 and 4-4 at different magnifications, respectively. The deposit surface appears cauliflower-like, indicating nodular growth, with occasional cracks around the circumference of individual nodules.

Compositional analyses were made by means of Energy Dispersive X-ray Analysis (EDX) and Glow Discharge Optical Emission Spectrometry (GDOES). The crystal structure of the electrodeposits was determined by X-Ray Diffraction (XRD).

4. 1. 3 Compositional Investigations of Thick Deposits

The compositions were measured in the centre of the deposited area. In the case of nickel-iron deposits; both EDX and GDOES gave comparable results. Initially that was also done for the nickel-zinc deposits, but it was found that EDX and GDOES results are not as comparable as in the case of nickel-iron electrodeposits. Compositional results of nickel-zinc deposits by EDX spot analyses deviated when neighbouring spots were analyzed, indicating localized constituent segregation [102]. In EDX spot analysis the

electron beam is focused to 0.1 μm diameter, the expected excitation volume is approximately 2 μm in diameter for a 20 kV electron beam as applied here. GDOES averages the composition of a circle four millimetres in diameter and was therefore used to determine the composition of nickel-zinc deposits.

It was found that compositional data generally are largely dependent upon the area on the sample from which they are obtained. Therefore compositional results are only comparable if they are taken from the same area of the samples. For convenience it was decided, that analyses were to be taken from the centre of the samples.

4. 1. 3. 1 Compositional Investigations of Thick NiFe Deposits

Nickel-Iron Solution 1

Compositional investigations on deposits produced in *Nickel-Iron Solution 1* at individual current densities were performed by EDX and GDOES. In table 4-20 the compositions obtained using these two analytical techniques are compared. Compositional results are largely comparable, i.e. having a deviation of less than 4 mass per cent at the highest found in the sample produced at 30 mA cm^{-2}. Within the current density range investigated, the iron content of deposits produced in *Nickel-Iron Solution 1* increased with increasing current density. It was lowest at the lowest current density, i.e. about 34 mass per cent and 32 mass per cent utilizing EDX and GDOES, respectively, and highest at the highest current density investigated (60 mA cm^{-2}), i.e. about 40 mass per cent measured with both EDX and GDOES.

The elemental composition was found to be uniform over the sample surface. Analyses were made in the middle of the sample, i.e. position '1' (see fig. 4-5).

It was found that compositional results obtained from EDX and GDOES are largely comparable in the case of nickel-iron electrodeposits. Because of this and the fact that GDOES measurements were quicker to carry out the results relating to nickel-iron deposits in this section were obtained using this technique.

Nickel-Iron Solution 3

In table 4-21 compositional results are given for deposits prepared from *Nickel-Iron Solution 3* in the current density range of 10 to 60 mA cm^{-2}. The compositions were measured with GDOES.

The lowest iron content was found in the deposit produced at the lowest current density, i.e. about 39 mass per cent at 10 mA cm^{-2}. With increasing current density the iron content is initially increased and reaches its maximum of 65 mass per cent at 40 mA cm^{-2}. Further increasing current density leads to decreasing iron content.

Nickel-Iron Solution 4

Compositional results measured with GDOES obtained from deposits formed in *Nickel-Iron Solution 4* are compiled in table 4-22. In the current density range investigated, the iron content of the deposits increased as the current density increased, i.e. was lowest (about 59 mass per cent) at 10 mA cm^{-2} and highest at 60 mA cm^{-2} (about 70 mass per cent). In *Nickel-Iron Solution 4* the diffusion limit of the iron species was not exceeded in the current density range investigated.

4. 1. 3. 2 Compositional Investigations of Thick NiZn Deposits

On the basis of the results obtained from tests of nickel-zinc electrolytes in the Hull Cell, it was decided that only *Nickel-Zinc Solution 8* was suitable for further investigation using individual current densities. It was found that the elemental composition of the nickel-zinc electrodeposit was not as uniform over the sample surface as that of the nickel-iron deposit. In contrast to analyses done on nickel-iron electrodeposits, where only the centre of the deposits was investigated, nickel-zinc electrodeposits formed in *Nickel-Zinc Solution 8* were analyzed at different areas of the deposited area. In figure 4-5 the analyzed areas are indicated.

Table 4-23 gives the compositional results obtained using GDOES. Numbers describing different positions on the samples in table 4-23 refer to areas numbered in figure 4-5.

Compositional results obtained from GDOES analyses show that differing compositions were found at different areas on the samples, i.e. the composition varied locally. Compositional analyses were made by GDOES since with this method the composition is averaged over a circular area of 4 mm in diameter. In contrast with EDX compositional information of an excitation volume of approximately 2 μm in diameter could be obtained. Thus GDOES measurements covering a larger specimen area gave more of an average composition than spot analyses by EDX. For convenience the composition measured in the centre of the sample was taken as representative and particular care was taken to take all analyses in the centre of the specimens, i.e. position '1' in figure 4-5.

4. 1. 4 Partial Current Efficiencies

On the basis of the compositional results and a knowledge of the mass of alloy deposited during electrolyses the partial current efficiencies for the deposition for individual metals were calculated using Faraday's Law. The current efficiency for the total metal deposition was taken as the sum of the partial current efficiencies of the individual metals. The current used for hydrogen evolution was taken as the difference between the total current used during electrolyses and that used to discharge metallic species.

However, in view of the uncertainty in elemental composition and the possible variation over the specimen's area this section means to indicate trends only rather than absolute values.

4. 1. 4. 1 Partial Current Efficiencies of Nickel-Iron Solutions

Nickel-Iron Solution 1

The partial current efficiencies calculated from the weight gain of the samples before and after the deposition in *Nickel-Iron Solution 1* using and the composition measured with EDX and GDOES are shown in figures 4-6 and 4-7, respectively. Figures 4-6 and 4-7 show that the partial current efficiency for iron deposition increased while that of nickel deposition decreased with increasing current density.

Nickel-Iron Solution 3

Figure 4-8 shows the partial current efficiencies for species deposited from *Nickel-Iron Solution 3*. The partial current efficiency for iron deposition initially increases with increasing current density until a maximum of about 64 per cent is reached at 40 mA cm^{-2}. At 60 mA cm^{-2}, the highest current density investigated, the partial current efficiency for iron deposition was about 63 per cent. The partial current efficiency for nickel deposition was highest at 58 per cent for the lowest current density considered, 10 mA cm^{-2}, and then decreased as the current density increased until it dropped to 35 per cent at 60 mA cm^{-2}.

Nickel-Iron Solution 4

Figure 4-9 shows the partial current efficiencies for nickel, iron and hydrogen discharge as well as the efficiency for total metal discharge from *Nickel-Iron Solution 4.* The partial current efficiency for nickel discharge decreased from approximately 40 to 30 per cent as the current density increased from 10 to 60 mA cm^{-2}. The partial current efficiency for iron deposition increased with increasing current density, being about 60 and 70 per cent at 10 and 60 mA cm^{-2}, respectively. The current efficiency for total metal deposition was 100 per cent with the exception of the deposit formed at 40 mA cm^{-2} where the current efficiency was about 95 per cent.

4. 1. 4. 2 Partial Current Efficiencies of Nickel-Zinc Solutions

Nickel-Zinc Solution 8

Figure 4-10 shows current density versus partial current efficiencies calculated from compositional GDOES results. At the lowest current density investigated (10 mA cm^{-2}) the total current efficiency for discharge of metallic species was 57 mass per cent and the proportion of current used for cathodic hydrogen reduction highest, i.e. 43 per cent. The partial current efficiency for zinc deposition initially increased with increasing current density, eventually reaching its maximum, in this case 57 per cent at 40 mA cm^{-2}. The partial current density for zinc deposition was approximately 49 per cent at the highest current density investigated, i.e. 60 mA cm^{-2}. The partial current efficiency for nickel deposition was lowest, i.e. about 27 per cent at the current density with the highest partial current efficiency value for zinc deposition at 30 mA cm^{-2}. The total current efficiency for metal deposition increased initially with increasing current density, reaching its maximum of about 83 per cent at 30 mA cm^{-2}, and decreased as the current density was increased further. The partial current efficiency for cathodic hydrogen reduction was highest at the lowest current density considered, i.e. approximately 43 per cent at 10 mA cm^{-2}, as the current density was increased it was decreased initially, reaching its minimum of about 17 per cent at 30 mA cm^{-2}. Further increasing current density leads to increased current efficiency for hydrogen reduction, i.e. approximately 22 per cent at 60 mA cm^{-2}.

4. 1. 5 X-Ray Diffraction Investigations of Thick Deposits

The nickel-iron and nickel-zinc electrodeposits of approximately 30 μm thickness deposited onto copper sheet were studied by X-Ray Diffraction (XRD) analyses.

4. 1. 5. 1 X-Ray Diffraction Studies on Copper Sheet Substrate

In table 4-24 the raw data, i.e. the calculated statistical value of distribution of diffracting planes {hkl} in a randomly orientated powdered specimen, '$R_{\{hkl\}}$', the measured intensity '$I_{\{hkl\}}$' of the reflections, and the computed planar distribution, of the copper substrate are set out.

In figure 4-11 the reflecting planes of the fcc structured copper substrate are shown in terms of their contribution in per cent values.

The X-Ray Diffraction (XRD) measurement was taken parallel to the rolling direction of the copper sheet. The (200) was the strongest, i.e. 40 % of all reflections found, indicative of a {100} texture.

Interplanar spacings 'd' and the lattice parameter 'a' of the copper sheet substrate were calculated on the basis of their positions of reflections in terms of Bragg angles 2θ. The absolute value 'a' was determined from a Cohen-Wagner Plot [91] (see fig. 4-12). In the literature the lattice parameter 'a' in a copper sample has been reported to be 0.36150 nm [88]. The value 'a' calculated for the copper sheet substrate used in this work was 0.36161 nm, i.e. approximately 0.03 per cent larger than the lattice parameter reported.

4. 1. 5. 2 XRD-Studies on Bulk Ni-Fe Electrodeposits

The crystal structure of deposits obtained from *Nickel-Iron Solution 1, 3* and *4*, described in detail in table 3-1, were investigated by X-Ray Diffraction. Deposits had been produced at 10, 30, and 60 mA cm^{-2} from the nickel-iron solutions.

Deposits formed from Nickel-Iron Solution 1

X-Ray Diffraction spectra of deposits, obtained at 10, 30 and 60 mA cm^{-2} are shown in figure 4-13. Deposits had the fcc crystal structure.

Raw data obtained from deposits produced from *Nickel-Iron Solution 1* in the order of increasing current density are listed in table 4-26.

From the raw data the actual texture of the samples was calculated. In table 4-27 and figure 4-14 the distribution of the planes is presented in tabular form and as a bar chart respectively.

Electrodeposits produced from *Nickel-Iron Solution 1* at 10, 30 and 60 mA cm^{-2} crystallized with fcc lattices, see figure 4-13. A bar chart showing the progressive changes in texture when the current density is increased from 10 to 60 mA cm^{-2} is shown in figure 4-14. In the coating deposited at 10 mA cm^{-2} the distribution of crystallograpic orientations was almost random, each reflection contributing between 20 and 30 per cent of the total measured. As the current density was increased to 60 mA cm^{-2} the distribution of orientations became less random with increases in both the {311} and {111} orientations. At 60 mA cm^{-2} the {111} and {311} orientations represented 37 and 41 per cent respectively of the total reflections measured.

In table 4-28 the positions of the reflections as Bragg angles 2θ are compiled. Table 4-29 shows the lattice parameters calculated on the basis of the 2θ positions.

Interplanar spacings within the fcc structured nickel-iron electrodeposits, determined from the positions of the Bragg angles, were found to increase with increasing current density probably due to stress as can be seen from table 4-29.

Deposits formed from Nickel-Iron Solution 3

In figure 4-15 the X-Ray Diffraction spectra of the deposits obtained at 10 and 30 mA cm^{-2} formed in *Nickel-Iron Solution 3* are shown.

The fcc crystal structure was obtained when current densities of 10 and 30 mA cm^{-2} were used. A mixed structure of fcc and bcc was found when the current density was 60 mA cm^{-2} (see figure 4-16).

Raw data obtained from fcc-structured deposits produced in *Nickel-Iron Solution 3* at current densities of 10 and 30 mA cm^{-2} are given in table 4-30.

The deposit obtained from *Nickel-Iron Solution 3* at 60 mA cm^{-2} had a mixed fcc/bcc structure. Raw data $R_{\{hkl\}}$ and $I_{\{hkl\}}$ are compiled in table 4-31.

From the raw data compiled in table 4-30 the actual texture of the fcc-structured deposits produced from *Nickel-Iron Solution 3* at current densities of 10 and 30 mA cm^{-2} was calculated. In table 4-32 and figure 4-17 the distribution of the planes is presented in tabular form and as a bar chart respectively.

Electrodeposits produced in *Nickel-Iron Solution 3* at the current densities of 10 and 30 mA cm^{-2} had fcc crystal lattices. The {311} and the {111} were the main reflections detected, and were both present in a higher proportion in the deposit produced at the higher current density. In contrast to the deposit produced from *Nickel-Iron Solution 1* at 10 mA cm^{-2}, in which the distribution of orientations was random, when deposited at the same current density the deposit produced from *Nickel-Iron Solution 3* exhibited a mixed {111}/{311} texture. Both fcc structured nickel-iron deposits produced from *Nickel-Iron Solution 3* had {111}/{311} textures, with the {111} being slightly less pronounced and whose proportions were increased at the expense of the weaker {200} and {220} orientations in the specimen prepared at the higher current density.

When the deposition current density used was increased to 60 mA cm^{-2} a mixed fcc/bcc crystal structure was obtained. The proportional distribution of detected reflections, calculated from the raw data $R_{\{hkl\}}$ and $I_{\{hkl\}}$ (see table 4-31), is set out in table 4-33. In figure 4-18 the orientation of the fcc/bcc deposit is presented diagrammatically.

The calculated distribution of planes in the mixed fcc/bcc structured deposit infers a {111} texture which represented 52.2 per cent of the total fcc reflections measured, likewise for its fcc and bcc portion. The {222} reflections of the bcc structured component are predominant, contributing to about 72.6 per cent of the total bcc reflections measured. This finding does not contradict the information given by the XRD spectrum in figure 4-16. The {222} reflection in the bcc lattice is weak, i.e. its intensity $R_{\{hkl\}}$ in a randomly orientated, powdered, untextured sample is low (compare $R_{\{hkl\}}$ values in table 4-31). Thus {222} reflections of bcc the lattice structure in the XRD spectra with low intensities at first sight contribute generally to a greater extent to the texture of the sample.

The positions of the 2θ Bragg angles of fcc reflections detected from the nickel-iron deposits produced from Solution *3* at 10 and 30 mA cm^{-2} are set out in table 4-34. Interplanar spacings calculated on the basis of these 2θ positions are stated in table 4-36. A tendency was observed that the deposit formed at the higher current density (i = 30 mA cm^{-2}) has slightly larger interplanar spacings, i.e. 0.2 per cent, which might be indicative of a stress effect.

Positions of 2θ Bragg angles from reflections found in the fcc/bcc crystal structured deposit produced from *Nickel-Iron Solution 3* with 60 mA cm^{-2} are given in table 4-35. The calculated interplanar spacings computed on this basis are compiled in table 4-37. The interplanar spacings of the fcc portion in the deposit are on average approximately 5 per cent greater than those of the fcc mono-structured deposit formed at 10 mA cm^{-2} from the same solution. The higher deposition rate caused by the higher current density possibly causes more deposit stress.

Deposits formed from Nickel-Iron Solution 4

Figure 4-19 shows the X-Ray Diffraction spectrum of the fcc structured nickel-iron deposit formed at 10 mA cm^{-2} from Solution *4*.

In figure 4-20 the X-Ray Diffraction spectra of bcc structured nickel-iron deposits prepared from Solution *4* at current densities of 30 and 60 mA cm^{-2} are shown.

Nickel-iron deposits obtained from Solution *4* using a current density of 10 mA cm^{-2} developed the fcc crystal structure. Deposits produced at higher current densities, i.e. 30 and 60 mA cm^{-2}, were found to be bcc structured. Raw data, i.e. $R_{\{hkl\}}$ and $I_{\{hkl\}}$, of the fcc and bcc structured deposits are set out in tables 4-38 and 4-39 respectively.

The distribution of the detected planes in the fcc and bcc lattice was calculated from the raw data, i.e. '$R_{\{hkl\}}$' the calculated statistical intensity of planes in a corresponding randomly orientated powdered specimen and '$I_{\{hkl\}}$', the measured intensity. The results of these calculations are shown in tables 4-40 and 4-41 respectively.

The planar distribution of the fcc and bcc reflections are shown as bar charts in figures 4-21 and 4-22 respectively.

As shown in figure 4-21, the fcc structured deposit formed at 10 mA cm^{-2} had a pronounced {111} texture, with about 91 per cent of the {111} planes aligned parallel to the surface. XRD spectra of the bcc structured deposits obtained with 30 and 60 mA cm^{-2} showed strong reflections from the {222} planes, see figure 4-20. The proportion of the {111} planes lying parallel to the surface was computed to amount to about 98 and 99 per cent of the total in the case of deposits formed at current densities of 30 and 60 mA cm^{-2} respectively (table 4-41, fig. 4-22).

Deposits formed in *Nickel-Iron Solution 4* generally had pronounced preferred orientation with {111} planes parallel to the surface in the case of both, fcc and bcc structured deposits. This {111} orientation in the texture of deposits was found to intensify with increasing current density.

The 2θ Bragg angle positions of the reflections measured from the fcc structured deposit, produced at a current density of 10 mA cm^{-2}, are given in table 4-42.

Bragg angles (2θ°) obtained from X-Ray Diffraction measurements of deposits produced with a current density of 30 and 60 mA cm^{-2} and having the bcc crystal lattice are compiled in table 4-43.

From the Bragg angle positions 2θ°, the interplanar spacing 'd' was calculated. These are compiled in tables 4-44 and 4-45 for fcc and bcc structured nickel-iron deposits respectively.

The interplanar spacings 'd' of the fcc structured deposit formed at 10 mA cm^{-2} from *Nickel-Iron Solution 4* are larger than those of deposits formed at the same current density from *Nickel-Iron Solutions 1* and *3*. In fcc nickel-iron deposits produced at 10 mA cm^{-2}, the average 'd'-spacings for deposits from Solutions *1* and *3* are 0.8 and 0.6 per cent, respectively, greater than that of the deposit from Solution *4*. This may result from the differences in elemental composition of the deposits. The interplanar spacings 'd' were increased in the same fashion as the iron content was found to have increased. Iron has a larger atomic radius than nickel, c.f. atomic radius [103]: Fe = 0.172 nm; Ni = 0.162 nm. Consequently, with the substitution of iron in the fcc nickel lattice there is an increased portion the interplanar spacings are wider.

4. 1. 5. 3 XRD-Studies on Bulk Ni-Zn Electrodeposits

The crystal structure of deposits, approximately 30 μm in thickness, obtained in the current density range of 10 to 60 mA cm^{-2} from *Nickel-Zinc Solution 8* was investigated by XRD analysis. The deposits were plated onto copper sheet substrates. Therefore the X-Ray Diffraction spectra contained reflections from the fcc lattice of copper in addition to reflections from the nickel-zinc deposits. An inherent feature of electrodeposited, in contrast to metallurgically produced alloys, is that the peaks are broadened and weaker reflections appear to merge into the background noise in the X-Ray Diffraction spectra [102]. Nickel-zinc deposits had generally weaker reflections compared to the nickel-iron alloy electrodeposits investigated in this work. Nevertheless the predominant phases could be identified. Yet detailed quantification of the individual reflections, as in the case of the nickel-iron deposits, appeared to be less feasible. An alternative approach was chosen for the characterization of the nickel-zinc electrodeposits: X-Ray Diffraction spectra of nickel-zinc deposits in their 'as-deposited' state and subsequent to heat treatment (260°C for 720 hours) were surveyed.

As-Deposited Condition

The results of structural investigations using X-Ray Diffraction given in table 4-46 clearly show two different types of structure depending upon the current density used to produce the deposits. A single phase complex bcc γ structure was obtained using current densities from 10 to 30 mA cm^{-2}. Figure 4-23a, 4-24a and 4-25a show typical X-Ray Diffraction patterns obtained from such deposits. In contrast a more complex structure containing both bcc γ- and fcc α-phases was obtained using current densities in the range 40 to 50 mA cm^{-2}. X-Ray Diffraction traces obtained from this type of deposit are shown in figures 4-26a and 4-27a. At 60 mA cm^{-2} the structure reverts back to a single complex bcc γ-phase (figure 4-28a). At the higher current densities, i.e. at 40 mA cm^{-2} and above, the deposits show a strong {110} preferred orientation as shown in figures 4-26a, 4-27a and 4-28a. Lattice parameter measurements of both γ- and α-phases are included in table 4-47.

Heat - Treated Condition

The results of the X-Ray Diffraction investigations after heat treatment are given in table 4-46. Subsequent to heat treatment there was a distinct sharpening of the peaks in many of the nickel-zinc deposits. In contrast to the as-plated deposits the majority of the deposits examined after heat treatment contained the tetragonal β_1-phase. For the coatings containing the single phase complex bcc γ-phase in the as-deposited condition, the apparent volume fraction of β_1-phase formed during heat treatment increased with increasing nickel content. In the specimen deposited at 10 mA cm^{-2} with a nickel content of 45.8 mass per cent the complex bcc γ-phase transformed, during heat treatment, almost completely to the tetragonal β_1-phase (figure 4-23b). Specimens deposited at 20 and 60 mA cm^{-2} containing 27.5 and 24.5 mass per cent nickel, respectively, showed only minimal transformation of the complex bcc γ-phase to β_1-phase during heat treatment (figures 4-24b and 4-28b), whilst that deposited at 30 mA cm^{-2} and containing 21.9 mass per cent nickel did not show any transformation to β_1-phase after heat treatment (figure 4-25b).

For the more complex structures containing both bcc γ- and fcc α-phases in the as-deposited condition there was evidence of transformation of both the bcc γ- and fcc α-phases to the β_1-phase (figures 4-26b and 4-27b). The coating deposited at 50 mA cm^{-2} containing the higher nickel content, i.e. 52.4 mass per cent, had a higher apparent volume fraction of β_1-phase than the deposit formed at 40 mA cm^{-2} with lower nickel content, i.e. 39.3 mass per cent nickel.

A comparison of the lattice parameters of the γ-phase in the as-deposited and heat treated conditions is included in table 4-48.

Current Density: 10 mA cm^{-2}

In figure 4-23 a and b X-Ray Diffraction spectra of the nickel-zinc deposit formed from *Nickel-Zinc Solution 8* at 10 mA cm^{-2}, in their as-deposited and heat-treated condition respectively, are shown. Prior to heat-treatment, the bcc γ-phase was identified in addition to reflections from the copper substrate. In its recrystallized state, β_1-phase was additionally identified besides γ-phase and reflections from the copper substrate.

Current Density: 20 mA cm^{-2}

The XRD-spectra of the deposit produced at 20 mA cm^{-2} in *Nickel-Zinc Solution 8*, prior and subsequent to heat-treatment, are shown in figure 4-24a and b respectively. In the as-deposited state reflections from the bcc γ-phase and the copper substrate were identified. In the heat-treated condition β_1 was additionally identified besides γ-phase and reflections from the copper substrate.

Current Density: 30 mA cm^{-2}

Figures 4-25 a and b show the XRD-spectra of the deposit produced with 30 mA cm^{-2} from *Nickel-Zinc Solution 8* prior and subsequent to heat-treatment respectively. In both spectra reflections from the bcc γ-phase and the copper substrate were identified. Spectra differed insofar that in the heat-treated condition peaks from the γ-phase were more distinct than in the as-deposited state. Furthermore weaker reflections that were not identified in the as-deposited state were found subsequent to heat-treatment.

Current Density: 40 mA cm^{-2}

Figures 4-26 a and b show the XRD-spectra of the deposit produced at 40 mA cm^{-2} from *Nickel-Zinc Solution 8* prior and subsequent to heat-treatment respectively. In the as-deposited state reflections from the bcc γ-phase, fcc α-phase and the copper substrate were identified. In the heat-treated condition β_1 was additionally identified besides bcc γ- and fcc α-phase and reflections from the copper substrate.

Current Density: 50 mA cm^{-2}

In figure 4-27 a and b X-Ray Diffraction spectra of the nickel-zinc deposit formed from *Nickel-Zinc Solution 8* with 50 mA cm^{-2} in their as-deposited and heat-treated condition respectively, are shown. Prior to heat-treatment, nickel-zinc bcc γ- and fcc α-phases were identified besides reflections from the copper substrate. Subsequent to heat-treatment, tetragonal fcc β_1-phase was additionally identified besides fcc α- and bcc γ-phase and reflections from the copper substrate.

Current Density: 60 mA cm^{-2}

Figures 4-28 a and b show the XRD-spectra of the deposit produced at 60 mA cm^{-2} from *Nickel-Zinc Solution 8* prior and subsequent to heat-treatment, respectively. In the as-deposited state reflections from the bcc γ-phase and the copper substrate were identified. In the heat-treated condition β_1 was additionally identified in addition to bcc γ-phase and reflections from the copper substrate.

4. 1. 6 Compositionally Modulated NiFe Deposits

Multilayered compositionally modulated nickel-iron electrodeposits consisting of ten individual layers obtained by step-pulsed current cycles were investigated. Quantitative Surface Depth Profile Analysis (QSDPA) were obtained by Glow Discharge Optical Emission Spectroscopy (GDOES) and line-scanning of cross-sectioned specimens was performed through Energy Dispersive X-ray (EDX) analysis. Nickel-iron multilayers were identical for both techniques, but sample preparation for Scanning Electron Microscopy (SEM) required a protective copper electrodeposit and cross-sectioning, whereas for GDOES no such sample preparation was needed, since the surface was sputtered off inwards.

4. 1. 6. 1 SEM Study of NiFe Multilayered Deposit

Figure 4-29a and b show the secondary electron image (SEI) and the backscattered image (BSI) respectively, of the cross-sectioned nickel-iron multilayered deposit. In the SEI mode of the SEM information is obtained regarding surface topography and material contrast. In figure 4-29a the layers produced at the higher current density, i.e. iron rich appear darker than those produced at a lower current density, the copper substrate and copper electrodeposit can be seen. The backscattered image, figure 4-29b, gives atomic number contrast. The iron richer layers appear darker, since iron has a lower atomic number than nickel and copper respectively. A further backscattered image of the same multilayered specimen is shown in figure 4-30, where additionally energy dispersive X-ray line-scans of the elements involved, i.e. nickel, iron and copper, are identified.

In figures 4-29a, 4-29b and 4-30 individual layers are not entirely uniform. The first layer, deposited with low current density, marked as layer '2' in figure 4-29b, appears having been plated iron-richer in its initial state. This is indicative for an iron rich diffusion layer at the beginning of this low current density step, which resulted in an increased iron content in the deposited alloy. In the course of further deposition equilibrium conditions were stabilized, with respect to mass transfer and diffusion control, which resulted in the following layers becoming more uniform.

4. 1. 6. 2 GDOES Study of NiFe Multilayered Deposit

A depth profile by GDOES is depicted in figure 4-31, generated by stepped pulse current from a nickel-iron electrodeposit consisting of ten single layers of alternating fcc and bcc crystal structure. It can be seen that the resolution deteriorates with depth. As the depth profiling is set by sputtering, the bottom of the sputtering crater (about 4 mm in diameter) advances through the deposit, expositing various depth of a layer, or even more than one single layer, at a time. The topography of the surface changes during the course of the sputtering as it develops a new micro-topography. Thus compositions are obtained from areas at distances different from the original surface at any instant. Such averaging effects add to the rounding of composition profiles as exemplified in figure 4-31. The steady loss of resolution with sputtering depth is due to the spatially varying rates of sputtering. This is clearly indicated by the copper composition detected, which in figure 4-31 appears to gradually increase from about 13 to 27 μm. In fact, however, the surface of the initial copper cathode had a 0.25 μm finish.

4. 2 Depth Profiles of Thin Electrodeposits

Thin deposits discussed in this section were produced in *Nickel-Iron Solution 4* and *Nickel-Zinc Solution 8* described in tables 3-1 and 3-2 at current densities of 10 and 60 mA cm^{-2}, respectively. Depth profiles were obtained via GDOES.

4. 2. 1 Depth Profiles of NiFe Electrodeposits on Copper Substrates

In figures 4-32 and 4-33 the depth profiles of nickel-iron deposits, produced at 10 and 60 mA cm^{-2} respectively onto copper, are set out. These indicate that there is no significant compositional gradation within the electrodeposit's initial nucleation site at the deposit/substrate interface to the remainder of the deposit. The gradual increase of the copper concentration and corresponding decrease in nickel and iron concentration is possibly due to the relatively large surface roughness, i.e. 0.25 μm finish of the unplated copper substrate, in comparison to the thickness of the nickel-iron electrodeposit, i.e. 0.05 μm. Figures 4-32 and 4-33 show that deposits have a higher iron than nickel content, but that the iron to nickel ratio is larger in the deposit produced with the higher current density (fig. 4-33).

4. 2. 2 Depth Profiles of NiZn Electrodeposits on Copper Substrates

Depth profiles of nickel-zinc electrodeposits, plated at 10 and 60 mA cm^{-2} on copper substrates, are shown in figures 4-34 and 4-35 respectively. No compositional gradation is evident at the initial nucleation site, i.e. interface deposit/substrate, in comparison to within the bulk of the nickel-zinc electrodeposit. The gradual transition of low copper and high nickel-zinc to high and low concentrations respectively, with increasing sputter depth is likely to result from the relatively low deposit thickness compared with the surface finish. Nickel-zinc deposits formed at 10 and 60 mA cm^{-2} are zinc-rich, with the zinc-nickel ratio being somewhat higher in the deposit produced with the higher current density (fig. 4-35).

4. 2. 3 Depth Profiles of NiZn Electrodeposits on Steel Substrates

As in the previous depth profiles of alloy deposits on copper, in the nickel-zinc deposits on steel the interface, nickel-zinc deposit/steel substrate, was not clearly resolved due to the deposit thickness being only one fifth of the steel substrate's surface finish prior to plating. In contrast to the electrodeposition of nickel-zinc onto copper, the electrocrystallization onto a steel substrate resulted in compositional variation of the alloy at the interface steel substrate/deposit compared with the subsequently deposited alloy of relatively uniform composition. In figures 4-36 and 4-37 the depth profiles of nickel-zinc deposits, electrocrystallized onto steel with 10 and 60 mA cm^{-2} respectively, are set out. Both depth profiles indicate that the nickel content is higher in the initial electrocrystallized deposit at the deposit/steel substrate interface in comparison with the subsequently deposited alloy. The depth profile obtained from the nickel-zinc alloy plated at 10 mA cm^{-2} shows this tendency to be particularly pronounced, with the nickel content being three times as high as the zinc content at the initial nucleation stage onto the steel substrate, but in the further course of the electrocrystallization as nickel-zinc alloy grows upon itself, the nickel content is about two thirds of the zinc content. In the nickel-zinc electrodeposit obtained at 60 mA cm^{-2} on steel (fig. 4-37) compositional variation within the deposit are also observed but not as pronounced as in figure 4-36. Again the nickel content was higher than the zinc content in the initial nucleation stage at the interface alloy deposit/steel substrate, but the zinc content increased in the course of deposit formation to become higher than the nickel content. Figures 4-36 and 4-37 indicate, that the composition of the deposited alloy is dependent upon the substrate material since electrodeposition onto steel results in nickel-rich deposit, whereas in the further course of electrodeposition, once nickel-zinc is being plated onto itself, the composition becomes zinc-rich and then remains relatively uniform.

4. 3 Investigations on the TEM

Microstructural observations were made on the Transmission Electron Microscope (TEM) generating bright/dark field images. Structural investigations were obtained by Selected Area Diffraction Patterns (SADP), compositional information was obtained by Energy Dispersive X-ray Analysis (EDX) using the TEM in its Scanning Transmission Electron Microscopy (STEM) mode. Quantitative results were calculated using the PMTHIN software (EDAX).

In this section the microstructural observations of the cross-sectioned electrodeposits obtained with the TEM are set out. Micrographs were taken in the form of dark and/or bright field images. Compositional results obtained using the TEM in its STEM mode are given as well as structural information obtained through SADP.

4. 3. 1 Nickel-Iron Electrodeposits

Nickel-iron electrodeposits deposited at 10 and 60 mA cm^{-2} had fcc and bcc crystal structures respectively. The fcc lattice structure of copper substrates extended into nickel-iron deposits produced at 10 mA cm^{-2}. In contrast nickel-iron deposits produced at 60 mA cm^{-2} on copper substrates had bcc structures.

4. 3. 1. 1 Single-layered NiFe fcc Electrodeposits on Copper Substrates

Microstructural Observations

Figure 4-38 shows a bright/dark field pair of a nickel-iron electrodeposit, produced at 10 mA cm^{-2}, on a copper substrate and the copper overplate. The nickel-iron electrodeposit has a columnar structure made up of individual banded grains. The bright field image (fig. 4-38a) reveals that grains appear to grow perpendicular to the substrate/coating interface, with the twin bands growing parallel to the substrate surface from the nucleation site at the copper substrate/electrodeposit interface. Some of the individual grains appear to have become wider as they grew out from the interface at the

expense of other grains. It cannot be taken for granted, that the current field lines were one hundred per cent perpendicular to the cathode surface during electrodeposition, thus explaining a slight deviation of the growth from normal. Additionally the cross-section of the specimen might not have been prepared exactly perpendicular to the electrodeposit's growth direction, which may have led to grains appearing due to the effect of sectioning.

Figures 4-39a and b show montages of bright fields and the corresponding dark fields, respectively, starting at the copper substrate, going across the cross-section of the fcc structured nickel-iron electrodeposit to the copper overplate. For the generation of the dark fields the <111> direction was used. Thus only grains with the <111> growth direction perpendicular to the substrate surface appear bright. The electrodeposit seems finer grained near to the nucleation site, as compared with that in the bulk deposit, due to the competitive growth of favoured grains which resulted in them growing broader and longer at the expense of less favoured grains. At the copper substrate/fcc deposit interface, the diameter of the grain was approximately 25 nm. In the mid-position of the deposit's cross-section the average grain diameter was approximately 50 nm, and increased further to about 120 nm at about 2 μm deposit thickness, i.e. interface deposit/copper overplate. Again the electrodeposit was characterized by twins within the grains.

Figure 4-40 shows the interface of a copper substrate and the nickel-iron electrodeposit produced at 10 mA cm^{-2}. The dark field (fig. 4-40b) was produced with the <111> direction, pointed at in SADP(III) (top right, fig. 4-40). Thus only grains having the <111> growth direction parallel to an imagined line between that spot and the zero-order spot allowed transmission of the beam and therefore to appear as a bright image. A characteristic feature of the nickel-iron electrodeposits was the occurrence of twins. These twins also manifest themselves as an array of spots between the zero-order spot and the spot corresponding to the reflection from the <111> direction in the selected area diffraction patterns. Diffraction patterns taken in adjacent areas either side of the coating/substrate interface (fig. 4-40 SADP(I), fig. 4-40 SADP(II)), show parallel growth direction, indicative of a degree of local epitaxy. The slightly darker areas in the

interfacial region seen in the bright field (fig. 4-40a) are evidence of a higher dislocation density as compared to that in the remaining areas of the deposit. This increase in dislocation density is probably due to lattice mismatch between substrate and deposit. The corresponding dark field (fig. 4-40b) indicates that the deposit appears to be a continuation of growth of grains within the copper substrate.

The bright/dark field images of the fcc-structured nickel-iron electrodeposit nucleated on a copper substrate are shown in figure 4-41a and b, respectively, along with a SADP of the coating. Twins are evident as twin spots in the SADP, and as sub-grain boundaries in the columnar grains in the micrographs. In the dark field, grains with <111> directional growth are highlighted, the alternate dark and light contrast of the twinned grains indicates a degree of distortion within the columnar grains.

In figure 4-42 a bright/dark field pair of a local nucleation site can be seen. Continuation of grain boundaries of the copper substrate into the twinned fcc nickel-iron deposit are visible. The twin boundaries are parallel to the local substrate.

Figure 4-43 shows a bright field of the copper substrate/nickel-iron electrodeposit interface together with corresponding selected area diffraction patterns taken in the copper substrate (I), at the interface copper substrate/nickel-iron electrodeposit (II), and in the well developed fcc deposit (III). Continuation of the structure of the copper substrate into the nickel-iron deposit, i.e. epitaxy, is indicated in figure 4-43 (SADP(I) and SADP(II) taken from the copper substrate and in the interface, respectively). The <111> spots corresponding to the <111> growth direction of SADP(I) and (II) align perfectly, hence the {111} planes of the fcc nickel-iron electrodeposit continue to grow on the {111} planes of the copper substrate perpendicular to the substrate surface. The <111> growth direction present in the copper substrate continues into the fcc nickel-iron electrodeposit, as can be seen from SADP(II), where the single diffraction spots from the copper substrate lie in the same direction as the spots from the fcc nickel-iron electrodeposit. The structural transition on going from the copper substrate to the electrodeposit is indicated in the SADP(II) by the single spots from the copper substrate transforming into the twin spots characteristic of the fcc structured nickel-iron

electrodeposit. The 'arcing' of the twin spots seen in SADP(III) indicates that the angle between grains having the major <111> growth direction increases as the coating develops.

Epitaxial growth of the fcc nickel-iron electrodeposit on the copper substrate is further exemplified in figure 4-44. Again the perfect alignment of the <111> spots in the selected area diffraction patterns from the copper substrate and <111> twin spots from the initially nucleated fcc nickel-iron deposit gives strong indication of epitaxy. In the well developed fcc nickel-iron electrodeposit the angle between grains showing the major growth direction deviates increasingly.

In figure 4-45 a bright/dark field pair of the bulk deposit and the deposit/copper overplate interface together with the selected area diffraction pattern used to generate the dark field image is shown. The dark field indicates that grains with the <111> growth direction increase in diameter, which stifles grains with less favourable growth directions. As shown in figure 4-42, the growth direction is always almost perpendicular to the local substrate surface. When the substrate surface is uneven the growth directions of grains, nucleated in localized regions, deviate from area to area of the deposit as growth proceeds. In the selected area diffraction pattern (fig. 4-45c) the 'arcing' observed reflects the greater or lesser variations in growth direction in the different regions of the coating.

Further indication of slight deviation from the major growth direction in the case of some grains is shown in figure 4-46. It shows a bright/dark field pair and the selected area diffraction pattern near to the interface of the nickel-iron and the copper overplate. The bright field micrograph shows grains which grow perpendicular to the predominant growth direction, as indicated by twins, and are thus parallel to the copper surface. In the dark field image, grains that appear bright deviate slightly from the predominant growth direction perpendicular to the copper surface, see figure 4-46b. In figure 4-46, the detected diffraction spot (<111>, see fig. 4-46c) indicates that the growth direction is not parallel to the general growth direction of the deposit, see fig. 4-46a. The <111>

spot pointed at in figure 4-46c aligns with the slightly inclined growth direction of the twinned grain, that appears bright in the dark field micrograph.

Compositional Analysis

Compositional investigations were done using the TEM in its STEM mode utilizing the PMTHIN software (EDAX). Results obtained using a spot size of 5 nm going across the breadth of the nickel-iron electrodeposit showed that the elemental composition of the nickel-iron electrodeposit remained largely unchanged. The elemental composition of the nickel-iron deposit in relation to increasing distance from the copper substrate/deposit interface are set out in table 4-49 which indicates an average composition of about 63 mass per cent iron and 37 mass per cent nickel.

4. 3. 1. 2 Single-layered NiFe bcc Electrodeposits on Copper Substrates

Microstructural Observations

Figure 4-47 shows a cross-section of a bcc structured nickel-iron deposit obtained at 60 mA cm^{-2} on a copper substrate and overplated with copper. At the substrate/deposit interface the grain size of the coating was much finer than in the bulk of the deposit. In the bulk of the deposit selected grains grow at the expense of less favoured ones. There is an indication that the copper substrate/bcc nickel-iron electrodeposit interface is smoother than the deposit's outer surface.

Figure 4-48 shows a montage of bright fields across the bcc structure of a nickel-iron electrodeposit on a copper substrate and overplated with copper. At the interfacial nucleation sites the deposit appears to be fine grained, and the microstructure formed in this region is indicative of a high dislocation density, possibly due to the local lattice mismatch between the fcc copper substrate and the bcc nickel-iron electrodeposit. The dislocation density decreases with the growth of the deposit, as indicated by decreasing image contrast. As growth proceeds the growth direction of larger grains, relative to

that for smaller grains, deviates increasingly from the perpendicular. This process results in an increase in surface roughness of the deposit's outer surface.

A montage of bright fields along the bcc structured nickel-iron electrodeposit/fcc copper substrate interface is shown in figure 4-49. During the initial stage of deposition the grains formed are very fine, and the micrographs show further evidence of high dislocation density.

Further indication of fine grained morphology at the nucleation site can be seen in the bright/dark field micrographs in figure 4-50 where grains that appear light in the dark field image have <110> growth direction.

As the electrodeposit grows, the extending cathode surface is becoming increasingly rough and its grain structure becomes coarser. Thus figure 4-51 shows an uneven copper overplate/thick nickel-iron electrodeposit interface.

A bright/dark field pair of images showing a nickel-iron electrodeposit in its advanced stage of growth is shown in figure 4-52. In the dark field (fig. 4-52b), grains having the <211> growth direction appear bright.

Figure 4-53 exemplifies another bright/dark field pair of the surface of the bcc structured nickel-iron electrodeposit. Grains appearing bright in the dark field (figure 4-53b) have <211> growth direction.

Compositional Analysis

Compositional investigations done with the TEM in its STEM mode utilizing the PMTHIN software (EDAX), using a spot size of 5 nm across the breadth of the nickel-iron electrodeposit produced at 60 mA cm^{-2} showed it to be homogeneous with an average composition of about 71 mass per cent iron and 29 mass per cent nickel, see table 4-50.

4. 3. 1. 3 Double-layered NiFe Electrodeposits on Copper Substrates

So far single layered nickel-iron electrodeposits produced at 10 and 60 mA cm^{-2} resulting in fcc and bcc lattice structure respectively, have been considered. These coatings had been deposited on a polished copper substrate having a fcc lattice.

Multilayered deposits have gained increasing interest in the past. The deviation of their properties in comparison to conventional single layered deposits of similar nominal composition, is most likely due to the higher number of nucleation interfaces in multilayers than in single layered deposits. The study of electrodeposits having different 're-nucleation' interfaces therefore appeared to be of potential interest in relation to a better understanding of multilayers.

With the intention of studying the initial nucleation at more than one type of interface, i.e. copper/nickel-iron deposit, double layered deposits of the fcc and bcc nickel-iron alloys were formed. Thus bcc nickel-iron was nucleated on fcc nickel-iron, which in turn had been nucleated on fcc copper. Fcc-nickel-iron was nucleated on bcc-nickel-iron previously plated on a polished copper substrate. In each case the first electrodeposited layer was thick enough to ensure that no epitaxial effects from the copper substrate were present which might affect the second alloy layer deposited. Therefore these specimen had two additional interfaces not previously studied (i) the bcc- re-nucleated on fcc nickel-iron, (ii) fcc- re-nucleated on bcc nickel-iron electrodeposit.

4. 3. 1. 3. 1 Bcc NiFe Nucleated on fcc NiFe Electrodeposits

Microstructural Observations

Figure 4-54a and b show the montages of bright and dark field images respectively, from a copper substrate plated with a duplex coating, bcc on fcc nickel-iron, with the entire overplated with copper. The duplex layer consisted of a 2 μm thick layer of 'bcc structured' nickel-iron deposited at 60 mA cm^{-2} on top of a 0.5 μm thick 'fcc structured'

layer deposited at 10 mA cm^{-2}. The bright field montage (fig. 4-54a) indicates, that the layer of fcc-structured nickel-iron is similar in terms of grains size and morphology, to that of the single layered fcc structure in the early stages, i.e. fine columnar grains with twins, see figs. 4-41a, 4-42a, 4-43a. Grains of the bcc-phase seem to have grown on top of the existing fcc columnar grains, with a grain size similar to the fcc-phase. In this case, unlike the bcc nickel-iron deposited on copper, which showed a very well defined interface, see figs. 4-47, 4-48, 4-49, 4-50, the bcc/fcc nickel-iron interface is less defined. The interfacial nucleation site of the bcc-phase on copper resulted in a fine grained structure accompanied by a high dislocation density. In comparison nucleating the bcc- on the fcc structured nickel-iron deposit showed a coarser grain size and lower dislocation density at the interface. The dark field micrographs (fig. 4-54b) were produced from fcc <111> and bcc <110> spots, which are both parallel to the dominant growth directions of the columnar grains. The grain size of the bcc-structured layer is coarser grained than the fcc-nickel-iron substrate initially deposited.

The bright/dark field pair in figure 4-55a and b respectively, typifies the interface of a substrate with a well developed fcc nickel-iron structure and the initial nucleation of the bcc nickel-iron electrodeposit.

A montage of bright field images along the interfacial nucleation site of the bcc nickel-iron on the well developed fcc nickel-iron electrodeposit is also shown in figure 4-56. The bcc nickel-iron appears to have nucleated on the fcc nickel-iron with a similar grain size and morphology to that of the latter. The columnar grain structure of the fcc-structured nickel-iron deposit was similar to the respective single layered deposits nucleated on copper, see figures 4-45, 4-46. Figure 4-54 shows that the copper/fcc nickel-iron alloy is much better defined than the corresponding fcc nickel-iron/bcc nickel-iron interface. In comparison to the polished copper/single layered bcc-phase deposit interface, which was characterized by a fine grain size and high dislocation density and hence very distinct, the nucleation sites at the bcc-phase/fcc nickel-iron electrodeposit interfaces were less clear. The grains appeared to be coarser and the dislocation density lower when nucleating the bcc structure on a fcc structured nickel-iron deposit as compared to its nucleation on polished copper.

Comparing the nucleation of the bcc-phase on a less developed 0.5 μm thick (fig. 4-54) to the well developed 2 μm thick fcc nickel-iron deposit (fig. 4-56, 4-57) shows the transition of the fcc into the bcc deposit appears to be smoother, i.e. a lower dislocation density and coarse grains of the nucleated bcc-phase, on the latter. Figures 4-57a and b are montages of bright and dark field pairs showing the copper substrate/fcc nickel-iron interface and the nucleation site of the bcc nickel-iron deposited onto the approximately 2 μm thick fcc nickel-iron. The dark field image (fig. 4-57b) covering the fcc and the bcc phase of the nickel-iron deposit was generated from parallel fcc <111> and bcc <110> reflections. The approximate d-spacing calculated from the XRD results are 0.2066 nm between fcc {111} planes and 0.2022 nm between bcc {110} planes, see section 4.4.

Figures 4-54, 4-55, 4-56, and 4-57 indicate that the transition from a fcc to a bcc structured nickel-iron electrodeposit is characterized by continuation of the fcc nickel-iron substrate grain structure accompanied by a lower dislocation density, whereas nucleation on polished copper gives rise to a comparatively high dislocation density. There appears to be a greater mismatch between bcc nickel-iron and copper, than between bcc and fcc nickel-iron.

Compositional Analyses

Quantitative investigations showed that uniform composition throughout the nickel-iron coating is obtained in the cases of both the fcc- and the bcc phased deposits. Therefore it was assumed that there is no significant compositional gradient within the individual layers of the double layered electrodeposits. Using the cross-section of the double layered deposit consisting of 2 μm fcc and 2 μm bcc nickel-iron electrocrystallized on top, three spot analyses were made in each layer. The results of these analyses are given in table 4-51. The fcc structured nickel-iron deposit has an average composition of approximately 40 mass per cent nickel and 60 mass per cent iron, the bcc structure is made up of about 26 mass per cent nickel and 74 mass per cent iron.

4. 3. 1. 3. 2 Fcc NiFe Nucleated on bcc NiFe Electrodeposits

Microstructural Observations

A cross-section of a copper substrate plated with a duplex coating, fcc on bcc nickel-iron, and overplated with copper is shown in figure 4-58. The duplex layer consisted of a 2 μm thick layer of 'fcc structured' nickel-iron deposited at 10 mA cm^{-2} on top of a 0.5 μm thick 'bcc structured' layer deposited at 60 mA cm^{-2}.

Figure 4-59 shows the characteristics of the individual nickel-iron layers in the duplex alloy layer. In this montage of bright fields the nucleation site of (i) the bcc structured nickel-iron on the copper substrate, and (ii) that of the fcc on the bcc structured nickel-iron are shown. The fcc phase is nucleated with a fine grained morphology with high dislocation density on top of the uneven surface of the bcc layer. In the competition for growth between the initial grains nucleated selected grains are favoured and there is a transition from the very fine grain size in the early stage to a coarser columnar structure with the presence of twins within the larger grains. Since the growth direction of nucleating grains is normal to the local surface, as exemplified in figures 4-42, 4-43, the growth direction of individual grains deviates from perpendicular to the copper substrate in this case, possibly as a result of the roughness of the underlying bcc structured layer.

Different areas along the interface of the well developed, 2 μm thick, bcc phase and the nucleation site of the fcc phased nickel-iron electrodeposit grown on top are shown in figures 4-60a, b and 4-61. Comparing figures 4-59 and 4-60a, the surface of the bcc structured nickel-iron coating appears to be slightly more uneven in the latter. This is likely to have resulted from the greater deposit thickness since roughness increases with deposit thickness. Since grain growth is perpendicular to the 'local' substrate, the increased surface roughness causes a higher degree of deviation in grains of the fcc-structure during competitive growth (fig. 4-60a, b) than in the case of grains nucleating on the smoother surface of the underlying bcc-phase (fig. 4-59). In contrast nucleation on a polished copper surface, as exemplified in figures 4-38 to 4-43, led to a high degree

of parallel ordering of the twinned grains and low dislocation density at the nucleation sites.

Compositional Analyses

Quantitative investigations showed a uniformity of composition within the individual layers of double layered nickel-iron coatings however formed. Therefore it was assumed that there is no significant compositional gradient within the individual layers of the double layers.

Using the cross-section of the double layered electrodeposit, consisting of 2 μm fcc electrocrystallized on 2 μm bcc nickel-iron deposit, three spot analyses were made in each single layer. The averaged results of the STEM analyses are shown in table 4-52. The bcc structure has the composition of about 26 mass per cent nickel and 74 mass per cent iron, the nickel-iron deposit with the fcc lattice consists of approximately 37 per cent nickel and 63 mass per cent iron.

4. 3. 2 Nickel-Zinc Electrodeposits

The γ-phases of nickel-zinc electrodeposits produced at 10 and 60 mA cm^{-2} both had the bcc structure. To investigate the nucleation and growth process on different substrates they were plated onto copper as well as mild steel substrates. The intention was to nucleate the bcc structured nickel-zinc alloys on a fcc structured substrate (copper) and on a substrate with bcc structure (mild steel).

4. 3. 2. 1 Single-layered NiZn Electrodeposits on Copper Substrates

4. 3. 2. 1. 1 Nickel-Zinc deposited with 10 mA cm^{-2}

Microstructural Observations

A cross-section of the columnar nickel-zinc coating electrodeposited at 10 mA cm^{-2} on a copper substrate including the copper overplate is shown in figure 4-62. The bright field image indicates a fine grained morphology at the interfacial nucleation site. Near the surface, the well developed nickel-zinc deposit consists of relatively large grains which make the boundary to the copper overplate very rough.

Figure 4-63 is a further example showing competitive grain growth. The initially fine grained structure develops into a coarser, columnar grained morphology.

In figures 4-64 and 4-65 the respective morphologies of the nucleation sites and the boundary of the well developed nickel-zinc deposit with the copper overplate are compared. On the polished copper the nickel-zinc nucleates with a comparatively fine grain size with a columnar morphology (fig. 4-64). On nucleation the average diameter of these columnar grains is around 0.1 μm. The grains become increasingly coarse until at the outer surface of the well developed coating (fig. 4-65) they reach diameters up to 0.5 μm.

Compositional Analyses

Compositional investigations were done using the TEM in its STEM mode utilizing the PMTHIN software (EDAX). Results obtained, using a spot size of 5 nm transversing the nickel-zinc electrodeposit, showed that the nickel-zinc electrodeposit was of relatively uniform composition when nucleated on copper. The elemental compositions of the nickel-zinc coating deposited at a current density of 10 mA cm^{-2} at increasing distances from the copper substrate/deposit interface are set out in table 4-53. The deposit composition is relatively homogenous with an average composition of approximately 32 mass per cent nickel and 68 mass per cent zinc.

4. 3. 2. 1. 2 Nickel-Zinc deposited with 60 mA cm^{-2}

Microstructural Observations

Figures 4-66a and b show a bright and a dark field image, respectively, of a cross-sectioned nickel-zinc alloy deposited at 60 mA cm^{-2} on a copper substrate. Initially the grain structure was fine but became increasingly coarse due to grain growth. Grains that appear bright in the dark field image (fig. 4-66b) have the <110> growth direction.

Competitive grain growth can be observed in figure 4-67 where again bright grains in the dark field image have <110> growth direction.

Figures 4-68 and 4-69 also show the nucleation site of the nickel-zinc coating electrodeposited at 60 mA cm^{-2} as bright and dark field pairs, a and b, respectively. In the dark field micrograph in figure 4-68b grains having the <110> growth direction appear bright, whereas grains with the <211> growth direction appear bright in figure 4-69b.

Compositional Analyses

The elemental compositions of the nickel-zinc coating deposited with a current density of 60 mA cm^{-2} at increasing distances from the copper substrate/deposit interface are set out in table 4-54. The compositions of individually analyzed spots in the nickel-zinc

deposit produced with 60 mA cm^{-2} appear to deviate to a larger extend as compared to the nickel-zinc deposit plated with 10 mA cm^{-2}.

A further set of spot analyses was made in different individual grains but at similar distances from the interface. It was found, that the compositional variation also occurs from grain to grain. Results obtained in these analyses are given in table 4-55.

4. 3. 2. 2 Single-layered NiZn Electrodeposits on Steel Substrates

Microstructural Observations

Cross-sections of nickel-zinc deposited at 10 mA cm^{-2} on steel substrates showed columnar growth as in the case of deposition on copper substrates. In the TEM the interfacial nucleation sites in the nickel-zinc deposit were darker than the bulk of the deposit indicative for a higher dislocation density. In the initial stage of electrodeposition epitaxial growth was evident. Results of competitive grain growth, i.e. preferred growth of selected grains, were observed to have taken place in the course of electrodeposition.

Compositional Analyses

The quantitative analysis by STEM, using a spot size of 5 nm, transversing from the interfacial nucleation site into the nickel-zinc electrodeposit, revealed that there is a compositional gradient in the deposit nucleated on a steel substrate. The compositions measured are given in table 4-56 in relation to their distance from the interfacial nucleation site. In the case of a steel substrate the zinc content is apparently lower near the interfacial nucleation site than in the subsequently deposited nickel-zinc alloy.

In figure 4-70 the nickel and zinc content of the deposit versus distance from the interface copper substrate/deposit are given, i.e. results from table 4-56 are shown graphically. At the interface, the nickel concentration is higher than the zinc content. With increasing distance from the interface the nickel content increases, the zinc content decreases. At 15 nm deposit thickness the zinc content was higher than the nickel content.

4. 4 Structural Investigations using XRD

Deposits of nickel-iron and nickel-zinc were investigated. The substrate was copper for nickel-iron, and mild steel for nickel-zinc electrodeposits. In this section results are presented in the form of raw data, i.e. '$R_{\{hkl\}}$' and '$I_{\{hkl\}}$'. '$R_{\{hkl\}}$' is the theoretical intensity calculated for a powdered 'random' specimen without preferred orientation and having the same nominal composition as the corresponding coating. In the calculation of the '$R_{\{hkl\}}$' values allowance was made for the different amounts of absorption due to differences in the thickness of the deposits investigated. '$I_{\{hkl\}}$' is the experimentally measured intensity of the {hkl} reflection from the specimen investigated. On the basis of the raw data the actual distribution of the reflections from different planes in the specimens were determined. Thus the reflection from a particular plane could be found as a percentage of the sum of all the reflections from different planes. The interplanar spacings and the lattice parameters were calculated from the positions of the measured 2θ Bragg angles according to Bragg's law, $\lambda = 2d \sin \theta$.

4. 4. 1 Nickel-Iron Electrodeposits

X-Ray Diffraction analyses showed that the nickel-iron electrodeposits formed at 10 mA cm^{-2} had face centred cubic lattices. Deposits obtained at a current density of 60 mA cm^{-2} had body centred cubic crystal structures.

4. 4. 1. 1 Structure of the Copper Substrate

Nickel-iron coatings were plated onto copper disc substrates which were machined from rod material. In table 4-57 the raw data and the computed planar distribution in the copper disc substrate are set out. The distribution of planes detected in the copper rod substrate is graphically displayed in percentage terms in figure 4-71. X-Ray Diffraction studies on the copper substrate showed that the highest proportion of the five reflections related to the {200} and {111} planes, which is indicative of a mixed {100}/{111} texture. The {100} and {111} orientation possibly resulted from working of the copper rod from which the substrates had been machined.

The interplanar spacings 'd' and the lattice parameter 'a' were calculated from the positions of the 2θ Bragg angles, see table 4-58. The lattice parameter 'a' of the cubic fcc copper disc was determined to be 0.36175 nm from a Cohen-Wagner plot [91] (see fig. 4-72). In the literature the lattice parameter of copper is given as 0.36150 nm [88]. Thus the lattice parameter determined in this work was approximately 0.08 per cent higher than the accepted literature value.

4. 4. 1. 2 Nickel-Iron Electrodeposits with fcc Crystal Structure

The nickel-iron electrodeposits formed at a current density of 10 mA cm^{-2} had fcc structures. Raw data obtained from fcc structured nickel-iron electrodeposits having different thicknesses on copper substrates are given in table 4-59.

The actual texture of the fcc structured nickel-iron electrodeposits was calculated from the raw data set out in table 4-59. In table 4-60 the distribution of the planes is set out in terms of percentage, which are displayed as a column chart in figure 4-73.

In the single layered fcc nickel-iron electrodeposits on copper substrates the {111} and the {220} reflections only were detected in the thickness range between 0.3 and 3 μm. The proportion of {111} orientation was higher than that of the {220} in all deposits studied regardless of their thickness. Apart from one exception, the 2 μm thick specimen, the {111} reflection increased, whereas in contrast the {220} decreased with increasing coating thickness.

The Bragg angles (2θ) of fcc nickel-iron deposits of different thickness are given in table 4-61. The interplanar d-spacings were calculated from the '2θ' Bragg angles measured for coatings of different thickness. The interplanar spacing of the {111} and {220} planes were calculated according to Bragg's law, $\lambda = 2d \sin \theta$.

In table 4-62 the computed d-spacings of fcc structured nickel-iron electrodeposits of deposit thicknesses ranging from 0.3 to 3 µm are compiled. Figure 4-74 indicates that the interplanar spacing of the {111} planes decreases with increasing deposit thickness in the case of the fcc nickel-iron deposit. The d-spacing of the underlying copper disc substrate is 0.20886 nm. This indicates that in the initial stage of deposition, the structure of the copper substrate was taken over and the lattice mismatch between the wider copper substrate and fcc nickel-iron deposit was compensated through widened lattice in the initial stages of deposit formation. As the deposit grew the substrate's influence gradually became less until the deposit is put down with equilibrium lattice spacings.

4. 4. 1. 3 Nickel-Iron Electrodeposits with bcc Crystal Structure

Raw data obtained from bcc structured nickel-iron electrodeposits having different thicknesses on copper substrates are given in table 4-63. The texture of the samples was calculated from the raw data in terms of the planes present together with their relative predominance expressed as percentages for coatings of different thickness. The results of these calculations are given in table 4-64 and figure 4-75.

In the 0.4 µm thick bcc nickel-iron deposits only {110} reflections were observed during X-Ray Diffraction analysis. The proportions of {211} and {110} reflections increased and decreased respectively for deposits of increasing thickness up to one micron. As a general rule {222} reflections were detected, when the bcc nickel-iron deposit exceeded one µm in thickness which, apart from slight inconsistencies at 1.5 and 2 µm, increased until it was found to have become the major texture at a deposit thickness of 20 µm. Additionally negligible amounts of {200} reflections were found in the 20 µm thick sample.

In table 4-65 the Bragg angles measured for reflections at individual deposit thicknesses of the bcc nickel-iron on copper are compiled. Interplanar d-spacings for deposits calculated on the basis of positions of the Bragg angles are stated in table 4-66.

4. 4. 1. 4 Fcc Nickel-Iron Electrodeposits on Various Substrates

Double layered nickel-iron electrodeposits were studied by means of X-Ray Diffraction to investigate the influence of the underlying substrate upon the planar distribution of the respective surface deposits. In table 4-67 the raw data, $R_{\{hkl\}}$ and $I_{\{hkl\}}$ from a 0.5 µm thick fcc structured nickel-iron electrodeposit electrocrystallized on (i) a copper disc substrate, (ii) a 0.5 µm thick and (iii) a 2 µm thick bcc structured nickel-iron electrodeposit are set out. Using the raw data from table 4-67 as a basis the distribution of the planes detected was calculated in percentage terms (see table 4-68 and figure 4-76). The intensity of the {111} reflection of the 0.5 µm thick fcc nickel-iron deposit is lower when deposited on the 2µm thick bcc than on the 0.5 µm thick bcc nickel-iron deposit.

In the case of an underlying polished copper substrate the predominant texture of 0.5 µm thick fcc nickel-iron electrodeposit was {111} accompanied with a smaller amount of {220}. In contrast only {111} orientation was detected when fcc nickel-iron layers were deposited on either 0.5 or 2 µm thick bcc nickel-iron deposit.

In table 4-69 the raw data $R_{\{hkl\}}$ and $I_{\{hkl\}}$ for a 2 µm thick fcc structured nickel-iron deposit electrocrystallized on (i) a copper substrate, (ii) a 0.5 µm thick and (iii) a 2 µm thick bcc structured nickel-iron electrodeposit are set out. Using the raw data from table 4-69 as a basis the distribution of the planes detected was calculated in percentage terms (see table 4-70 and figure 4-77).

The 2 µm thick fcc nickel-iron electrodeposits had pronounced {111} textures regardless of the substrate material present. This texture was most pronounced when the fcc nickel-iron was deposited onto a 0.5 µm thick bcc structured nickel-iron electrodeposit and was found to be less pronounced when deposited on a polished copper substrate. When 2 µm thick fcc nickel-iron was deposited onto a 2 µm thick bcc structured nickel-iron deposit, the {111} texture was still present, but less dominant and accompanied by {200}, {220}, and {311} reflections.

Rocking Angle X-Ray Diffraction Analyses

Rocking angle X-Ray Diffraction analyses were made to determine the degree of deviation of the strongly preferred (111) orientation of the nickel-iron deposits from the fibre texture. Spectra of 'Ω-scans' of 2 μm thick fcc structured nickel-iron deposited on copper, 0.5 μm bcc nickel-iron and 2 μm nickel-iron are shown in figure 4-78.

The full width, at half height, of the {111} reflections was taken as a measure in determining the sharpness of the peaks. The 2 μm thick fcc structured nickel-iron deposit electrocrystallized onto 0.5 μm thick bcc nickel-iron had the strongest texture of the deposits studied. Thus the peak was judged sharpest, since the full width at half height was smallest. The green curve in figure 4-78 gives the rocking angle X-Ray Diffraction spectrum of the fcc structured 2 μm thick nickel-iron deposit plated onto 2 μm bcc structured nickel-iron. The full width at half height was larger than that of the deposit plated onto 0.5 μm bcc nickel-iron, but smaller than in the rocking angle Diffraction trace of the 2 μm thick fcc structured deposit plated onto copper (green curve in figure 4-78).

Rocking angle X-Ray Diffraction analyses of 2 μm thick fcc structured nickel-iron electrodeposits indicated that the development of a preferred orientation is dependant on the substrate. A thin 0.5 μm bcc structured nickel-iron deposit appears to be an ideal precondition for strongly textured fcc deposit growth. The fcc nickel-iron appears to show a less developed texture if electrocrystallized onto thicker (2 μm) bcc nickel-iron. The Rocking Angle X-Ray Diffraction spectrum of the fcc structured nickel-iron on polished copper substrate indicates, that polished copper is least favourable for {111} texture formation of the substrate materials investigated.

4. 4. 1. 5 Bcc Nickel-Iron Electrodeposits on Various Substrates

The planar distribution of the bcc nickel-iron electrodeposits with respect to the underlying substrates was studied. The substrates used with respect to the final coating studied, were (i) polished copper substrate, (ii) 0.5μm thick, and (iii) 2μm thick fcc structured nickel-iron electrodeposits. Outer layers of either 0.5 μm or 2 μm thick bcc structured nickel-iron were deposited onto the different substrates listed. Table 4-71 shows the raw data, $R_{\{hkl\}}$ and $I_{\{hkl\}}$ determined from the 0.5 μm thick bcc structured nickel-iron deposited on the substrates examined. In table 4-72 and figure 4-79 the distribution of detected reflections are presented.

The 0.5 μm thick bcc nickel-iron surface layer had a strong {211} texture when deposited on a polished copper substrate, when the only other reflection detected was the {110}. The relative proportions of {110} to {211} reflections found in the 0.5 μm thick outer bcc nickel-iron electrodeposit was found to depend upon the substrate as can be seen from figure 4-79. Thus the ratio of {110} to {211} texture was lowest for the polished copper substrate, and highest for the 2 μm fcc nickel-iron substrate, with the value of the ratio lying between the two for a 0.5 μm thick fcc nickel-iron substrate.

The results of the X-Ray Diffraction investigations of 2 μm thick bcc nickel-iron electrodeposits plated on a polished copper substrate, 0.5 μm and 2 μm thick fcc structured nickel-iron deposits are given in tables 4-73, 4-74 and figure 4-80.

The 2 μm thick bcc nickel iron electrodeposit was found to be mostly random orientated when deposited onto 2 μm fcc nickel-iron. Thus reflections from three planes were observed whose percentage intensities decreased in the order {222}>{211}>{110}. The most dominant reflecting planes for 2 μm bcc structured electrodeposits on all three substrates investigated were {211} and {222}. However the {211} plane was more prevalent than the {222} plane for the deposit on the copper substrate with the reverse being true for deposits on fcc nickel-iron substrates. Furthermore the ratio of the {222} to {211} was much greater in the case of the bcc nickel-iron formed on the thinner fcc nickel-iron substrate than that for the coating formed on the thicker fcc substrate.

Although the {110} orientation was present in the bcc nickel-iron deposits formed on all three substrates it was only present in significant amounts in the deposit formed on a 2 μm thick fcc nickel-iron substrate. The 2 μm thick bcc nickel-iron coating deposited onto a 0.5 μm thick fcc coating was found to have the highest proportion of {222} orientation of the samples compared in figure 4-73, along with {211} and {110}. The 2 μm thick nickel-iron nucleated onto 2 μm fcc nickel-iron had the {222}, {211}, and {110} orientations, with the {222} orientation having the highest proportion and {110} the lowest. The {110} component was the greatest in the coating with the best developed {111} texture in the substrate, i.e. the 2 μm thick fcc nickel-iron coating, see figure 4-73.

In addition 0.5, 2, and 10 μm thick bcc structured nickel-iron coatings were deposited on 2 μm thick fcc nickel-iron substrates for comparison purposes. Raw data, '$R_{\{hkl\}}$' and '$I_{\{hkl\}}$' are compiled in table 4-75 and the corresponding calculated planar distributions presented in table 4-76 and figure 4-81.

As indicated in table 4-76 and figure 4-81 the degree of {222} orientation increased with increasing deposit thickness when the bcc nickel-iron was deposited on a 2 μm fcc nickel-iron deposit. No {222} orientations were detectable in the 0.5 μm thick bcc nickel-iron deposit, but it was found to account for about 50 and 97 per cent in the 2 and 10 μm thick nickel-iron deposits respectively.

The measured 2θ Bragg angles for the 0.5, 2, and 10 μm thick bcc nickel-iron specimens, deposited on 2 μm fcc nickel-iron, are compiled in table 4-77. From the positions of the 2θ Bragg angles the interplanar d-spacings were calculated and are given in table 4-78.

4. 4. 2 Nickel-Zinc Electrodeposits

The γ-phase in nickel-zinc electrodeposits formed at both 10 and 60 mA cm^{-2} had bcc structures. Preliminary tests indicated that the major reflections from the bcc γ-phase nickel-zinc electrodeposits occurred at similar Bragg 2θ angle positions to reflections from the copper substrate, and were therefore difficult to identify. Further nickel-zinc coatings were therefore plated onto mild steel substrates.

Fifteen reflections were found in all the spectra obtained, four of which were second order reflections. Thus eleven 'real' reflections were recognizable. The main reflection was the {330}, individual peaks in the spectra were identified on the basis of the Bragg angles 2θ.

4. 4. 2. 1 Structure of the Mild Steel Substrate

Raw data relating to the mild steel substrate, together with the computed distribution of reflections, are compiled in table 4-79.

Reflections were found relating to five planes in the mild steel substrate. Their calculated distribution in percentage terms is shown in figure 4-82. The closest packed, {110} plane, was calculated to account for the highest proportion of the total reflections with regard to planar distribution, followed by the {310}, {211}, {222}, and {200}. Thus the results show that the mild steel substrate had a weak {110} texture.

The interplanar d-spacings and the lattice parameter 'a' were calculated from the measured Bragg angle positions, see table 4-80. The lattice parameter determined from a Cohen-Wagner [91] plot presented in figure 4-83 was found to be 0.28706 nm. In the literature [88] the lattice parameter of bcc iron was stated to be 0.28664 nm, the lattice parameter calculated in this work is about 0.15 per cent larger.

4. 4. 2. 2 Nickel-Zinc Electrodeposits, bcc γ-Phase, 10 mA cm^{-2}

In tables 4-81 and 4-82 the raw data from the X-Ray Diffraction analyses of nickel-zinc deposited at a current density of 10 mA cm^{-2} are given. For convenience, the calculated '$R_{\{hkl\}}$' values and the measured intensities, '$I_{\{hkl\}}$', are compiled in separate tables, 4-81 and 4-82, respectively. The '$R_{\{hkl\}}$' values were computed assuming a powdered specimen of the same nominal composition as the deposit, i.e. 31.5 mass per cent nickel and 68.5 mass per cent zinc, and allowing for the absorption variations due to the varying thicknesses of the deposits. The intensities '$I_{\{hkl\}}$' were measured.

In table 4-83 the per cent distribution of reflections from the nickel-zinc deposits produced at 10 mA cm^{-2} and having various thicknesses are compiled. Results are presented as bar chart in figure 4-84.

The {330} was the major reflection from the γ-phased nickel-zinc electrodeposit produced at 10 mA cm^{-2} with bcc crystal structure. In the 0.1 and 0.2 μm thick deposits it was the only reflection detected. On the other hand there is a possibility that other reflections were present in minor proportions but were not detected because the deposits were too thin, hence a lower X-ray intensity. However, the presence of the {330} reflection was found to decrease with increasing deposit thickness for thicknesses up to 10 μm, but was found to be very intense in the case of the 20 μm thick deposit. With the exception of the 10 μm thick deposit, the {330} reflection was the major reflection in all samples. The nickel-zinc coatings electrodeposited at 10 mA cm^{-2} all had a {110} texture apart from the 10 μm thick one. The proportion of the reflection due to the {222} plane increased steadily with increasing deposit thickness up to 10 μm and then dropped to a low value in the 20 μm thick deposit. The 10 μm thick sample was an exception, for it was the only one whose X-Ray Diffraction results were indicative for a dominant {111} texture, whereas the deposits with other thicknesses showed dominant {110} texture.

The occurrence of {552} reflection as a function of deposit thickness showed a maximum for thicknesses in the region of 0.5 to 1 μm where these reflections accounted for approximately a quarter of all reflections measured. With increasing deposit thickness above 1 μm the percentage proportion of the {552} reflection decreased. The {332} reflections were found in nickel-zinc deposits with thicknesses above 2 μm. Its contribution as a proportion of the total reflections was minor, and was greatest in the case of the 10 μm thick sample, but even there contributed only about three per cent of the total reflections detected. Only the 10 and 20 μm thick deposits produced reflections from the {600} planes. At the most the {600} reflection only contributed 20 to 14 per cent of the total reflections in the 10 and 20 μm thick deposits, respectively.

Positions of reflections in terms of Bragg angles are set out in table 4-84. Interplanar d-spacings were determined from the measured Bragg angle positions. In table 4-85, the interplanar spacing measured at individual deposit thicknesses is set out. There is evidence that the interplanar spacings are increased with deposit thickness, see figure 4-86.

4. 4. 2. 3 Nickel-Zinc Electrodeposits, bcc γ-Phase, 60 mA cm^{-2}

Raw data from X-Ray Diffraction studies of nickel-zinc deposited on mild steel substrates at 60 mA cm^{-2} and having various thicknesses are being discussed in this section. Calculated $R_{\{hkl\}}$ and measured intensities $I_{\{hkl\}}$ are compiled in two separate tables 4-86 and 4-87 respectively.

The distribution in per cent of the individual reflections relative to the total reflections were computed from the raw data given in tables 4-86 and 4-87. The results of these calculations are presented in table 4-88 and figure 4-85.

In the 0.2, 0.5, 1 and 2 μm thick nickel-zinc deposits formed at 60 mA cm^{-2} the {222} reflection was found, with the highest proportion of about six per cent occurring in the 0.2 μm thick coating. With increasing thickness the proportion of the {222} increased, with the exception of the 1 μm thick deposit. Nevertheless, it was not detected in the 10 and 20 μm thick deposits. The predominant reflections detected in all nickel-zinc deposits produced at a current density of 60 mA cm^{-2} and investigated using X-Ray Diffraction analyses were {330} reflections. In the thin, 0.1 μm thick nickel-zinc deposit produced at 60 mA cm^{-2}, only the {330} reflections were found as in the case of the nickel-zinc formed at 10 mA cm^{-2} with similar thickness. Further orientations may still have been present which might not have been detected due to the very thin coating studied, hence low X-ray intensity. The occurrence of {330} reflection was highest in the thickest coating studied, i.e. 20 μm, and accounted for almost 100 per cent of the total reflections, with only minute amounts of {600}, {552}, and {741} being present. In coatings of all thickness studied {330} reflections constituted the major proportion of all the reflections produced, i.e. being at least 60 per cent of the total. Thus a {110} texture was present in all of the coatings.

In the 0.2, 0.5, 1 and 2 μm thick deposits only, the {332} reflection was detected, but hardly exceeded one per cent of the total of the other planes detected. Thus its contribution was very small. The {600} reflection was found in deposits above 0.5 μm in thickness and its contribution was found to be highest in the 10 μm thick coating, i.e.

about 14 per cent of the total reflections detected. In the thickest coating studied, i.e. 20 μm, the {600} reflection was found to be relatively weak. In all nickel-zinc coatings exceeding 0.2 μm in thickness, the {552} reflection was detected and its highest contribution to the total reflections, about one 21 per cent, was measured in the 0.5 μm thick sample. Deposits with thicknesses greater than 0.5 μm showed {741} reflections. The proportion of {741} reflections as a function of nickel-zinc deposit thickness between 0.5 and 20 μm showed a maximum at a thickness of 10 μm, where the {741} reflections accounted for approximately 5 per cent of the total reflections, and was very small in the 20 μm thick deposit, i.e. 0.1 per cent. Only in the 10 μm thick deposit was the {820} reflection detected where it contributed about 7 per cent to the total measured reflections. Since reflections from the {510}, {521}, and {631} planes occurred only in traces smaller than one per cent in the 10 μm thick deposit, they have been included in table 4-88 but neglected in figure 4-85. However, all of the γ-phase nickel-iron specimens, produced at 60 mA cm^{-2} had a strong {110} texture.

Bragg angle positions of reflections of nickel-zinc deposited at 60 mA cm^{-2} are given in table 4-89. Interplanar d-spacings were calculated from the positions of the Bragg angles and are set out in table 4-90.

Table 4-90 indicates that the interplanar d-spacings are increased with deposit thickness in the nickel-zinc deposited at 60 mA cm^{-2}. A similar tendency was being observed in nickel-zinc deposited under comparable conditions at 10 mA cm^{-2}. In figure 4-86, the interplanar spacings between the predominant {330} planes versus deposit thickness are shown for nickel-zinc deposits formed at 10 and 60 mA cm^{-2}. In addition the d-spacing of the {110} planes of the steel substrate is presented. The smaller values of the {330} d-spacings found in thinner deposits indicate epitaxy in the initial stages of electrodeposition, i.e. the deposit takes over the lattice spacing given by the substrate. As the substrate's influence becomes less and the deposit thickness increases equilibrium deposition conditions prevail, the d-spacings take on their equilibrium values. The deposit formed at the higher current density appears to have a greater interplanar spacings possibly caused by the higher deposition rate and induced stress.

5 Discussion

5. 1 Electrolytes and Deposits Obtained

Preliminary work involving Hull Cell tests and electrolyses carried out at individual current densities established suitable solution compositions and operating conditions which produced coherent dense nickel-iron and nickel-zinc alloy deposits. These deposits were of a quality commensurate with commercial electrodeposits and robust enough to allow thinned specimens to be prepared for TEM studies. A characteristic feature of the nickel-zinc solutions tested was that they were stable in the unworked condition but turned turbid during use. In contrast the nickel-iron solutions investigated became turbid even on standing as well as during working. For this reason all solutions were freshly prepared prior to use and continuously filtered.

5. 1. 1 Nickel-Iron Solutions

Previous workers have considered the electrolyte's instability to be related to the oxidation of ferrous ions to ferric and the subsequent precipitation of hydrolysis products, such as $Fe(OH)^{++}$ and $Fe(OH)_2^{+}$, which become adsorbed in the growing cathodic deposits [104]. Ferric and ferrous hydroxides have been found to precipitate at pH values of 3.5 and 6 respectively and even in electrolytes containing reducing agents air oxidation has been found to produce some ferric ions [6, 105]. Electrolytes with basic compositions (i. e. *Nickel-Iron Solutions 1* and *2* in table 3-1) were found to oxidize in very short time. The rate of oxidation of ferrous ions has been found to be reduced in the presence of complexing agents, including citric- [104] and ascorbic acids [6, 22, 106, 107] as well as ammonium ions [6, 108]. For this reason more advanced formulations were developed containing complexants such as ascorbic acid and saccharine in *Nickel-Iron Solution 3* (see table 3-1). Saccharine was used to try to offset some of the inevitable increased incidence of internal stress [22, 104, 106, 109, 110] resulting from the use of the low pH adopted to avoid hydroxide precipitation.

A further addition of a wetting agent, sodium lauryl sulphate, in *Nickel-Iron Solution 3* rendered the application of nitrogen agitation unfeasible due to the foam generated in the presence of this agent. For this reason the electrolyte was agitated using a magnetic stirrer.

To increase the iron content in the deposits, the concentration of ferrous sulphate in the electrolyte was increased and the nickel sulphate concentration correspondingly decreased, so as to maintain a similar total molar metal ion content as in *Nickel-Iron Solution 1* and *2* (see table 3-1). *Nickel-Iron Solution 4* had almost the same formulation as *Solution 3* (see table 3-1) except that sodium lauryl sulphate was omitted, which allowed the solution to be purged with nitrogen. Agitation with an inert gas, i.e. nitrogen which also de-aerated the solution, was found to give deposits of satisfactory quality and properties.

The solutions were required to remain stable over an appreciable period of time and produce nickel-iron deposits with good adhesion and smoothness. A further aim was to develop an electrolyte from which deposits having different crystal structures could be obtained. According to the nickel-iron alloys thermal equilibrium diagram fcc γ-phase and bcc α-phase occur in the composition ranges of approximately 75 to 100 and 0 to 10 weight per cent nickel respectively [111]. Equilibrium diagrams are a guide insofar as they show those phases which might be deposited. Electrodeposited alloys only form phases that are obtained from the molten state, but some phases present in the equilibrium diagram cannot be obtained by electrocrystallization [112]. Since electrodeposited alloys are produced under non-equilibrium conditions, the composition range of individual phases may deviate from corresponding phases in the thermal equilibrium diagram. The *Nickel-Iron Solution 4* (see table 3-1) could be used to produce fcc γ- and bcc α-phases at 10 and 60 mA cm^{-2} respectively.

5. 1. 2 Bulk Structure and Nature of Nickel-Iron Deposits

Nickel-iron electrodeposits had either single fcc or bcc phase structures or mixed fcc/bcc crystal structures.

5. 1. 2. 1 Nickel-Iron Deposits with fcc Crystal Structure

The speed of electrocrystallization is influenced by the applied current density. Deposits generated using a higher current density generally exhibited higher degrees of preferred orientations than those produced in the same solution at lower current density (see fig. 4-14, 4-17). The {311}/{111} texture was found in all fcc nickel-iron deposits produced in *Nickel-Iron Solution 1* and *3*. These deposits contained more than fifty per cent nickel, inferring that the fcc nickel-lattice accommodates the iron atoms.

In the fcc lattice the {111} plane has the highest packing density and the fcc {311} plane has low packing density, see table 5-6. Fcc {111} and {311} textured deposits would be expected to be associated with relatively lower and higher 'local' overpotential respectively with respect to the accepted overall overpotential for metal discharge [49].

The occurrence of fcc {311} texture in nickel electrodeposition has not been found reported in the literature, indicating that its occurrence in nickel-iron deposition may be related to the co-deposition of hydrogen which possibly resulted in adsorption of iron- and/or mixed nickel-iron hydroxyl/hydroxide compounds thus hindering metallic discharge. This is in line with the literature where the nickel surface is described as being inert but very receptive to every chemical species capable of being absorbed on it [3, 113]. This could be an important factor in the pulse plating of nickel and its alloys, since periodic adsorption/desorption of species might be expected to be associated with changes during on/off periods. The increased iron content in the deposit produced in *Nickel-Iron Solution 4* may have favoured the discharge of metallic species involving a lower overpotential for metal discharge. Thus competitive hydrogen discharge would be less prevalent, resulting in the formation of {111} texture, see figure 4-21.

5. 1. 2. 2 Nickel-Iron Deposits with bcc Crystal Structure

The higher the iron content in the electrolyte the higher the iron content in the deposit. Nickel-iron deposits that had bcc crystal structure had generally a high iron content. Since relatively pure iron at room temperature has a bcc lattice, it can be assumed that iron atoms were being replaced by nickel atoms in the lattice. In the bcc lattice the {111} plane has low packing density, see table 5-7, indicating high overpotential during electrodeposition [49].

The observation that under otherwise comparable conditions the bcc {111} texture was more dominant in deposits produced at higher current densities, indicates that higher overpotential and faster deposit growth promotes one degree texture formation (see figs. 4-20, 4-22).

5. 1. 2. 3 Nickel-Iron Deposits with mixed fcc/bcc Crystal Structure

Solution agitation promoted a higher iron content in deposits (compare figs. 4-8, 4-9) because iron, the less concentrated metallic species in the solution, tended to deplete more quickly in the cathodic diffusion layer during electrodeposition. This provides an explanation for the observation that in solutions with similar metal ion concentration (*Nickel-Iron Solutions 3* and *4*) operated at the same current density the deposits formed with and without agitation had bcc and mixed fcc/bcc structure, respectively. In the nickel-iron deposit with mixed fcc/bcc lattice the {111} texture was dominant in both the fcc and the bcc phases (see figs. 4-16, 4-18). This infers that fcc and bcc {111} textures deposited with low and high overpotentials respectively.

5. 1. 3 Nickel-Zinc Solutions

Following trials and modification of a bath reported in the literature a suitable bath for depositing nickel-zinc alloys was developed based upon the metal sulphates, boric acid and p-toluene sulfonic acid, (see table 3-2) [114]. The use of nitrogen agitation was found to be more beneficial in producing quality deposits than the addition of sodium lauryl

sulphate. The use of p-toluene sulfonic acid which resulted in brighter deposits has been reported to act as a grain refiner [114].

5. 1. 4 Bulk Structure and Nature of Nickel-Zinc Deposits

Nickel-zinc deposits have bcc γ-phased crystal structure (see figs. 4-23 to 4-25; 4-28), occasionally accompanied by the fcc α-phase (see figs. 4-26, 4-27), which has been described as a nickel-rich solid solution [115]. The occurrence of α-phase in the deposits obtained in the present work cannot be assigned to a particular compositional range as reported, where α-phase occurred in deposits containing up to 50 per cent nickel, deposits with higher nickel concentrations contained γ-phase [115]. The β- and δ-phase present in the thermal equilibrium diagram [116] were not present in the as-deposited coatings, but the tetragonal β_1-phase was formed during subsequent heat-treatment of the deposits (see figs. 4-23; 4-24; 4-26; 4-27; 4-28). This is in keeping with similar observations already reported [115]. The amount of transformed β_1-phase from γ- and α-phase, where present, was directly related to the nickel content in the deposit. Thus the apparent volume fraction of β_1-phase formed during heat-treatment increased with increasing nickel content significantly, the deposit with the lowest nickel content did not transform to the β_1-phase.

The observation regarding the quality of the γ-phased deposits in the present work disagreed with previously reported work [115]. The morphology of the γ-phased nickel-zinc deposits was described as being easily pulverized, of a loose consistency, dark and occasionally black in colour [115]. In the present studies the quality of γ-phased nickel-zinc electrodeposits was found to be satisfactory and samples could even be prepared to a state of electron-transparency, which requires deposits of reasonable mechanical stability. In comparison to nickel-iron deposits the preparation of nickel-zinc deposits for TEM was more problematic due to their greater brittleness.

The rate of deposit formation is related directly to the applied current density. If the current density is increased, deposition conditions are moved further away from the equilibrium conditions and thus more energy is available for nucleation, i.e. a higher

number of nuclei associated with finer grained deposits might be expected. On the other hand at the higher current density where deposition is presumably mainly mass-transfer controlled, more hydrogen discharge may be expected since in the competition for discharge between metallic and hydrogen cations the latter may be more successful due to their smaller atomic size, thus superior mobility, compared with the competing the metallic species.

Comparison of TEM micrographs of γ-phased nickel-zinc electrodeposits produced with the lower current density, figures 4-62 and 4-63, with those deposited with the higher current density, figures 4-66, 4-67 and 4-68, suggests that the higher current density produces coarser grained deposits. This infers, that at the higher current density, nucleation of new grains is more inhibited than at the lower current density resulting in finer grained deposits at the lower current density. This inhibition may be ascribed to successive adsorption of either hydrogen or metallic hydroxyl/hydroxides in the latter stages with increasing pH at the cathodic interface.

5. 2 Nucleation and Growth of Electrodeposits

Finch et al. first postulated, that the development of electrodeposits is characterized by three stages: (i) the initial stage, (ii) the transitional, and (iii) the final stage [2].

The initial nucleation of the alloy electrodeposits investigated was found to confirm Finch's statement that the substrate predominates the structure of the deposit during the initial stages [2]. The subsequent growth of the electrodeposits is mainly influenced by the electrolyte and operating parameters conditions in the final stages of growth. The deposit structure developed in the final stage may vary from that at the substrate/deposit interface, in which case a transitional deposit structure may develop (transitional stage).

5. 2. 1 Initial Nucleation

The initial stage of growth is characterized by initial nucleation and continuation of the substrate lattice, i.e. epitaxy. Epitaxy has been defined as the "oriented growth of a crystalline substance on a crystalline substrate with a fixed orientation between the two crystal lattices" [117]. It has been considered that one of the preconditions for lattice continuation to occur is "that the difference between lattice spacings in parallel directions of the contact planes of substrate and deposit is less than fifteen per cent", i.e. the fifteen per cent criterion [2].

In the present work all deposits and substrate materials had cubic structures, where by definition crystallographic directions are perpendicular to corresponding planes [118]. The deposit's growth direction is perpendicular to the substrate's/deposit's interface, see fig 5-1. Therefore Finch's postulation can be interpreted as showing epitaxial lattice continuation occurs, if lattice spacings of planes parallel to the deposit growth direction differ by less than 15 per cent.

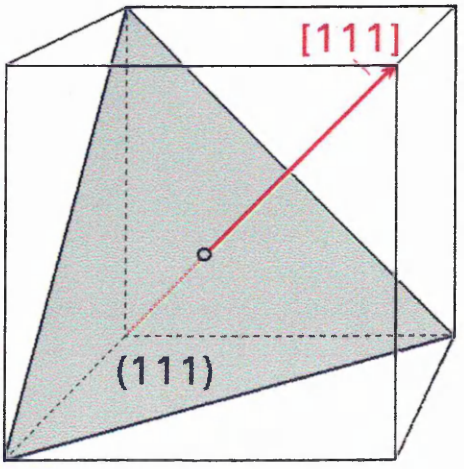

However, if substrate and deposit have dissimilar lattice structures, then the alloy orientation nucleating will be that atoms fit approximately in the positions of substrate atoms, see figures 5-3 to 5-11 showing nickel-iron and 5-13 to 5-15 showing nickel-zinc. In other words, depositing atoms fit into the recesses between the substrate atoms.

It is worthy of note that the orientation of deposits in the initial stages of growth was that of the most densely packed plane parallel to the substrate in all deposits investigated in the present work.

XRD and TEM, i.e. SADP, were used as complementary techniques for the determination of crystallographic structure and textures of electrodeposits. XRD measures the intensity of reflections parallel with the surface of the deposit (see figures 3-14; 3-15), whilst the growth direction from SADP is perpendicular to this (see figure 3-13). To evaluate Finch's fifteen per cent criterion, planes parallel to the growth directions needed determining, i.e. zones from SADPs. Zones are the planes perpendicular to the electron beam and parallel to the growth direction at 0° tilt (see figure 5-1).

The SADPs, e.g. in figure 4-43, are interpreted as substrate and deposit having {110} zone, i.e. the {110} plane perpendicular to the electron beam. At 0° tilt, the {110} plane is parallel to the growth direction of the deposit. Planes producing reflections (spots in SADPs) are all perpendicular to this plane. Thus, the patterns in figure 4-43 showing substrate and deposit infer that the {111} planes of copper and fcc nickel-iron are parallel to the surface of the electrodeposit and {110} planes parallel to the growth direction, i.e. {111} $\perp$ {110}, and thus Finch's fifteen per cent rule is the difference between fcc {110} planes of nickel-iron and copper.

5. 2. 2 Deposit Growth and Re-Nucleation

In the course of electrodeposition the deposit thickness increases and the predominance of the substrate's effect upon the orientation of the electrodeposit decreases. The relative importance of nucleation and growth changes as the influence of the substrate decreases subsequent to the initial nucleation and as the influence of the electrolyte and deposition parameters become increasingly important as the deposit grows. In the absence of further nucleation initially nucleated crystals may continue to grow, but further nucleation may take place within the mass of the growing deposit. If the latter is the case then the growth of crystals nucleated at the substrate/deposit interface have to compete with the growth of crystals nucleated in the bulk of the deposit. The preferred growth of selected orientations leads to increased surface roughness and since deposit electrocrystallization occurs on the local surface with a particular orientation, the orientation of newly nucleating grains may deviate slightly from the parallel order of the initial cathode surface.

TEM micrographs of cross-sectioned electrodeposits show that all electrodeposits investigated have a columnar grain structure growing with an orientation approximately perpendicular to the substrate surface, i.e. parallel to the deposit growth direction. Generally, the initially deposited layer at the nucleating interface is finer grained and appears darker in comparison to the bulk of the deposit further away from the initial nucleation site. The dark layer at the substrate/deposit interface indicates a high dislocation density due to the lattice mismatch between substrate and deposit. Near the nucleating interface grains are fine and narrow. However in the competition for growth, i.e. as the distance from the initial nucleating interface increases, the structure becomes coarser and the columnar grains become wider due to their lateral growth at the expense of less favourably orientated grains. Grains, orientated favourably to start with and re-nucleating grains with an orientation favourable in the competition for growth, develop columnar structure and supersede less favourably orientated grains.

During deposit growth the roughness of the electrodeposit's surface is increased since grains are not equally favoured in the competition for growth. Furthermore growth at protruding areas is inherently preferred since current field lines concentrate on protrusions leading to increased deposition rate, see figure 5-2a. In contrast to grain growth perpendicular to the 'local' surface may result in columnar grains growing in recessed areas impeding each other during growth, see figure 5-2b, leading to levelling through the geometric effect. Hence, in the absence of levelling additives in the electrolyte or other levelling effects, the surface roughness increases as the deposit grows due to relatively higher deposition rates at protrusions compared with recessed areas on the surface.

5. 2. 3 Theoretical Considerations

In tables 5-3, 5-4, and 5-5 the interplanar spacings of substrate and deposit lattices are listed that theoretically fulfil the 15 per cent criterion.

The data in table 5-1 were calculated in order to see whether or not Finch's 15 per cent postulation applied to those systems studied in the present work. Calculations are based on the lattice parameters 'a', i. e. the distances between {100} planes, taken from literature [88]. The interplanar spacings were calculated using

$$d = \frac{a}{\sqrt{h^2 + k^2 + l^2}} \qquad [5.1]$$

where: a = lattice parameter

d = interplanar spacing

Table 5-1 indicates that d-spacings between analogous planes for the pure fcc structured copper, nickel and iron are very similar. The unit cell of the fcc structured nickel-iron alloy is somewhat larger than that of the pure nickel, i.e. about 2 per cent, yet smaller than that of fcc structured iron, i.e. about 0.1 per cent, possibly due to lattice dilation caused by the iron atoms occupying sites within the nickel lattice. The lattice parameter of bcc structured iron and nickel-iron are comparable, with the latter being 0.6 per cent larger, indicating lattice strain possibly due to nickel atoms occupying sites in the iron lattice. The intermetallic compound Ni_5Zn_{21} has the largest unit cell with a lattice parameter approximately three times as large as that of the iron bcc lattice.

Table 5-2 gives an overview of planes that are perpendicular to one another in the cubic system. In tables 5-3, 5-4, and 5-5, substrate/deposit combinations investigated in present work are set out, that fulfil the 15 per cent criterion.

The unit cell of the nickel-zinc γ-phase is approximately three times as large as that of the substrate materials copper and steel, see table 5-1. Therefore epitaxial growth of e.g.{110} $Ni_{21}Zn_5$ can occur on {110} orientated bcc iron, see table 5-5.

5. 2. 4 Texture Formation During Electrodeposition

Grains orientated with the most densely packed planes parallel to the substrate are more favoured than grains with other orientations in the competition of growth [2]. In tables 5-6 and 5-7 the packing density of various planes in terms of atoms per unit area are compiled for cubic fcc and bcc lattices, respectively. The order of packing densities of planes is $\delta_{\{111\}} > \delta_{\{100\}} > \delta_{\{110\}} > \delta_{\{311\}} > \delta_{\{210\}} > \delta_{\{211\}}$ and $\delta_{\{110\}} > \delta_{\{100\}} > \delta_{\{310\}} > \delta_{\{111\}} > \delta_{\{211\}}$ for the fcc and bcc lattices, respectively. The higher the packing density, the stronger the binding forces amongst the atoms making up the plane. Thus, the generation of planes with high packing density parallel to the given substrate surface appears plausible from the thermodynamic view-point of the principle of minimized energy.

The lattice parameter 'a' for the fcc and bcc nickel-iron are 0.3596 nm and 0.28681 nm, respectively [88]. Thus for fcc and bcc nickel iron the unit areas of the {100} planes 'a^2' are 0.1293 nm^2 and 0.08226 nm^2, respectively. The number of atoms per nm^2 are given in line 3 in tables 5-6 and 5-7. Due to the smaller lattice parameter of the bcc in comparison to the fcc structured nickel-iron, the atomic density in respect to a defined area, i.e. 1 nm^2, is very similar for the densest populated plane of either lattice, i.e. {111} for fcc and {110} for bcc nickel-iron.

The geometric aspect of substrate/deposit compatibility, i.e. 'fifteen per cent guide criterion' and the energetic/thermodynamic aspect, that low index, close packed planes parallel to the substrate surface, are dominant in the initial deposit's structure. Further parameters, such as hydrogen co-deposition, bath constituents, e.g. anions, surfactants and their decomposition products, determine the development of a deposit's crystal structure [2, 7, 53]. With increasing overpotential during electrodeposition Pangarov's theory of the preferred selection of planes with high packing density in the competition for growth is invalidated and reversed [49]. Co-deposition of hydrogen is a significant competing process during electrocrystallization of metallic species.

For example the texture of nickel electrodeposits results directly and indirectly from the competitive cathodic discharge between nickel and hydrogen ions resulting in the prevalence of certain species adsorbed at the cathode/catholyte interface [113]. Thus the formation of {110} texture was attributed to the inhibiting influence of adsorbed hydrogen (H_{ads}), the {210} texture formed in the presence of molecular hydrogen (H_2), and {211} texture formation was ascribed to the inhibition by nickel-hydroxide ($Ni(OH)_2$), whereas the {100} mode of crystal growth was considered as relatively free from inhibiting species [53, 113].

There was no evidence of {100}, {210}, or {211} orientations in the fcc structured nickel-iron electrodeposits investigated in the present work. The formation of {210} and {211} textures appears rather unlikely since these planes have relatively low packing densities, see table 5-6, but fcc structured nickel-iron electrodeposits are mainly {111} textured, indicating that electrodeposition takes place with relatively low overpotential. However, in present work the {111} and {110} textures were found, but no {100}, which would be expected from a consideration of the packing densities of these planes, i.e. $\delta_{\{111\}} > \delta_{\{100\}} > \delta_{\{110\}}$. Even in the thinnest deposit there was no evidence of {100} orientation, see figure 4-73, despite the fact that the copper substrate is {100} textured, see figure 4-71, and epitaxial nucleation would have involved very little strain.

Assuming the classical metallurgical homogenous nucleation theory from the molten to the solid state a solid nucleus is generated once the total free energy of the particle is minimized. For convenience, the nucleus is assumed to be spherical.

Thus the total free energy can be expressed as [50]

$$\Delta F = -\frac{4}{3}\pi r^3 \Delta F_v + 4\pi r^2 \sigma \qquad [5.2]$$

With ΔF : Total free energy

r : Radius of the spherical nucleus

ΔF_v : Difference in volume free energy of molten and solid state

σ : Surface energy per unit area of the solid/liquid interface

$\frac{4}{3}\pi r^3$: Volume of the sphere

$4\pi r^2$: Surface of the sphere

The first an second term in equation [5. 2] represent the volume energy term and the surface energy term of the spherical nucleus, respectively. A stable solid nucleus is generated, once the critical radius is exceeded. Once the surface energy term is smaller than the volume energy term and the total free energy is zero or has negative values the critical radius is exceeded and a stable solid nucleus is formed. Equation [5. 2] can be simplified as

$$\Delta F = -volume\ energy + surface\ energy \qquad [5.3]$$

In electrodeposition, not only the metallic species are adsorbed and/or discharged at the cathode and thus there is no 'homogeneous' nucleation in keeping with equations [5.2] and [5.3]. Hence a further general term, i.e. strain, can be introduced.

In the thermodynamic consideration of the generation of certain orientations during electrodeposition, the total free energy can be described as

$$\Delta F_{\{hkl\}} = -volume\,energy_{\{hkl\}} + surface\,energy_{\{hkl\}} + strain_{\{hkl\}} \qquad [5.4]$$

with *volume energy* $_{\{hkl\}}$: Proportional to the polarization of the cathode ΔF_P, i.e. driving force for nucleation, and the atomic packing density of considered plane.

surface energy $_{\{hkl\}}$: Proportional to surface area and liquid/solid surface energy per unit area σ.

strain $_{\{hkl\}}$: Strain is the mismatch between ideal and actual atomic positions. Strain may be forced upon the system by adsorption, discharge or incorporation of species.

A possible explanation for the generation of {110} rather than the {100} orientation in present work is that the combined surface energy and strained energy term for {110} oriented planes under the prevailing deposition conditions is considerably less than the combined surface energy and strained energy term for {100} oriented planes, resulting in lower total free energy $\Delta F_{\{hkl\}}$ for the generation of {110} orientated planes.

5. 3 Interfacial Effects and Initial Nucleation

The influence of the initial substrate upon the first stage of deposition may be influenced by crystallographic (fifteen per cent criterion) [2, 51], electrochemical [3] (potential of the electrode in the solution; inhibition of the metal discharge reaction), and thermodynamic factors [49, 120, 121].

If the crystallographic factors during initial growth were the only influence, electrocrystallized atoms might develop an initial texture that fitted onto the substrate. Then the initial deposit structure was maintained throughout the growing deposit apart from gradual lattice dilation or contraction of the growing electrodeposit associated with a reduction of the inherent deposit stress caused by substrate/deposit lattice mismatch. Initial lattice strain, i.e. broadened lattice, as a result of epitaxial growth was observed in fcc structured nickel-iron electrodeposits nucleated on copper. The lattice spacings relax to equilibrium size with increasing deposit thickness as the deposit grows, see table 4-62, and figure 4-74.

The electrochemical behaviour of a cathodic surface is affected by the relative ease of hydrogen co-discharge along with the competing discharge of metallic species, see Piontelli's classification [3]. Thus, the cathodic surface has a potential influence upon the developing texture and especially on any elemental composition changes in the deposit as it grows and as the major influencing factor changes from that of the initial substrate to those of the bath and the operating conditions.

Thermodynamic considerations suggest that planes with high packing density, thus strong interatomic forces, parallel to the surface are most easily formed at low overpotential, i.e. under conditions close to equilibrium. Increasing overpotential results in random deposit texture and higher overpotential eventually causes, nucleation resulting in the lowest packed planes parallel to the surface being formed [49]. Amongst other things the overpotential to be overcome during metal deposition is determined by the substrate surface, species adsorbed on the cathode, the electrochemical conductivity and electrolysis parameters.

5. 3. 1 Initial Interfacial Nucleation

Continuation of the substrate structure in the electrodeposited coating confirmed the fifteen per cent criterion. Even though the substrate materials were polycrystalline having preferred orientation, deposits had dominant textures (not one degree textures) from which it can be inferred that epitaxial growth occurs, since the major textures of substrate/deposit combinations were in agreement with the fifteen per cent criterion.

For initial three- and two- dimensional nucleation to occur, see figures 2-2; 2-3, surface energy is required for nuclei generation. This annexation energy for atoms depositing in later stages is lower due to the increased number of neighbouring atoms, kink sites etc. Therefore in the initial stage, the energy input, i.e. negative polarization of the cathode, is used up primarily for nuclei formation, so that initially formed nuclei have textures formed under low overpotential close to their equilibrium value. The initial formation of closest packed planes parallel to the substrate as the major textures in both fcc and bcc lattices was evident in all the electrodeposits investigated irrespective of the substrate surface.

5. 3. 1. 1 Fcc Nickel-Iron Electrodeposition on Copper Substrates

The initially formed deposit is influenced by the original cathodic surface. In fcc nickel-iron deposit, the three stages of deposit formation postulated by Finch [2] were identified as (i) initial stage, depending on the initial cathode: {111} texture under low inhibiting conditions accompanied by {110} texture if metallic discharge is inhibited on the cathodic surface; (ii) transitional stage, similar to (iii) final stage, {111} texture, inferring low overpotential [49].

Deposition of fcc nickel-iron on a copper substrate with {100}/{111} orientation (see table 4-57, fig. 4-71) initially resulted in lattice continuation and epitaxial growth of the {111} and {110} orientated fcc nickel-iron on {111} and {100} copper planes parallel to the substrate/deposit interface, see table 4-60 and figure 4-73. This suggests that the relative order of nucleating sequence of planes in relation to the atomic packing density, see table 5-6, was changed such that the total free energy for deposition of {110} oriented planes was less than for {100} oriented deposits. Lattice spacings between {110} planes, i.e. zones, in the thinnest fcc nickel-iron deposit measured was only about 0.6 per cent smaller than that of the copper substrate, hence the 15 per cent criterion for epitaxy was fulfilled. The densest packed planes have strongest binding energy and fcc grains with {111} orientation are favoured in the competition for growth under conditions where deposition is not strongly inhibited [49]. The atoms of the fcc {111} planes in the nickel-iron deposit fall very close to the recesses between atoms in the copper {111} plane. Epitaxial nucleation of {111} orientated grains onto {111} copper appears to be connected with lower lattice strain than nucleation on a {100} orientated copper substrate, compare figures 5-3 and 5-4.

Nucleation of {110} nickel-iron deposits on {111} and {100} textured copper substrates is shown in figures 5-5 and 5-6 respectively, which indicate that lattice strain within the deposit occurs in both cases, but to a somewhat larger extent on the latter. An explanation for the decrease in the occurrence of {110} orientation with increasing deposit thickness could be that initial two dimensional nucleation produces strained (fig. 5-5; 5-6), hence less stable nuclei. In contrast, {111} orientated nuclei are less strained, particularly when epitaxially grown on a {111} substrate, see figure 5-3, and therefore favoured in the competition for growth. Thus the {111} crystallographic texture became increasingly dominant with increasing deposit thickness, see XRD-results figure 4-73.

Furthermore during electrocrystallization there is constant competition for growth between new nucleation and growth of existing grains. Crystals having the {111} orientation are more favoured during competitive growth than those with {110} texture since the {110} planes involve lower interatomic binding force than the {111} planes, with the highest packing density in the fcc lattice (see table 5-6). Therefore more energy is required for the formation of {110} than for {111} planes.

In the literature nickel electrodeposition is frequently cited as an example of a process taking place with relatively high overpotential during metal discharge as compared to that for some other metals [2, 3, 7, 53]. For low current densities, involving relatively low overpotential during metal discharge, only planes with strong interatomic binding forces are expected to form. At higher current densities, involving higher overpotentials, the generation of other planes requiring higher energies becomes possible [49]. Deposition of fcc nickel on polished copper substrates was reported to result in random orientation in thin deposits, and {110} orientation in thick deposits [51]. A parallel to the present work may be drawn since the nickel-iron electrodeposit discussed here had a fcc crystal structure only, inferring that the iron substituted for nickel atoms in the fcc lattice. Therefore initial co-deposition of {110} and {111} textured grains appears plausible. In the further development of the deposit existing grains grew but also further nucleation of new grains occurred and in the competition for growth, planes with higher packing densities and stronger interatomic forces, i.e. fcc {111} textured grains, were favoured. Therefore the fcc {110} texture was not revealed in XRD investigations of thick deposits (fig. 4-73).

The {110} texture was reported to occur when adsorbed hydrogen (H_{ads}) inhibits nickel deposition [113]. In view of the fact that copper and nickel have similar structures this might suggest that the {110} texture in the initially deposited nickel-iron on copper substrates found in the present work results from a similar inhibition effect; possibly caused by co-discharged hydrogen.

TEM examinations of cross-sectioned deposits indicate the co-existence of {111} and {110} textured grains in the initial stage, e.g. in figure 4-38 the small interfacial deposit region appears diffuse, fine-grained, with only a few grains having twin lines parallel to the interface, indicating that they have {111} texture. As twin bands are only expected along fcc {111} planes, since they are the closest packed planes, it can be concluded that grains with twin bands parallel to the interface are definitively {111} textured. From approximately 0.1 μm distance into the deposit from the substrate/deposit interface grains become more distinct with the effect that {111} textured grains became dominant. From then on a columnar grain structure and a predominance of {111} texture is observed, grains then become wider and are eventually entirely {111} textured. Figures 4-39 a and b also indicate that only at the actual interfacial boundary some grains are do not show twinning suggesting the absence of any {111} texture. Further away from the interface columnar growth of grains occurs with twin bands parallel to the interface and grains becoming wider as the deposit thickness increases. Figures 4-41 and 4-42 indicate that grain boundaries of the substrate continue into the deposit, with the majority of deposit grains having twins with a few appearing diffuse inferring, from XRD results, that they have {110} texture. Verification that the {111} texture of the fcc nickel-iron deposit results from a continuation of the copper substrate's structure is given by Selected Area Diffraction Patterns (SADP) in figures 4-40, 4-43 and 4-44. 'Arcing' of the twin spots of SADPs taken in the established, advanced developed, bulk deposit (see figures 4-40, 4-43, 4-44, 4-45, 4-46) indicate that {111} planes of different grains were not exactly parallel to the initial substrate, i.e. deviate from the fibre axis, inferring that the actual surface during electrocrystallization was roughened and grain growth occurred perpendicular to the local surface orientation.

5. 3. 1. 2 Fcc NiFe Nucleation on Bcc NiFe Electrodeposited Substrates

In contrast to what was found using copper substrates, bcc structured electrodeposited nickel-iron substrates appear to promote development of an initial pure {111} texture of the nucleating fcc nickel-iron, (see figs. 4-76, 4-77), indicating that the degree of inhibition for metal deposition is higher on copper surfaces than on bcc structured nickel-iron surfaces.

Rocking Angle XRD investigations infer that the {111} texture of the 2 μm thick fcc structured nickel-iron electrodeposit deviates least from the fibre axis when electrocrystallized on a 0.5 μm thick bcc structured nickel-iron deposited substrate. On a 2 μm thick bcc structured electrodeposited nickel-iron substrate, the deposited fcc structured nickel-iron is less strongly textured, the {111} texture of fcc structured nickel-iron electrodeposit deviated more from the fibre axis, but the polished copper substrate appears to be least suited for {111} texture formation, see figure 4-78. The degree of deviation of the {111} texture from the normal to the substrate, i.e. fibre axis, illustrated in figure 4-78 indicates that the 0.5 μm thick bcc structured electrodeposited substrate is the best precursor for a perfectly {111} textured fcc nickel-iron deposit.

On the thin bcc structured nickel-iron deposit, with {211} and {110} texture (see figs. 4-76 and 4-77), the fcc nickel-iron nucleates almost entirely with {111} texture. Thus, although the substrate surface is less even than the polished copper surface, the 0.5 μm thick bcc structured nickel-iron deposit supplies more favourable conditions for {111} texture formation than other substrate material and surface conditions investigated.

The 0.5 μm thick electrodeposited bcc structured nickel-iron substrate is {211}/{110} textured. Possible atomic arrangements of {111} textured fcc nuclei nucleated onto bcc {110} oriented nickel-iron electrodeposited substrate is depicted in figure 5-7.

Atomic arrangement of fcc structured {111} oriented nickel-iron nucleated on a bcc structured {211} electrodeposited substrate is depicted in figure 5-8. For clarity, figure 5-8a shows only the {211} textured bcc nickel-iron substrate and figure 5-8b depicts a {111} oriented fcc nickel-iron nucleated on the same substrate.

Deposition of {111} orientated fcc structure onto {211} bcc orientated nickel-iron appears to be connected with less lattice strain than when deposited onto {110}, compare figure 5-7 with figure 5-8b.

The findings that thin (0.5 μm thick) fcc structured deposits are {111} textured only when deposited onto bcc nickel-iron substrate, but have {110} besides {111} orientation when plated onto fcc copper indicates that discharge on copper is associated with the co-deposition of the inhibiting adsorbed hydrogen (H_{ads}) which reportedly results in {110} texture, whereas deposition on the nickel-iron surface gives {111} texture which forms under non-inhibiting conditions only [113].

When deposited onto a 2 μm thick bcc electrodeposited substrate, the thinner (0.5 μm thick) fcc nickel-iron electrodeposit had a strong {111} texture, whereas the thicker (2 μm thick) had other orientations besides the dominant {111}, compare figures 4-76 and 4-77, respectively. Deposition, i.e. texture formation, occurred parallel to the local cathode surface and due to increased surface roughness of the 2 μm thick bcc nickel-iron substrate other than the fcc {111} texture, i.e. {100}, {110}, and {311} were found, see figure 4-77. The surface of the 0.5 μm thick bcc nickel-iron substrate is relatively smooth, see figure 4-59, the crystal growth normal to the local substrate has resulted in little deviation from the {111} fibre texture. In contrast the surface of the 2 μm thick bcc structured substrate was rougher, see figure 4-60a, crystal growth perpendicular to the local substrate orientation thus resulted in greater deviation from the fibre axis.

Furthermore, in contrast to the 0.5 µm thick bcc structured nickel-iron substrate, the 2 µm thick bcc substrate exhibits additionally a {111} component, see table 4-64 and figure 4-75. Figure 5-9a shows the possible atomic arrangement of the {111} plane in the bcc nickel-iron electrodeposited substrate. The {111} textured fcc nickel-iron nucleated on this substrate (fig. 5-9a) is depicted in figure 5-9b, indicating that nucleation of {111} fcc onto {111} bcc nickel-iron is connected with little strain.

TEM-micrographs of the fcc structured nickel-iron electrodeposited onto the 0.5 µm thick bcc structured nickel-iron are shown in figures 4-58 to 4-61. The comparison of the overall views of fcc nickel-iron deposited on the copper substrate (fig. 4-38) and the 0.5 µm thick bcc structured nickel-iron electrodeposit (fig. 4-58) reveals, that the interface between the polished copper and the deposit is smoother than that between bcc and fcc nickel-iron electrodeposit. However, this does not hamper the development of the {111} texture closer to the fibre axis when electrodeposited onto the bcc nickel-iron deposits than on the copper substrate. The fcc deposit close to the interfacial bcc/fcc deposit site appears to be finer grained at the substrate/deposit interface than in the bulk deposit. The dark region is indicative for high dislocation density due to lattice mismatch (see fig. 4-59). However in the course of further growth nucleation of a {111} texture results in competitive growth, as indicated by an increase in column diameter with increasing distance from the interface. A comparison of the 0.5 and 2 µm thick deposits shows that as the deposits have become thicker the twins are no longer orientated parallel to the original copper substrate, see figures 4-60 a, b and 4-61.

5. 3. 1. 3 Bcc Nickel-Iron Electrodeposition on Copper Substrates

The bcc structured nickel-iron electrodeposits show characteristics of electrodeposits in accordance with Finch's general ideas insofar that they exhibit the three stages of growth [2]. The present work suggests that these correspond to three different crystal orientations: (i) Initial stage with {110} texture, highest packing density; (ii) intermediate stage, {211} texture, lowest packing density; (iii) final stage {111} texture, intermediate packing density.

In the initial stage of deposition of bcc structured nickel-iron on fcc structured copper disc substrates, the nucleation of {110} orientated grains predominates, see figure 4-75, table 4-64. Low inhibition in the initial stage is inferred, since bcc {110} planes have the highest packing density (see table 5-7).

The deposition is furthermore geometrically favoured since is takes place with little strain on the copper substrate. The schematic diagrams of the atomic arrangement of nickel-iron bcc {110} deposited on the {111} and {100} plane of the copper fcc substrate are shown in figures 5-10 and 5-11, respectively.

As the deposit thickness increased the {211} orientation was detected besides the {110}, which became stronger with increasing deposit thickness at the expense of the {110} (fig. 4-75). The occurrence of {211} orientated grains was furthermore confirmed by the TEM images in figures 4-52 and 4-53, where the zone is $(\bar{1}11)$, hence this indicates that the initial growth direction [100] changed to [111] as the initial {110} orientation changed to {211}. In the thicker deposits the {211} and (222) reflections were observed until in the thickest deposits the (222) reflection, i.e. almost only {111} texture was observed in the bulk, see figure 4-75.

It has been established that in some cases the initial deposition is associated with a sub-potential, i.e. a potential lower than that normally associated with the deposition of thick deposits. It is probable that this sub-potential effect arises as a result of the strong binding effect between the initially deposited metal atoms and those of the substrate. The closer the packing in any given system the stronger the binding energy and the

likelihood of initial sub-potential deposition. As deposition proceeds the overpotential increases to the 'normal' value for that associated with the formation of thicker deposits. It has been suggested that this change in overpotential can be correlated to the structures associated with the three stages of deposition [51, 52]. The magnitude of the packing density of planes is inversely proportional to the overpotential conditions [49, 120, 121].

The increase of the overvoltage from the sub-potential may be connected with the following changes at the cathodic surface.

- Transition of cathode metallic surface from (a) copper to (b) increasing proportion of nickel-iron to copper and finally to (c) nickel-iron only.
- Change in the cathodic layer during electrodeposition hindering discharge of metallic species.
- Change in the nickel-iron deposit textures on the cathodic surface.

By its nature the initial cathodic surface influences nucleation of the initial deposit. In the course of the deposition process it becomes covered with a coating of different composition to that of the original surface and one which becomes a new sub-surface with respect to further deposited metal and determines the magnitude of overpotential to be overcome for further metal ion discharge. Thus, the initial substrate not only has a direct influence on the initial - but a further reaching, indirect influence on to the later stages of deposition.

The occurrence of {211} orientation and <111> zone axis corresponds to the transitional stage. It does not seem unreasonable to infer that the low packing density (see table 5-7) indicates the presence of a high overpotential during electrodeposition and can be interpreted as being due to a transitional re-arrangement of crystals as the initial texture changes from {110} to final {111}. Hence, the overpotential decreased so that in the final stage the {111} texture predominates, which is in agreement with the ideas and work of Finch [2, 51] and Pangarov [49, 120, 121].

5. 3. 1. 4 Bcc NiFe Nucleation on Fcc NiFe Electrodeposited Substrates

Bcc structured nickel-iron deposited onto different substrates indicates that the substrate influences the extension of the initial and the transitional deposition stages. In figure 4-79 electrocrystallization on the copper substrate occurred initially under sub-potential conditions before the potential increased until deposition has occurred under 'normal' overpotential conditions as suggested by previous work [10] . Whereas on fcc electrodeposited nickel-iron substrates the apparent effects of the initial sub-potential deposition persists further into the deposit the thicker the fcc electrodeposited substrate. The preponderance of close packed planes parallel with the surface in the 2 μm thick nickel-iron deposit is greater than in the corresponding copper substrate which explains the apparent increased evidence for sub-potential deposition in the former as reflected in the greater presence of {110} bcc orientated grains.

The 2 μm thick bcc nickel-iron electrodeposited on copper and fcc nickel-iron of various thicknesses (see fig. 4-80) had the highest proportion of {110} orientation when deposited on the 2 μm thick fcc nickel-iron electrodeposited substrate. The 0.5 μm thick fcc structured substrate led to the highest proportion of bcc {111}, which was the texture of the final stage, inferring that during the formation the overlying deposit quickly attained its final texture corresponding to the third stage of growth. On the copper substrate, the bcc nickel-iron deposit had a dominant {211} texture, inferring that the intermediate stage was rather pronounced.

TEM micrographs of bcc electrodeposited onto copper and fcc nickel-iron supported the conclusions drawn from XRD studies. The interfacial nucleation site between the copper substrate and bcc structured nickel-iron deposit is characterized by fine grains with high dislocation density, see figures 4-47 to 4-50. The interface between the 0.5 μm thick fcc and bcc structured nickel-iron has lower dislocation density (see figs. 4-54a and b), but the nucleation of bcc onto 2 μm thick nickel-iron almost appeared as a continuation of grains with a lower dislocation density (see figs. 4-55 to 4-57). The initial nucleation of the bcc densest packed {110} texture was maintained further into the deposit thickness on the 2 μm thick substrate, less on the 0.5 μm thick fcc nickel-iron substrate and least on the copper substrate. This infers that the bcc {110} possibly sub-potentially nucleated with ease onto the well developed {111} textured fcc nickel-iron. The 0.5 μm thick fcc nickel-iron has {110} as well as {111} texture which may have inhibited the nucleation of the bcc {110} texture further into the nickel-iron deposit (see fig. 4-79) as compared to when deposited on the thicker (2 μm) fcc nickel-iron electrodeposited substrate, which had less {110} but more {111} texture (see fig. 4-73).

Summary:

The present work suggests that not only does the substrate influence the initial stage of deposition in terms of structure but also how the texture develops with increasing thickness. During electrodeposition there is a constant growth of existing grains and additional nucleation of new grains. New sub-surfaces are generated and it appears from the results that the sub-surface existing at the time of nucleation determines the prevalent local overpotential condition. Where the electrochemical characteristics of the initial nuclei formed on the substrate are similar to that of the substrate then the onset of the intermediate and final stage are delayed. This results in a relatively thick deposit being formed during the initial deposition stage and having the structural characteristic of that stage.

5. 3. 1. 5 Compositionally Modulated NiFe Electrodeposits

Inevitably at the onset of electrodeposition changes and perturbations occur at the electrode/electrolyte interface before equilibrium conditions are established. Clearly this leads to the possibility that the initial deposit will have different characteristics from that formed under relatively steady state conditions. It therefore follows that one might expect a deposit of a given thickness formed in one step might have different properties to a deposit of the same overall thickness but formed in several steps during which the current is interrupted.

The clearly layered structure of the cross-sectioned nickel-iron multilayer generated with step pulsed direct current is shown in figure 4-29. Figure 4-30 shows the elemental composition of the multilayer obtained via SEM/EDX line-scans, which is not perfectly stepped possibly due to inherent features of the technique used to give signals from the excitation volume. The loss of resolution is brought about if the 'analyzing spot' is set on the interface between the fcc/bcc layers when the average composition from the excitation volume of the specimen is measured on the assumption of a gradual composition change although the composition change is stepped. Thus the compositional changes occur abruptly at the interface, with each single layer over the cross-section having uniform composition.

Bright field and dark field images of the fcc/bcc structured interfaces of the cross-sectioned multilayered nickel iron deposit show that the interface is clearly defined, see figures 4-54a/b, 4-55, 4-56, 4-57a/b (bcc nucleated on fcc nickel-iron) and figures 4-58, 4-59, 4-60a/b, 4-61 (fcc nucleated on bcc nickel-iron). Near the interface the newly nucleated layer generally has finer grain size and higher dislocation density in comparison to distances further away from the interface indicating competition for growth among grains. Additionally nucleating interfaces not only have finer grain size, but the initial deposits have different structural orientation, i.e. texture, that is mainly the densest packed plane parallel to the substrate, thus the 'mechanically' most resistant texture, in contrast to the subsequently grown deposit where grains are coarser and orientations are more random. The increased number of interfaces within the multilayered deposit, which are artificially generated by the stepped pulsed current, and each of which would have given rise to a new initial stage may be one of the causes for the difference in properties between compositionally modulated and bulk alloy deposits. In other words a multilayered deposit might be expected for example to contain a higher volume fraction of fine grained alloy than a single layered of the same thickness.

5. 3. 1. 6 Nickel-Zinc Bcc Crystal Structure

Texture formation in the initial stage of deposition of the closest packed plane also occurs in nickel-zinc deposition on various substrates. Nickel-zinc electrodeposits considered here have bcc γ-phase. The formula Ni_5Zn_{21} has been assigned to the γ-phase, a solid solution with a high solubility for nickel and zinc, and has a complex bcc structure with 52 atoms in its unit cell [122]. Each γ-phased unit cell can be considered as three cells extended along the axes in the cubic system resulting in a unit cell of 3×3×3=27 cubic body centred sub cells. Of the 54 possible accommodation sites for atoms of the unit cell two are missing, which is the central and the corner atoms, such that the new unit cell consists of 52 atoms [36], see figure 5-12.

Literature reports agreed with the results found in the present work regarding the structure to be expected for certain alloy compositions; thus it was reported that within the range approximately 50 to 90 weight per cent zinc the γ-phase developed in the nickel-zinc alloy [115].

The major textures of nickel-zinc deposits and the mild steel substrate was the {110} orientation, see figures 4-84, 4-85 and 4-82 respectively. The lattice parameter of the nickel-zinc γ-phase is approximately three times that of the substrate bcc iron (table 5-1). Epitaxial growth of for example {110} textured $Ni_{21}Zn_5$ can occur on {110} orientated mild steel, see table 5-5. Atoms of nickel-zinc {110} planes fit closely into the recesses between atoms on the mild steel {110} planes, see figure 5-13.

When nickel-zinc was deposited onto copper it had {110} zone, i.e. growth direction. Figure 5-14 depicts a model of {110} orientated nickel-zinc nucleated on a {111} textured copper substrate. The atoms of the nickel-zinc {110} planes fit closely into the recesses between atoms on the copper {111} planes, thus the strain within the nucleated nickel-zinc is very low.

In figure 5-15 nucleation of {110} orientated nickel-zinc on a {100} textured copper substrate is shown. Here the strain required for the atoms of the {110} nickel-zinc plane to fit into the recesses between the atoms of the {110} textured copper substrate is somewhat higher than for nucleation on the {111} orientated copper, compare figures 5-15 and 5-14.

5. 3. 2 Compositional Changes in Nickel-Zinc Bcc Structured Electrodeposits

In the initial stages of deposition there is a competition for discharge between hydrogen and the two metals present, i.e. nickel and zinc. The degree of competition will very much depend upon the relative ease of hydrogen and metal discharge and on the different substrate surfaces involved. In Piontelli's classification [3] initial substrate surfaces of copper and iron are 'normal' and 'inert', respectively; and the electrodeposited metals nickel and zinc are 'inert' and 'intermediate', respectively. Therefore one might expect relatively little hydrogen discharge from copper substrates, especially at low current densities, but from a steel substrate hydrogen discharges fairly readily. Once the original substrate becomes covered by the alloy coating and takes on a new composition, i.e. that of the deposit, and then the competition between hydrogen and the metal ions present is governed by the relative ease of hydrogen and metal ions discharge from the surface of the alloy deposit. Therefore compositional changes from initially nucleated to bulk deposit may be ascribable to the changing competitive situation especially with respect to metal and hydrogen discharge as the composition of the active surface changes. Changes in the crystallographic structure of the original and new deposited surface might also influence the relative ease of discharge of the ionic species present. For example the results of the present work suggest the possibility of marked epitaxial growth favours sub-potential deposition. Whatever the metal surface one might expect increased competition from hydrogen discharge with increasing current density.

Depth profiles from GDOES investigations of nickel-zinc electrodeposited on copper and steel substrates (see figs. 4-34, 4-35 and 4-36, 4-37, respectively), indicate that the initial substrate surface does indeed play a determining role regarding the compositional properties in the initial stage of deposit formation. Nickel-zinc alloys deposited onto copper substrates have uniform alloy composition along their cross-section as depicted in figures 4-34 and 4-35. This suggests that comparable overpotential conditions for metallic and hydrogen species prevails on either the original copper surface and the newly created nickel-zinc sub-surface. In other words that hydrogen is discharged only

with difficulty at both copper and nickel-zinc surfaces and therefore the composition of the alloy is mainly dependent upon the relative ease of discharge of nickel and zinc.

However, when deposited onto mild steel the composition of the deposits initially appear to be richer in nickel near the interfacial nucleation site as compared with the bulk deposits where the substrate's influence has decreased and uniform composition is observed, see figures 4-36 and 4-37. This compositional gradient is more pronounced in the deposit generated with the lower, i.e. 10 mA cm^{-2}, compared with that produced with the higher current density, i.e. 60 mA cm^{-2} , see figures 4-36 and 4-37, respectively. It is possible that the tendency to produce an initial nickel deposit on steel surfaces is less pronounced at higher current densities due to the fact that a significant proportion of the zinc ions present have enough energy to enable them to overcome any overpotential effects as well as the hydrogen and nickel ions. These findings are most likely a result of the fact that hydrogen and nickel ions are discharged with relative ease at the steel surface as compared to zinc ions. It is a well known fact in industrial circles that during zinc plating of steel hydrogen evolution takes place in the initial stages which stops as soon as the entire surface is covered with zinc [123].

It is noticeable that thicker deposits on both copper and steel substrates take a very similar course, reflecting the nature of the deposit, once the initial surfaces have been, covered (compare figs. 4-34, 4-35 with figs. 4-36, 4-37, respectively). In this connection it is worth noting that a copper strike [124] is often used to overcome problems of hydrogen co-deposition during initial plating when iron is plated with other metals.

Compositional results from depth profiles inferring an influence of the substrate material on the composition of the initially nucleated deposit were confirmed by EDX analyses with the STEM. With the STEM higher spatial resolution was realized, analyses of the cross-sectioned deposits were made with spot sizes of 5 nm diameter, whereas the GDOES results are averaged from 4 mm diameter areas.

Irrespective of the substrate material compositional variations were found with the STEM when analyzing different grains at equal distance from the nucleation site, see table 4-55, and analyses of grains along their growth direction, see table 4-54, indicated localized constituent segregation of nickel-zinc deposits, as found in previous work [102]. Nevertheless, overall compositional variation in the initial nucleating stage was dependent on the substrate, i.e. steel, compared with the bulk nickel-zinc electrodeposit is indicated, since GDOES compositional results are averaged over a larger deposit area.

Other workers reported that nickel-zinc deposition is preceded by a zinc rich layer [125]. On first sight this appears to contradict the results of the present work which is perhaps understandable since experimental conditions were different in the two cases. In both cases the substrate materials were electrochemically similar (i.e. both inert) but the zinc to nickel ratio in solution were significantly different. However on both substrate materials steel and glassy carbon (as used in the cited work [125]) hydrogen discharges fairly readily [7]. The different electrolyte composition reported infers, that the pH value for zinc hydroxide precipitation was lower than for nickel hydroxide precipitation as demonstrated below, which led to initial zinc deposition [125].

$K_L\ Ni(OH)_2 = 1.6 \cdot 10^{-16}$

$K_L\ Ni(OH)_2 = c(Ni^{2+}) \cdot c^2(OH^-)$; $c(Ni^{2+}) = 0.1\ mol \cdot l^{-1}$

$c(OH^-) = 4 \cdot 10^{-8}\ mol \cdot l^{-1}$; pOH = 7.4; pH = 6.6

$K_L\ Zn(OH)_2 = 4.5 \cdot 10^{-17}$

$K_L\ Zn(OH)_2 = c(Zn^{2+}) \cdot c^2(OH^-)$; $c(Zn^{2+}) = 0.05\ mol \cdot l^{-1}$

$c(OH^-) = 3 \cdot 10^{-8}\ mol \cdot l^{-1}$; pOH = 7.5; pH = 6.5

(Solubility products $K_L\ Ni(OH)_2 = 1.6 \cdot 10^{-16}$ and $K_L\ Zn(OH)_2 = 4.5 \cdot 10^{-17}$ taken from the literature [126])

An alternative approach for explaining the occurrence of the initial nickel rich layer found in the present work to that suggested above can therefore be postulated. Thus, that the higher nickel content of the initially nucleated nickel-zinc deposited with the lower current density onto steel compared to that in the alloy deposited with the higher current density may possibly be explained as resulting from the increased hydrogen discharge at the higher current density at the expense of both, nickel and zinc. Whereas, in contrast at the lower current density the hydrogen discharge occurs mainly at the expense of the zinc species higher current density is accompanied by increased hydrogen discharge leading to a higher degree of alkalization in the cathodic layer than would be the case at the lower current density. With the electrolyte used, i.e. *Nickel-Zinc Solution 8*, (see table 3-2), $Ni(OH)_2$ and $Zn(OH)_2$ would form at pH values of 6.1 and 6.4, respectively as shown by the following calculation.

$K_L\ Ni(OH)_2 = 1.6 \cdot 10^{-16}$

$K_L\ Ni(OH)_2 = c(Ni^{2+}) \cdot c^2(OH^-)$; $c(Ni^{2+}) = 1.2\ mol \cdot l^{-1}$

$c(OH^-) = 1.155 \cdot 10^{-8}\ mol \cdot l^{-1}$; $pOH = 7.9$; $pH = 6.1$

$K_L\ Zn(OH)_2 = 4.5 \cdot 10^{-17}$

$K_L\ Zn(OH)_2 = c(Zn^{2+}) \cdot c^2(OH^-)$; $c(Zn^{2+}) = 0.07\ mol \cdot l^{-1}$

$c(OH^-) = 2.54 \cdot 10^{-8}\ mol \cdot l^{-1}$; $pOH = 7.6$; $pH = 6.4$

Thus as the pH-value rises during the onset of deposition, $Ni(OH)_2$ precipitation and adsorption will precede that of $Zn(OH)_2$. At the higher current density a higher degree of hydrogen adsorption will take place and hence, through the faster increase of pH in the cathode film, the ratio of nickel to zinc hydroxides is lower than at the lower current density. If the nickel and zinc deposition takes place through adsorbed mixed nickel-zinc hydroxides or hydroxyl ions, as suggested by previous workers then the amount of zinc deposited would be higher at the higher current density than at the lower current density [36]. This is in line with the observations made in the present work where the nickel content is lower in the initially nucleated layer at the higher current density in comparison to that deposited at the lower current density.

6 Conclusions and Future Work

6. 1 Conclusions

In the present work the nucleation and growth habits of electrocrystallized nickel, alloyed with iron and zinc were investigated. The prominent findings can be summarized as follows:

- The present work has confirmed, integrated and extended the ideas of Finch et al. [2, 51] Piontelli et al. [3] and Pangarov [49, 120, 121] as applicable to alloy deposition. It has shown that a better understanding of alloy deposition, particularly in the initial stages, by considering crystallographic, energy and electrochemical aspects in combination rather than individually.

- A method involving the heavy overplating of deposits prior to preparation for the examination by TEM has been developed for the study of deposit nucleation and growth characteristics.

- The initial substrate influences the initial nucleation and growth characteristics of both nickel-iron and nickel-zinc electrodeposits.

- The effect of substrate on deposit structure persists further into the deposit in the case of nickel-iron than nickel-zinc.

- Nickel-iron deposits tend to have a more uniform composition throughout than those of nickel-zinc.

- Two explanations can be put forward for the changes in the nickel-zinc deposits during its initial stages of growth. One based on the electrochemical characteristics of the system and one based on the upon hydroxide precipitation in the cathodic layer resulting from local pH changes.

- A semi-quantitative model can be used to explain the structure and preferred orientation of nickel-iron alloys deposited.

- A similar explanation has been developed to explain the structure and composition of nickel-zinc deposits.

- A parallel between the established classical metallurgical homogenous nucleation theory [50] and electrodeposition can be drawn to interpret the occurrence or absence of certain crystal orientations in electrodeposits.

- Both nickel-iron and nickel-zinc deposits became coarser grained with increasing thickness. The consequence of this is that the dislocation density is greater in the initial stages than in the latter stages of growth.

- The results of the present work, i.e. evidence of densely packed planes, fine gains associated with high dislocation densities probably explain why deposits obtained by pulse plating, i.e. a technique effectively involving 'repeated initial stage' deposition, have characteristics different to those produced by normal direct current plating.

6. 2 Future Work

- With the findings relating to nucleation interfaces made in the present work, it appears sensible to investigate further the initial stages of deposition with respect to multilayered electrodeposits. Since the present work gives valid evidence that the difference in properties between mono- and multilayered deposits is due to the increased number of interfacial nucleation sites in the latter, nucleation interfaces of electrodeposits could be investigated in more detail, possibly with alternative investigative techniques to consolidate above conclusions. Whereas in the present work particularly *ex situ* techniques, i.e. on the previously deposited coatings, were used the development of similar deposits might be studied with *in situ* techniques, i.e. during electrodeposition, or on extremely thin deposits using more sensitive techniques. Among these voltammetry and scanning tunnelling microscopy appear to be promising.

- However, when using *ex situ* methods, i.e. the approach made in this work, to study similar deposits of different thicknesses appears suitable. This is particularly true for methods applied to the deposit's surface and not its cross-section, e.g. XRD and GDOES.

- It would be useful to study other systems to confirm whether, as found in the present work, the orientation of the initially nucleated layers is generally that with the highest packing density parallel to the surface.

- Further deposition studies involving other substrate/alloy systems having various combinations of electrochemical characteristics would probably give a further insight into the relative importance of the electrochemical and structural factors effecting the initial stage of deposition.

7 References

[1] T. Akiyama, H. Fukushima, "Recent Study on the Mechanism of the Electrodeposition of Iron-group Metal Alloys", *ISIJ International,* **32**, 7 (1992) pp 787-789.

[2] G. I. Finch, H. Wilman, L. Yang, "Crystal Growth at the Cathode", *Disc. Faraday Soc.,* **1** (1947) pp 144-158.

[3] R. Piontelli, C. Guerci, "Influence du matériau cathodique sur l'éléctrodeposition des métaux", in International Committee of Electrochemical Thermodynamics and Kinetics, Proceedings of the 2nd meeting 1950. Libreria Editrice Politecnica Cesare Tamburini Milano (1951) pp 149-159.

[4] C. E. Mortimer: Das Basiswissen der Chemie, 5th edition. Georg Thieme Verlag, Stuttgart, Germany (1987) pp 335-337.

[5] E. Raub, K. Müller: Fundamentals of Metal Deposition. Elsevier, Amsterdam, Netherlands (1967).

[6] F. Lowenheim: Modern Electroplating, 3rd edition. Electrochemical Society Inc., New York, USA (1973).

[7] J. M. West: Electrodeposition and Corrosion Processes, 2nd edition. Van Nostrand Reinhold Company, London, UK (1970) p 119.

[8] R. Winand, "Electrocrystallization - Theory and Application", *Hydrometallurgy,* **29**, 1-3 (1992) pp 567-598.

[9] D. Ross, "Symposium Report: Current Developments in Surface Finishing in the UK", *Trans. IMF,* **74**, 1 (1996) pp 2-3.

[10] S. Swathirajan, "Potentiodynamic and Galvanostatic Stripping Methods for Characterization of Alloy Electrodeposition Process and Product", *J. Electrochem. Soc.*, **133** (1986) pp 671-680.

[11] R. Brdicka: Grundlagen der physikalischen Chemie, 15th edition. Deutscher Verlag der Wissenschaften, Berlin, Germany (1981) p 636.

[12] A. Brenner: Electrodeposition of Alloys, Principles and Practice, Vol. 2. Academic Press, New York, USA (1963).

[13] H. Dahms, "The Influence of Hydrolysis on the Deposition and the Co-Deposition of Iron-Group Metals (Fe, Co, Ni) at the Dropping Mercury Electrode", *J. Electroanal. Chem.*, **8** (1964) pp 5-12.

[14] H. Dahms, I. M. Croll, "The Anomalous Codeposition of Nickel-Iron Alloys", *J. Electrochem. Soc.*, **112**, 8 (1965) pp 771-775.

[15] J. Bielinski, J. Przyluski, "Selected Problems in the Continuous Electrodeposition of Ni-Fe Alloys", *Surf. Technol.*, **9**, 1 (1979) pp 53-64; "Modification of Solution Composition in the Electrochemical Deposition of Ni-Fe Alloy Films", *Surf. Technol.*, **9**, 1 (1979) pp 65-75.

[16] J. Horkans, "On the Role of Buffers and Anions in NiFe Electrodeposition", *J. Electrochem. Soc.*, **126**, 11 (1979) pp 1861-1867; "Effect of Plating Parameters on Electrodeposited NiFe", *J. Electrochem. Soc.*, **128**, 1 (1981) pp 45-49.

[17] E. Beltowska-Lehmann, A. Riesenkampf, "Investigation of the Electrodeposition Kinetics of Permalloy Thin Films using a Rotating Disc Electrode ", *Surf. Technol.*, **11**, 5 (1980) pp 349-355.

[18] L. T. Romankiw, "pH-Changes at the Cathode during Electrolysis of Ni, Fe, Cu and Their Alloys and a Simple Technique for Measuring pH-Changes at the Electrodes", in the Electrochemical Society Proceedings of the Symposium on "Electrodeposition Technology, Theory and Practice", L. T. Romankiw and D. R. Turner, eds., Vol. 87-17 (1987) pp 301-325.

[19] S. Hessami, C. W. Tobias, "A Mathematical Model for Anomalous Codeposition of Nickel-Iron on a Rotating Disc Electrode", *J. Electrochem. Soc.,* **136**, 12 (1989) pp 3611-3616.

[20] J. O'M. Bookris, D. Drazic, A. R. Despic, "The Electrode Kinetics of the Deposition and Dissolution of Iron", *Electrochim. Acta,* **4** (1961) pp 325-361.

[21] J. Matulis, R. Slizys, "On some Characteristics of Cathodic Processes in Nickel Deposition", *Electrochim. Acta,* **9** (1964) pp 1177-1188.

[22] D. L. Grimmett, M. Schwarz, K. Nobe, "Pulsed Electrodeposition of Iron-Nickel Alloys", *J. Electrochem. Soc.,* **137**, 11 (1990) pp 3414-3418.

[23] E. Raub, E. Walter, "Galvanische Niederschläge von Nickel-Eisen-Legierungen", *Zeitschrift Elektrochemie,* **41**, 3 (1935) pp 169-174.

[24] C. E. Lehmberg, "Investigations into a Nickel-Iron Electrolyte and its Deposits", unpublished results.

[25] W. Alberth, A. F. Bogenschütz, J. L. Jostan, A. von Krusenstjern, "Die galvanische Abscheidung von Superinvar-Legierungen", *Galvanotechnik,* **66**, 4 (1975) pp 291-300.

[26] G. H. Cockett, E. S. Spencer-Timms, "Variation of Composition with Thickness in Thin Electrodeposited Films of Nickel-Iron Alloys", *J. Electrochem. Soc.,* **108**, 9 (1961) pp 906-908.

[27] F. H. Edelman, "Controlled Electrode Potential Deposition of Nickel-Iron Films", *J. Electrochem. Soc.,* **109** (1962) p 440.

[28] M. E. Henstock, E. S. Spencer-Timms, "The Composition of Thin Electrodeposited Alloy Films with Special Reference to Nickel-Iron", *Trans. Inst. Met. Finish.,* **40** (1963) pp 179-185.

[29] W. O. Freitag, J. S. Mathias, G. DiGuilio, "The Electrodeposition of Nickel-Iron Phosphorous Thin Films for Computer Memory Use", *J. Electrochem. Soc.,* **111**, 1 (1964) pp 35-39.

[30] H. Dahms, "Composition Gradients in Electroplated Permalloy Films", *Electrochem. Technol.,* **4**, 11-12 (1966) pp 530-532.

[31] D. R. Eastham, P. J. Boden, M. E. Henstock, "Factors Affecting the Composition Gradient in Electrodeposited Permalloy Films", *Trans. IMF,* **46** (1968) pp 37-43.

[32] I. Ohno, "The Electroplating of Fe-Ni Films", *J. Met. Finish. Soc. Jpn.,* **23** (1972) pp 163-176.

[33] Z. Kovac, "The Effect of Superimposed A.C. on D. C. in Electrodeposition of Ni-Fe Alloys", *J. Electrochem. Soc.,* **118**, 1 (1971) pp 51-57.

[34] B. S. Sheshadri, V. Koppa, B. S. Prakash, S. M. Mayanna, "The Effect of Superposition of an Alternating Current on a Direct Current on the Electrodeposition of Ni-Fe Alloys", *Surf. Technol.,* **13** (1981) pp 111-117.

[35] M. Pushpavanam, K. Balakrishnan, "Internal Stress and Hydrogen Permeability of Zinc-Nickel Alloy Electrodeposits", *Trans. IMF,* **74**, 1 (1996) pp 33-35.

[36] A. Knödler, "Über den Einfluß von Zink auf die elektrolytische Abscheidung des Nickels", *Metalloberfläche,* **21**, 11 (1967) pp 321-328.

[37] E. Raub, A. Knödler, A. Disam, H. Kawase, "Der Einfluß von Elektrolytzusätzen auf die Vorgänge in der Phasengrenzschicht", *Metalloberfläche,* **23**, 10 (1969) pp 293-302.

[38] A. Knödler, "Über den Einfluß von Zink und Cadmium auf die elektrolytische Abscheidung des Kobalts und die Bildung von Kobalt-Zink und Kobalt-Cadmium-Legierungen", *Surf. Technol.,* **4** (1976) pp 441-463.

[39] K. Higashi, H. Fukushima, T.Urakawa, T. Adaniya, K. Matsudo, "Mechanism of the Electrodeposition of Zinc Containing a Small Amount of Cobalt", *J. Electrochem. Soc.,* **128**, 10 (1981) pp 2081-2085.

[40] H. Fukushima, T. Akiyama, J.-H. Lee, M. Yamaguchi, K. Higashi, "Mechanism of the Electrodeposition of Zn with Iron-group Metals from Sulfate Baths", *J. Met. Finish. Soc. Jpn.,* **33** (1982) pp 574-578.

[41] L. Felloni, R. Fratesi, E. Quadrini, G. Roventi, "Electrodeposition of Zinc-Nickel Alloys from Chloride Solution", *J. Appl. Electrochem.,* **17**, 3 (1987) pp 574-582.

[42] M. F. Mathias, T. W. Chapman, "The Composition of Electrodeposited Zinc-Nickel Coatings", *J. Electrochem. Soc.,* **134**, 6 (1987) pp 1408-1416.

[43] M. F. Mathias, T. W. Chapman, "A Zinc-Nickel Alloy Electrodeposition Kinetics Model from Thickness and Composition Measurement on the Rotating Disc Electrode", *J. Electrochem. Soc.,* **137**, 1 (1990) pp 102-111.

[44] M. F. Mathias, C. M. Villa, T. W. Chapman, "A Model of Zinc-Nickel Alloy Electrodeposition in an industrial-scale Cell", *J. Appl. Electrochem.,* **20**, 1 (1990) pp 1-10.

[45] V. G. Roev, N. V. Gudin, "New Aspects of Zinc-Nickel Alloy Co-deposition", *Trans. IMF,* **74**, 5 (1996) pp 153-157.

[46] W. Hume-Rothery: Electrons, Atoms, Metals, and Alloys, 3rd edition. Dover Publications, New York, USA (1955) p 284.

[47] F. C. Frank, "The Influence of Dislocations on Crystal Growth", *Disc. Faraday Soc.,* **5** (1949) pp 48-54.

[48] H. Fischer, "Grundsätzliches zur Elektrokristallisation im Vergleich zum Aufdampfen von Metallen", 16th William Blum Lecture Feb. 1976. Conference Proceedings of the 62nd American Electroplaters Society, Toronto, Canada, June 23 (1975).

[49] N. A. Pangarov, "The Crystal Orientation of Electrodeposited Metals", *Electrochim. Acta,* **7** (1962) pp 139-146.

[50] J. W. Martin: Precipitation Hardening. Pergamon Press Ltd., London, UK (1968) pp 15-18.

[51] G. I. Finch, C. H. Sun, "An Electron Diffraction Study of the Structure of Electrodeposited Metals", *Trans. Faraday Soc.,* **32** (1936) pp 852-863.

[52] G. I. Finch, A. L. Williams, "The Structure of Electrodeposited Nickel", *Trans. Faraday Soc.,* **33** (1937) pp 564-569.

[53] K. C. Chan, N. S. Qu, D. Zhu, "Quantitative Texture Analysis in Pulse Reverse Current Electroforming of Nickel", to be published.

[54] F. Kotzia, C. Kollia, N. Spyrellis, "Influence of Butyne-2-diol 1,4 in Nickel Electrocrystallization under Pulse Reversed Current regime", *Trans. IMF*, **71**, 1 (1993) pp 34-36.

[55] J. Macheras, D. Vouros, C. Kollia, N. Spyrellis, "Nickel Electrocrystallization: Influence of Unsaturated Organic Additives on the Mechanism of Orientated Crystal Growth", *Trans. IMF*, **74**, 2 (1996) pp 55-58.

[56] U. Cohen, F. B. Koch, R. Sard, "Electroplating of Cyclic Multilayered Alloy (CMA) Coatings", *J. Electrochem. Soc.,* **130**, 10 (1983) pp 1987-1995.

[57] S. Menezes, D. P. Anderson, "Wavelength-Property Correlation in Electrodeposited Ultrastructured Cu-Ni Multilayers", *J. Electrochem. Soc.,* **137**, 2 (1990) pp 440-444.

[58] D. M. Tench, J. T. White, "Considerations in Electrodeposition of Compositionally Modulated Alloys", *J. Electrochem. Soc.,* **137**, 10 (1990) pp 3061-3066.

[59] D. S. Lashmore, M. P. Dariel, "Electrodeposited Cu-Ni Textured Superlattices", *J. Electrochem. Soc.,* **135**, 5 (1988) pp 1218-1221.

[60] J. Yaholm, O. Zadok, U.S. Patent 4,652,352,348 (1987).

[61] J. Yaholm, O. Zadok, "Formation of Composition-Modulated Alloys by Electrodeposition", *J. Mater. Sci.,* **22** (1987) pp 499-503.

[62] M. Svensson, U. Wahlström, G. Holmbon, "Compositionally Modulated Cobalt-Tungsten Alloys Deposited from Single Ammoniacal Electrolyte", to be published.

[63] V. A. Zabludovsky, E. F. Shapenko, "The Obtaining of Cobalt Multilayers by Programme-controlled Pulse Current", *Trans. IMF*, **75**, 5 (1997) pp 203-204.

[64] Metals Handbook, 9th edition Vol. 10: Materials Characterization. "Glossary of Terms", Ohio, USA (1986) pp 672-684.

[65] E. Langiewka, A. Budniok, "In Situ X-ray Study of the Structure of electrolytic Coatings", *Surf. Coat. Technol.,* **27**, 1 (1986) pp 57-66.

[66] Z. Chen, J. Li, E. Wang, "In Situ Scanning Tunnelling Microscopic Study of Nickel Electrodeposition on HOPG", *J. Electroanal. Chem.,* **373** (1994) pp 83-87.

[67] A. Gonzáles-Martín, R. C. Bhardwaj, J. O'M. Bookris, "Some in situ STM Contributions to the Characterization of electrochemical Systems", *J. Applied Electrochem.,* **21**, 6 (1993) pp 531-546.

[68] R. S. Robinson, "Real-time Scanning Tunnelling Microscopic Study of Surfaces under Active Chemical Control", *J. Microsc.,* **152**, 2 (1988) pp 541-546.

[69] M. Pushvanam, K. Balakrishnan, L. R. Sharma, "Electrodeposition of Zinc-Nickel Alloy: A Voltammetric Study", in 4th International Symposium on Frontiers of Electrochemistry (Science & Technology), Madras, India, 14-15 Nov. 1989, *Trans. Saest,* **24** (1989) p 3.

[70] P. C. Andriacos, J. Tabib, L. T. Romanikiw, "Stripping Voltammetry of Nickel-Iron Films Electrodeposited on Platinum Using a Rotating Disc Electrode", *J. Electrochem. Soc.,* **135**, 5 (1988) pp 1172-1174.

[71] W. J. Lorenz, E. Schmidt, G. Staikow, H. Bort, "Metal Ion Adsorption and Electrocrystallization", in Faraday Symposia of the Chemical Society, No 12. Chaucer Press, Bungay, Suffolk, Great Britain (1978) pp 14-23.

[72] A. Bewick, J. Jovicevic, B. Thomas, "Phase Formation in the Underpotential Deposition of Metals", in Faraday Symposia of the Chemical Society, No 12. Chaucer Press, Bungay, Suffolk, Great Britain (1978) pp 24-35.

[73] M. Y. Abyaneh, M. Fleischman, "The Electrocrystallization of Nickel", *Trans. IMF.*, **58**, 3 (1980) pp 91-96.

[74] Buehler Ltd.: BUEHLER DIALOG ™ Microstructural Analysis Reference Manual. Lake Bluff, Illinois, USA (1989).

[75] W. Canning: The Canning Handbook Surface Finishing Technology, 23rd edition. Spon, New York, USA (1982).

[76] DIN 50957, "Galvanisierungsprüfung mit der Hullzelle" (1978).

[77] W. Nohse: Die Untersuchung galvanischer Bäder in der HULL-ZELLE, 3rd edition. Eugen G. Leuze Verlag, Saulgau, Germany (1984).

[78] Reference Handbook: The Sparcatron Manual for E. D. M. Operators. Sparcatron Ltd., Glouster, UK.

[79] Gatan Ltd.: Instruction Manual for Precision Dimple Grinder MODEL 656/3. Gatan Ltd., Corby, Northants, UK.

[80] Gatan Ltd.: Instruction Manual for Precision Ion Polishing System MODEL 691 PIPS™. Gatan Ltd., Corby, Northants, UK.

[81] W. Dohmke: Werkstoffkunde und Werkstoffprüfung, 10th edition. Giradet, Düsseldorf, Germany (1986) p 376.

[82] Published with kind permission of Dr. D. B. Lewis, Materials Research Institute, Sheffield Hallam University, Sheffield, UK.

[83] M. Rühe, "Transmission Electron Microscopy", in Metals Handbook, 9 th edition Vol. 9, "Metallography and Microstructures". American Society for Metals, Ohio, USA (1985) pp 103-122.

[84] M. Ives, D. B. Lewis, C. E. Lehmberg, "Depth Profile Analysis of Multilayer Ni-Fe Alloy Coatings by Glow Discharge Optical Emission Spectroscopy (GDOES) and Energy Dispersive X-ray (EDX) Linescan - a Comparative Study", *Surf. Interface Anal.*, **25**, 3 (1997).

[85] Instruction Manual: Quantitative Electron Probe Microanalysis. Link Analytical Ltd., High Wycombe, UK.

[86] PV9900 EDAX, General User's Guide 9 499.140.50 000, April 1991, Version 23.

[87] B. D. Cullity: Elements of X-Ray Diffraction. Addison-Wesley Publishing Company Inc., Massachusetts, USA (1959).

[88] Hanawalt Search Manual, Powder Diffraction File, JCPDS, International Centre for Data Diffraction Data. Swarthmore, Pennsylvania, USA (1992).

[89] Software ADP (Automated Powder Diffraction) version 3.6. Philips Analytical X-Ray, Almelo, Netherlands.

[90] C. S. Barrett: Structure of Metals, 2nd edition. Mc Graw-Hill Book Company, New York, USA (1952).

[91] J. B. Cohen, C. N. J. Wagner, "Determination of Twin Fault Probabilities from the Diffraction Patterns of fcc Metals and Alloys", *J. Appl. Phys.*, **33**, 6 (1962) pp 2073-2077.

[92] S. Kadlec, J. Musil, W. D. Münz, G. Håkanson, J. E. Sundgren, "Reactive Deposition of TiN Films Using an Unbalanced Magnetron", *Surface Coating Technol.*, **39/40** (1989) pp 487-497.

[93] D. B. Lewis, F. B. Pickering, "Development of Recrystallization Textures in Ferritic Stainless Steels and their Relationship to Formability", *Metals Technology*, **10** (1983) pp 264.

[94] K. W. Andrews: Physical Metallurgy, Techniques and Applications, Vol. 1. George Allen & Unwin Ltd. (1973) p 219.

[95] International Tables for X-Ray Crystallography, Vol. 3., J. A. Ibers, W. C. Hamilton eds., Kynoch Press Birmingham, UK (1974) pp 233-235.

[96] Philips Instruction Manual: PW1752/00 Monochromator, PW1753/00 Spare Crystal for PW1752/00. Reference Leaflet 4822 870 23311 890808.

[97] International Tables for X-Ray Crystallography, Revised and Supplementary Tables, Vol. 4. J. A. Ibers, W. C. Hamilton eds., Kynoch Press Birmingham, UK (1974) pp 71-97.

[98] International Tables for X-Ray Crystallography, Revised and Supplementary Tables, Vol. 4. J. A. Ibers, W. C. Hamilton eds., Kynoch Press Birmingham, UK (1974) pp 148-151.

[99] R. Kuzel, Jr., R. Cerny, V. Valvoda, M. Blomberg, M. Merisalo, S. Kadlec, "Complex XRD microstructural studies of hard coatings applied to PVD-deposited TiN films. Part II. Transition from porous to compact films and microstructural inhomogeneity of the layers", *Thin Solid Films*, **268** (1995) pp 72-82.

[100] K. W. Andrews, D. J. Dyson, S. R. Keown: Interpretation of Electron Diffraction Patterns. Hilger Watts Ltd., London, UK (1967).

[101] S. Hadian, "Control of Electrodeposit Properties of Nickel and Nickel Alloy by Pulse Plating", MPhil. Thesis, Sheffield Hallam University, UK (1980) p 112.

[102] D. B. Lewis, C. E. Lehmberg, G. W. Marshall, "The Structure of High Nickel Content Zinc-Nickel Electrodeposits from Sulphate Baths", to be published.

[103] Table of Periodic Properties of the Elements. Sargent-Welch Scientific Company, 7300 Linder Avenue, Skokie, Illinois 60077, USA (1980) p 2.

[104] H. V. Venkasetty, "Electrodeposition of Thin Magnetic Permalloy Films", *J. Electrochem. Soc.*, **117**, 3 (1970) pp 403-407.

[105] R. J. Clauss, R. A. Tremmel, R. W. Klein, "Decorative Nickel-Iron Alloy Electrodeposits: Present Status and Future Possibilities," *Trans. Inst. Metal Finish.*, **53** (1975) pp 22-27.

[106] D. L. Grimmett, M. Schwartz, K. Nobe, "A Comparison of DC and Pulsed Fe-Ni Alloy Deposits", *J. Electrochem. Soc.*, **140**, 4 (1993) pp 973-978.

[107] R. Sivakumar, T. L. Rama Char, "Electrodeposition of ternary alloys of nickel-iron-cadmium from the sulphate bath", *Metal Finishing,* **18**, 206 (1972) pp 65-70.

[108] L. Domnikow, "Electrodeposition of Iron from Neutral Solutions", *Metal Finishing,* **69**, 12 (1971) pp 40-43.

[109] K. Nakamura, T. Hayashi, "Effect of Addition Agents on the Electrodeposition of Ni-Fe Alloys", *Bull. Univ. of Osaka Pref.*, **32**, 2 (1983) pp 127-137.

[110] B. N. Popov, K.-M. Yin, R. E. White, "Galvanostatic Pulse and Pulse Reverse Plating of Nickel-Iron Alloys from Electrolytes Containing Organic Compounds on a Rotating Disc Electrode", *J. Electrochem. Soc.*, **140**, 5 (1993) pp 1321-1330.

[111] M. Hansen, K. Anderko: Constitution of Binary Alloys. Mc Graw-Hill Book Company Inc., New York, USA (1958) pp 677-684.

[112] E. Raub, K. Müller: Fundamentals of Metal Deposition. Elsevier, Amsterdam, Netherlands (1967) p 144.

[113] J. Amblard, M. Froment, "New Interpretation of Texture Formation in Nickel Electrodeposits", in Faraday Symposia of the Chemical Society, No 12; Electrocrystallisation, Nucleation and Phase Formation, The Electrochemical Society, London, UK (1977) pp 136-144.

[114] S. R. Rajagopalan, "Electrodeposition of Nickel-Zinc Alloys", *Metal Finishing,* **70**, 12 (1972) pp 52-58.

[115] E. Raub, F. Elser, "Der Aufbau galvanischer Legierungsniederschläge (XI.)*. Die Nickel-Zink-Legierungen", *Metalloberfläche,* **11**, 5 (1957) pp 165-168.

[116] M. Hansen, K. Anderko: Constitution of Binary Alloys. Mc Graw-Hill Book Company Inc., New York, USA (1958) pp 1059-1062.

[117] Metals Handbook, 9th edition Vol. 10: Materials Characterization. "Glossary of Terms", Ohio, USA (1986) pp 673.

[118] W. Dohmke: Werkstoffkunde und Werkstoffprüfung, 10th edition. Giradet, Düsseldorf, Germany (1986) p 23.

[119] C. S. Barrett: Structure of Metals, 2nd edition. Mc Graw-Hill Book Company, New York, USA (1952) p 36.

[120] N. A. Pangarov, "On the Crystal Orientation of Electrodeposited Metals", *Electrochim. Acta,* **9** (1964) pp 721-726.

[121] N. A. Pangarov, "Preferred Orientations in Electro-Deposited Metals", *J. Electroanal. Chem.,* **9** (1965) pp 70-85.

[122] J. Schramm, O. Vaupel, "Röntgenographische Untersuchungen an dem Dreistoffsystem Ni-Cu-Zn", *Metallwirtschaft,* **15**, 31 (1936) pp 723-726.

[123] Candidate's practical work experience.

[124] B. Gaida: Galvanotechnik in Frage und Antwort, 4th edition. Eugen G. Leuze Verlag, Saulgau, Germany (1983) p 210.

[125] M. Eyraud, Z. Hanane, J. Crousier, "Galvanostatic Study of the Electrocrystallisation of Binary Nickel Base Alloys. 1- Zinc -Nickel Alloy on Glassy Carbon", to be published.

[126] C. E. Mortimer: Das Basiswissen der Chemie, 5th edition. Georg Thieme Verlag, Stuttgart, Germany (1987) pp 402.

Structure of Nickel-Iron and Nickel-Zinc Electrodeposits

Volume II

Claudia Erdmuthe Lehmberg

A thesis submitted in partial fulfilment of the requirements of Sheffield Hallam University for the degree of Doctor of Philosophy

November 1998

8 Tables and Figures

8. 1 Tables

Table 2-1: Comparison of Investigative Techniques Used in Present Work.

	GDOES	XRD	TEM				SEM		
			electron diffraction SADP	imaging mode BF	imaging mode DF	STEM/ EDX	imaging mode SEI	imaging mode BSI	EDX
Parameters									
Excitation	ions	X-rays	e^-	e^-	e^-	e^-	e^-	e^-	e^-
Transmission	*hv* (optical)	X-rays	e^-	e^-	e^-	X-rays	secondary e^-	backscattered e^-	X-rays
Information									
Nucleation and Growth	no	no	cross-section only	cross-section only	cross-section only	cross-section only	no	no	no
Composition	yes	no	no	no	no	yes	no	no	yes
Texture	no	surf. texture	local texture	no	local texture	no	no	no	no
Overall Structure	no	no	no	local	local	no	surf. topography	atomic number contrast	no
Grain Size	no	no	no	yes	yes	no	no	no	no
Dislocation Density	no	no	no	yes	yes	no	no	no	no
Depth Profile									
Composition	yes	no	no	no	no	cross-section only	no	no	cross-section only
Texture	no	yes	cross-section only	no	cross-section only	no	no	no	no
Application	ex situ	ex situ, also in situ [65]	ex situ	ex situ	ex situ	ex situ	ex situ	ex situ	ex situ

Table 2-2: Comparison of Alternative Investigative Techniques not Used in Present Work.

	XRF	AES	STM	Voltammetry
Parameters				
Excitation	X-rays	e^-	voltage	(i) voltage (ii) current
Transmission	fluorescent radiation	e^-	tunnelling e^-	(i) current (ii) voltage
Information				
Nucleation and Growth	no	no	no	indirect
Composition	no	yes	no	no
Texture	no	no	no	no
Overall Structure	no	no	surf. topography	no
Grain Size	no	no	no	no
Dislocation Density	no	no	no	no
Depth Profile	no	no	no	no
Composition	no	no	no	no
Texture	no	no	no	no
Application	ex situ	ex situ	ex situ, also in situ [66, 67, 68].	in situ

Table 3-1: Composition and Working Parameters of Nickel-Iron Electrolytes.

Component		Solution 1 mol l^{-1}	2 mol l^{-1}	3 mol l^{-1}	4 mol l^{-1}
Nickel(II)-sulphate	$NiSO_4*6H_2O$	0.81	0.45	0.69	0.69
Nickel(II)-chloride	$NiCl_2*6H_2O$	0.21	0.21	0.21	0.21
Boric acid	H_3BO_3	0.48	0.48	0.48	0.48
Ferrous(II)-sulphate	$FeSO_4*7H_2O$	0.1	0.47	0.29	0.29
Citric acid	$C_3H_4(OH)(COOH)_3*H_2O$	0.003	0.003	0.003	0.003
Sodium lauryl sulphate	$NaC_{12}H_{25}SO_4$	-	0.002	0.002	-
Saccharine	$C_6H_4CONHSO_2$	-	-	0.003	0.003
Ascorbic acid	$C_6H_8O_6$	-	-	0.003	0.003

Working Condition	Solution 1	2	3	4
agitation	N_2-agitation 1. uncontrolled 2. 1 l min^{-1} 3. 3 l min^{-1} 4. 6 l min^{-1}	magnetic stirrer on hot plate; speed 7	submersible magnetic stirrer in water bath: speed: 7; reverse mode: 10	N_2-agitation: 1 l min^{-1}

Table 3-2: Composition and Working Parameters of Nickel-Zinc Electrolytes.

Component		Solution							
		1	2	3	4	5	6	7	8
		mol l^{-1}	mol l^{-1}	mol l^{-1}	mol l^{-1}	mol l^{-1}	mol l^{-1}	mol l^{-1}	mol l^{-1}
Nickel(II)-sulphate	$NiSO_4*6H_2O$	0.57	0.57	0.57	0.57	0.57	0.57	1.11	1.2
Zinc(II)-sulphate	$ZnSO_4*7H_2O$	0.7	0.7	0.7	0.7	0.7	0.7	0.16	0.07
Boric acid	H_3BO_3	0.32	0.32	0.32	0.64	0.64	0.64	0.32	0.32
p-toluene sulfonic acid	$C_7H_8O_3S*H_2O$	0.01	0.01	-	-	0.01	0.01	0.01	0.01
Sodium lauryl sulphate	$NaC_{12}H_{25}SO_4$	-	0.002	-	-	-	0.002	-	-

Working	Solution							
Condition	1	2	3	4	5	6	7	8
Anodes	nickel	nickel	nickel	nickel	nickel	nickel	inert	inert
pH	3 (*/**)	3 (**)	3 (**)	~2 (***)	~2 (***)	~2 (***)	3 (**)	3 (**)
Volume	500 ml	500 ml	500 ml	500 ml	500 ml	500 ml	1500 ml	1500 ml
Agitation	a); b)	a); b)	a)	a); b)	a); b)	a)	b)	b)

*pH-value adjusted with ammonia solution
**pH-value adjusted with sodium hydroxide solution
***no pH-value adjusted; solution had ~2
agitation: a) submersible magnetic stirrer: speed 5, reverse mode 5
b) agitated with nitrogen gas; 1.5 l min^{-1}

Table 3-3: Description of Degreasing Agent for Copper and Brass.

Trade name	*KLEENAX*
Manufacturer	Canning (Birmingham, UK)
Remarks	Contains cyanide
Concentration	125 g l^{-1}
Operating parameters	i_c: 30 mA cm^{-2} *T*: 40 °C *t*: 1 - 2 min

Table 3-4: Description of Degreasing Agent for Steel.

Trade name	*Activax*
Manufacturer	Canning (Birmingham, UK)
Remarks	Cyanide-free
Concentration	50 g l^{-1}
Operating parameters	i_a: 30 mA cm^{-2} *T*: 70 °C *t*: 30 s

Table 3-5: Description of Activating Agent.

Trade name	*Activator No. 2*
Manufacturer	Lea Ronal (Buxton, UK)
Concentration	50 g l^{-1}
Operating parameters	*T*: room temperature *t*: 1 min

Table 3-6: Composition and Operating Parameters of the Cyanide Copper Electrolyte.

Constituents	Concentration [g l^{-1}]
CuCN	40
KCN	66
K_2CO_3	39
$NaKC_4H_4O_6$	60

T	40-60 °C
Anodes	Electrolytic Copper
Anode:Cathode	1:2
i_c	10 mA cm^{-2}

Table 3-7: Composition and Operating Parameters of the Acid Copper Electrolyte.

Constituents	Concentration [g l^{-1}]
$CuSO_4 \cdot 5H_2O$	200
H_2SO_4	50

T	40 °C
Anodes	Electrolytic Copper
Anode:Cathode	1:2
i_c	100 mA cm^{-2}

Table 3-8: *K* Emission Lines (Weighted Mean) [89] and Mass Absorption Coefficients K_{edge} [90].

Element	Atomic Number	K_α [nm]	K_β [nm]	K_{edge} [nm]
Cobalt	27	0.179026	0.162080	0.1608
Nickel	28	...	...	0.1488
Copper	29	0.154186	0.139222	0.1380
Molybdenum	42	0.071073	0.063229	0.061977

Table 3-9: Steps of Angular Ranges to Diffract Planes of fcc Nickel-Iron.

Angular range °2θ	Reflection
41.4 - 46.5	{111}
49 - 53	{200}
72 - 78	{220}
87 - 93	{311}
132 - 149	{331}

Table 3-10: Steps of Angular Ranges to Diffract Planes of bcc Nickel-Iron.

Angular range 2θ	Reflection
41.4 - 46.5	{110}
62 - 68	{200}
79 - 85	{211}
112 - 120	{310}
132 - 149	{222}

Table 4-1: Composition and Visual Evaluation of Quiescent Nickel-Iron Solution 1 Employing 1A Cell Current.

current density [mA cm^{-2}]	composition mass-% Ni	mass-% Fe	observation deposit appearance
4	73.1	26.9	dull; dark, brownish-grey; no pitting
10	69.7	30.3	dull; brownish-grey; slightly pitted
15	71.1	28.9	dull; brownish-grey; slightly pitted
20	71.0	29.0	dull; brownish-grey; pitted
30	76.3	23.7	dull; brownish-grey; pitted
40	78.3	21.7	dull; brownish-grey; pitted
50	83.1	16.9	dull; brownish-grey; pitted

Table 4-2: Composition and Visual Evaluation of Quiescent Nickel-Iron Solution 1 Employing 3A Cell Current.

current density [mA cm^{-2}]	composition mass-% Ni	mass-% Fe	observation deposit appearance
12	71.6	28.4	dull; brownish-grey; slightly pitted
30	76.3	23.7	dull; brownish-grey; slightly pitted
60	81.6	18.4	dull; brownish-grey; slightly pitted
90	84.2	15.8	dull; brownish-grey; slightly pitted
150	87.1	12.9	dull; brownish-grey; pitted

Table 4-3: Composition and Visual Evaluation of Quiescent Nickel-Iron Solution 1 Employing 7A Cell Current.

current density [mA cm^{-2}]	composition mass-% Ni	mass-% Fe	observation deposit appearance
52.5	83.6	16.4	dull; brownish-grey; slightly pitted
140	88.5	11.5	dull; brownish-grey; slightly pitted
210	87.7	12.3	dull; brownish-grey; pitted
350	90.2	9.8	dull; brownish-grey; pitted

Table 4-4: Composition and Visual Evaluation of Nitrogen Agitated Nickel-Iron Solution 1 Employing 1A Cell Current.

current density [mA cm^{-2}]	composition mass-% Ni	mass-% Fe	observation deposit appearance
4	67.7	30.3	dull; yellowish-grey; no pitting
10	64.5	35.5	dull; yellowish-grey; no pitting
15	64.6	35.4	dull; yellowish-grey; slightly pitted
20	65.4	34.6	dull; yellowish-grey; pitted
30	61.4	38.6	dull; yellowish-grey; pitted
40	57.5	42.5	dull; yellowish-grey; pitted
50	59.1	40.9	dull; brownish-grey; pitted

Table 4-5: Composition and Visual Evaluation of Nitrogen Agitated Nickel-Iron Solution 1 Employing 3A Cell Current.

current density [mA cm^{-2}]	composition mass-% Ni	mass-% Fe	observation deposit appearance
15	60.3	39.7	dull; yellowish-grey; slightly pitted
30	56.7	43.3	dull; yellowish-grey; slightly pitted
60	53.9	46.1	dull; grey; slightly pitted
90	56.6	43.4	dull; grey; slightly pitted
150	58.6	41.4	dull; grey; slightly pitted

Table 4-6: Composition and Visual Evaluation of Nitrogen Agitated Nickel-Iron Solution 1 Employing 7A Cell Current.

current density [mA cm^{-2}]	composition mass-% Ni	mass-% Fe	observation deposit appearance
52.5	65.7	34.3	dull; yellowish-grey; slightly pitted
140	62.8	37.2	dull; grey; slightly pitted
210	64.8	35.2	dull; grey; slightly pitted
350	71.9	28.1	dull; grey; slightly pitted

Table 4-7: Composition and Visual Evaluation of Quiescent Nickel-Iron Solution 4 Employing 1A Cell Current.

current density [mA cm^{-2}]	composition mass-% Ni	mass-% Fe	observation deposit appearance
4	53.2	46.8	shiny; silverish-grey; smooth
5	51.5	48.5	shiny; silverish-grey; smooth
7.5	48.1	51.9	shiny; silverish-grey; smooth
10	45.8	54.2	shiny; silverish-grey; smooth
12.5	45.8	54.2	shiny; silverish-grey; smooth
15	45.3	54.7	shiny; silverish-grey; smooth
20	45.8	54.2	shiny; silverish-grey; smooth
30	47.3	52.7	shiny; silverish-grey; slightly pitted
40	50.9	49.1	shiny; silverish-grey; slightly pitted
50	53.5	46.5	slightly dull; silverish-grey; slightly pitted

Table 4-8: Composition and Visual Evaluation of Quiescent Nickel-Iron Solution 4 Employing 3A Cell Current.

current density [mA cm^{-2}]	composition mass-% Ni	mass-% Fe	observation deposit appearance
12	49.9	50.1	shiny; silverish-grey; smooth
15	49.2	50.8	shiny; silverish-grey; smooth
22.5	48.6	51.4	shiny; silverish-grey; smooth
30	51.8	48.2	shiny; silverish-grey; slightly pitted
37.5	51.4	48.6	shiny; silverish-grey; slightly pitted
45	53.8	46.2	shiny; silverish-grey; slightly pitted
60	55.9	44.1	dull; silverish-grey; slightly pitted
90	60.6	39.4	dull; silverish-grey; slightly pitted
120	64.2	35.8	dull; silverish-grey; slightly pitted
150	68.3	31.7	dull; silverish-grey; slightly pitted

Table 4-9: Composition and Visual Evaluation of Quiescent Nickel-Iron Solution 4 Employing 7A Cell Current.

current density [mA cm^{-2}]	composition		observation
	mass-% Ni	mass-% Fe	deposit appearance
28	54.1	45.9	shiny; silverish-grey; smooth
35	54.4	45.6	shiny; silverish-grey; smooth
52.5	58.9	41.1	shiny; silverish-grey; smooth
70	61.4	38.6	dull; silverish-grey; slightly pitted
87.5	64.4	35.6	dull; silverish-grey; slightly pitted
105	66.1	33.9	dull; silverish-grey; slightly pitted
140	68.9	31.1	dull; silverish-grey; slightly pitted
210	70.8	29.3	dull; silverish-grey; slightly pitted
280	61.1	38.9	burnt; non-adherent deposit
350	57.6	42.4	burnt; non-adherent deposit

Table 4-10: Composition and Visual Evaluation of Nitrogen Agitated Nickel-Iron Solution 4 Employing 1A Cell Current.

current density [mA cm^{-2}]	composition		observation
	mass-% Ni	mass-% Fe	deposit appearance
4	55.0	45.0	shiny; silverish-grey; smooth
5	52.6	47.4	shiny; silverish-grey; smooth
7.5	47.8	52.2	shiny; silverish-grey; smooth
10	45.4	54.6	shiny; silverish-grey; smooth
12.5	43.1	56.9	shiny; silverish-grey; smooth
15	39.8	60.2	shiny; silverish-grey; smooth
20	36.5	63.5	shiny; silverish-grey; smooth
30	35.1	64.9	shiny; silverish-grey; smooth
40	34.0	66.0	shiny; silverish-grey; smooth
50	32.5	67.5	shiny; silverish-grey; smooth

Table 4-11: Composition and Visual Evaluation of Nitrogen Agitated Nickel-Iron Solution 4 Employing 3A Cell Current.

current density [mA cm^{-2}]	composition		observation
	mass-% Ni	mass-% Fe	deposit appearance
12	43.3	56.7	shiny; silverish-grey; smooth
15	41.9	58.1	shiny; silverish-grey; smooth
22.5	39.3	60.7	shiny; silverish-grey; smooth
30	36.5	63.5	shiny; silverish-grey; smooth
37.5	36.0	64.0	shiny; silverish-grey; smooth
45	35.0	65.0	shiny; silverish-grey; smooth
60	34.1	65.9	shiny; silverish-grey; smooth
90	34.0	66.0	shiny; silverish-grey; smooth
120	34.0	66.0	shiny; silverish-grey; fine cracks
150	33.4	66.6	shiny; silverish-grey; pitted, fine cracks

Table 4-12: Composition and Visual Evaluation of Nitrogen Agitated Nickel-Iron Solution 4 Employing 7A Cell Current.

current density [mA cm^{-2}]	composition		observation
	mass-% Ni	mass-% Fe	deposit appearance
28	48.1	51.9	shiny; silverish-grey; smooth
35	46.9	53.1	shiny; silverish-grey; smooth
52.5	46.5	53.5	shiny; silverish-grey; smooth
70	43.5	56.5	shiny; silverish-grey; smooth
87.5	43.9	56.1	shiny; silverish-grey; smooth
105	39.1	60.9	shiny; silverish-grey; smooth
140	40.7	59.3	shiny; silverish-grey; pitted, fine cracks
210	44.6	55.4	less shiny; silverish-grey; pitted, fine cracks
280	40.4	59.6	less shiny; silverish-grey; pitted, fine cracks
350	41.0	59.1	less shiny; silverish-grey; pitted, fine cracks

Table 4-13: Composition and Visual Evaluation of Nitrogen Agitated Nickel-Zinc Solution 7 Employing 1A Cell Current.

current density [mA cm^{-2}]	composition		observation
	mass-% Ni	mass-% Zn	deposit appearance
5	38.8	61.2	shiny; brownish-grey
10	29.5	70.5	dull; brownish-grey
20	19.4	80.6	dull; yellowish-grey
30	19.0	81.0	shiny; silverish-grey
40	18.9	81.1	shiny; silverish-grey
50	19.8	80.2	shiny; silverish-grey

Table 4-14: Composition and Visual Evaluation of Quiescent Nickel-Zinc Solution 8 Employing 1A Cell Current.

current density [mA cm^{-2}]	composition mass-% Ni	mass-% Zn	observation deposit appearance
4	64.2	35.8	shiny; brownish-grey
5	54.0	46.0	shiny; brownish-grey
15	37.5	62.5	dull; silver-grey
20	35.7	64.3	dull; silver-grey
30	34.4	65.6	dull; silverish-grey
50	41.3	58.7	dull; silverish-grey

Table 4-15: Composition and Visual Evaluation of Quiescent Nickel-Zinc Solution 8 Employing 3A Cell Current.

current density [mA cm^{-2}]	composition mass-% Ni	mass-% Zn	observation deposit appearance
12	88.2	11.8	dull; brownish-grey, silver-grey patches
15	56.1	43.9	dull; brownish-grey, silver-grey patches
30	63.3	36.7	dull; brownish-grey, silver-grey patches
60	74.5	25.5	dull; brownish-grey, silver-grey patches
120	81.2	18.8	burnt, black powdery deposit
150	95.4	4.6	burnt, black powdery deposit

Table 4-16: Composition and Visual Evaluation of Quiescent Nickel-Zinc Solution 8 Employing 5A Cell Current.

current density [mA cm^{-2}]	composition mass-% Ni	mass-% Zn	observation deposit appearance
20	71.7	28.3	dull; brownish-grey
25	86.8	13.2	dull; brownish-grey
50	89.4	10.6	dull, brownish-grey; deposit cracked
75	87.3	12.7	dull; brownish-grey; deposit cracked
100	93.1	6.9	dull; brownish-grey; deposit cracked
150	86.3	13.7	burnt, black powdery deposit
200	78.1	21.9	burnt, black powdery deposit
250	84.3	15.7	burnt, black powdery deposit

Table 4-17: Composition and Visual Evaluation of Nitrogen Agitated Nickel-Zinc Solution 8 Employing 1A Cell Current.

current density [mA cm^{-2}]	composition		observation
	mass-% Ni	mass-% Zn	deposit appearance
4	63.0	36.9	shiny; brownish-grey
5	60.7	39.3	shiny; brownish-grey
15	45.9	54.1	shiny; brownish-grey
20	32.1	67.9	slightly dull; silverish-grey
30	26.4	73.6	dull; silverish-grey
40	25.9	74.1	dull; silverish-grey
50	44.9	55.1	dull; silverish-grey

Table 4-18: Composition and Visual Evaluation of Nitrogen Agitated Nickel-Zinc Solution 8 Employing 3A Cell Current.

current density [mA cm^{-2}]	composition		observation
	mass-% Ni	mass-% Zn	deposit appearance
12	32.3	67.7	shiny; silverish-grey
15	30.4	69.6	shiny; silverish-grey
30	41.0	59.0	dull; silverish-grey
45	58.4	41.6	dull; silverish-grey
60	64.8	35.2	dull; silverish-grey
120	71.7	28.3	dull; silverish-grey
150	77.7	22.3	burnt, black, powdery deposit

Table 4-19: Composition and Visual Evaluation of Nitrogen Agitated Nickel-Zinc Solution 8 Employing 5A Cell Current.

current density [mA cm^{-2}]	composition		observation
	mass-% Ni	mass-% Zn	deposit appearance
20	89.1	10.9	dull; brownish-grey with silver patches
25	89.1	10.9	dull; brownish-grey with silver patches
62.5	72.3	27.7	dull; silverish-grey
75	70.8	29.2	dull; silverish-grey
100	72.3	27.7	dull; silverish-grey
150	95.8	4.2	burnt, black, powdery deposit
200	95.5	4.5	burnt, black, powdery deposit
250	97.4	2.6	burnt, black, powdery deposit

Table 4-20: Elemental Compositions Determined by EDX and GDOES of Deposits Produced in Nickel-Iron Solution 1 at Individual Current Densities.

Current Density [mA cm^{-2}]	Composition (**EDX**)		Composition (**GDOES**)	
	mass-% Ni	mass-% Fe	mass-% Ni	mass-% Fe
10	66.5	33.5	68.1	31.9
20	62.2	37.8	65.7	34.3
30	60.8	39.2	64.5	35.5
40	60.2	39.8	62.3	37.7
60	60.7	39.3	59.7	40.3

Table 4-21: Elemental Compositions Determined by GDOES of Deposits Produced in Nickel-Iron Solution 3 at Individual Current Densities.

Current Density [mA cm^{-2}]	Composition (**GDOES**)	
	mass-% Ni	mass-% Fe
10	61.3	38.7
20	57.5	42.5
30	56.0	44.0
40	35.5	64.5
60	36.5	63.5

Table 4-22: Elemental Compositions Determined by GDOES of Deposits Produced in Nickel-Iron Solution 4 at Individual Current Densities.

Current Density [mA cm^{-2}]	Composition (**GDOES**)	
	mass-% Ni	mass-% Fe
10	41.4	58.6
20	33.2	66.8
30	32.9	67.1
40	31.6	68.4
60	30.3	69.7

Table 4-23: Elemental Compositions Determined by GDOES at Various Areas of Deposits Produced in Nickel-Zinc Solution 8 at Individual Current Densities.

Current Density [mA cm^{-2}]	Area on Sample (see fig. 4-5)	Composition	
		mass-% Ni	mass-% Zn
10	1	45.8	54.2
10	2	37.0	63.0
10	3	29.5	70.5
20	1	27.5	72.5
20	2	29.2	70.8
20	3	24.0	76.0
30	1	30.0	70.0
30	2	28.6	71.4
30	3	25.2	74.8
40	1	24.9	75.1
40	2	23.6	76.4
40	3	33.7	66.3
50	1	52.4	47.6
50	2	44.6	45.4
50	3	37.9	62.1
60	1	34.2	65.8
60	2	36.9	63.1
60	3	38.0	62.0

Table 4-24: Raw Data $R_{\{hkl\}}$, $I_{\{hkl\}}$ and Planar Distribution in per cent of the Copper Sheet Substrate.

	Planes: Copper Sheet Substrate									
	111		**200**		**220**		**311**		**331**	
Raw Data	$R_{\{hkl\}}$	$I_{\{hkl\}}$	$R_{\{hkl\}}$	$I_{\{hkl\}}$	$R_{\{hkl\}}$	$I_{\{hkl\}}$	$R_{\{hkl\}}$	$I_{\{hkl\}}$	$R_{\{hkl\}}$	$I_{\{hkl\}}$
	245.3	1335	112.9	2083	59.5	396	65.4	352	48.7	449
%	12.1		40.9		14.7		11.9		20.4	

Table 4-25: Raw Data: Measured 2θ Bragg Angles. Calculated Interplanar Spacings 'd' and Lattice Parameter 'a' of Copper Sheet Substrate.

	Reflections						
Copper	**111**	**200**	**220**	**311**	**222**	**400**	**331**
°2θ	43.3	50.4	74.1	89.9	95.1	116.9	136.4
d [nm]	0.20874	0.18091	0.12786	0.10905	0.10437	0.09041	0.08296
a [nm]	0.36155	0.36182	0.36164	0.36169	0.36154	0.36164	0.36160

Table 4-26: Raw Data $R_{\{hkl\}}$ and $I_{\{hkl\}}$ of fcc NiFe Electrodeposits on Copper Sheet Substrates Deposited in NiFe Solution 1.

Current	***Planes***							
Density	**111**		**200**		**220**		**311**	
[mA cm^{-2}]	$R_{\{hkl\}}$	$I_{\{hkl\}}$	$R_{\{hkl\}}$	$I_{\{hkl\}}$	$R_{\{hkl\}}$	$I_{\{hkl\}}$	$R_{\{hkl\}}$	$I_{\{hkl\}}$
10	89.9	1468	41.0	479	21.5	356	24.0	342
30	83.7	1742	38.0	305	20.1	184	22.4	553
60	76.7	1807	34.8	276	18.4	118	20.5	541

Table 4-27: Planar Distribution in per cent of fcc NiFe Electrodeposits on Copper Sheet Substrates Deposited in NiFe Solution 1.

i	*Planes Distribution in per cent*			
[mA cm^{-2}]	**111**	**200**	**220**	**311**
10	27.8	19.9	28.1	24.2
30	33.2	12.8	14.6	39.4
60	36.6	12.4	9.9	41.1

Table 4-28: Raw Data: Measured 2θ Bragg Angles of fcc NiFe Electrodeposits on Copper Sheet Substrates Deposited in NiFe Solution 1.

i	*Reflections:* 2θ° Bragg Angles			
[mA cm^{-2}]	**111**	**200**	**220**	**311**
10	44.04	51.32	75.55	91.81
30	43.97	51.32	75.44	91.78
60	43.85	51.22	75.31	91.60

Table 4-29: Calculated d-Spacings of fcc NiFe Electrodeposits on Copper Sheet Substrates Deposited in NiFe Solution 1.

i	*Reflections:* Calculated d-Spacings [nm]			
[mA cm^{-2}]	**111**	**200**	**220**	**311**
10	0.20543	0.17789	0.12575	0.10726
30	0.20578	0.17789	0.12591	0.10728
60	0.20628	0.17821	0.12609	0.10745

Table 4-30: Raw Data $R_{\{hkl\}}$ and $I_{\{hkl\}}$ of fcc NiFe Electrodeposits on Copper Sheet Substrates Deposited in NiFe Solution 3.

Current Density	*Planes*							
	111		200		220		311	
[mA cm^{-2}]	$R_{\{hkl\}}$	$I_{\{hkl\}}$	$R_{\{hkl\}}$	$I_{\{hkl\}}$	$R_{\{hkl\}}$	$I_{\{hkl\}}$	$R_{\{hkl\}}$	$I_{\{hkl\}}$
10	78.8	1346	35.8	244	18.9	126	21.0	414
30	72.1	1222	32.8	144	17.2	78	19.2	370

Table 4-31: Raw Data $R_{\{hkl\}}$ and $I_{\{hkl\}}$ of fcc/bcc NiFe Electrodeposits on Copper Sheet Substrates Deposited in NiFe Solution 3 (i = 60 mA cm^{-2}).

Planes (fcc)							
111		200		220		311	
$R_{\{hkl\}}$	$I_{\{hkl\}}$	$R_{\{hkl\}}$	$I_{\{hkl\}}$	$R_{\{hkl\}}$	$I_{\{hkl\}}$	$R_{\{hkl\}}$	$I_{\{hkl\}}$
55.9	788	25.7	90	13.6	72	15.3	65

Planes (bcc)									
110		200		211		310		222	
$R_{\{hkl\}}$	$I_{\{hkl\}}$	$R_{\{hkl\}}$	$I_{\{hkl\}}$	$R_{\{hkl\}}$	$I_{\{hkl\}}$	$R_{\{hkl\}}$	$I_{\{hkl\}}$	$R_{\{hkl\}}$	$I_{\{hkl\}}$
74.8	557	10.3	20	18.7	130	2.7	46	1.1	94.8

Table 4-32: Planar Distribution in per cent of fcc NiFe on Copper Sheet Substrates Deposited at 10 and 30 mA cm^{-2} in NiFe Solution 3.

i	*Planes: Distribution in per cent*			
[mA cm^{-2}]	111	200	220	311
10	34.0	13.6	13.2	39.2
30	37.5	9.7	10.1	42.7

Table 4-33: Planar Distribution in per cent of fcc/bcc NiFe on Copper Sheet Substrates Deposited at 60 mA cm^{-2} in NiFe Solution 3.

Planes (fcc): Distribution in per cent			
111	**200**	**220**	**311**
51.9	12.9	19.6	15.6

Planes (bcc): Distribution in per cent				
110	**200**	**211**	**310**	**222**
6.1	1.6	5.7	14.0	72.6

Table 4-34: Raw Data: Measured 2θ Bragg Angles of fcc NiFe Electrodeposits on Copper Sheet Substrates Deposited in NiFe Solution 3 at 10 and 30 mA cm^{-2}.

i	*Reflections:* 2θ° Bragg Angles			
[mA cm^{-2}]	**111**	**200**	**220**	**311**
10	43.87	51.20	75.36	91.66
30	43.77	51.06	75.26	91.52

Table 4-35: Raw Data: Measured 2θ Bragg Angles of fcc/bcc NiFe Electrodeposits on Copper Sheet Substrates Deposited in NiFe Solution 3 at 60 mA cm^{-2}.

Reflections / 2θ° Bragg Angles *(fcc)*			
111	**200**	**220**	**311**
43.70	50.85	74.95	90.97
Reflections / 2θ° Bragg Angles *(bcc)*			
110	**200**	**211**	**310**	**222**
44.61	65.40	82.58	117.74	138.52

Table 4-36: Calculated d-Spacings of fcc NiFe Electrodeposits on Copper Sheet Substrates Deposited in NiFe Solution 3.

i	*Reflections* / calculated d-Spacings [nm]			
[mA cm^{-2}]	**111**	**200**	**220**	**311**
10	0.20622	0.17826	0.12602	0.10739
30	0.20666	0.17874	0.12617	0.10752

Table 4-37: Calculated d-Spacings of fcc/bcc Electrodeposits on Copper Sheet Substrates Deposited in NiFe Solution 3.

Reflections / calculated d-Spacings [nm] *(fcc)*			
111	**200**	**220**	**311**
0.20696	0.17942	0.12660	0.10803
Reflections / calculated d-Spacings [nm] *(bcc)*			
110	**200**	**211**	**310**	**222**
0.20295	0.14259	0.11680	0.09076	0.82852

Table 4-38: Raw Data $R_{\{hkl\}}$ and $I_{\{hkl\}}$ of fcc NiFe Electrodeposit on Copper Sheet Substrate Deposited in NiFe Solution 4 (i = 10 mA cm^{-2}).

Planes							
111		**200**		**220**		**311**	
$R_{\{hkl\}}$	$I_{\{hkl\}}$	$R_{\{hkl\}}$	$I_{\{hkl\}}$	$R_{\{hkl\}}$	$I_{\{hkl\}}$	$R_{\{hkl\}}$	$I_{\{hkl\}}$
59.0	8331	26.8	128	14.5	52	16.1	88

Table 4-39: Raw Data $R_{\{hkl\}}$ and $I_{\{hkl\}}$ of bcc NiFe Electrodeposits on Copper Sheet Substrates Deposited in NiFe Solution 4 (i = 30 mA cm^{-2}), (i = 60 mA cm^{-2}).

Current	*Planes*									
Density	**110**		**200**		**211**		**310**		**222**	
[mA cm^{-2}]	$R_{\{hkl\}}$	$I_{\{hkl\}}$	$R_{\{hkl\}}$	$I_{\{hkl\}}$	$R_{\{hkl\}}$	$I_{\{hkl\}}$	$R_{\{hkl\}}$	$I_{\{hkl\}}$	$R_{\{hkl\}}$	$I_{\{hkl\}}$
30	72.2	77	10.0	*	18.3	58	9.7	*	3.8	1074
60	69.5	17	9.8	*	17.7	37	9.5	*	3.7	1473

* not detectable

Table 4-40: Planar Distribution in per cent of fcc NiFe Electrodeposit on Copper Sheet Substrate Deposited in NiFe Solution 4 (i = 10 mA cm^{-2}).

Planes: Distribution in per cent			
111	**200**	**220**	**311**
91.1	3.1	2.3	3.5

Table 4-41: Planar Distribution in per cent of bcc NiFe Electrodeposits on Copper Sheet Substrates deposited in NiFe Solution 4 (i = 30 mA cm^{-2}), (i = 60 mA cm^{-2}).

i	*Planes: Distribution in per cent*				
[mA cm^{-2}]	**110**	**200**	**211**	**310**	**222**
30	0.4	*	1.1	*	98.5
60	0.1	*	0.5	*	99.4

* not detectable

Table 4-42: Raw Data: Measured 2θ Bragg Angles of fcc NiFe Electrodeposit on Copper Sheet Substrate Deposited in NiFe Solution 4 (i = 10 mA cm^{-2}).

Reflections / 2θ° Bragg Angles *(fcc)*			
111	**200**	**220**	**311**
43.71	51.02	74.63	90.87

Table 4-43: Raw Data: Measured 2θ Bragg Angles of bcc NiFe Electrodeposits on Copper Sheet Substrates Deposited in NiFe Solution 4 (i = 30 mA cm^{-2}), (i = 60 mA cm^{-2}).

i	*Reflections* / 2θ° Bragg Angles *(bcc)*				
[mA cm^{-2}]	**110**	**200**	**211**	**310**	**222**
30	44.61	*	82.31	*	137.65
60	44.68	*	82.36	*	137.61

* not detectable

Table 4-44: Calculated d-Spacings of fcc NiFe Electrodeposit on Copper Sheet Substrate Deposited in NiFe Solution 4 (i = 10 mA cm^{-2}).

Reflections / calculated d-Spacings [nm]			
111	**200**	**220**	**311**
0.20694	0.17885	0.12707	0.10812

Table 4-45: Calculated d-Spacings of bcc NiFe Electrodeposits on Copper Sheet Substrates Deposited in NiFe Solution 4 (i = 30 mA cm^{-2}), (i = 60 mA cm^{-2}).

i	*Reflections* / calculated d-Spacings [nm]				
[mA cm^{-2}]	**110**	**200**	**211**	**310**	**222**
30	0.20295	*	0.11705	*	0.08261
60	0.20266	*	0.11699	*	0.08262

Table 4-46: Structure of Nickel-Zinc Deposited at Various Current Densities in As-Deposited and Heat-Treated State.

Current Density [mA cm^{-2}]	Structure As - Deposited	Structure Heat - Treated
10	bcc γ-phase	Tetragonal β_1-phase + bcc γ-phase
20	bcc γ-phase	Tetragonal β_1-phase + bcc γ-phase
30	bcc γ-phase	bcc γ-phase
40	bcc γ-phase + fcc α-phase	Tetragonal β_1-phase + bcc γ-phase + fcc α-phase
50	bcc γ-phase + fcc α-phase	Tetragonal β_1-phase + bcc γ-phase + fcc α-phase
60	bcc γ-phase	Tetragonal β_1-phase + bcc γ-phase

Table 4-47: Comparison Between Lattice Parameters of Nickel-Zinc Alloys Crystallized under Equilibrium Conditions and Through Electrocrystallization at Current Densities from 10 to 60 mA cm^{-2}.

	Lattice Parameter [nm]		Approximate Chemical Formula
	γ-phase	α-phase	
JCPDS	0.892		Ni_5Zn_{21}
i [mA cm^{-2}]			
10	0.8704		NiZn
20	0.8801		Ni_3Zn_7
30	0.8903		Ni_6Zn_{19}
40	0.8850	0.3535	-
50	0.8850	0.3532	-
60	0.8865		$Ni_{13}Zn_{36}$

Table 4-48: Comparison between Lattice Parameters of γ-Phase Nickel-Zinc Alloy Deposits in As-Deposited and Heat-Treated State.

Current Density [mA cm^{-2}]	Lattice Parameter [nm]		
	γ-phase as-deposited	γ-phase heat treated	Δ a
10	0.8704	0.8840	0.0136
20	0.8801	0.8869	0.0068
30	0.8903	0.8878	0.0025
40	0.8850	0.8850	0
50	0.8850	0.8850	0
60	0.8865	0.8860	0.0005

Table 4-49: Elemental Composition of fcc Nickel-Iron Deposit at Different Distances from Copper Substrate/Deposit Interface.

Distance from Interface Substrate/Deposit [nm]	Composition Mass-%	
	Ni	Fe
5	37.54	62.46
10	36.38	63.62
15	37.54	62.46
20	37.93	62.07
25	37.02	62.98
30	37.25	62.75
35	36.58	63.42
40	37.59	62.41
45	38.32	61.68
50	36.25	63.75
55	36.56	63.44
60	35.96	64.04
65	36.03	63.97
70	36.50	63.50
75	36.70	63.30
80	36.84	63.15
85	35.98	64.02
90	35.96	64.04

Table 4-50: Elemental Composition of bcc Nickel-Iron Deposit at Different Distances from Copper Substrate/Deposit Interface.

Distance from Interface Substrate/Deposit [nm]	Composition Mass-%	
	Ni	Fe
5	29.48	70.52
10	29.39	70.61
15	29.43	70.57
20	29.05	70.95
25	28.84	71.16
30	28.88	71.12
35	28.93	71.07
40	28.95	71.05
45	29.00	71.00
50	29.37	70.63
55	29.15	70.85
60	29.09	70.91
65	29.08	70.92
70	29.01	70.99
75	28.95	71.05
80	28.83	71.17
85	28.57	71.43
90	28.64	71.36

Table 4-51: Elemental Composition of Double Layered fcc/bcc Nickel-Iron Deposit.

Structure	Composition [Mass-%]	
	Ni	Fe
fcc	41.07	58.93
fcc	40.74	59.26
fcc	39.56	60.44
bcc	26.01	73.99
bcc	26.10	73.90
bcc	26.05	73.95

Table 4-52: Elemental Composition of Double Layered bcc/fcc Nickel-Iron Deposit.

Structure	Composition [Mass-%]	
	Ni	Fe
bcc	26.06	73.94
fcc	37.12	62.88

Table 4-53: Elemental Composition of bcc Nickel-Zinc Deposit (i = 10 mA cm^{-2}) at Different Distances from Copper Substrate/Deposit Interface.

Distance from Interface Substrate/Deposit [nm]	Composition Mass-%	
	Ni	Zn
5	31.43	68.57
10	31.50	68.50
15	31.57	68.43
20	31.53	68.47
25	31.87	68.13
30	31.56	68.44
35	31.66	68.34
40	31.49	68.51
45	31.41	68.59
50	31.63	68.37
55	31.59	68.41
60	31.36	68.64
65	31.30	68.70
70	30.94	69.06
...		
...		
middle of deposit	31.02	68.98

Table 4-54: Elemental Composition of bcc Nickel-Zinc Deposit (i = 60 mA cm^{-2}) at Different Distances from Copper Substrate/Deposit Interface.

Distance from Interface Substrate/Deposit [nm]	Composition Mass-%	
	Ni	Zn
5	35.42	64.58
10	38.21	61.79
15	38.38	61.62
20	34.34	65.66
25	34.17	65.75
30	33.25	66.75
35	34.71	65.29
40	34.10	65.90
45	33.70	66.30
50	34.49	65.51
55	33.79	66.21

Table 4-55: Elemental Composition of bcc Nickel-Zinc Deposit (i = 60 mA cm^{-2}) at Similar Distance from Copper Substrate/Deposit Interface but in Different Grains.

Spot	Composition Mass-%	
	Ni	Zn
1	32.88	67.12
2	30.52	69.48
3	29.93	70.07

Table 4-56: Elemental Composition of bcc Nickel-Zinc Deposit (i = 10 mA cm^{-2}) at Different Distances from Steel Substrate/Deposit Interface.

Distance from Interface Substrate/Deposit [nm]	Composition Mass-%	
	Ni	Zn
5	59.13	40.87
10	51.92	48.08
15	42.34	57.66
20	34.31	65.69
25	34.16	65.84
30	31.64	68.36
35	33.01	66.99
40	34.89	65.11
45	30.56	69.44

Table 4-57: Raw Data $R_{\{hkl\}}$, $I_{\{hkl\}}$ and Planar Distribution in per cent of the Copper Disc Substrate.

	Planes: Copper Disc Substrate									
	111		**200**		**220**		**311**		**331**	
Raw	$R_{\{hkl\}}$	$I_{\{hkl\}}$	$R_{\{hkl\}}$	$I_{\{hkl\}}$	$R_{\{hkl\}}$	$I_{\{hkl\}}$	$R_{\{hkl\}}$	$I_{\{hkl\}}$	$R_{\{hkl\}}$	$I_{\{hkl\}}$
Data	245.5	9344	112.9	4711	59.6	170	65.5	698	48.7	103
%	39.9		43.7		3.0		11.2		2.2	

Table 4-58: Raw Data: Measured 2θ Bragg Angles. Calculated Interplanar Spacings 'd' and Lattice Parameter 'a' of Copper Disc Substrate.

	Reflections						
Copper	**111**	**200**	**220**	**311**	**222**	**400**	**331**
°2θ	43.31	50.41	74.09	89.86	95.10	116.76	136.35
d [nm]	0.20873	0.18089	0.12787	0.10907	0.10439	0.09046	0.08298
a [nm]	0.36153	0.36177	0.36166	0.36174	0.36162	0.36184	0.36169

Table 4-59: Raw Data, $R_{\{hkl\}}$ and $I_{\{hkl\}}$, of fcc NiFe Electrodeposits on Copper Disc Substrates.

	Planes							
Thickness	111		200		220		311	
[μm]	$R_{\{hkl\}}$	$I_{\{hkl\}}$	$R_{\{hkl\}}$	$I_{\{hkl\}}$	$R_{\{hkl\}}$	$I_{\{hkl\}}$	$R_{\{hkl\}}$	$I_{\{hkl\}}$
0.3	13.8	1622	5.6	*	2.2	209	2.1	*
0.4	17.6	1440	7.2	*	2.9	132	2.7	*
0.5	21.1	1553	8.6	*	3.4	91	3.4	*
0.75	28.5	2377	11.8	*	4.8	*	4.8	*
1	34.3	6463	14.4	*	6.0	226	6.0	*
1.5	42.6	7451	18.2	*	8.0	(70)	8.1	*
2	47.8	6246	20.8	*	9.4	159	9.7	*
3	52.8	33760	23.5	*	11.3	(66)	11.9	*

* Not detectable

( ) Values in brackets are intensities below $3 \times \sqrt{\text{Background}}$

Table 4-60: Planar Distribution in per cent of fcc NiFe Electrodeposits on Copper Disc Substrates.

	Planes: Distribution in per cent			
[μm]	111	200	220	311
0.3	55.2	*	44.8	*
0.4	63.8	*	36.2	*
0.5	73.4	*	26.6	*
0.75	100	*	*	*
1	83.4	*	16.6	*
1.5	100	*	**	*
2	88.5	*	11.5	*
3	100	*	**	*

* Not detectable

** Intensities below $3 \times \sqrt{\text{Background}}$

Table 4-61: Raw Data: Measured 2θ Bragg Angles of fcc Nickel-Iron Deposits.

	Reflections / 2θ° Bragg Angles			
[μm]	111	200	220	311
0.3	43.58	*	74.52	*
0.4	43.63	*	74.57	*
0.5	43.65	*	74.87	*
0.75	43.74	*	*	*
1	43.72	*	74.86	*
1.5	43.75	*	(74.94)	*
2	43.77	*	75.04	*
3	42.72	*	(74.93)	*

* Not detectable

( ) Values in brackets are intensities below $3 \times \sqrt{\text{Background}}$

Table 4-62: Calculated d-Spacings of fcc NiFe Substrates of Various Thicknesses on Copper.

	Reflections / Calculated d-spacings [nm]			
[μm]	111	200	220	311
0.3	0.20751	*	0.12723	*
0.4	0.20727	*	0.12716	*
0.5	0.20721	*	0.12672	*
0.75	0.20681	*	*	*
1	0.20689	*	0.12674	*
1.5	0.20673	*	(0.12663)	*
2	0.20666	*	0.12647	*
3	0.20688	*	(0.12664)	*

* Not detectable

( ) Values in brackets are calculated from Bragg angle positions with intensities below $3 \times \sqrt{\text{Background}}$

Table 4-63: Raw Data, $R_{\{hkl\}}$ and $I_{\{hkl\}}$, of bcc NiFe Electrodeposits on Copper Disc Substrates.

	Planes									
Thickness	110		200		211		310		222	
[μm]	$R_{\{hkl\}}$	$I_{\{hkl\}}$	$R_{\{hkl\}}$	$I_{\{hkl\}}$	$R_{\{hkl\}}$	$I_{\{hkl\}}$	$R_{\{hkl\}}$	$I_{\{hkl\}}$	$R_{\{hkl\}}$	$I_{\{hkl\}}$
0.4	22.9	181	2.4	*	3.6	(88)	1.6	*	0.6	*
0.5	27.3	414	2.9	*	4.4	3120	1.9	*	0.7	*
0.75	36.5	552	4.0	*	6.2	519	2.7	*	1.0	*
1	43.8	598	4.9	*	7.8	693	3.4	*	1.3	(76)
1.5	53.6	333	6.3	*	10.2	810	4.6	*	1.7	309
2	59.6	249	7.3	(43)	12.0	1228	5.6	*	2.1	91
3	65.4	510	8.5	(58)	14.5	856	7.0	*	2.6	243
20	68.2	149	9.4	34	17.3	119	9.2	(18)	3.6	7032

* Not detectable

( ) Values in brackets are intensities below $3 \times \sqrt{\text{Background}}$

Table 4-64: Planar Distribution in per cent of bcc NiFe Electrodeposits on Copper Disc Substrates.

	Planes: Distribution in per cent				
[μm]	110	200	211	310	222
0.4	100	*	**	**	*
0.5	17.4	*	82.6	*	*
0.75	15.3	*	84.7	*	*
1	13.3	*	86.4	*	**
1.5	2.3	*	29.6	*	68.1
2	2.8	**	67.8	*	29.4
3	4.9	**	37.0	*	58.1
20	0.1	0.2	0.3	**	99.4

* Not detectable

** $I(hkl) < 3 \times \sqrt{\text{Background}}$

Table 4-65: Raw Data: Measured 2θ Bragg Angles of bcc Nickel-Iron Electrodeposits of Individual Thickness on Copper Disc Substrates.

	Reflections / 2θ° Bragg Angles				
[µm]	110	200	211	310	222
0.4	44.85	*	(82.66)	*	*
0.5	44.86	*	82.67	*	*
0.75	44.82	*	82.61	*	*
1	44.85	*	82.67	*	(137.52)
1.5	44.79	*	82.58	*	137.67
2	44.79	(65.37)	82.64	*	137.78
3	44.79	(65.40)	82.59	*	137.76
20	44.63	65.40	82.29	(116.70)	137.74

* Not detectable

( ) Values in brackets are Bragg angles where intensities were below $3 \times \sqrt{\text{Background}}$

Table 4-66: Calculated d-Spacings of bcc NiFe Electrodeposits of Individual Thickness on Copper Disc Substrates.

	Reflections / Calculated d-spacings [nm]				
[µm]	110	200	211	310	222
0.4	0.20191	*	(0.11642)	*	*
0.5	0.20190	*	0.11663	*	*
0.75	0.20207	*	0.11670	*	*
1	0.20194	*	0.11663	*	(0.08247)
1.5	0.20219	*	0.11673	*	0.08260
2	0.20217	(0.14289)	0.11667	*	0.08250
3	0.20218	(0.14296)	0.11673	*	0.08257
20	0.20287	0.14258	0.11707	(0.09049)	0.08258

* Not detectable

( ) Values in brackets are calculated from Bragg angle positions with intensities below $3 \times \sqrt{\text{Background}}$

Table 4-67: Raw Data $R_{\{hkl\}}$ and $I_{\{hkl\}}$ of 0.5μm Thick fcc NiFe Electrodeposited on Various Substrates.

Substrate	*Planes* 111		200		220		311	
	$R_{\{hkl\}}$	$I_{\{hkl\}}$	$R_{\{hkl\}}$	$I_{\{hkl\}}$	$R_{\{hkl\}}$	$I_{\{hkl\}}$	$R_{\{hkl\}}$	$I_{\{hkl\}}$
Copper Disc Substrate	21.1	1553	8.6	*	3.4	91	3.4	*
0.5μm bcc NiFe Electrodeposit	21.1	1889	8.6	*	3.4	(49)	3.4	*
2μm bcc NiFe Electrodeposit	21.1	775	8.6	*	3.4	(48)	3.4	*

* Not detectable

( ) Values in brackets are intensities below $3 \times \sqrt{\text{Background}}$

Table 4-68: Texture (Planar Distribution in per cent) of 0.5μm thick fcc NiFe Electrodeposits on Various Substrates.

Substrate	*Planes: Distribution in per cent* 111	200	220	311
Copper Disc Substrate	73.4	*	26.6	*
0.5μm bcc NiFe Electrodeposit	100	*	**	*
2μm bcc NiFe Electrodeposit	100	*	**	*

* Not detectable

** $I(hkl) < 3 \times \sqrt{\text{Background}}$

Table 4-69: Raw Data $R_{\{hkl\}}$ and $I_{\{hkl\}}$ of 2μm Thick fcc NiFe Electrodeposited on Various Substrates.

Substrate	*Planes*							
	111		200		220		311	
	$R_{\{hkl\}}$	$I_{\{hkl\}}$	$R_{\{hkl\}}$	$I_{\{hkl\}}$	$R_{\{hkl\}}$	$I_{\{hkl\}}$	$R_{\{hkl\}}$	$I_{\{hkl\}}$
Copper Disc Substrate	47.8	6246	20.7	*	9.4	159	9.7	*
0.5μm bcc NiFe Electrodeposit	47.8	12873	20.7	*	9.4	(59)	9.7	*
2μm bcc NiFe Electrodeposit	47.8	8759	20.7	2701	9.4	133	9.7	228

* Not detectable

( ) Values in brackets are intensities below $3 \times \sqrt{\text{Background}}$

Table 4-70: Texture (Planar Distribution in per cent) of 2μm Thick fcc NiFe Electrodeposits on Various Substrates.

Substrate	*Planes: Distribution in per cent*			
	111	200	220	311
Copper Disc Substrate	88.5	*	11.5	*
0.5μm bcc NiFe Electrodeposit	100	*	**	*
2μm bcc NiFe Electrodeposit	52.1	37.3	4.0	6.6

* Not detectable

** $I(hkl) < 3 \times \sqrt{\text{Background}}$

Table 4-71: Raw Data $R_{\{hkl\}}$ and $I_{\{hkl\}}$ of 0.5μm Thick bcc NiFe Electrodeposits on Various Substrates.

Substrate	*Planes*									
	110		200		211		310		222	
	$R_{\{hkl\}}$	$I_{\{hkl\}}$	$R_{\{hkl\}}$	$I_{\{hkl\}}$	$R_{\{hkl\}}$	$I_{\{hkl\}}$	$R_{\{hkl\}}$	$I_{\{hkl\}}$	$R_{\{hkl\}}$	$I_{\{hkl\}}$
Copper Disc Substrate	27.3	414	2.9	*	4.4	317	1.9	*	0.7	*
0.5μm fcc NiFe Electrodeposit	27.3	889	2.9	(9)	4.4	313	1.9	*	0.7	(34)
2μm fcc NiFe Electrodeposit	27.3	1433	2.9	(4)	4.4	312	1.9	*	0.7	(50)

* Not detectable

( ) Values in brackets are intensities below $3 \times \sqrt{\text{Background}}$

Table 4-72: Texture (planar Distribution in per cent) of 0.5μm Thick bcc NiFe Electrodeposits on Various Substrates.

Substrate	*Planes: Distribution in per cent*				
	110	200	211	310	222
Copper Disc Substrate	17.4	*	82.6	*	*
0.5μm fcc NiFe Electrodeposit	31.5	**	68.5	*	**
2μm fcc NiFe Electrodeposit	42.6	**	57.4	*	**

* Not detectable

** $I(hkl) < 3 \times \sqrt{\text{Background}}$

Table 4-73: Raw Data $R_{\{hkl\}}$ and $I_{\{hkl\}}$ of 2μm Thick bcc NiFe Electrodeposits on Various Substrates.

Substrate	*Planes* 110		200		211		310		222	
	$R_{\{hkl\}}$	$I_{\{hkl\}}$	$R_{\{hkl\}}$	$I_{\{hkl\}}$	$R_{\{hkl\}}$	$I_{\{hkl\}}$	$R_{\{hkl\}}$	$I_{\{hkl\}}$	$R_{\{hkl\}}$	$I_{\{hkl\}}$
Copper Disc Substrate	59.6	249	7.3	(43)	12.0	1228	5.6	*	2.1	91
0.5μm fcc NiFe Electrodeposit	59.6	292	7.3	(38)	12.0	509	5.6	*	2.1	621
2μm fcc NiFe Electrodeposit	59.6	2200	7.3	(20)	12.0	714	5.6	*	2.1	204

* Not detectable

( ) Values in brackets are intensities below $3 \times \sqrt{\text{Background}}$

Table 4-74: Texture (planar Distribution in per cent) of 2μm Thick bcc NiFe Electrodeposits on Various Substrates.

Substrate	*Planes: Distribution in per cent* 110	200	211	310	222
Copper Disc Substrate	2.8	**	67.8	*	29.4
0.5μm fcc NiFe Electrodeposit	1.4	**	12.1	*	86.5
2μm fcc NiFe Electrodeposit	18.8	**	30.7	*	50.5

* Not detectable

** $I(hkl) < 3 \times \sqrt{\text{Background}}$

Table 4-75: Raw Data $R_{\{hkl\}}$ and $I_{\{hkl\}}$ of 0.5, 2, and 10μm Thick bcc NiFe Electrodeposited on 2μm thick NiFe Substrate.

Thickness	*Planes*									
	110		200		211		310		222	
	$R_{\{hkl\}}$	$I_{\{hkl\}}$	$R_{\{hkl\}}$	$I_{\{hkl\}}$	$R_{\{hkl\}}$	$I_{\{hkl\}}$	$R_{\{hkl\}}$	$I_{\{hkl\}}$	$R_{\{hkl\}}$	$I_{\{hkl\}}$
0.5 μm	27.3	1433	2.9	(4)	4.4	312	1.9	*	0.7	(50)
2 μm	59.6	2200	7.3	(20)	12.0	724	5.6	*	2.1	204
10 μm	68.7	77	9.4	60	17.5	160	9.3	79	3.6	2735

* Not detectable

( ) Values in brackets are intensities below $3 \times \sqrt{\text{Background}}$

Table 4-76: Texture (planar Distribution in per cent) of 0.5, 2, and 10μm Thick bcc NiFe Electrodeposits on 2μm thick fcc NiFe Substrate.

Thickness	*Planes: Distribution in per cent*				
	110	200	211	310	222
0.5 μm	42.6	*	57.4	*	**
2 μm	18.8	**	30.7	*	50.5
10 μm	0.1	0.8	1.2	1.1	96.8

* Not detectable

** $I(hkl) < 3 \times \sqrt{\text{Background}}$

Table 4-77: Raw Data: Measured 2θ Bragg Angles of 0.5µm, 2µm, and 10 µm Thick bcc NiFe Electrodeposits on 2µm fcc NiFe.

	Reflections / 2θ Bragg Angles				
Thickness	**110**	**200**	**211**	**310**	**222**
0.5 µm	44.77	(65.71)	82.61	*	(137.52)
2 µm	44.73	(65.23)	82.57	*	137.64
10 µm	44.77	65.50	82.44	116.82	137.78

Table 4-78: Calculated d-Spacings of bcc NiFe of 0.5, 2, and 10µm Thick Electrodeposits on 2µm fcc NiFe Substrates.

	Reflections / Calculated d-spacings [nm]				
Thickness	**110**	**200**	**211**	**310**	**222**
0.5 µm	0.20236	(0.14310)	0.11683	*	(0.08261)
2 µm	0.20235	(0.14383)	0.11683	*	0.08261
10 µm	0.20226	0.14302	0.11677	0.09045	0.08257

Table 4-79: Raw Data $R_{\{hkl\}}$, $I_{\{hkl\}}$ and Planar Distribution in per cent of Mild Steel Substrate.

	Planes									
Mild	**110**		**200**		**211**		**310**		**222**	
Steel	$R_{\{hkl\}}$	$I_{\{hkl\}}$	$R_{\{hkl\}}$	$I_{\{hkl\}}$	$R_{\{hkl\}}$	$I_{\{hkl\}}$	$R_{\{hkl\}}$	$I_{\{hkl\}}$	$R_{\{hkl\}}$	$I_{\{hkl\}}$
Raw Data	262.2	700	37.4	39	68.3	99	37.3	64	14.6	18
%	32.9		12.7		17.8		21.1		15.5	

Table 4-80: Raw Data: Measured 2θ Bragg Angles. Calculated Interplanar Spacings 'd' and Lattice Parameter 'a' of Mild Steel Substrate.

Mild Steel	*Reflections*					
	110	200	211	220	310	222
°2θ	44.82	65.08	82.39	98.77	116.27	136.98
d [nm]	0.20205	0.14322	0.11696	1.01470	0.09070	0.08280
a [nm]	0.285738	0.28643	0.28650	0.28703	0.28682	0.28682

Table 4-81: Calculated $R_{\{hkl\}}$ Values of an Untextured Nickel-Zinc Powder Specimen of Similar Nominal Composition and Thickness to the Electrodeposit formed at 10 mA cm^{-2}.

Thickness	*Planes: $R_{\{hkl\}}$-Values*										
[μm]	222	321	330	332	510	521	600	631	552	741	820
0.1	12.4	54.9	8.2	10.6	7.3	10.5	0.8	3.8	1.3	1.7	0.8
0.2	24.3	107.2	16.0	20.8	14.3	20.6	1.7	7.3	2.5	3.2	1.5
0.5	56.6	253.9	38.1	49.7	34.4	49.6	4.0	17.9	6.1	7.9	3.7
1	105.2	474.3	71.7	94.1	65.4	94.7	7.7	34.5	11.8	15.2	7.1
2	183.4	837.3	128.4	175.1	119.1	173.5	14.3	64.3	22.1	28.6	13.5
10	407.2	1939	318.4	457.7	324.7	489.9	42.2	199.8	70.8	95.2	45.1
20	420.6	2025	340.6	497.2	362.3	556.4	49.3	240.3	86.9	120.4	57.3

Table 4-82: Measured Intensities $I_{\{hkl\}}$ of NiZn, Electrodeposited at 10 mA cm^{-2}, on Mild Steel Substrates.

Thickness	*Planes: $I_{\{hkl\}}$-Values*										
[µm]	222	321	330	332	510	521	600	631	552	741	820
0.1	*	*	2205	*	*	*	*	*	*	*	*
0.2	*	*	1053	*	*	*	*	*	*	*	*
0.5	125	*	1169	*	*	*	*	*	69	*	*
1	305	*	1965	*	*	*	*	*	121	*	*
2	1356	*	2473	(50)	*	*	*	*	91	*	*
10	4990	*	2155	322	*	*	217	*	71	*	*
20	2143	*	14390	417	*	*	404	*	215	*	*

* Not detectable

( ) Values in brackets are intensities below $3 \times \sqrt{\text{Background}}$

Table 4-83: Planar Distribution of Nickel-Zinc Deposit of Various Thicknesses, Electrodeposited at 10 mA cm^{-2}, on Mild Steel Substrates.

	Planes: Distribution in per cent										
[μm]	**222**	**321**	**330**	**332**	**510**	**521**	**600**	**631**	**552**	**741**	**820**
0.1	*	*	100	*	*	*	*	*	*	*	*
0.2	*	*	100	*	*	*	*	*	*	*	*
0.5	5.0	*	69.4	*	*	*	*	*	25.6	*	*
1	7.2	*	67.6	*	*	*	*	*	25.2	*	*
2	24.0	*	62.6	**	*	*	*	*	13.4	*	*
10	47.4	*	26.2	2.7	*	*	19.9	*	3.8	*	*
20	8.7	*	71.8	1.4	*	*	13.9	*	4.2	*	*

* Not detectable

** $I(hkl) < 3 \times \sqrt{\text{Background}}$

Table 4-84: Raw Data: Bragg Angles of bcc Nickel-Zinc, Electrodeposited at 10 mA cm^{-2}, on Mild Steel Substrates.

	Reflections / 2θ Bragg Angles										
[μm]	222	321	330	332	510	521	600	631	552	741	820
0.1	*	*	44.24	*	*	*	*	*	*	*	*
0.2	*	*	43.98	*	*	*	*	*	*	*	*
0.5	35.42	*	43.62	*	*	*	*	*	80.2	*	*
1	35.34	*	43.52	*	*	*	*	*	79.95	*	*
2	35.35	*	43.48	(48)	*	*	*	*	79.84	*	*
10	35.32	*	43.44	47.9	*	*	63.07	*	79.81	*	*
20	35.3	*	43.41	47.95	*	*	62.96	*	79.80	*	*

* Not detectable

( ) Values in brackets are intensities below $3 \times \sqrt{\text{Background}}$

Table 4-85: Calculated d-Spacings of bcc Nickel-Zinc (i = 10 mA cm^{-2}) at Various Thicknesses.

	Reflections / Calculated d-Spacings [nm]										
[μm]	222	321	330	332	510	521	600	631	552	741	820
0.1	*	*	0.20456	*	*	*	*	*	*	*	*
0.2	*	*	0.20571	*	*	*	*	*	*	*	*
0.5	0.25391	*	0.20732	*	*	*	*	*	0.11970	*	*
1	0.25449	*	0.20779	*	*	*	*	*	0.11997	*	*
2	0.25471	*	0.20796	(0.1881)	*	*	*	*	0.12007	*	*
10	0.25491	*	0.20814	0.18827	*	*	0.14717	*	0.12017	*	*
20	0.25509	*	0.20828	0.18840	*	*	0.14728	*	0.12025	*	*

* Not detectable

( ) Values in brackets are calculated from 2θ Bragg angles with intensities below $3 \times \sqrt{\text{Background}}$

Table 4-86: Calculated $R_{\{hkl\}}$ Values of an Untextured Nickel-Zinc Powder Specimen of Similar Nominal Composition and Thickness to the Electrodeposit Formed at 60 mA cm^{-2}.

Thickness	*Planes: $R_{\{hkl\}}$-Values*										
[μm]	222	321	330	332	510	521	600	631	552	741	820
0.1	12.3	54.2	8.1	10.4	7.2	10.3	0.8	3.7	1.3	1.6	0.8
0.2	23.2	104.7	15.6	19.9	14.0	20.1	1.6	7.2	2.4	3.2	1.5
0.5	55.1	249.4	37.4	50.0	33.8	48.7	4.1	17.6	5.9	7.9	3.6
1	104.0	468.1	71.5	96.1	64.4	93.3	7.8	34.0	11.7	15.3	7.0
2	178.4	820.3	125.8	171.6	116.8	170.1	14.2	63.0	21.6	28.2	13.1
10	390.8	1839	302.3	422.8	313.4	462.7	40.2	189.3	67.7	90.6	43.6
20	412.9	1968	331.2	473.5	352.6	514.8	47.9	234.0	84.4	116.9	55.4

Table 4-87: Measured Intensities $I_{\{hkl\}}$ of NiZn, Electrodeposited at 60 mA cm^{-2}, on Mild Steel Substrates.

Thickness	*Planes: $I_{\{hkl\}}$-Values*										
[μm]	222	321	330	332	510	521	600	631	552	741	820
0.1		*	2256	*	*	*	*	*	*	*	*
0.2	249	*	2352	(29)	*	*	*	*	(18)	*	*
0.5	428	*	5994	106	*	*	(30)	*	265	(32)	*
1	1463	*	12685	253	*	*	243	*	303	98	*
2	410	*	28807	111	*	*	301	*	507	227	*
10	*	*	19870	*	456	(62)	627	109	947	499	336
20	*	*	355824	*	*	*	(86)	*	392	137	*

* Not detectable

( ) Values in brackets are intensities below $3 \times \sqrt{\text{Background}}$

Table 4-88: Planar Distribution of Nickel-Zinc Deposit of Various Thicknesses, Electrodeposited at 60 mA cm^{-2}, on Mild Steel Substrates.

	Planes: Distribution in per cent										
[µm]	222	321	330	332	510	521	600	631	552	741	820
0.1	*	*	100	*	*	*	*	*	*	*	*
0.2	6.6	*	93.4	**	*	*	*	*	**	*	*
0.5	3.6	*	74.6	1.0	*	*	**	*	20.8	**	*
1	5.5	*	68.9	1.0	*	*	12.1	*	10.0	2.5	*
2	0.8	*	80.4	0.2	*	*	7.5	*	8.3	2.8	*
10	*	*	59.4	*	1.3	**	14.1	0.5	12.7	5.0	7.0
20	*	*	99.5	*	*	*	**	*	0.4	0.1	*

* Not detectable

** $I(hkl) < 3 \times \sqrt{\text{Background}}$

Table 4-89: Raw Data: Bragg Angles of bcc Nickel-Zinc, Electrodeposited at 60 mA cm^{-2}, on Mild Steel Substrates.

	Reflections / 2θ Bragg Angles										
[µm]	222	321	330	332	510	521	600	631	552	741	820
0.1	*	*	44.20	*	*	*	*		*	*	*
0.2	35.56	*	43.71	(48.86)	*	*	*	*	80.50	*	*
0.5	35.40	*	43.50	48.09	*	*	(63.63)	*	80.10	(89.72)	*
1	35.40	*	43.49	48.09	*	*	62.63	*	80.10	89.72	*
2	35.28	*	43.31	47.82	*	*	62.75	*	79.54	89.56	*
10	*	*	43.16	*	52.26	(56.81)	62.65	72.12	79.11	89.41	90.57
20	*	*	43.17	*	*	*	62.63	*	79.32	89.49	*

* Not detectable

( ) Values in brackets are calculated from 2θ Bragg angles with intensities below $3 \times \sqrt{\text{Background}}$

Table 4-90: Calculated d-Spacings of bcc Nickel-Zinc (i = 60 mA cm^{-2}) at Various Thicknesses.

	Reflections / Calculated d-Spacings [nm]										
[µm]	222	321	330	332	510	521	600	631	552	741	820
0.1	*	*	0.20474	*	*	*	*		*	*	*
0.2	0.25345	*	0.20694	(0.18728)	*	*	*	*	(0.11948)	*	*
0.5	0.25463	*	0.20790	0.18806	*	*	(0.14822)	*	0.12003	(0.10920)	*
1	0.25463	*	0.20790	0.18806	*	*	0.14822	*	0.12003	0.10920	*
2	0.25565	*	0.20874	0.18881	*	*	0.14796	*	0.12052	0.10936	*
10	*	*	0.20942	*	0.17424	(0.16922)	0.14815	0.13087	0.12097	0.10950	0.10840
20	*	*	0.20939	*	*	*	0.14806	*	0.12089	0.19352	*

* Not detectable

( ) Values in brackets are calculated from 2θ Bragg angles with intensities below $3 \times \sqrt{\text{Background}}$

Table 5-1: Interplanar Spacings of Substrate Metals, Alloy Electrodeposits Investigated, and Individual Metals Contained in Alloy Electrodeposits Investigated, based on JCPDS Data [88].

		Cu	NiFe	NiFe	Ni	Fe	Fe	Ni_5Zn_{21}
	lattice	fcc	fcc	bcc	fcc	fcc	bcc	bcc
	JCPDS	4-836	23-297	37-474	4-850	31-619	6-696	6-653
$h^2+k^2+l^2$	plane	*d-spacings [nm]*						
1	100	**0.3615**	**0.3596**	**0.28681**	**3.5238**	**0.36**	**0.28664**	**0.892**
2	110	0.25562	0.25428	0.20281	0.24917	0.25456	0.20269	0.63074
3	111	0.20871	0.20762	0.16559	0.20345	0.20785	0.16550	0.515
5	210	0.16167	0.16082	0.12827	0.15759	0.161	0.12819	0.39892
6	211	0.14758	0.14681	0.11709	0.14386	0.14697	0.11702	0.36416
9	221	0.1205	0.11987	0.09560	0.11746	0.12	0.09555	0.29733
10	310	0.11432	0.11372	0.0907	0.11143	0.11384	0.09064	0.28208
11	311	0.1090	0.10842	0.08648	0.10625	0.10854	0.08643	0.26895
13	320	0.10026	0.09974	0.07955	0.09773	0.09985	0.07950	0.2474
14	321	0.09661	0.09611	0.07665	0.09418	0.09621	0.07661	0.2384

Table 5-2: Crystallographic Planes (Directions) with Corresponding Perpendicular Planes (Directions) in the Cubic System [119].

{hkl}	Planes Perpendicular (⊥) to {hkl}
100	100; 110; 210; 310; 320
110	110; 211; 221
111	110; 211; 321
210	100; 210; 221; 321
211	110; 111; 311; 321
221	110; 210; 221
310	100; 110; 310
311	110; 211; 310
320	100; 320
321	111; 210; 211

Table 5-3: Interplanar Spacings of fcc and bcc Nickel-Iron Compatible for Initial Deposition on Copper Substrate According to Finch's 15 per Cent Criterion. Data are Based on JCPDS Lattice Parameters.

	Substrate	Electrodeposit	
	Cu	NiFe	NiFe
Lattice	*fcc*	*fcc*	*bcc*
	100	100	-
	110	110	100
	111	111	110
	210	210; 211	111
	211	210; 211	111; 210
	221	221; 310; 311	210; 211
	310	221; 310; 311	210; 211
	311	221; 310; 311; 320; 321	211; 221

Table 5-4: Interplanar Spacings of fcc and bcc Nickel-Iron Compatible for Initial Deposition According to Finch's 15 per Cent Criterion. Data are Based on JCPDS Lattice Parameters.

	NiFe	NiFe
Lattice	*fcc*	*bcc*
	100	-
	110	100
	111	110
	210	111
	211	111; 210
	221	210; 211
	310	210; 211; 220
	311	211; 221
	320	211; 221; 310; 311
	321	221; 310; 311

Table 5-5: Interplanar Spacings of Ni_5Zn_{21}, that Fulfil Finch's 15 per cent Criterion and Fit on the d-Spacings of the Copper and Iron Substrate Multiplied by Three.

	Substrate	Electrodeposit
	Cu	Ni_5Zn_{21}
Lattice	*fcc*	*bcc*
	100	-
	110	300
	111	330
	210	333
	211	333; 630
	221	630; 633
	310	630; 633; 663
	311	633 ;663; 930
	320	663; 930; 933
	321	663; 930; 933; 960

Substrate	Electrodeposit
Fe	Ni_5Zn_{21}
bcc	*bcc*
100	300
110	330
111	333
210	630; 633
211	630; 633; 663
221	663; 930;933; 960
310	663; 930;933; 960; 963
311	663; 930; 933; 960; 963
320	930, 933, 960; 963
321	933; 960;963

Table 5-6: Atomic Density $\delta_{\{hkl\}}$ of Different Crystal Planes {hkl} in the fcc Lattice.

{hkl}	{111}	{100}	{110}	{311}	{210}	{211}
$\delta_{\{hkl\}}$ (at/a^2)	2.3094	2	1.4142	0.9177	0.8944	0.6666
$\delta_{\{hkl\}}$ (at/nm^2)	17.8591	15.4664	10.9364	7.0965	6.9168	5.1555

Table 5-7: Atomic Density $\delta_{\{hkl\}}$ of Different Crystal Planes {hkl} in the bcc Lattice.

{hkl}	{110}	{100}	{310}	{111}	{211}
$\delta_{\{hkl\}}$ (at/a^2)	1.4142	1	0.6325	0.5774	0.3333
$\delta_{\{hkl\}}$ (at/nm^2)	17.1920	12.1566	7.6885	7.0186	4.0522

8. 2 Figures

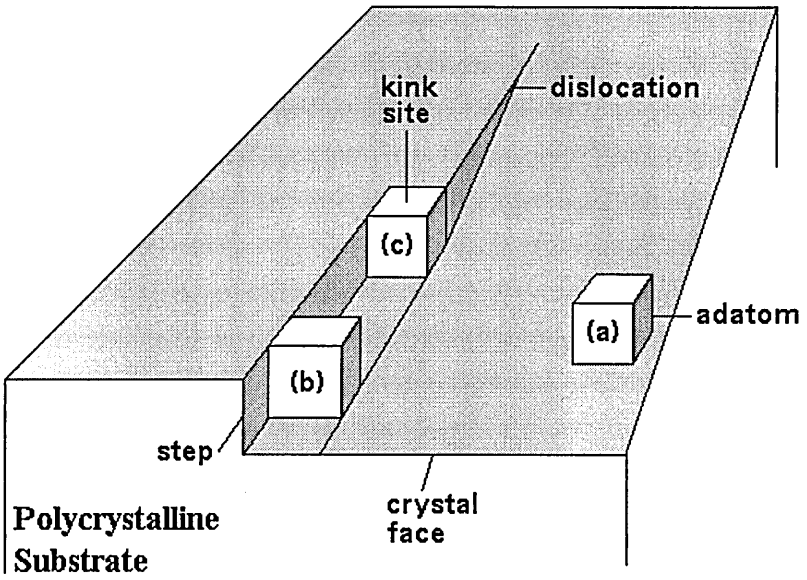

Fig. 2-1: Schematic Drawing of the Electrocrystallization Process of an Atom on a polycrystalline Substrate from (a) being discharged, (b) diffusing over the Surface to a Step, and (c) diffusing along the Step to kink Site in a Screw Dislocation.

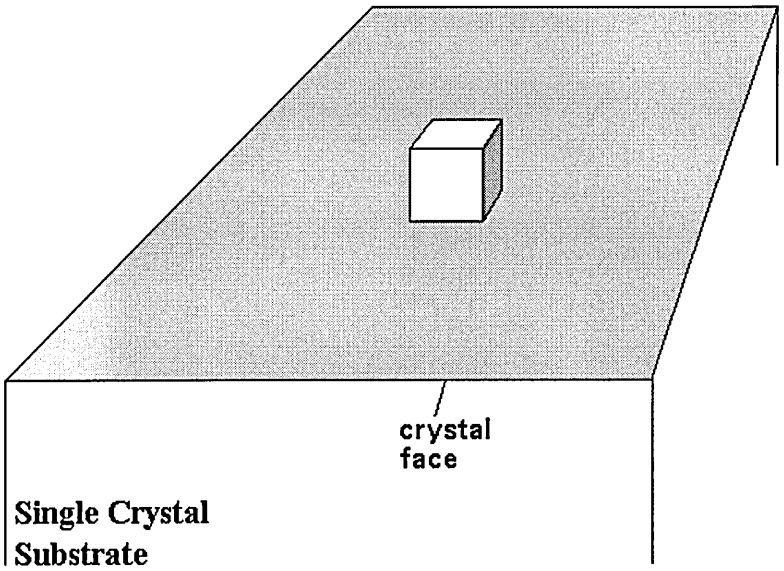

Fig. 2-2: Schematic Drawing of the three-dimensional Electrocrystallization Process of an Atom on a single Crystal Substrate (Island Growth).

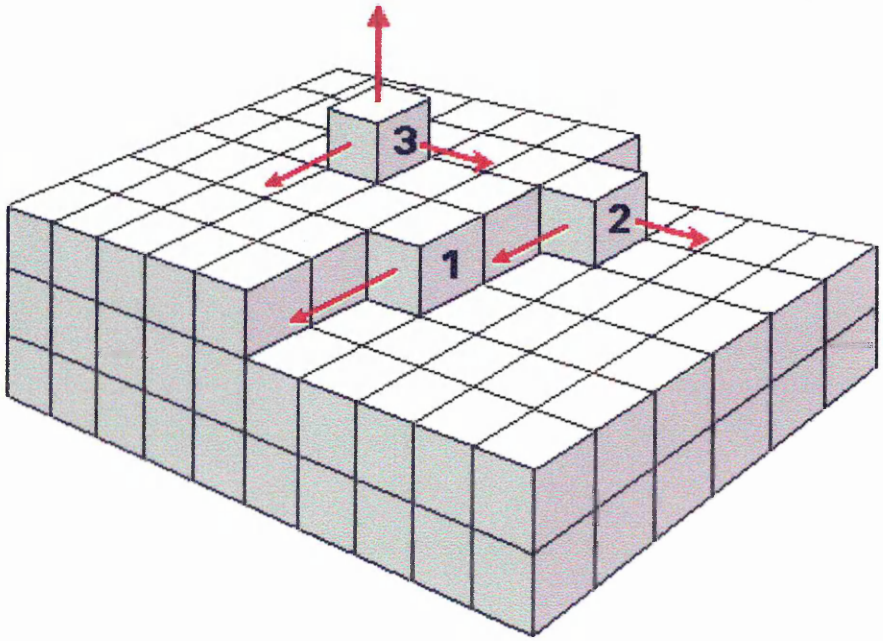

Fig. 2-3: Schematic Drawing of linear Growth at Kink Site '1', two-dimensional Growth '2', and three-dimensional Growth '3'.

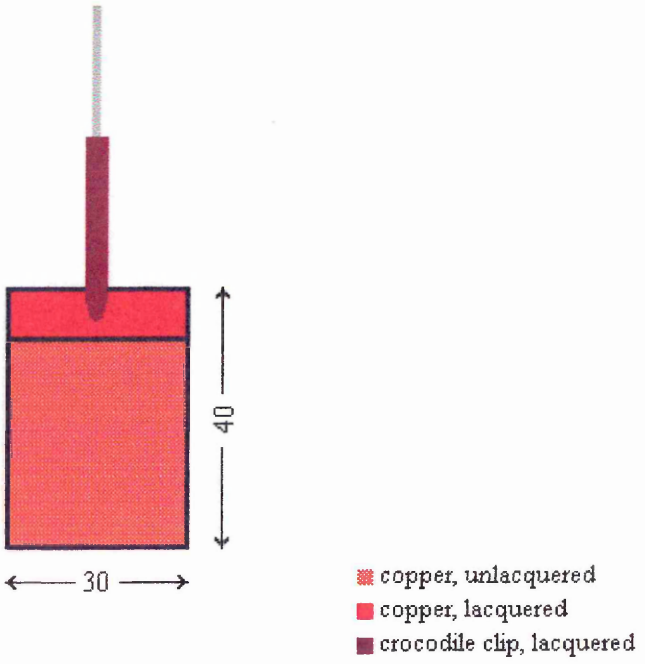

Fig. 3-1: Copper Cathodes, Used for Thick Deposits at Individual Current Densities for subsequent XRD, GDOES, EDX Investigations.

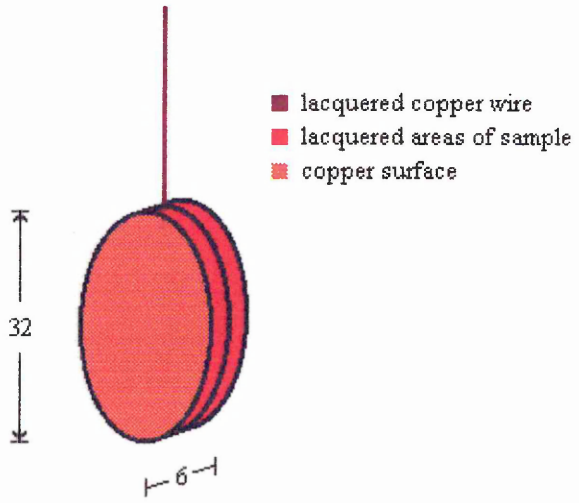

Fig. 3-2: Copper Disc Cathodes, Used to Deposit Thin Deposits for Subsequent XRD, GDOES, EDX Investigations.

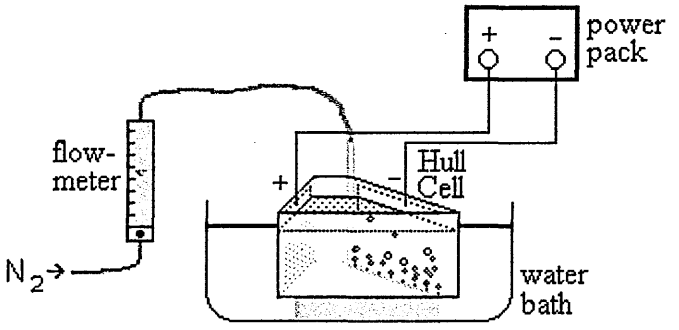

Fig. 3-3: Schematic Diagram of Experimental Electroplating Set-up with the Hull Cell.

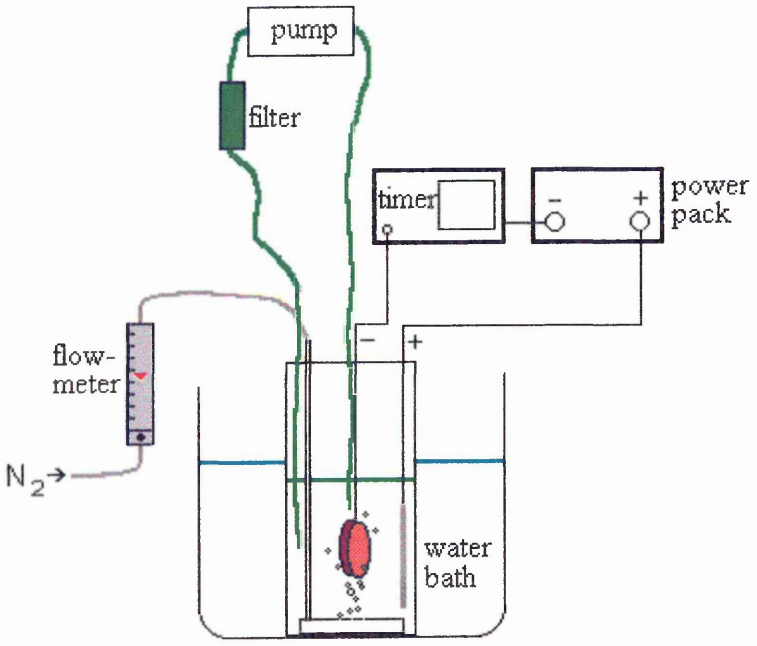

Fig. 3-4: Schematic Diagram of Experimental Electroplating Set-up.

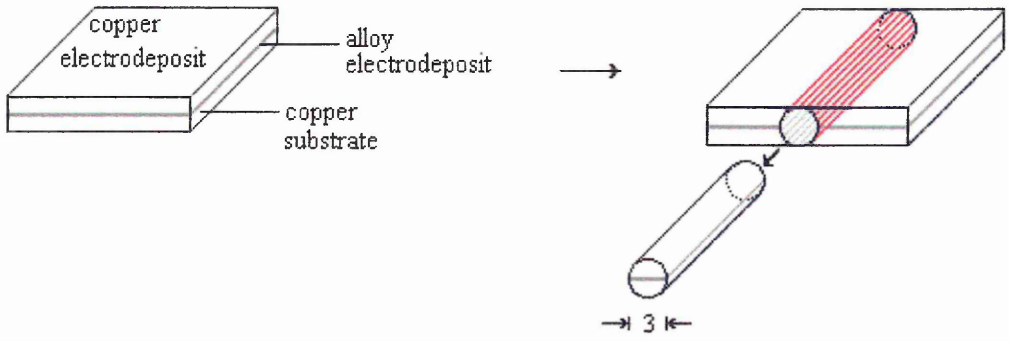

Fig. 3-5: Spark Erosion of a Cylinder.

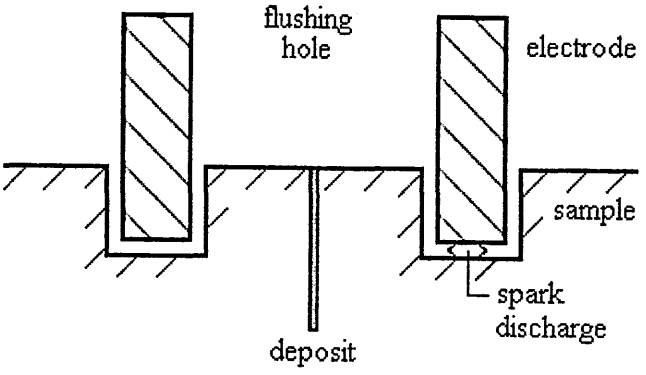

Fig. 3-6: Cross-sectional View of Spark Erosion Process.

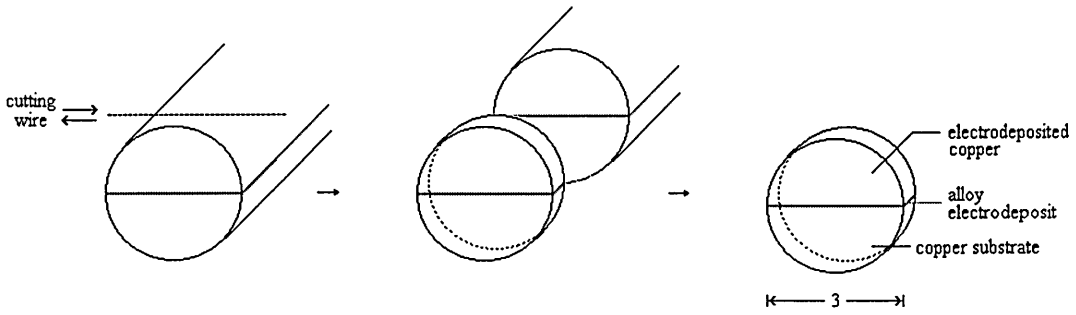

Fig. 3-7: Cutting off Discs.

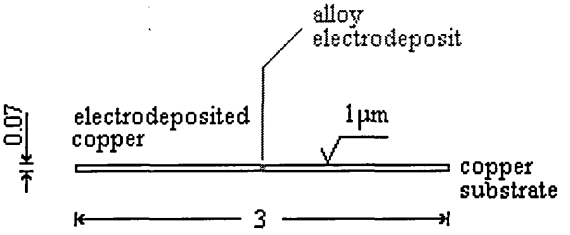

Fig. 3-8: Ground 3 mm Diameter Disc, Ready for Dimpling.

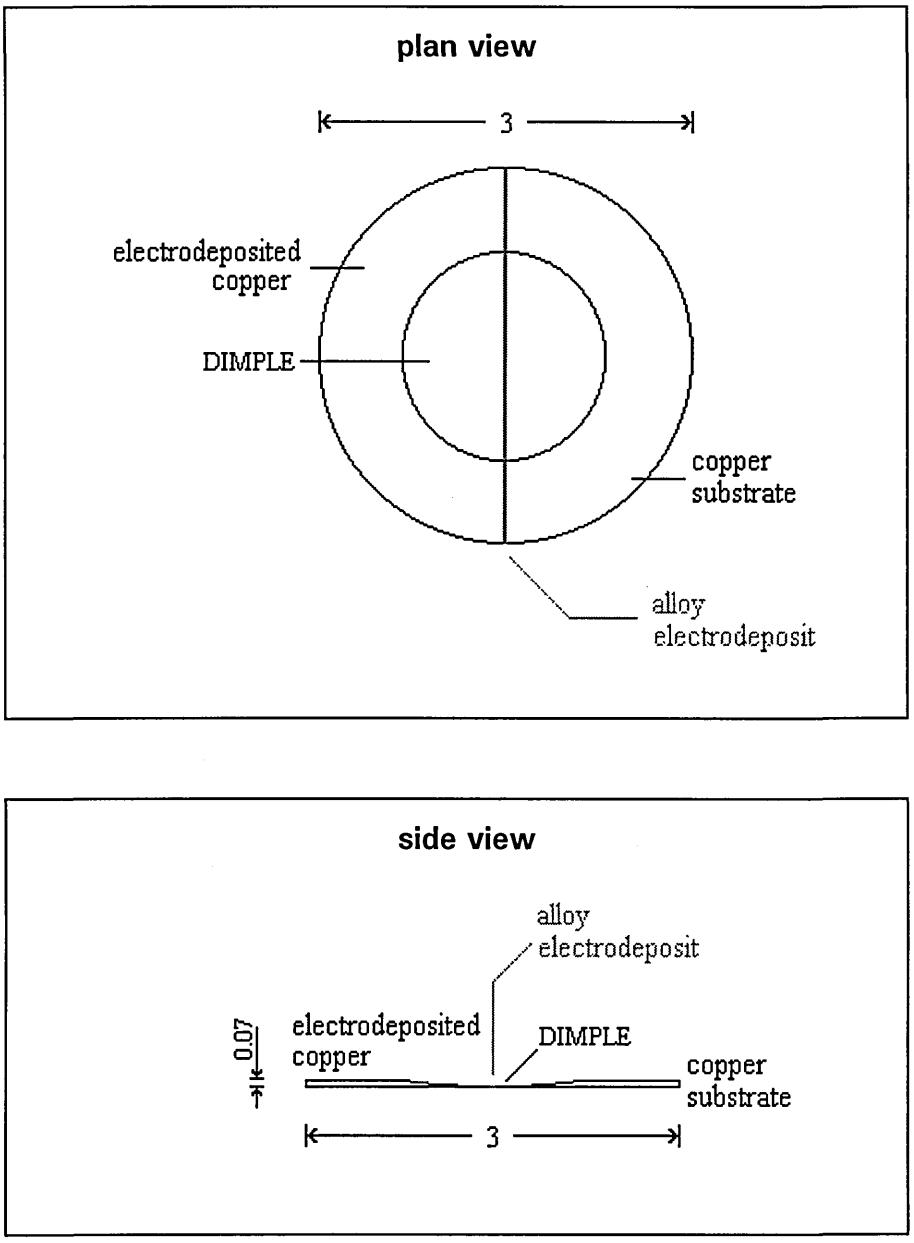

Fig. 3-9: Dimpled 3 mm Diameter Disc.

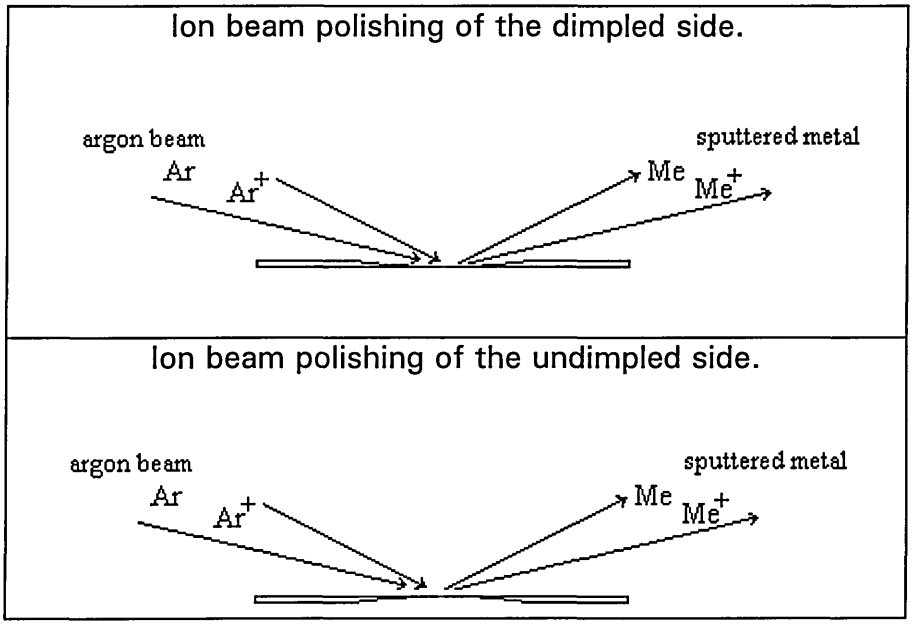

Fig. 3-10: Ion Beam Thinning.

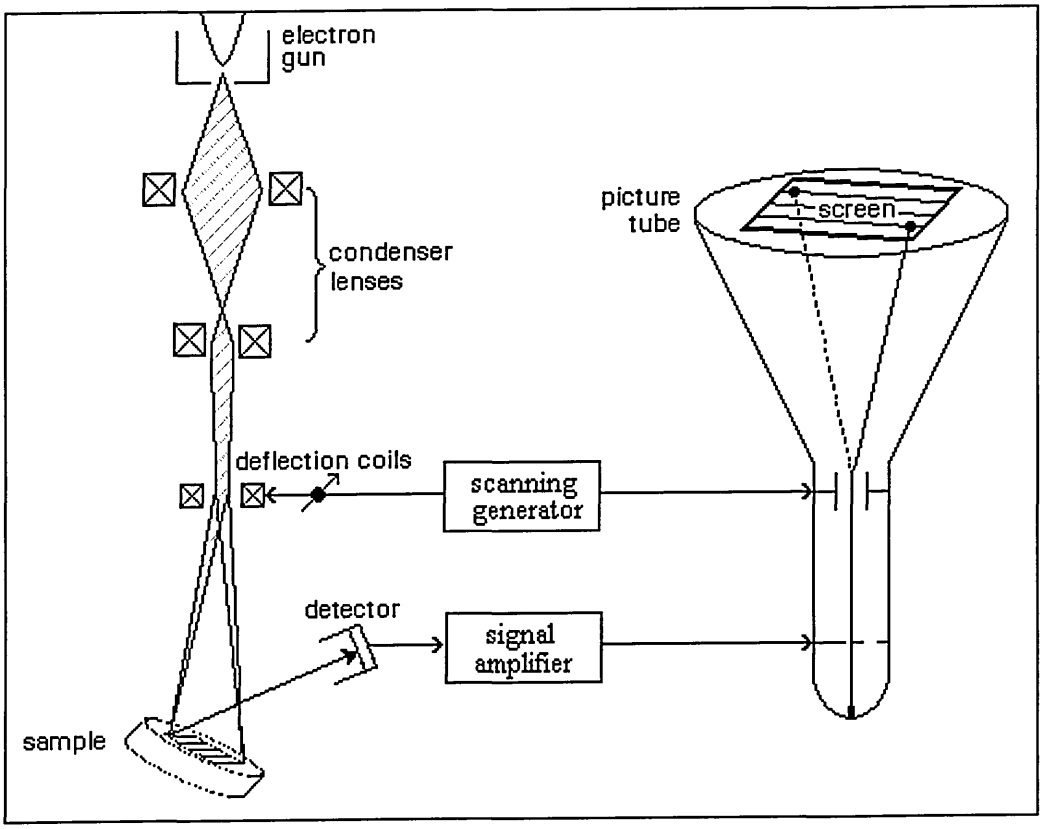

Fig. 3-11: Schematic Diagram of the SEM [81].

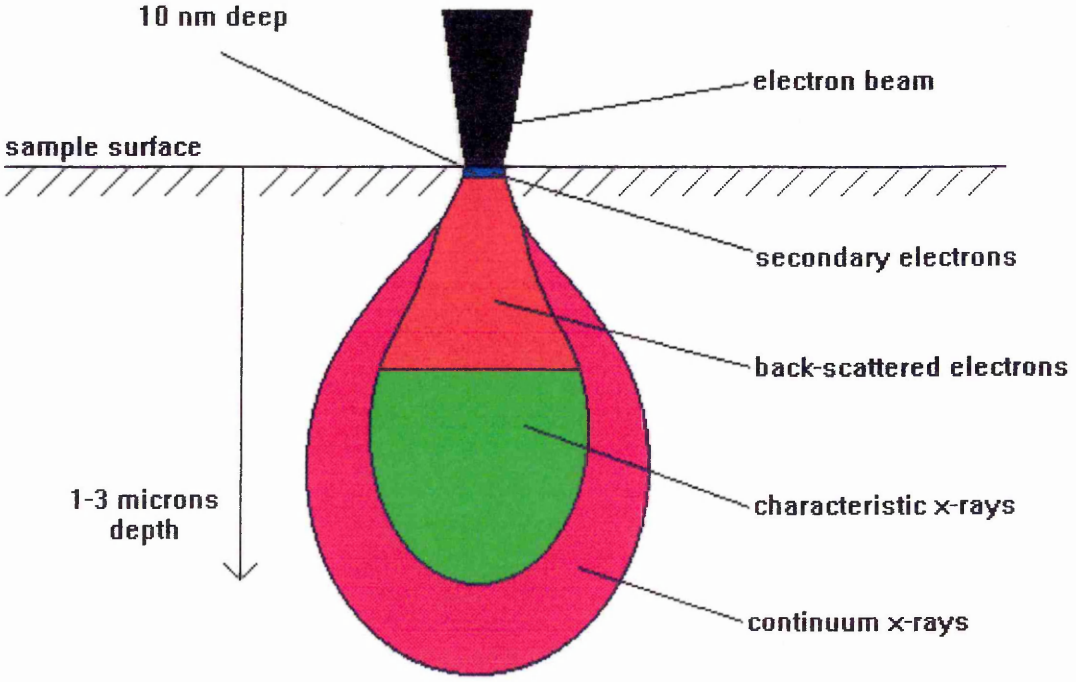

Fig. 3-12 [82]: Schematic Diagram of Excitation Volume for Major SEM Sample Emissions.

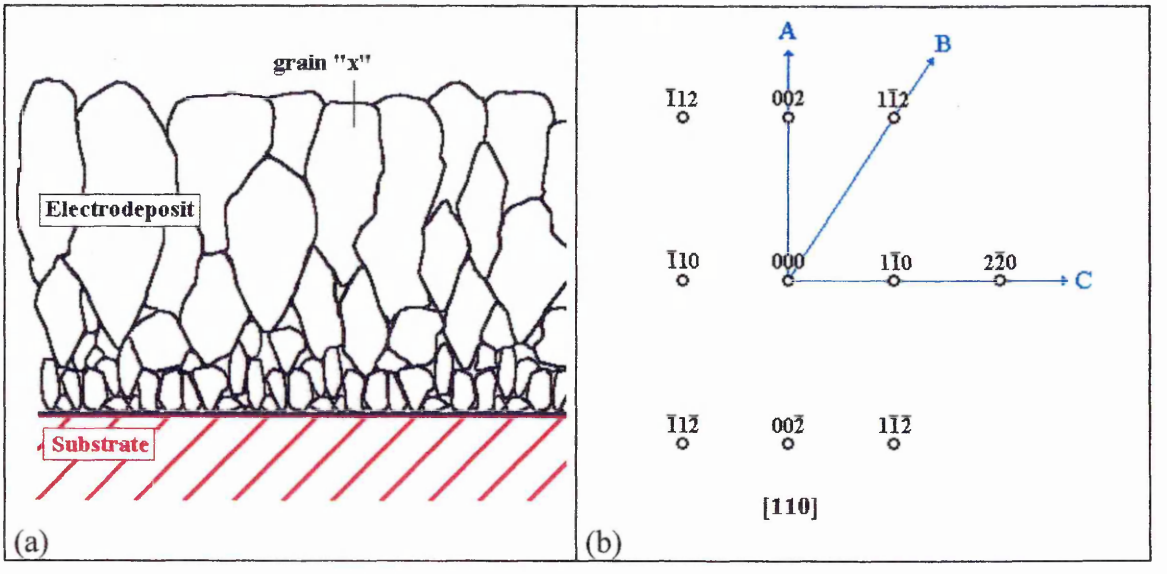

Fig. 3-13: a) Schematic Representation of a Cross-Sectional Transmission Electron Micrograph of a bcc Nickel-Iron Electrodeposit on a Copper Substrate.
b) Schematic Representation of an Electron Diffraction Pattern from Grain 'x' in a).

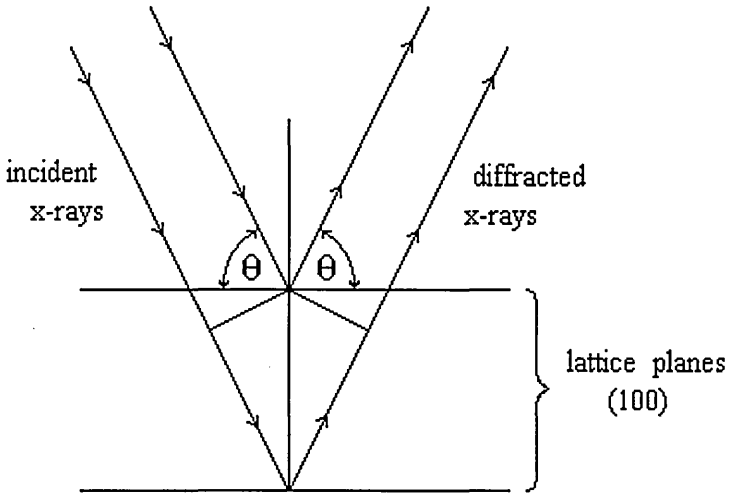

Fig. 3-14: Diffraction of X-rays by Lattice Planes.

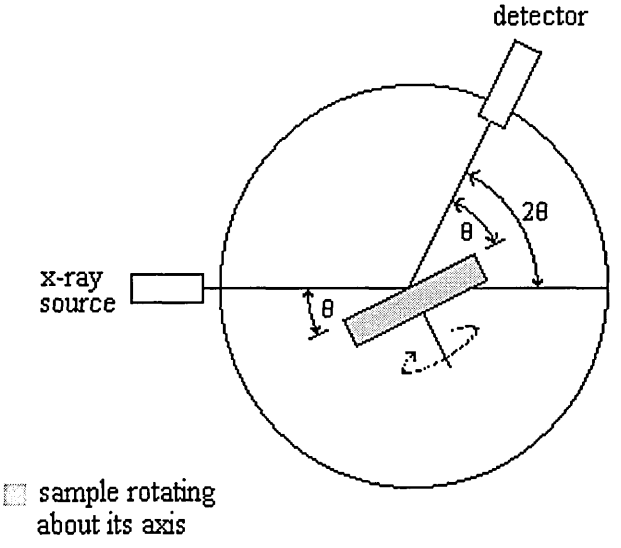

Fig. 3-15: X-ray Spectrometer Operated under Bragg-Brentano Conditions.

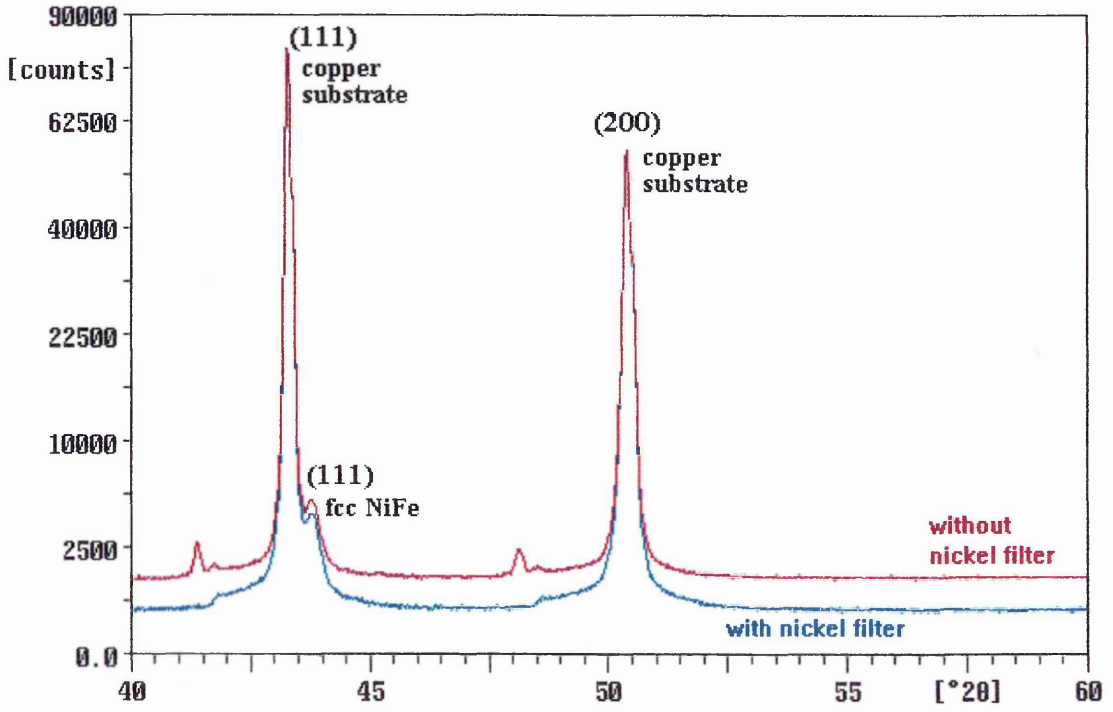

Fig. 3-16: X-ray Diffraction Spectra of Nickel-Iron Electrodeposit on Copper Substrate. Filtering Monochromatic CuK_{α} Radiation Through a Nickel Foil Resulted in Lower Background Noise.

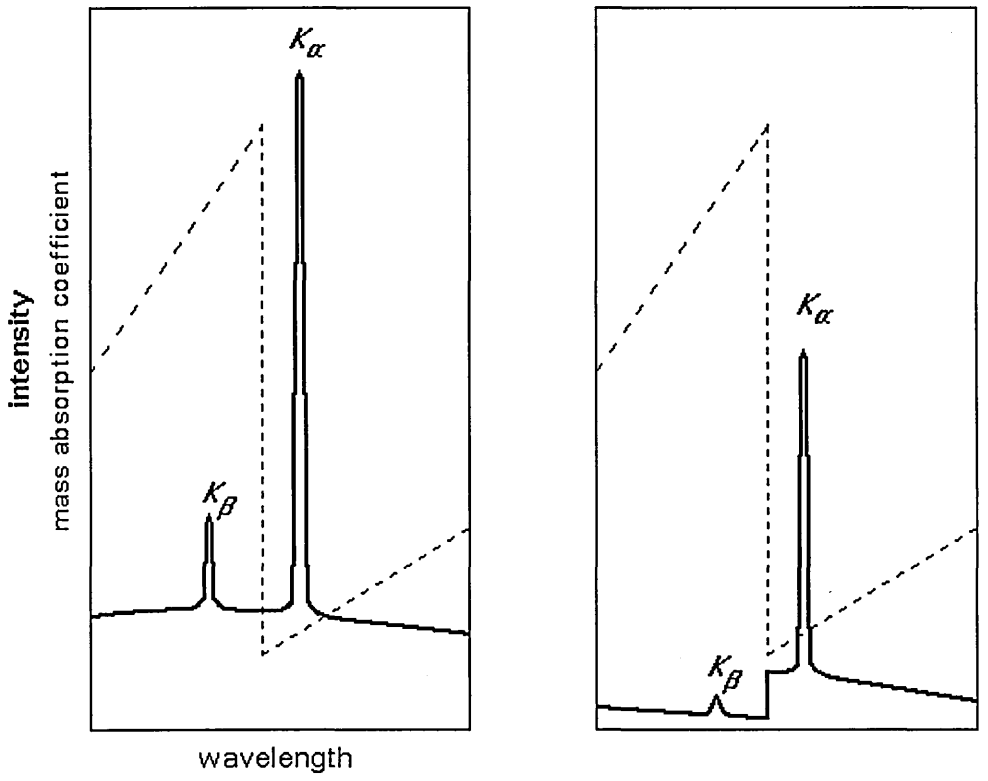

(a) No filter *(b) Nickel filter*

Fig. 3-17[87]: Schematic Comparison of the Spectra of Copper Radiation *(a)* Before and *(b)* After Passage Through a Nickel Filter. The Dashed Line Is the Mass Absorption Coefficient of Nickel.

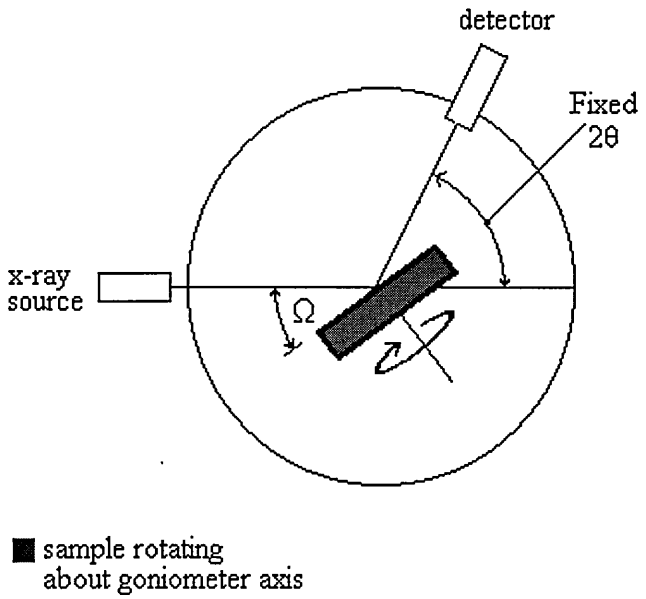

Fig. 3-18: X-ray Spectrometer operated under Omega Scan Conditions.

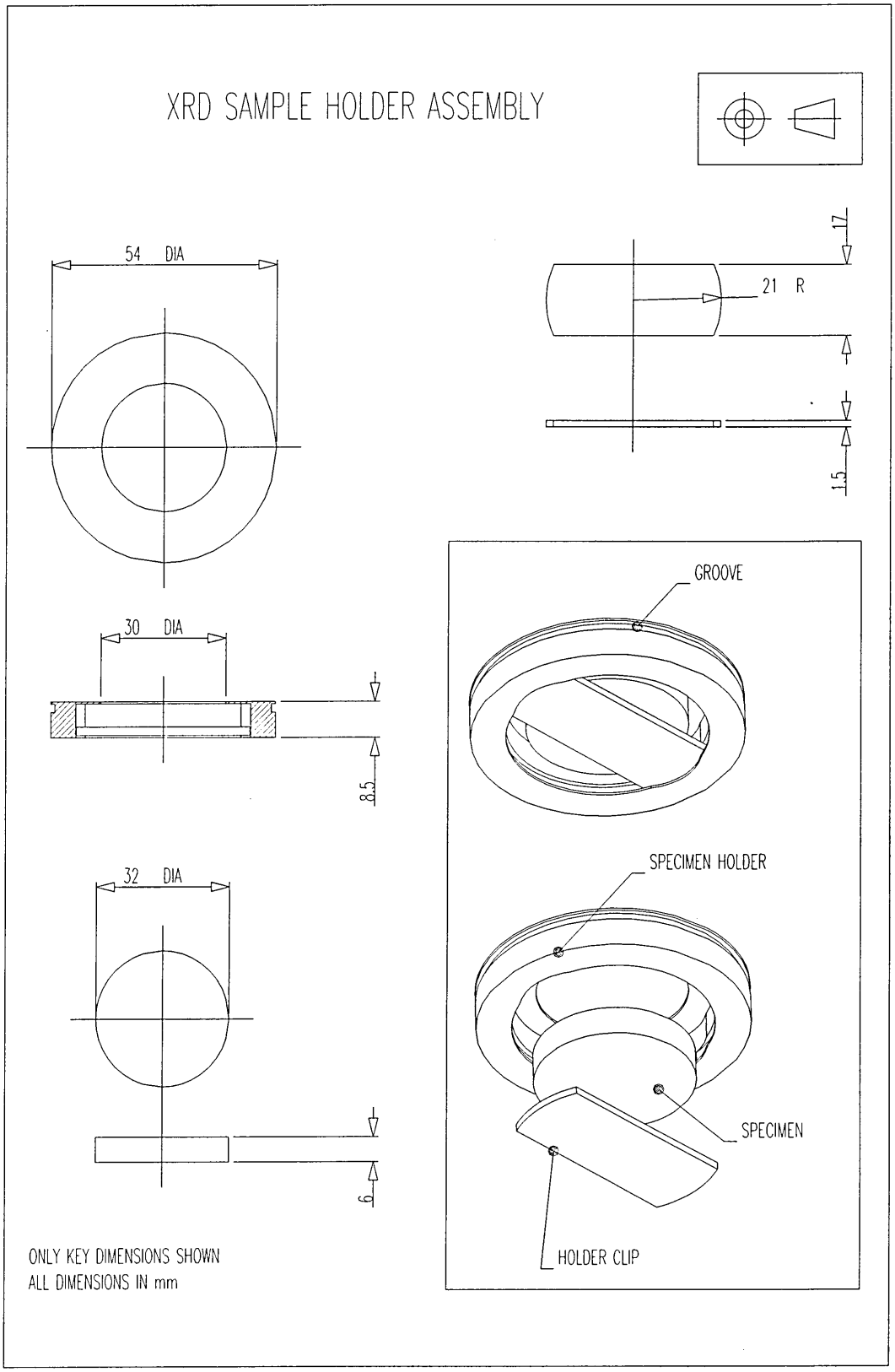

Fig. 3-19: Specimen Holder Assembly for X-ray Diffraction Investigations of Disc Samples.

Fig. 4-1: Surface Morphology of Deposit Produced in NiFe Solution 4 at 10 mA cm^{-2}.

200 µm

Fig. 4-2: Surface Morphology of Deposit Produced in NiFe Solution 4 at 30 mA cm^{-2}.

10 µm

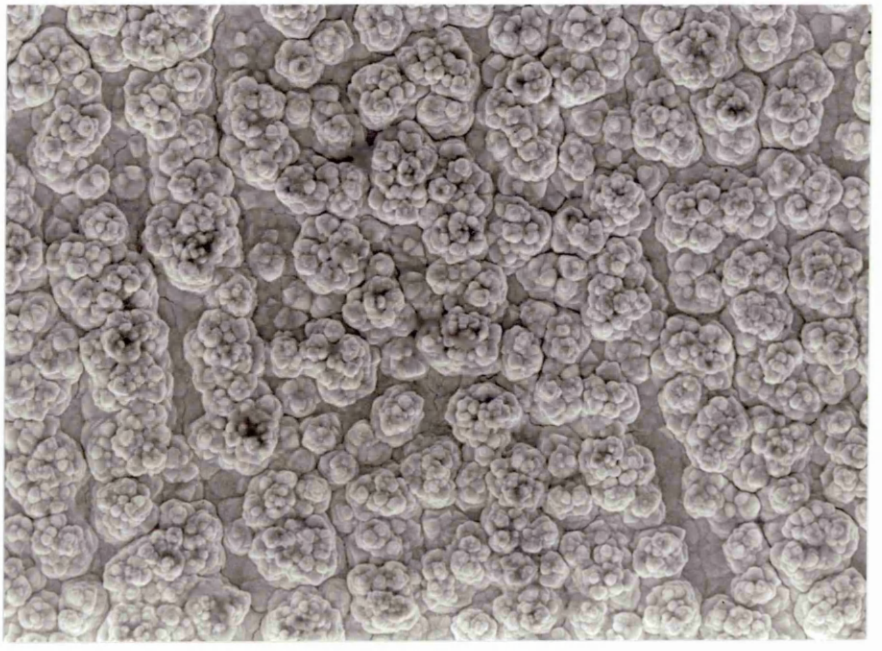

Fig. 4-3: Surface Morphology of Deposit Produced in NiZn Solution 8 at 10 mA cm^{-2}.

1 µm

Fig. 4-4: Surface Morphology of Deposit Produced in NiZn Solution 8 at 10 mA cm^{-2}.

2 µm

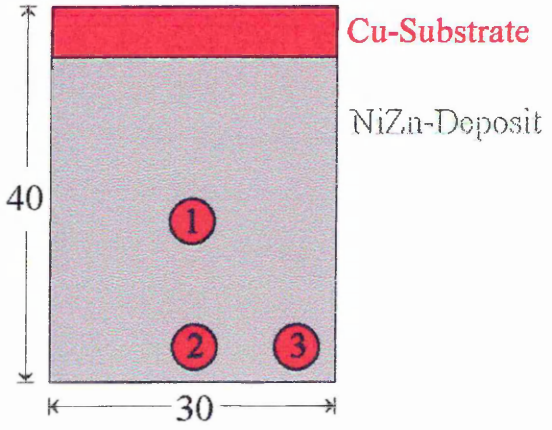

Fig. 4-5: Schematic Diagram of Nickel-Zinc Deposited Sample, Analyzed Areas Indicated with Numbers.

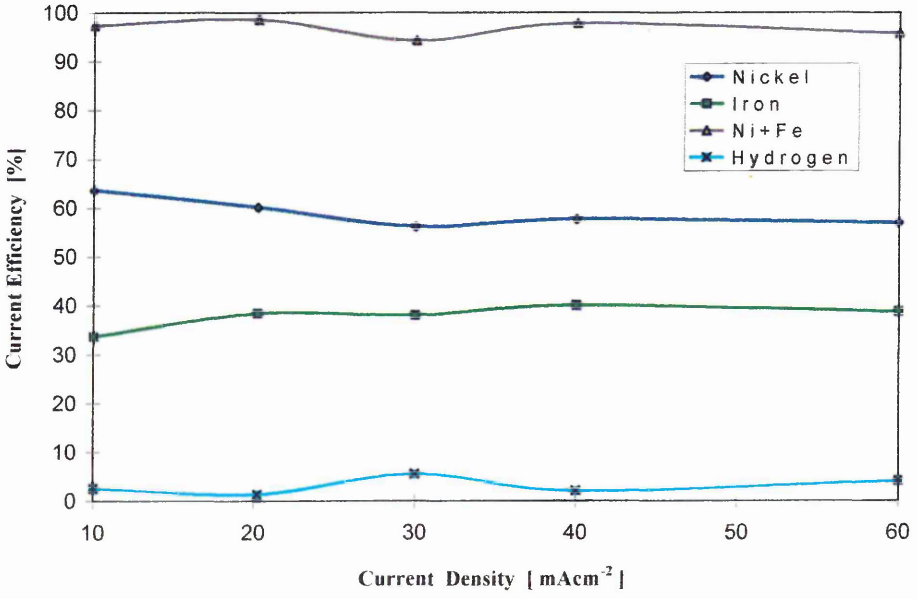

Fig. 4-6: Partial Current Efficiencies of Nickel-Iron Solution 1 at Individual Current Densities Using Compositional Results from EDX.

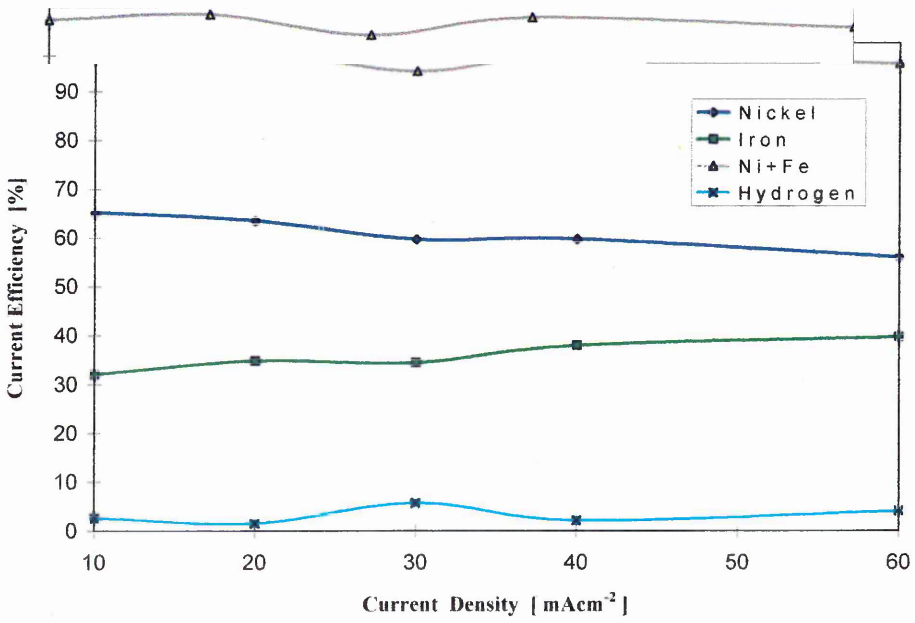

Fig. 4-7: Partial Current Efficiencies of Nickel-Iron Solution 1 at Individual Current Densities Using Compositional Results from GDOES.

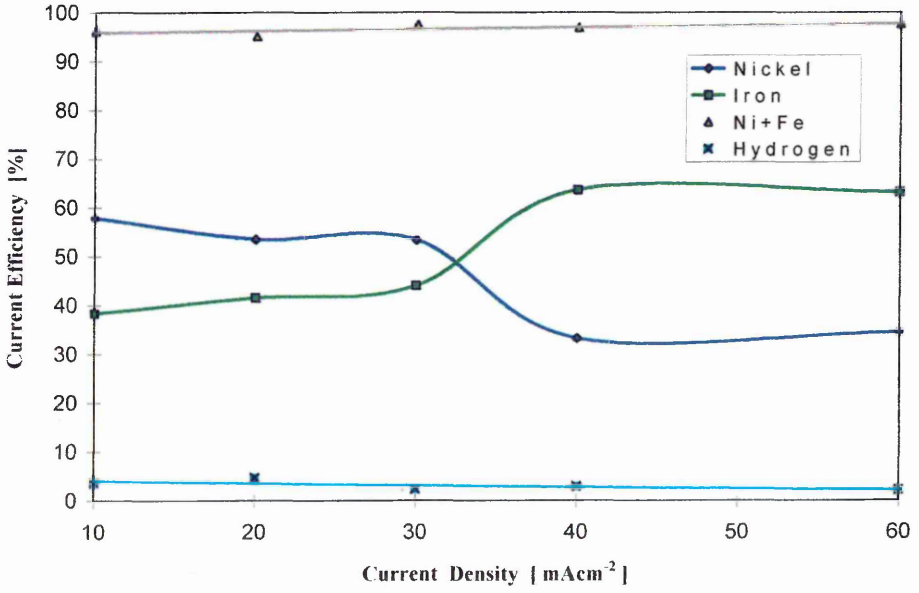

Fig. 4-8: Partial Current Efficiencies of Nickel-Iron Solution 3 at Individual Current Densities Using Compositional Results from GDOES.

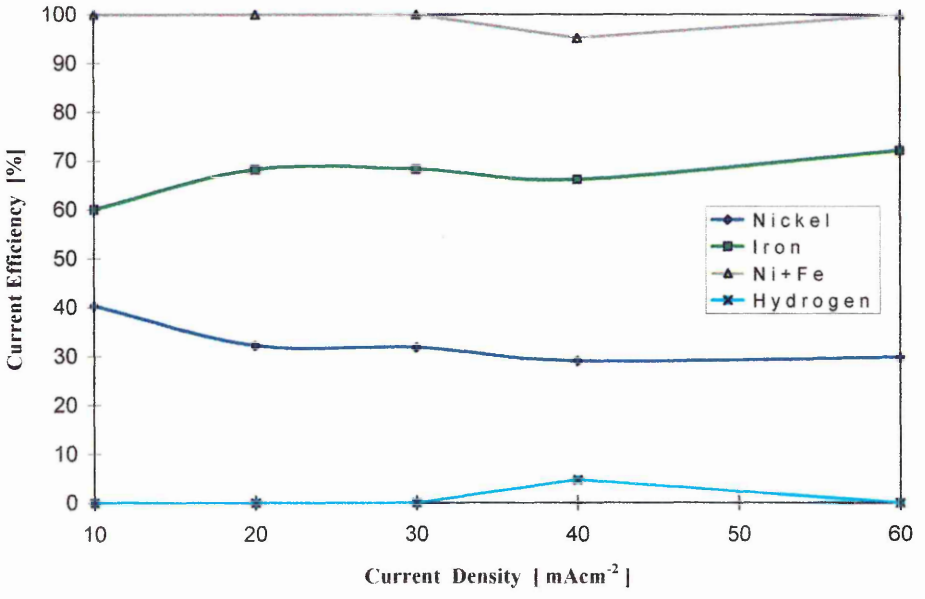

Fig. 4-9: Partial Current Efficiencies of Nickel-Iron Solution 4 at Individual Current Densities Using Compositional Results from GDOES.

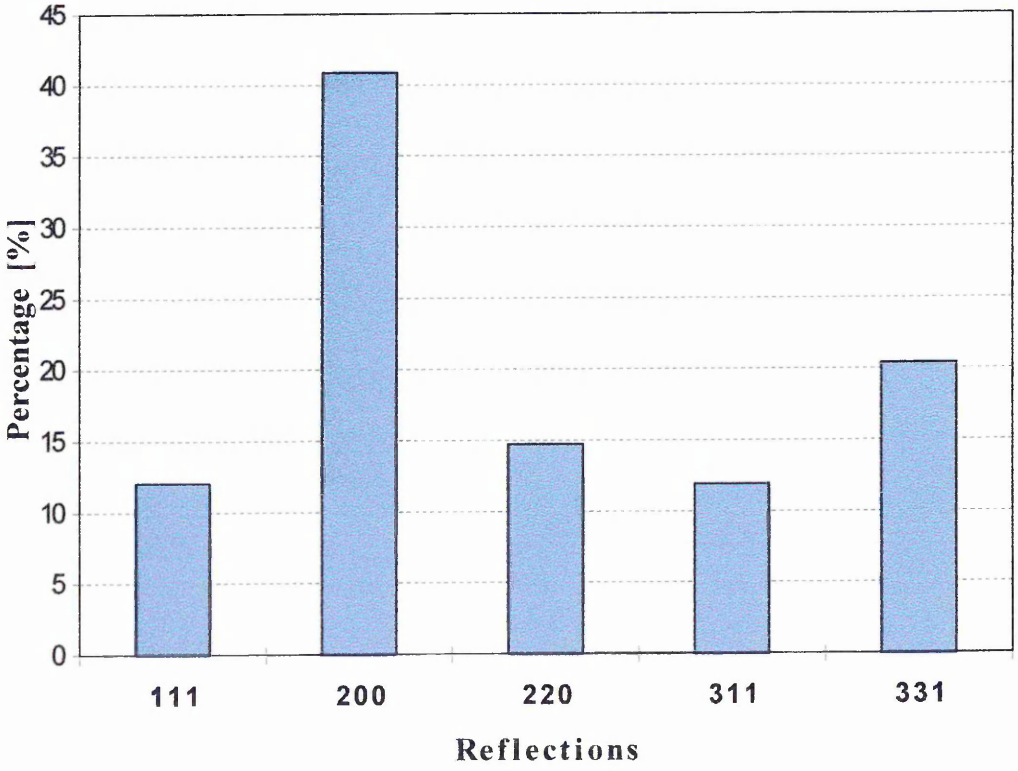

Fig. 4-11: Distribution of Reflecting Planes Detected in the Copper Sheet Substrate.

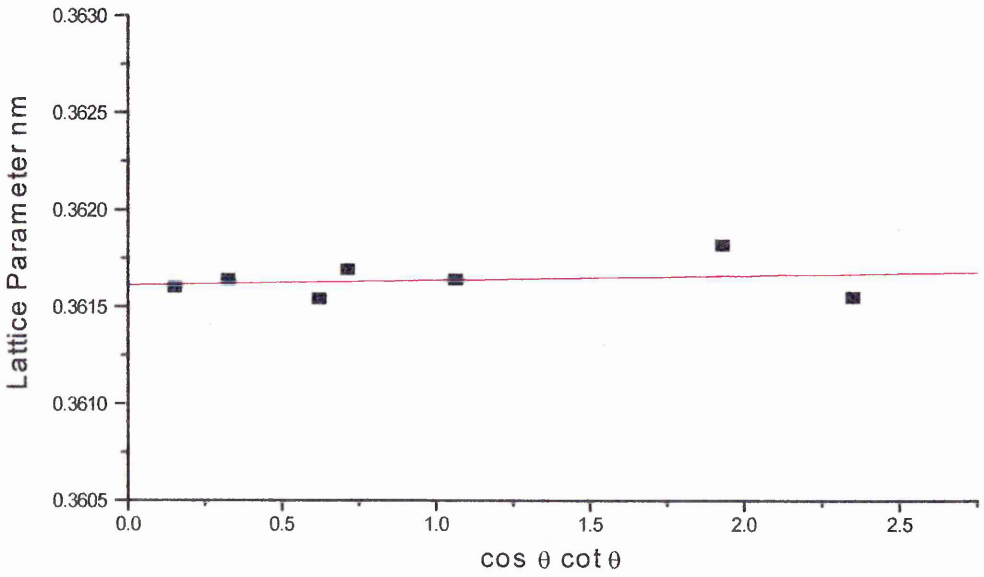

Fig. 4-12: Copper Sheet Substrate: Lattice Parameter [nm] Versus cosθ cotθ; Cohen-Wagner Plot for Extrapolation of Lattice Parameter 'a'.

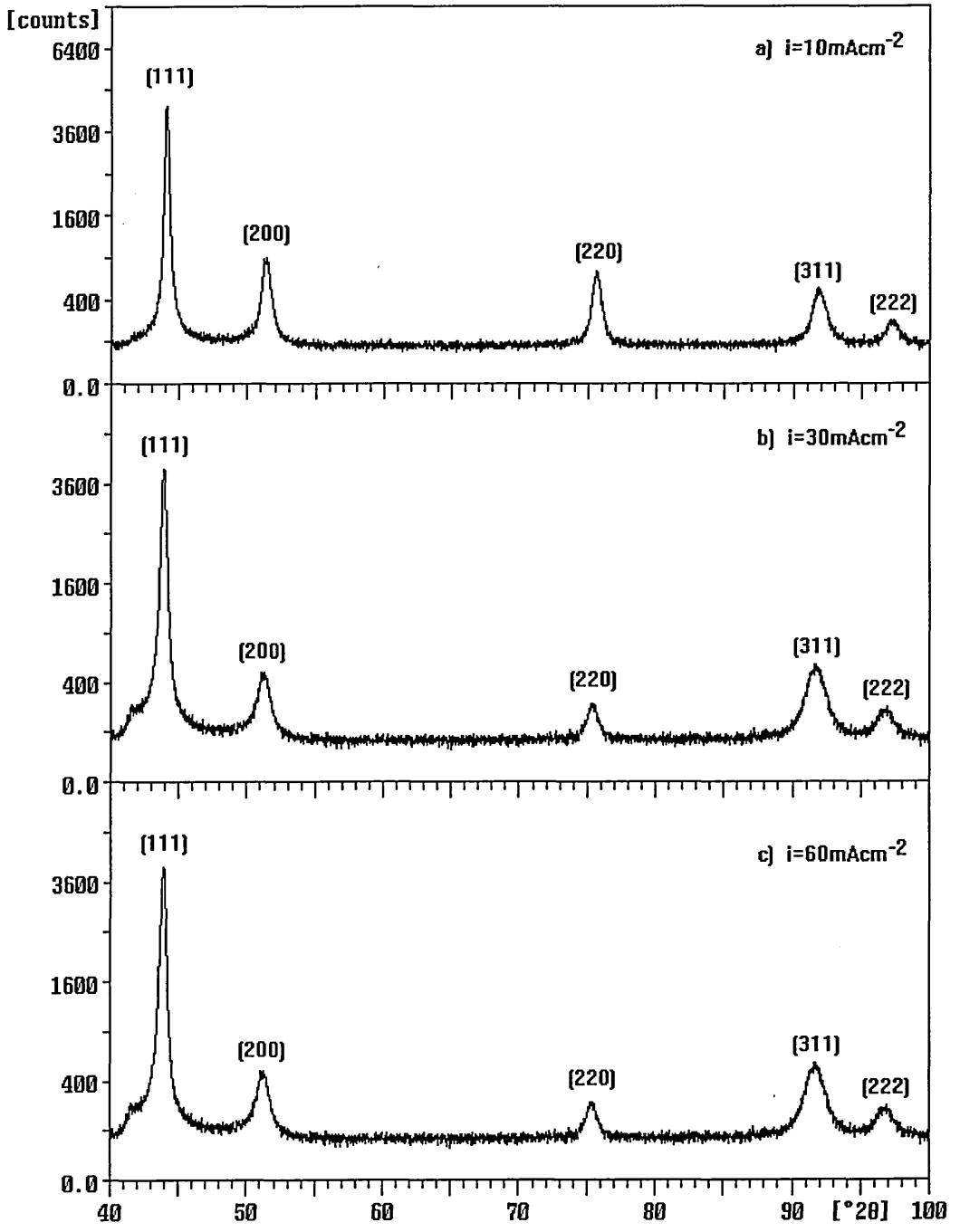

Fig. 4-13: X-Ray Diffraction Spectra of fcc Structured NiFe Deposits Obtained from Solution 1 at Different Current Densities:
a) i = 10 mA cm^{-2}, b) i = 30 mA cm^{-2}, c) i = 60 mA cm^{-2}.

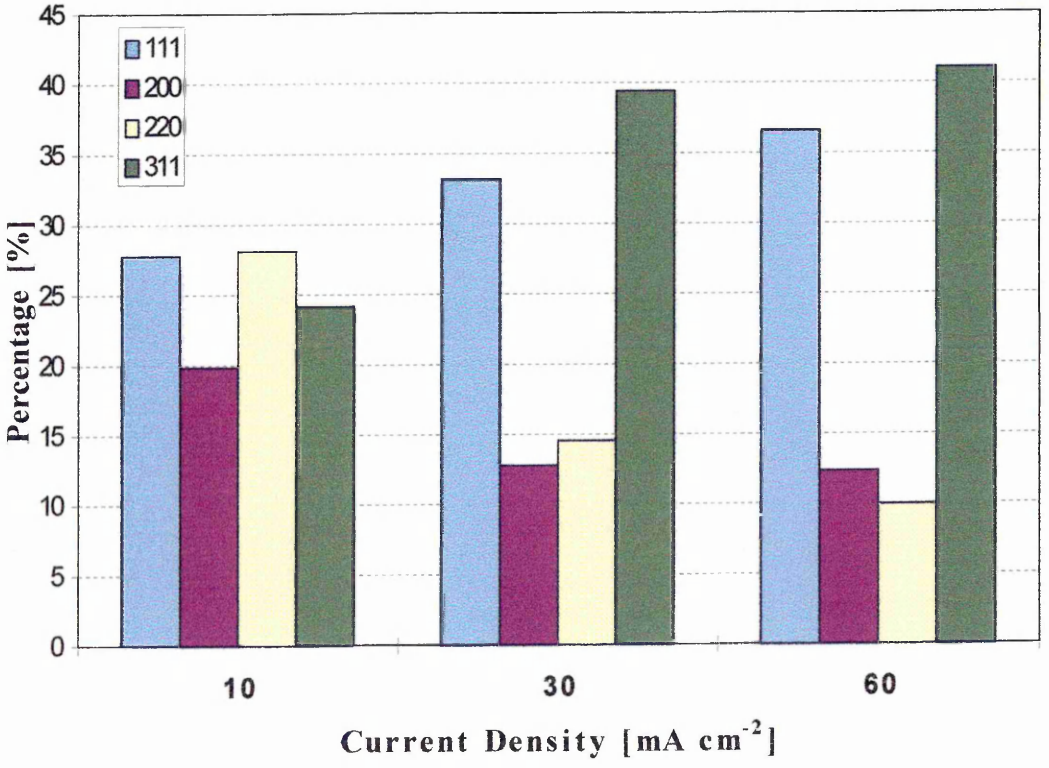

Fig. 4-14: Distribution of Reflections Detected in fcc NiFe Electrodeposits on Copper Sheet Substrates Deposited in NiFe Solution 1 at 10, 30 and 60 mA cm^{-2}.

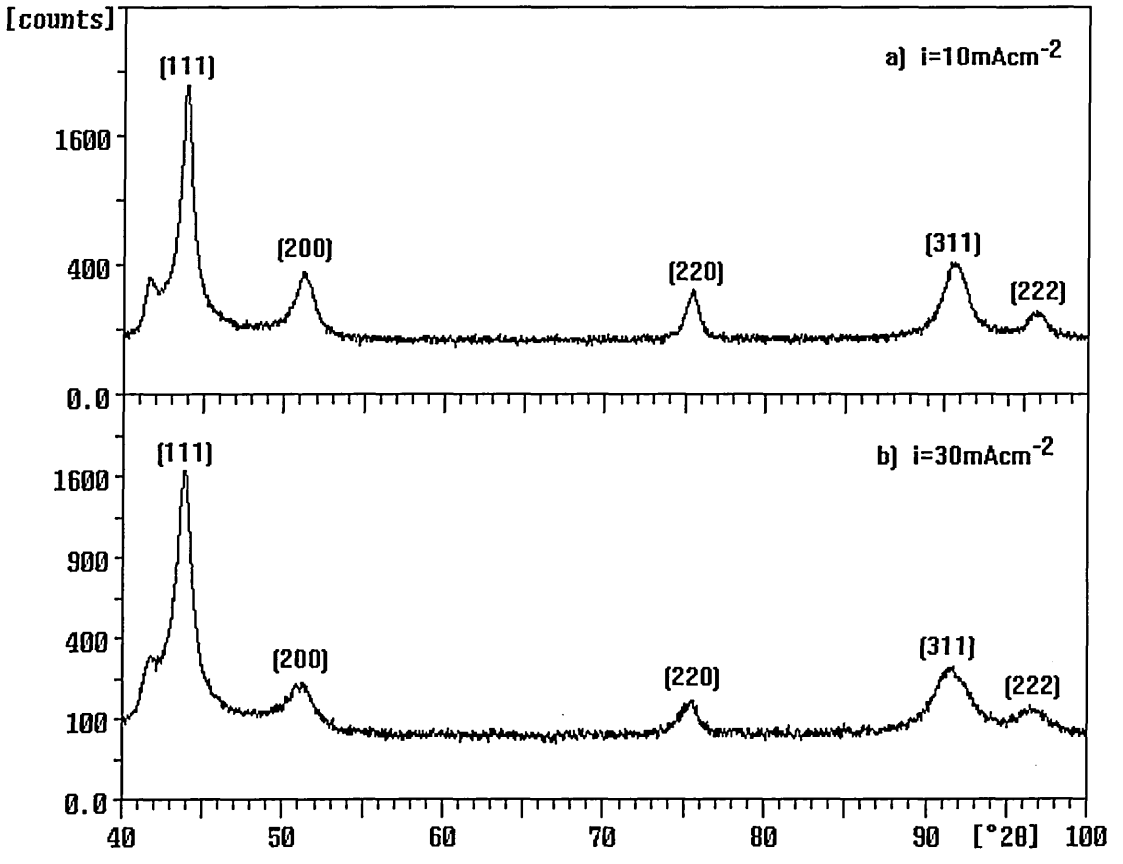

Fig. 4-15: X-Ray Diffraction Spectra of fcc Structured NiFe Deposits Obtained from Solution 3 at Different Current Densities:
a) i = 10 mA cm^{-2}, b) i = 30 mA cm^{-2}.

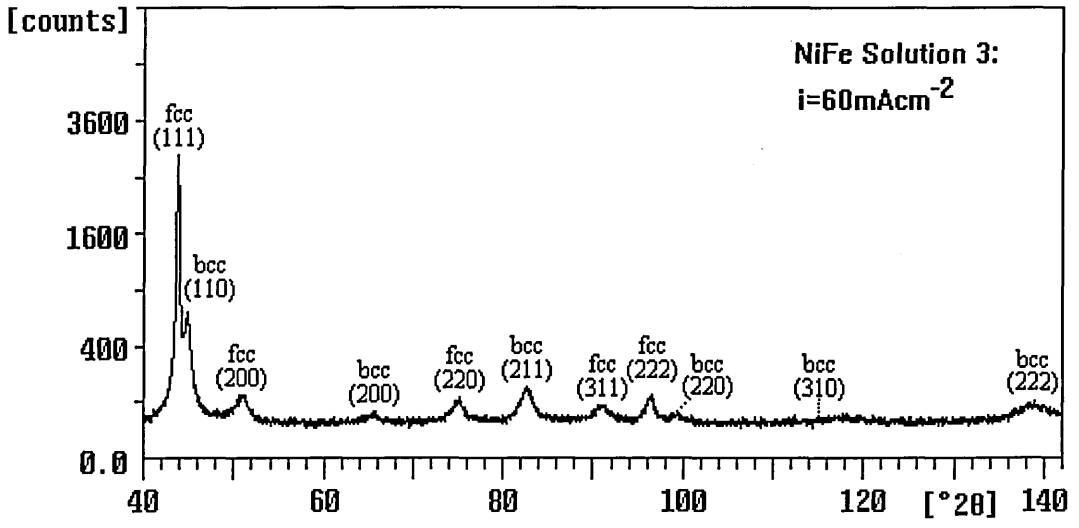

Fig. 4-16: X-Ray Diffraction Spectrum of Mixed fcc/bcc Structured NiFe Deposits Obtained from Solution 3 at i = 60 mA cm^{-2}.

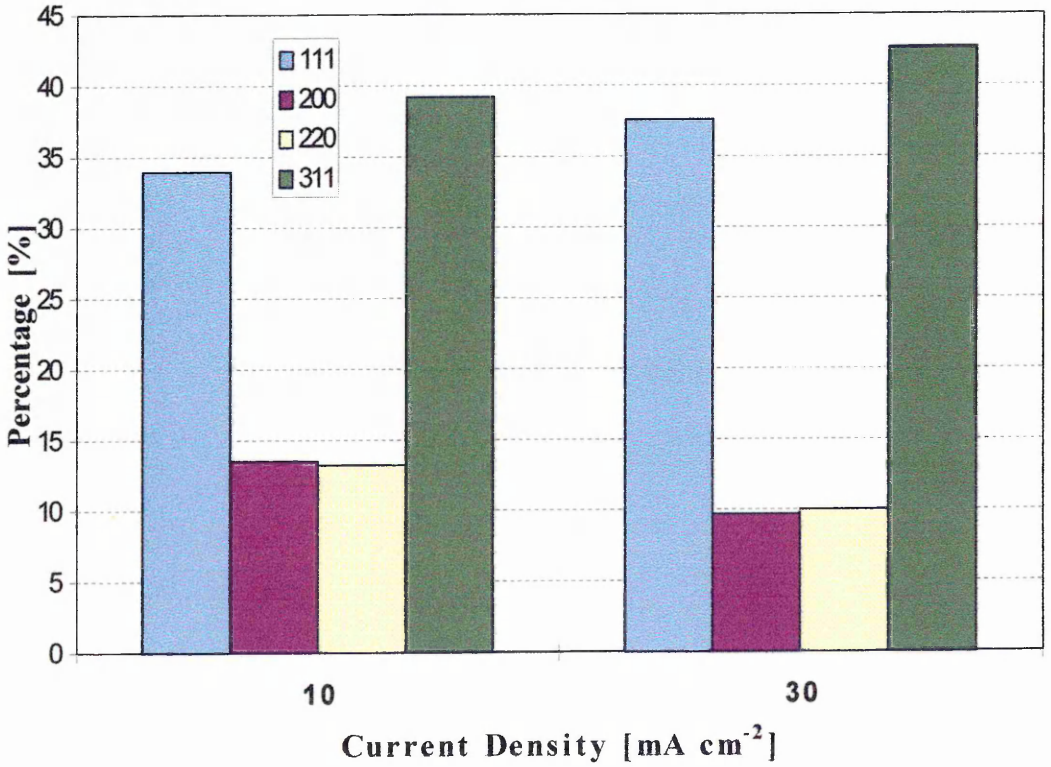

Fig. 4-17: Distribution of Reflections Detected in fcc NiFe Electrodeposits on Copper Sheet Deposited at 10 and 30 mA cm^{-2} in NiFe Solution 3.

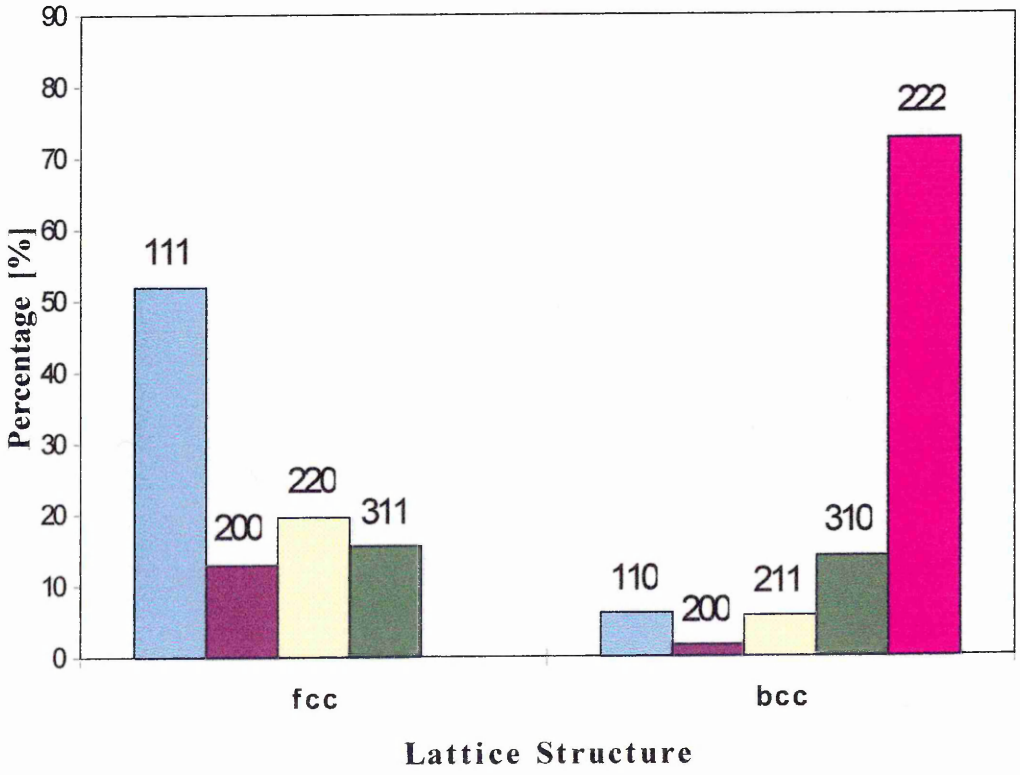

Fig. 4-18: Distribution of Reflections Detected in fcc/bcc NiFe Electrodeposits on Copper Sheet Deposited at 60 mA cm^{-2} in NiFe Solution 3.

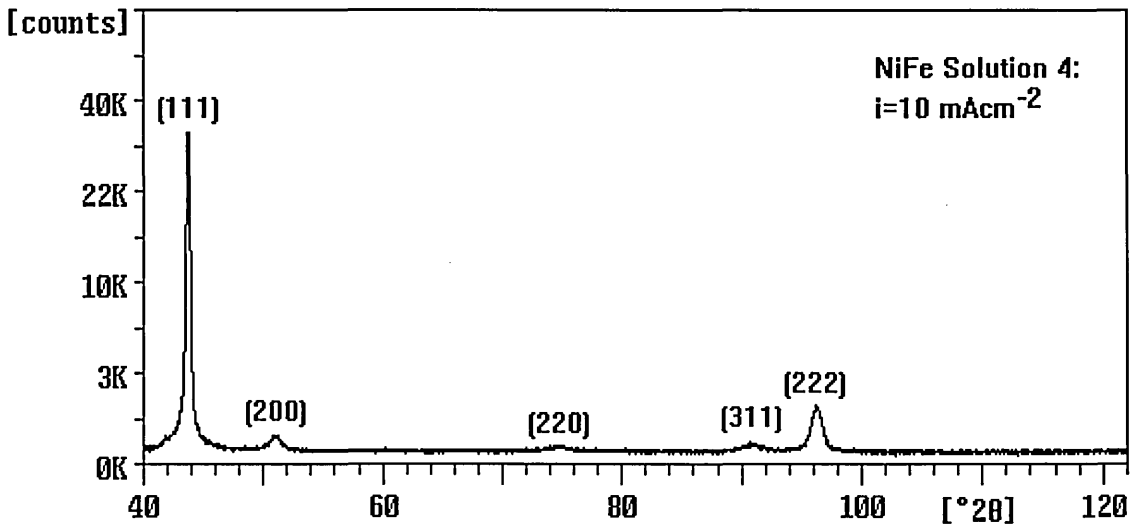

Fig. 4-19: X-Ray Diffraction Spectrum of fcc Structured NiFe Deposits Obtained from Solution 4 (i = 10 mA cm^{-2}).

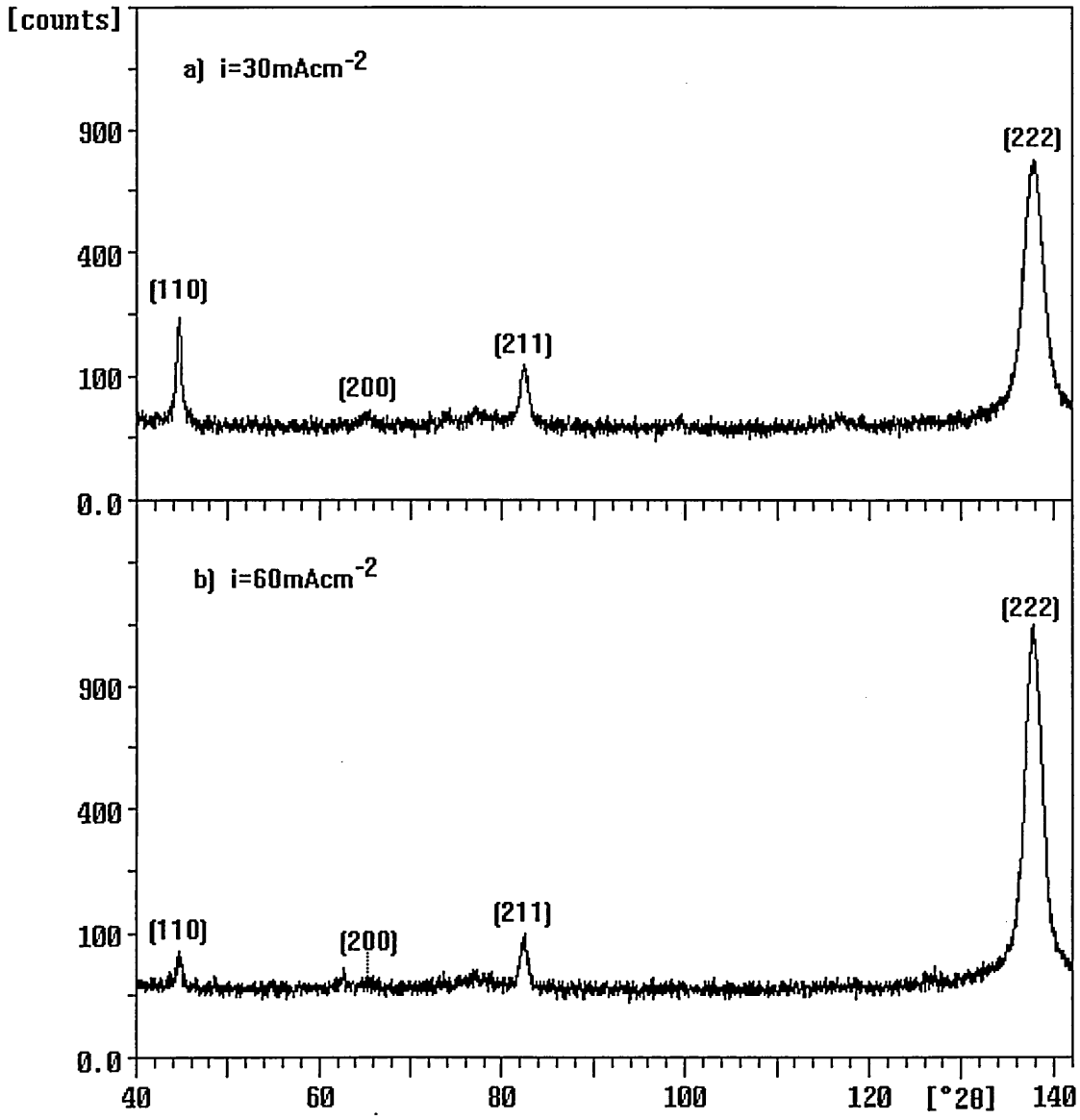

Fig. 4-20: X-Ray Diffraction Spectra of bcc Structured NiFe Deposits Obtained from Solution 4 at Different Current Densities:
a) i = 30 mA cm^{-2}, b) i = 60 mA cm^{-2}.

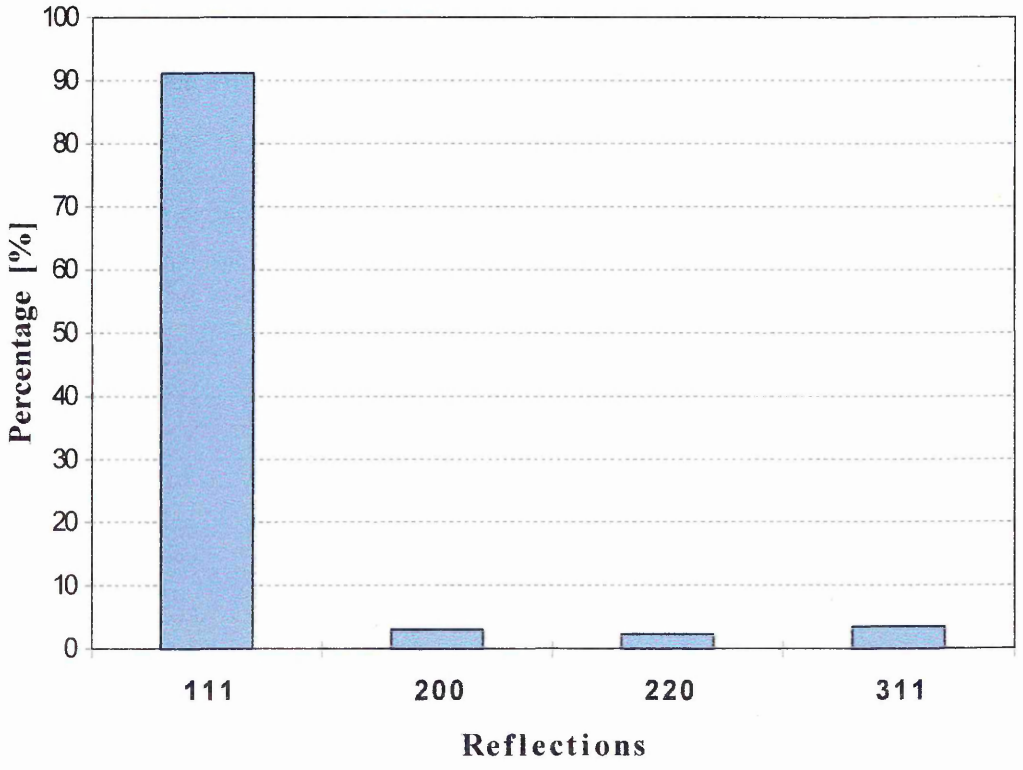

Fig. 4-21: Distribution of Reflections Detected in fcc NiFe Electrodeposit on Copper Sheet Deposited at 10 mA cm^{-2} in NiFe Solution 4.

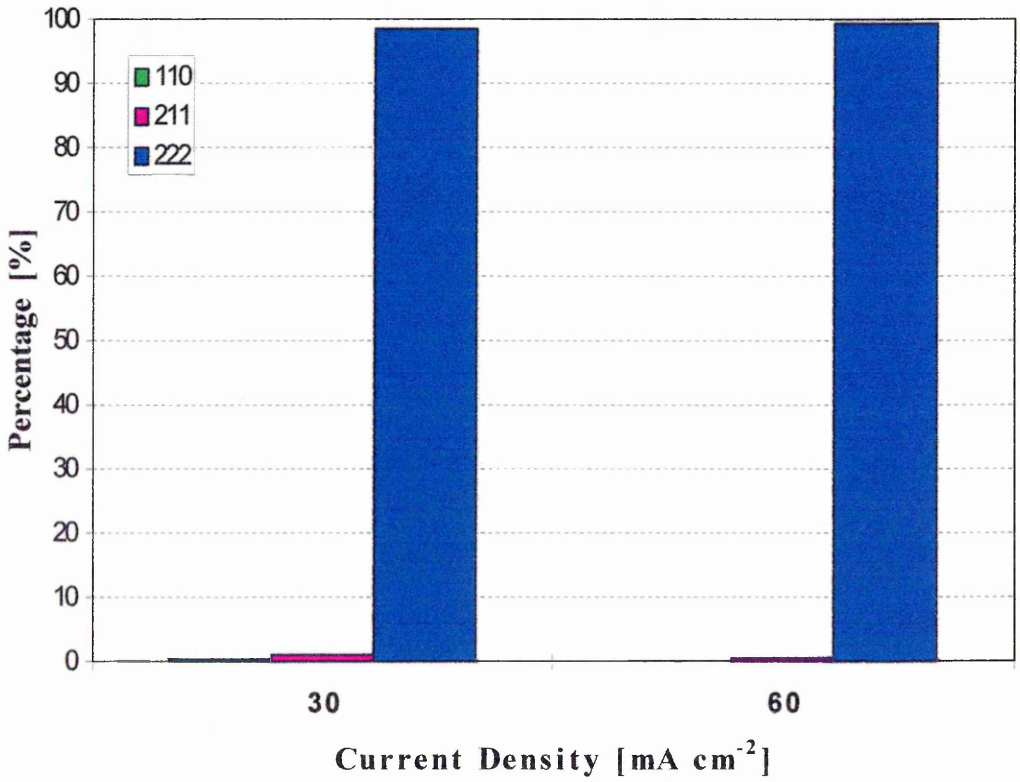

Fig. 4-22: Distribution of Reflections Detected in bcc NiFe Electrodeposit on Copper Sheet Deposited at 30 and 60 mA cm^{-2} in NiFe Solution 4.

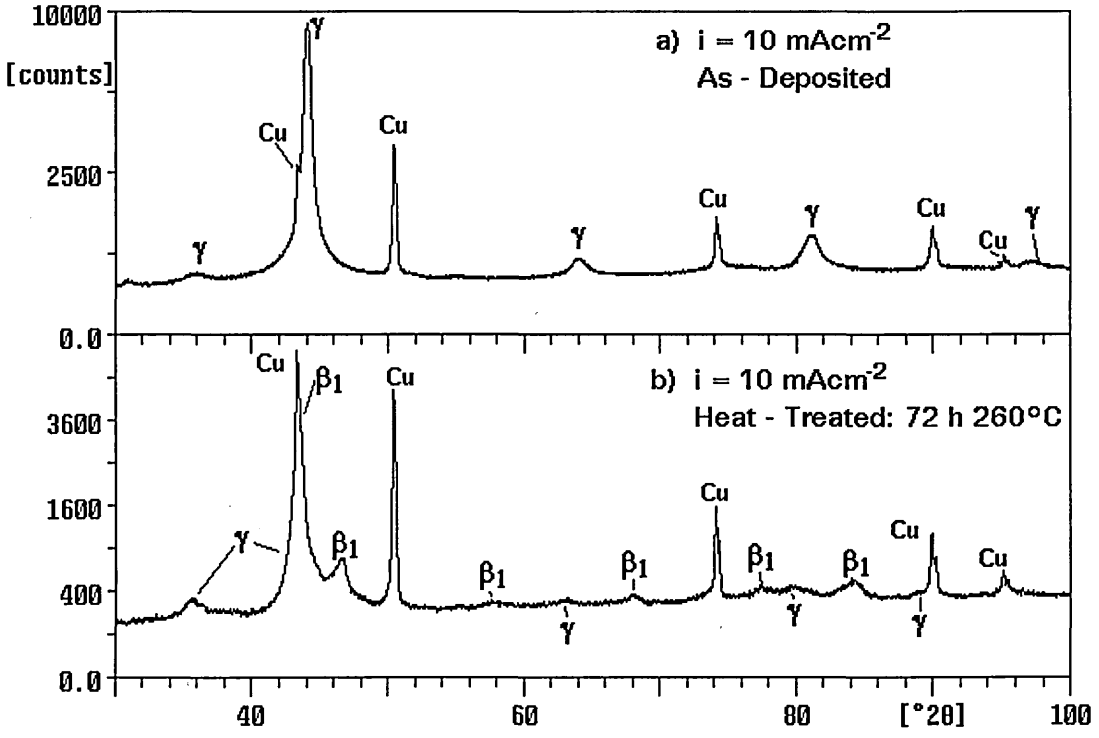

Fig. 4-23: XRD Spectra of Deposit Produced in Nickel-Zinc Solution 8, (i = 10 mA cm^{-2}) in a) As-Deposited, b) Heat-Treated Condition.

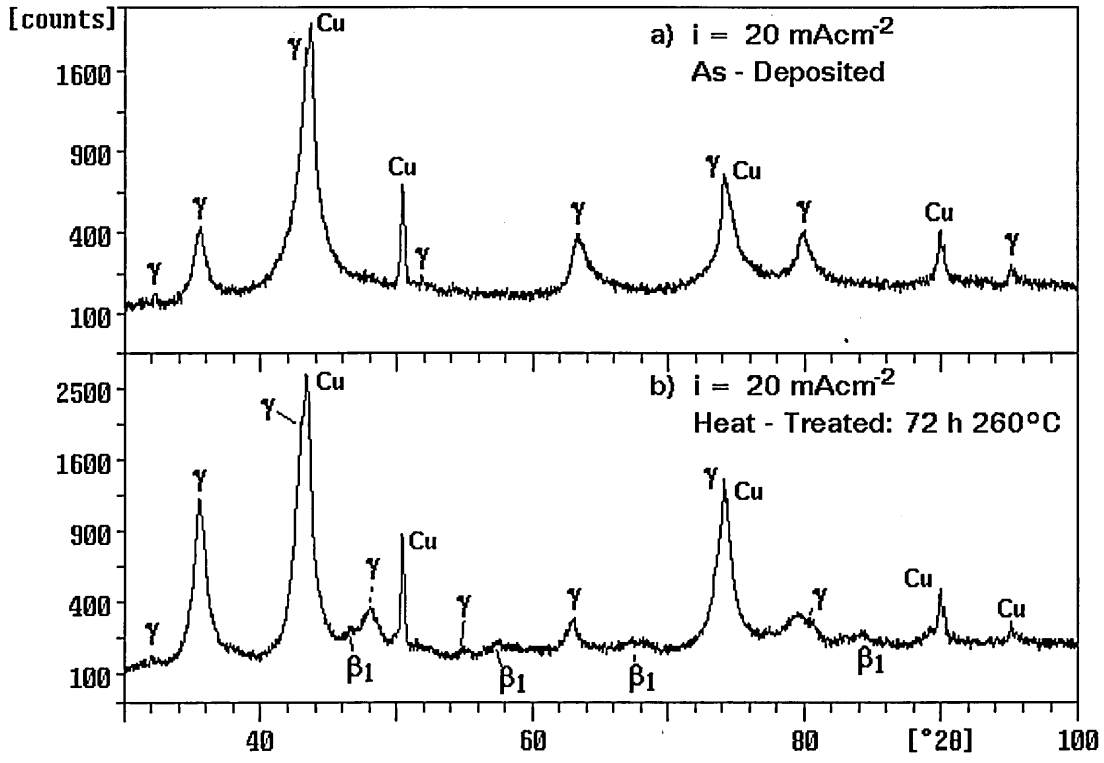

Fig. 4-24: XRD Spectra of Deposit Produced in Nickel-Zinc Solution 8, ($i = 20$ mA cm^{-2}) in a) As-Deposited, b) Heat-Treated Condition.

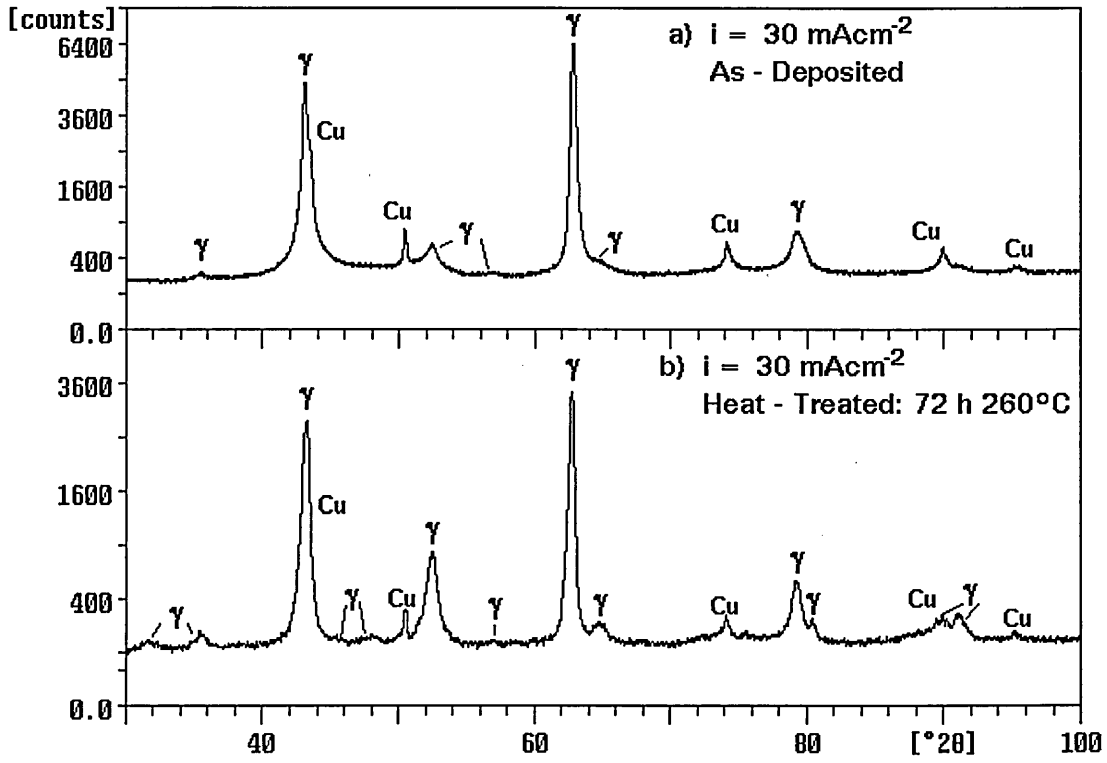

Fig. 4-25: XRD Spectra of Deposit Produced in Nickel-Zinc Solution 8, ($i = 30$ mA cm^{-2}) in a) As-Deposited, b) Heat-Treated Condition.

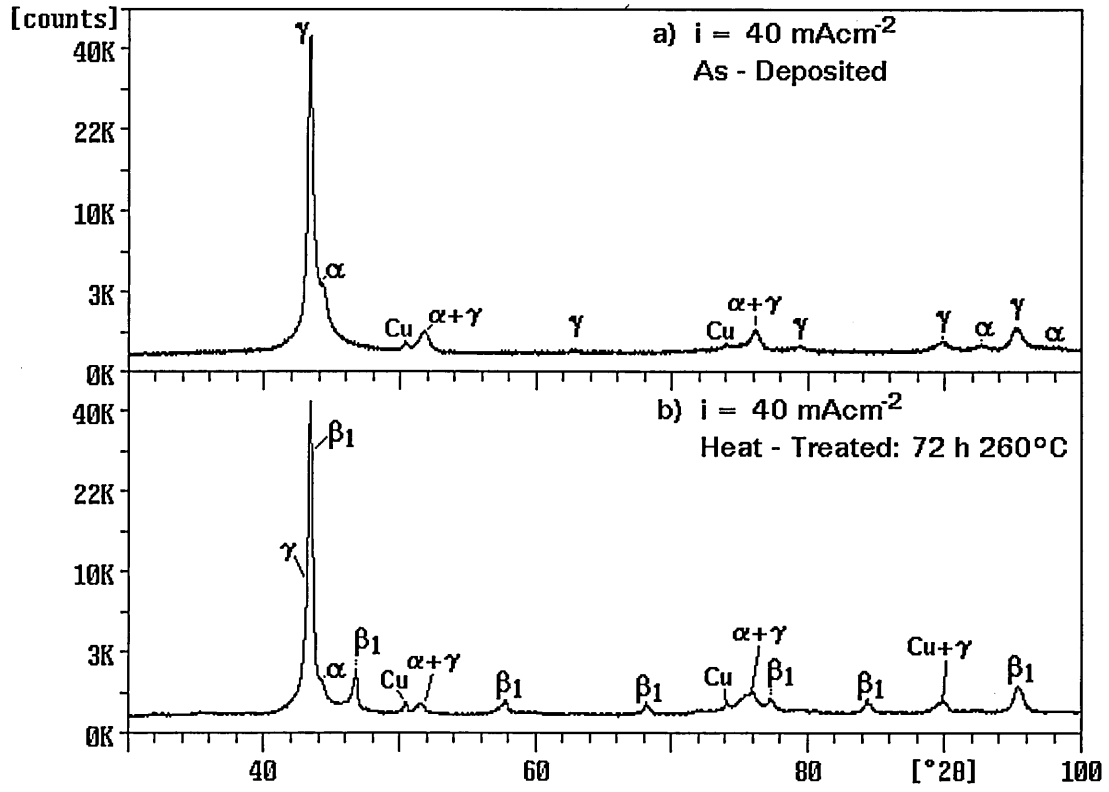

Fig. 4-26: XRD Spectra of Deposit Produced in Nickel-Zinc Solution 8, ($i = 40$ mA cm^{-2}) in a) As-Deposited, b) Heat-Treated Condition.

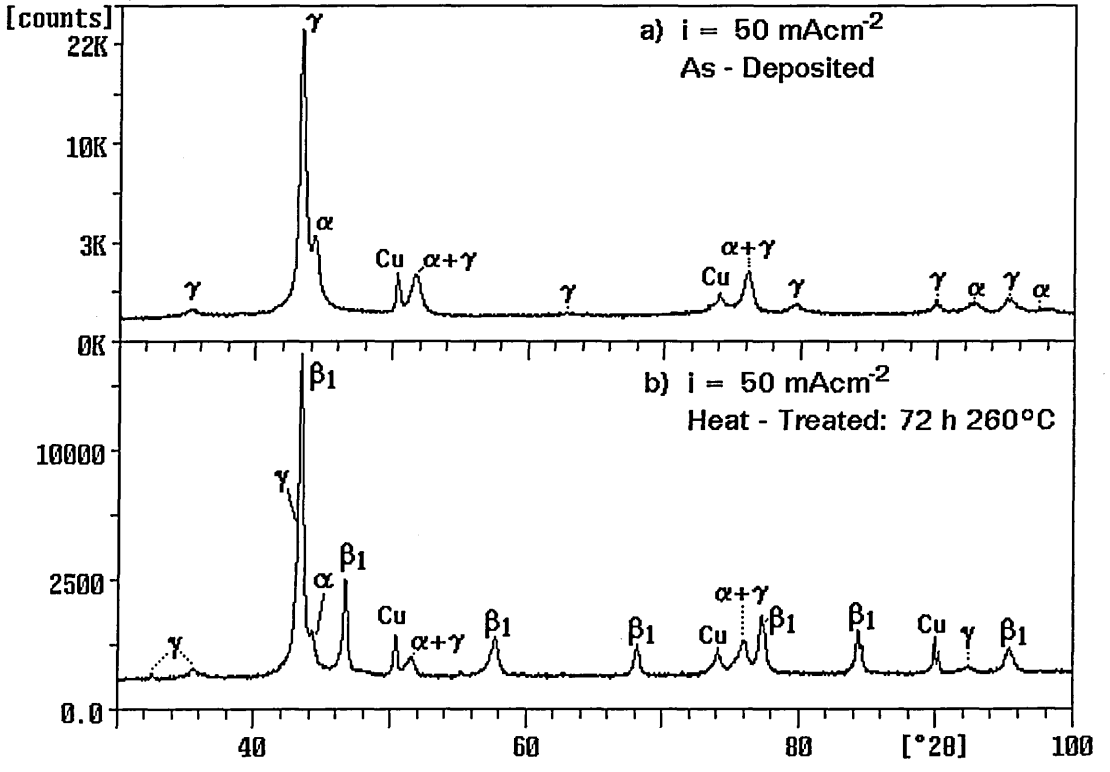

Fig. 4-27: XRD Spectra of Deposit Produced in Nickel-Zinc Solution 8, (i = 50 mA cm^{-2}) in a) As-Deposited, b) Heat-Treated Condition.

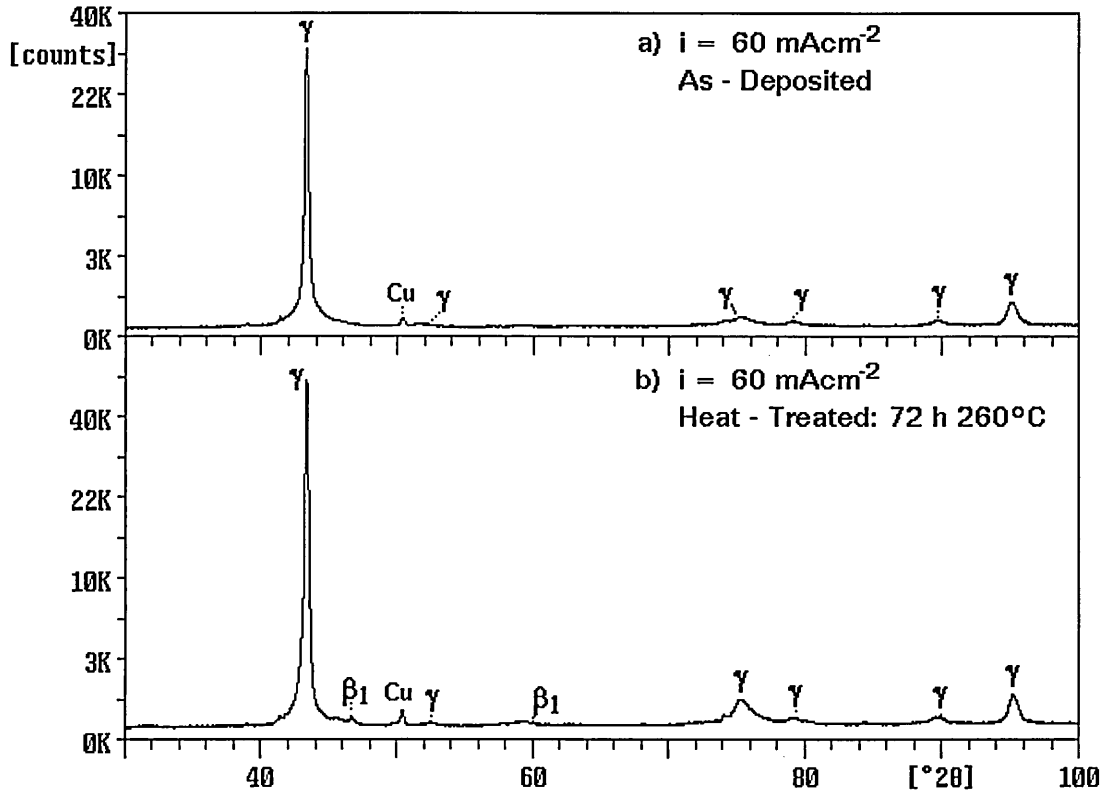

Fig. 4-28: XRD Spectra of Deposit Produced in Nickel-Zinc Solution 8, ($i = 60$ mA cm^{-2}) in a) As-Deposited, b) Heat-Treated Condition.

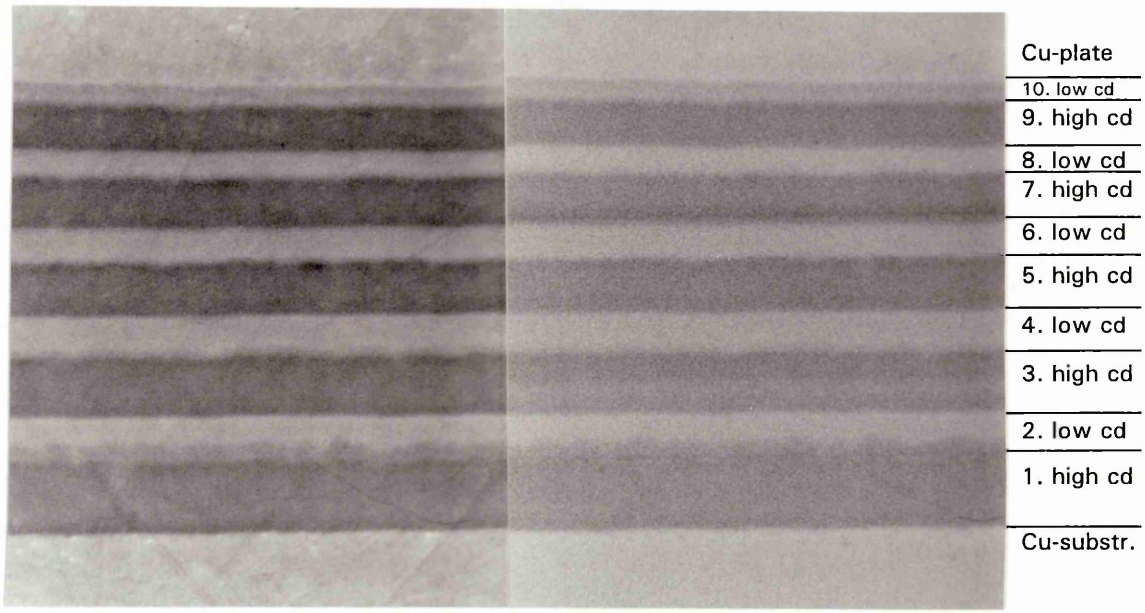

Fig. 4-29:
a) SEI
of Multilayered NiFe Deposit.

b) BSI
of Multilayered NiFe Deposit.

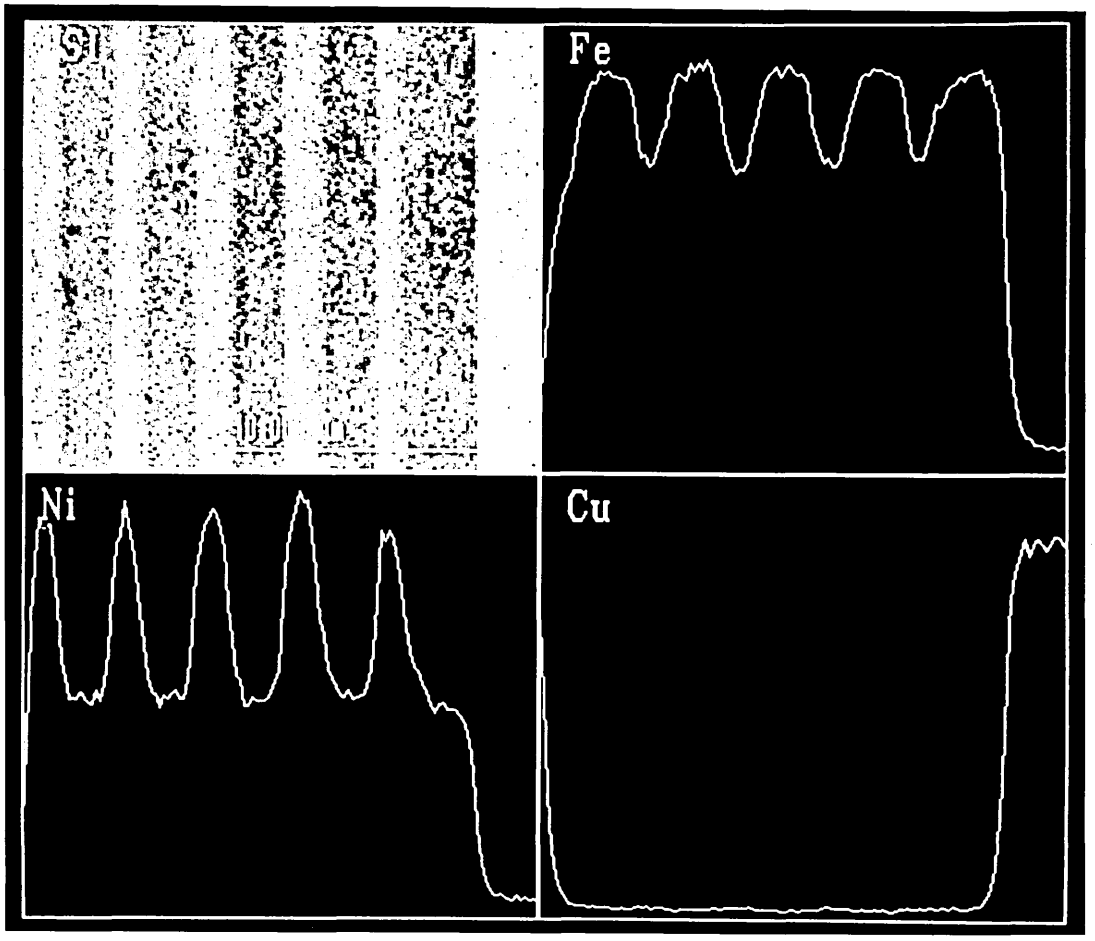

Fig. 4-30: Cross-sectioned Nickel-Iron Electrodeposit.
Digitized BSI (top left).
Energy Dispersive Line-Scans of Multilayered Nickel-Iron Electrodeposit: Iron (top right); Nickel (bottom left); Copper (bottom right).

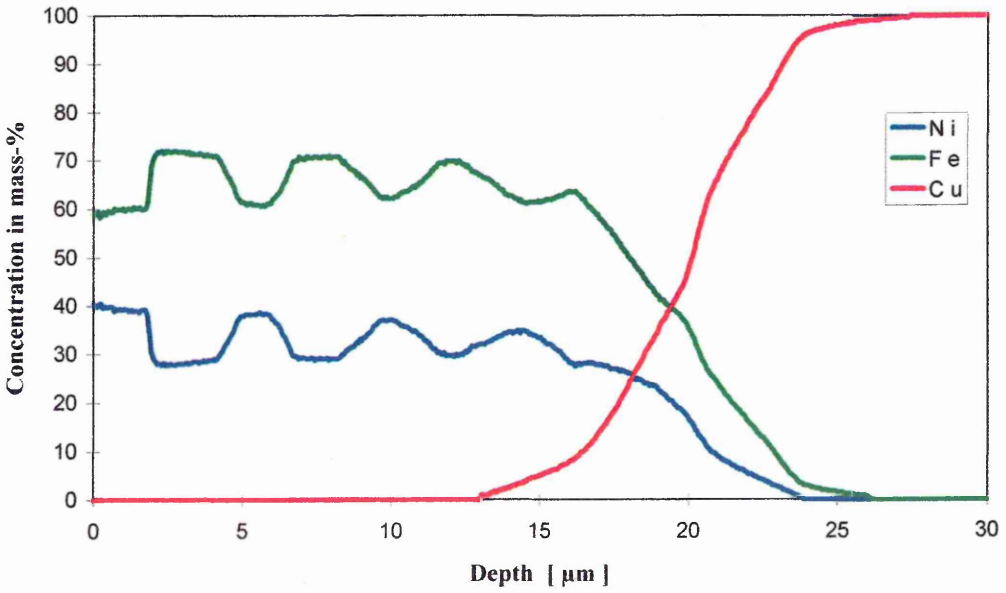

Fig. 4-31: Quantitative Depth Profile of Nickel-Iron Multilayer Obtained by GDOES.

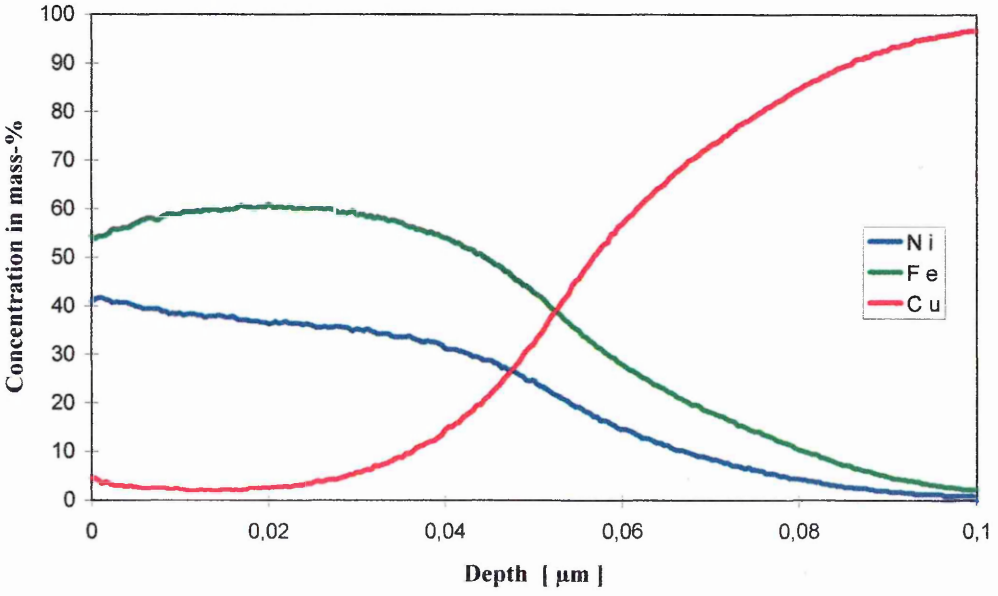

Fig. 4-32: Quantitative Depth Profile of 0.05 µm Thick fcc Nickel-Iron Electrodeposit (i = 10 mA cm^{-2}).

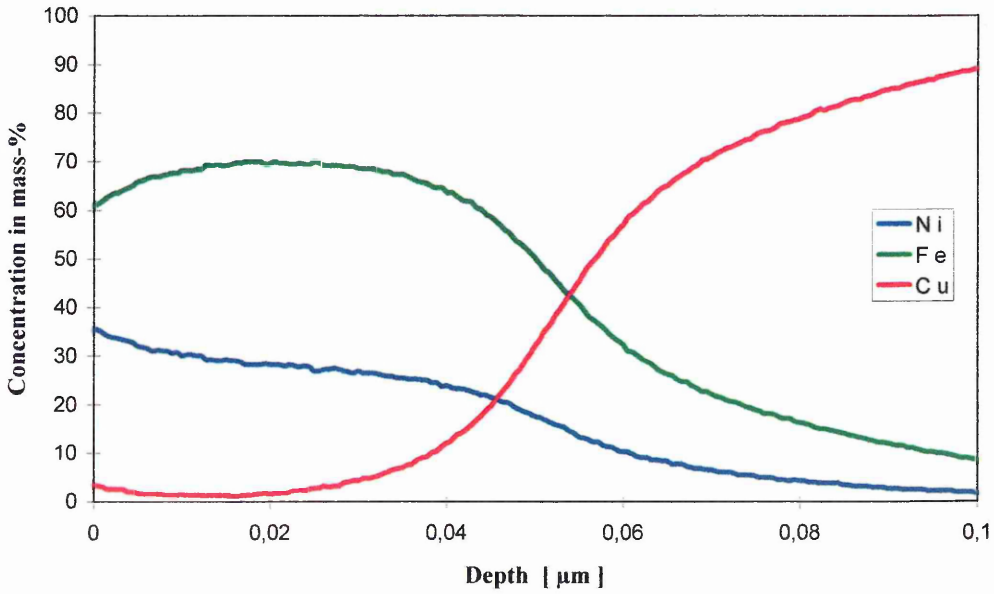

Fig. 4-33: Quantitative Depth Profile of 0.05 µm Thick bcc Nickel-Iron Electrodeposit (i = 60 mA cm^{-2}).

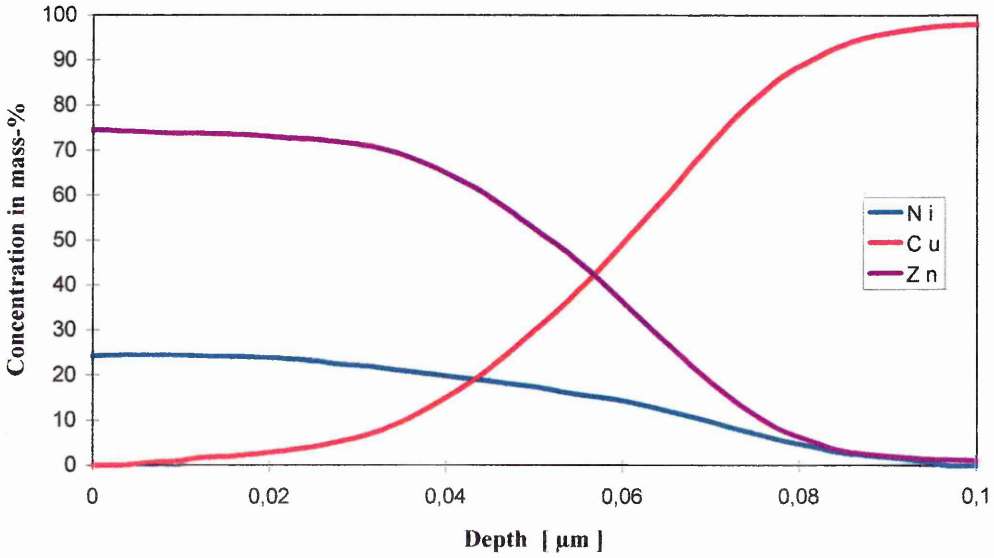

Fig. 4-34: Quantitative Depth Profile of 0.05 µm Thick Nickel-Zinc Electrodeposited with 10 mA cm^{-2} onto Copper Substrate.

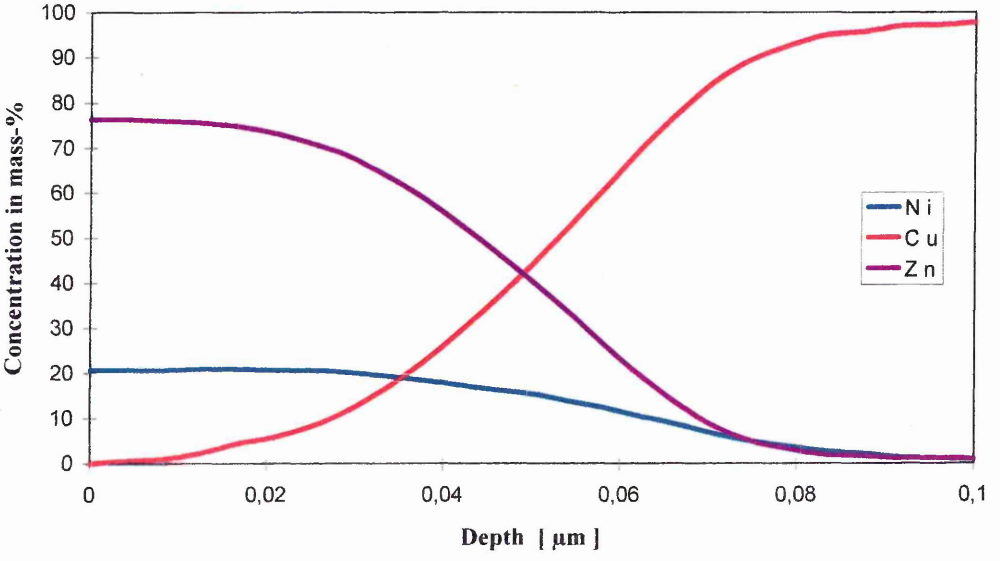

Fig. 4-35: Quantitative Depth Profile of 0.05 µm thick Nickel-Zinc Electrodeposited with 60 mA cm^{-2} onto Copper Substrate.

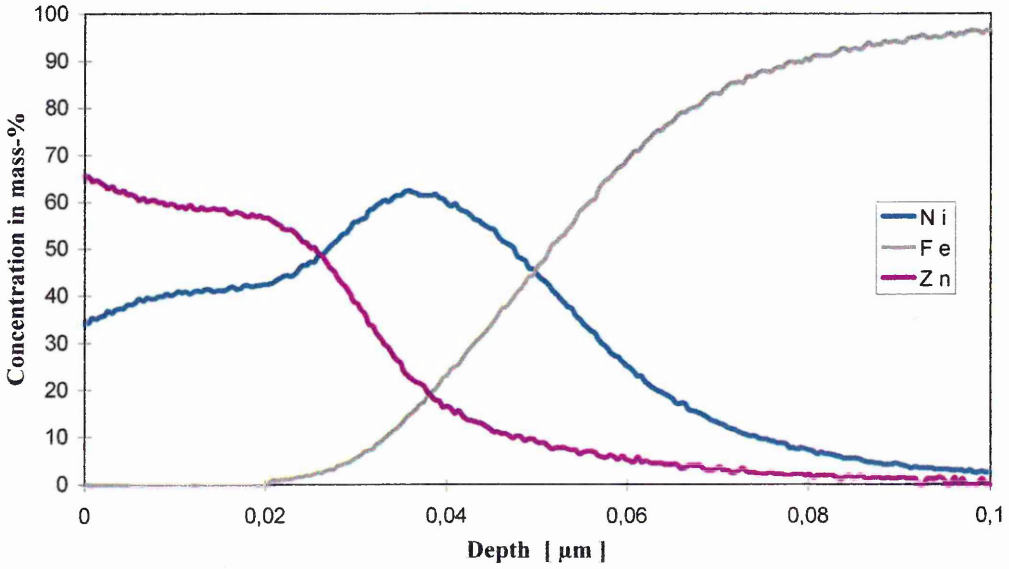

Fig. 4-36: Quantitative Depth Profile of 0.05 µm Thick Nickel-Zinc Electrodeposited with 10 mA cm^{-2} onto Steel Substrate.

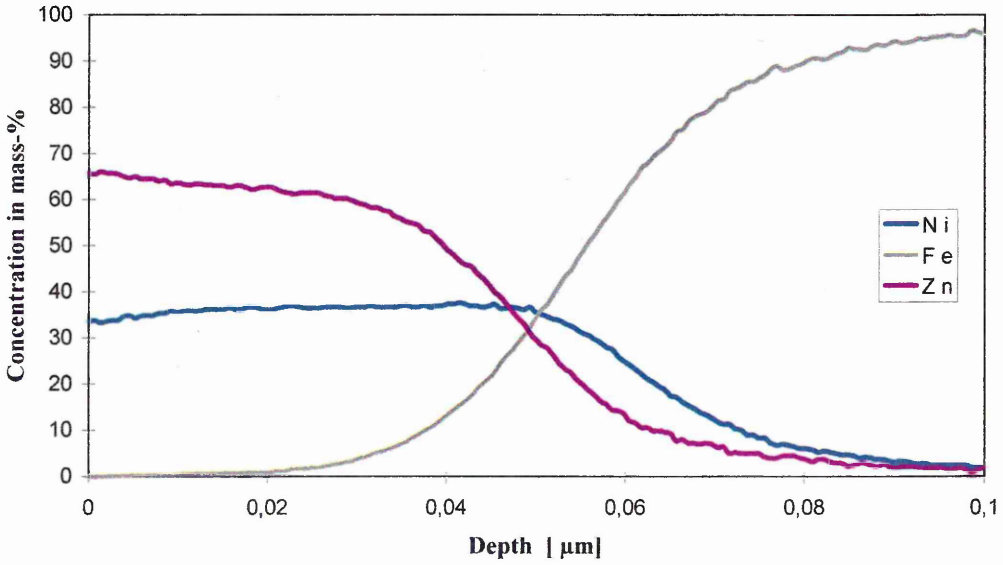

Fig. 4-37: Quantitative Depth Profile of 0.05 µm Thick Nickel-Zinc Electrodeposited with 60 mA cm^{-2} onto Steel Substrate.

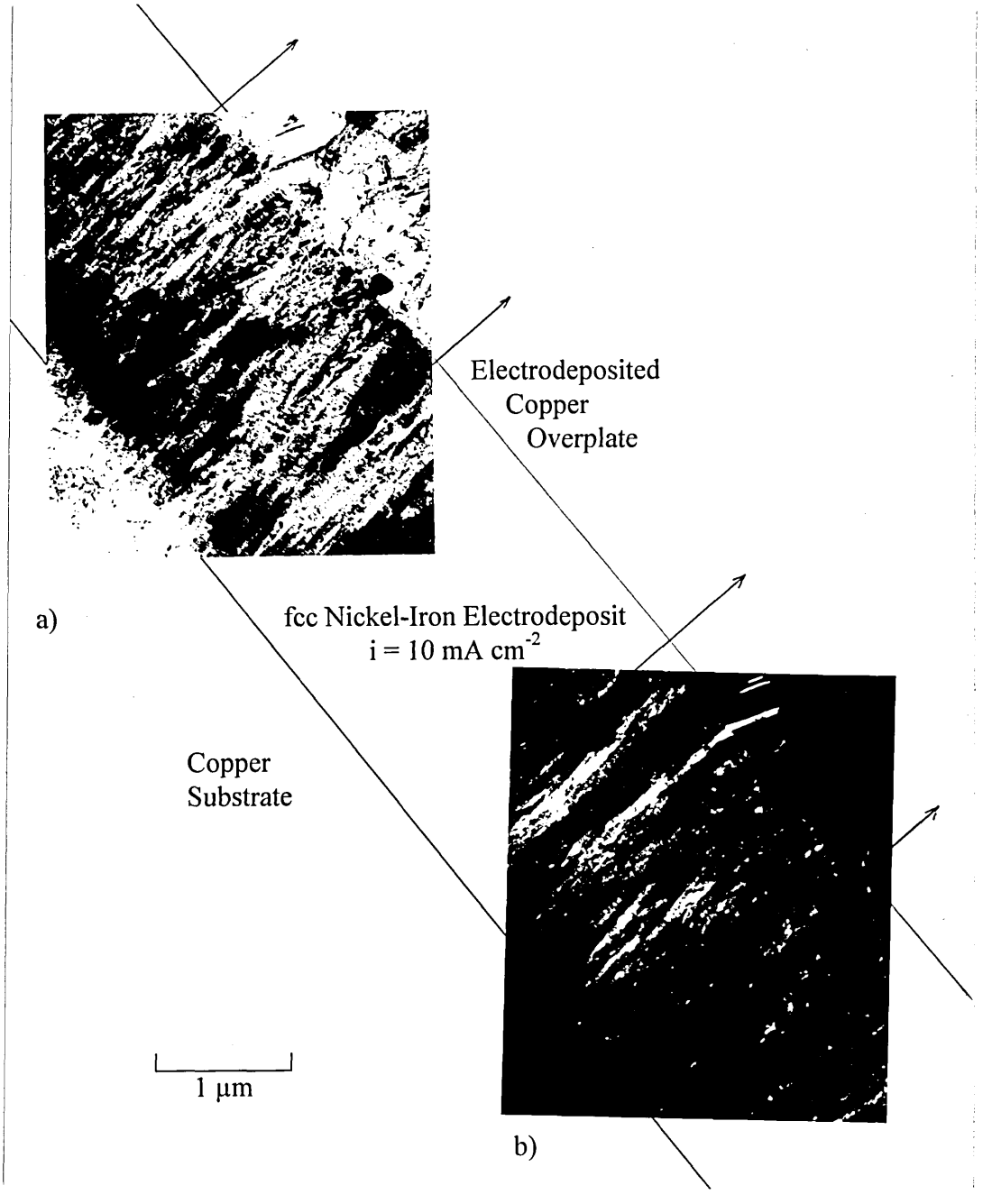

Fig. 4-38: (a) Bright and (b) Dark Field Image of Cross-Sectioned fcc Nickel-Iron Electrodeposit.

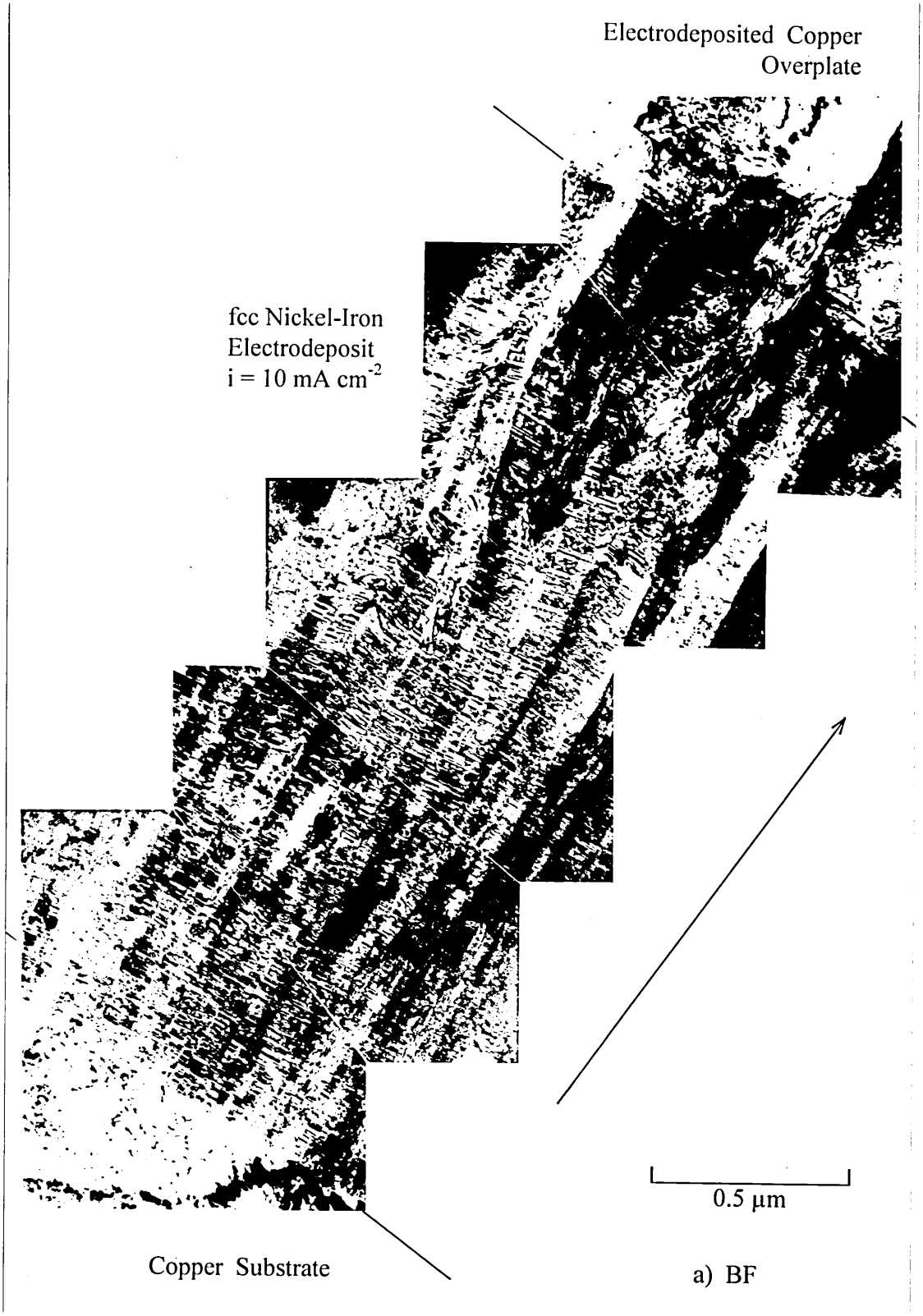

Fig. 4-39a: Montage of Bright Field Images Across Cross-Sectioned fcc Nickel-Iron Electrodeposit.

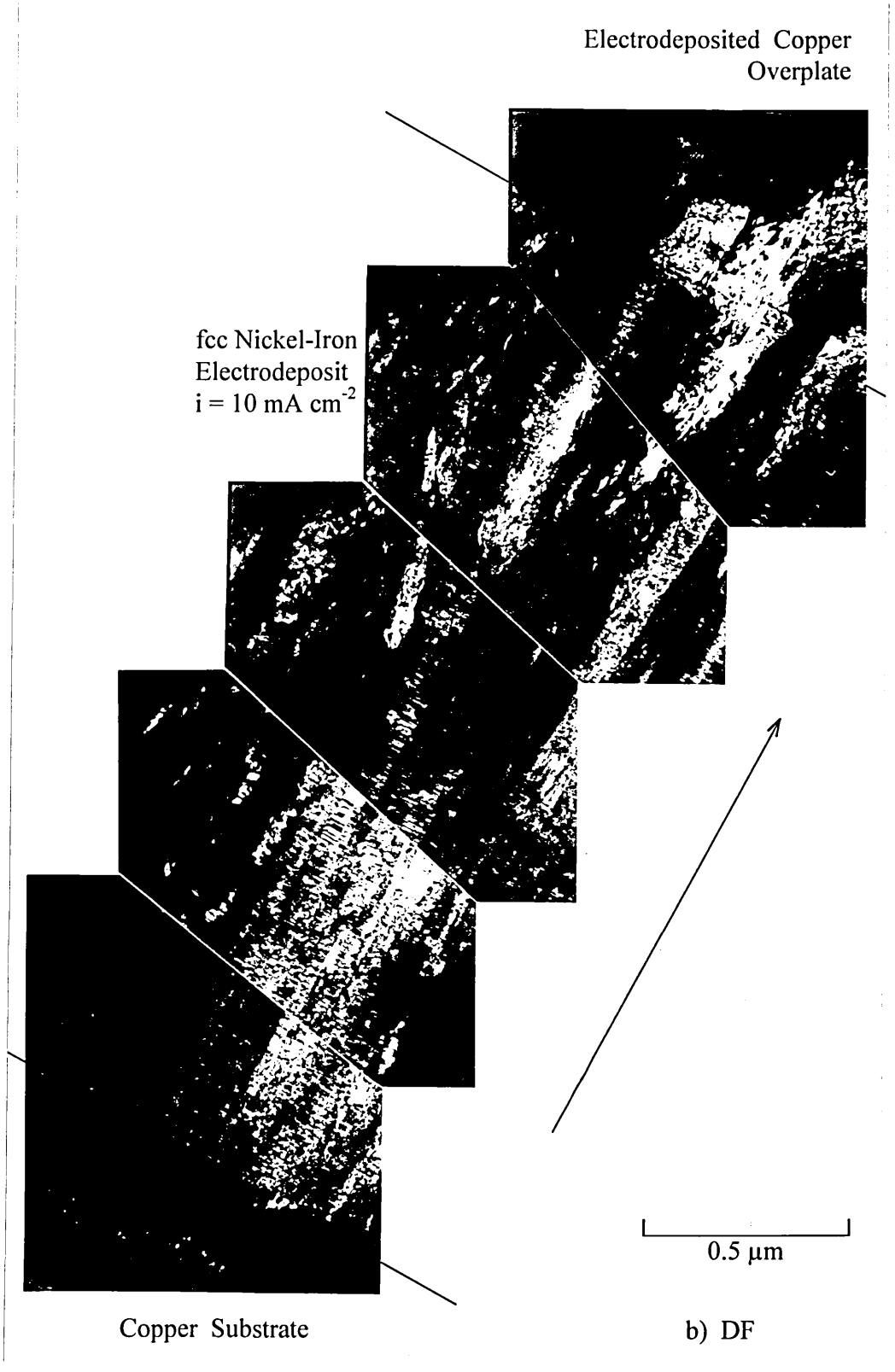

Fig. 4-39b: Montage of Dark Field Images Across Cross-Sectioned fcc Nickel-Iron Electrodeposit.

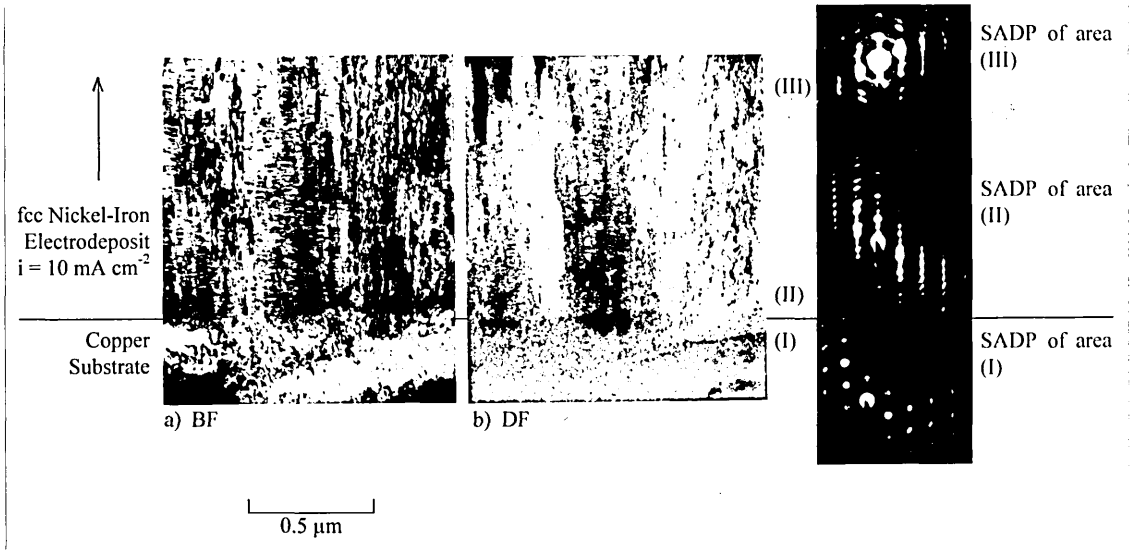

Fig. 4-40: (a) Bright and (b) Dark Field Pair of Interface Between Copper Substrate and fcc Nickel-Iron Electrodeposit.
SADPs: (I) Copper Substrate, (II) Nucleation Site of fcc Nickel-Iron Deposit, (III) Advanced Developed fcc Nickel-Iron Deposit.

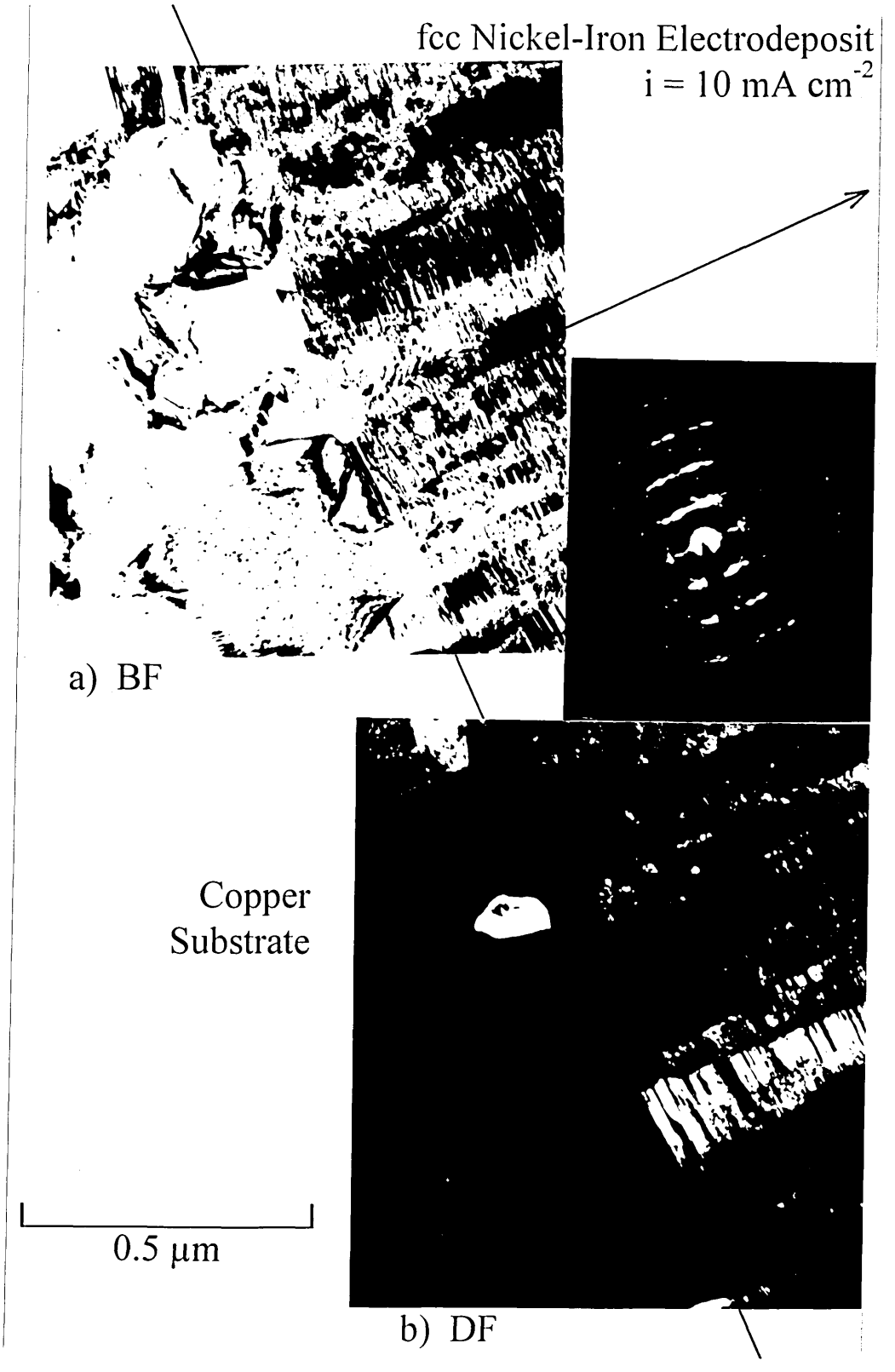

Fig. 4-41: (a) Bright and (b) Dark Field Pair of Initial Nucleation Site of fcc Nickel-Iron Electrodeposit on Copper Substrate, Including SADP of fcc Coating.

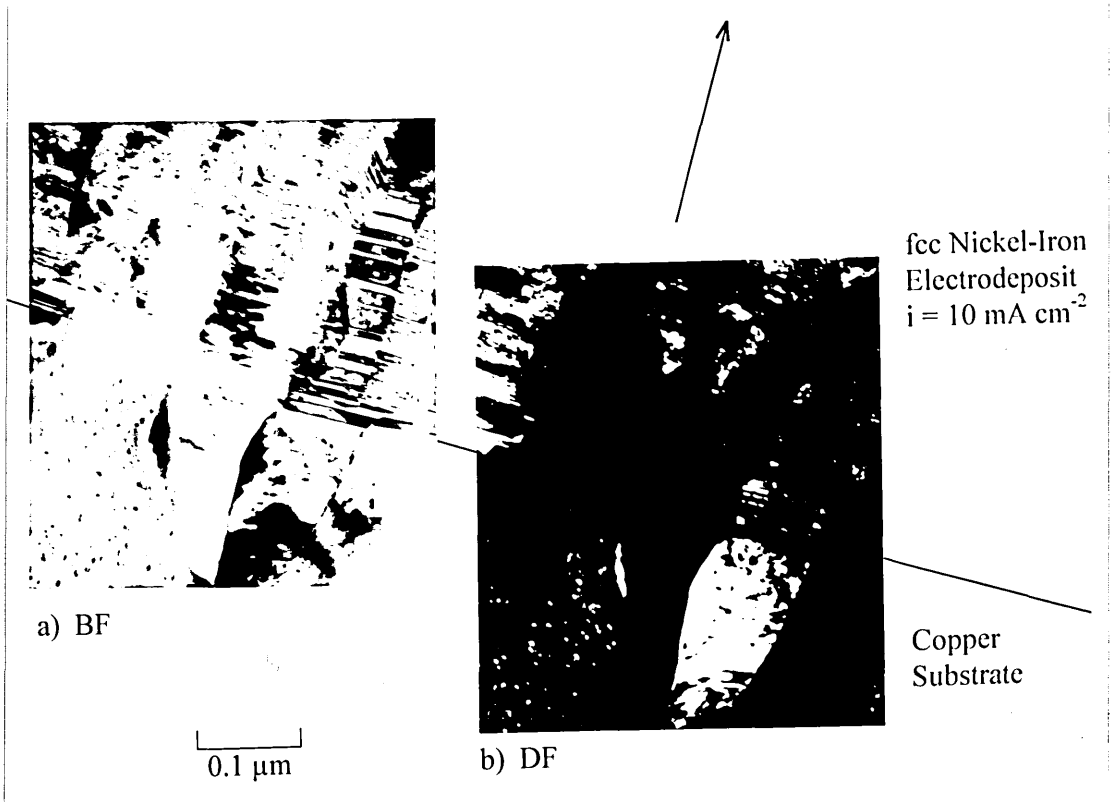

Fig. 4-42: (a) Bright and (b) Dark Field Pair of Interface Copper Substrate/fcc Nickel-Iron Electrodeposit.

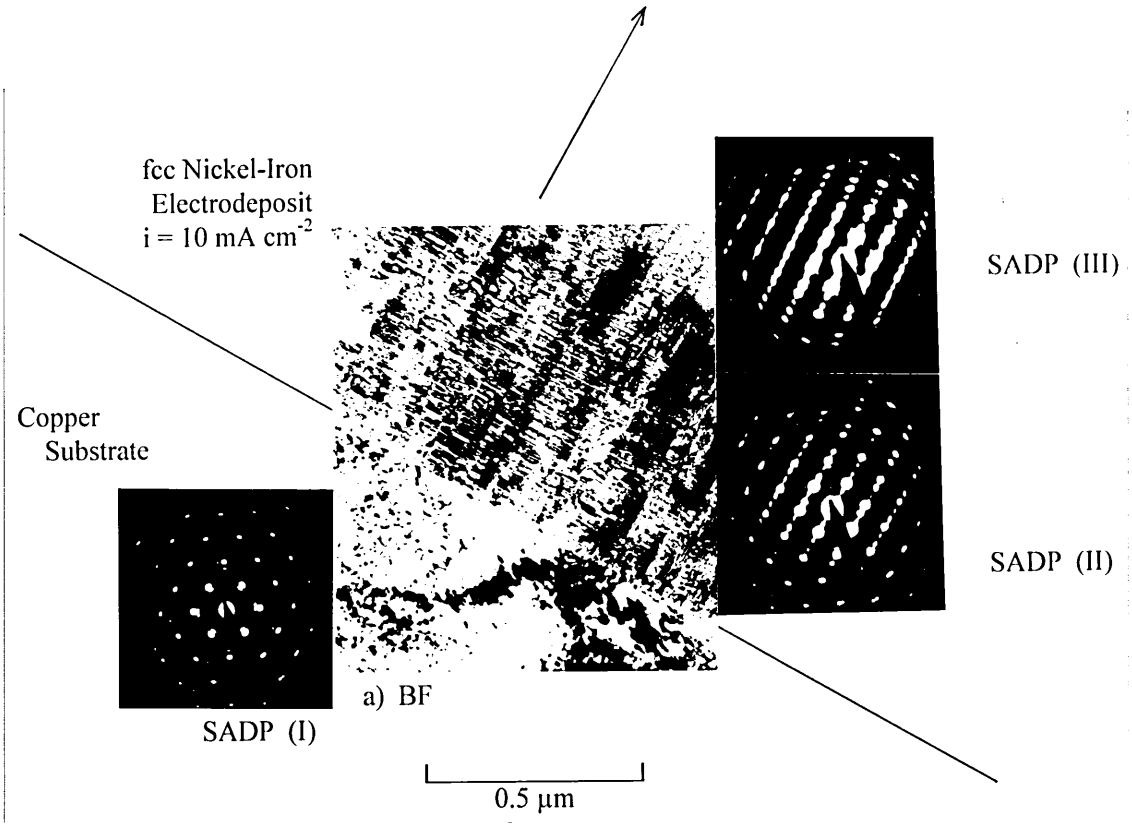

Fig. 4-43: (a) Bright Field Image of Interface Copper Substrate/fcc Nickel-Iron Electrodeposit.
SADPs: (I) Copper Substrate, (II) Interface Copper Substrate/fcc NiFe Deposit, (III) Advanced Developed fcc NiFe Deposit.

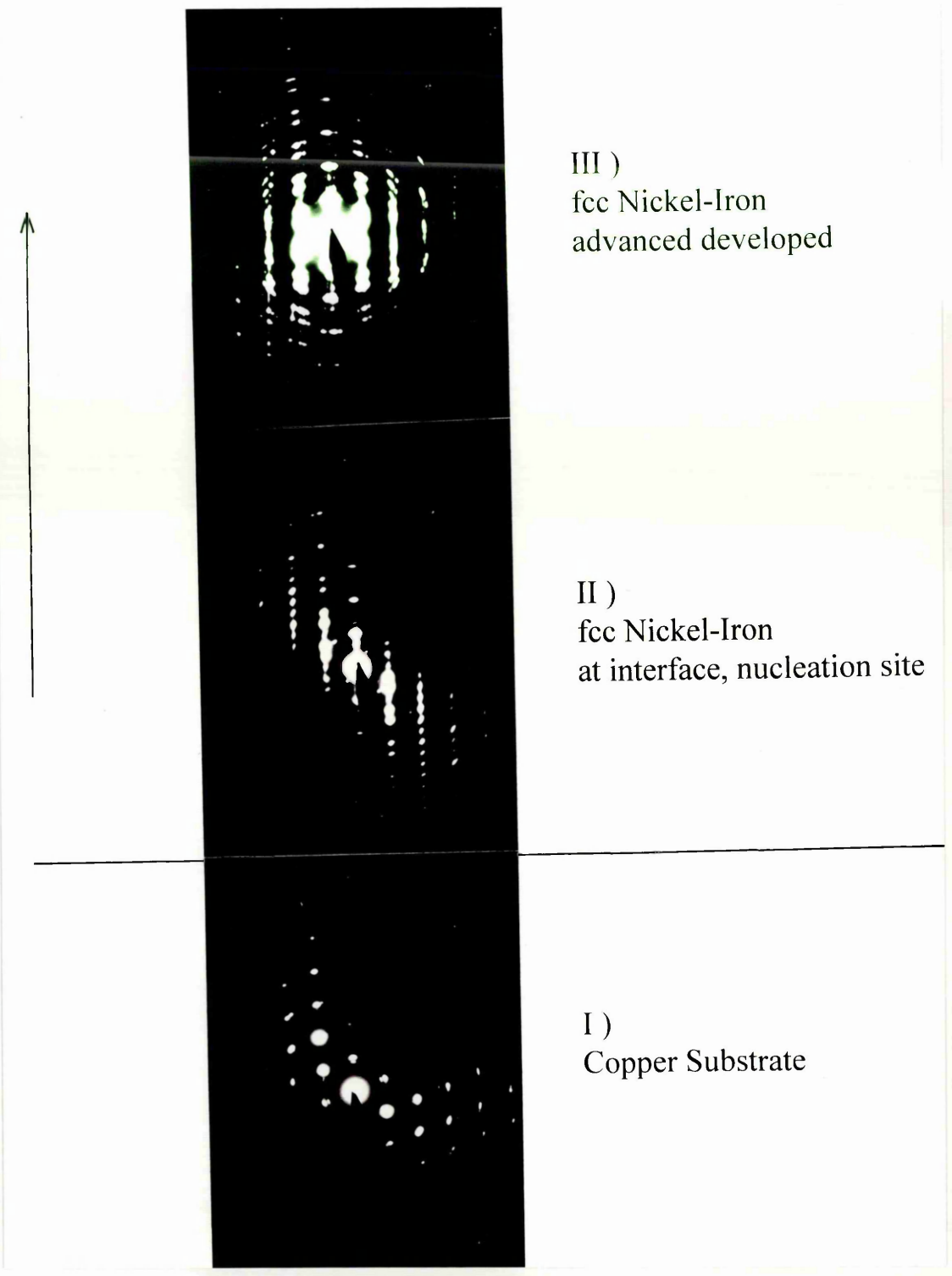

Fig. 4-44: Series of Selected Area Diffraction Patterns Indicating Initial Epitaxial Growth and 'Arcing' of Twin Spots in Advanced Developed fcc NiFe Deposit.
SADPs: (I) Copper Substrate, (II) fcc Nickel-Iron Electrodeposit at Nucleation Site, (III) Advanced Developed fcc NiFe Electrodeposit.

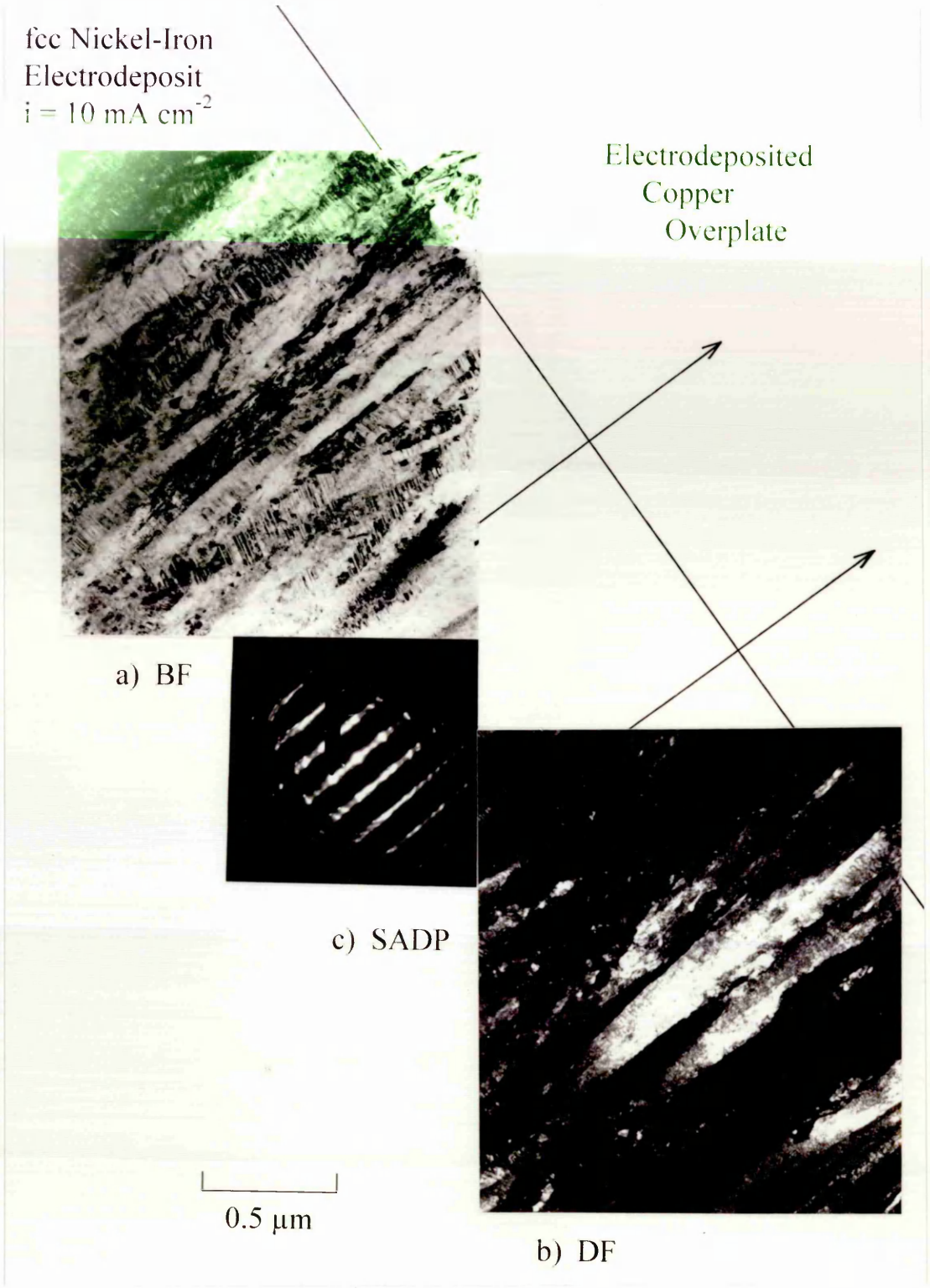

Fig. 4-45: a) Bright, (b) Dark Field Image and (c) Selected Area Diffraction Pattern of Advanced Developed fcc Nickel-Iron Electrodeposit.

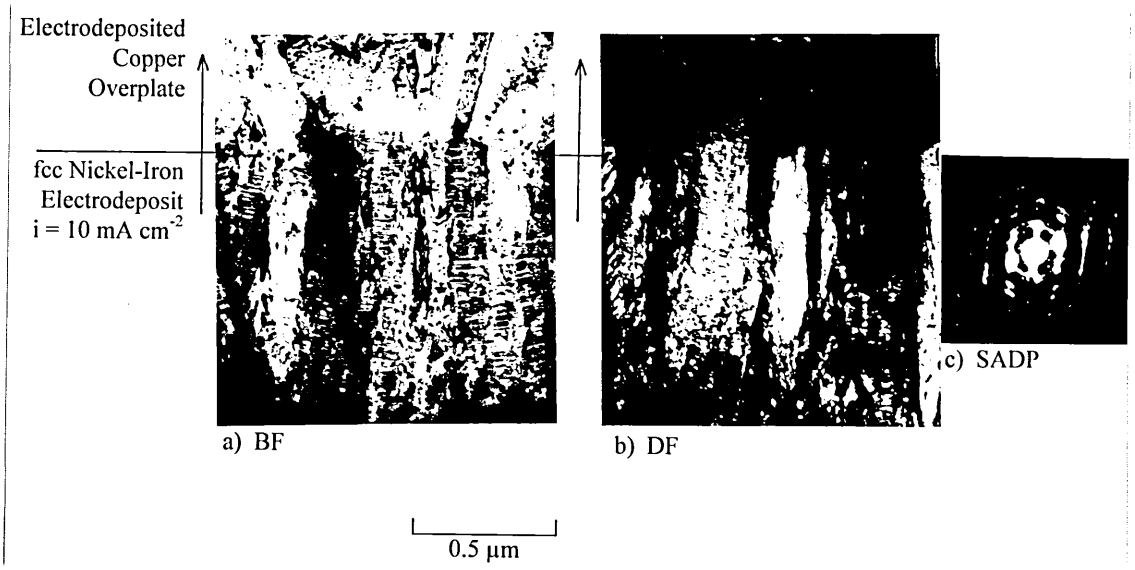

Fig. 4-46: (a) Bright, (b) Dark Field Image and (c) Selected Area Diffraction Pattern of Advanced Developed fcc Nickel-Iron Electrodeposit.

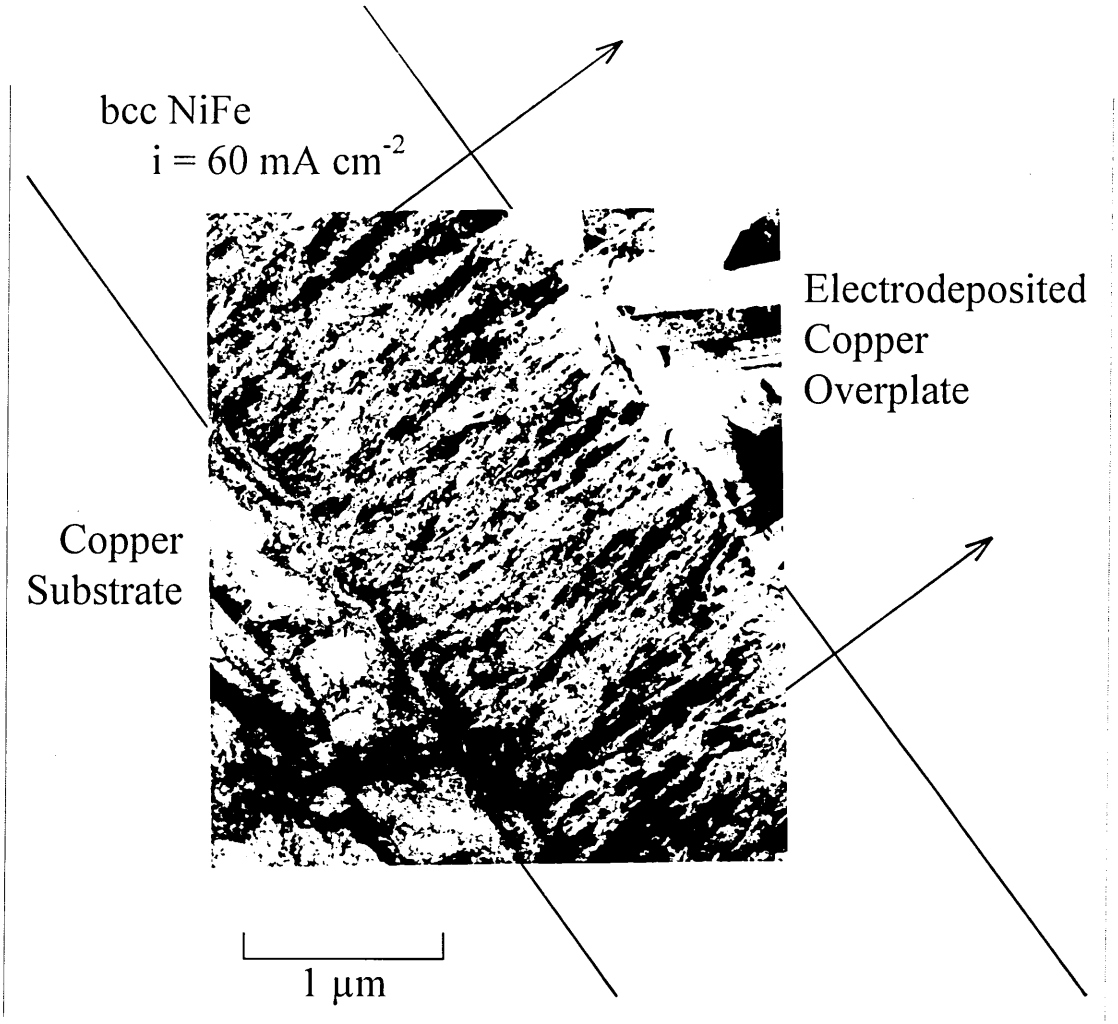

Fig. 4-47: Bright Field Image Showing General Overall View of Cross-Sectioned bcc Nickel-Iron Electrodeposit Nucleated on a Copper Substrate, Overplated with Copper.

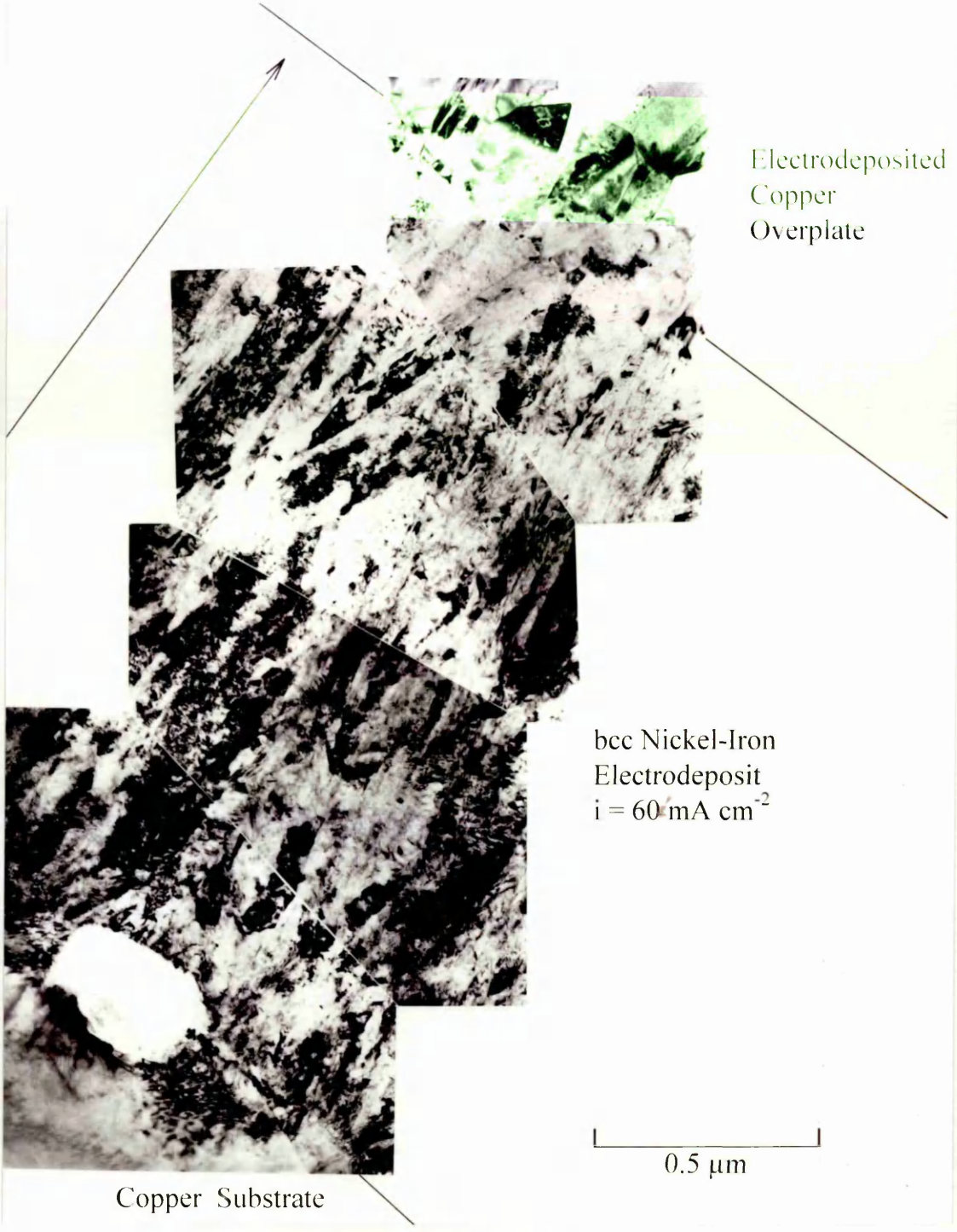

Fig. 4-48: Montage of Bright Field Images Showing General Overall View of Cross-Sectioned bcc Nickel-Iron Electrodeposit Nucleated on a Copper Substrate, Overplated with Copper.

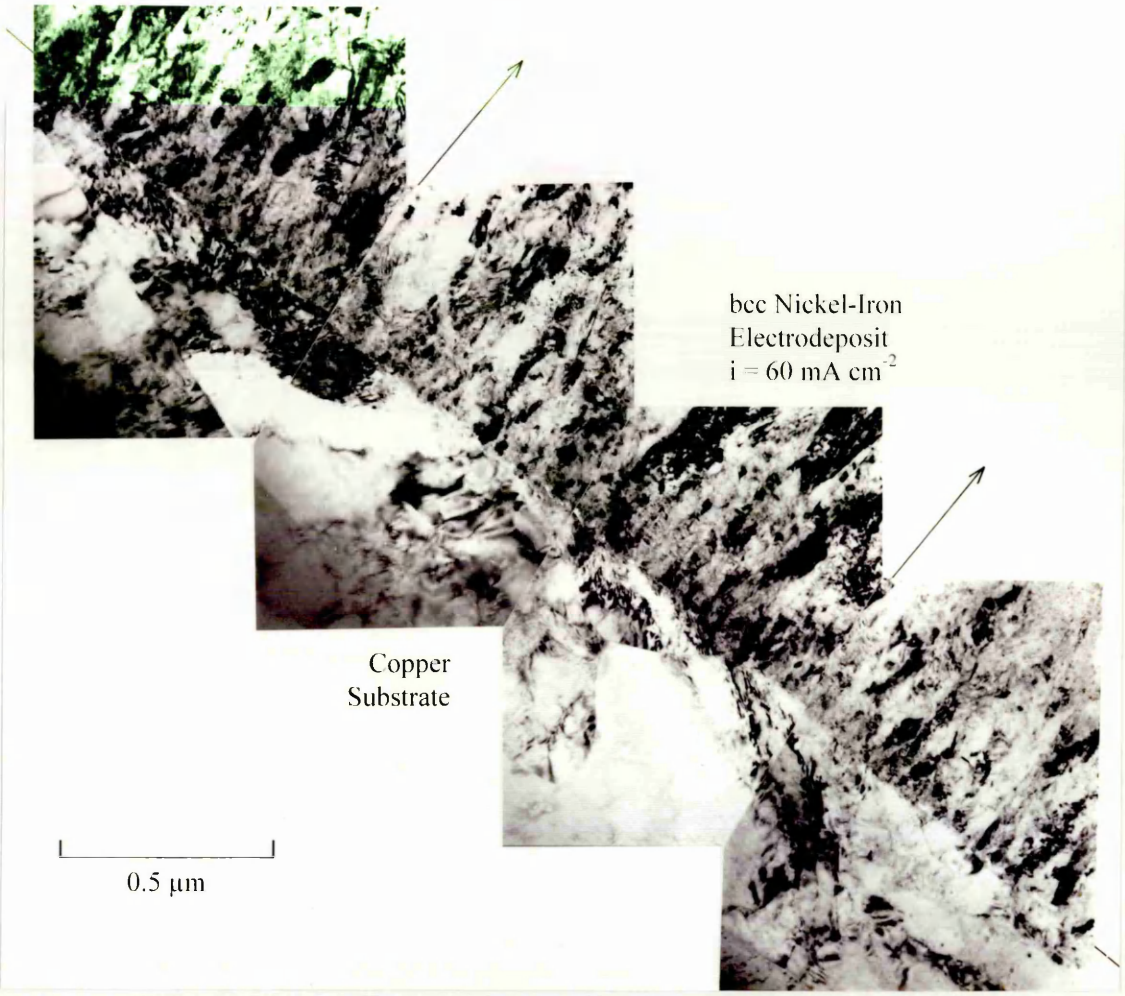

Fig. 4-49: Montage of Bright Field Images Along the Interface Between the bcc Nickel-Iron Electrodeposit and the Copper Substrate.

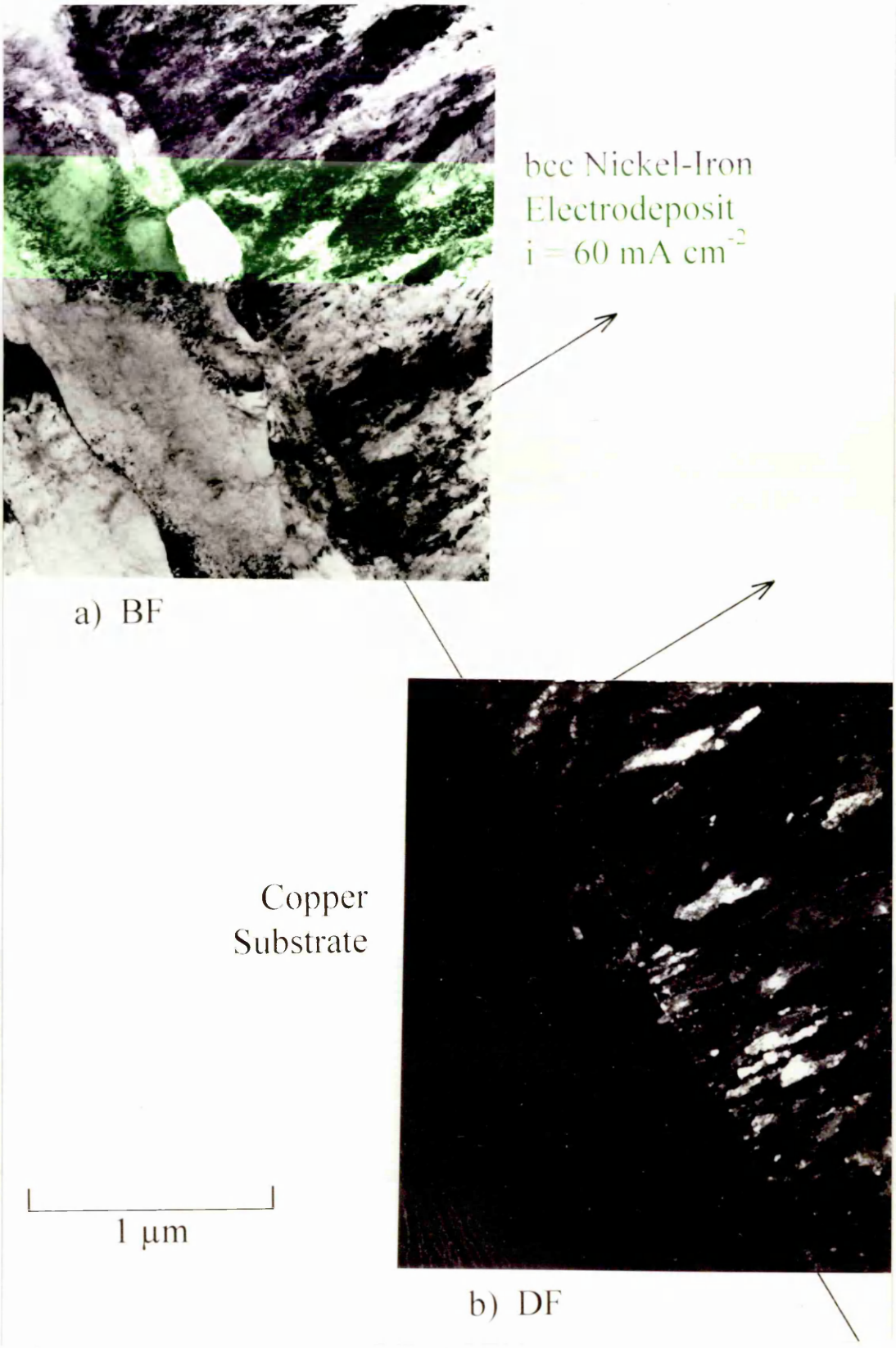

Fig. 4-50: (a) Bright and (b) Dark Field Micrograph of Copper Substrate/bcc Nickel-Iron Electrodeposit Interface.

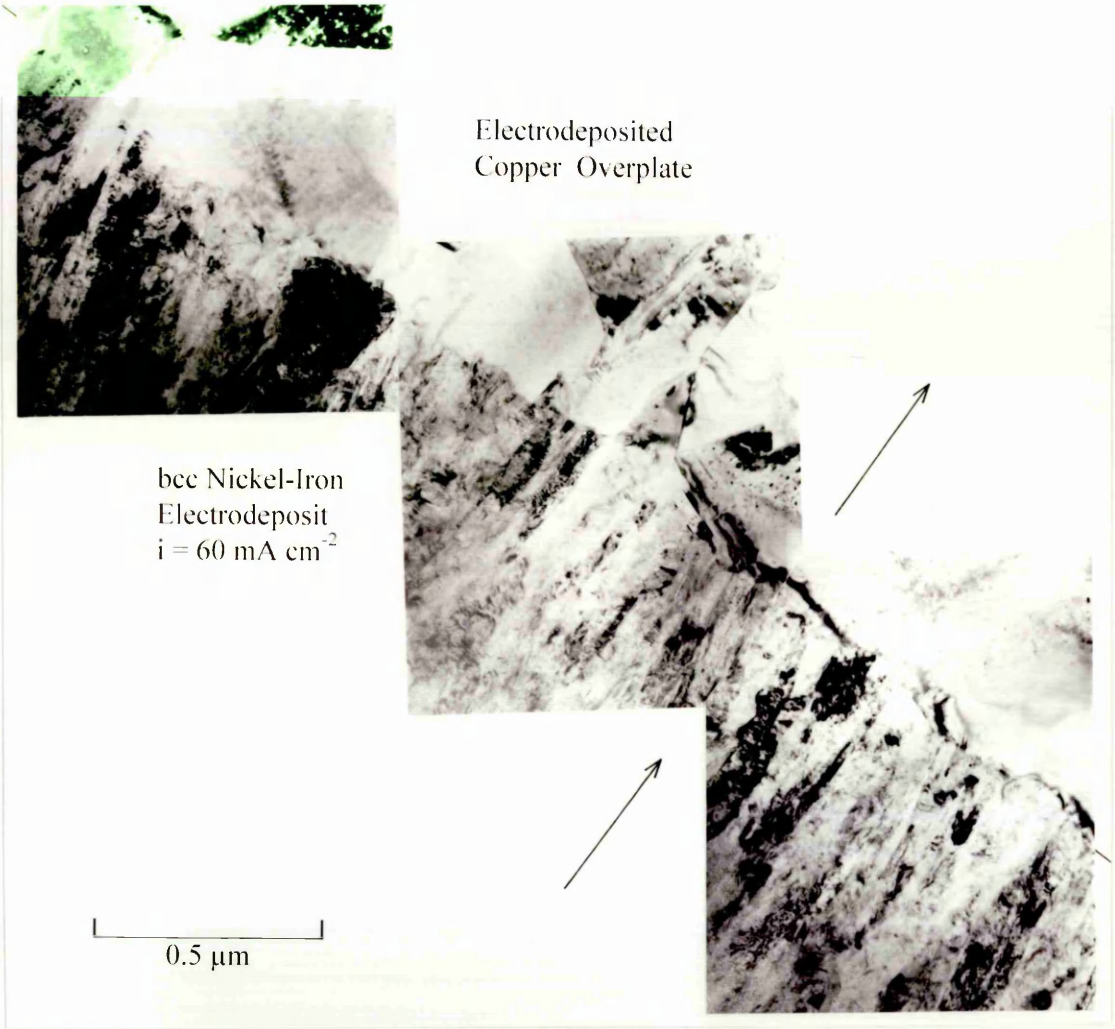

Fig. 4-51: Montage of Bright Field Images Showing the Interface Between the Surface of the Advanced Developed bcc Nickel-Iron Electrodeposit and the Overplated Copper.

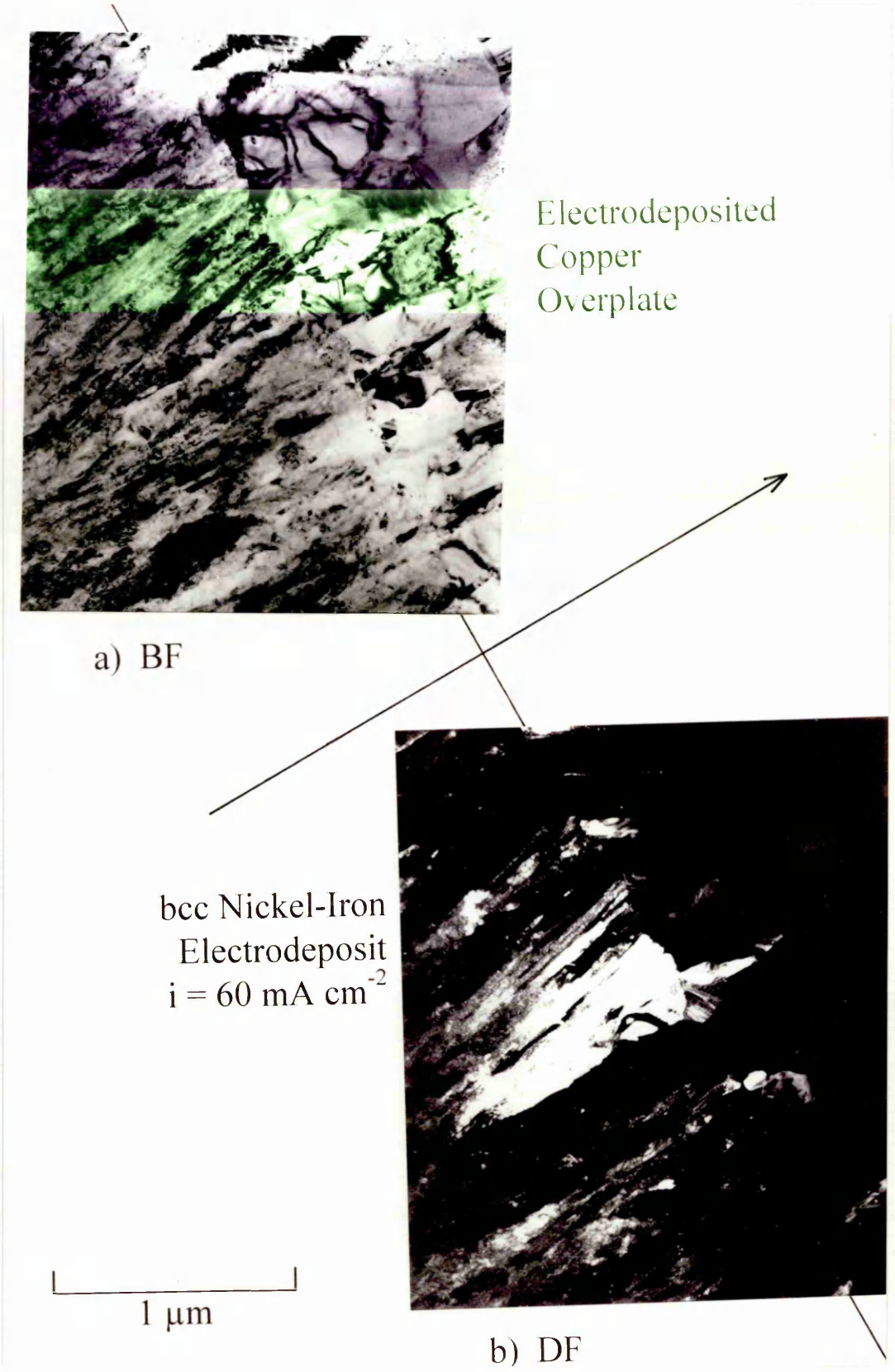

Fig. 4-52: (a) Bright and (b) Dark Field Pair of bcc Nickel-Iron Deposit/Copper Overplate Interface. Bright Grains in (b) Have <211> Growth Direction.

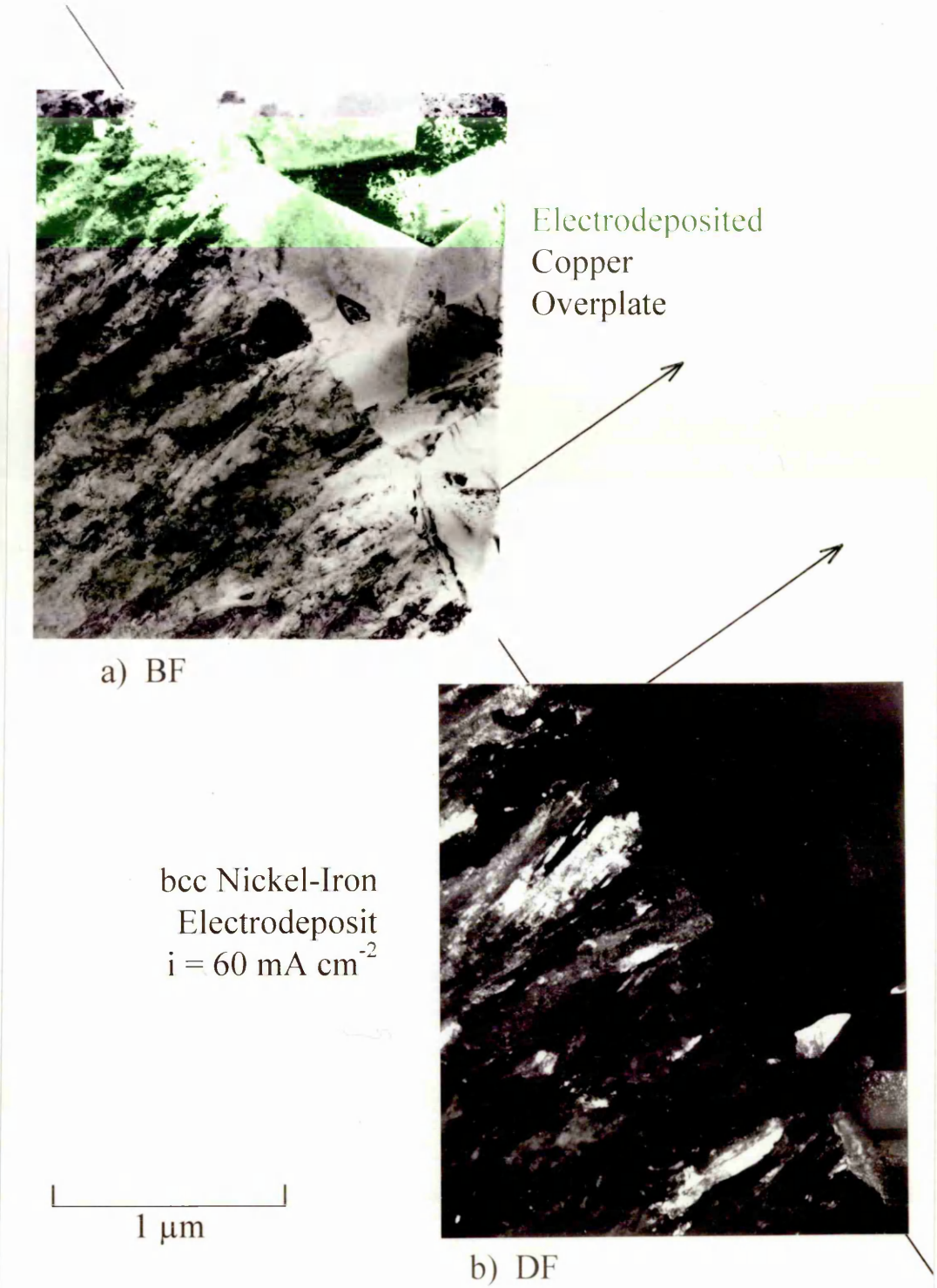

Fig. 4-53: (a) Bright and (b) Dark Field Pair of bcc Nickel-Iron Deposit/Copper Overplate Interface. Bright Grains in (b) Have <211> Growth Direction.

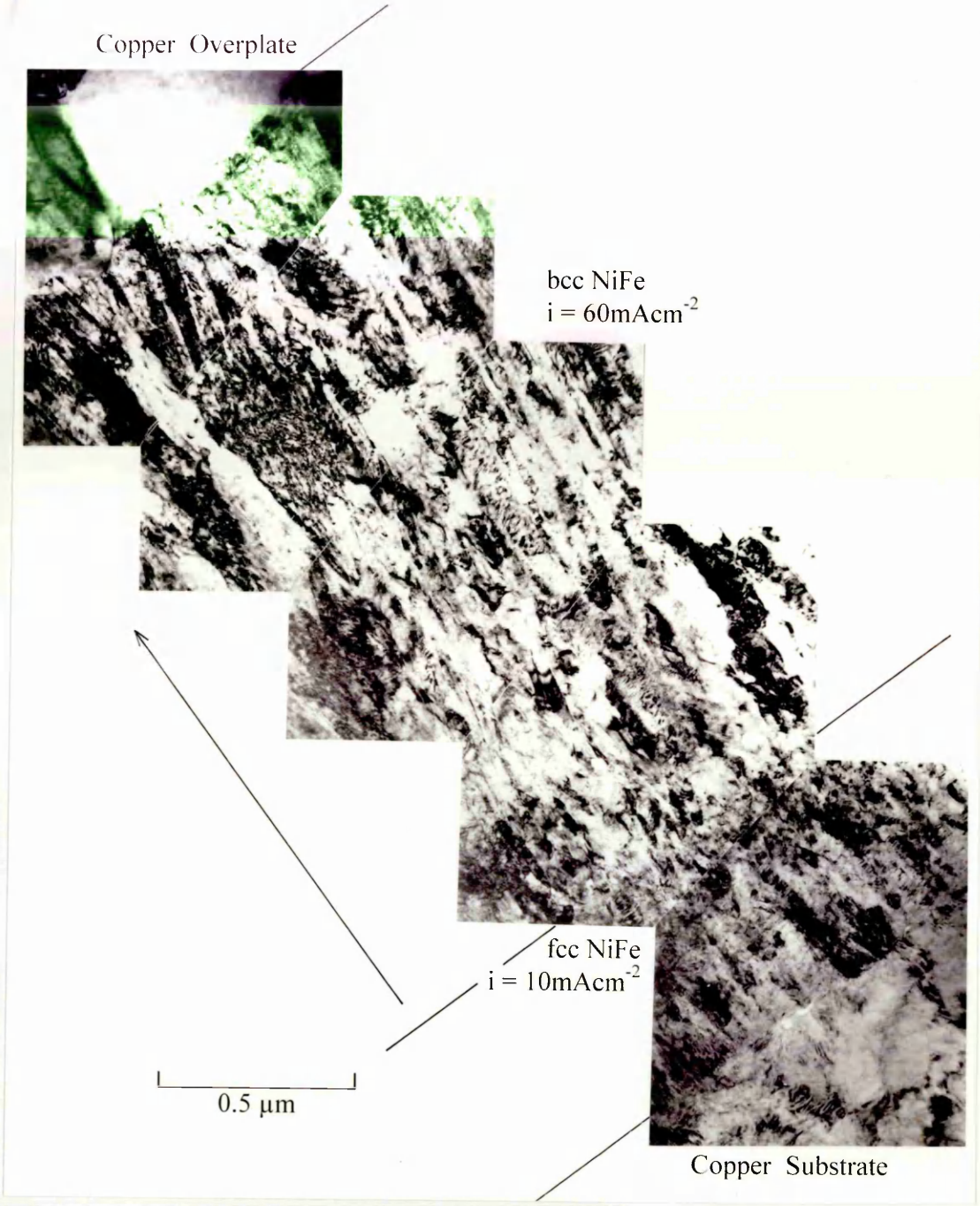

Fig. 4-54a: Montage of Bright Field Images Showing Double Layered 2µm Thick bcc NiFe Nucleated on 0.5µm Thick fcc NiFe Deposit.

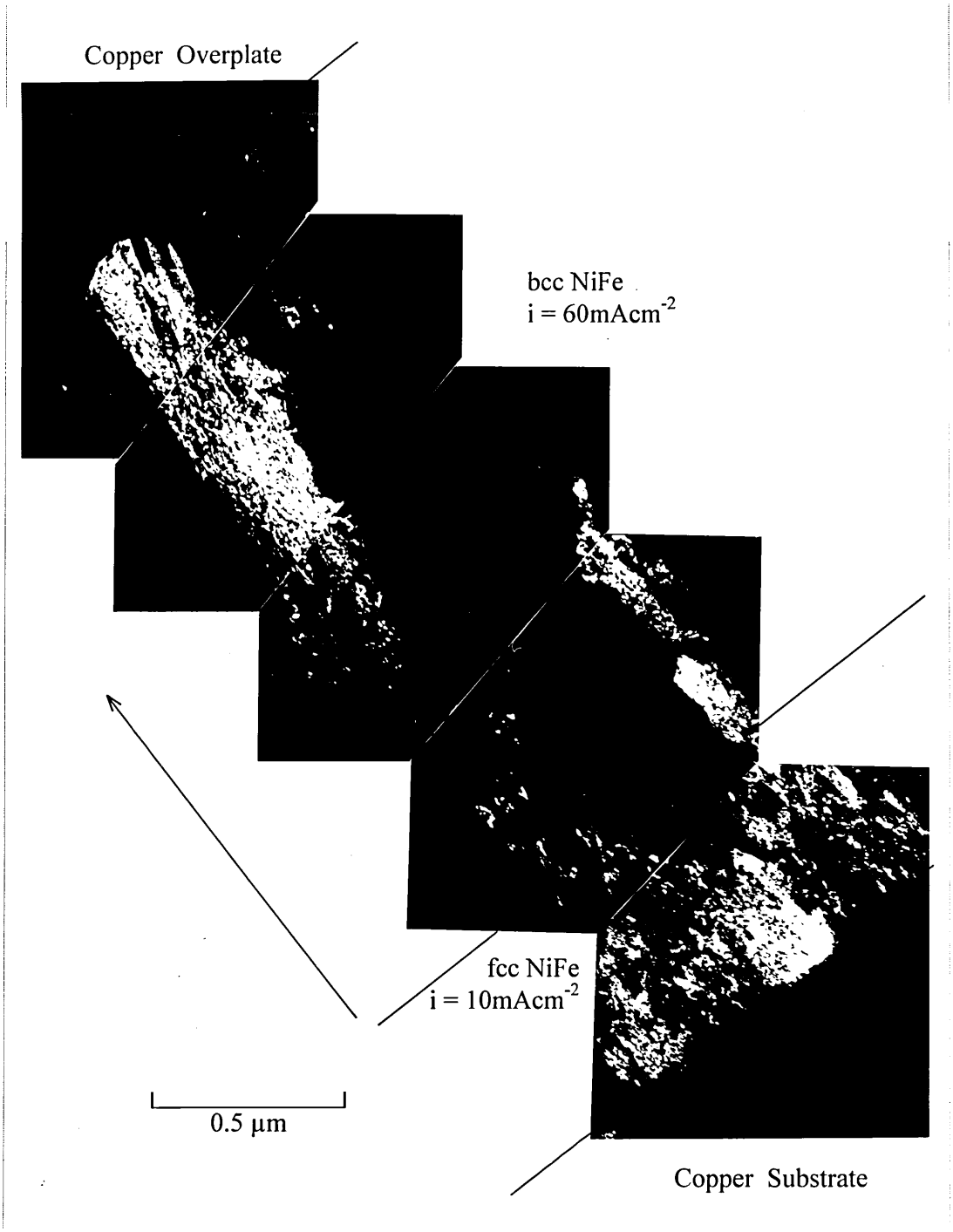

Fig. 4-54b: Montage of Dark Field Images Showing Double Layered 2μm Thick bcc NiFe Nucleated on 0.5μm Thick fcc NiFe Deposit.

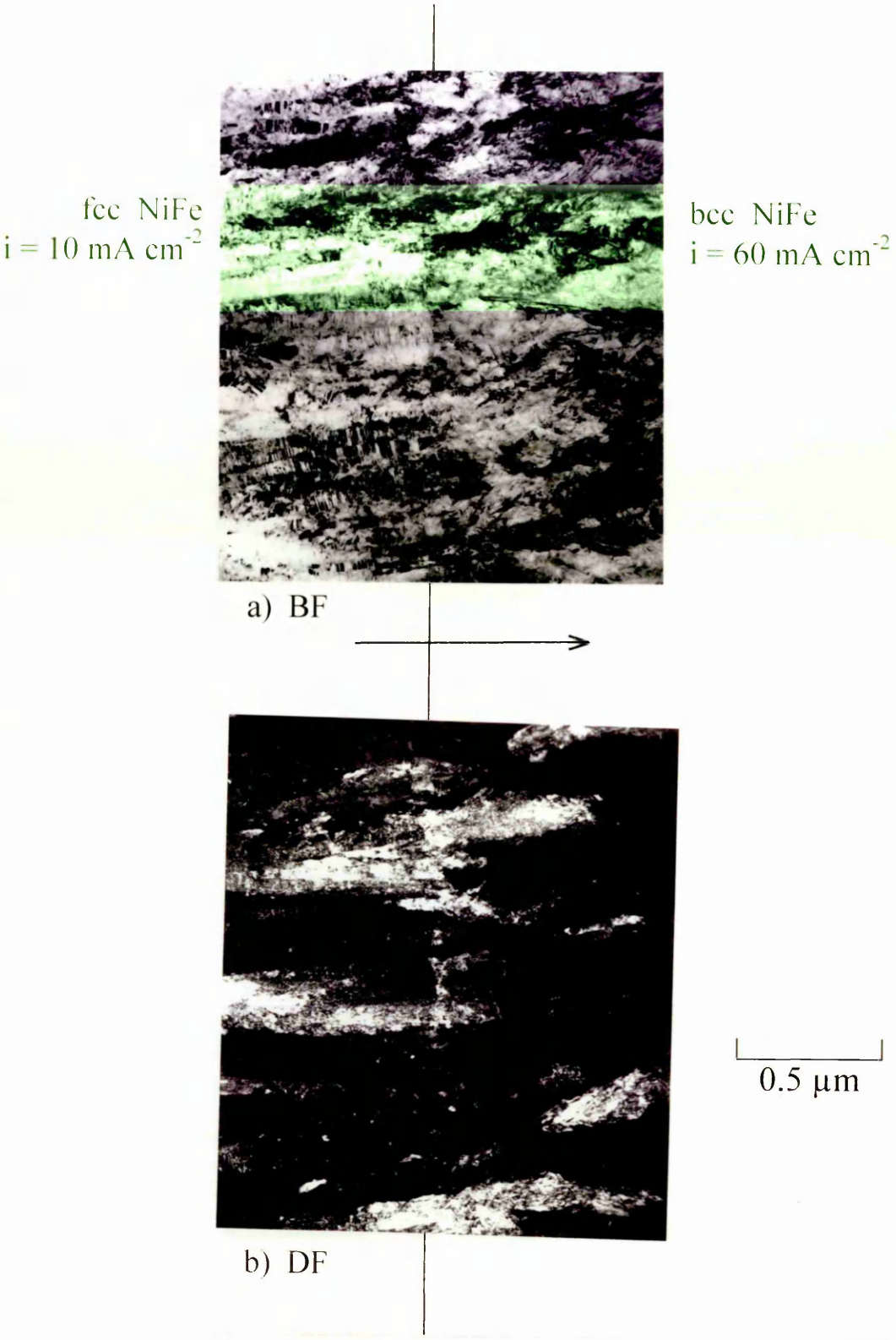

Fig. 4-55: (a) Bright and (b) Dark Field Pair of Interface Between Advanced Developed, 2µm Thick fcc NiFe Deposit and Nucleation Site of bcc NiFe Deposit.

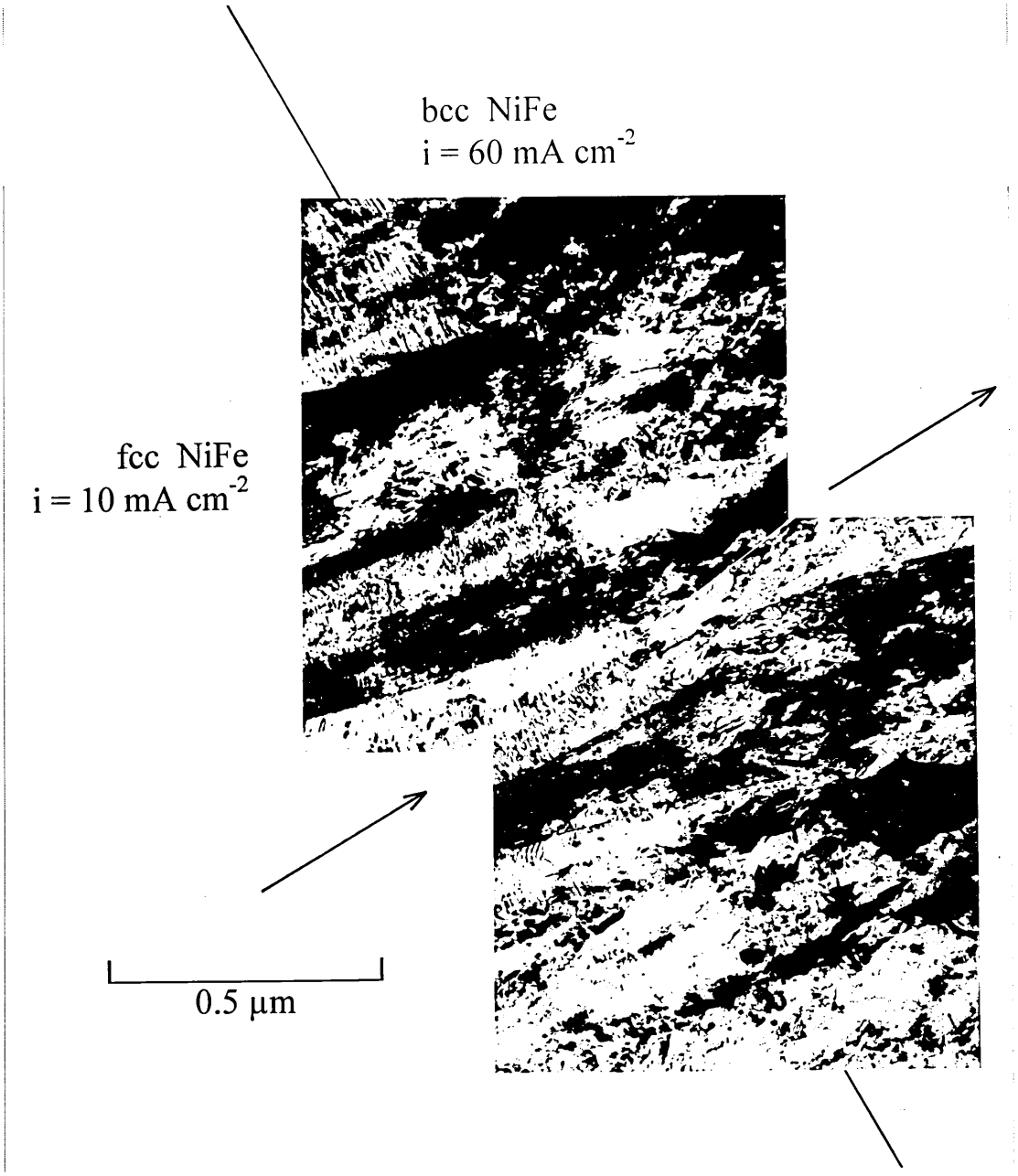

Fig. 4-56: Montage of Bright Field Image Showing Interface Between 2µm Thick, Advanced Developed fcc NiFe Deposit and Nucleation Site of bcc NiFe Deposit.

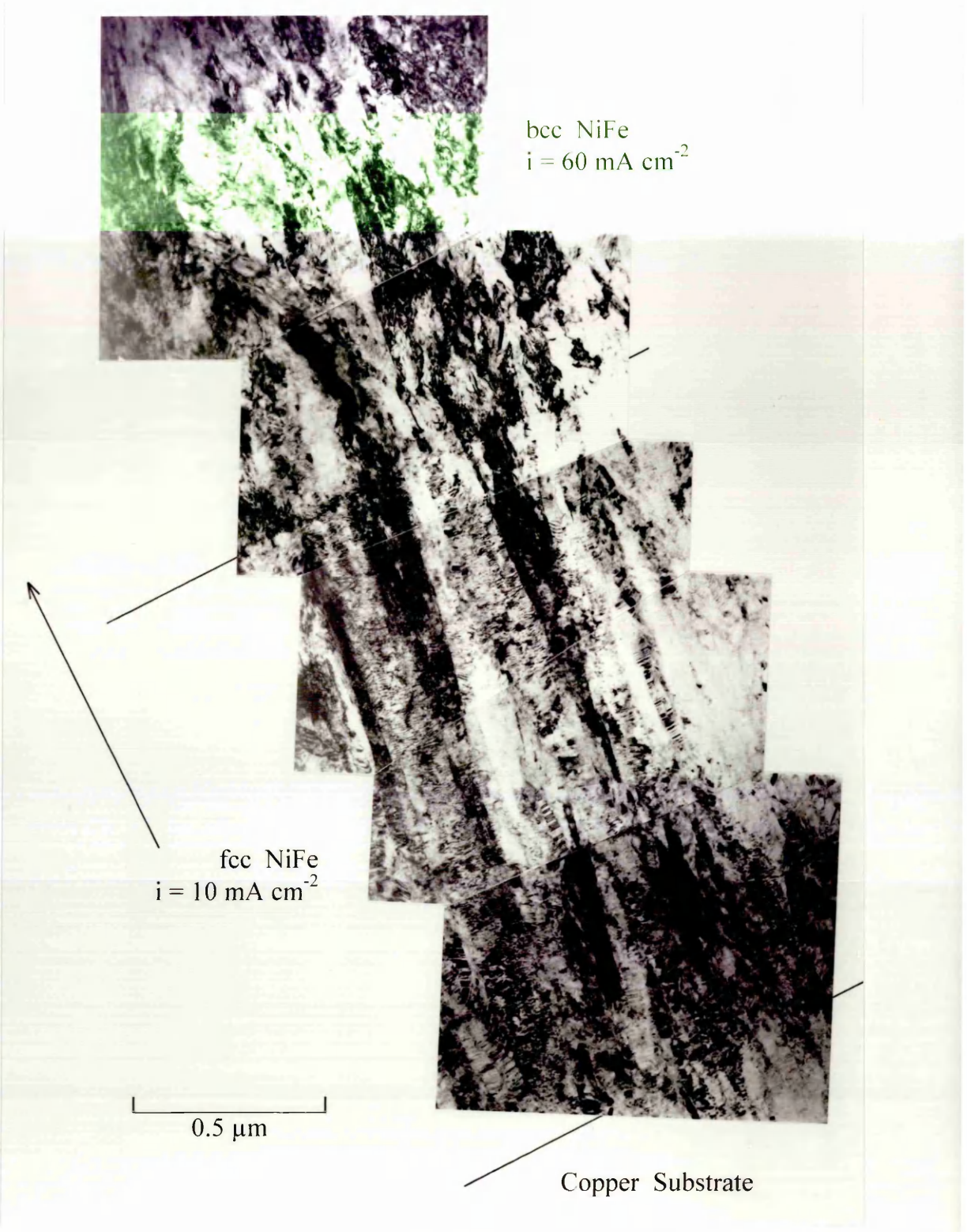

Fig. 4-57a: Bright Field Images of Double Layered 2µm Thick bcc NiFe-Nucleated on 2µm Thick fcc NiFe Deposit.

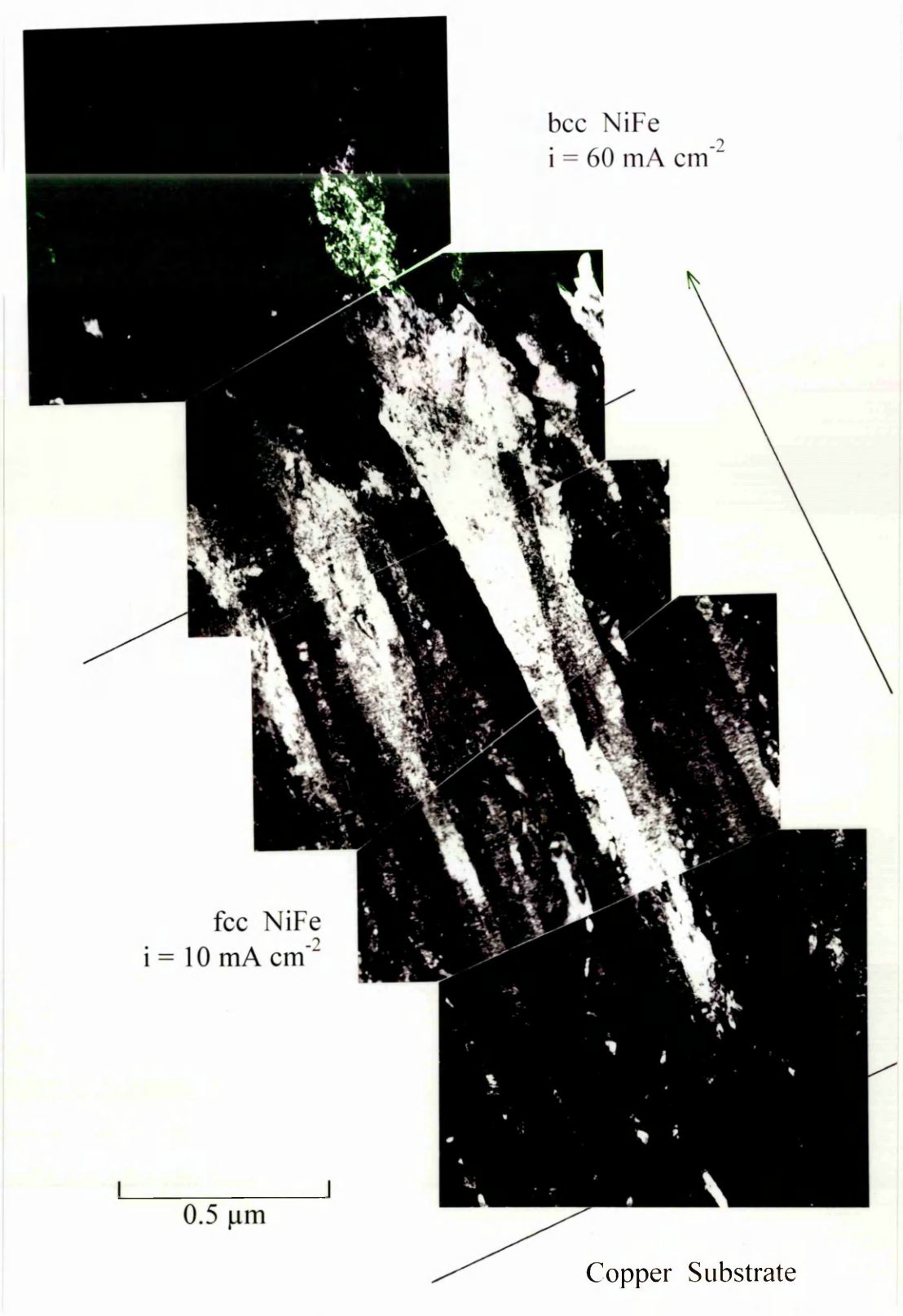

Fig. 4-57b: Dark Field Images of Double Layered 2μm Thick bcc NiFe-Nucleated on 2μm Thick fcc NiFe Deposit.

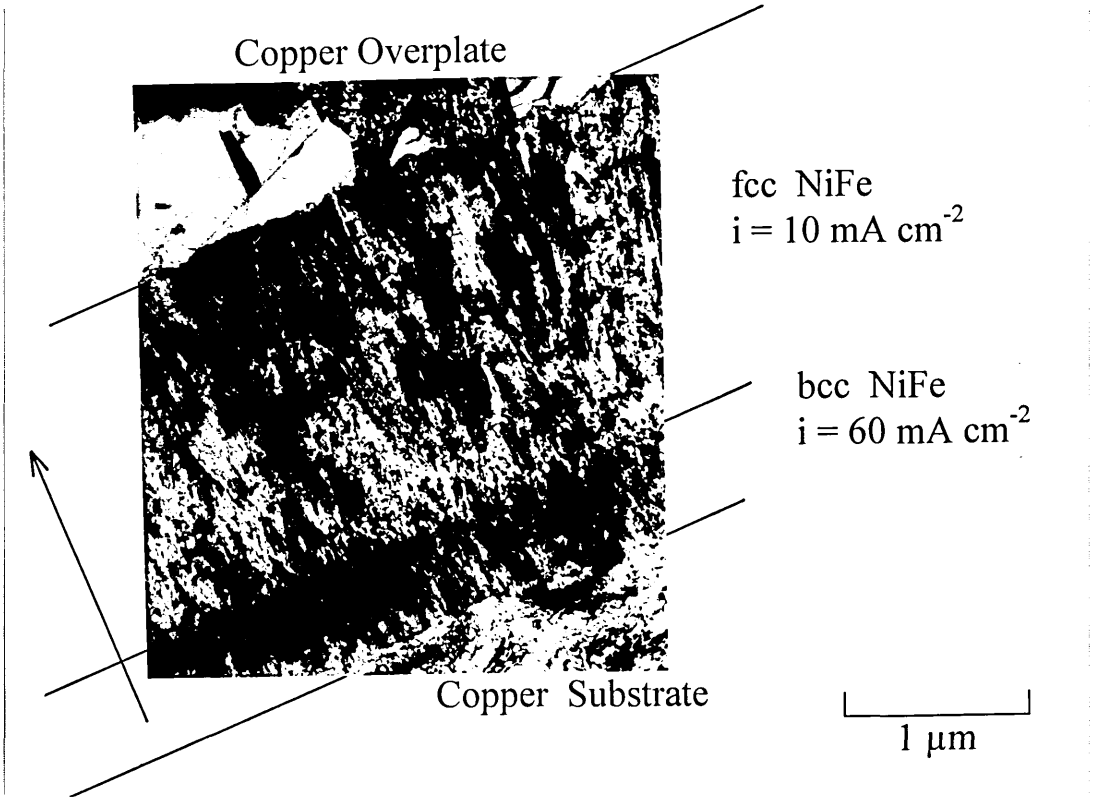

Fig. 4-58: Bright Field Image of Double Layered 2μm Thick fcc NiFe Nucleated on 0.5μm Thick bcc NiFe Deposit.

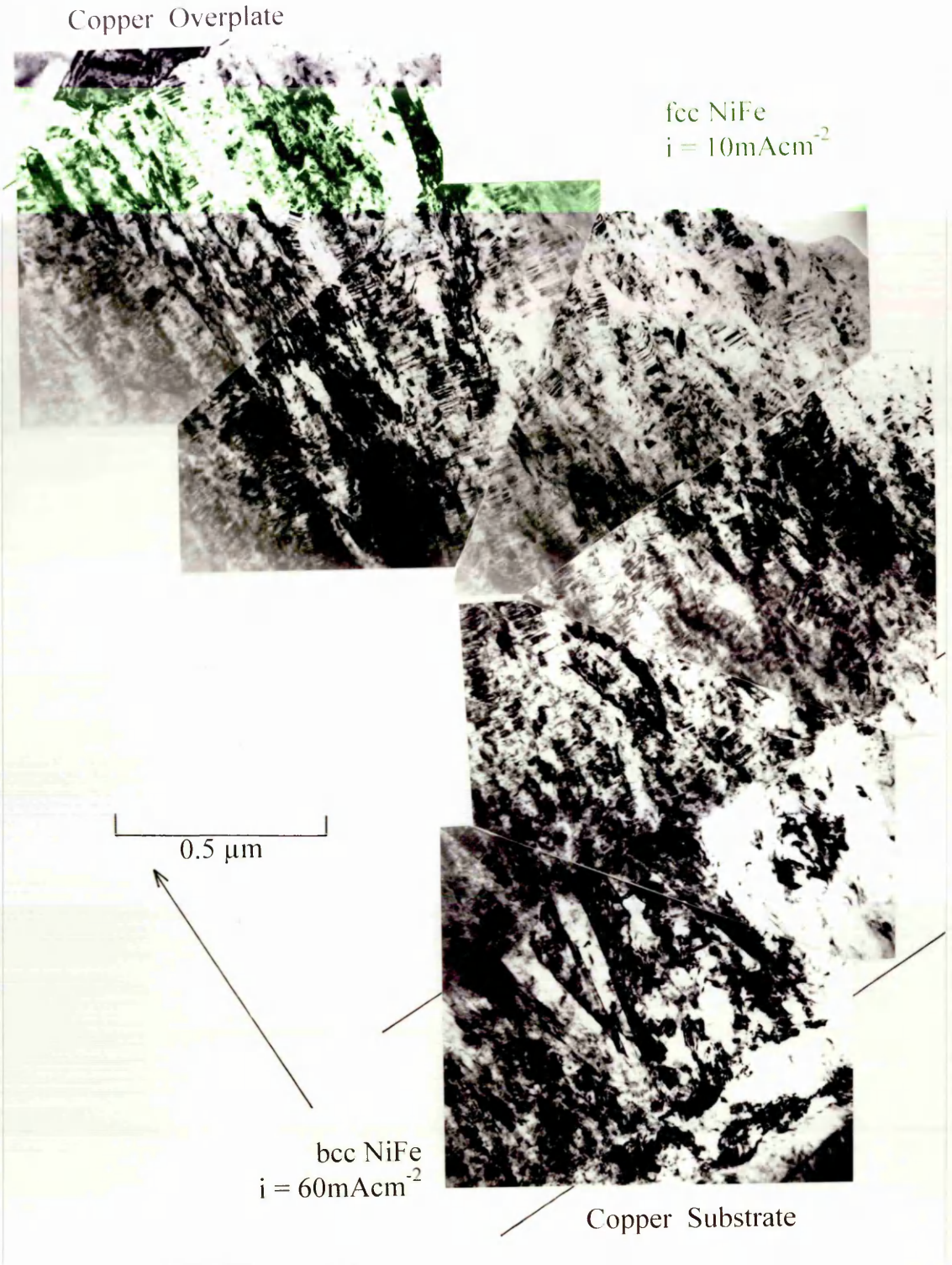

Fig. 4-59: Montage of Bright Field Images of Double Layered 2µm thick fcc NiFe Nucleated on 0.5µm Thick bcc NiFe Deposit.

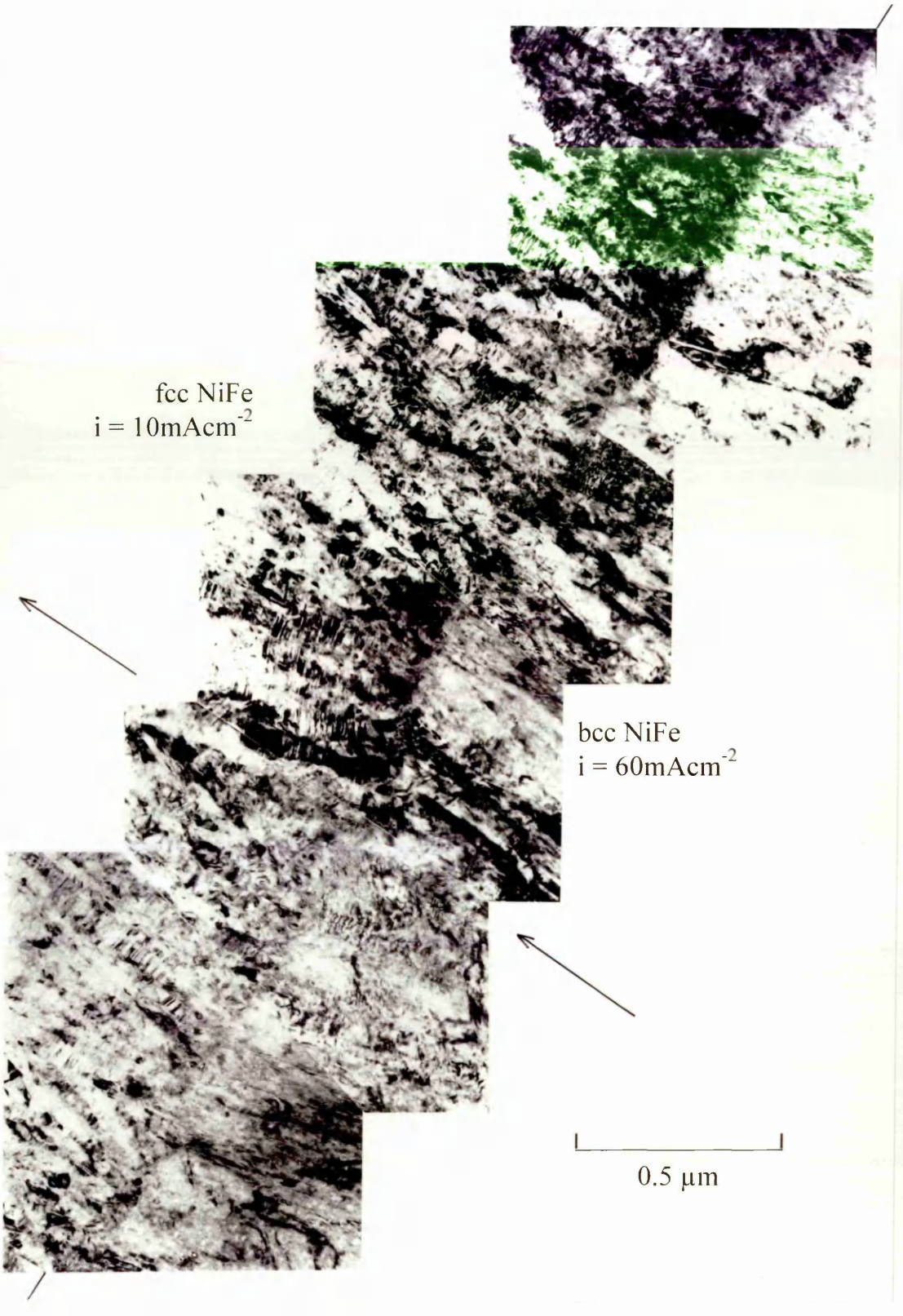

Fig. 4-60a: Montage of Bright Fields Along Interface of Double Layered, 2μm Thick fcc NiFe Deposit Nucleated on 2μm Thick bcc NiFe Deposit.

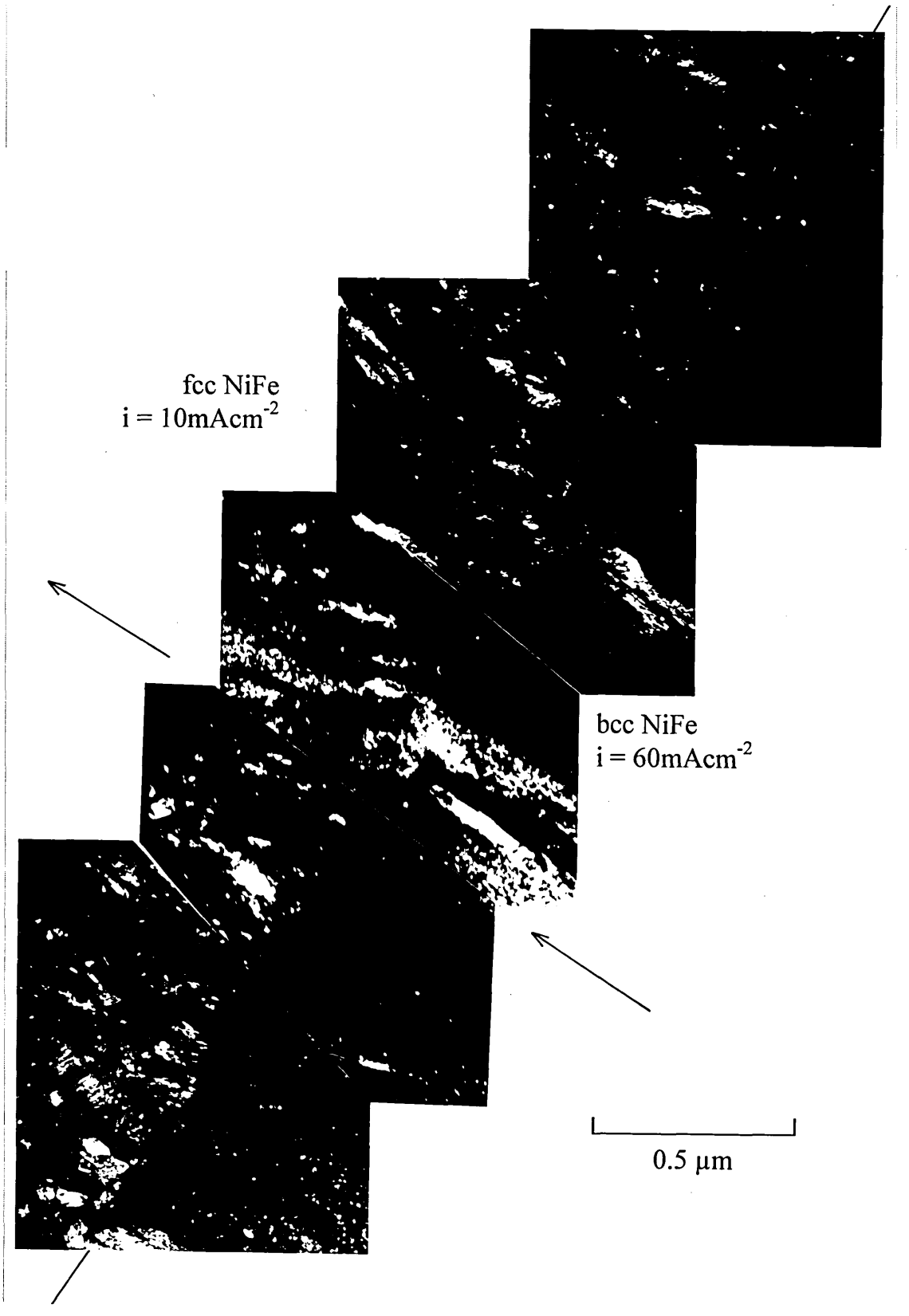

Fig. 4-60b: Montage of Dark Fields Along Interface of Double Layered, 2μm Thick fcc NiFe Deposit Nucleated on 2μm Thick bcc NiFe Deposit.

Fig. 4-61: Montage of Bright Fields Along Interface of Double Layered 2μm Thick fcc NiFe Deposit Nucleated on 2μm Thick bcc NiFe Deposit.

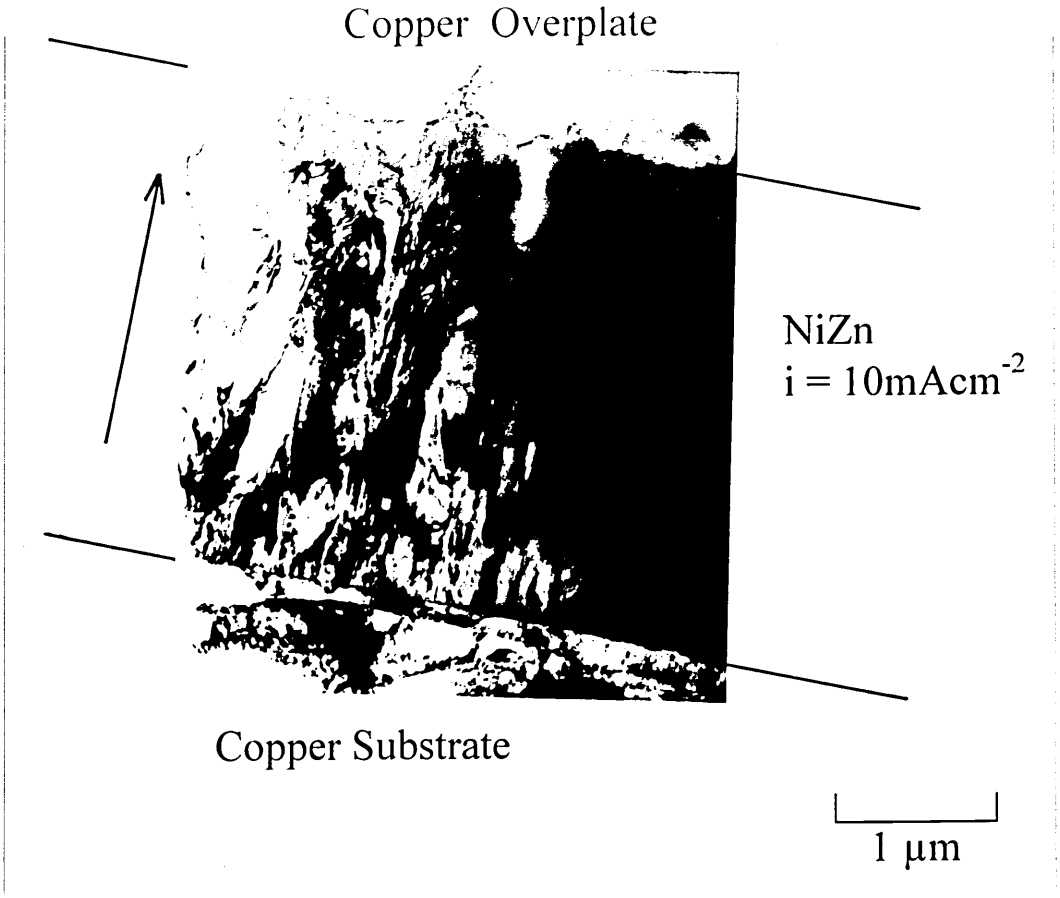

Fig. 4-62: Bright Field Image of NiZn Deposit (i = 10 mA cm^{-2}) on Copper Substrate.

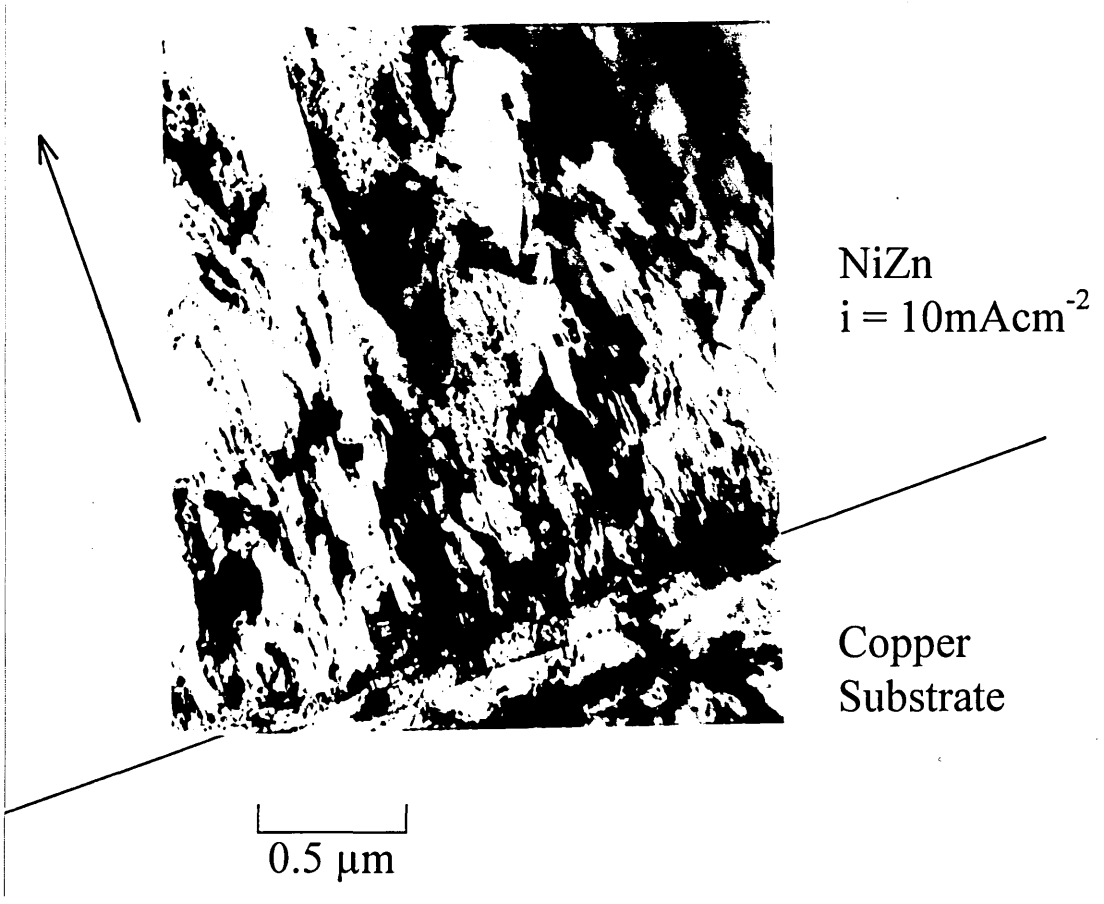

Fig. 4-63: Bright Field Image of Interface between Copper Substrate and Nucleated NiZn Deposit (i = 10 mA cm^{-2}).

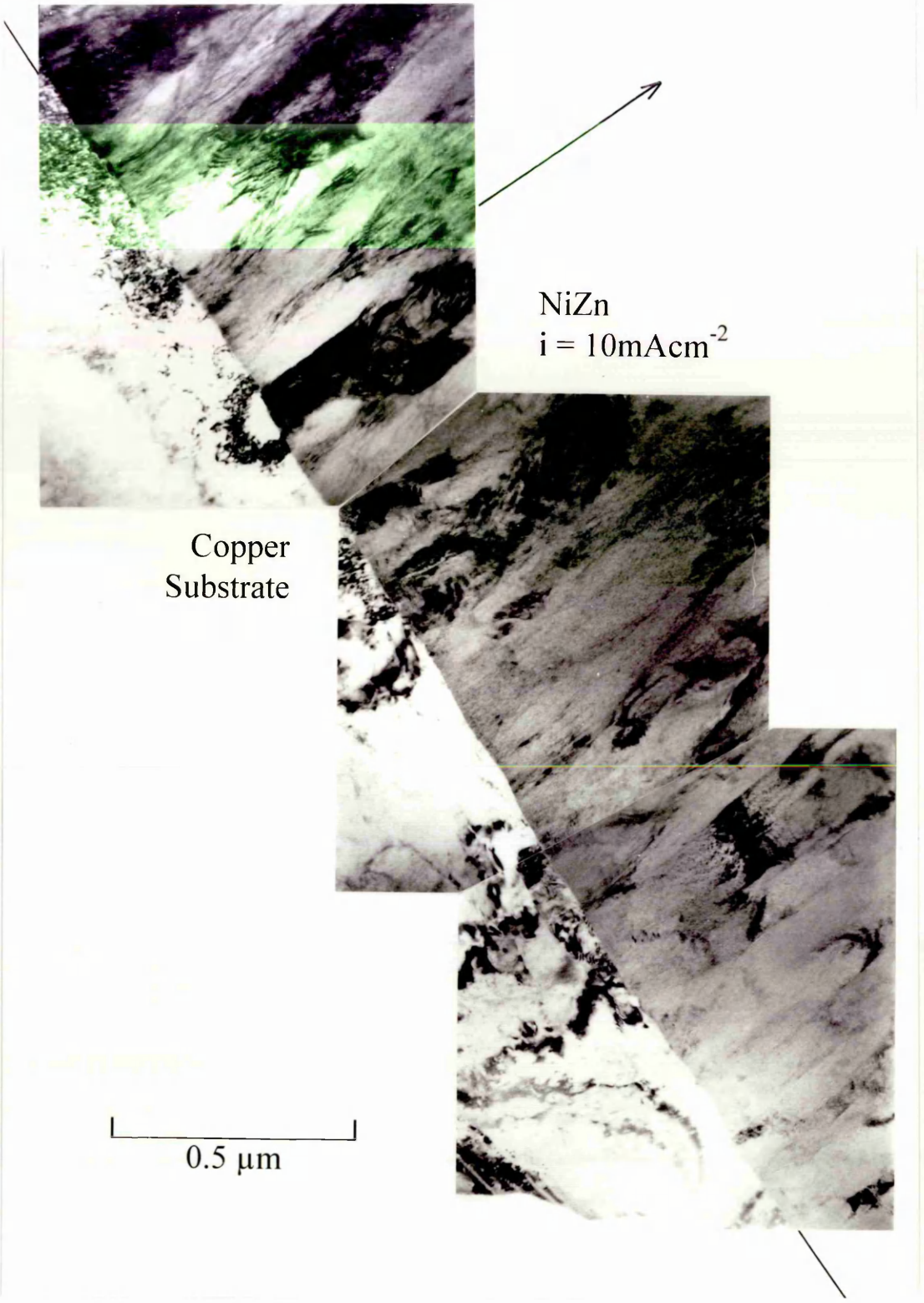

Fig. 4-64: Bright Field Images Along Interface Between Copper Substrate and Nucleated NiZn Deposit (i = 10 mA cm^{-2}).

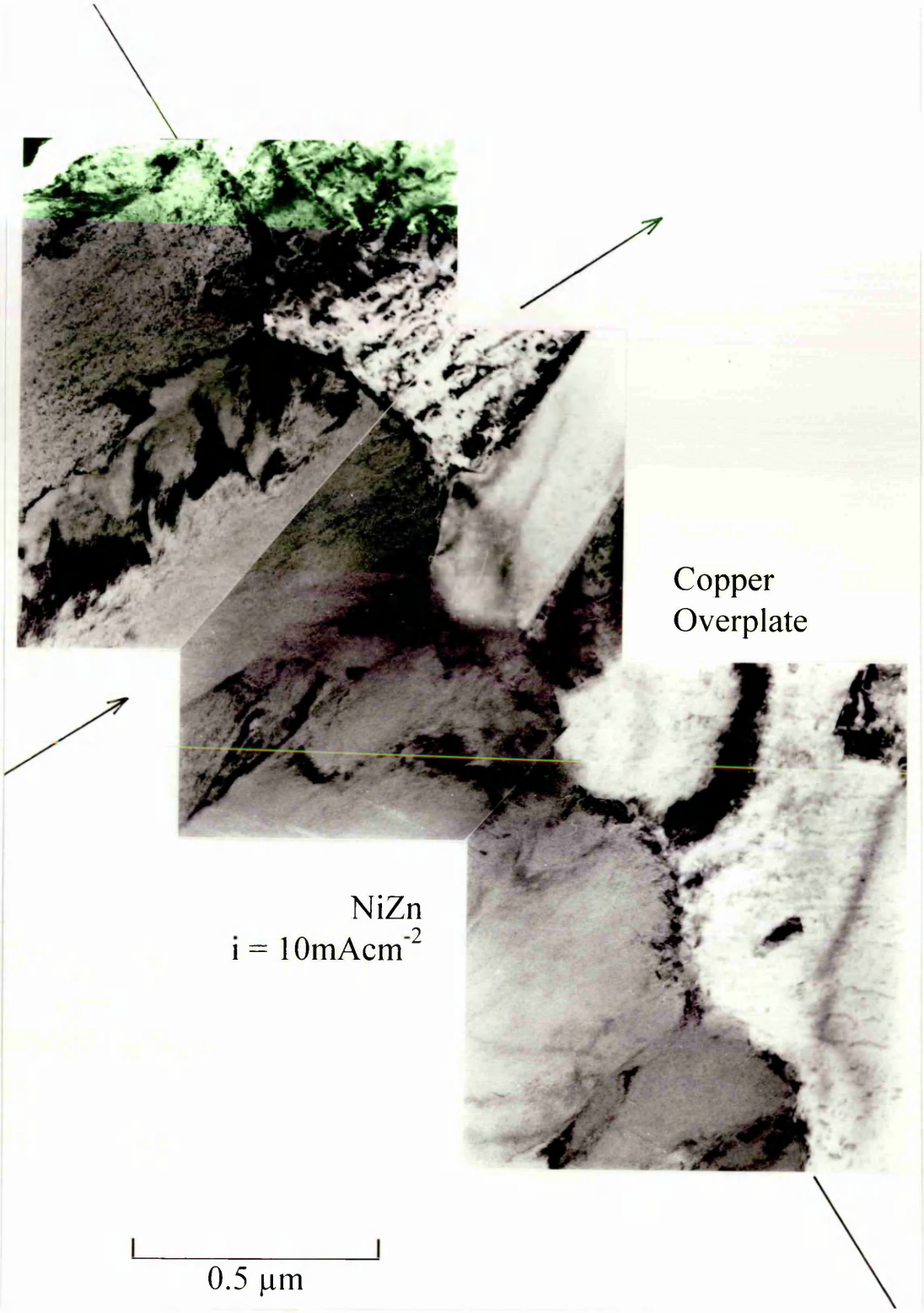

Fig. 4-65: Bright Field Images Along Interface Between Advanced Developed, Approximately 2µm Thick, Coarse Grained NiZn Deposit (i = 10 mA cm^{-2}) and Copper Overplate.

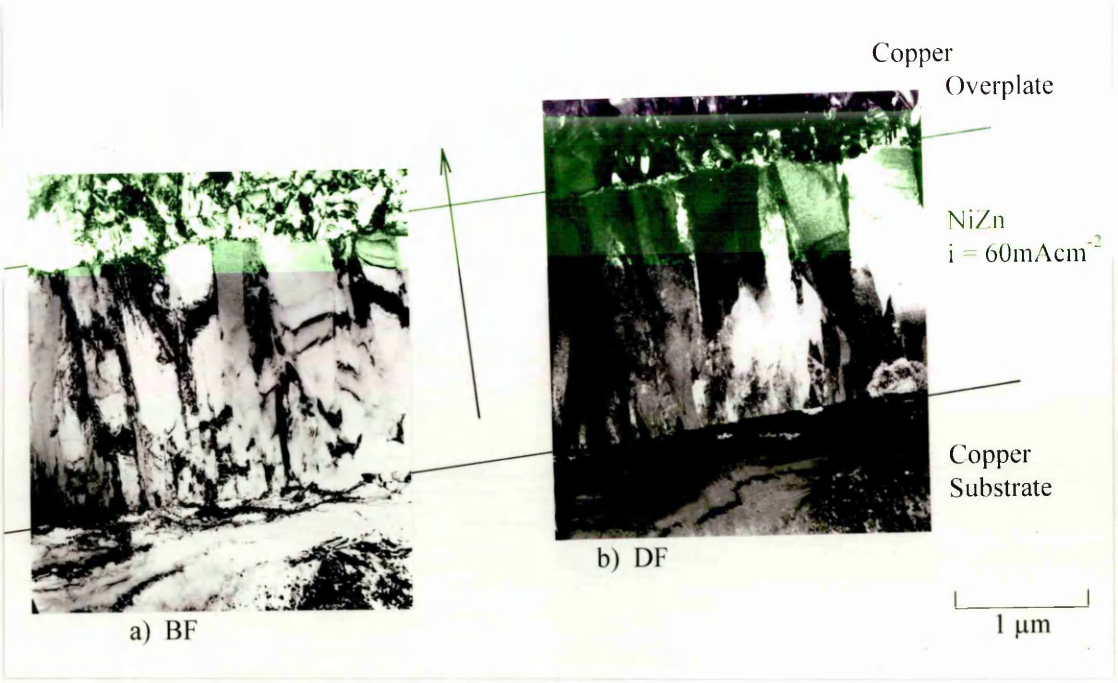

Fig. 4-66: (a) Bright Field and (b) Dark Field Image of Cross-Sectioned NiZn Deposit (i = 60 mA cm^{-2}) Nucleated on Copper.

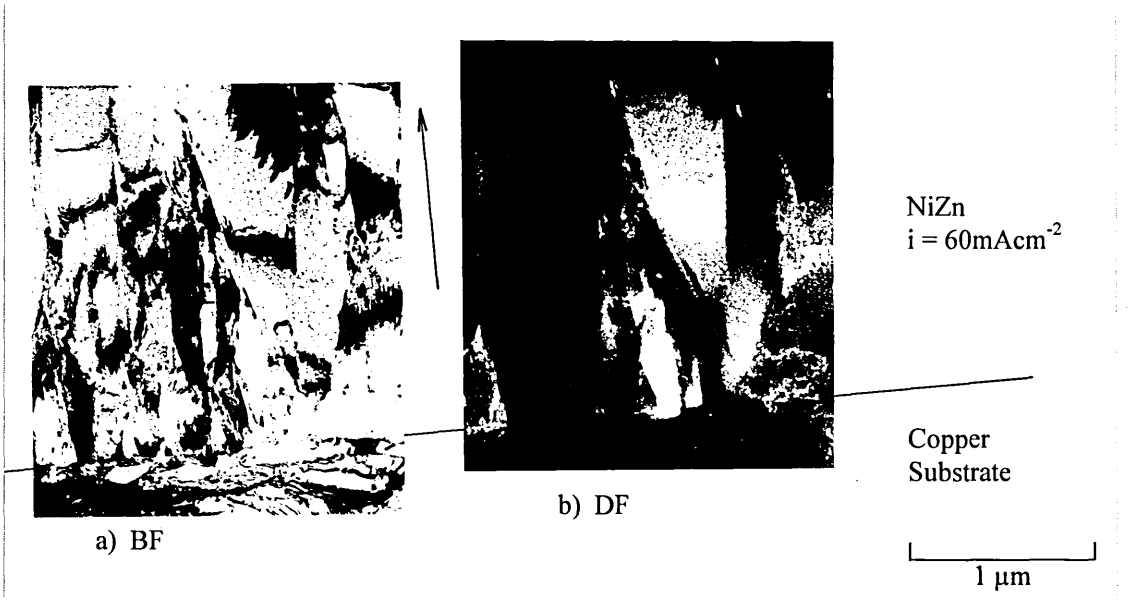

Fig. 4-67: (a) Bright and (b) Dark Field Image of Nucleation Site of NiZn Deposit (i = 60 mA cm^{-2}) on Copper.

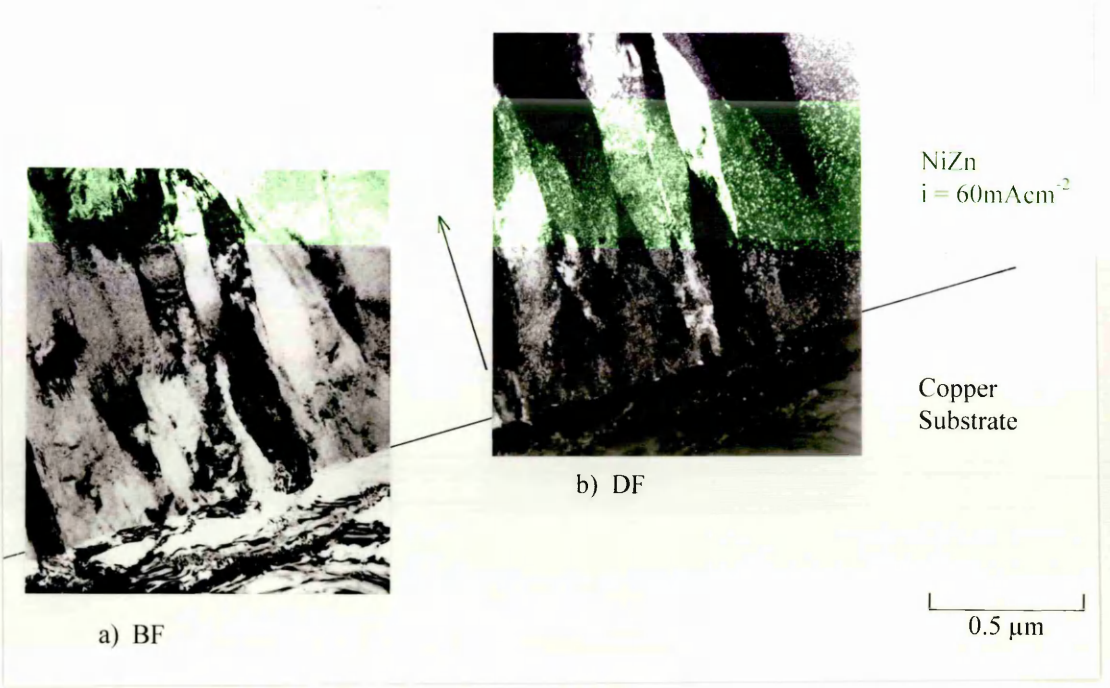

Fig. 4-68: (a) Bright and (b) Dark Field Image of Nucleation Site of NiZn Deposit (i = 60 mA cm^{-2}) on Copper.

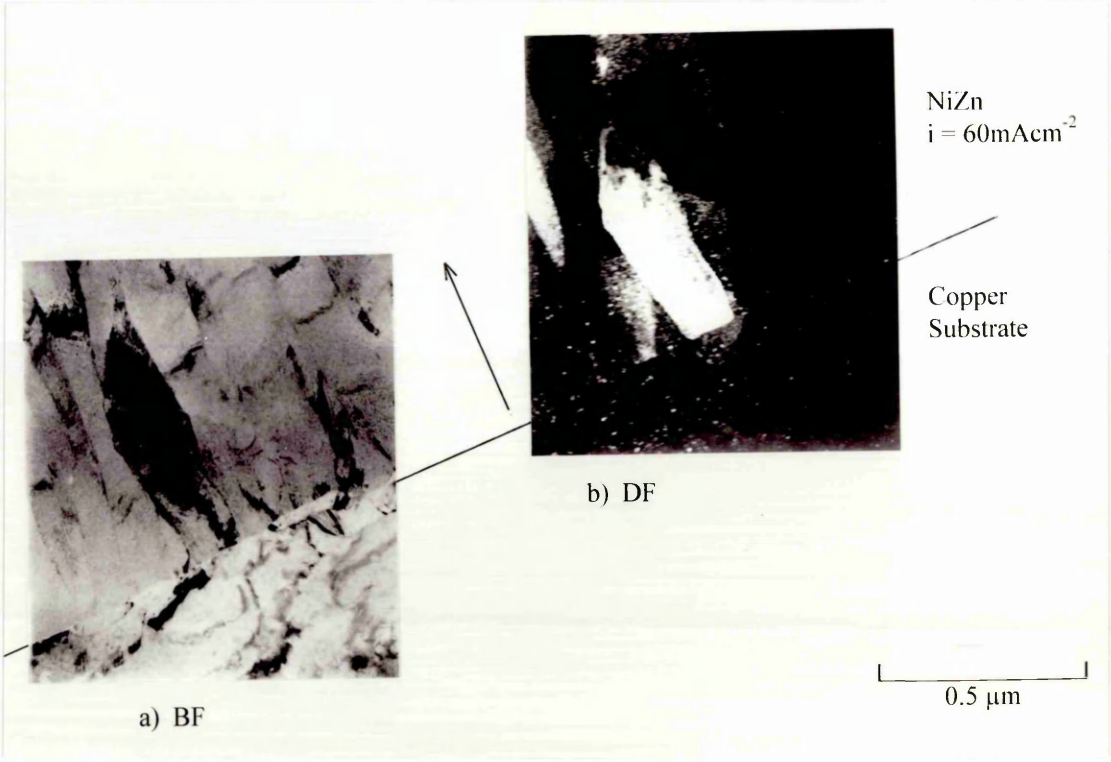

Fig. 4-69: (a) Bright and (b) Dark Field Image of Nucleation Site of NiZn Deposit (i = 60 mA cm^{-2}) on Copper.

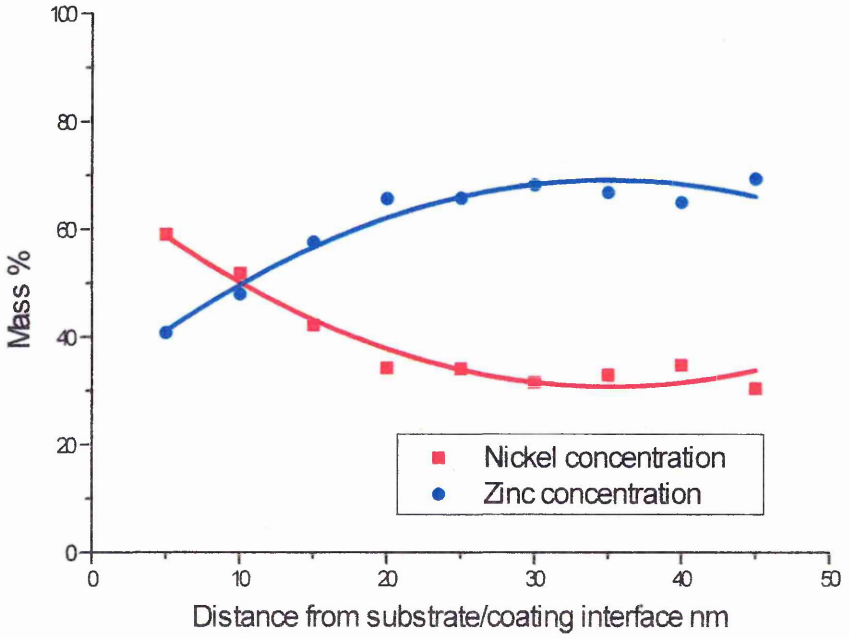

Fig. 4-70: Composition of Nickel Zinc Deposit (i = 10 mA cm^{-2}) versus Distance from Interface Steel Substrate/Nickel Zinc Deposit.

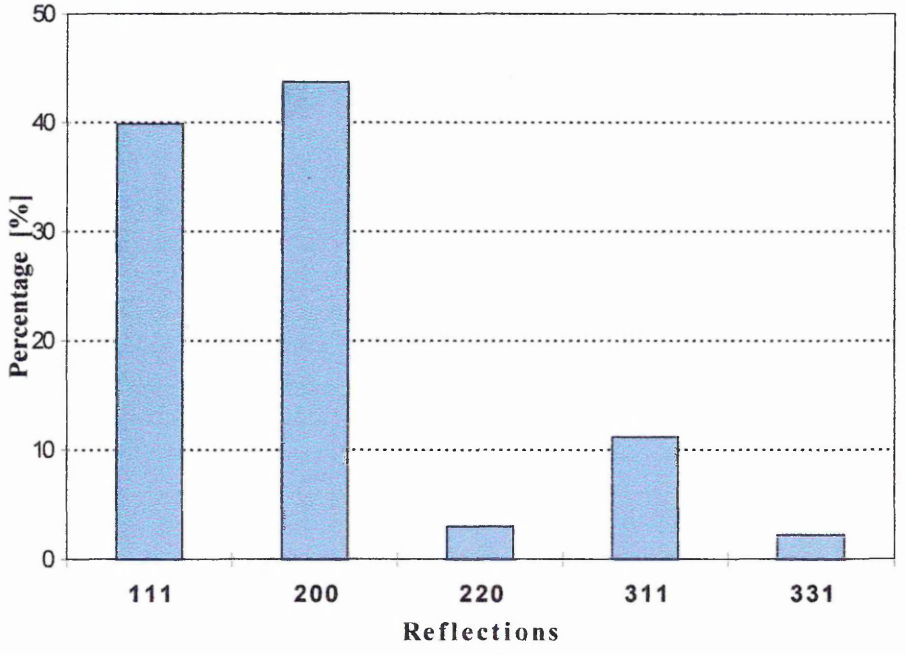

Fig. 4-71: Distribution of Reflections Detected in the Copper Disc Substrate.

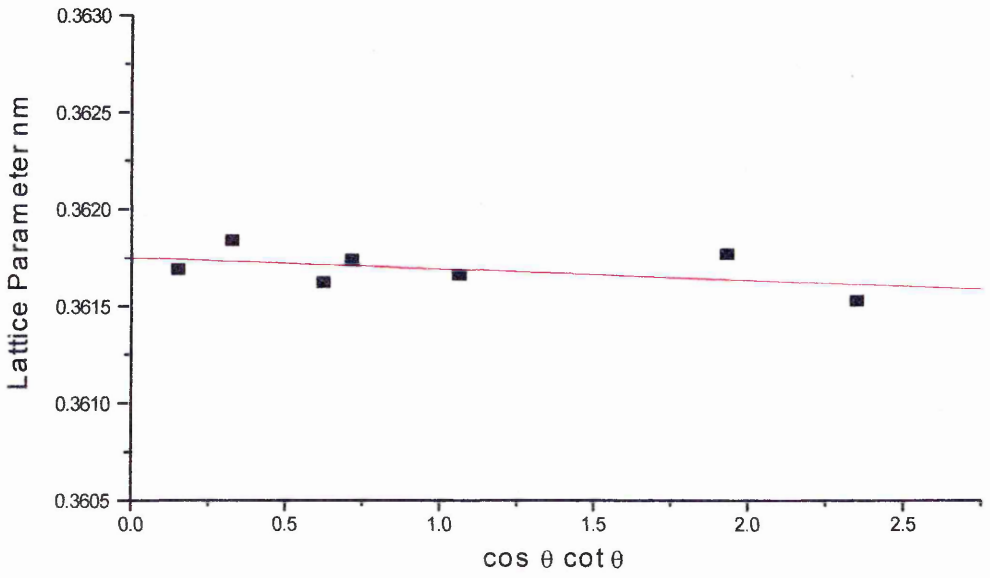

Fig. 4-72: Copper Rod Substrate: Lattice Parameter [nm] Versus cosθ cotθ; Cohen-Wagner Plot for Extrapolation of Lattice Parameter 'a'.

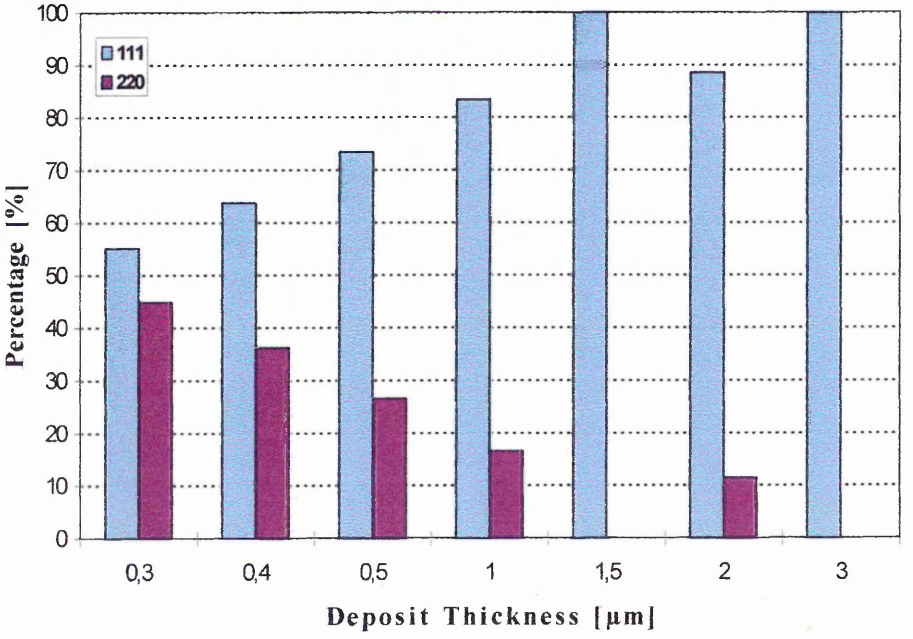

Fig. 4-73: Distribution of Reflections Detected at Various Thicknesses in the fcc NiFe Electrodeposits.

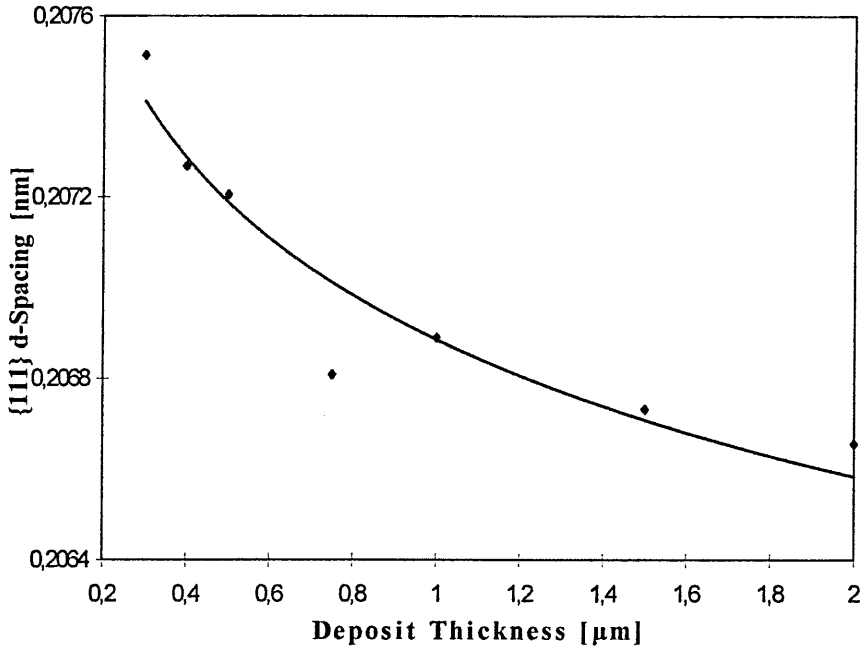

Fig. 4-74: Deposit Thickness Versus {111} Interplanar d-Spacing in fcc NiFe Electrodeposit.

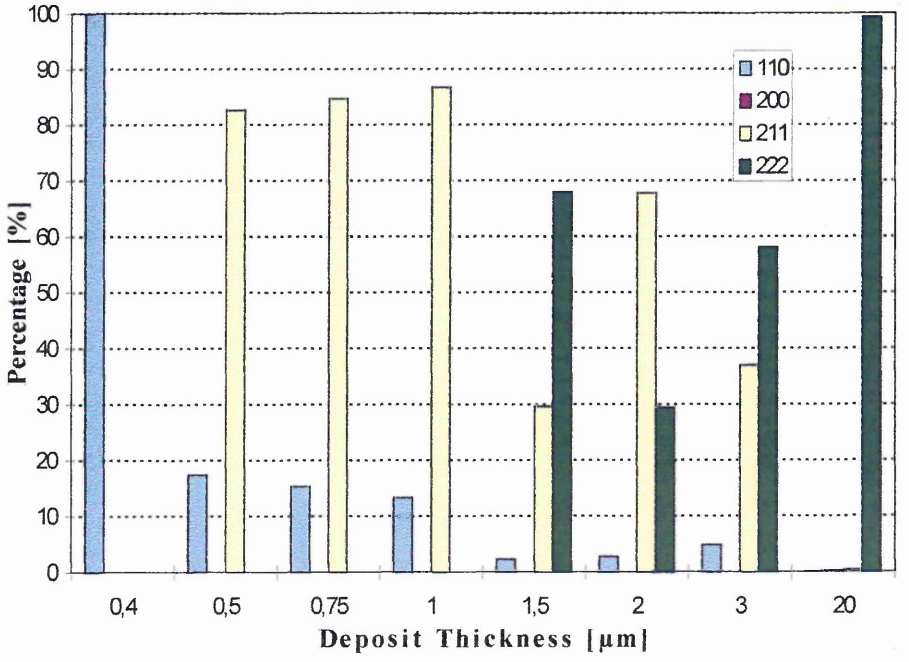

Fig. 4-75: Distribution of Reflections Detected at Various Thicknesses in the bcc NiFe Electrodeposits.

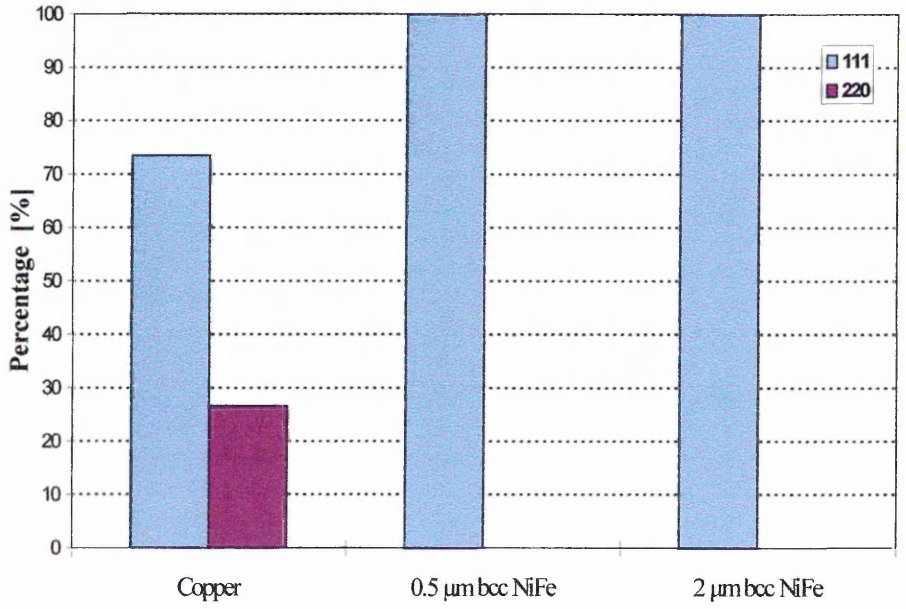

Fig. 4-76: Planar Distribution of 0.5µm Thick fcc NiFe on Copper, 0.5µm bcc NiFe, and 2µm bcc NiFe Electrodeposited Substrates.

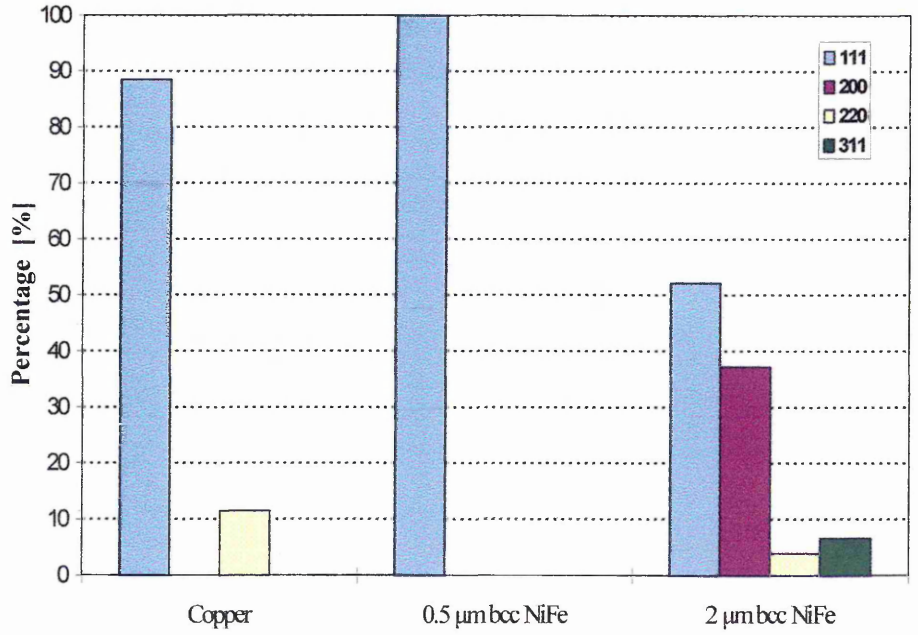

Fig. 4-77: Planar Distribution in per cent of 2µm Thick fcc NiFe Electrodeposits on Copper, 0.5µm bcc NiFe, and 2µm bcc NiFe Electrodeposited Substrates.

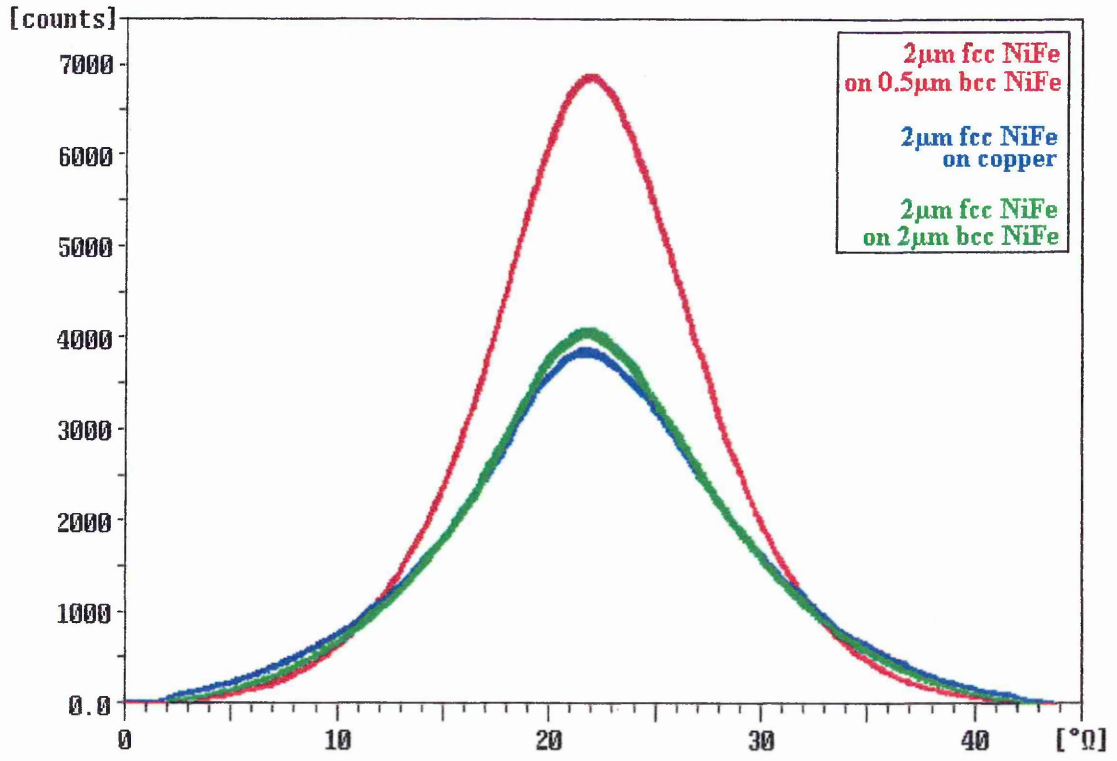

Fig. 4-78: Ω-Scan Spectra of 2µm Thick fcc Structured Nickel-Iron Deposit Electrocrystallized onto Different Substrates, i.e. Copper, 0.5µm bcc NiFe, and 2µm bcc NiFe Electrodeposits.

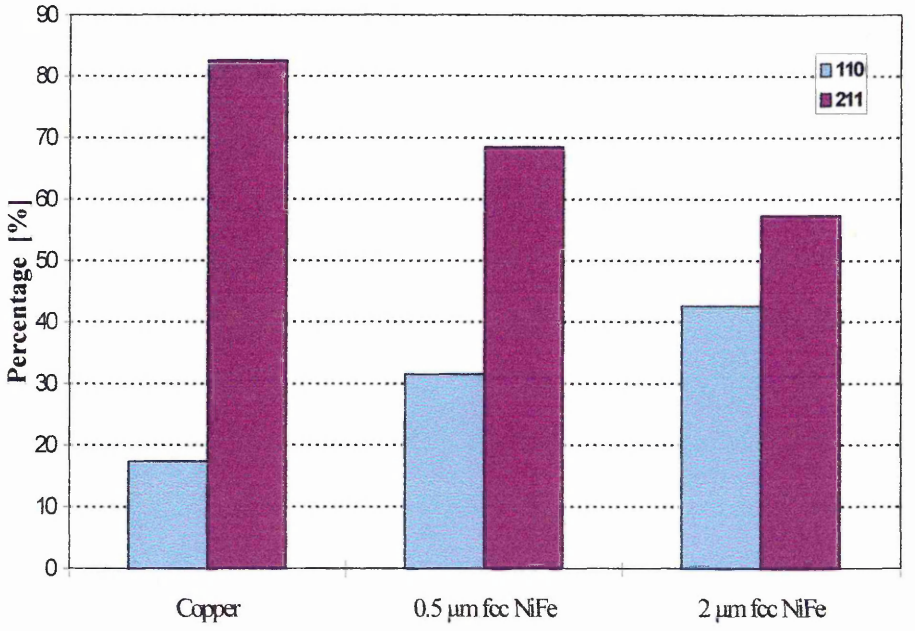

Fig. 4-79: Planar Distribution of 0.5µm Thick bcc NiFe on Copper, 0.5µm fcc NiFe, and 2µm fcc NiFe Electrodeposited Substrates.

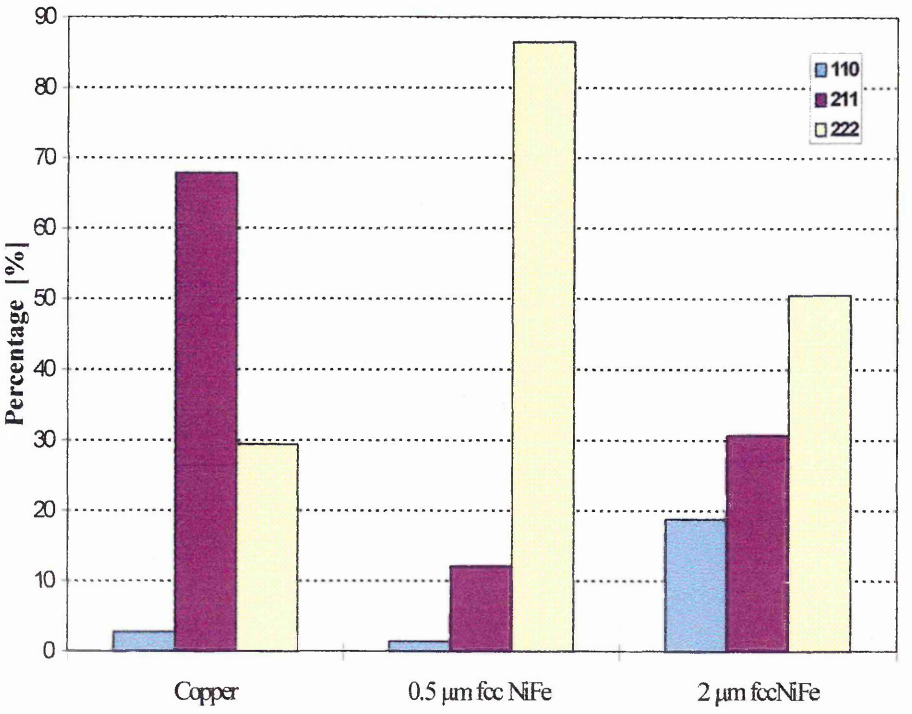

Fig. 4-80: Planar Distribution of 2µm Thick bcc NiFe on Copper, 0.5µm fcc NiFe, and 2µm fcc NiFe Electrodeposited Substrates.

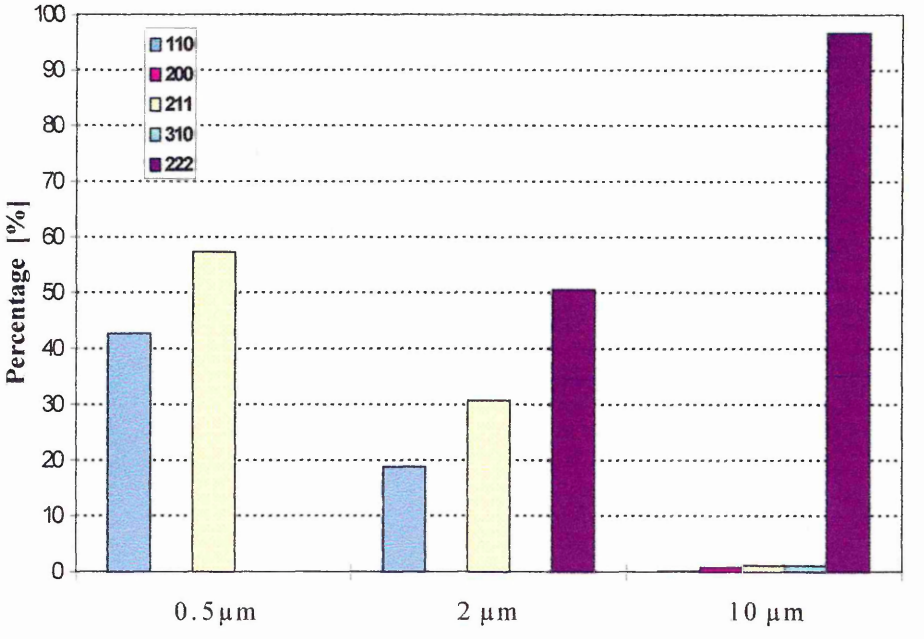

Fig. 4-81: Planar Distribution of 0.5µm, 2µm, and 10µm thick bcc NiFe Electrodeposit on 2µm fcc NiFe Substrate.

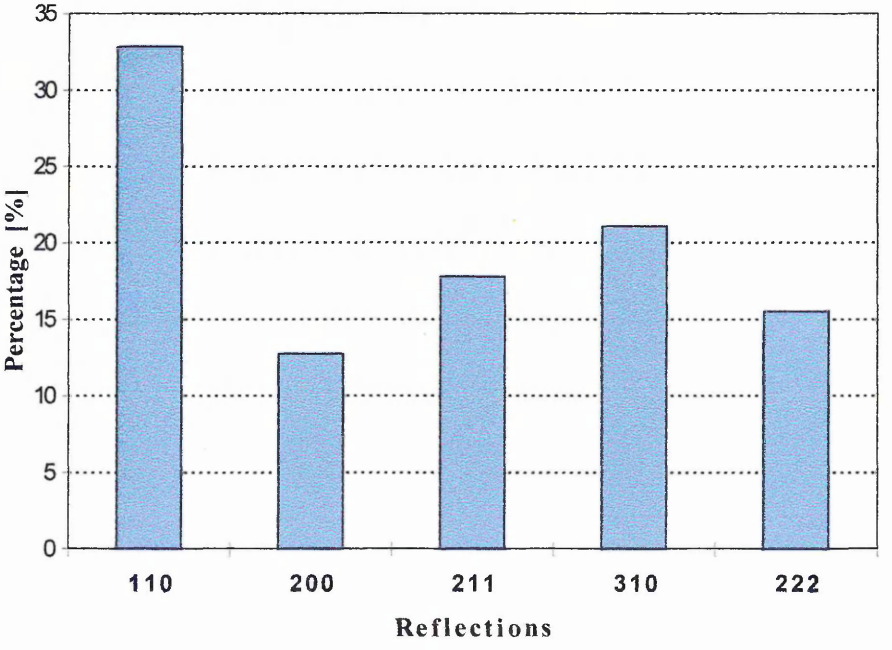

Fig. 4-82: Distribution of Reflections detected in the Mild Steel Disc Substrate.

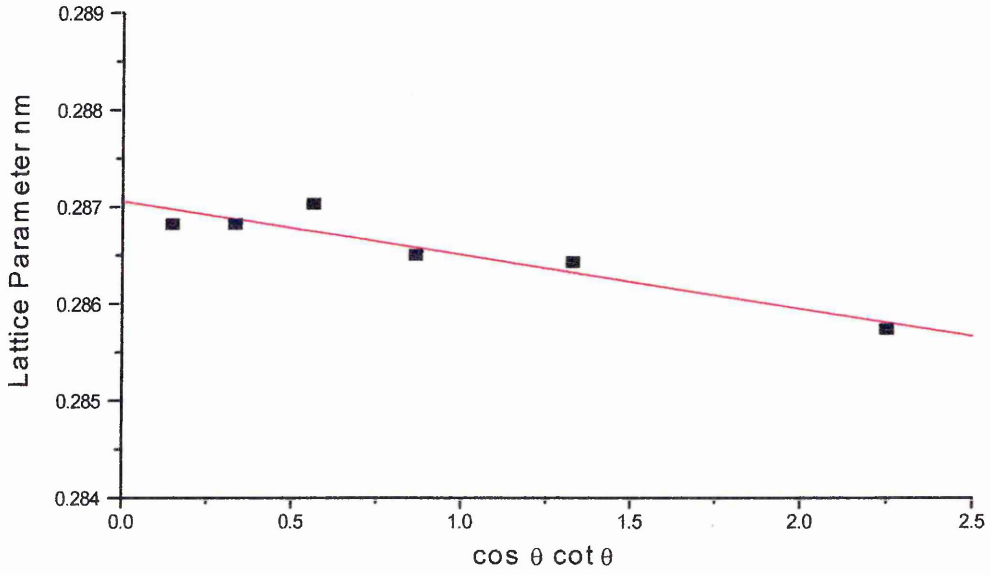

Fig. 4-83: Mild Steel Substrate: Lattice Parameter [nm] Versus cosθ cotθ; Cohen-Wagner Plot for Extrapolation of Lattice Parameter 'a'.

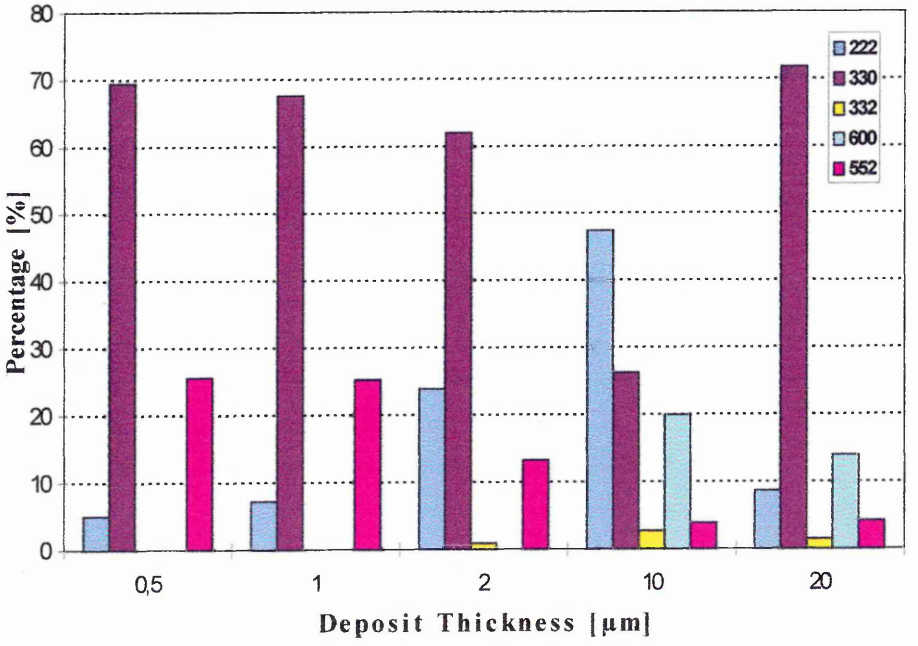

Fig. 4-84: Distribution of Reflections Detected in Nickel-Zinc of Various Thicknesses, Deposited with 10 mA cm^{-2} on Mild Steel Substrates.

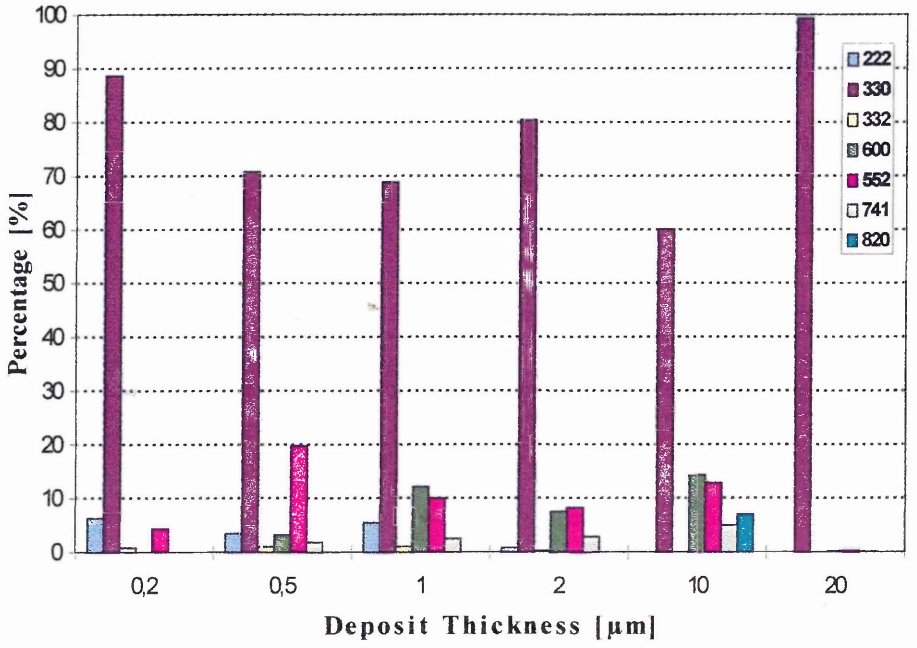

Fig. 4-85: Distribution of Reflections Detected in Nickel-Zinc of Various Thicknesses, Deposited with 60 mA cm^{-2} on Mild Steel Substrates.

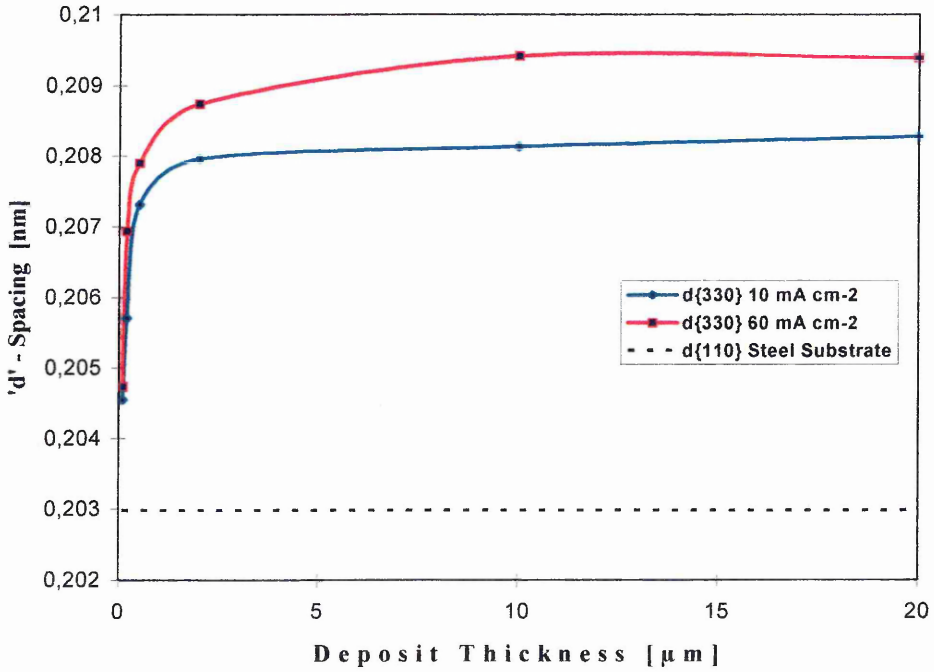

Fig. 4-86: Interplanar {330} d-Spacings of γ-Phase NiZn Deposits Formed at 10 and 60 mA cm^{-2} Versus Deposit Thickness and {110} d-Spacing of Steel Substrate.

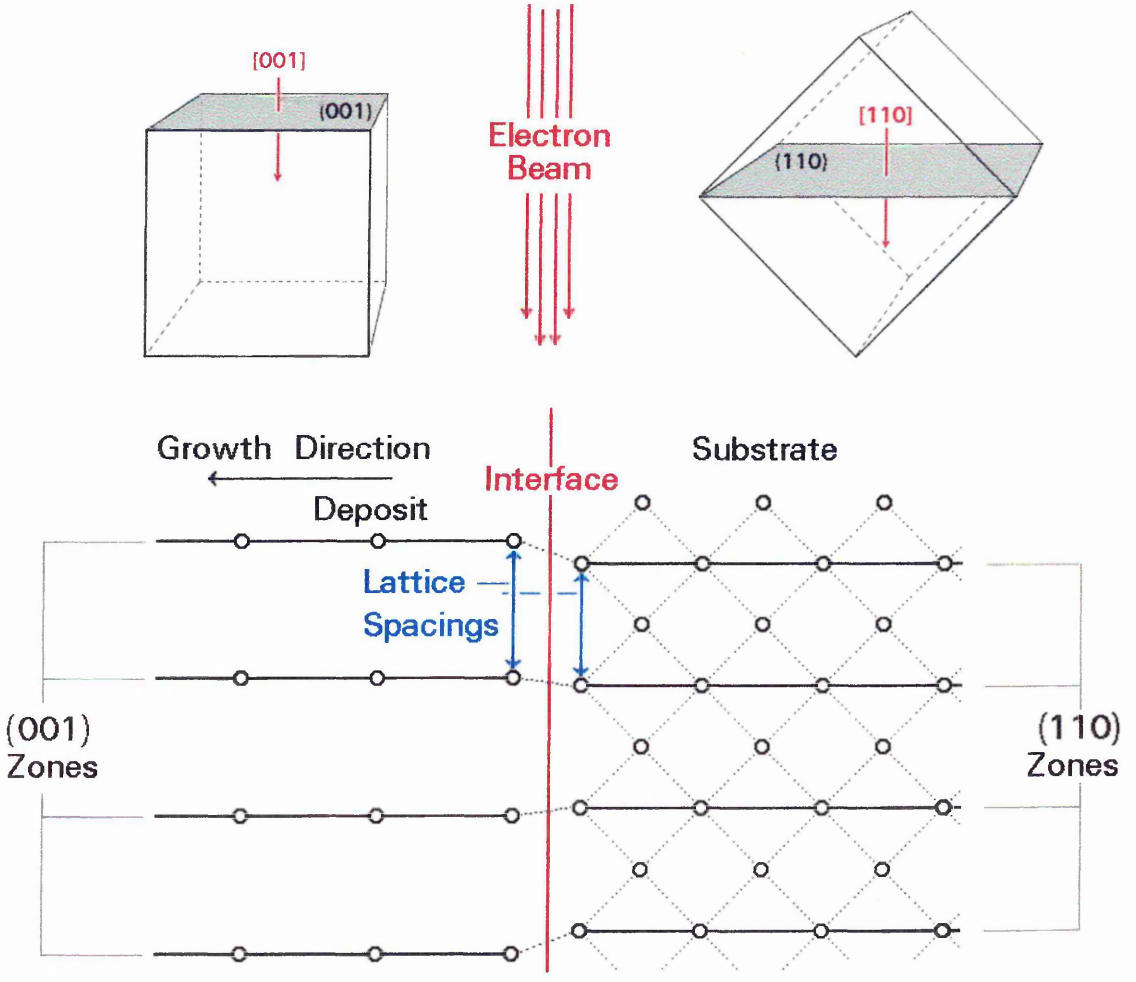

Fig. 5-1: Model of the Electron Beam Interacting with a Cross-Sectioned Specimen, i.e. bcc Nickel-Iron Electrodeposited on a Copper Substrate.

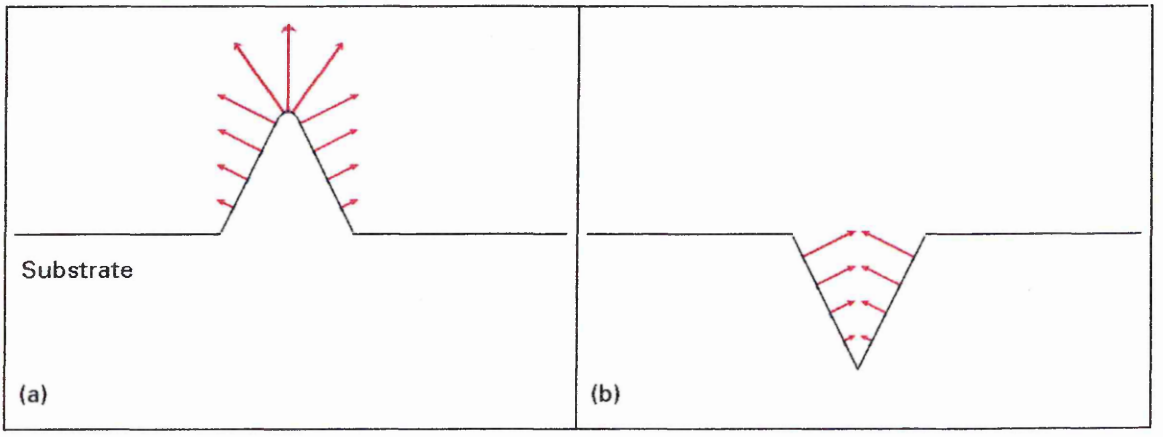

Fig. 5-2: Schematic Representation of Grain Growth (a) at a Protrusion and (b) on a Recessed Area of the Substrate Perpendicular to the Surface.

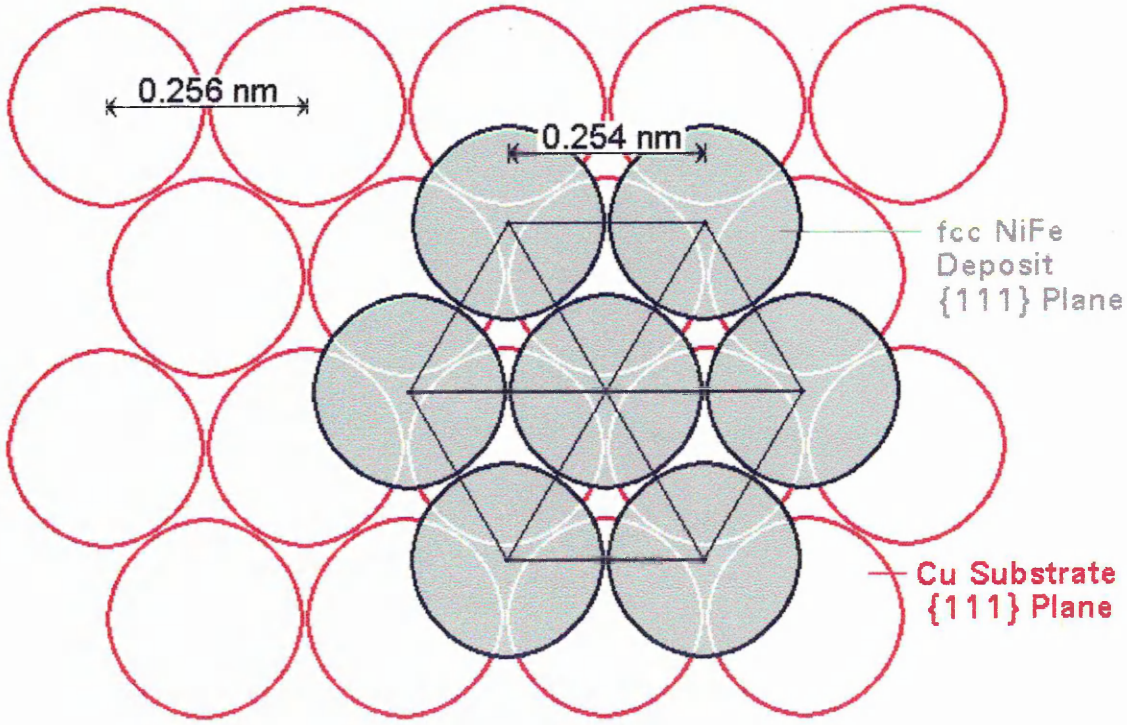

Fig. 5-3: Model of Atoms in {111} Orientated fcc Nickel-Iron Deposit Nucleated onto {111} Textured Copper Substrate (Plan View).

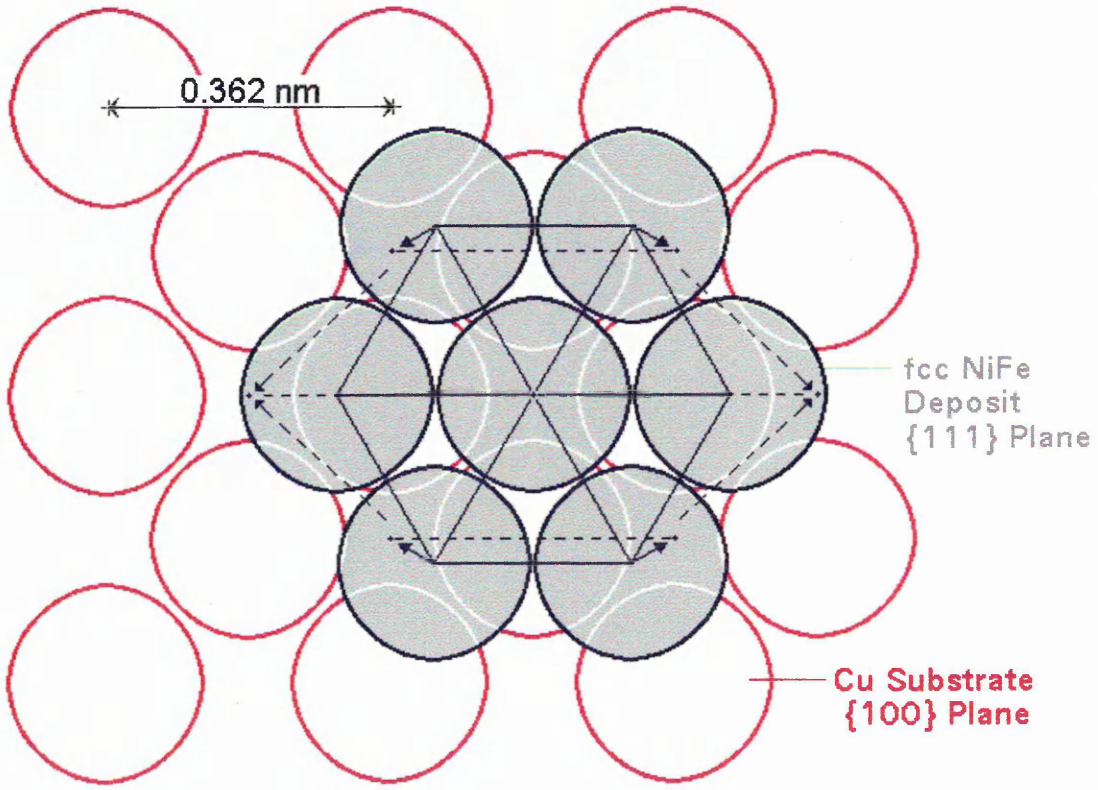

Fig. 5-4: Model of Atoms in {111} Orientated fcc Nickel-Iron Deposit Nucleated onto {100} Textured Copper Substrate (Plan View).

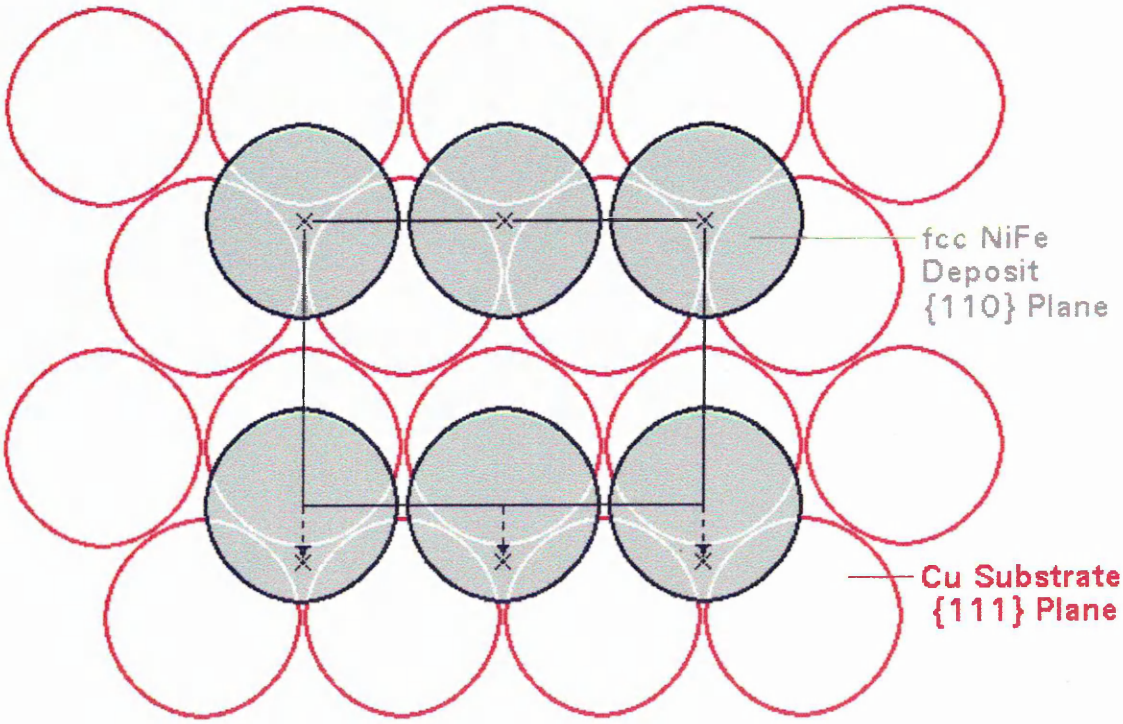

Fig. 5-5: Model of Atoms in {110} Orientated fcc Nickel-Iron Deposit Nucleated onto {111} Textured Copper Substrate (Plan View).

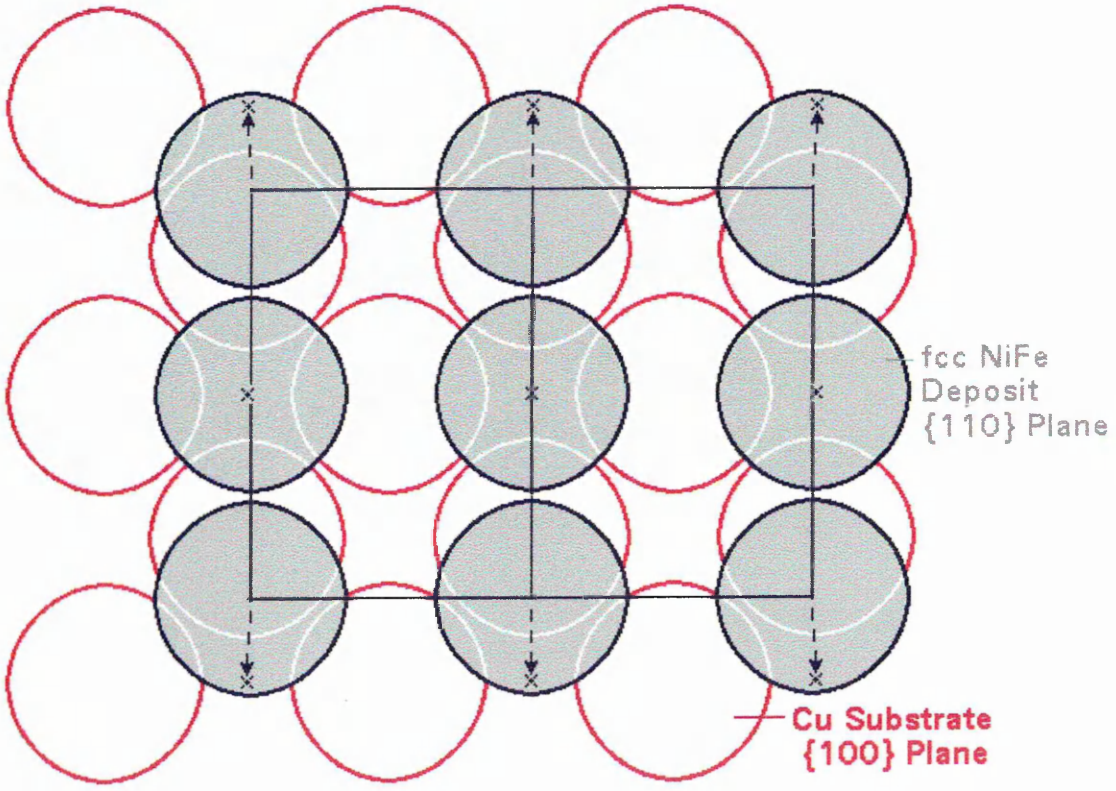

Fig. 5-6: Model of Atoms in {110} Orientated fcc Nickel-Iron Deposit Nucleated onto {100} Textured Copper Substrate (Plan View).

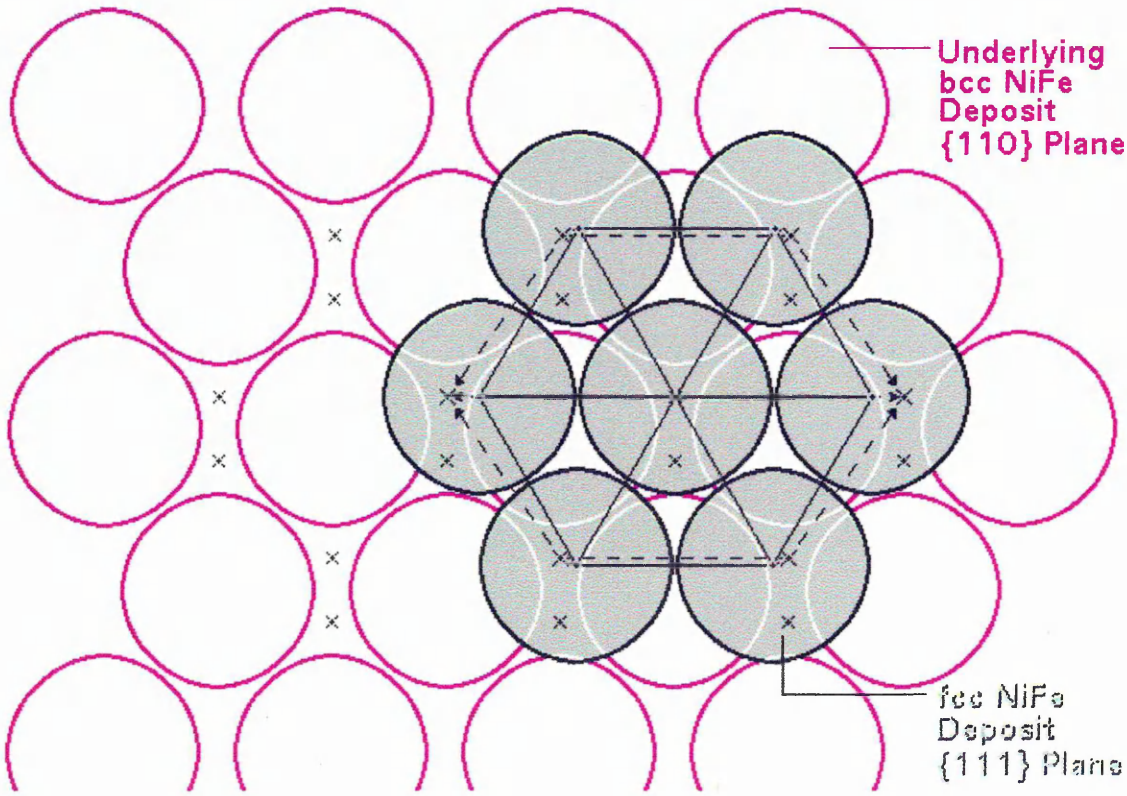

Fig. 5-7: Model of Atoms in {111} Orientated fcc Nickel-Iron Deposit Nucleated onto {110} Textured bcc Structured Nickel-Iron Electrodeposited Substrate (Plan View).

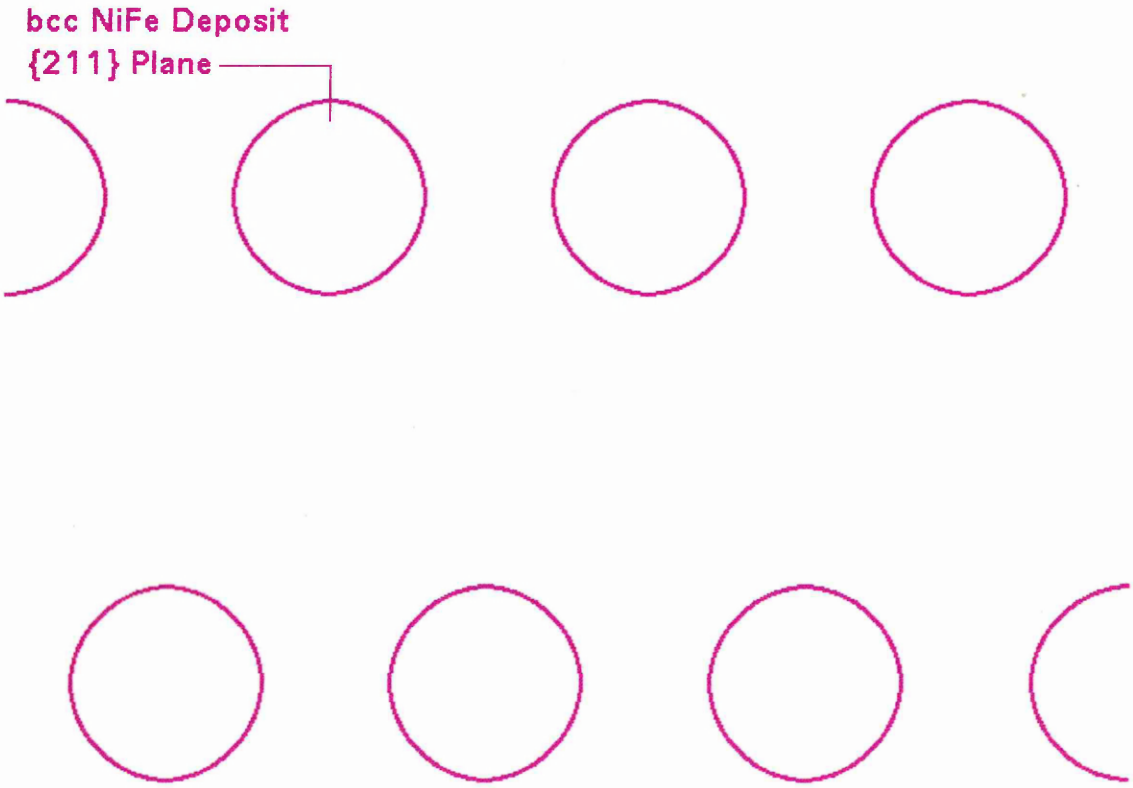

Fig. 5-8a: Model of Atoms in {211} Orientated bcc Nickel-Iron Electrodeposited Substrate (Plan View).

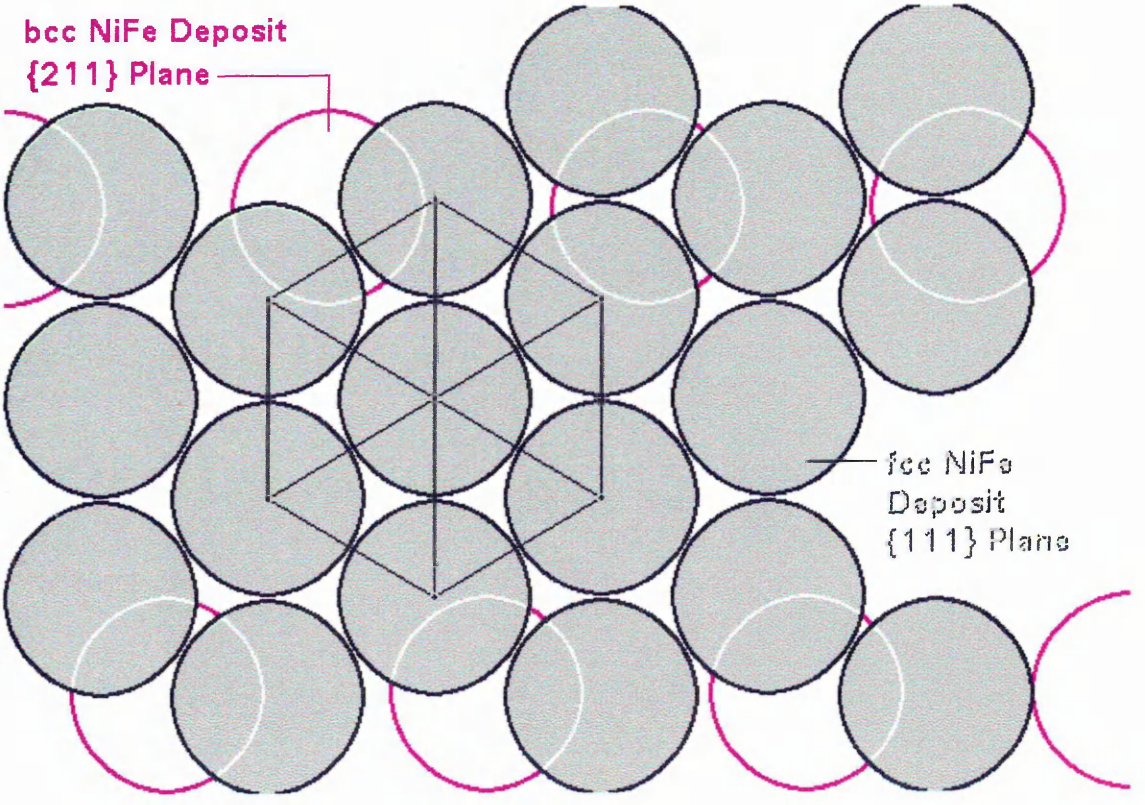

Fig. 5-8b: Model of Atoms in {111} Orientated fcc Nickel-Iron Deposit Nucleated onto {211} Textured bcc Structured Nickel-Iron Electrodeposited Substrate (Plan View).

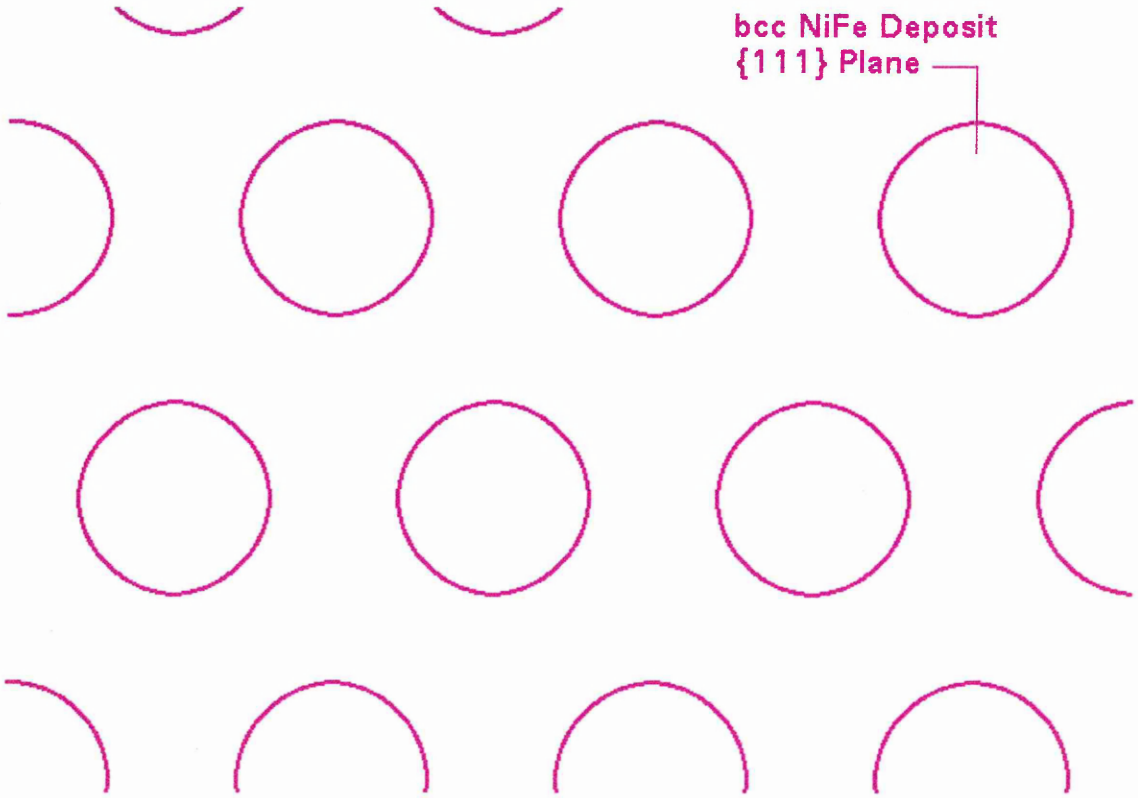

Fig. 5-9a: Model of Atoms in {111} Orientated bcc Nickel-Iron Electrodeposited Substrate (Plan View).

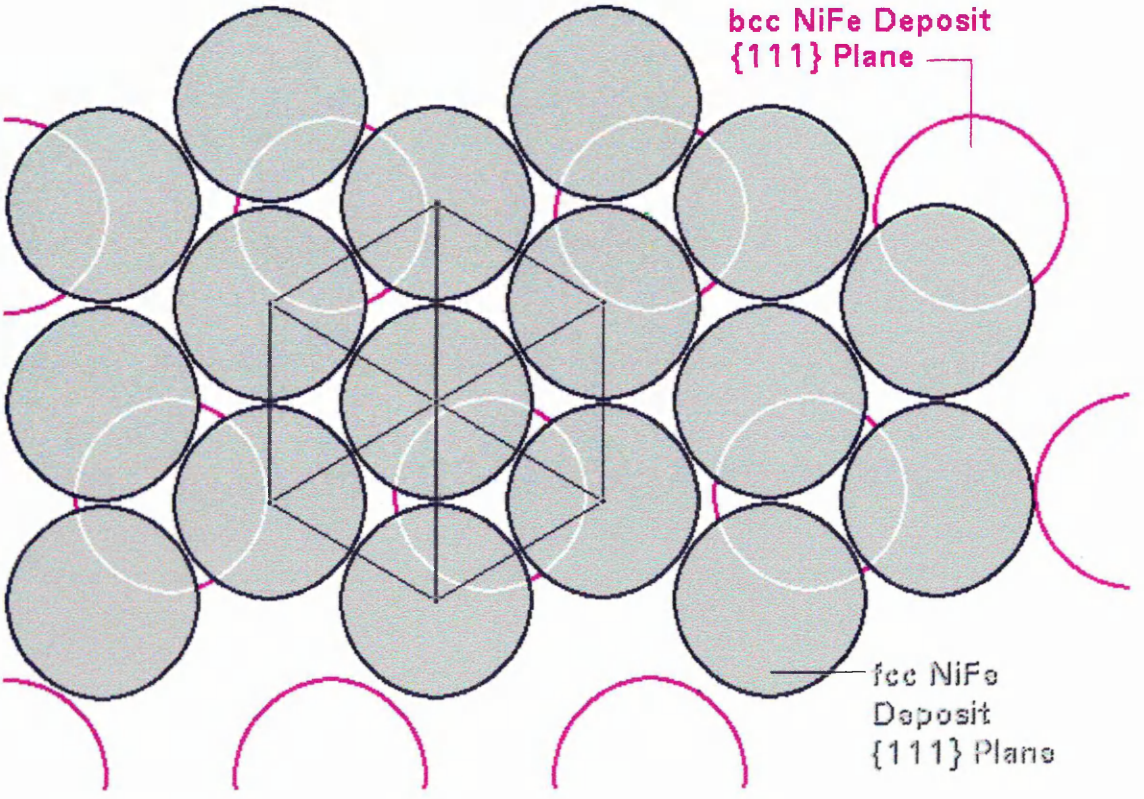

Fig. 5-9b: Model of Atoms in {111} Orientated fcc Nickel-Iron Deposit Nucleated onto {111} Textured bcc Structured Nickel-Iron Electrodeposited Substrate (Plan View).

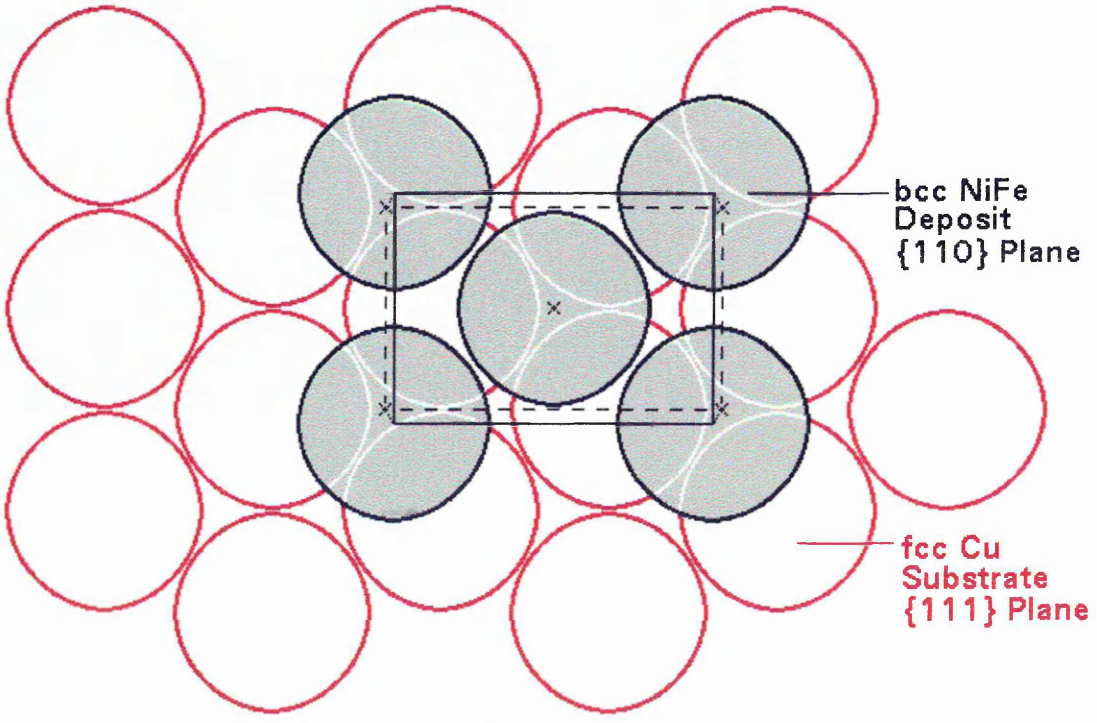

Fig. 5-10: Model of Atoms in {110} Orientated bcc Nickel-Iron Deposit Nucleated onto {111} Textured fcc Copper Substrate (Plan View).

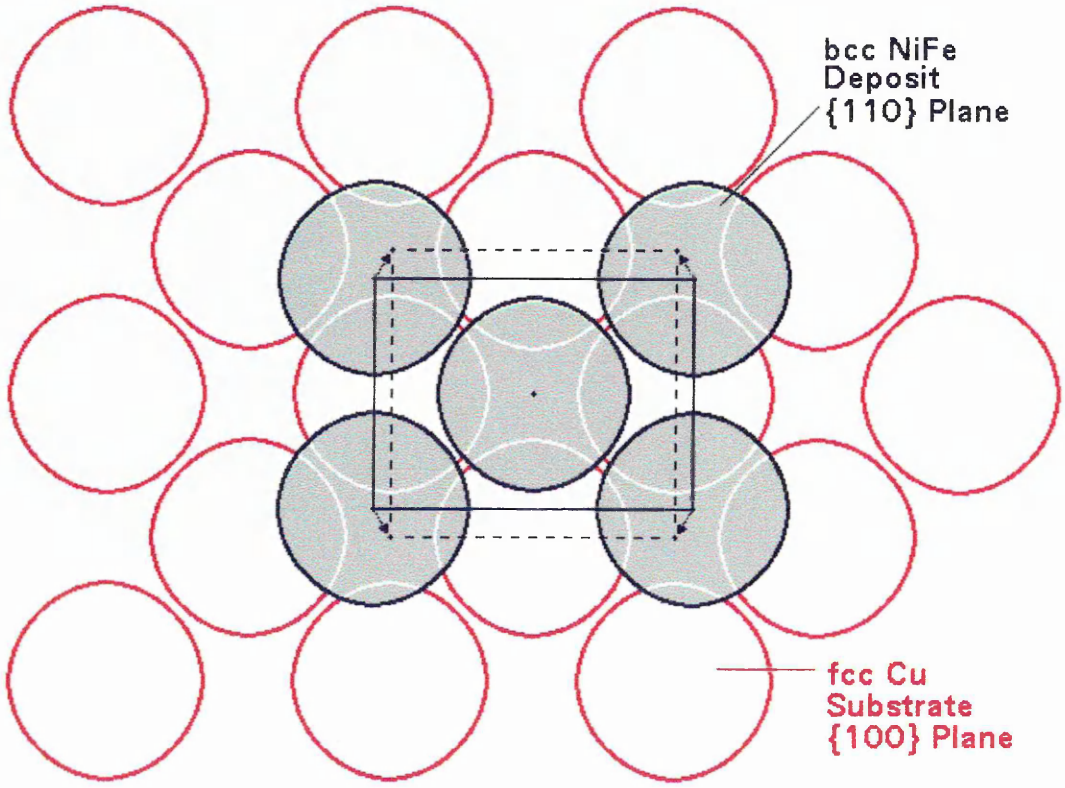

Fig. 5-11: Model of Atoms in {110} Orientated bcc Nickel-Iron Deposit Nucleated onto {100} Textured fcc Copper Substrate (Plan View).

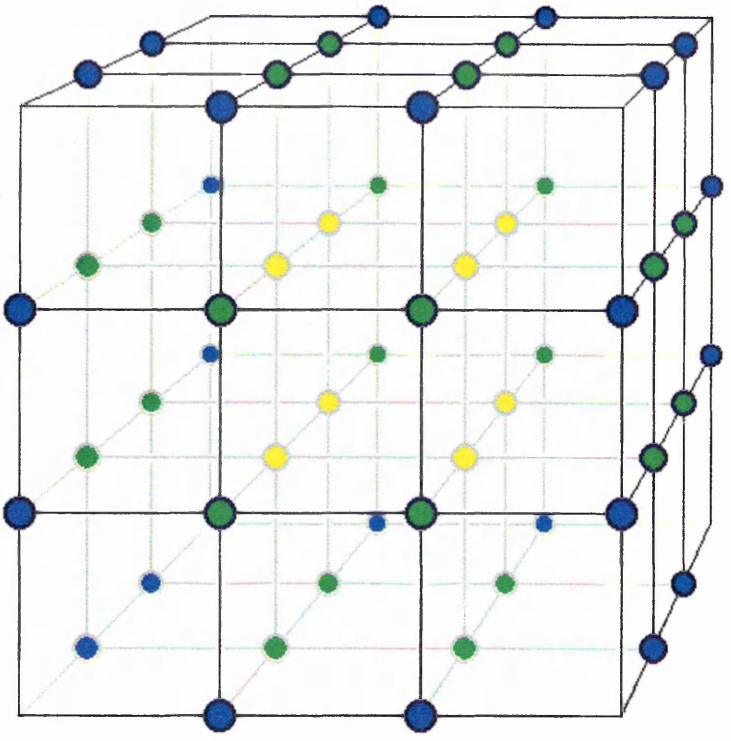

Unit Cell, consisting of 27 Sub Cells, 52 Atoms.

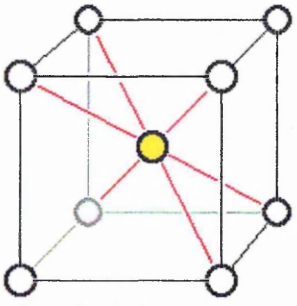

Bcc Sub Cell

● : **Atoms on edges, shared by 4 unit cells.**

$$\frac{24}{4} = 6$$

● : **Atoms on face sides, shared by 2 unit cells.**

$$\frac{24}{2} = 12$$

● : **Atoms inside the unit cell (8 atoms), and accommodated within each sub cell, except the central atom (26 atoms per unit cell), not shared.**

$$8 + 26 = 34$$

Fig. 5-12: Model Depicting the Atomic Arrangement within the Ni_5Zn_{21} Unit Cell, which Consists of 27 Bcc Sub Cells, thus Working out at 52 Atoms per Unit Cell.

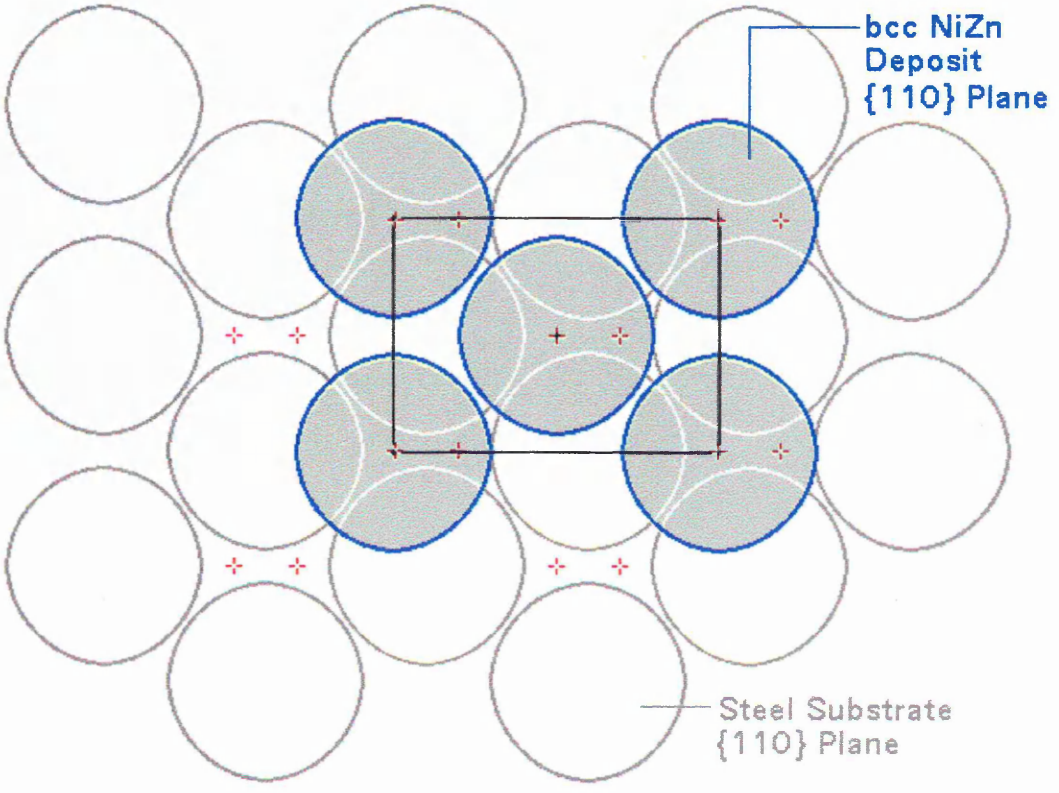

Fig. 5-13: Model of Epitaxial Growth of {110} Orientated bcc γ-Phased Nickel-Zinc Deposit Nucleated onto {110} Textured Steel Substrate (Plan View).

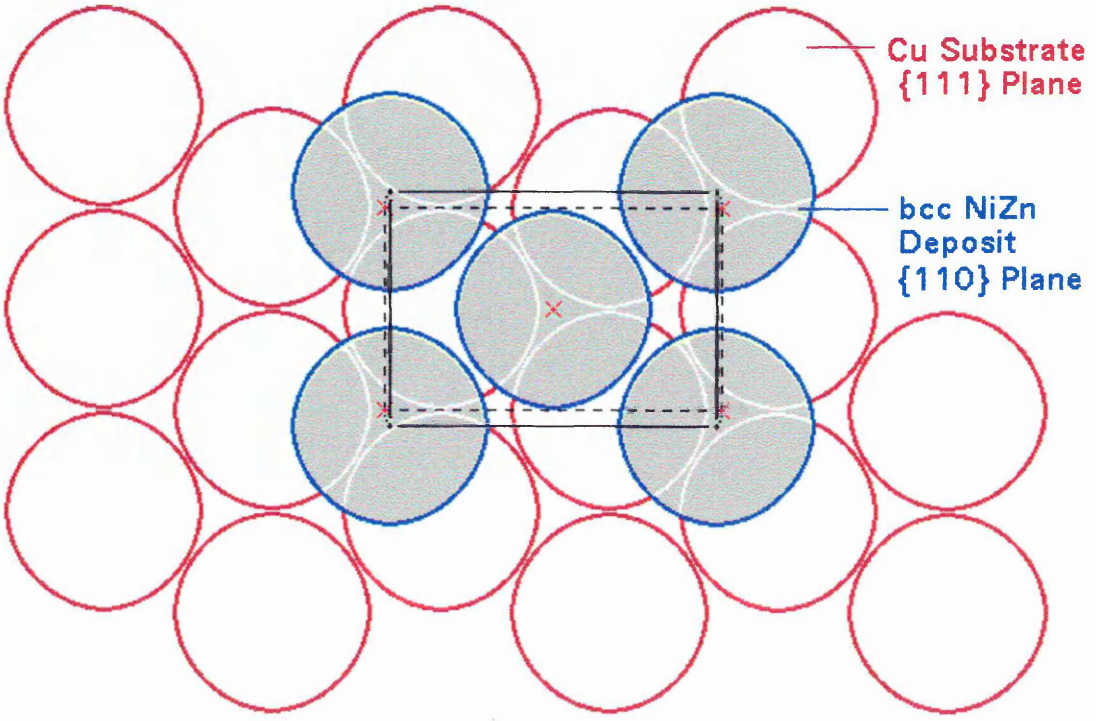

Fig. 5-14: Model of {110} Orientated bcc γ-Phased Nickel-Zinc Deposit Nucleated onto {111} Textured Copper Substrate (Plan View).

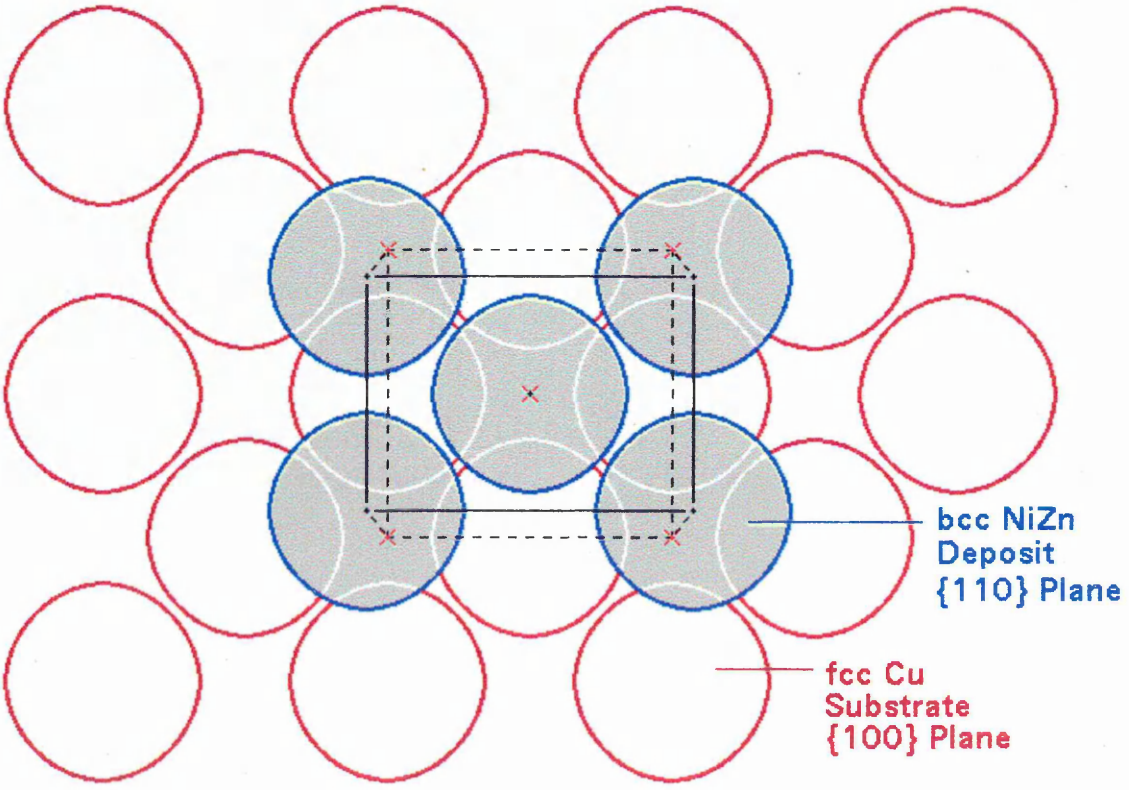

Fig. 5-15: Model of {110} Orientated bcc γ-Phased Nickel-Zinc Deposit Nucleated onto {100} Textured Copper Substrate (Plan View).

Structure of Nickel-Iron and Nickel-Zinc Electrodeposits

Volume II

Claudia Erdmuthe Lehmberg

A thesis submitted in partial fulfilment of the requirements of Sheffield Hallam University for the degree of Doctor of Philosophy

November 1998

8 Tables and Figures

8. 1 Tables

Table 2-1: Comparison of Investigative Techniques Used in Present Work.

	GDOES	XRD	TEM				SEM		
			electron diffraction SADP	imaging mode BF	imaging mode DF	STEM/ EDX	imaging mode SEI	imaging mode BSI	EDX
Parameters									
Excitation	ions	X-rays	e^-	e^-	e^-	e^-	e^-	e^-	e^-
Transmission	*hv* (optical)	X-rays	e^-	e^-	e^-	X-rays	secondary e^-	backscattered e^-	X-rays
Information									
Nucleation and Growth	no	no	cross-section only	cross-section only	cross-section only	cross-section only	no	no	no
Composition	yes	no	no	no	no	yes	no	no	yes
Texture	no	surf. texture	local texture	no	local texture	no	no	no	no
Overall Structure	no	no	no	local	local	no	surf. topography	atomic number contrast	no
Grain Size	no	no	no	yes	yes	no	no	no	no
Dislocation Density	no	no	no	yes	yes	no	no	no	no
Depth Profile									
Composition	yes	no	no	no	no	cross-section only	no	no	cross-section only
Texture	no	yes	cross-section only	no	cross-section only	no	no	no	no
Application	ex situ	ex situ, also in situ [65]	ex situ	ex situ	ex situ	ex situ	ex situ	ex situ	ex situ

Table 2-2: Comparison of Alternative Investigative Techniques not Used in Present Work.

	XRF	AES	STM	Voltammetry
Parameters				
Excitation	X-rays	e^-	voltage	(i) voltage (ii) current
Transmission	fluorescent radiation	e^-	tunnelling e^-	(i) current (ii) voltage
Information				
Nucleation and Growth	no	no	no	indirect
Composition	no	yes	no	no
Texture	no	no	no	no
Overall Structure	no	no	surf. topography	no
Grain Size	no	no	no	no
Dislocation Density	no	no	no	no
Depth Profile	no	no	no	no
Composition	no	no	no	no
Texture	no	no	no	no
Application	ex situ	ex situ	ex situ, also in situ [66, 67, 68].	in situ

Table 3-1: Composition and Working Parameters of Nickel-Iron Electrolytes.

Component		Solution 1 mol l^{-1}	2 mol l^{-1}	3 mol l^{-1}	4 mol l^{-1}
Nickel(II)-sulphate	$NiSO_4*6H_2O$	0.81	0.45	0.69	0.69
Nickel(II)-chloride	$NiCl_2*6H_2O$	0.21	0.21	0.21	0.21
Boric acid	H_3BO_3	0.48	0.48	0.48	0.48
Ferrous(II)-sulphate	$FeSO_4*7H_2O$	0.1	0.47	0.29	0.29
Citric acid	$C_3H_4(OH)(COOH)_3*H_2O$	0.003	0.003	0.003	0.003
Sodium lauryl sulphate	$NaC_{12}H_{25}SO_4$	-	0.002	0.002	-
Saccharine	$C_6H_4CONHSO_2$	-	-	0.003	0.003
Ascorbic acid	$C_6H_8O_6$	-	-	0.003	0.003

Working Condition	Solution 1	2	3	4
agitation	N_2-agitation 1. uncontrolled 2. 1 l min^{-1} 3. 3 l min^{-1} 4. 6 l min^{-1}	magnetic stirrer on hot plate; speed 7	submersible magnetic stirrer in water bath: speed: 7; reverse mode: 10	N_2-agitation: 1 l min^{-1}

Table 3-2: Composition and Working Parameters of Nickel-Zinc Electrolytes.

Component		Solution							
		1	2	3	4	5	6	7	8
		mol l^{-1}	mol l^{-1}	mol l^{-1}	mol l^{-1}	mol l^{-1}	mol l^{-1}	mol l^{-1}	mol l^{-1}
Nickel(II)-sulphate	$NiSO_4*6H_2O$	0.57	0.57	0.57	0.57	0.57	0.57	1.11	1.2
Zinc(II)-sulphate	$ZnSO_4*7H_2O$	0.7	0.7	0.7	0.7	0.7	0.7	0.16	0.07
Boric acid	H_3BO_3	0.32	0.32	0.32	0.64	0.64	0.64	0.32	0.32
p-toluene sulfonic acid	$C_7H_8O_3S*H_2O$	0.01	0.01	-	-	0.01	0.01	0.01	0.01
Sodium lauryl sulphate	$NaC_{12}H_{25}SO_4$	-	0.002	-	-	-	0.002	-	-

Working	Solution							
Condition	1	2	3	4	5	6	7	8
Anodes	nickel	nickel	nickel	nickel	nickel	nickel	inert	inert
pH	3 (*/**)	3 (**)	3 (**)	~2 (***)	~2 (***)	~2 (***)	3 (**)	3 (**)
Volume	500 ml	500 ml	500 ml	500 ml	500 ml	500 ml	1500 ml	1500 ml
Agitation	a); b)	a); b)	a)	a); b)	a); b)	a)	b)	b)

*pH-value adjusted with ammonia solution
**pH-value adjusted with sodium hydroxide solution
***no pH-value adjusted; solution had ~2
agitation: a) submersible magnetic stirrer: speed 5, reverse mode 5
b) agitated with nitrogen gas; 1.5 l min^{-1}

Table 3-3: Description of Degreasing Agent for Copper and Brass.

Trade name	*KLEENAX*
Manufacturer	Canning (Birmingham, UK)
Remarks	Contains cyanide
Concentration	125 g l^{-1}
Operating parameters	i_c: 30 mA cm^{-2} *T*: 40 °C *t*: 1 - 2 min

Table 3-4: Description of Degreasing Agent for Steel.

Trade name	*Activax*
Manufacturer	Canning (Birmingham, UK)
Remarks	Cyanide-free
Concentration	50 g l^{-1}
Operating parameters	i_a: 30 mA cm^{-2} *T*: 70 °C *t*: 30 s

Table 3-5: Description of Activating Agent.

Trade name	*Activator No. 2*
Manufacturer	Lea Ronal (Buxton, UK)
Concentration	50 g l^{-1}
Operating parameters	*T*: room temperature *t*: 1 min

Table 3-6: Composition and Operating Parameters of the Cyanide Copper Electrolyte.

Constituents	Concentration [g l^{-1}]
CuCN	40
KCN	66
K_2CO_3	39
$NaKC_4H_4O_6$	60

T	40-60 °C
Anodes	Electrolytic Copper
Anode:Cathode	1:2
i_c	10 mA cm^{-2}

Table 3-7: Composition and Operating Parameters of the Acid Copper Electrolyte.

Constituents	Concentration [g l^{-1}]
$CuSO_4 \cdot 5H_2O$	200
H_2SO_4	50

T	40 °C
Anodes	Electrolytic Copper
Anode:Cathode	1:2
i_c	100 mA cm^{-2}

Table 3-8: *K* Emission Lines (Weighted Mean) [89] and Mass Absorption Coefficients K_{edge} [90].

Element	Atomic Number	K_α [nm]	K_β [nm]	K_{edge} [nm]
Cobalt	27	0.179026	0.162080	0.1608
Nickel	28	...	...	0.1488
Copper	29	0.154186	0.139222	0.1380
Molybdenum	42	0.071073	0.063229	0.061977

Table 3-9: Steps of Angular Ranges to Diffract Planes of fcc Nickel-Iron.

Angular range °2θ	Reflection
41.4 - 46.5	{111}
49 - 53	{200}
72 - 78	{220}
87 - 93	{311}
132 - 149	{331}

Table 3-10: Steps of Angular Ranges to Diffract Planes of bcc Nickel-Iron.

Angular range 2θ	Reflection
41.4 - 46.5	{110}
62 - 68	{200}
79 - 85	{211}
112 - 120	{310}
132 - 149	{222}

Table 4-1: Composition and Visual Evaluation of Quiescent Nickel-Iron Solution 1 Employing 1A Cell Current.

current density [mA cm^{-2}]	composition		observation
	mass-% Ni	mass-% Fe	deposit appearance
4	73.1	26.9	dull; dark, brownish-grey; no pitting
10	69.7	30.3	dull; brownish-grey; slightly pitted
15	71.1	28.9	dull; brownish-grey; slightly pitted
20	71.0	29.0	dull; brownish-grey; pitted
30	76.3	23.7	dull; brownish-grey; pitted
40	78.3	21.7	dull; brownish-grey; pitted
50	83.1	16.9	dull; brownish-grey; pitted

Table 4-2: Composition and Visual Evaluation of Quiescent Nickel-Iron Solution 1 Employing 3A Cell Current.

current density [mA cm^{-2}]	composition		observation
	mass-% Ni	mass-% Fe	deposit appearance
12	71.6	28.4	dull; brownish-grey; slightly pitted
30	76.3	23.7	dull; brownish-grey; slightly pitted
60	81.6	18.4	dull; brownish-grey; slightly pitted
90	84.2	15.8	dull; brownish-grey; slightly pitted
150	87.1	12.9	dull; brownish-grey; pitted

Table 4-3: Composition and Visual Evaluation of Quiescent Nickel-Iron Solution 1 Employing 7A Cell Current.

current density [mA cm^{-2}]	composition		observation
	mass-% Ni	mass-% Fe	deposit appearance
52.5	83.6	16.4	dull; brownish-grey; slightly pitted
140	88.5	11.5	dull; brownish-grey; slightly pitted
210	87.7	12.3	dull; brownish-grey; pitted
350	90.2	9.8	dull; brownish-grey; pitted

Table 4-4: Composition and Visual Evaluation of Nitrogen Agitated Nickel-Iron Solution 1 Employing 1A Cell Current.

current density [mA cm^{-2}]	composition mass-% Ni	mass-% Fe	observation deposit appearance
4	67.7	30.3	dull; yellowish-grey; no pitting
10	64.5	35.5	dull; yellowish-grey; no pitting
15	64.6	35.4	dull; yellowish-grey; slightly pitted
20	65.4	34.6	dull; yellowish-grey; pitted
30	61.4	38.6	dull; yellowish-grey; pitted
40	57.5	42.5	dull; yellowish-grey; pitted
50	59.1	40.9	dull; brownish-grey; pitted

Table 4-5: Composition and Visual Evaluation of Nitrogen Agitated Nickel-Iron Solution 1 Employing 3A Cell Current.

current density [mA cm^{-2}]	composition mass-% Ni	mass-% Fe	observation deposit appearance
15	60.3	39.7	dull; yellowish-grey; slightly pitted
30	56.7	43.3	dull; yellowish-grey; slightly pitted
60	53.9	46.1	dull; grey; slightly pitted
90	56.6	43.4	dull; grey; slightly pitted
150	58.6	41.4	dull; grey; slightly pitted

Table 4-6: Composition and Visual Evaluation of Nitrogen Agitated Nickel-Iron Solution 1 Employing 7A Cell Current.

current density [mA cm^{-2}]	composition mass-% Ni	mass-% Fe	observation deposit appearance
52.5	65.7	34.3	dull; yellowish-grey; slightly pitted
140	62.8	37.2	dull; grey; slightly pitted
210	64.8	35.2	dull; grey; slightly pitted
350	71.9	28.1	dull; grey; slightly pitted

Table 4-7: Composition and Visual Evaluation of Quiescent Nickel-Iron Solution 4 Employing 1A Cell Current.

current density [mA cm^{-2}]	composition mass-% Ni	mass-% Fe	observation deposit appearance
4	53.2	46.8	shiny; silverish-grey; smooth
5	51.5	48.5	shiny; silverish-grey; smooth
7.5	48.1	51.9	shiny; silverish-grey; smooth
10	45.8	54.2	shiny; silverish-grey; smooth
12.5	45.8	54.2	shiny; silverish-grey; smooth
15	45.3	54.7	shiny; silverish-grey; smooth
20	45.8	54.2	shiny; silverish-grey; smooth
30	47.3	52.7	shiny; silverish-grey; slightly pitted
40	50.9	49.1	shiny; silverish-grey; slightly pitted
50	53.5	46.5	slightly dull; silverish-grey; slightly pitted

Table 4-8: Composition and Visual Evaluation of Quiescent Nickel-Iron Solution 4 Employing 3A Cell Current.

current density [mA cm^{-2}]	composition mass-% Ni	mass-% Fe	observation deposit appearance
12	49.9	50.1	shiny; silverish-grey; smooth
15	49.2	50.8	shiny; silverish-grey; smooth
22.5	48.6	51.4	shiny; silverish-grey; smooth
30	51.8	48.2	shiny; silverish-grey; slightly pitted
37.5	51.4	48.6	shiny; silverish-grey; slightly pitted
45	53.8	46.2	shiny; silverish-grey; slightly pitted
60	55.9	44.1	dull; silverish-grey; slightly pitted
90	60.6	39.4	dull; silverish-grey; slightly pitted
120	64.2	35.8	dull; silverish-grey; slightly pitted
150	68.3	31.7	dull; silverish-grey; slightly pitted

Table 4-9: Composition and Visual Evaluation of Quiescent Nickel-Iron Solution 4 Employing 7A Cell Current.

current density [mA cm^{-2}]	composition		observation
	mass-% Ni	mass-% Fe	deposit appearance
28	54.1	45.9	shiny; silverish-grey; smooth
35	54.4	45.6	shiny; silverish-grey; smooth
52.5	58.9	41.1	shiny; silverish-grey; smooth
70	61.4	38.6	dull; silverish-grey; slightly pitted
87.5	64.4	35.6	dull; silverish-grey; slightly pitted
105	66.1	33.9	dull; silverish-grey; slightly pitted
140	68.9	31.1	dull; silverish-grey; slightly pitted
210	70.8	29.3	dull; silverish-grey; slightly pitted
280	61.1	38.9	burnt; non-adherent deposit
350	57.6	42.4	burnt; non-adherent deposit

Table 4-10: Composition and Visual Evaluation of Nitrogen Agitated Nickel-Iron Solution 4 Employing 1A Cell Current.

current density [mA cm^{-2}]	composition		observation
	mass-% Ni	mass-% Fe	deposit appearance
4	55.0	45.0	shiny; silverish-grey; smooth
5	52.6	47.4	shiny; silverish-grey; smooth
7.5	47.8	52.2	shiny; silverish-grey; smooth
10	45.4	54.6	shiny; silverish-grey; smooth
12.5	43.1	56.9	shiny; silverish-grey; smooth
15	39.8	60.2	shiny; silverish-grey; smooth
20	36.5	63.5	shiny; silverish-grey; smooth
30	35.1	64.9	shiny; silverish-grey; smooth
40	34.0	66.0	shiny; silverish-grey; smooth
50	32.5	67.5	shiny; silverish-grey; smooth

Table 4-11: Composition and Visual Evaluation of Nitrogen Agitated Nickel-Iron Solution 4 Employing 3A Cell Current.

current density [mA cm^{-2}]	composition		observation
	mass-% Ni	mass-% Fe	deposit appearance
12	43.3	56.7	shiny; silverish-grey; smooth
15	41.9	58.1	shiny; silverish-grey; smooth
22.5	39.3	60.7	shiny; silverish-grey; smooth
30	36.5	63.5	shiny; silverish-grey; smooth
37.5	36.0	64.0	shiny; silverish-grey; smooth
45	35.0	65.0	shiny; silverish-grey; smooth
60	34.1	65.9	shiny; silverish-grey; smooth
90	34.0	66.0	shiny; silverish-grey; smooth
120	34.0	66.0	shiny; silverish-grey; fine cracks
150	33.4	66.6	shiny; silverish-grey; pitted, fine cracks

Table 4-12: Composition and Visual Evaluation of Nitrogen Agitated Nickel-Iron Solution 4 Employing 7A Cell Current.

current density [mA cm^{-2}]	composition		observation
	mass-% Ni	mass-% Fe	deposit appearance
28	48.1	51.9	shiny; silverish-grey; smooth
35	46.9	53.1	shiny; silverish-grey; smooth
52.5	46.5	53.5	shiny; silverish-grey; smooth
70	43.5	56.5	shiny; silverish-grey; smooth
87.5	43.9	56.1	shiny; silverish-grey; smooth
105	39.1	60.9	shiny; silverish-grey; smooth
140	40.7	59.3	shiny; silverish-grey; pitted, fine cracks
210	44.6	55.4	less shiny; silverish-grey; pitted, fine cracks
280	40.4	59.6	less shiny; silverish-grey; pitted, fine cracks
350	41.0	59.1	less shiny; silverish-grey; pitted, fine cracks

Table 4-13: Composition and Visual Evaluation of Nitrogen Agitated Nickel-Zinc Solution 7 Employing 1A Cell Current.

current density [mA cm^{-2}]	composition		observation
	mass-% Ni	mass-% Zn	deposit appearance
5	38.8	61.2	shiny; brownish-grey
10	29.5	70.5	dull; brownish-grey
20	19.4	80.6	dull; yellowish-grey
30	19.0	81.0	shiny; silverish-grey
40	18.9	81.1	shiny; silverish-grey
50	19.8	80.2	shiny; silverish-grey

Table 4-14: Composition and Visual Evaluation of Quiescent Nickel-Zinc Solution 8 Employing 1A Cell Current.

current density [mA cm^{-2}]	composition mass-% Ni	mass-% Zn	observation deposit appearance
4	64.2	35.8	shiny; brownish-grey
5	54.0	46.0	shiny; brownish-grey
15	37.5	62.5	dull; silver-grey
20	35.7	64.3	dull; silver-grey
30	34.4	65.6	dull; silverish-grey
50	41.3	58.7	dull; silverish-grey

Table 4-15: Composition and Visual Evaluation of Quiescent Nickel-Zinc Solution 8 Employing 3A Cell Current.

current density [mA cm^{-2}]	composition mass-% Ni	mass-% Zn	observation deposit appearance
12	88.2	11.8	dull; brownish-grey, silver-grey patches
15	56.1	43.9	dull; brownish-grey, silver-grey patches
30	63.3	36.7	dull; brownish-grey, silver-grey patches
60	74.5	25.5	dull; brownish-grey, silver-grey patches
120	81.2	18.8	burnt, black powdery deposit
150	95.4	4.6	burnt, black powdery deposit

Table 4-16: Composition and Visual Evaluation of Quiescent Nickel-Zinc Solution 8 Employing 5A Cell Current.

current density [mA cm^{-2}]	composition mass-% Ni	mass-% Zn	observation deposit appearance
20	71.7	28.3	dull; brownish-grey
25	86.8	13.2	dull; brownish-grey
50	89.4	10.6	dull, brownish-grey; deposit cracked
75	87.3	12.7	dull; brownish-grey; deposit cracked
100	93.1	6.9	dull; brownish-grey; deposit cracked
150	86.3	13.7	burnt, black powdery deposit
200	78.1	21.9	burnt, black powdery deposit
250	84.3	15.7	burnt, black powdery deposit

Table 4-17: Composition and Visual Evaluation of Nitrogen Agitated Nickel-Zinc Solution 8 Employing 1A Cell Current.

current density [mA cm^{-2}]	composition		observation
	mass-% Ni	mass-% Zn	deposit appearance
4	63.0	36.9	shiny; brownish-grey
5	60.7	39.3	shiny; brownish-grey
15	45.9	54.1	shiny; brownish-grey
20	32.1	67.9	slightly dull; silverish-grey
30	26.4	73.6	dull; silverish-grey
40	25.9	74.1	dull; silverish-grey
50	44.9	55.1	dull; silverish-grey

Table 4-18: Composition and Visual Evaluation of Nitrogen Agitated Nickel-Zinc Solution 8 Employing 3A Cell Current.

current density [mA cm^{-2}]	composition		observation
	mass-% Ni	mass-% Zn	deposit appearance
12	32.3	67.7	shiny; silverish-grey
15	30.4	69.6	shiny; silverish-grey
30	41.0	59.0	dull; silverish-grey
45	58.4	41.6	dull; silverish-grey
60	64.8	35.2	dull; silverish-grey
120	71.7	28.3	dull; silverish-grey
150	77.7	22.3	burnt, black, powdery deposit

Table 4-19: Composition and Visual Evaluation of Nitrogen Agitated Nickel-Zinc Solution 8 Employing 5A Cell Current.

current density [mA cm^{-2}]	composition		observation
	mass-% Ni	mass-% Zn	deposit appearance
20	89.1	10.9	dull; brownish-grey with silver patches
25	89.1	10.9	dull; brownish-grey with silver patches
62.5	72.3	27.7	dull; silverish-grey
75	70.8	29.2	dull; silverish-grey
100	72.3	27.7	dull; silverish-grey
150	95.8	4.2	burnt, black, powdery deposit
200	95.5	4.5	burnt, black, powdery deposit
250	97.4	2.6	burnt, black, powdery deposit

Table 4-20: Elemental Compositions Determined by EDX and GDOES of Deposits Produced in Nickel-Iron Solution 1 at Individual Current Densities.

Current Density [mA cm^{-2}]	Composition (**EDX**)		Composition (**GDOES**)	
	mass-% Ni	mass-% Fe	mass-% Ni	mass-% Fe
10	66.5	33.5	68.1	31.9
20	62.2	37.8	65.7	34.3
30	60.8	39.2	64.5	35.5
40	60.2	39.8	62.3	37.7
60	60.7	39.3	59.7	40.3

Table 4-21: Elemental Compositions Determined by GDOES of Deposits Produced in Nickel-Iron Solution 3 at Individual Current Densities.

Current Density [mA cm^{-2}]	Composition (**GDOES**)	
	mass-% Ni	mass-% Fe
10	61.3	38.7
20	57.5	42.5
30	56.0	44.0
40	35.5	64.5
60	36.5	63.5

Table 4-22: Elemental Compositions Determined by GDOES of Deposits Produced in Nickel-Iron Solution 4 at Individual Current Densities.

Current Density [mA cm^{-2}]	Composition (**GDOES**)	
	mass-% Ni	mass-% Fe
10	41.4	58.6
20	33.2	66.8
30	32.9	67.1
40	31.6	68.4
60	30.3	69.7

Table 4-23: Elemental Compositions Determined by GDOES at Various Areas of Deposits Produced in Nickel-Zinc Solution 8 at Individual Current Densities.

Current Density [mA cm^{-2}]	Area on Sample (see fig. 4-5)	Composition	
		mass-% Ni	mass-% Zn
10	1	45.8	54.2
10	2	37.0	63.0
10	3	29.5	70.5
20	1	27.5	72.5
20	2	29.2	70.8
20	3	24.0	76.0
30	1	30.0	70.0
30	2	28.6	71.4
30	3	25.2	74.8
40	1	24.9	75.1
40	2	23.6	76.4
40	3	33.7	66.3
50	1	52.4	47.6
50	2	44.6	45.4
50	3	37.9	62.1
60	1	34.2	65.8
60	2	36.9	63.1
60	3	38.0	62.0

Table 4-24: Raw Data $R_{\{hkl\}}$, $I_{\{hkl\}}$ and Planar Distribution in per cent of the Copper Sheet Substrate.

	Planes: Copper Sheet Substrate									
	111		**200**		**220**		**311**		**331**	
Raw Data	$R_{\{hkl\}}$	$I_{\{hkl\}}$	$R_{\{hkl\}}$	$I_{\{hkl\}}$	$R_{\{hkl\}}$	$I_{\{hkl\}}$	$R_{\{hkl\}}$	$I_{\{hkl\}}$	$R_{\{hkl\}}$	$I_{\{hkl\}}$
	245.3	1335	112.9	2083	59.5	396	65.4	352	48.7	449
%	12.1		40.9		14.7		11.9		20.4	

Table 4-25: Raw Data: Measured 2θ Bragg Angles. Calculated Interplanar Spacings 'd' and Lattice Parameter 'a' of Copper Sheet Substrate.

	Reflections						
Copper	**111**	**200**	**220**	**311**	**222**	**400**	**331**
°2θ	43.3	50.4	74.1	89.9	95.1	116.9	136.4
d [nm]	0.20874	0.18091	0.12786	0.10905	0.10437	0.09041	0.08296
a [nm]	0.36155	0.36182	0.36164	0.36169	0.36154	0.36164	0.36160

Table 4-26: Raw Data $R_{\{hkl\}}$ and $I_{\{hkl\}}$ of fcc NiFe Electrodeposits on Copper Sheet Substrates Deposited in NiFe Solution 1.

Current	***Planes***							
Density	**111**		**200**		**220**		**311**	
[mA cm^{-2}]	$R_{\{hkl\}}$	$I_{\{hkl\}}$	$R_{\{hkl\}}$	$I_{\{hkl\}}$	$R_{\{hkl\}}$	$I_{\{hkl\}}$	$R_{\{hkl\}}$	$I_{\{hkl\}}$
10	89.9	1468	41.0	479	21.5	356	24.0	342
30	83.7	1742	38.0	305	20.1	184	22.4	553
60	76.7	1807	34.8	276	18.4	118	20.5	541

Table 4-27: Planar Distribution in per cent of fcc NiFe Electrodeposits on Copper Sheet Substrates Deposited in NiFe Solution 1.

i	*Planes Distribution in per cent*			
[mA cm^{-2}]	**111**	**200**	**220**	**311**
10	27.8	19.9	28.1	24.2
30	33.2	12.8	14.6	39.4
60	36.6	12.4	9.9	41.1

Table 4-28: Raw Data: Measured 2θ Bragg Angles of fcc NiFe Electrodeposits on Copper Sheet Substrates Deposited in NiFe Solution 1.

i	*Reflections:* 2θ° Bragg Angles			
[mA cm^{-2}]	**111**	**200**	**220**	**311**
10	44.04	51.32	75.55	91.81
30	43.97	51.32	75.44	91.78
60	43.85	51.22	75.31	91.60

Table 4-29: Calculated d-Spacings of fcc NiFe Electrodeposits on Copper Sheet Substrates Deposited in NiFe Solution 1.

i	*Reflections:* Calculated d-Spacings [nm]			
[mA cm^{-2}]	**111**	**200**	**220**	**311**
10	0.20543	0.17789	0.12575	0.10726
30	0.20578	0.17789	0.12591	0.10728
60	0.20628	0.17821	0.12609	0.10745

Table 4-30: Raw Data $R_{\{hkl\}}$ and $I_{\{hkl\}}$ of fcc NiFe Electrodeposits on Copper Sheet Substrates Deposited in NiFe Solution 3.

Current Density	*Planes*							
	111		200		220		311	
[mA cm^{-2}]	$R_{\{hkl\}}$	$I_{\{hkl\}}$	$R_{\{hkl\}}$	$I_{\{hkl\}}$	$R_{\{hkl\}}$	$I_{\{hkl\}}$	$R_{\{hkl\}}$	$I_{\{hkl\}}$
10	78.8	1346	35.8	244	18.9	126	21.0	414
30	72.1	1222	32.8	144	17.2	78	19.2	370

Table 4-31: Raw Data $R_{\{hkl\}}$ and $I_{\{hkl\}}$ of fcc/bcc NiFe Electrodeposits on Copper Sheet Substrates Deposited in NiFe Solution 3 (i = 60 mA cm^{-2}).

Planes (fcc)							
111		200		220		311	
$R_{\{hkl\}}$	$I_{\{hkl\}}$	$R_{\{hkl\}}$	$I_{\{hkl\}}$	$R_{\{hkl\}}$	$I_{\{hkl\}}$	$R_{\{hkl\}}$	$I_{\{hkl\}}$
55.9	788	25.7	90	13.6	72	15.3	65

Planes (bcc)									
110		200		211		310		222	
$R_{\{hkl\}}$	$I_{\{hkl\}}$	$R_{\{hkl\}}$	$I_{\{hkl\}}$	$R_{\{hkl\}}$	$I_{\{hkl\}}$	$R_{\{hkl\}}$	$I_{\{hkl\}}$	$R_{\{hkl\}}$	$I_{\{hkl\}}$
74.8	557	10.3	20	18.7	130	2.7	46	1.1	94.8

Table 4-32: Planar Distribution in per cent of fcc NiFe on Copper Sheet Substrates Deposited at 10 and 30 mA cm^{-2} in NiFe Solution 3.

i	*Planes: Distribution in per cent*			
[mA cm^{-2}]	111	200	220	311
10	34.0	13.6	13.2	39.2
30	37.5	9.7	10.1	42.7

Table 4-33: Planar Distribution in per cent of fcc/bcc NiFe on Copper Sheet Substrates Deposited at 60 mA cm^{-2} in NiFe Solution 3.

Planes (fcc): Distribution in per cent			
111	**200**	**220**	**311**
51.9	12.9	19.6	15.6

Planes (bcc): Distribution in per cent				
110	**200**	**211**	**310**	**222**
6.1	1.6	5.7	14.0	72.6

Table 4-34: Raw Data: Measured 2θ Bragg Angles of fcc NiFe Electrodeposits on Copper Sheet Substrates Deposited in NiFe Solution 3 at 10 and 30 mA cm^{-2}.

i	*Reflections:* 2θ° Bragg Angles			
[mA cm^{-2}]	**111**	**200**	**220**	**311**
10	43.87	51.20	75.36	91.66
30	43.77	51.06	75.26	91.52

Table 4-35: Raw Data: Measured 2θ Bragg Angles of fcc/bcc NiFe Electrodeposits on Copper Sheet Substrates Deposited in NiFe Solution 3 at 60 mA cm^{-2}.

Reflections / 2θ° Bragg Angles *(fcc)*			
111	**200**	**220**	**311**
43.70	50.85	74.95	90.97
Reflections / 2θ° Bragg Angles *(bcc)*			
110	**200**	**211**	**310**	**222**
44.61	65.40	82.58	117.74	138.52

Table 4-36: Calculated d-Spacings of fcc NiFe Electrodeposits on Copper Sheet Substrates Deposited in NiFe Solution 3.

i	*Reflections* / calculated d-Spacings [nm]			
[mA cm^{-2}]	**111**	**200**	**220**	**311**
10	0.20622	0.17826	0.12602	0.10739
30	0.20666	0.17874	0.12617	0.10752

Table 4-37: Calculated d-Spacings of fcc/bcc Electrodeposits on Copper Sheet Substrates Deposited in NiFe Solution 3.

Reflections / calculated d-Spacings [nm] *(fcc)*			
111	**200**	**220**	**311**
0.20696	0.17942	0.12660	0.10803
Reflections / calculated d-Spacings [nm] *(bcc)*			
110	**200**	**211**	**310**	**222**
0.20295	0.14259	0.11680	0.09076	0.82852

Table 4-38: Raw Data $R_{\{hkl\}}$ and $I_{\{hkl\}}$ of fcc NiFe Electrodeposit on Copper Sheet Substrate Deposited in NiFe Solution 4 (i = 10 mA cm^{-2}).

Planes							
111		**200**		**220**		**311**	
$R_{\{hkl\}}$	$I_{\{hkl\}}$	$R_{\{hkl\}}$	$I_{\{hkl\}}$	$R_{\{hkl\}}$	$I_{\{hkl\}}$	$R_{\{hkl\}}$	$I_{\{hkl\}}$
59.0	8331	26.8	128	14.5	52	16.1	88

Table 4-39: Raw Data $R_{\{hkl\}}$ and $I_{\{hkl\}}$ of bcc NiFe Electrodeposits on Copper Sheet Substrates Deposited in NiFe Solution 4 (i = 30 mA cm^{-2}), (i = 60 mA cm^{-2}).

Current	*Planes*									
Density	**110**		**200**		**211**		**310**		**222**	
[mA cm^{-2}]	$R_{\{hkl\}}$	$I_{\{hkl\}}$	$R_{\{hkl\}}$	$I_{\{hkl\}}$	$R_{\{hkl\}}$	$I_{\{hkl\}}$	$R_{\{hkl\}}$	$I_{\{hkl\}}$	$R_{\{hkl\}}$	$I_{\{hkl\}}$
30	72.2	77	10.0	*	18.3	58	9.7	*	3.8	1074
60	69.5	17	9.8	*	17.7	37	9.5	*	3.7	1473

* not detectable

Table 4-40: Planar Distribution in per cent of fcc NiFe Electrodeposit on Copper Sheet Substrate Deposited in NiFe Solution 4 (i = 10 mA cm^{-2}).

Planes: Distribution in per cent			
111	**200**	**220**	**311**
91.1	3.1	2.3	3.5

Table 4-41: Planar Distribution in per cent of bcc NiFe Electrodeposits on Copper Sheet Substrates deposited in NiFe Solution 4 ($i = 30$ mA cm^{-2}), ($i = 60$ mA cm^{-2}).

i	*Planes: Distribution in per cent*				
[mA cm^{-2}]	**110**	**200**	**211**	**310**	**222**
30	0.4	*	1.1	*	98.5
60	0.1	*	0.5	*	99.4

* not detectable

Table 4-42: Raw Data: Measured 2θ Bragg Angles of fcc NiFe Electrodeposit on Copper Sheet Substrate Deposited in NiFe Solution 4 ($i = 10$ mA cm^{-2}).

Reflections / 2θ° Bragg Angles *(fcc)*			
111	**200**	**220**	**311**
43.71	51.02	74.63	90.87

Table 4-43: Raw Data: Measured 2θ Bragg Angles of bcc NiFe Electrodeposits on Copper Sheet Substrates Deposited in NiFe Solution 4 ($i = 30$ mA cm^{-2}), ($i = 60$ mA cm^{-2}).

i	*Reflections* / 2θ° Bragg Angles *(bcc)*				
[mA cm^{-2}]	**110**	**200**	**211**	**310**	**222**
30	44.61	*	82.31	*	137.65
60	44.68	*	82.36	*	137.61

* not detectable

Table 4-44: Calculated d-Spacings of fcc NiFe Electrodeposit on Copper Sheet Substrate Deposited in NiFe Solution 4 (i = 10 mA cm^{-2}).

Reflections / calculated d-Spacings [nm]			
111	**200**	**220**	**311**
0.20694	0.17885	0.12707	0.10812

Table 4-45: Calculated d-Spacings of bcc NiFe Electrodeposits on Copper Sheet Substrates Deposited in NiFe Solution 4 (i = 30 mA cm^{-2}), (i = 60 mA cm^{-2}).

i	*Reflections* / calculated d-Spacings [nm]				
[mA cm^{-2}]	**110**	**200**	**211**	**310**	**222**
30	0.20295	*	0.11705	*	0.08261
60	0.20266	*	0.11699	*	0.08262

Table 4-46: Structure of Nickel-Zinc Deposited at Various Current Densities in As-Deposited and Heat-Treated State.

Current Density [mA cm^{-2}]	Structure As - Deposited	Structure Heat - Treated
10	bcc γ-phase	Tetragonal β_1-phase + bcc γ-phase
20	bcc γ-phase	Tetragonal β_1-phase + bcc γ-phase
30	bcc γ-phase	bcc γ-phase
40	bcc γ-phase + fcc α-phase	Tetragonal β_1-phase + bcc γ-phase + fcc α-phase
50	bcc γ-phase + fcc α-phase	Tetragonal β_1-phase + bcc γ-phase + fcc α-phase
60	bcc γ-phase	Tetragonal β_1-phase + bcc γ-phase

Table 4-47: Comparison Between Lattice Parameters of Nickel-Zinc Alloys Crystallized under Equilibrium Conditions and Through Electrocrystallization at Current Densities from 10 to 60 mA cm^{-2}.

	Lattice Parameter [nm]		Approximate Chemical Formula
	γ-phase	α-phase	
JCPDS	0.892		Ni_5Zn_{21}
i [mA cm^{-2}]			
10	0.8704		NiZn
20	0.8801		Ni_3Zn_7
30	0.8903		Ni_6Zn_{19}
40	0.8850	0.3535	-
50	0.8850	0.3532	-
60	0.8865		$Ni_{13}Zn_{36}$

Table 4-48: Comparison between Lattice Parameters of γ-Phase Nickel-Zinc Alloy Deposits in As-Deposited and Heat-Treated State.

Current Density [mA cm^{-2}]	Lattice Parameter [nm]		
	γ-phase as-deposited	γ-phase heat treated	Δ a
10	0.8704	0.8840	0.0136
20	0.8801	0.8869	0.0068
30	0.8903	0.8878	0.0025
40	0.8850	0.8850	0
50	0.8850	0.8850	0
60	0.8865	0.8860	0.0005

Table 4-49: Elemental Composition of fcc Nickel-Iron Deposit at Different Distances from Copper Substrate/Deposit Interface.

Distance from Interface Substrate/Deposit [nm]	Composition Mass-%	
	Ni	Fe
5	37.54	62.46
10	36.38	63.62
15	37.54	62.46
20	37.93	62.07
25	37.02	62.98
30	37.25	62.75
35	36.58	63.42
40	37.59	62.41
45	38.32	61.68
50	36.25	63.75
55	36.56	63.44
60	35.96	64.04
65	36.03	63.97
70	36.50	63.50
75	36.70	63.30
80	36.84	63.15
85	35.98	64.02
90	35.96	64.04

Table 4-50: Elemental Composition of bcc Nickel-Iron Deposit at Different Distances from Copper Substrate/Deposit Interface.

Distance from Interface Substrate/Deposit [nm]	Composition Mass-%	
	Ni	Fe
5	29.48	70.52
10	29.39	70.61
15	29.43	70.57
20	29.05	70.95
25	28.84	71.16
30	28.88	71.12
35	28.93	71.07
40	28.95	71.05
45	29.00	71.00
50	29.37	70.63
55	29.15	70.85
60	29.09	70.91
65	29.08	70.92
70	29.01	70.99
75	28.95	71.05
80	28.83	71.17
85	28.57	71.43
90	28.64	71.36

Table 4-51: Elemental Composition of Double Layered fcc/bcc Nickel-Iron Deposit.

Structure	Composition [Mass-%]	
	Ni	Fe
fcc	41.07	58.93
fcc	40.74	59.26
fcc	39.56	60.44
bcc	26.01	73.99
bcc	26.10	73.90
bcc	26.05	73.95

Table 4-52: Elemental Composition of Double Layered bcc/fcc Nickel-Iron Deposit.

Structure	Composition [Mass-%]	
	Ni	Fe
bcc	26.06	73.94
fcc	37.12	62.88

Table 4-53: Elemental Composition of bcc Nickel-Zinc Deposit (i = 10 mA cm^{-2}) at Different Distances from Copper Substrate/Deposit Interface.

Distance from Interface Substrate/Deposit [nm]	Composition Mass-%	
	Ni	Zn
5	31.43	68.57
10	31.50	68.50
15	31.57	68.43
20	31.53	68.47
25	31.87	68.13
30	31.56	68.44
35	31.66	68.34
40	31.49	68.51
45	31.41	68.59
50	31.63	68.37
55	31.59	68.41
60	31.36	68.64
65	31.30	68.70
70	30.94	69.06
...		
...		
middle of deposit	31.02	68.98

Table 4-54: Elemental Composition of bcc Nickel-Zinc Deposit (i = 60 mA cm^{-2}) at Different Distances from Copper Substrate/Deposit Interface.

Distance from Interface Substrate/Deposit [nm]	Composition Mass-%	
	Ni	Zn
5	35.42	64.58
10	38.21	61.79
15	38.38	61.62
20	34.34	65.66
25	34.17	65.75
30	33.25	66.75
35	34.71	65.29
40	34.10	65.90
45	33.70	66.30
50	34.49	65.51
55	33.79	66.21

Table 4-55: Elemental Composition of bcc Nickel-Zinc Deposit (i = 60 mA cm^{-2}) at Similar Distance from Copper Substrate/Deposit Interface but in Different Grains.

Spot	Composition Mass-%	
	Ni	Zn
1	32.88	67.12
2	30.52	69.48
3	29.93	70.07

Table 4-56: Elemental Composition of bcc Nickel-Zinc Deposit (i = 10 mA cm^{-2}) at Different Distances from Steel Substrate/Deposit Interface.

Distance from Interface Substrate/Deposit [nm]	Composition Mass-%	
	Ni	Zn
5	59.13	40.87
10	51.92	48.08
15	42.34	57.66
20	34.31	65.69
25	34.16	65.84
30	31.64	68.36
35	33.01	66.99
40	34.89	65.11
45	30.56	69.44

Table 4-57: Raw Data $R_{\{hkl\}}$, $I_{\{hkl\}}$ and Planar Distribution in per cent of the Copper Disc Substrate.

	Planes: Copper Disc Substrate									
	111		**200**		**220**		**311**		**331**	
Raw	$R_{\{hkl\}}$	$I_{\{hkl\}}$	$R_{\{hkl\}}$	$I_{\{hkl\}}$	$R_{\{hkl\}}$	$I_{\{hkl\}}$	$R_{\{hkl\}}$	$I_{\{hkl\}}$	$R_{\{hkl\}}$	$I_{\{hkl\}}$
Data	245.5	9344	112.9	4711	59.6	170	65.5	698	48.7	103
%	39.9		43.7		3.0		11.2		2.2	

Table 4-58: Raw Data: Measured 2θ Bragg Angles. Calculated Interplanar Spacings 'd' and Lattice Parameter 'a' of Copper Disc Substrate.

	Reflections						
Copper	**111**	**200**	**220**	**311**	**222**	**400**	**331**
°2θ	43.31	50.41	74.09	89.86	95.10	116.76	136.35
d [nm]	0.20873	0.18089	0.12787	0.10907	0.10439	0.09046	0.08298
a [nm]	0.36153	0.36177	0.36166	0.36174	0.36162	0.36184	0.36169

Table 4-59: Raw Data, $R_{\{hkl\}}$ and $I_{\{hkl\}}$, of fcc NiFe Electrodeposits on Copper Disc Substrates.

	Planes							
Thickness	111		200		220		311	
[μm]	$R_{\{hkl\}}$	$I_{\{hkl\}}$	$R_{\{hkl\}}$	$I_{\{hkl\}}$	$R_{\{hkl\}}$	$I_{\{hkl\}}$	$R_{\{hkl\}}$	$I_{\{hkl\}}$
0.3	13.8	1622	5.6	*	2.2	209	2.1	*
0.4	17.6	1440	7.2	*	2.9	132	2.7	*
0.5	21.1	1553	8.6	*	3.4	91	3.4	*
0.75	28.5	2377	11.8	*	4.8	*	4.8	*
1	34.3	6463	14.4	*	6.0	226	6.0	*
1.5	42.6	7451	18.2	*	8.0	(70)	8.1	*
2	47.8	6246	20.8	*	9.4	159	9.7	*
3	52.8	33760	23.5	*	11.3	(66)	11.9	*

* Not detectable

( ) Values in brackets are intensities below $3 \times \sqrt{\text{Background}}$

Table 4-60: Planar Distribution in per cent of fcc NiFe Electrodeposits on Copper Disc Substrates.

	Planes: Distribution in per cent			
[μm]	111	200	220	311
0.3	55.2	*	44.8	*
0.4	63.8	*	36.2	*
0.5	73.4	*	26.6	*
0.75	100	*	*	*
1	83.4	*	16.6	*
1.5	100	*	**	*
2	88.5	*	11.5	*
3	100	*	**	*

* Not detectable

** Intensities below $3 \times \sqrt{\text{Background}}$

Table 4-61: Raw Data: Measured 2θ Bragg Angles of fcc Nickel-Iron Deposits.

	Reflections / 2θ° Bragg Angles			
[μm]	111	200	220	311
0.3	43.58	*	74.52	*
0.4	43.63	*	74.57	*
0.5	43.65	*	74.87	*
0.75	43.74	*	*	*
1	43.72	*	74.86	*
1.5	43.75	*	(74.94)	*
2	43.77	*	75.04	*
3	42.72	*	(74.93)	*

* Not detectable

( ) Values in brackets are intensities below $3 \times \sqrt{\text{Background}}$

Table 4-62: Calculated d-Spacings of fcc NiFe Substrates of Various Thicknesses on Copper.

	Reflections / Calculated d-spacings [nm]			
[μm]	111	200	220	311
0.3	0.20751	*	0.12723	*
0.4	0.20727	*	0.12716	*
0.5	0.20721	*	0.12672	*
0.75	0.20681	*	*	*
1	0.20689	*	0.12674	*
1.5	0.20673	*	(0.12663)	*
2	0.20666	*	0.12647	*
3	0.20688	*	(0.12664)	*

* Not detectable

( ) Values in brackets are calculated from Bragg angle positions with intensities below $3 \times \sqrt{\text{Background}}$

Table 4-63: Raw Data, $R_{\{hkl\}}$ and $I_{\{hkl\}}$, of bcc NiFe Electrodeposits on Copper Disc Substrates.

	Planes									
Thickness	110		200		211		310		222	
[µm]	$R_{\{hkl\}}$	$I_{\{hkl\}}$	$R_{\{hkl\}}$	$I_{\{hkl\}}$	$R_{\{hkl\}}$	$I_{\{hkl\}}$	$R_{\{hkl\}}$	$I_{\{hkl\}}$	$R_{\{hkl\}}$	$I_{\{hkl\}}$
0.4	22.9	181	2.4	*	3.6	(88)	1.6	*	0.6	*
0.5	27.3	414	2.9	*	4.4	3120	1.9	*	0.7	*
0.75	36.5	552	4.0	*	6.2	519	2.7	*	1.0	*
1	43.8	598	4.9	*	7.8	693	3.4	*	1.3	(76)
1.5	53.6	333	6.3	*	10.2	810	4.6	*	1.7	309
2	59.6	249	7.3	(43)	12.0	1228	5.6	*	2.1	91
3	65.4	510	8.5	(58)	14.5	856	7.0	*	2.6	243
20	68.2	149	9.4	34	17.3	119	9.2	(18)	3.6	7032

* Not detectable

( ) Values in brackets are intensities below $3 \times \sqrt{\text{Background}}$

Table 4-64: Planar Distribution in per cent of bcc NiFe Electrodeposits on Copper Disc Substrates.

	Planes: Distribution in per cent				
[µm]	110	200	211	310	222
0.4	100	*	**	**	*
0.5	17.4	*	82.6	*	*
0.75	15.3	*	84.7	*	*
1	13.3	*	86.4	*	**
1.5	2.3	*	29.6	*	68.1
2	2.8	**	67.8	*	29.4
3	4.9	**	37.0	*	58.1
20	0.1	0.2	0.3	**	99.4

* Not detectable

** $I(hkl) < 3 \times \sqrt{\text{Background}}$

Table 4-65: Raw Data: Measured 2θ Bragg Angles of bcc Nickel-Iron Electrodeposits of Individual Thickness on Copper Disc Substrates.

	Reflections / 2θ° Bragg Angles				
[µm]	110	200	211	310	222
0.4	44.85	*	(82.66)	*	*
0.5	44.86	*	82.67	*	*
0.75	44.82	*	82.61	*	*
1	44.85	*	82.67	*	(137.52)
1.5	44.79	*	82.58	*	137.67
2	44.79	(65.37)	82.64	*	137.78
3	44.79	(65.40)	82.59	*	137.76
20	44.63	65.40	82.29	(116.70)	137.74

* Not detectable

( ) Values in brackets are Bragg angles where intensities were below $3 \times \sqrt{\text{Background}}$

Table 4-66: Calculated d-Spacings of bcc NiFe Electrodeposits of Individual Thickness on Copper Disc Substrates.

	Reflections / Calculated d-spacings [nm]				
[µm]	110	200	211	310	222
0.4	0.20191	*	(0.11642)	*	*
0.5	0.20190	*	0.11663	*	*
0.75	0.20207	*	0.11670	*	*
1	0.20194	*	0.11663	*	(0.08247)
1.5	0.20219	*	0.11673	*	0.08260
2	0.20217	(0.14289)	0.11667	*	0.08250
3	0.20218	(0.14296)	0.11673	*	0.08257
20	0.20287	0.14258	0.11707	(0.09049)	0.08258

* Not detectable

( ) Values in brackets are calculated from Bragg angle positions with intensities below $3 \times \sqrt{\text{Background}}$

Table 4-67: Raw Data $R_{\{hkl\}}$ and $I_{\{hkl\}}$ of 0.5μm Thick fcc NiFe Electrodeposited on Various Substrates.

Substrate	*Planes* 111		200		220		311	
	$R_{\{hkl\}}$	$I_{\{hkl\}}$	$R_{\{hkl\}}$	$I_{\{hkl\}}$	$R_{\{hkl\}}$	$I_{\{hkl\}}$	$R_{\{hkl\}}$	$I_{\{hkl\}}$
Copper Disc Substrate	21.1	1553	8.6	*	3.4	91	3.4	*
0.5μm bcc NiFe Electrodeposit	21.1	1889	8.6	*	3.4	(49)	3.4	*
2μm bcc NiFe Electrodeposit	21.1	775	8.6	*	3.4	(48)	3.4	*

* Not detectable

( ) Values in brackets are intensities below $3 \times \sqrt{\text{Background}}$

Table 4-68: Texture (Planar Distribution in per cent) of 0.5μm thick fcc NiFe Electrodeposits on Various Substrates.

Substrate	*Planes: Distribution in per cent* 111	200	220	311
Copper Disc Substrate	73.4	*	26.6	*
0.5μm bcc NiFe Electrodeposit	100	*	**	*
2μm bcc NiFe Electrodeposit	100	*	**	*

* Not detectable

** $I(hkl) < 3 \times \sqrt{\text{Background}}$

Table 4-69: Raw Data $R_{\{hkl\}}$ and $I_{\{hkl\}}$ of 2μm Thick fcc NiFe Electrodeposited on Various Substrates.

Substrate	*Planes*							
	111		200		220		311	
	$R_{\{hkl\}}$	$I_{\{hkl\}}$	$R_{\{hkl\}}$	$I_{\{hkl\}}$	$R_{\{hkl\}}$	$I_{\{hkl\}}$	$R_{\{hkl\}}$	$I_{\{hkl\}}$
Copper Disc Substrate	47.8	6246	20.7	*	9.4	159	9.7	*
0.5μm bcc NiFe Electrodeposit	47.8	12873	20.7	*	9.4	(59)	9.7	*
2μm bcc NiFe Electrodeposit	47.8	8759	20.7	2701	9.4	133	9.7	228

* Not detectable

( ) Values in brackets are intensities below $3 \times \sqrt{\text{Background}}$

Table 4-70: Texture (Planar Distribution in per cent) of 2μm Thick fcc NiFe Electrodeposits on Various Substrates.

Substrate	*Planes: Distribution in per cent*			
	111	200	220	311
Copper Disc Substrate	88.5	*	11.5	*
0.5μm bcc NiFe Electrodeposit	100	*	**	*
2μm bcc NiFe Electrodeposit	52.1	37.3	4.0	6.6

* Not detectable

** $I(hkl) < 3 \times \sqrt{\text{Background}}$

Table 4-71: Raw Data $R_{\{hkl\}}$ and $I_{\{hkl\}}$ of 0.5μm Thick bcc NiFe Electrodeposits on Various Substrates.

Substrate	*Planes*									
	110		200		211		310		222	
	$R_{\{hkl\}}$	$I_{\{hkl\}}$	$R_{\{hkl\}}$	$I_{\{hkl\}}$	$R_{\{hkl\}}$	$I_{\{hkl\}}$	$R_{\{hkl\}}$	$I_{\{hkl\}}$	$R_{\{hkl\}}$	$I_{\{hkl\}}$
Copper Disc Substrate	27.3	414	2.9	*	4.4	317	1.9	*	0.7	*
0.5μm fcc NiFe Electrodeposit	27.3	889	2.9	(9)	4.4	313	1.9	*	0.7	(34)
2μm fcc NiFe Electrodeposit	27.3	1433	2.9	(4)	4.4	312	1.9	*	0.7	(50)

* Not detectable

( ) Values in brackets are intensities below $3 \times \sqrt{\text{Background}}$

Table 4-72: Texture (planar Distribution in per cent) of 0.5μm Thick bcc NiFe Electrodeposits on Various Substrates.

Substrate	*Planes: Distribution in per cent*				
	110	200	211	310	222
Copper Disc Substrate	17.4	*	82.6	*	*
0.5μm fcc NiFe Electrodeposit	31.5	**	68.5	*	**
2μm fcc NiFe Electrodeposit	42.6	**	57.4	*	**

* Not detectable

** $I(hkl) < 3 \times \sqrt{\text{Background}}$

Table 4-73: Raw Data $R_{\{hkl\}}$ and $I_{\{hkl\}}$ of 2μm Thick bcc NiFe Electrodeposits on Various Substrates.

Substrate	*Planes* 110		200		211		310		222	
	$R_{\{hkl\}}$	$I_{\{hkl\}}$	$R_{\{hkl\}}$	$I_{\{hkl\}}$	$R_{\{hkl\}}$	$I_{\{hkl\}}$	$R_{\{hkl\}}$	$I_{\{hkl\}}$	$R_{\{hkl\}}$	$I_{\{hkl\}}$
Copper Disc Substrate	59.6	249	7.3	(43)	12.0	1228	5.6	*	2.1	91
0.5μm fcc NiFe Electrodeposit	59.6	292	7.3	(38)	12.0	509	5.6	*	2.1	621
2μm fcc NiFe Electrodeposit	59.6	2200	7.3	(20)	12.0	714	5.6	*	2.1	204

* Not detectable

( ) Values in brackets are intensities below $3 \times \sqrt{\text{Background}}$

Table 4-74: Texture (planar Distribution in per cent) of 2μm Thick bcc NiFe Electrodeposits on Various Substrates.

Substrate	*Planes: Distribution in per cent* 110	200	211	310	222
Copper Disc Substrate	2.8	**	67.8	*	29.4
0.5μm fcc NiFe Electrodeposit	1.4	**	12.1	*	86.5
2μm fcc NiFe Electrodeposit	18.8	**	30.7	*	50.5

* Not detectable

** $I(hkl) < 3 \times \sqrt{\text{Background}}$

Table 4-75: Raw Data $R_{\{hkl\}}$ and $I_{\{hkl\}}$ of 0.5, 2, and 10μm Thick bcc NiFe Electrodeposited on 2μm thick NiFe Substrate.

Thickness	*Planes*									
	110		200		211		310		222	
	$R_{\{hkl\}}$	$I_{\{hkl\}}$	$R_{\{hkl\}}$	$I_{\{hkl\}}$	$R_{\{hkl\}}$	$I_{\{hkl\}}$	$R_{\{hkl\}}$	$I_{\{hkl\}}$	$R_{\{hkl\}}$	$I_{\{hkl\}}$
0.5 μm	27.3	1433	2.9	(4)	4.4	312	1.9	*	0.7	(50)
2 μm	59.6	2200	7.3	(20)	12.0	724	5.6	*	2.1	204
10 μm	68.7	77	9.4	60	17.5	160	9.3	79	3.6	2735

* Not detectable

( ) Values in brackets are intensities below $3 \times \sqrt{\text{Background}}$

Table 4-76: Texture (planar Distribution in per cent) of 0.5, 2, and 10μm Thick bcc NiFe Electrodeposits on 2μm thick fcc NiFe Substrate.

Thickness	*Planes: Distribution in per cent*				
	110	200	211	310	222
0.5 μm	42.6	*	57.4	*	**
2 μm	18.8	**	30.7	*	50.5
10 μm	0.1	0.8	1.2	1.1	96.8

* Not detectable

** $I(hkl) < 3 \times \sqrt{\text{Background}}$

Table 4-77: Raw Data: Measured 2θ Bragg Angles of 0.5µm, 2µm, and 10 µm Thick bcc NiFe Electrodeposits on 2µm fcc NiFe.

	Reflections / 2θ Bragg Angles				
Thickness	**110**	**200**	**211**	**310**	**222**
0.5 µm	44.77	(65.71)	82.61	*	(137.52)
2 µm	44.73	(65.23)	82.57	*	137.64
10 µm	44.77	65.50	82.44	116.82	137.78

Table 4-78: Calculated d-Spacings of bcc NiFe of 0.5, 2, and 10µm Thick Electrodeposits on 2µm fcc NiFe Substrates.

	Reflections / Calculated d-spacings [nm]				
Thickness	**110**	**200**	**211**	**310**	**222**
0.5 µm	0.20236	(0.14310)	0.11683	*	(0.08261)
2 µm	0.20235	(0.14383)	0.11683	*	0.08261
10 µm	0.20226	0.14302	0.11677	0.09045	0.08257

Table 4-79: Raw Data $R_{\{hkl\}}$, $I_{\{hkl\}}$ and Planar Distribution in per cent of Mild Steel Substrate.

	Planes									
Mild	**110**		**200**		**211**		**310**		**222**	
Steel	$R_{\{hkl\}}$	$I_{\{hkl\}}$	$R_{\{hkl\}}$	$I_{\{hkl\}}$	$R_{\{hkl\}}$	$I_{\{hkl\}}$	$R_{\{hkl\}}$	$I_{\{hkl\}}$	$R_{\{hkl\}}$	$I_{\{hkl\}}$
Raw Data	262.2	700	37.4	39	68.3	99	37.3	64	14.6	18
%	32.9		12.7		17.8		21.1		15.5	

Table 4-80: Raw Data: Measured 2θ Bragg Angles. Calculated Interplanar Spacings 'd' and Lattice Parameter 'a' of Mild Steel Substrate.

Mild Steel	*Reflections*					
	110	200	211	220	310	222
°2θ	44.82	65.08	82.39	98.77	116.27	136.98
d [nm]	0.20205	0.14322	0.11696	1.01470	0.09070	0.08280
a [nm]	0.285738	0.28643	0.28650	0.28703	0.28682	0.28682

Table 4-81: Calculated $R_{\{hkl\}}$ Values of an Untextured Nickel-Zinc Powder Specimen of Similar Nominal Composition and Thickness to the Electrodeposit formed at 10 mA cm^{-2}.

Thickness	*Planes: $R_{\{hkl\}}$-Values*										
[μm]	222	321	330	332	510	521	600	631	552	741	820
0.1	12.4	54.9	8.2	10.6	7.3	10.5	0.8	3.8	1.3	1.7	0.8
0.2	24.3	107.2	16.0	20.8	14.3	20.6	1.7	7.3	2.5	3.2	1.5
0.5	56.6	253.9	38.1	49.7	34.4	49.6	4.0	17.9	6.1	7.9	3.7
1	105.2	474.3	71.7	94.1	65.4	94.7	7.7	34.5	11.8	15.2	7.1
2	183.4	837.3	128.4	175.1	119.1	173.5	14.3	64.3	22.1	28.6	13.5
10	407.2	1939	318.4	457.7	324.7	489.9	42.2	199.8	70.8	95.2	45.1
20	420.6	2025	340.6	497.2	362.3	556.4	49.3	240.3	86.9	120.4	57.3

Table 4-82: Measured Intensities $I_{\{hkl\}}$ of NiZn, Electrodeposited at 10 mA cm^{-2}, on Mild Steel Substrates.

Thickness	*Planes: $I_{\{hkl\}}$-Values*										
[µm]	222	321	330	332	510	521	600	631	552	741	820
0.1	*	*	2205	*	*	*	*	*	*	*	*
0.2	*	*	1053	*	*	*	*	*	*	*	*
0.5	125	*	1169	*	*	*	*	*	69	*	*
1	305	*	1965	*	*	*	*	*	121	*	*
2	1356	*	2473	(50)	*	*	*	*	91	*	*
10	4990	*	2155	322	*	*	217	*	71	*	*
20	2143	*	14390	417	*	*	404	*	215	*	*

* Not detectable

( ) Values in brackets are intensities below $3 \times \sqrt{\text{Background}}$

Table 4-83: Planar Distribution of Nickel-Zinc Deposit of Various Thicknesses, Electrodeposited at 10 mA cm^{-2}, on Mild Steel Substrates.

	Planes: Distribution in per cent										
[μm]	**222**	**321**	**330**	**332**	**510**	**521**	**600**	**631**	**552**	**741**	**820**
0.1	*	*	100	*	*	*	*	*	*	*	*
0.2	*	*	100	*	*	*	*	*	*	*	*
0.5	5.0	*	69.4	*	*	*	*	*	25.6	*	*
1	7.2	*	67.6	*	*	*	*	*	25.2	*	*
2	24.0	*	62.6	**	*	*	*	*	13.4	*	*
10	47.4	*	26.2	2.7	*	*	19.9	*	3.8	*	*
20	8.7	*	71.8	1.4	*	*	13.9	*	4.2	*	*

* Not detectable

** $I(hkl) < 3 \times \sqrt{\text{Background}}$

Table 4-84: Raw Data: Bragg Angles of bcc Nickel-Zinc, Electrodeposited at 10 mA cm^{-2}, on Mild Steel Substrates.

	Reflections / 2θ Bragg Angles										
[μm]	222	321	330	332	510	521	600	631	552	741	820
0.1	*	*	44.24	*	*	*	*	*	*	*	*
0.2	*	*	43.98	*	*	*	*	*	*	*	*
0.5	35.42	*	43.62	*	*	*	*	*	80.2	*	*
1	35.34	*	43.52	*	*	*	*	*	79.95	*	*
2	35.35	*	43.48	(48)	*	*	*	*	79.84	*	*
10	35.32	*	43.44	47.9	*	*	63.07	*	79.81	*	*
20	35.3	*	43.41	47.95	*	*	62.96	*	79.80	*	*

* Not detectable

( ) Values in brackets are intensities below $3 \times \sqrt{\text{Background}}$

Table 4-85: Calculated d-Spacings of bcc Nickel-Zinc (i = 10 mA cm^{-2}) at Various Thicknesses.

	Reflections / Calculated d-Spacings [nm]										
[μm]	222	321	330	332	510	521	600	631	552	741	820
0.1	*	*	0.20456	*	*	*	*	*	*	*	*
0.2	*	*	0.20571	*	*	*	*	*	*	*	*
0.5	0.25391	*	0.20732	*	*	*	*	*	0.11970	*	*
1	0.25449	*	0.20779	*	*	*	*	*	0.11997	*	*
2	0.25471	*	0.20796	(0.1881)	*	*	*	*	0.12007	*	*
10	0.25491	*	0.20814	0.18827	*	*	0.14717	*	0.12017	*	*
20	0.25509	*	0.20828	0.18840	*	*	0.14728	*	0.12025	*	*

* Not detectable

( ) Values in brackets are calculated from 2θ Bragg angles with intensities below $3 \times \sqrt{\text{Background}}$

Table 4-86: Calculated $R_{\{hkl\}}$ Values of an Untextured Nickel-Zinc Powder Specimen of Similar Nominal Composition and Thickness to the Electrodeposit Formed at 60 mA cm^{-2}.

Thickness	*Planes: $R_{\{hkl\}}$-Values*										
[μm]	222	321	330	332	510	521	600	631	552	741	820
0.1	12.3	54.2	8.1	10.4	7.2	10.3	0.8	3.7	1.3	1.6	0.8
0.2	23.2	104.7	15.6	19.9	14.0	20.1	1.6	7.2	2.4	3.2	1.5
0.5	55.1	249.4	37.4	50.0	33.8	48.7	4.1	17.6	5.9	7.9	3.6
1	104.0	468.1	71.5	96.1	64.4	93.3	7.8	34.0	11.7	15.3	7.0
2	178.4	820.3	125.8	171.6	116.8	170.1	14.2	63.0	21.6	28.2	13.1
10	390.8	1839	302.3	422.8	313.4	462.7	40.2	189.3	67.7	90.6	43.6
20	412.9	1968	331.2	473.5	352.6	514.8	47.9	234.0	84.4	116.9	55.4

Table 4-87: Measured Intensities $I_{\{hkl\}}$ of NiZn, Electrodeposited at 60 mA cm^{-2}, on Mild Steel Substrates.

Thickness	*Planes: $I_{\{hkl\}}$-Values*										
[μm]	222	321	330	332	510	521	600	631	552	741	820
0.1		*	2256	*	*	*	*	*	*	*	*
0.2	249	*	2352	(29)	*	*	*	*	(18)	*	*
0.5	428	*	5994	106	*	*	(30)	*	265	(32)	*
1	1463	*	12685	253	*	*	243	*	303	98	*
2	410	*	28807	111	*	*	301	*	507	227	*
10	*	*	19870	*	456	(62)	627	109	947	499	336
20	*	*	355824	*	*	*	(86)	*	392	137	*

* Not detectable

( ) Values in brackets are intensities below $3 \times \sqrt{\text{Background}}$

Table 4-88: Planar Distribution of Nickel-Zinc Deposit of Various Thicknesses, Electrodeposited at 60 mA cm^{-2}, on Mild Steel Substrates.

	Planes: Distribution in per cent										
[µm]	222	321	330	332	510	521	600	631	552	741	820
0.1	*	*	100	*	*	*	*	*	*	*	*
0.2	6.6	*	93.4	**	*	*	*	*	**	*	*
0.5	3.6	*	74.6	1.0	*	*	**	*	20.8	**	*
1	5.5	*	68.9	1.0	*	*	12.1	*	10.0	2.5	*
2	0.8	*	80.4	0.2	*	*	7.5	*	8.3	2.8	*
10	*	*	59.4	*	1.3	**	14.1	0.5	12.7	5.0	7.0
20	*	*	99.5	*	*	*	**	*	0.4	0.1	*

* Not detectable

** $I(hkl) < 3 \times \sqrt{\text{Background}}$

Table 4-89: Raw Data: Bragg Angles of bcc Nickel-Zinc, Electrodeposited at 60 mA cm^{-2}, on Mild Steel Substrates.

	Reflections / 2θ Bragg Angles										
[µm]	222	321	330	332	510	521	600	631	552	741	820
0.1	*	*	44.20	*	*	*	*		*	*	*
0.2	35.56	*	43.71	(48.86)	*	*	*	*	80.50	*	*
0.5	35.40	*	43.50	48.09	*	*	(63.63)	*	80.10	(89.72)	*
1	35.40	*	43.49	48.09	*	*	62.63	*	80.10	89.72	*
2	35.28	*	43.31	47.82	*	*	62.75	*	79.54	89.56	*
10	*	*	43.16	*	52.26	(56.81)	62.65	72.12	79.11	89.41	90.57
20	*	*	43.17	*	*	*	62.63	*	79.32	89.49	*

* Not detectable

( ) Values in brackets are calculated from 2θ Bragg angles with intensities below $3 \times \sqrt{\text{Background}}$

Table 4-90: Calculated d-Spacings of bcc Nickel-Zinc (i = 60 mA cm^{-2}) at Various Thicknesses.

	Reflections / Calculated d-Spacings [nm]										
[µm]	222	321	330	332	510	521	600	631	552	741	820
0.1	*	*	0.20474	*	*	*	*		*	*	*
0.2	0.25345	*	0.20694	(0.18728)	*	*	*	*	(0.11948)	*	*
0.5	0.25463	*	0.20790	0.18806	*	*	(0.14822)	*	0.12003	(0.10920)	*
1	0.25463	*	0.20790	0.18806	*	*	0.14822	*	0.12003	0.10920	*
2	0.25565	*	0.20874	0.18881	*	*	0.14796	*	0.12052	0.10936	*
10	*	*	0.20942	*	0.17424	(0.16922)	0.14815	0.13087	0.12097	0.10950	0.10840
20	*	*	0.20939	*	*	*	0.14806	*	0.12089	0.19352	*

* Not detectable

( ) Values in brackets are calculated from 2θ Bragg angles with intensities below $3 \times \sqrt{\text{Background}}$

Table 5-1: Interplanar Spacings of Substrate Metals, Alloy Electrodeposits Investigated, and Individual Metals Contained in Alloy Electrodeposits Investigated, based on JCPDS Data [88].

		Cu	NiFe	NiFe	Ni	Fe	Fe	Ni_5Zn_{21}
	lattice	fcc	fcc	bcc	fcc	fcc	bcc	bcc
	JCPDS	4-836	23-297	37-474	4-850	31-619	6-696	6-653
$h^2+k^2+l^2$	plane	*d-spacings [nm]*						
1	100	**0.3615**	**0.3596**	**0.28681**	**3.5238**	**0.36**	**0.28664**	**0.892**
2	110	0.25562	0.25428	0.20281	0.24917	0.25456	0.20269	0.63074
3	111	0.20871	0.20762	0.16559	0.20345	0.20785	0.16550	0.515
5	210	0.16167	0.16082	0.12827	0.15759	0.161	0.12819	0.39892
6	211	0.14758	0.14681	0.11709	0.14386	0.14697	0.11702	0.36416
9	221	0.1205	0.11987	0.09560	0.11746	0.12	0.09555	0.29733
10	310	0.11432	0.11372	0.0907	0.11143	0.11384	0.09064	0.28208
11	311	0.1090	0.10842	0.08648	0.10625	0.10854	0.08643	0.26895
13	320	0.10026	0.09974	0.07955	0.09773	0.09985	0.07950	0.2474
14	321	0.09661	0.09611	0.07665	0.09418	0.09621	0.07661	0.2384

Table 5-2: Crystallographic Planes (Directions) with Corresponding Perpendicular Planes (Directions) in the Cubic System [119].

{hkl}	Planes Perpendicular (⊥) to {hkl}
100	100; 110; 210; 310; 320
110	110; 211; 221
111	110; 211; 321
210	100; 210; 221; 321
211	110; 111; 311; 321
221	110; 210; 221
310	100; 110; 310
311	110; 211; 310
320	100; 320
321	111; 210; 211

Table 5-3: Interplanar Spacings of fcc and bcc Nickel-Iron Compatible for Initial Deposition on Copper Substrate According to Finch's 15 per Cent Criterion. Data are Based on JCPDS Lattice Parameters.

	Substrate	Electrodeposit	
	Cu	NiFe	NiFe
Lattice	*fcc*	*fcc*	*bcc*
	100	100	-
	110	110	100
	111	111	110
	210	210; 211	111
	211	210; 211	111; 210
	221	221; 310; 311	210; 211
	310	221; 310; 311	210; 211
	311	221; 310; 311; 320; 321	211; 221

Table 5-4: Interplanar Spacings of fcc and bcc Nickel-Iron Compatible for Initial Deposition According to Finch's 15 per Cent Criterion. Data are Based on JCPDS Lattice Parameters.

	NiFe	NiFe
Lattice	*fcc*	*bcc*
	100	-
	110	100
	111	110
	210	111
	211	111; 210
	221	210; 211
	310	210; 211; 220
	311	211; 221
	320	211; 221; 310; 311
	321	221; 310; 311

Table 5-5: Interplanar Spacings of Ni_5Zn_{21}, that Fulfil Finch's 15 per cent Criterion and Fit on the d-Spacings of the Copper and Iron Substrate Multiplied by Three.

	Substrate	Electrodeposit
	Cu	Ni_5Zn_{21}
Lattice	*fcc*	*bcc*
	100	-
	110	300
	111	330
	210	333
	211	333; 630
	221	630; 633
	310	630; 633; 663
	311	633 ;663; 930
	320	663; 930; 933
	321	663; 930; 933; 960

Substrate	Electrodeposit
Fe	Ni_5Zn_{21}
bcc	*bcc*
100	300
110	330
111	333
210	630; 633
211	630; 633; 663
221	663; 930;933; 960
310	663; 930;933; 960; 963
311	663; 930; 933; 960; 963
320	930, 933, 960; 963
321	933; 960;963

Table 5-6: Atomic Density $\delta_{\{hkl\}}$ of Different Crystal Planes {hkl} in the fcc Lattice.

{hkl}	{111}	{100}	{110}	{311}	{210}	{211}
$\delta_{\{hkl\}}$ (at/a^2)	2.3094	2	1.4142	0.9177	0.8944	0.6666
$\delta_{\{hkl\}}$ (at/nm^2)	17.8591	15.4664	10.9364	7.0965	6.9168	5.1555

Table 5-7: Atomic Density $\delta_{\{hkl\}}$ of Different Crystal Planes {hkl} in the bcc Lattice.

{hkl}	{110}	{100}	{310}	{111}	{211}
$\delta_{\{hkl\}}$ (at/a^2)	1.4142	1	0.6325	0.5774	0.3333
$\delta_{\{hkl\}}$ (at/nm^2)	17.1920	12.1566	7.6885	7.0186	4.0522

8. 2 Figures

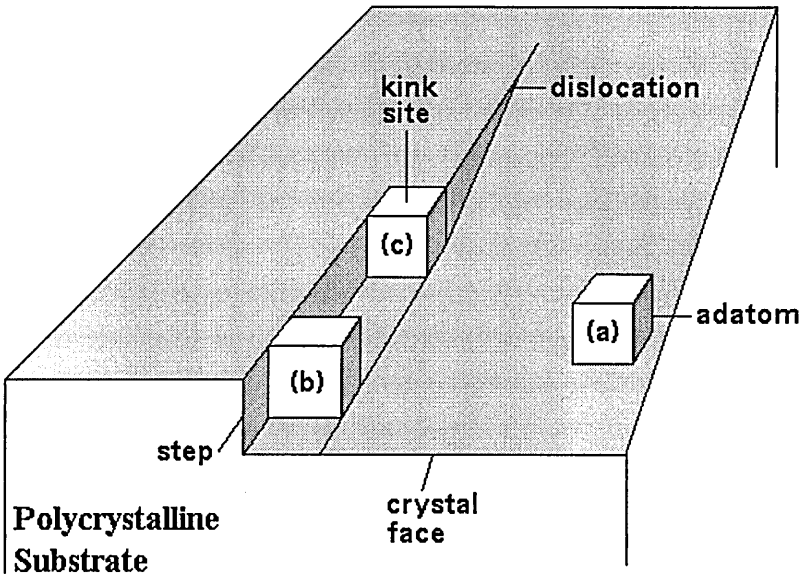

Fig. 2-1: Schematic Drawing of the Electrocrystallization Process of an Atom on a polycrystalline Substrate from (a) being discharged, (b) diffusing over the Surface to a Step, and (c) diffusing along the Step to kink Site in a Screw Dislocation.

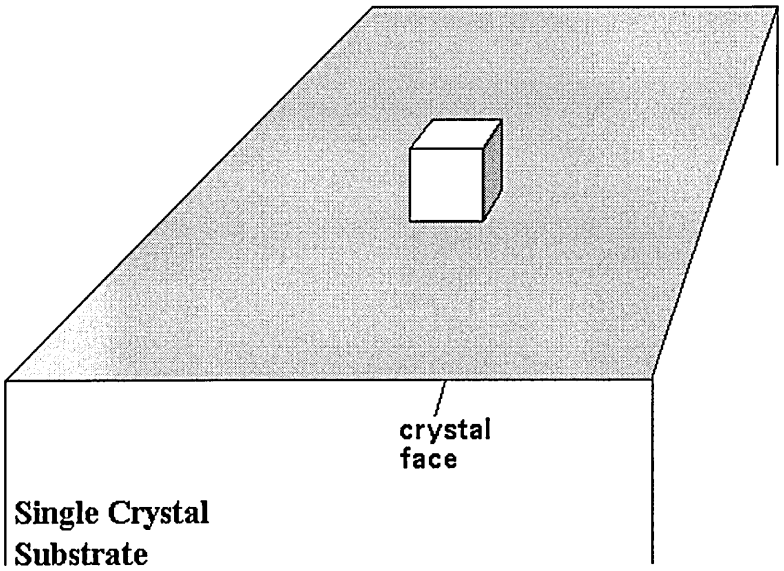

Fig. 2-2: Schematic Drawing of the three-dimensional Electrocrystallization Process of an Atom on a single Crystal Substrate (Island Growth).

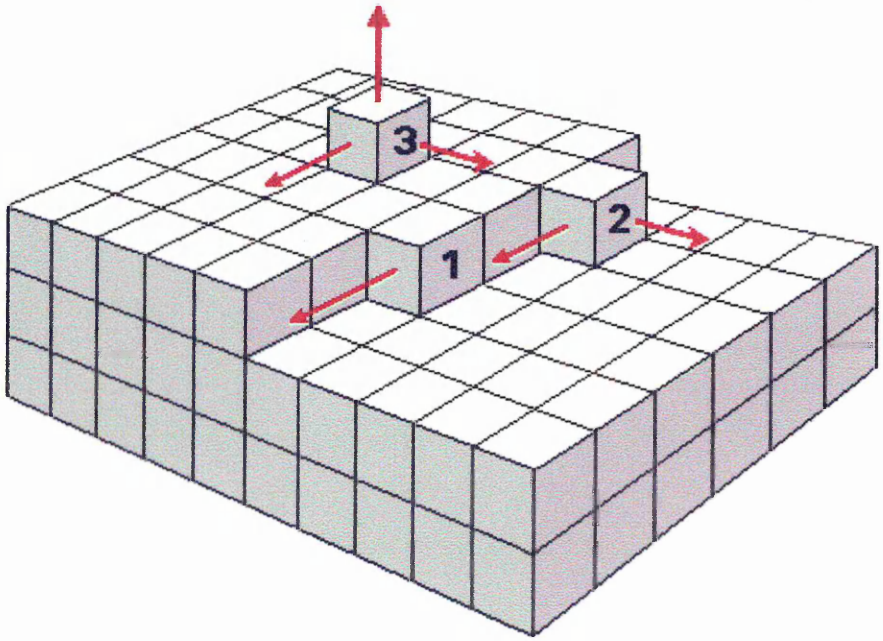

Fig. 2-3: Schematic Drawing of linear Growth at Kink Site '1', two-dimensional Growth '2', and three-dimensional Growth '3'.

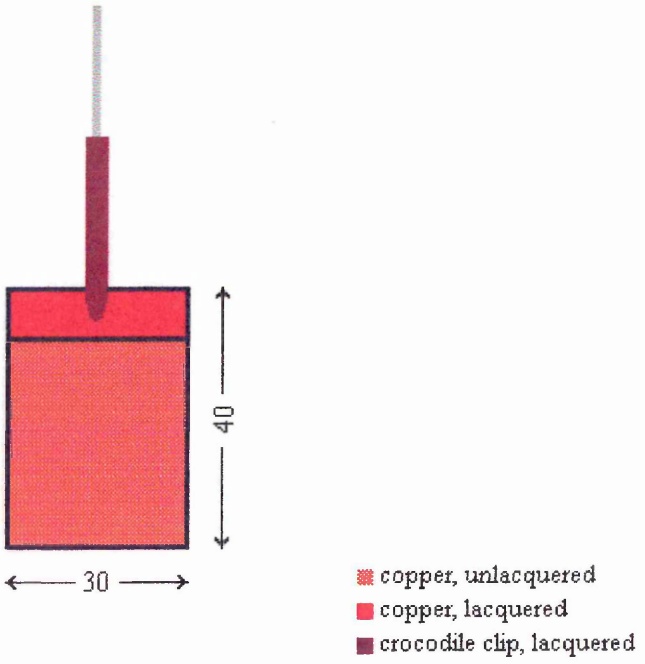

Fig. 3-1: Copper Cathodes, Used for Thick Deposits at Individual Current Densities for subsequent XRD, GDOES, EDX Investigations.

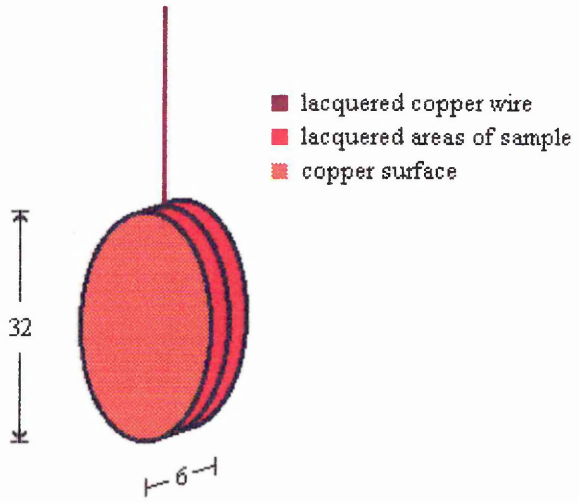

Fig. 3-2: Copper Disc Cathodes, Used to Deposit Thin Deposits for Subsequent XRD, GDOES, EDX Investigations.

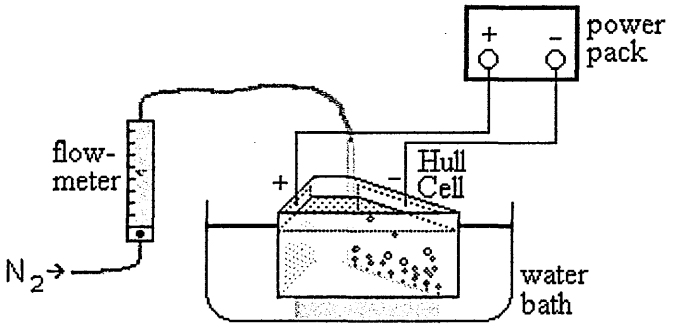

Fig. 3-3: Schematic Diagram of Experimental Electroplating Set-up with the Hull Cell.

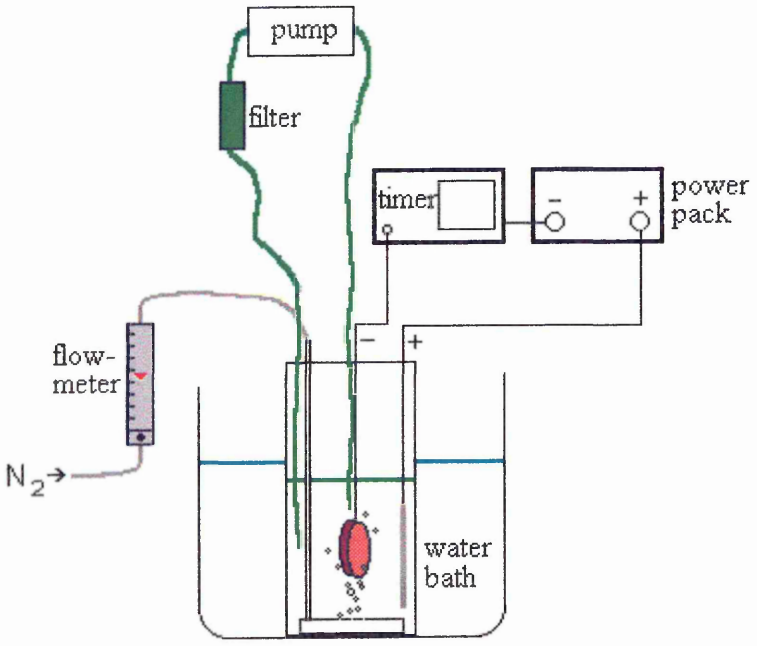

Fig. 3-4: Schematic Diagram of Experimental Electroplating Set-up.

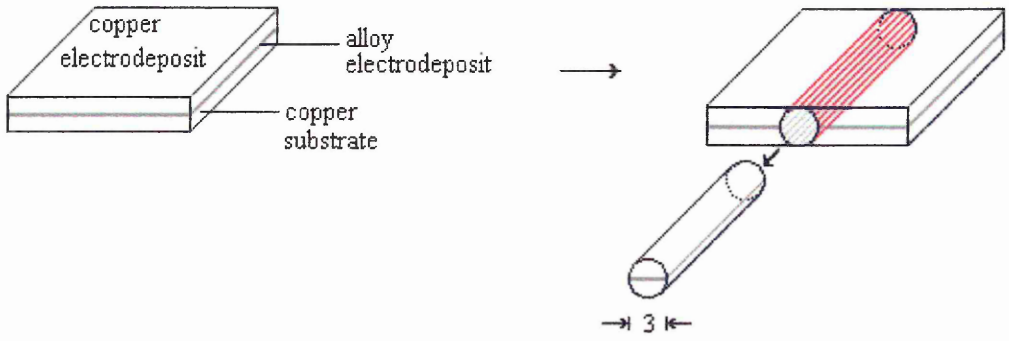

Fig. 3-5: Spark Erosion of a Cylinder.

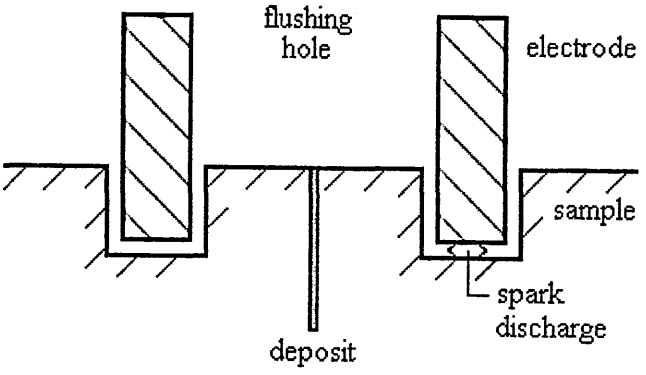

Fig. 3-6: Cross-sectional View of Spark Erosion Process.

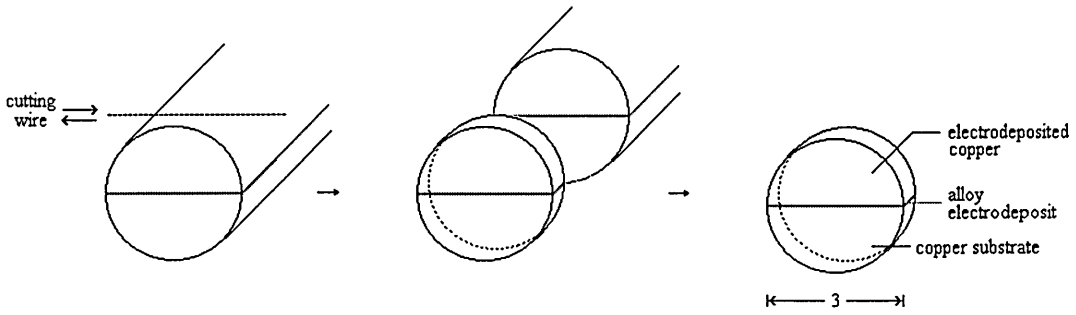

Fig. 3-7: Cutting off Discs.

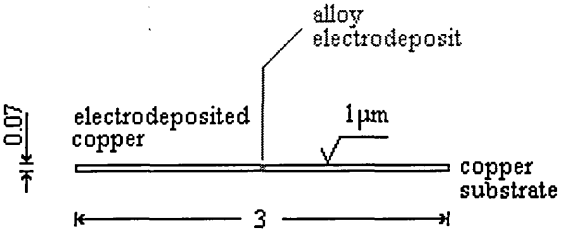

Fig. 3-8: Ground 3 mm Diameter Disc, Ready for Dimpling.

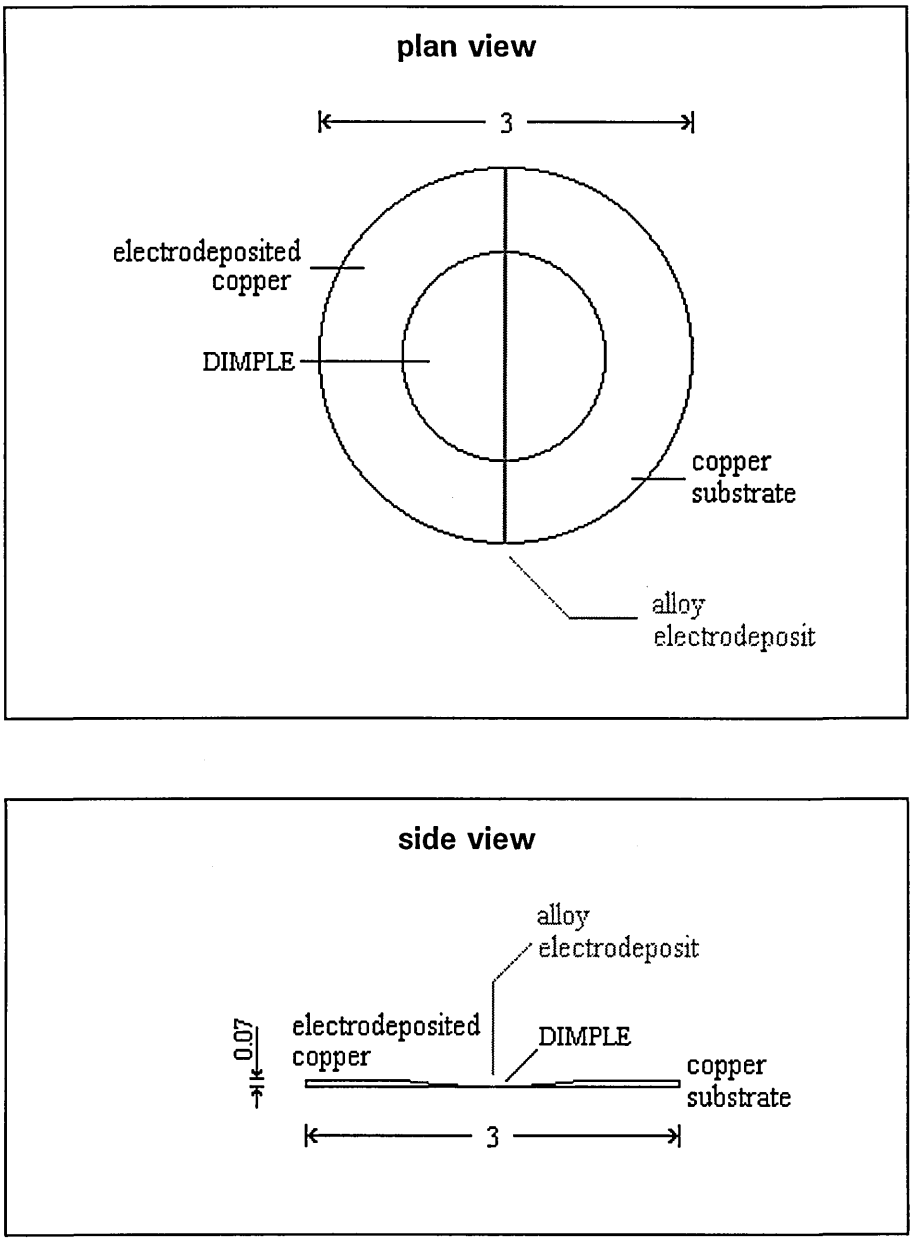

Fig. 3-9: Dimpled 3 mm Diameter Disc.

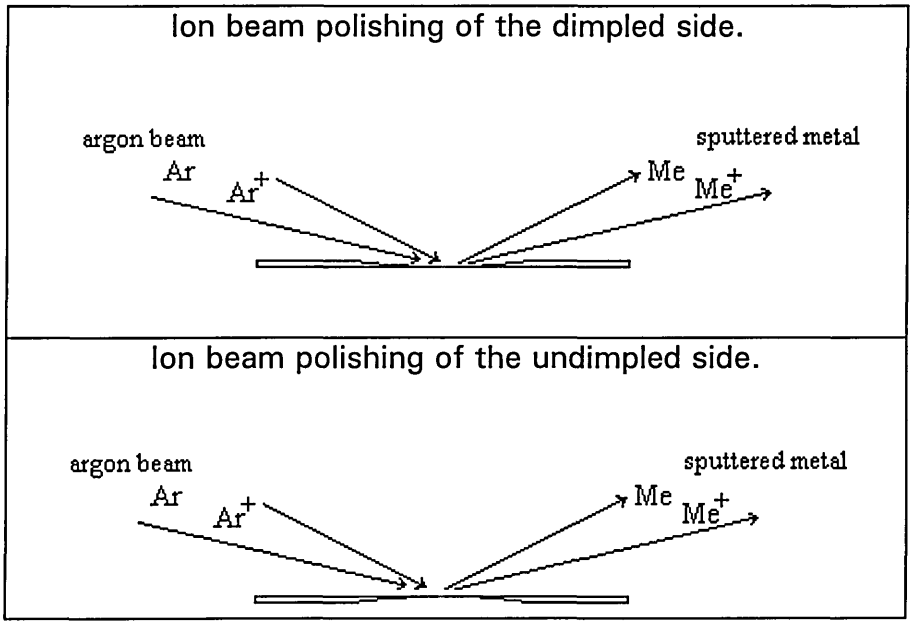

Fig. 3-10: Ion Beam Thinning.

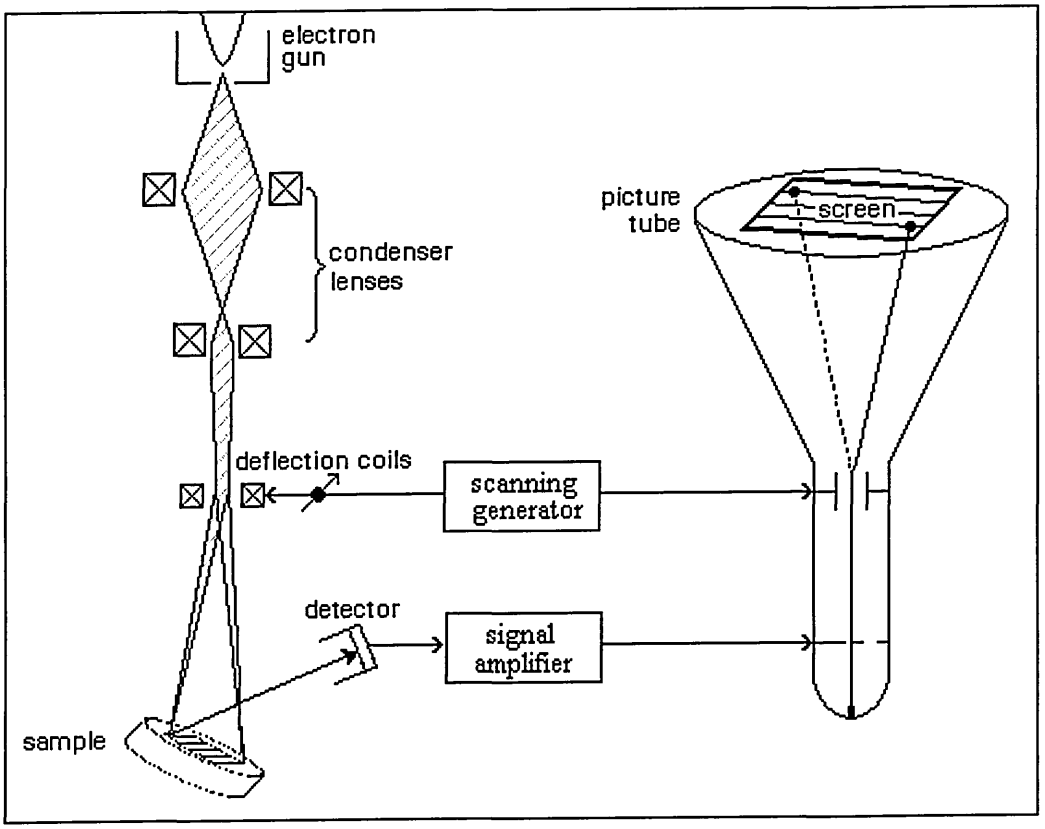

Fig. 3-11: Schematic Diagram of the SEM [81].

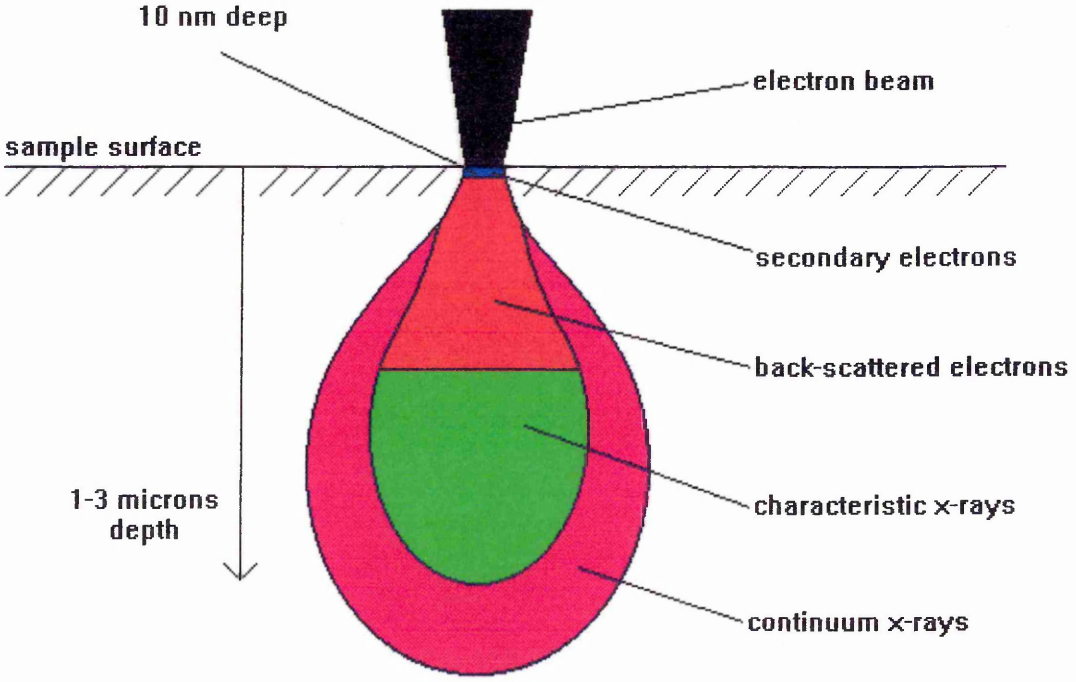

Fig. 3-12 [82]: Schematic Diagram of Excitation Volume for Major SEM Sample Emissions.

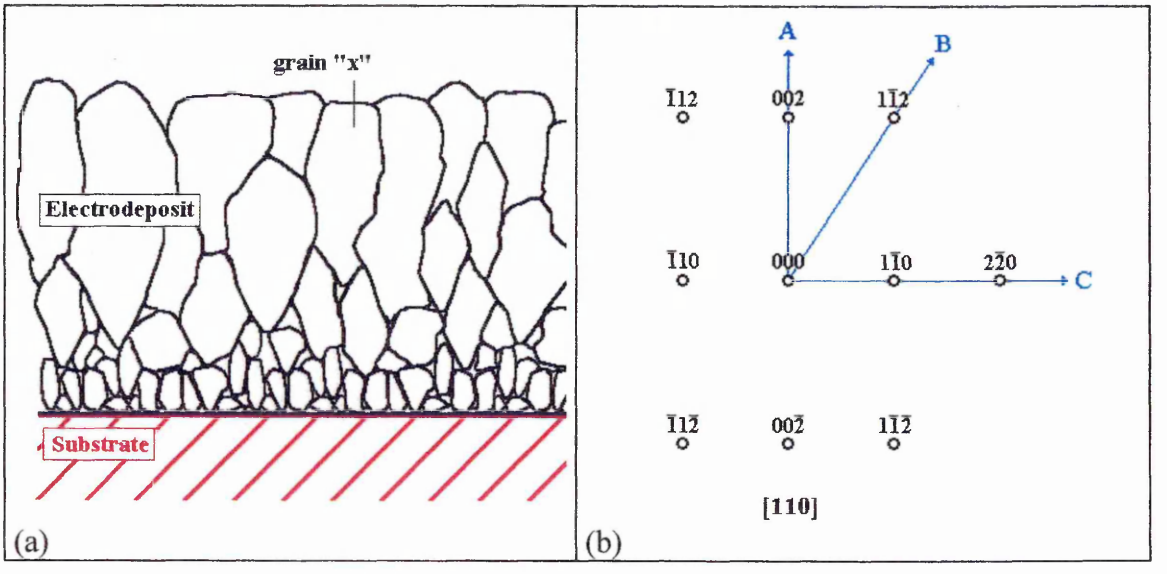

Fig. 3-13: a) Schematic Representation of a Cross-Sectional Transmission Electron Micrograph of a bcc Nickel-Iron Electrodeposit on a Copper Substrate.
b) Schematic Representation of an Electron Diffraction Pattern from Grain 'x' in a).

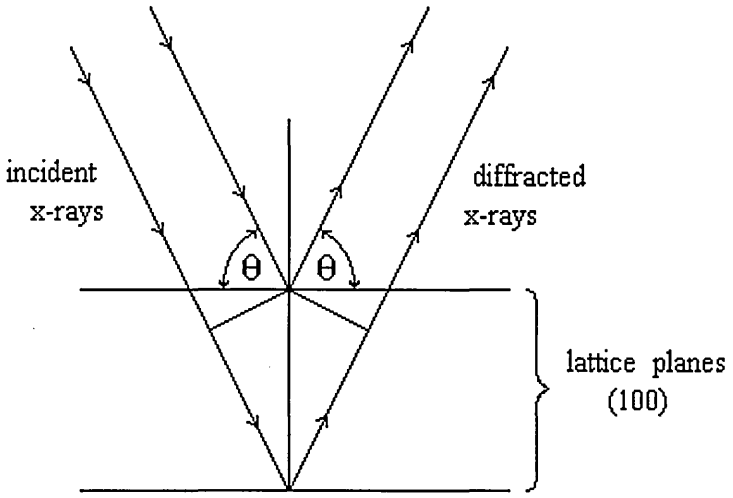

Fig. 3-14: Diffraction of X-rays by Lattice Planes.

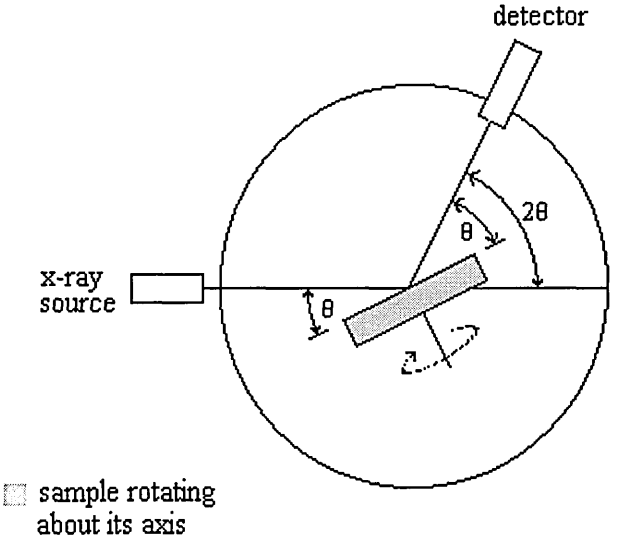

Fig. 3-15: X-ray Spectrometer Operated under Bragg-Brentano Conditions.

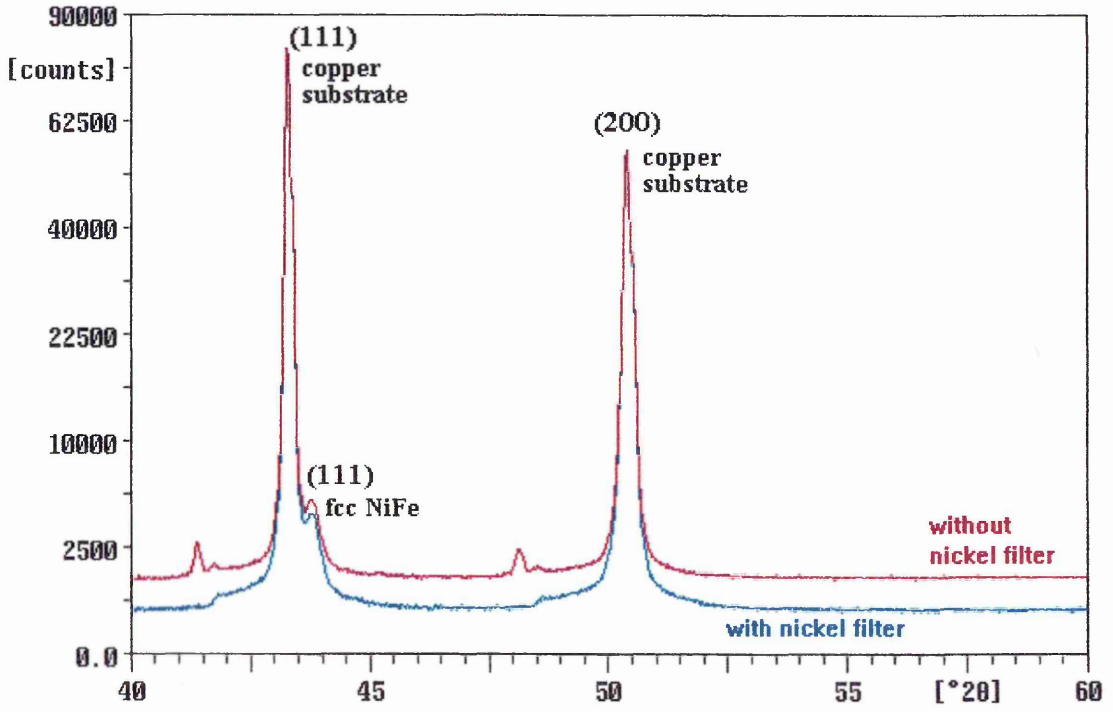

Fig. 3-16: X-ray Diffraction Spectra of Nickel-Iron Electrodeposit on Copper Substrate. Filtering Monochromatic CuK_{α} Radiation Through a Nickel Foil Resulted in Lower Background Noise.

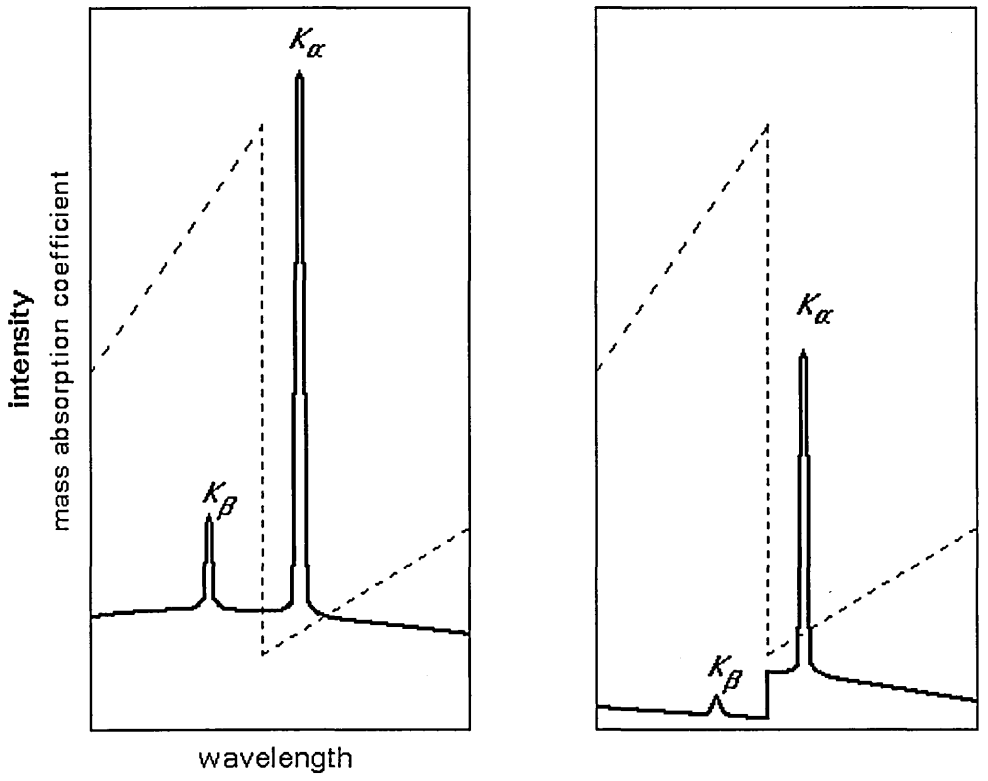

(a) No filter *(b) Nickel filter*

Fig. 3-17[87]: Schematic Comparison of the Spectra of Copper Radiation *(a)* Before and *(b)* After Passage Through a Nickel Filter. The Dashed Line Is the Mass Absorption Coefficient of Nickel.

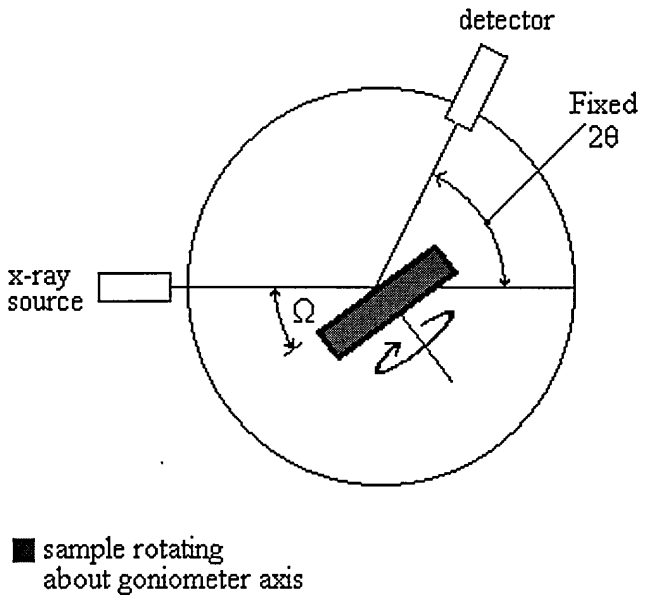

Fig. 3-18: X-ray Spectrometer operated under Omega Scan Conditions.

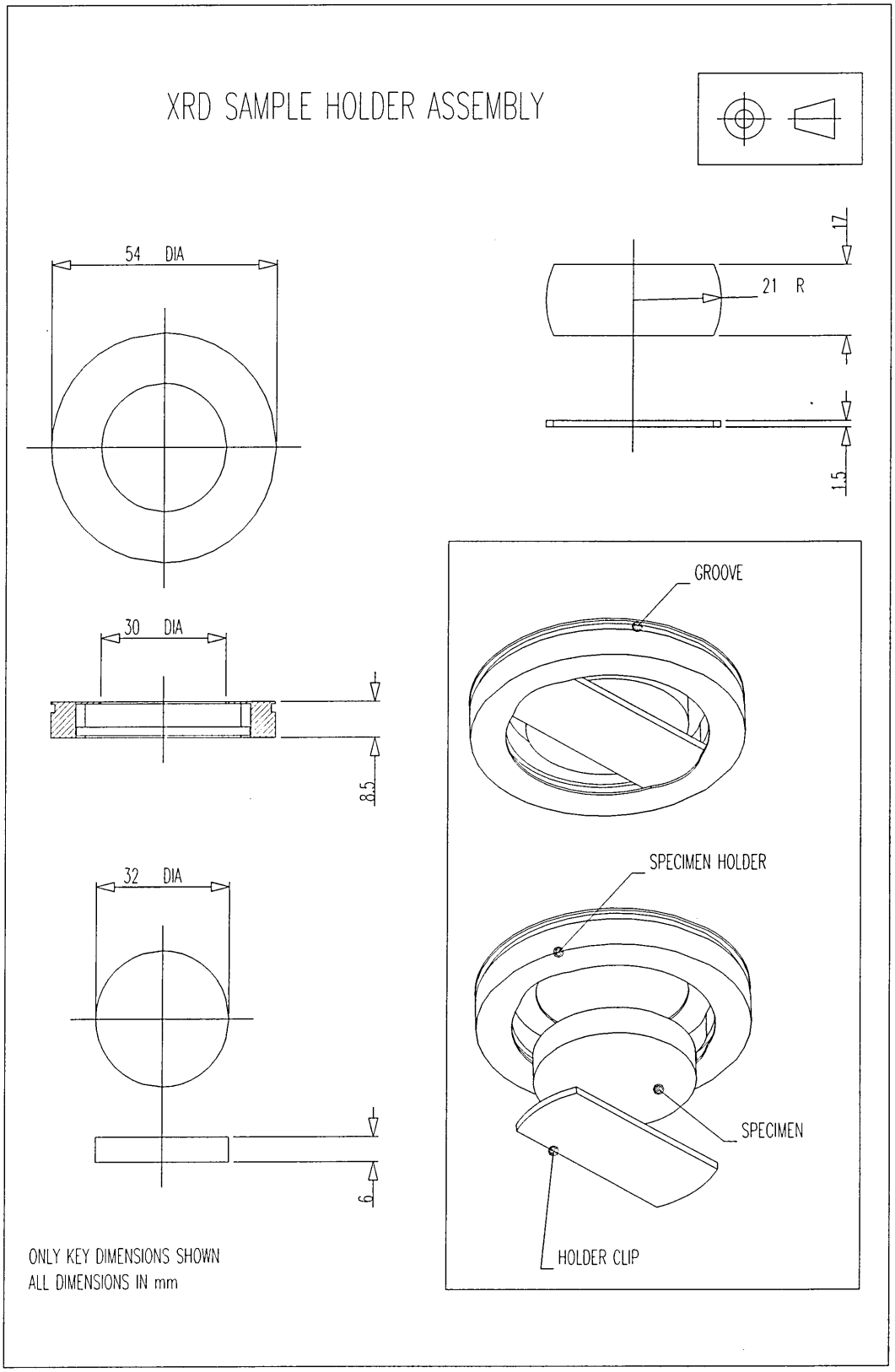

Fig. 3-19: Specimen Holder Assembly for X-ray Diffraction Investigations of Disc Samples.

Fig. 4-1: Surface Morphology of Deposit Produced in NiFe Solution 4 at 10 mA cm^{-2}.

200 µm

Fig. 4-2: Surface Morphology of Deposit Produced in NiFe Solution 4 at 30 mA cm^{-2}.

10 µm

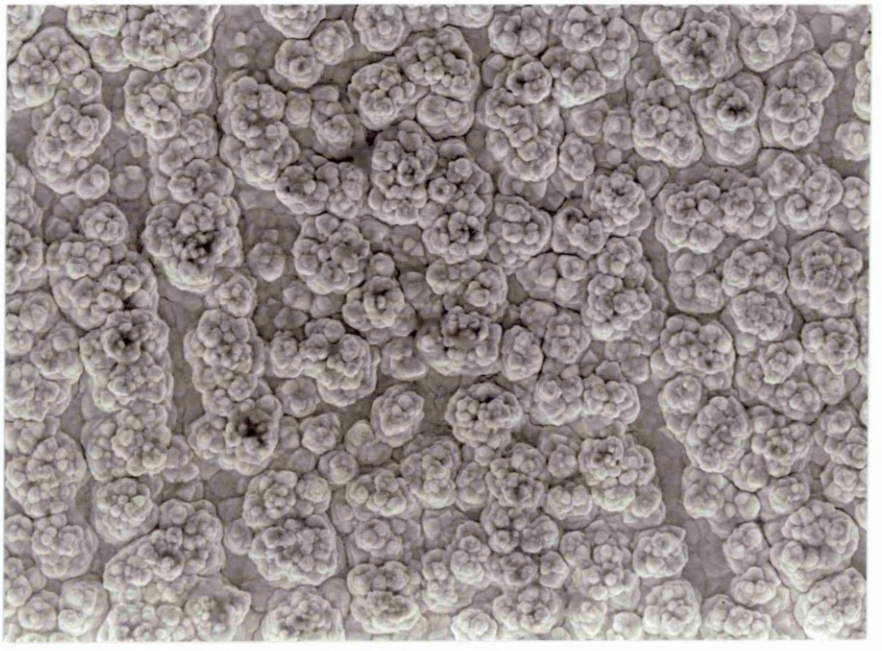

Fig. 4-3: Surface Morphology of Deposit Produced in NiZn Solution 8 at 10 mA cm^{-2}.

1 µm

Fig. 4-4: Surface Morphology of Deposit Produced in NiZn Solution 8 at 10 mA cm^{-2}.

2 µm

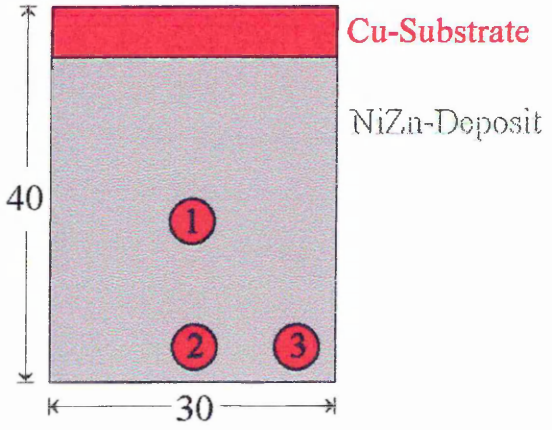

Fig. 4-5: Schematic Diagram of Nickel-Zinc Deposited Sample, Analyzed Areas Indicated with Numbers.

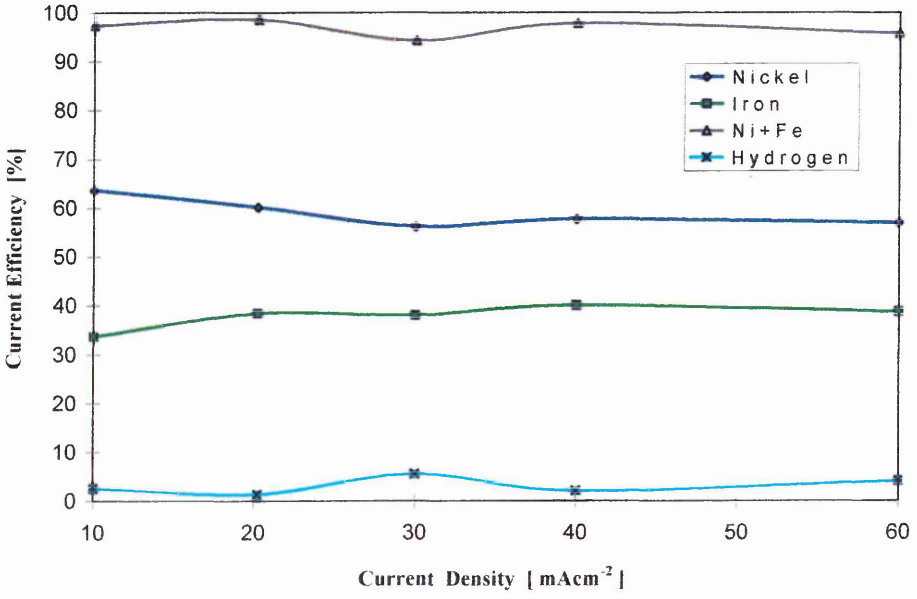

Fig. 4-6: Partial Current Efficiencies of Nickel-Iron Solution 1 at Individual Current Densities Using Compositional Results from EDX.

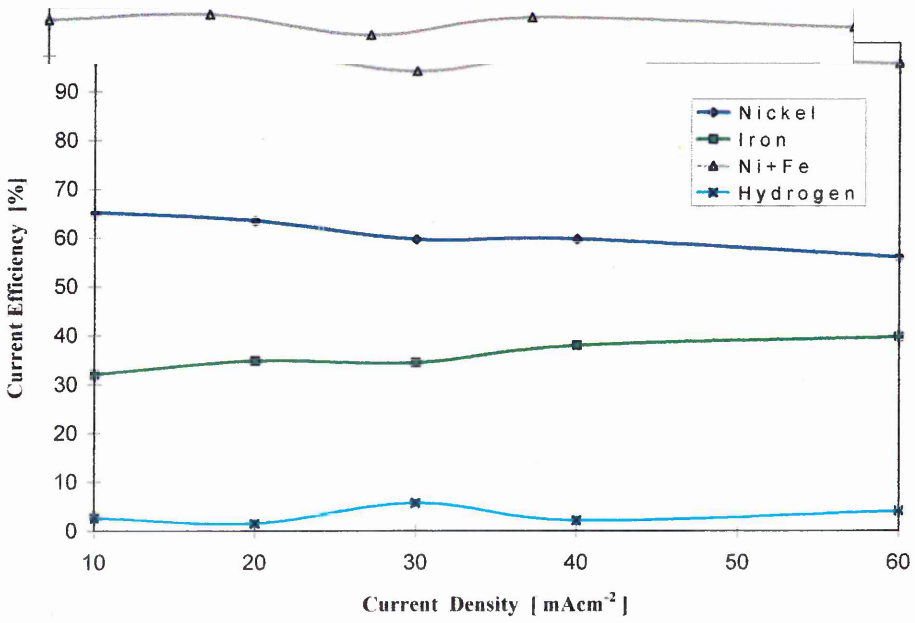

Fig. 4-7: Partial Current Efficiencies of Nickel-Iron Solution 1 at Individual Current Densities Using Compositional Results from GDOES.

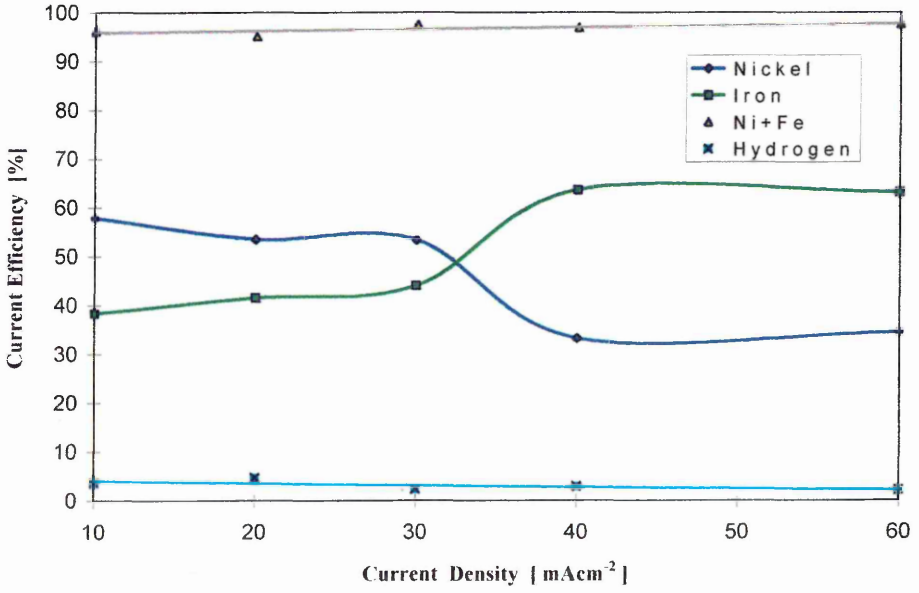

Fig. 4-8: Partial Current Efficiencies of Nickel-Iron Solution 3 at Individual Current Densities Using Compositional Results from GDOES.

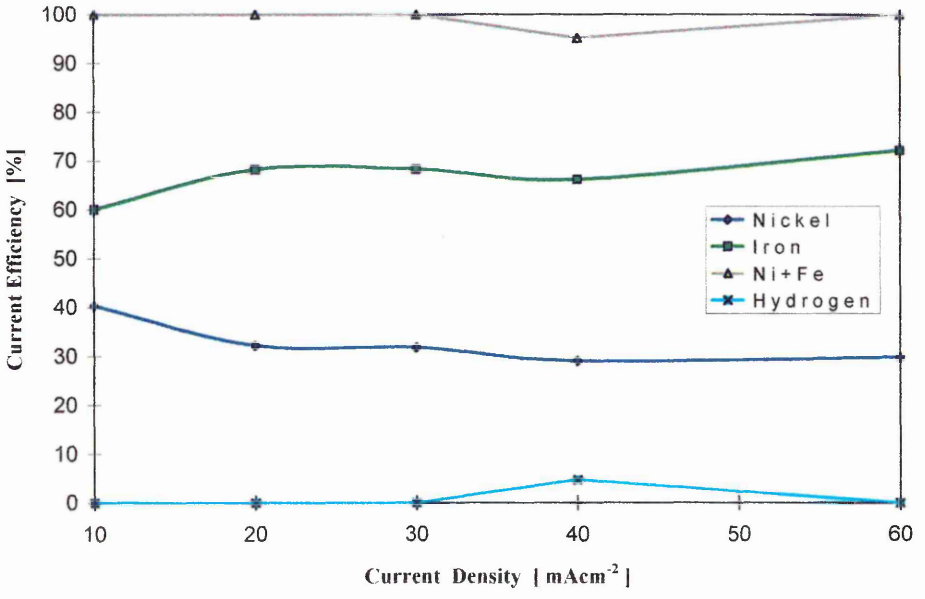

Fig. 4-9: Partial Current Efficiencies of Nickel-Iron Solution 4 at Individual Current Densities Using Compositional Results from GDOES.

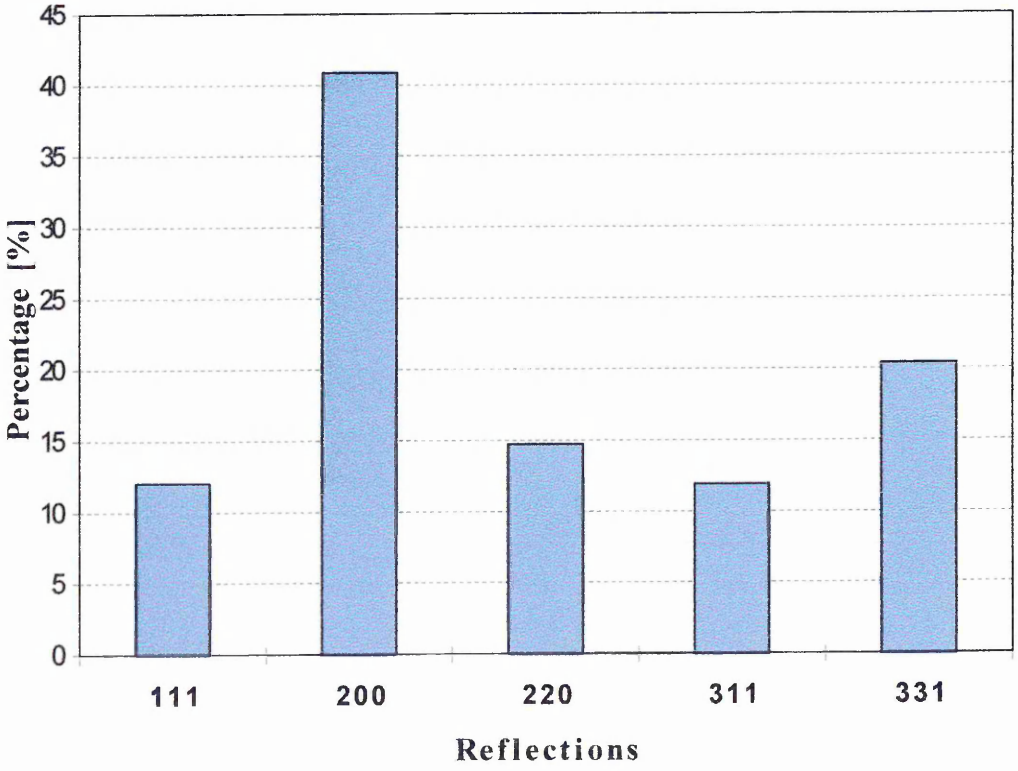

Fig. 4-11: Distribution of Reflecting Planes Detected in the Copper Sheet Substrate.

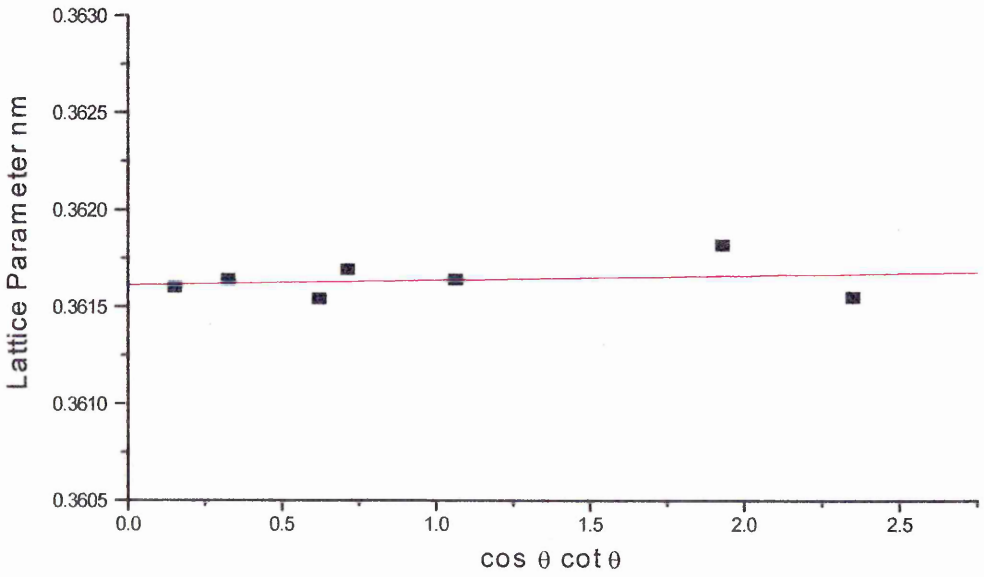

Fig. 4-12: Copper Sheet Substrate: Lattice Parameter [nm] Versus cosθ cotθ; Cohen-Wagner Plot for Extrapolation of Lattice Parameter 'a'.

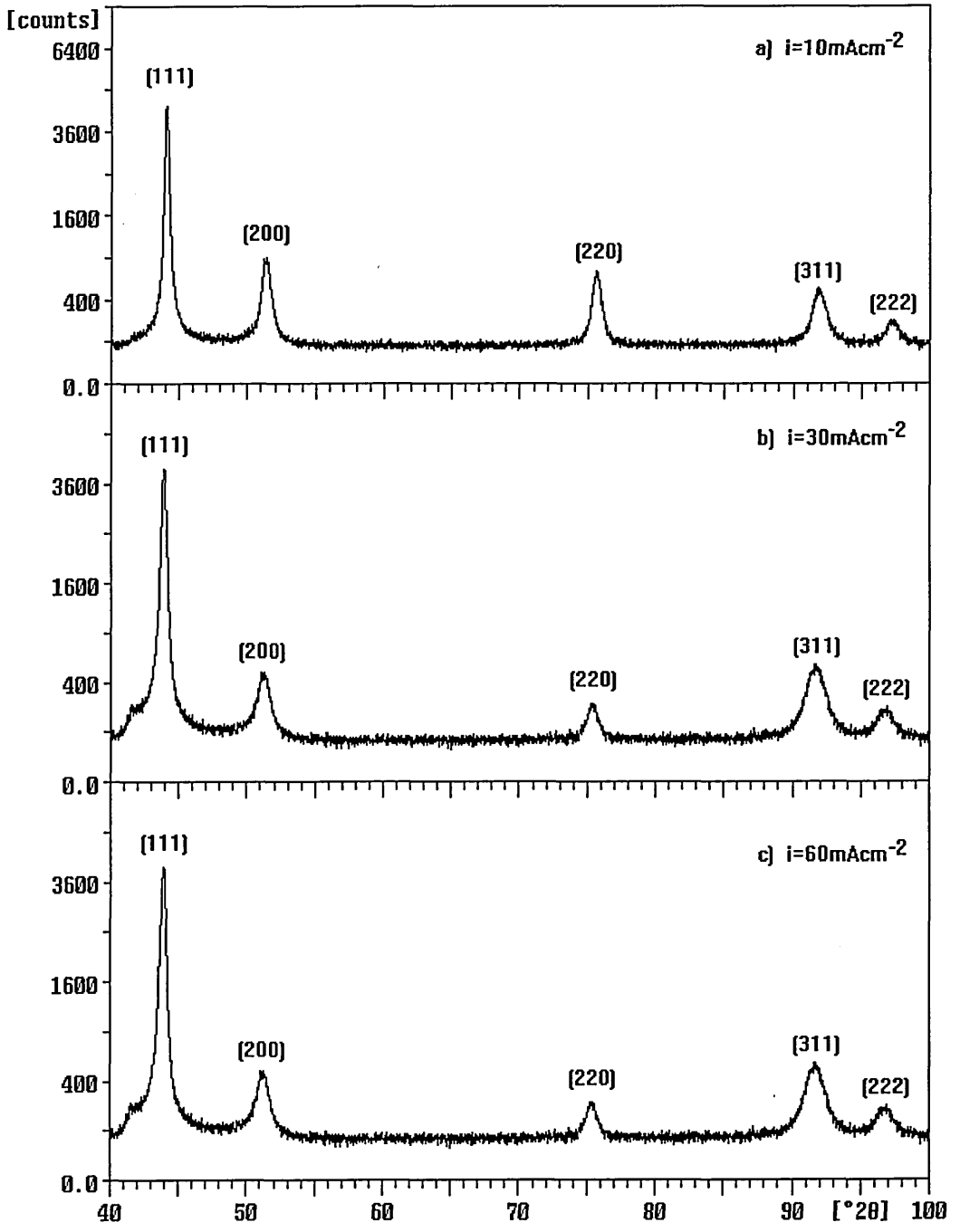

Fig. 4-13: X-Ray Diffraction Spectra of fcc Structured NiFe Deposits Obtained from Solution 1 at Different Current Densities:
a) i = 10 mA cm^{-2}, b) i = 30 mA cm^{-2}, c) i = 60 mA cm^{-2}.

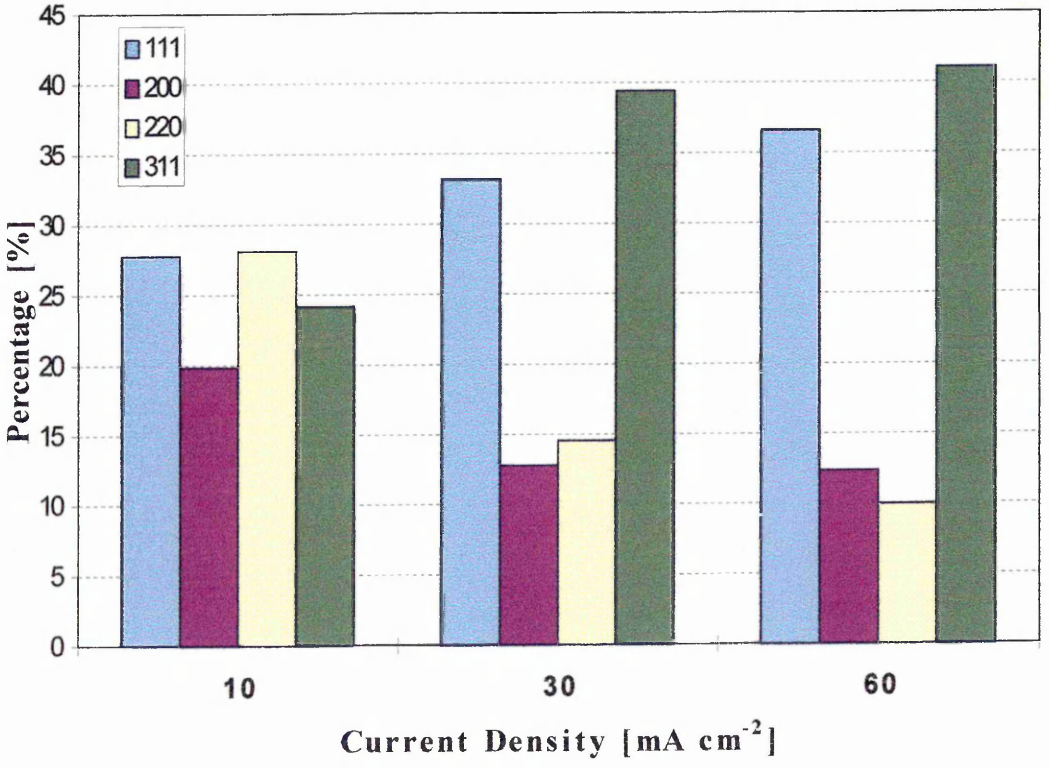

Fig. 4-14: Distribution of Reflections Detected in fcc NiFe Electrodeposits on Copper Sheet Substrates Deposited in NiFe Solution 1 at 10, 30 and 60 mA cm^{-2}.

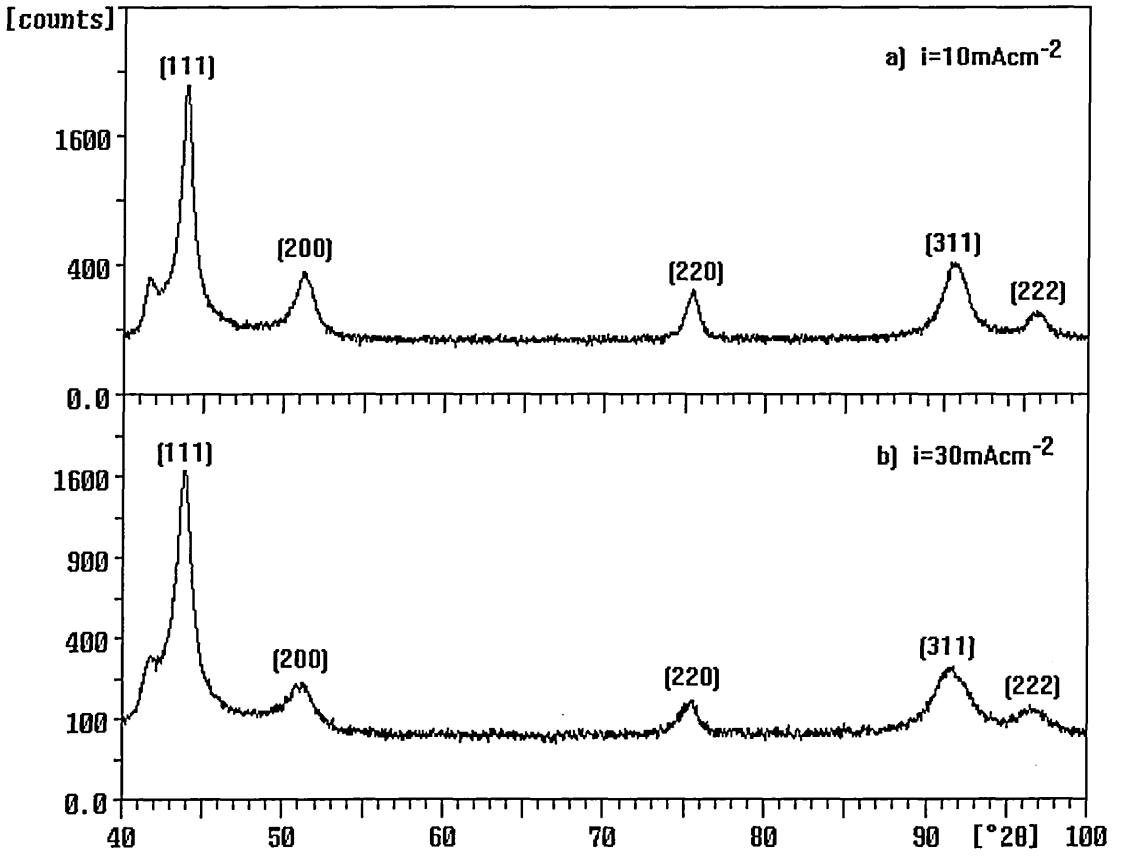

Fig. 4-15: X-Ray Diffraction Spectra of fcc Structured NiFe Deposits Obtained from Solution 3 at Different Current Densities:
a) i = 10 mA cm^{-2}, b) i = 30 mA cm^{-2}.

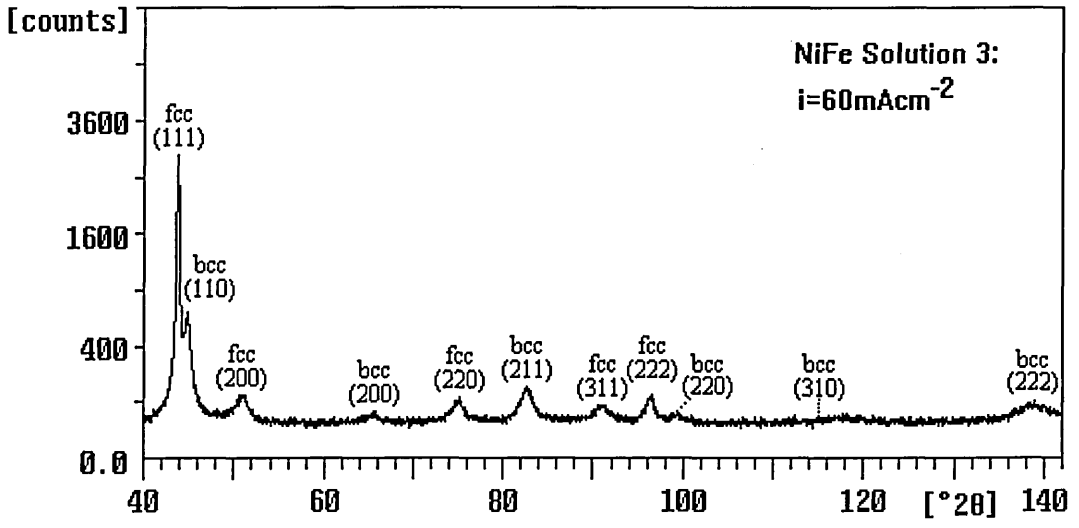

Fig. 4-16: X-Ray Diffraction Spectrum of Mixed fcc/bcc Structured NiFe Deposits Obtained from Solution 3 at i = 60 mA cm^{-2}.

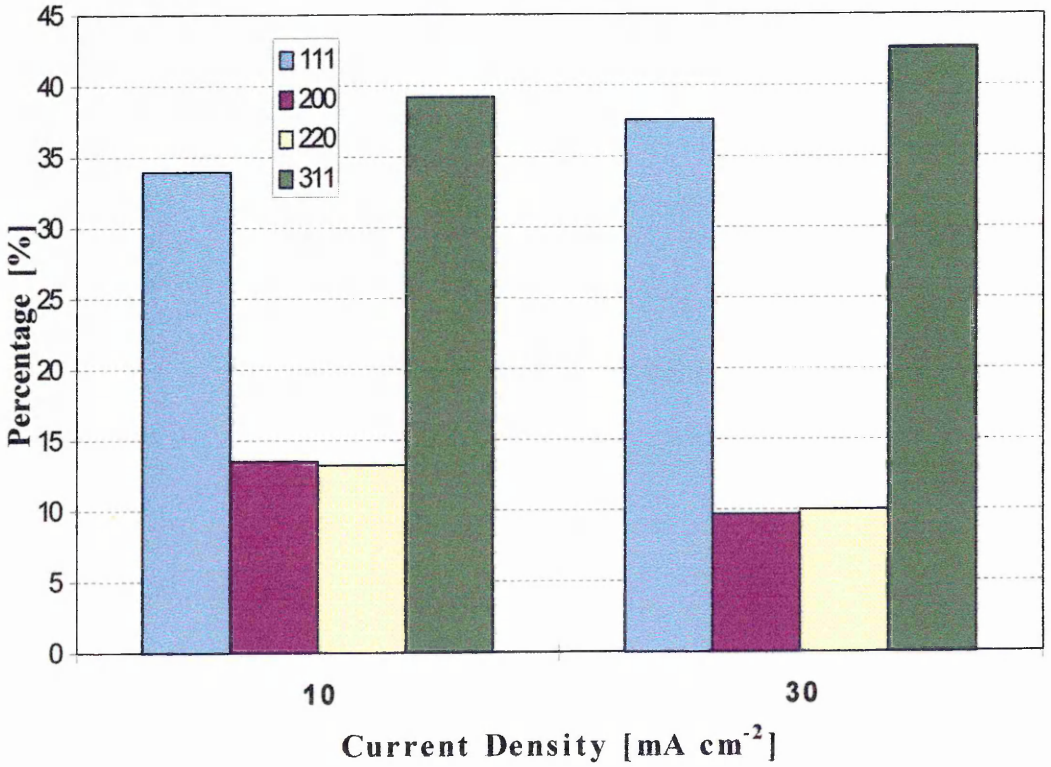

Fig. 4-17: Distribution of Reflections Detected in fcc NiFe Electrodeposits on Copper Sheet Deposited at 10 and 30 mA cm^{-2} in NiFe Solution 3.

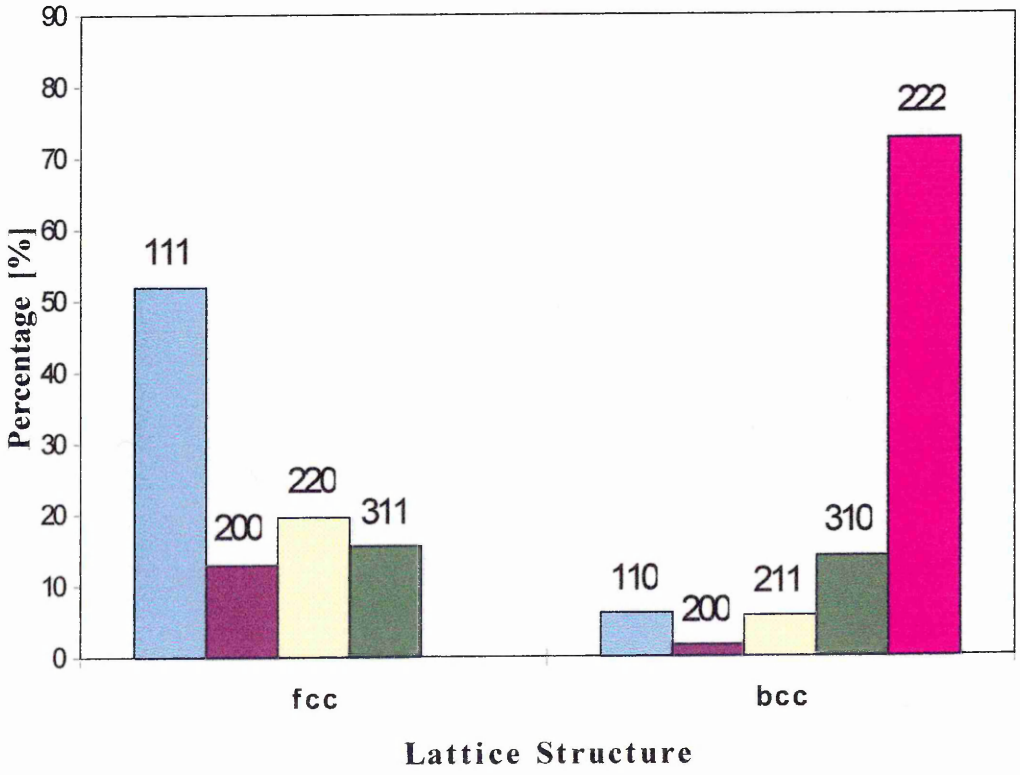

Fig. 4-18: Distribution of Reflections Detected in fcc/bcc NiFe Electrodeposits on Copper Sheet Deposited at 60 mA cm^{-2} in NiFe Solution 3.

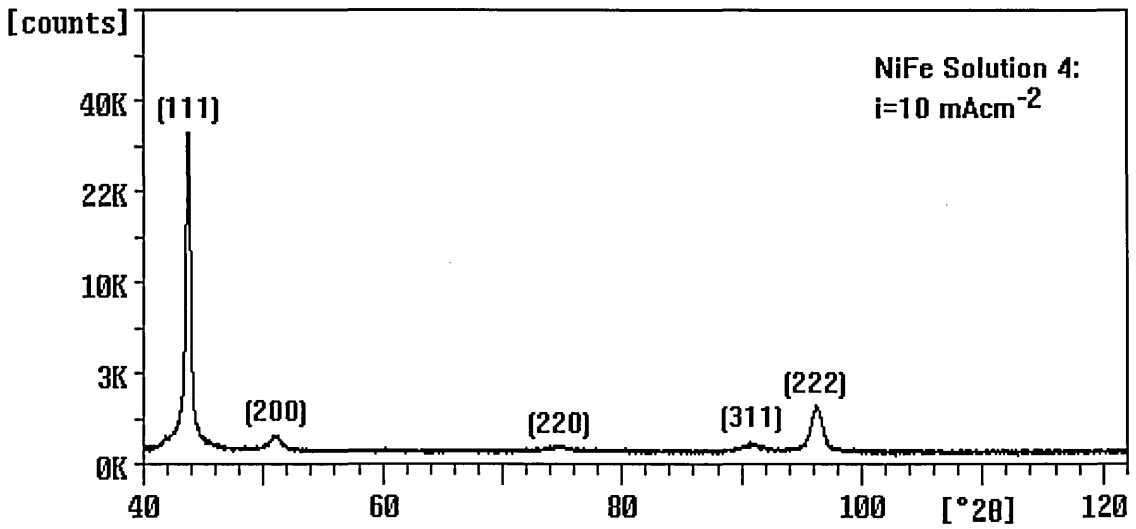

Fig. 4-19: X-Ray Diffraction Spectrum of fcc Structured NiFe Deposits Obtained from Solution 4 (i = 10 mA cm^{-2}).

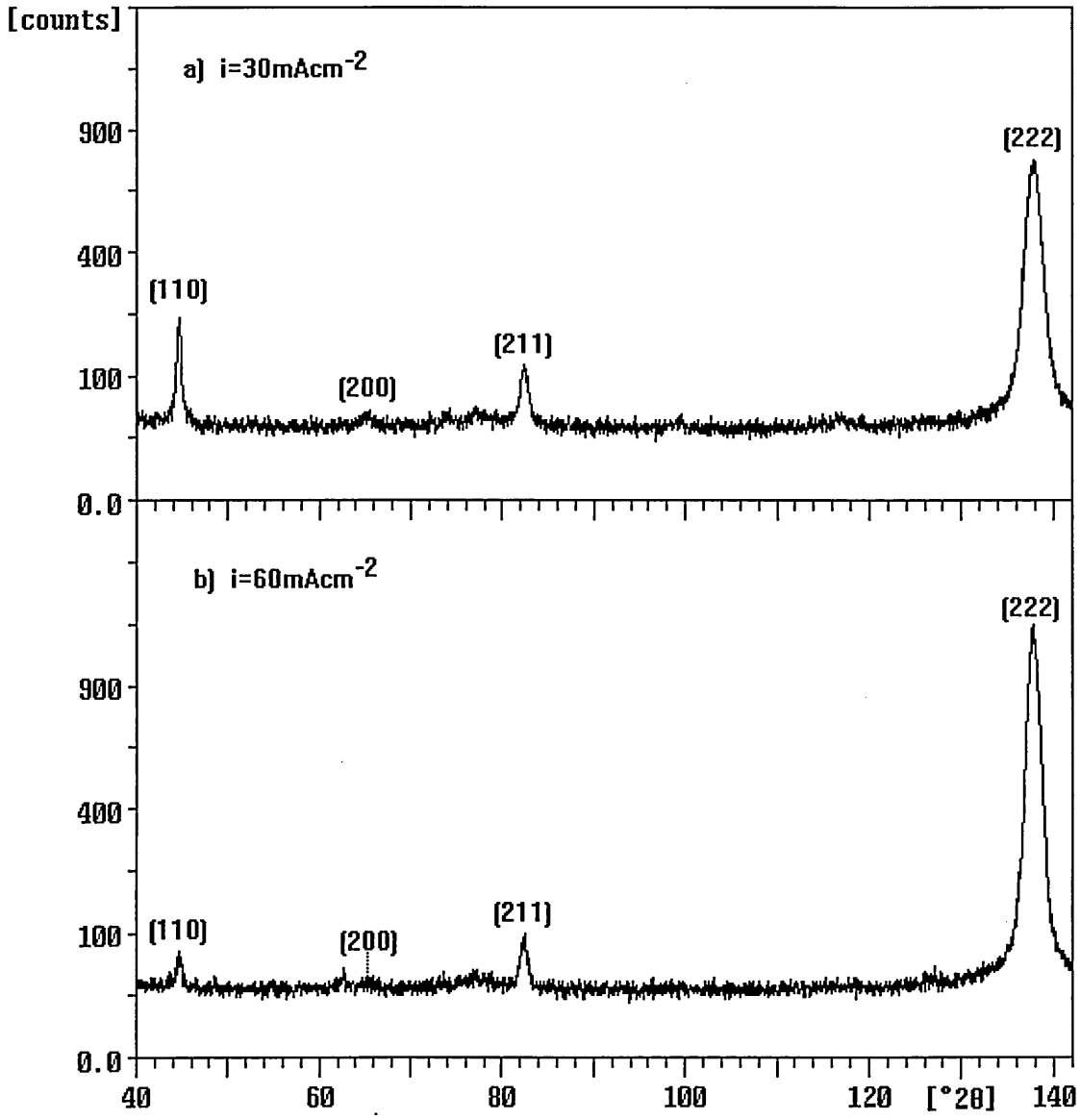

Fig. 4-20: X-Ray Diffraction Spectra of bcc Structured NiFe Deposits Obtained from Solution 4 at Different Current Densities:
a) i = 30 mA cm^{-2}, b) i = 60 mA cm^{-2}.

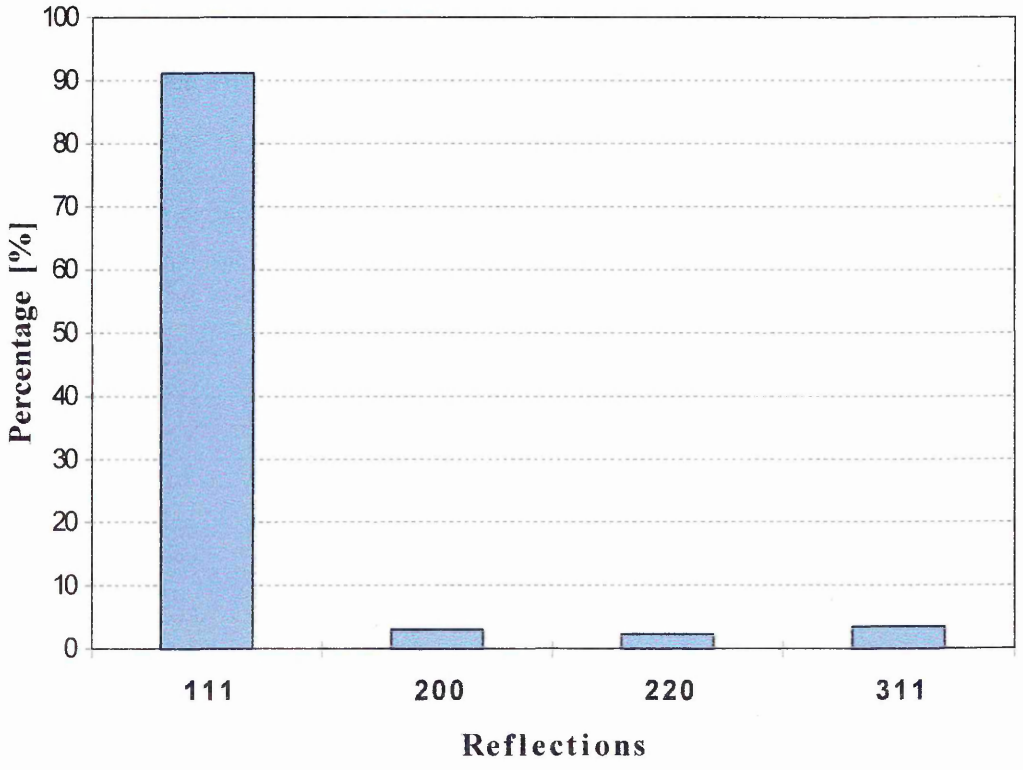

Fig. 4-21: Distribution of Reflections Detected in fcc NiFe Electrodeposit on Copper Sheet Deposited at 10 mA cm^{-2} in NiFe Solution 4.

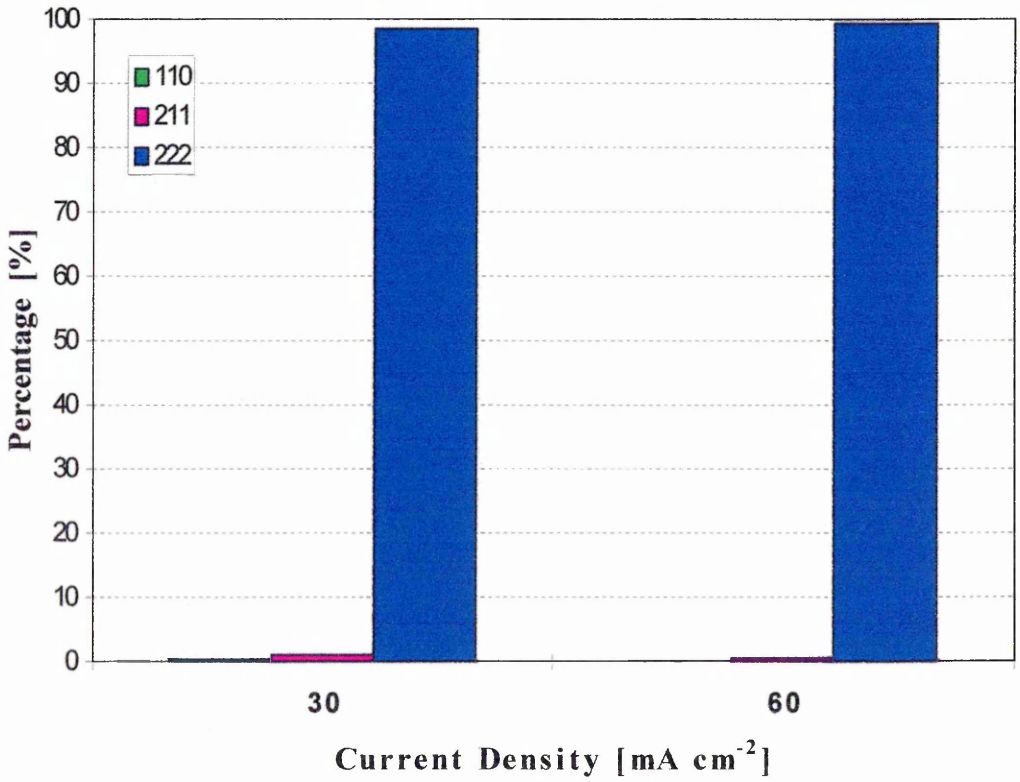

Fig. 4-22: Distribution of Reflections Detected in bcc NiFe Electrodeposit on Copper Sheet Deposited at 30 and 60 mA cm^{-2} in NiFe Solution 4.

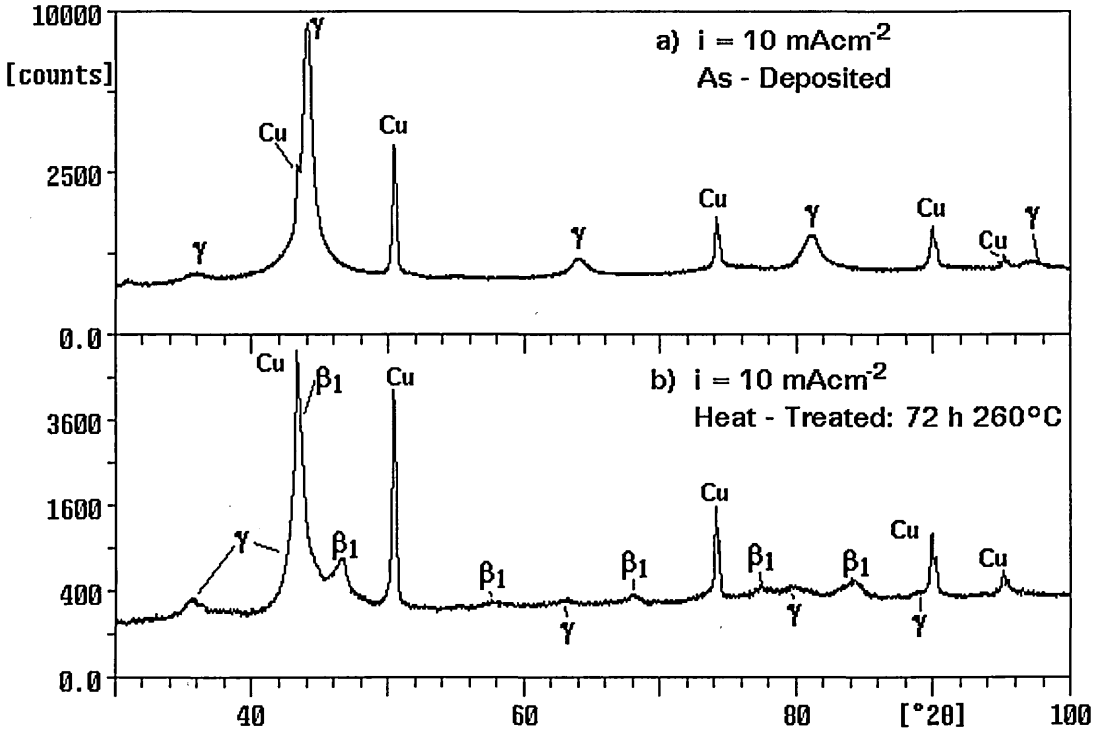

Fig. 4-23: XRD Spectra of Deposit Produced in Nickel-Zinc Solution 8, (i = 10 mA cm^{-2}) in a) As-Deposited, b) Heat-Treated Condition.

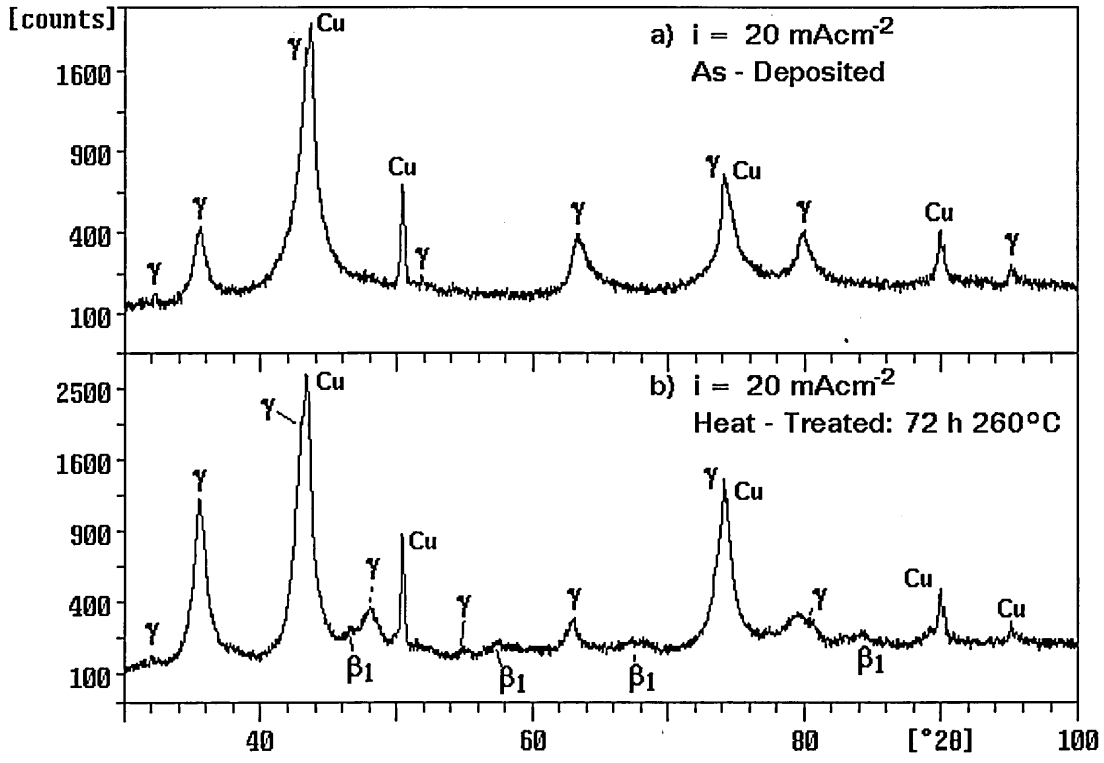

Fig. 4-24: XRD Spectra of Deposit Produced in Nickel-Zinc Solution 8, ($i = 20$ mA cm^{-2}) in a) As-Deposited, b) Heat-Treated Condition.

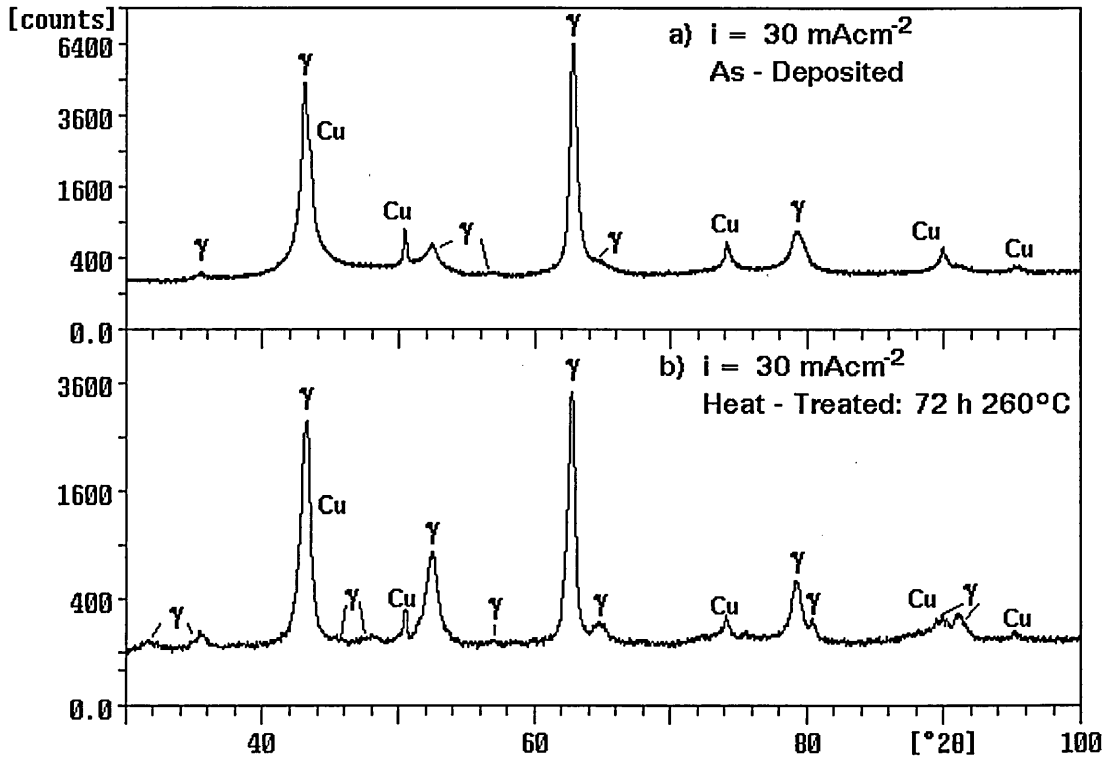

Fig. 4-25: XRD Spectra of Deposit Produced in Nickel-Zinc Solution 8, ($i = 30$ mA cm^{-2}) in a) As-Deposited, b) Heat-Treated Condition.

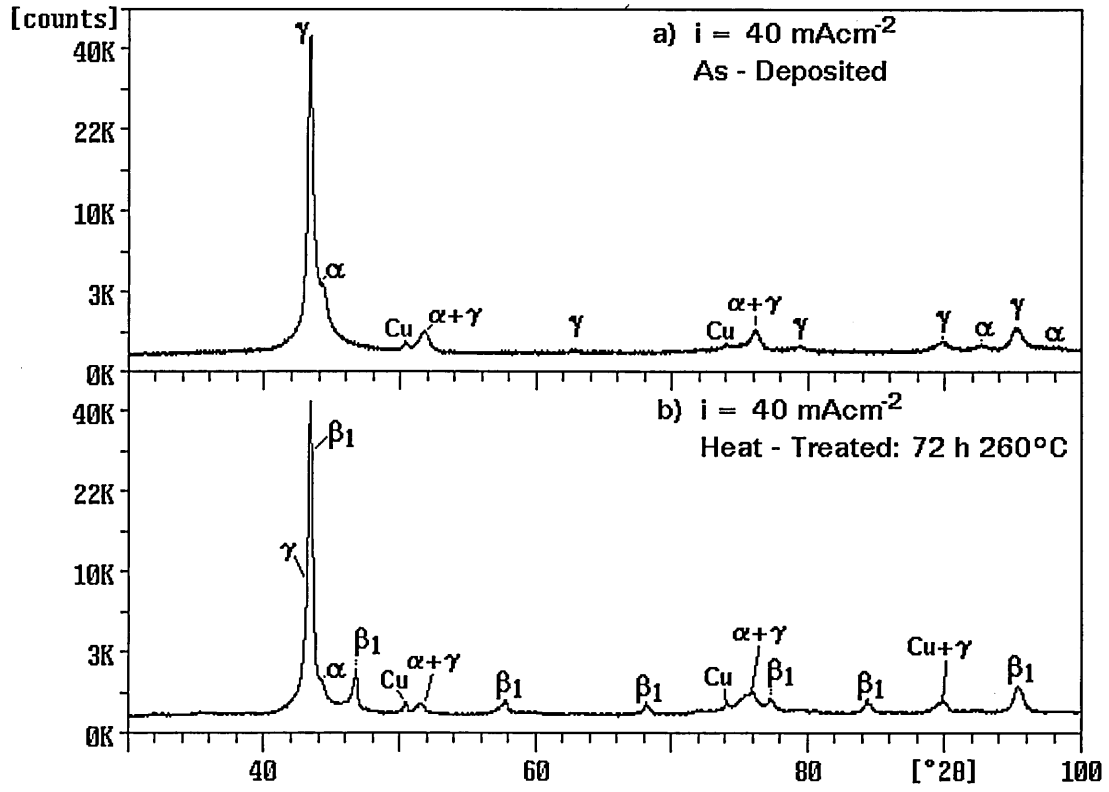

Fig. 4-26: XRD Spectra of Deposit Produced in Nickel-Zinc Solution 8, ($i = 40$ mA cm^{-2}) in a) As-Deposited, b) Heat-Treated Condition.

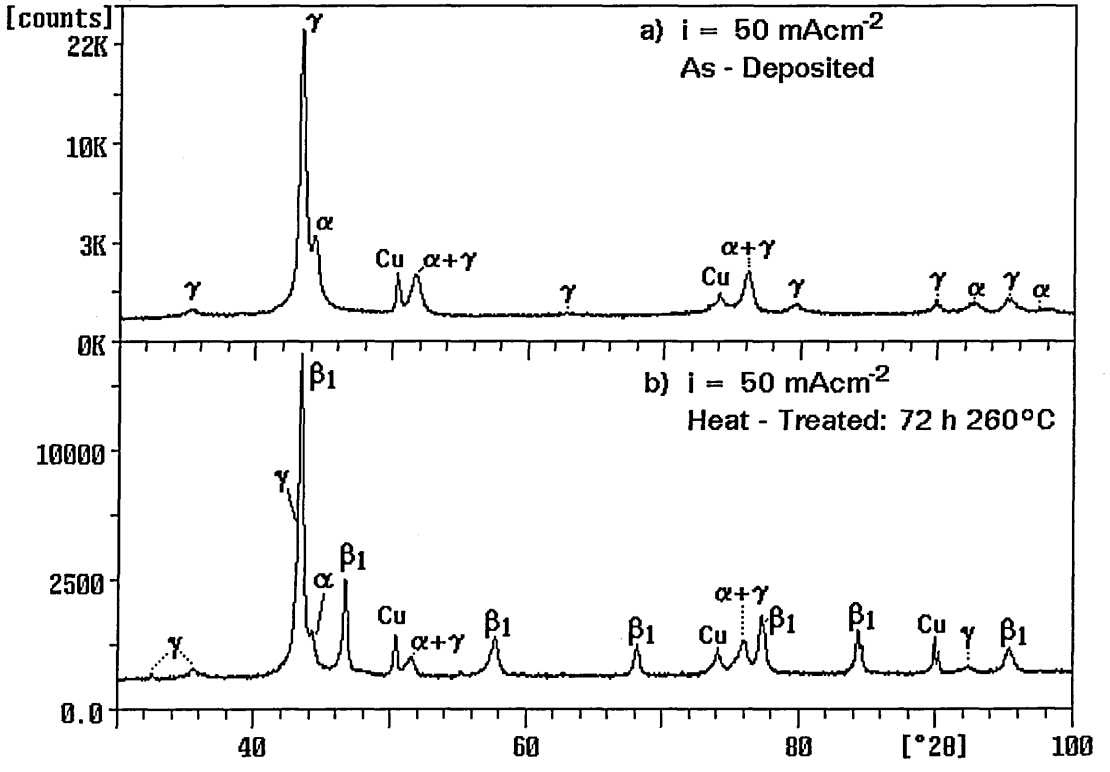

Fig. 4-27: XRD Spectra of Deposit Produced in Nickel-Zinc Solution 8, (i = 50 mA cm^{-2}) in a) As-Deposited, b) Heat-Treated Condition.

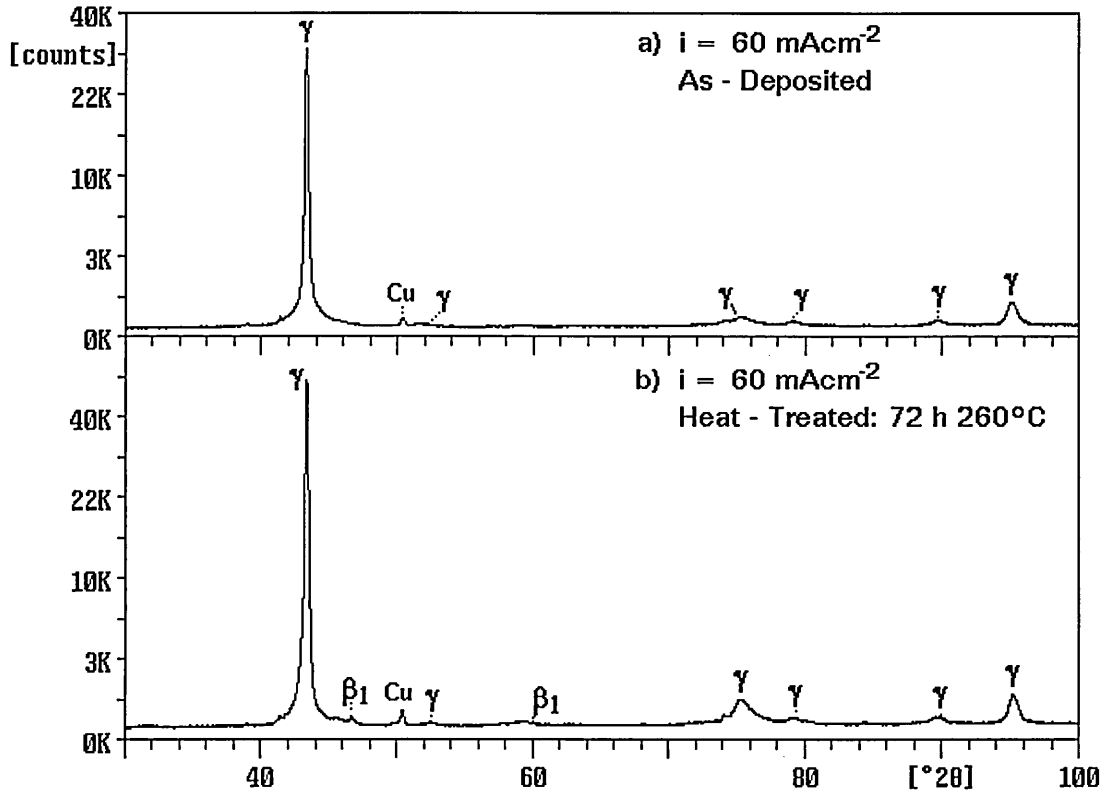

Fig. 4-28: XRD Spectra of Deposit Produced in Nickel-Zinc Solution 8, ($i = 60$ mA cm^{-2}) in a) As-Deposited, b) Heat-Treated Condition.

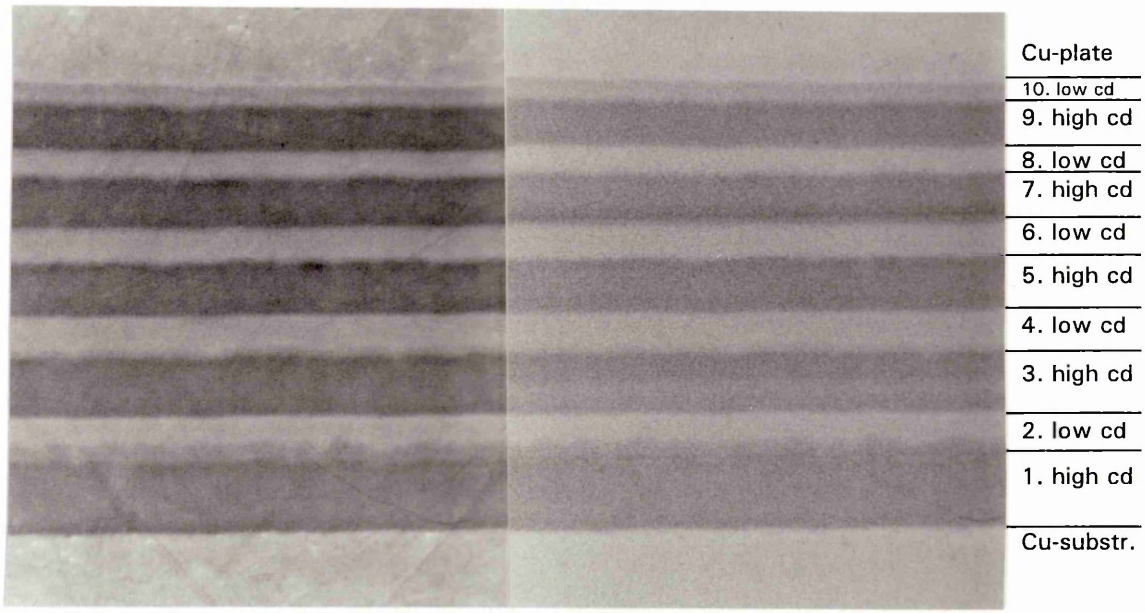

Fig. 4-29:
a) SEI
of Multilayered NiFe Deposit.

b) BSI
of Multilayered NiFe Deposit.

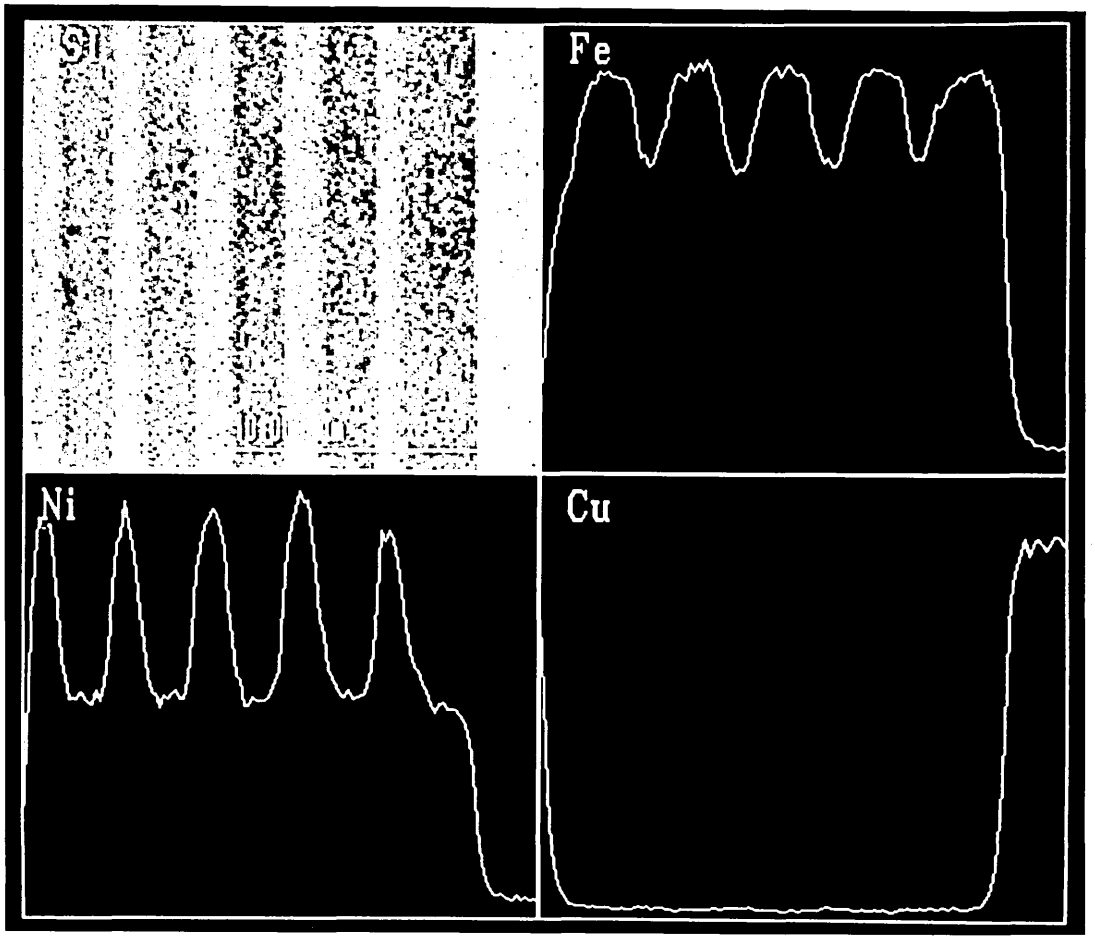

Fig. 4-30: Cross-sectioned Nickel-Iron Electrodeposit.
Digitized BSI (top left).
Energy Dispersive Line-Scans of Multilayered Nickel-Iron Electrodeposit: Iron (top right); Nickel (bottom left); Copper (bottom right).

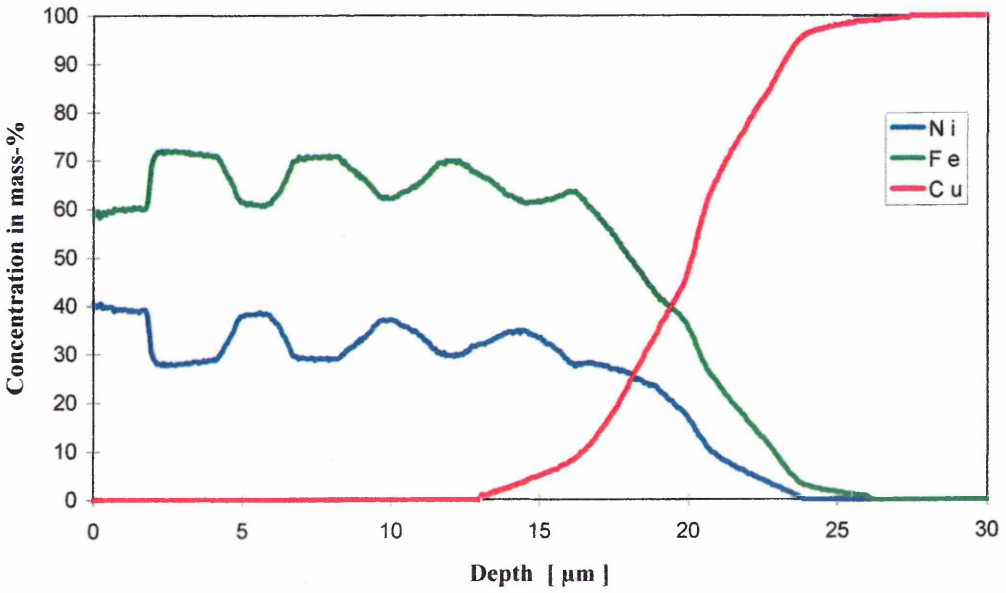

Fig. 4-31: Quantitative Depth Profile of Nickel-Iron Multilayer Obtained by GDOES.

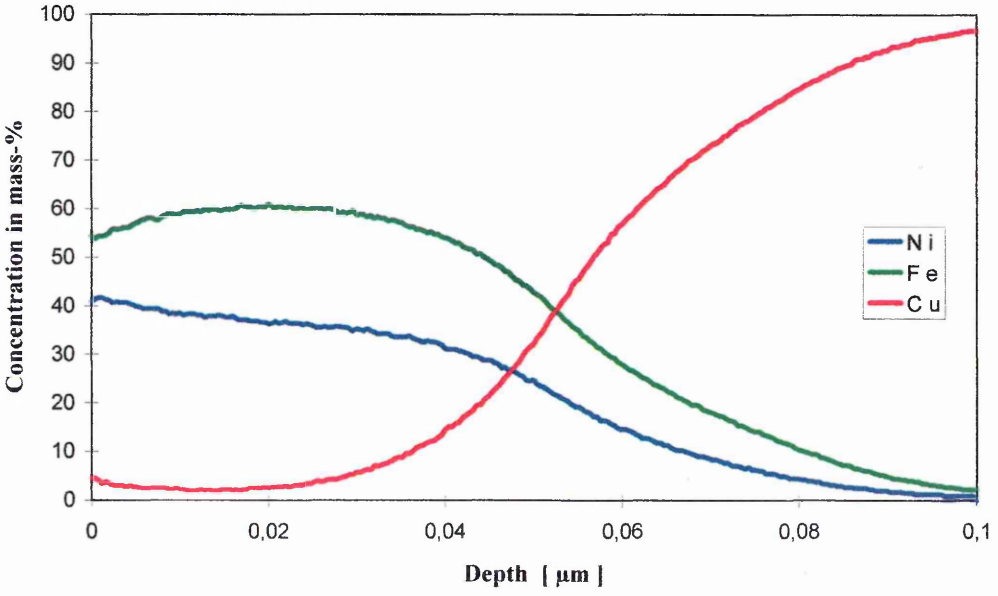

Fig. 4-32: Quantitative Depth Profile of 0.05 µm Thick fcc Nickel-Iron Electrodeposit (i = 10 mA cm^{-2}).

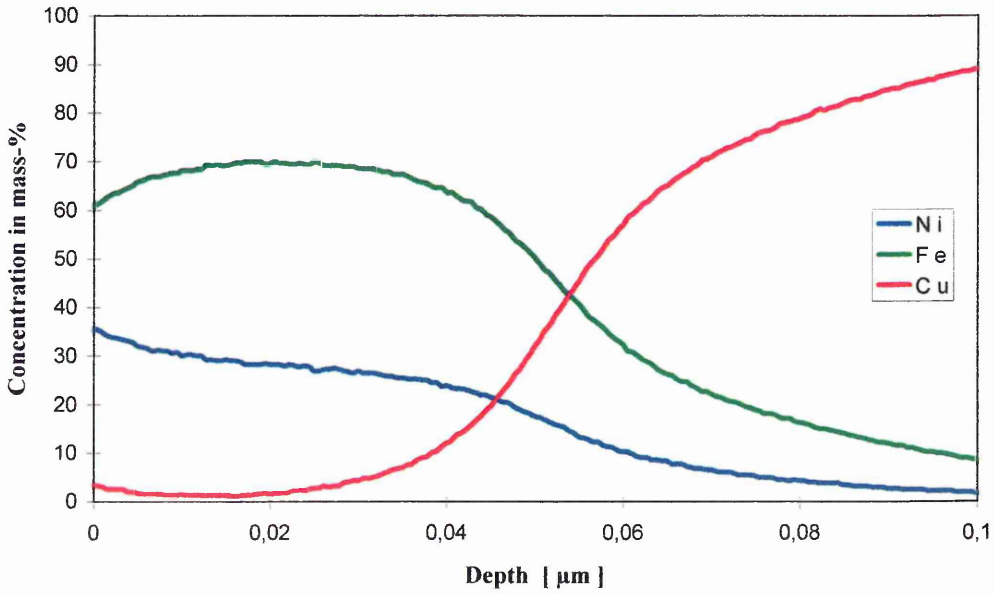

Fig. 4-33: Quantitative Depth Profile of 0.05 µm Thick bcc Nickel-Iron Electrodeposit (i = 60 mA cm^{-2}).

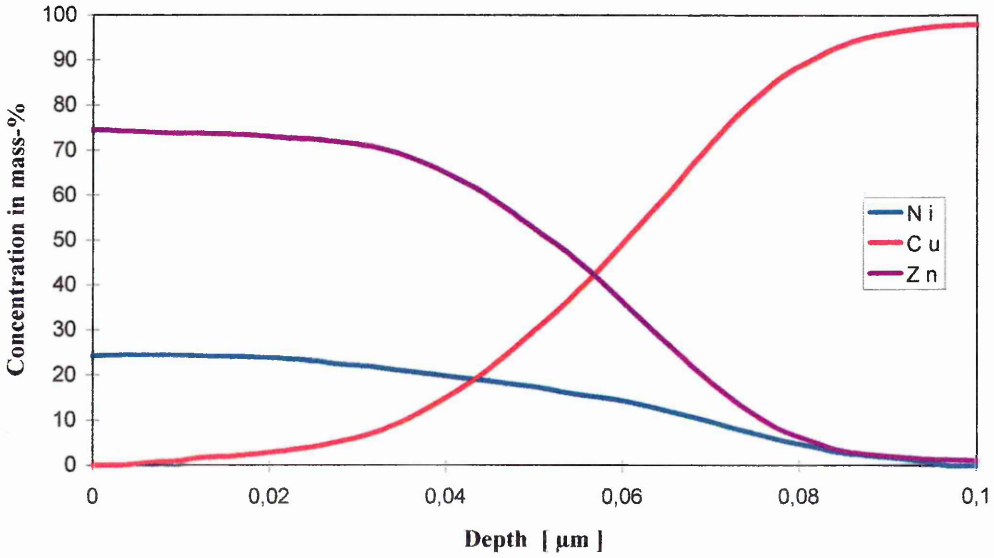

Fig. 4-34: Quantitative Depth Profile of 0.05 µm Thick Nickel-Zinc Electrodeposited with 10 mA cm^{-2} onto Copper Substrate.

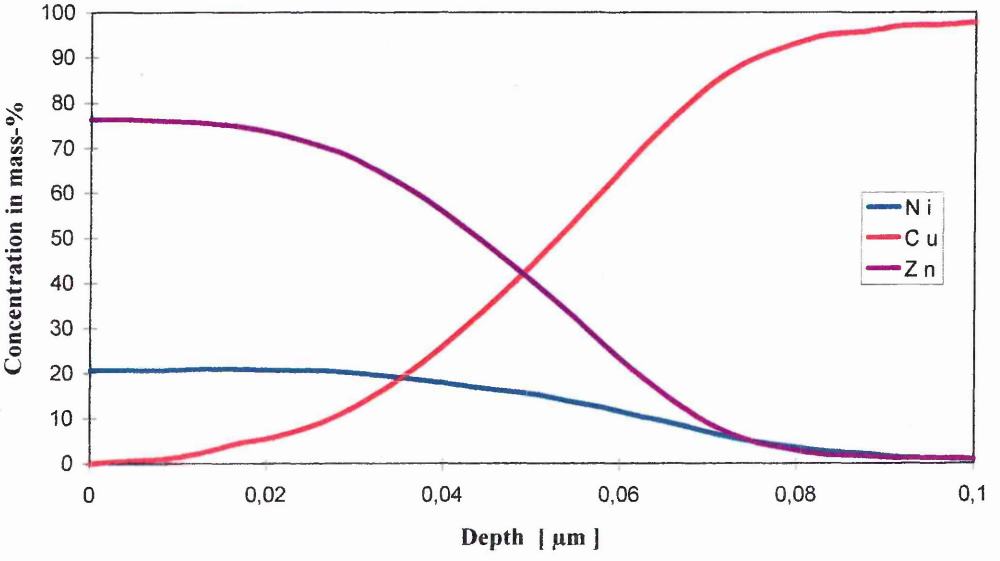

Fig. 4-35: Quantitative Depth Profile of 0.05 µm thick Nickel-Zinc Electrodeposited with 60 mA cm^{-2} onto Copper Substrate.

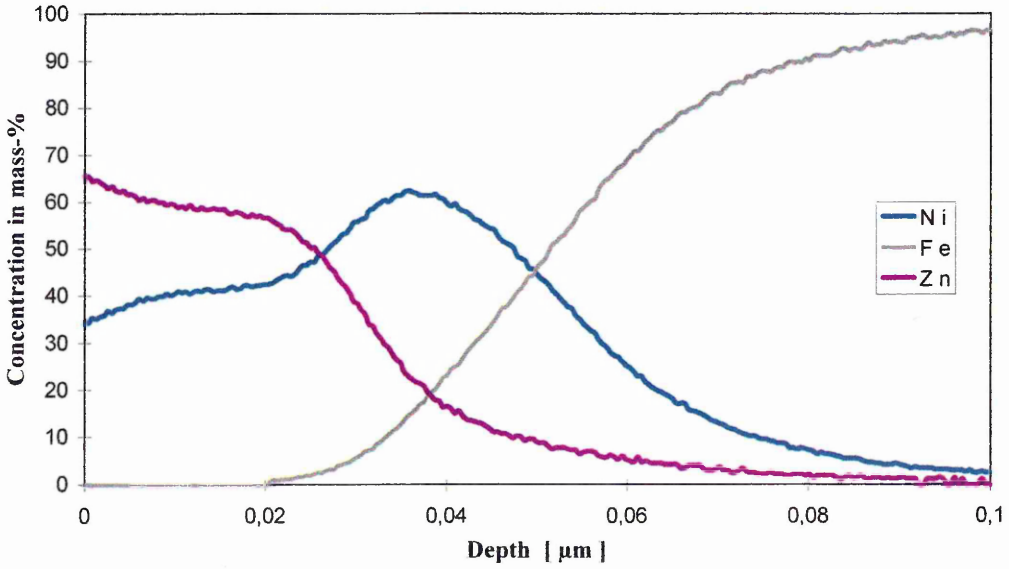

Fig. 4-36: Quantitative Depth Profile of 0.05 µm Thick Nickel-Zinc Electrodeposited with 10 mA cm^{-2} onto Steel Substrate.

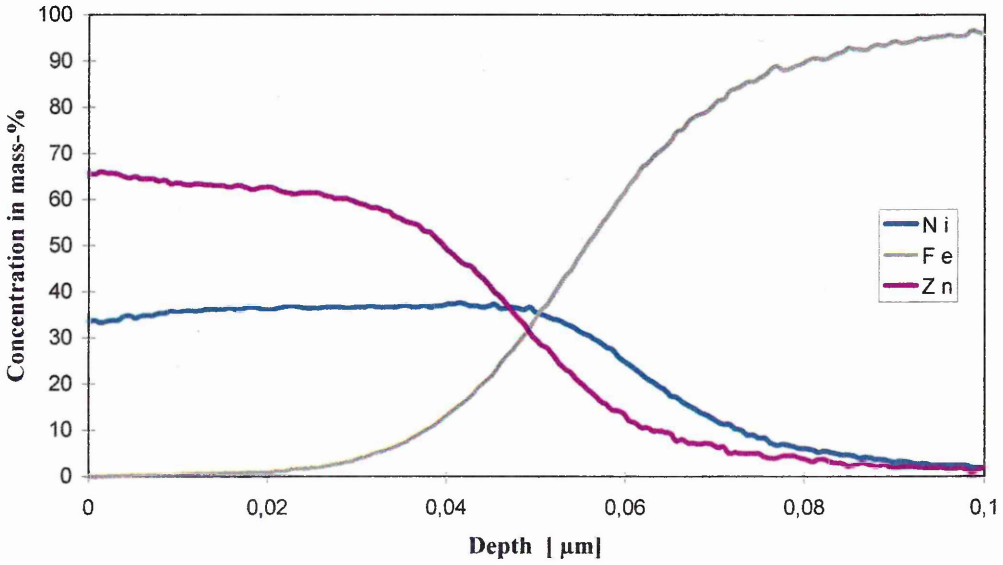

Fig. 4-37: Quantitative Depth Profile of 0.05 µm Thick Nickel-Zinc Electrodeposited with 60 mA cm^{-2} onto Steel Substrate.

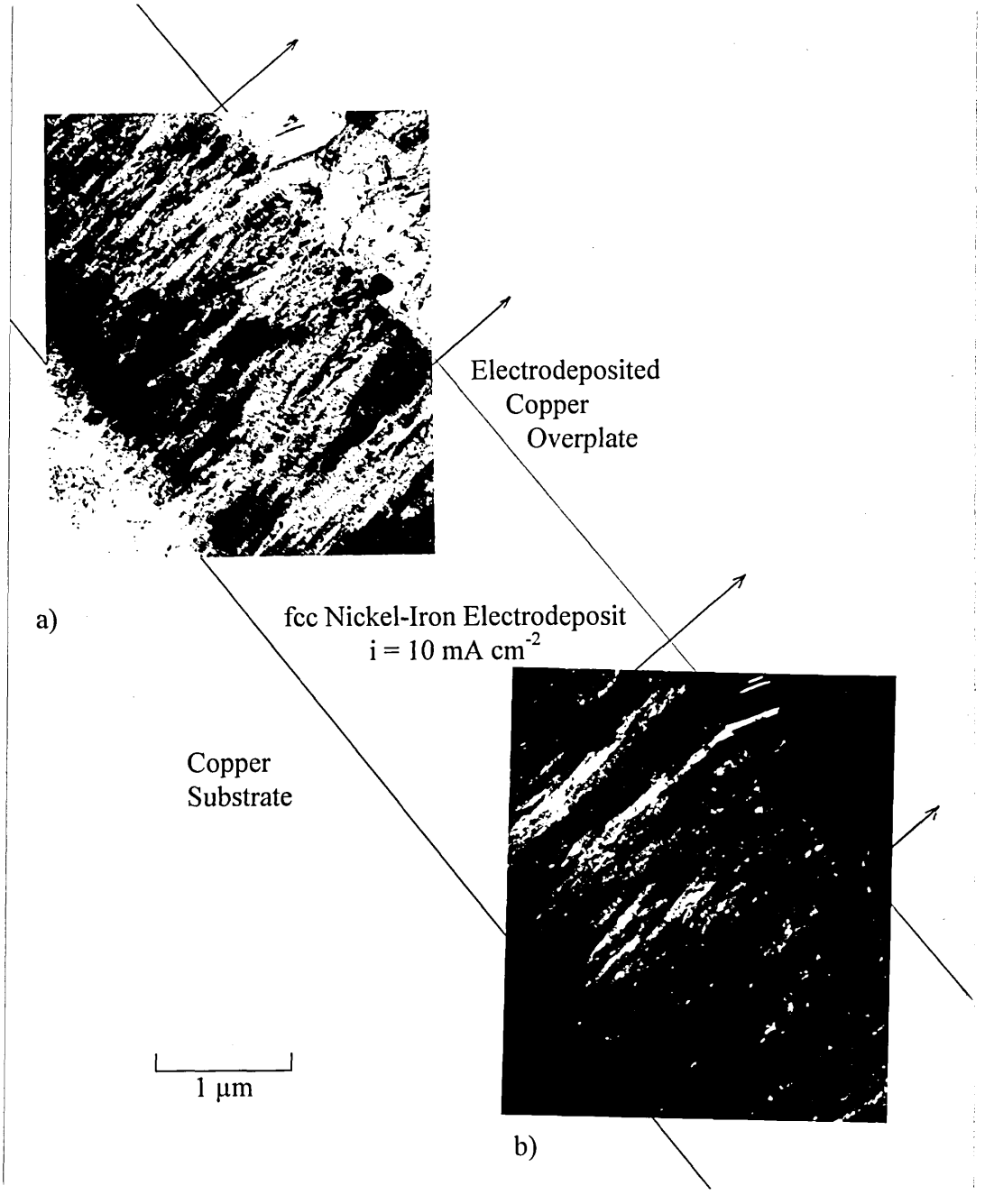

Fig. 4-38: (a) Bright and (b) Dark Field Image of Cross-Sectioned fcc Nickel-Iron Electrodeposit.

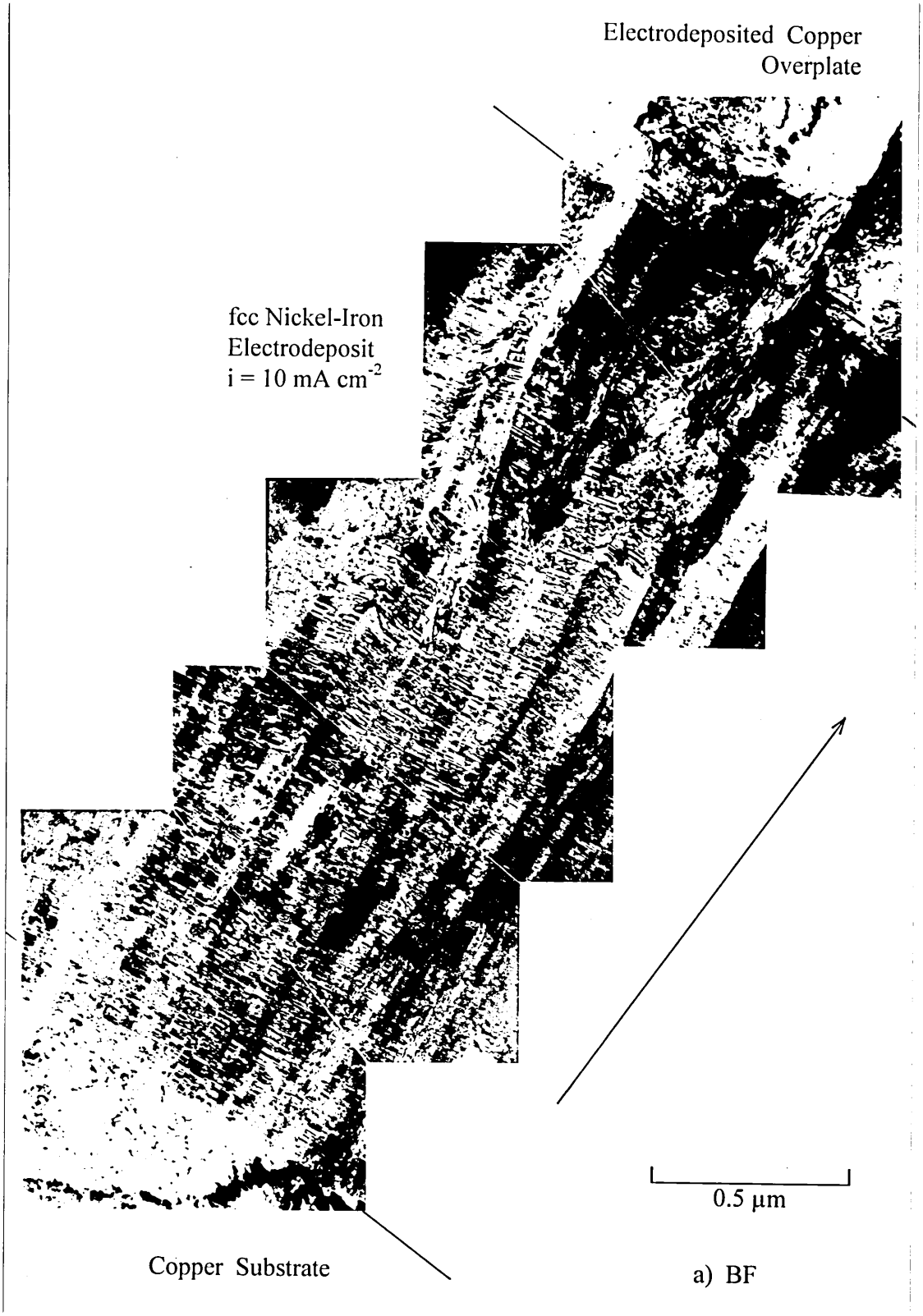

Fig. 4-39a: Montage of Bright Field Images Across Cross-Sectioned fcc Nickel-Iron Electrodeposit.

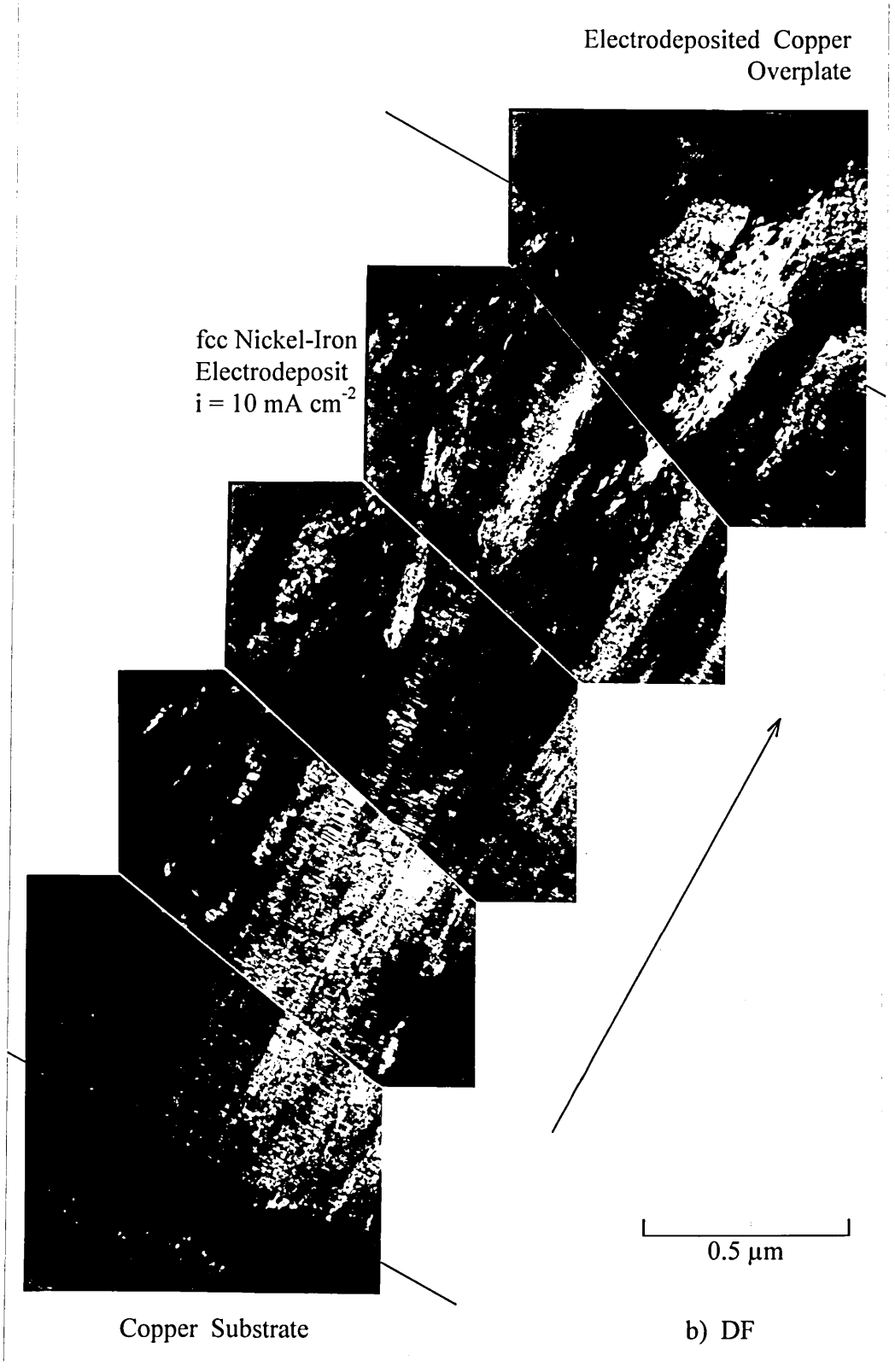

Fig. 4-39b: Montage of Dark Field Images Across Cross-Sectioned fcc Nickel-Iron Electrodeposit.

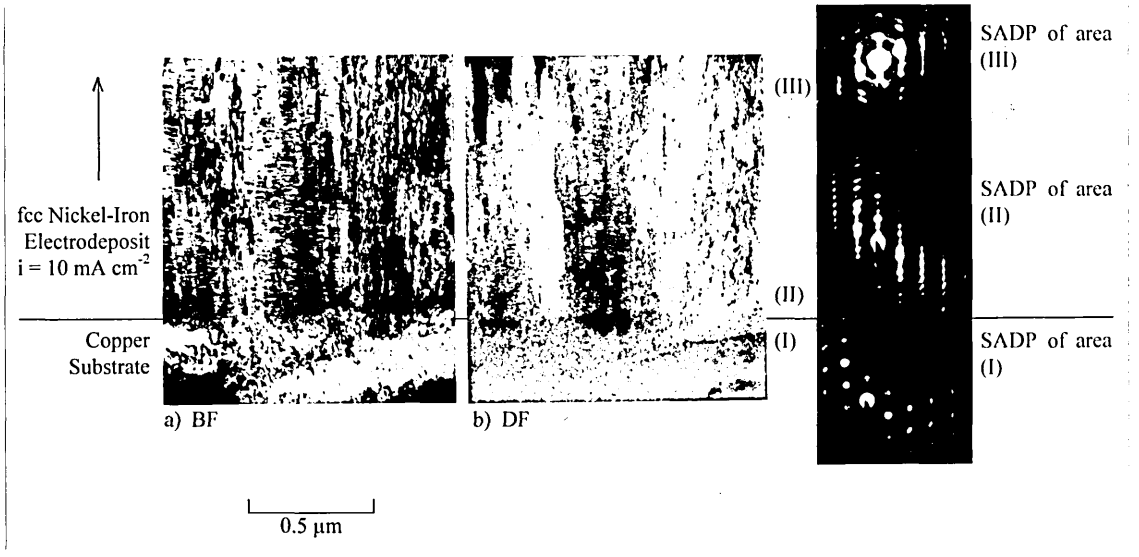

Fig. 4-40: (a) Bright and (b) Dark Field Pair of Interface Between Copper Substrate and fcc Nickel-Iron Electrodeposit.
SADPs: (I) Copper Substrate, (II) Nucleation Site of fcc Nickel-Iron Deposit, (III) Advanced Developed fcc Nickel-Iron Deposit.

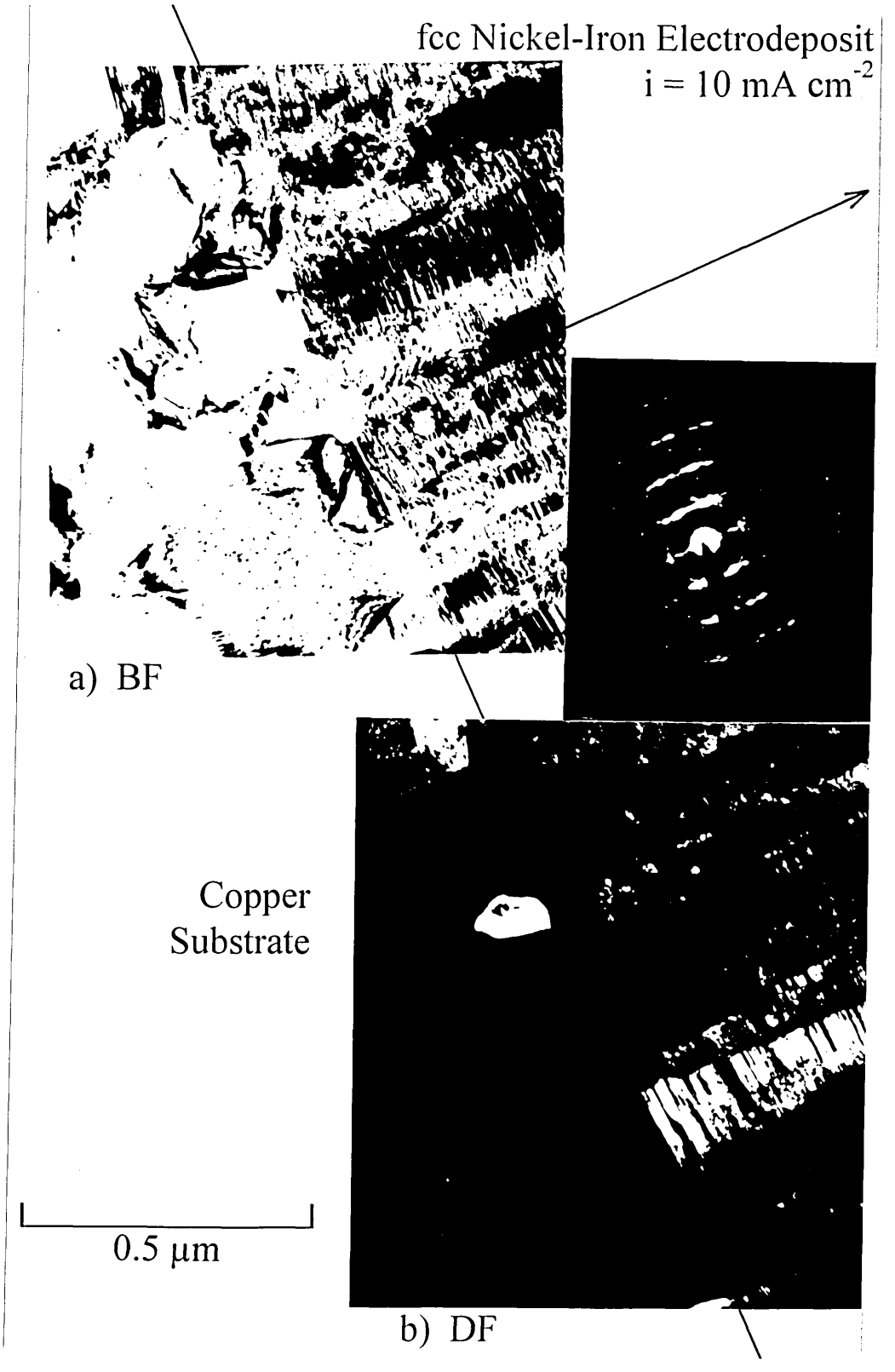

Fig. 4-41: (a) Bright and (b) Dark Field Pair of Initial Nucleation Site of fcc Nickel-Iron Electrodeposit on Copper Substrate, Including SADP of fcc Coating.

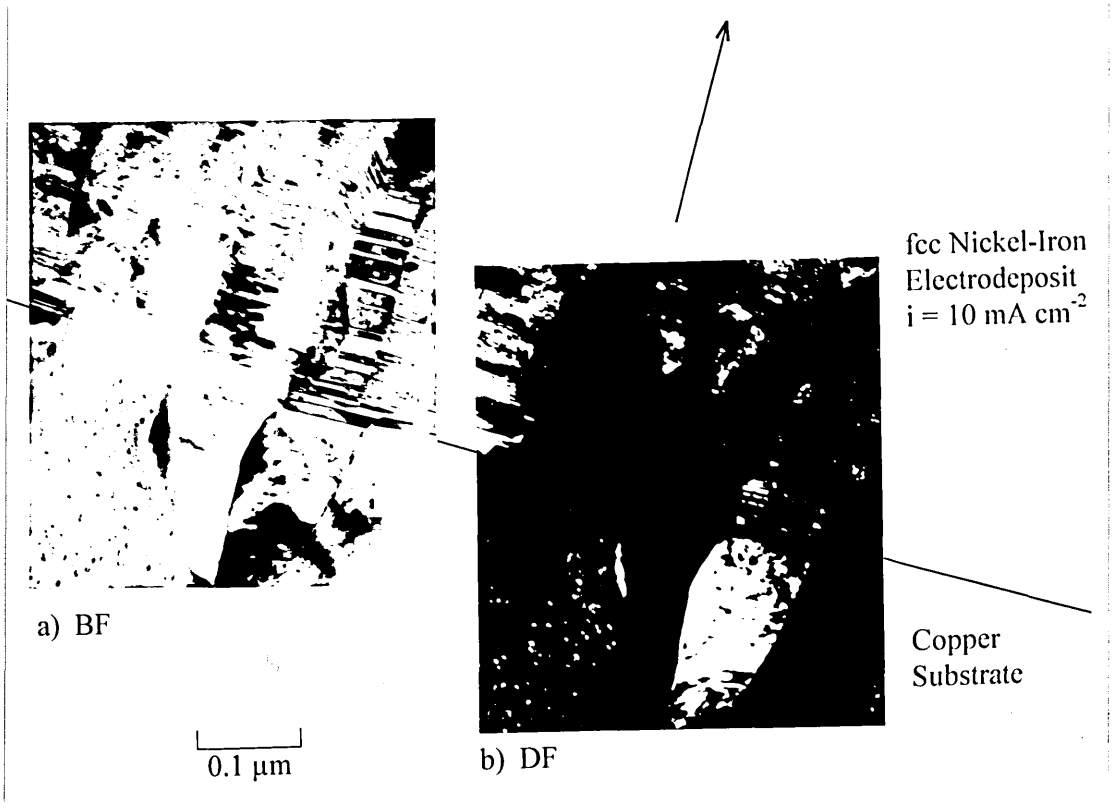

Fig. 4-42: (a) Bright and (b) Dark Field Pair of Interface Copper Substrate/fcc Nickel-Iron Electrodeposit.

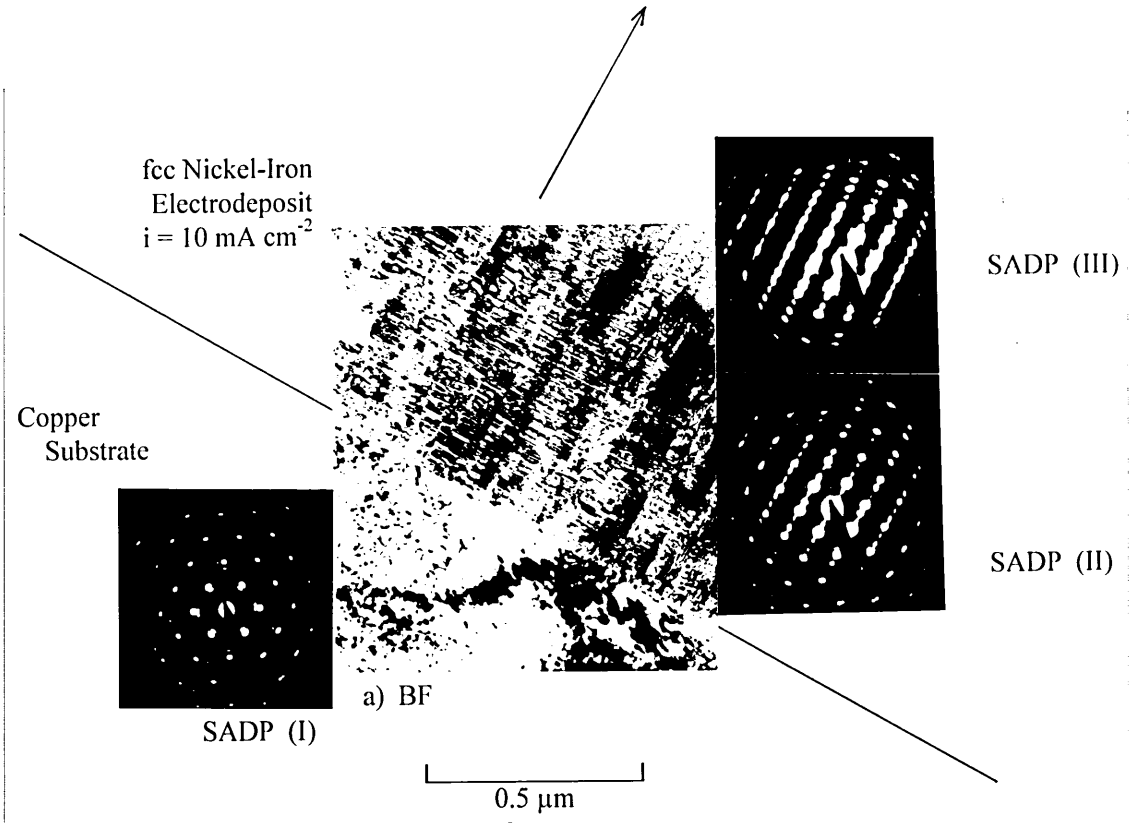

Fig. 4-43: (a) Bright Field Image of Interface Copper Substrate/fcc Nickel-Iron Electrodeposit.
SADPs: (I) Copper Substrate, (II) Interface Copper Substrate/fcc NiFe Deposit, (III) Advanced Developed fcc NiFe Deposit.

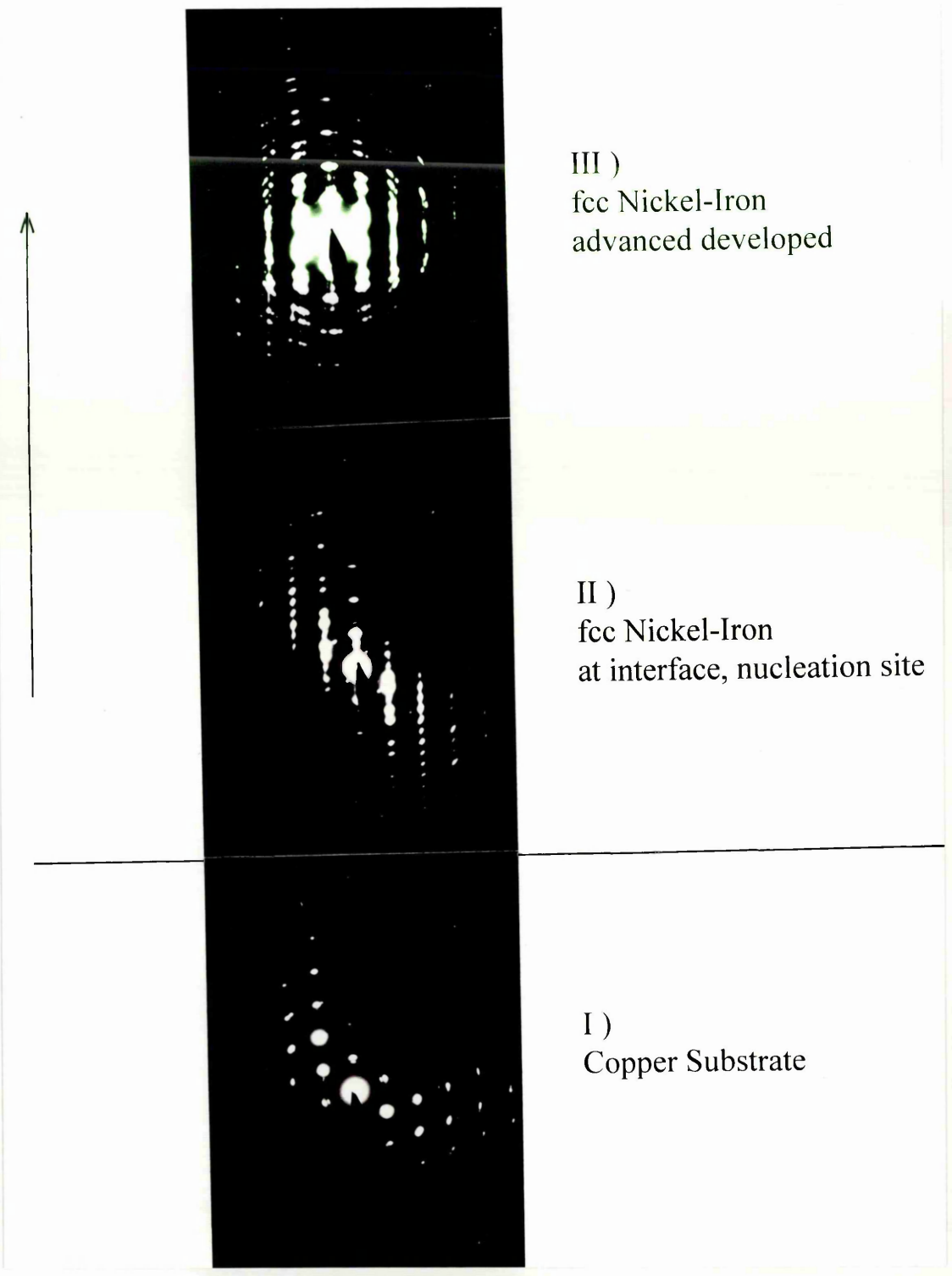

Fig. 4-44: Series of Selected Area Diffraction Patterns Indicating Initial Epitaxial Growth and 'Arcing' of Twin Spots in Advanced Developed fcc NiFe Deposit.
SADPs: (I) Copper Substrate, (II) fcc Nickel-Iron Electrodeposit at Nucleation Site, (III) Advanced Developed fcc NiFe Electrodeposit.

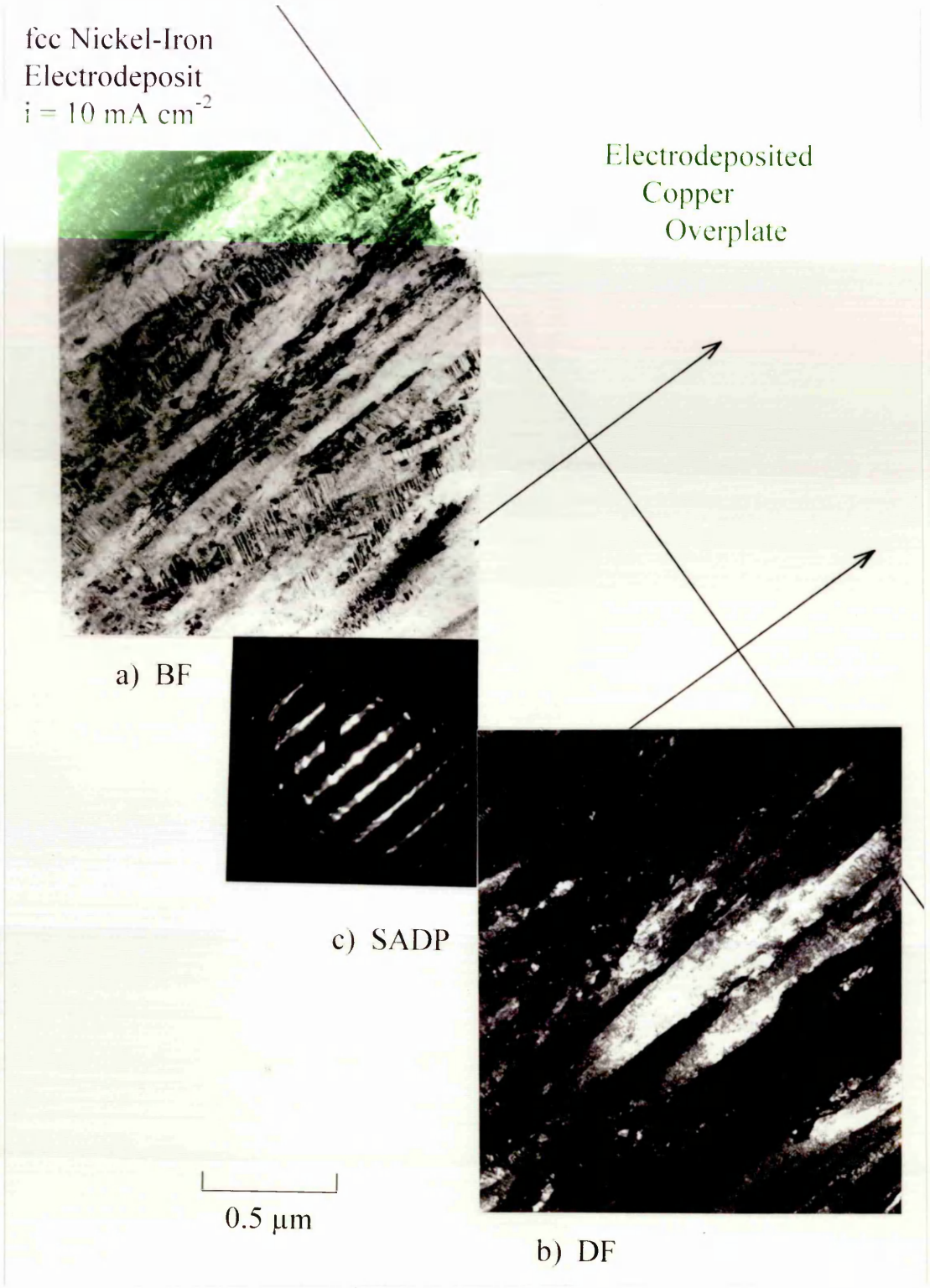

Fig. 4-45: a) Bright, (b) Dark Field Image and (c) Selected Area Diffraction Pattern of Advanced Developed fcc Nickel-Iron Electrodeposit.

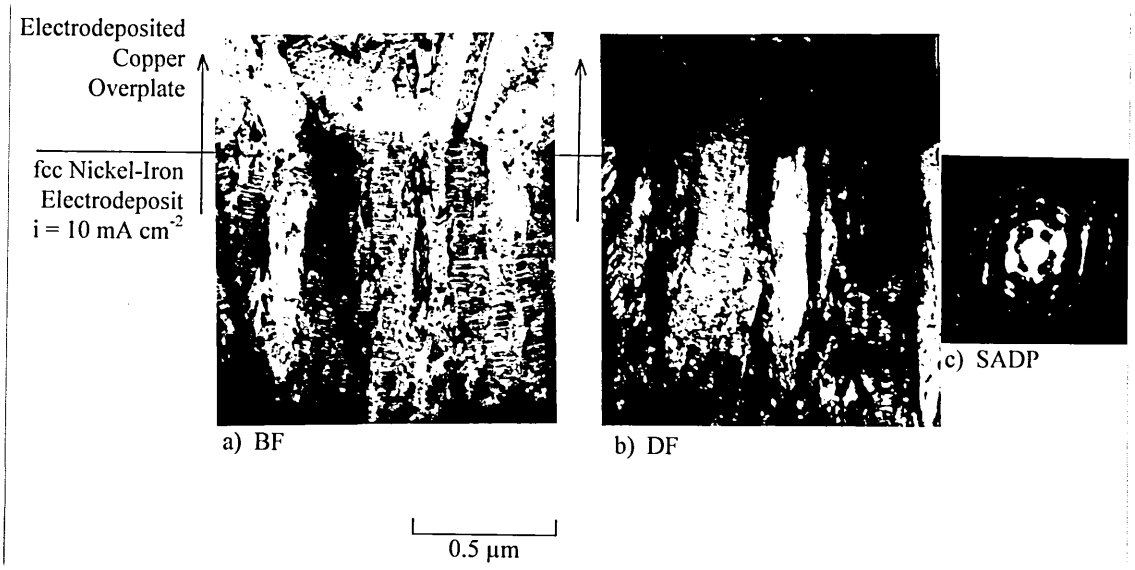

Fig. 4-46: (a) Bright, (b) Dark Field Image and (c) Selected Area Diffraction Pattern of Advanced Developed fcc Nickel-Iron Electrodeposit.

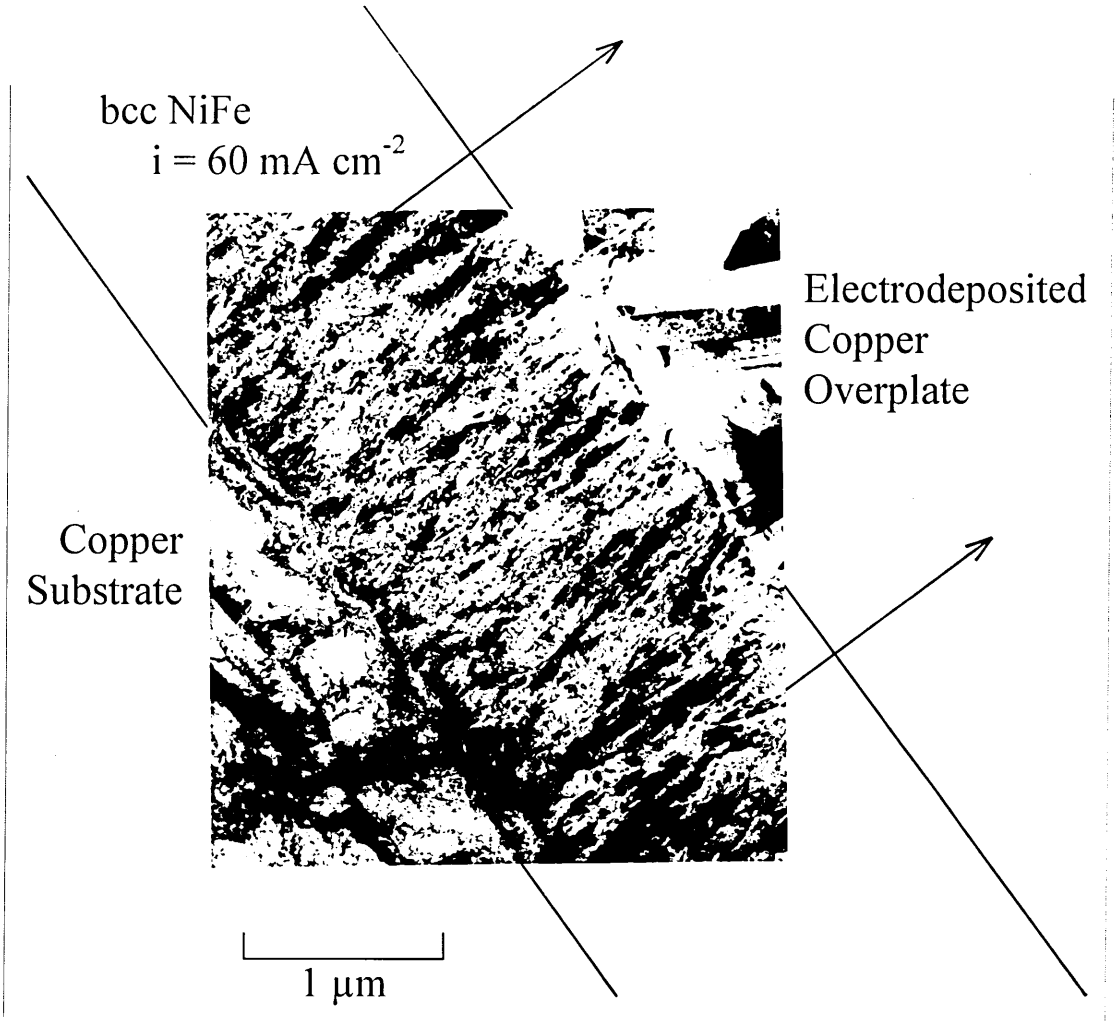

Fig. 4-47: Bright Field Image Showing General Overall View of Cross-Sectioned bcc Nickel-Iron Electrodeposit Nucleated on a Copper Substrate, Overplated with Copper.

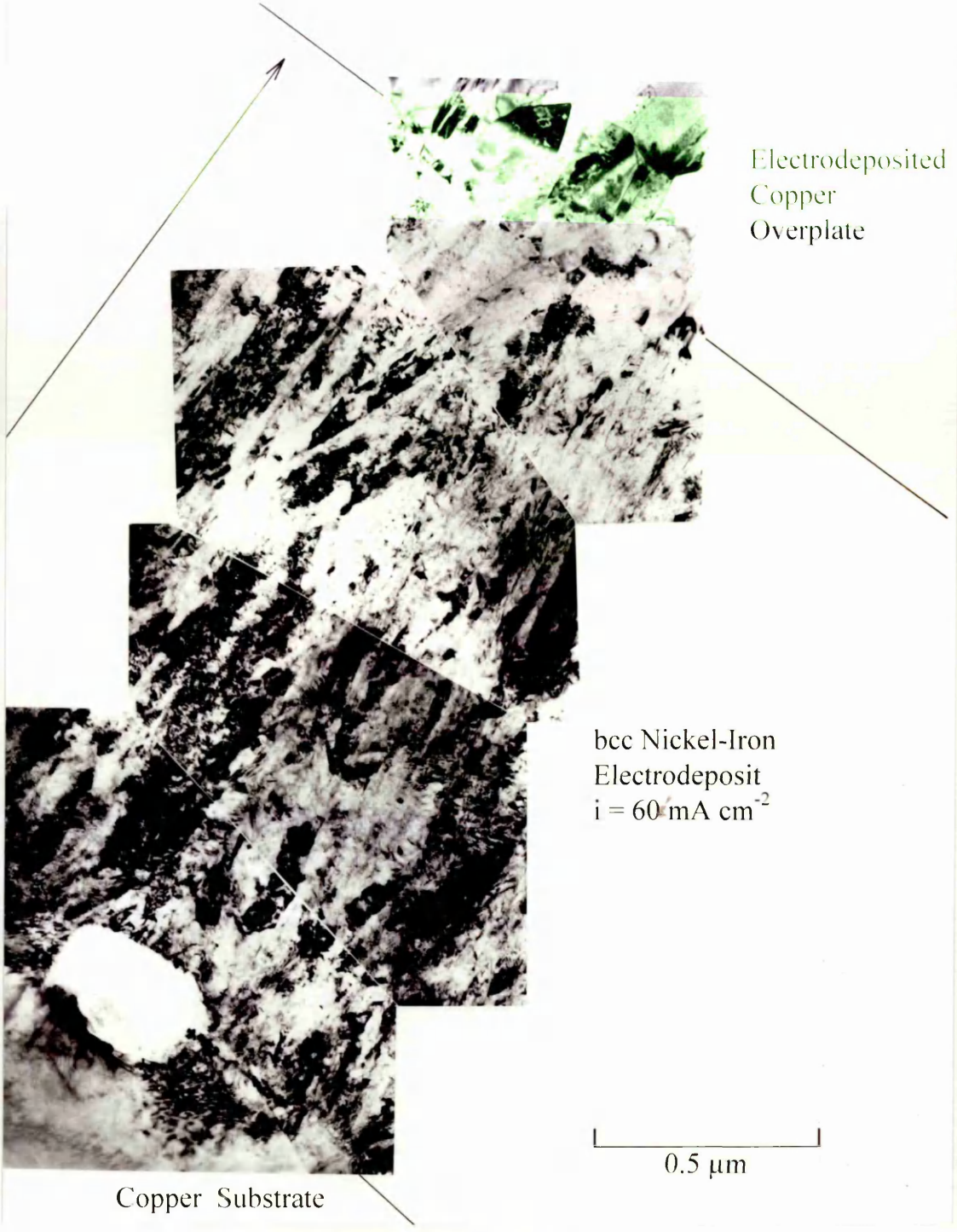

Fig. 4-48: Montage of Bright Field Images Showing General Overall View of Cross-Sectioned bcc Nickel-Iron Electrodeposit Nucleated on a Copper Substrate, Overplated with Copper.

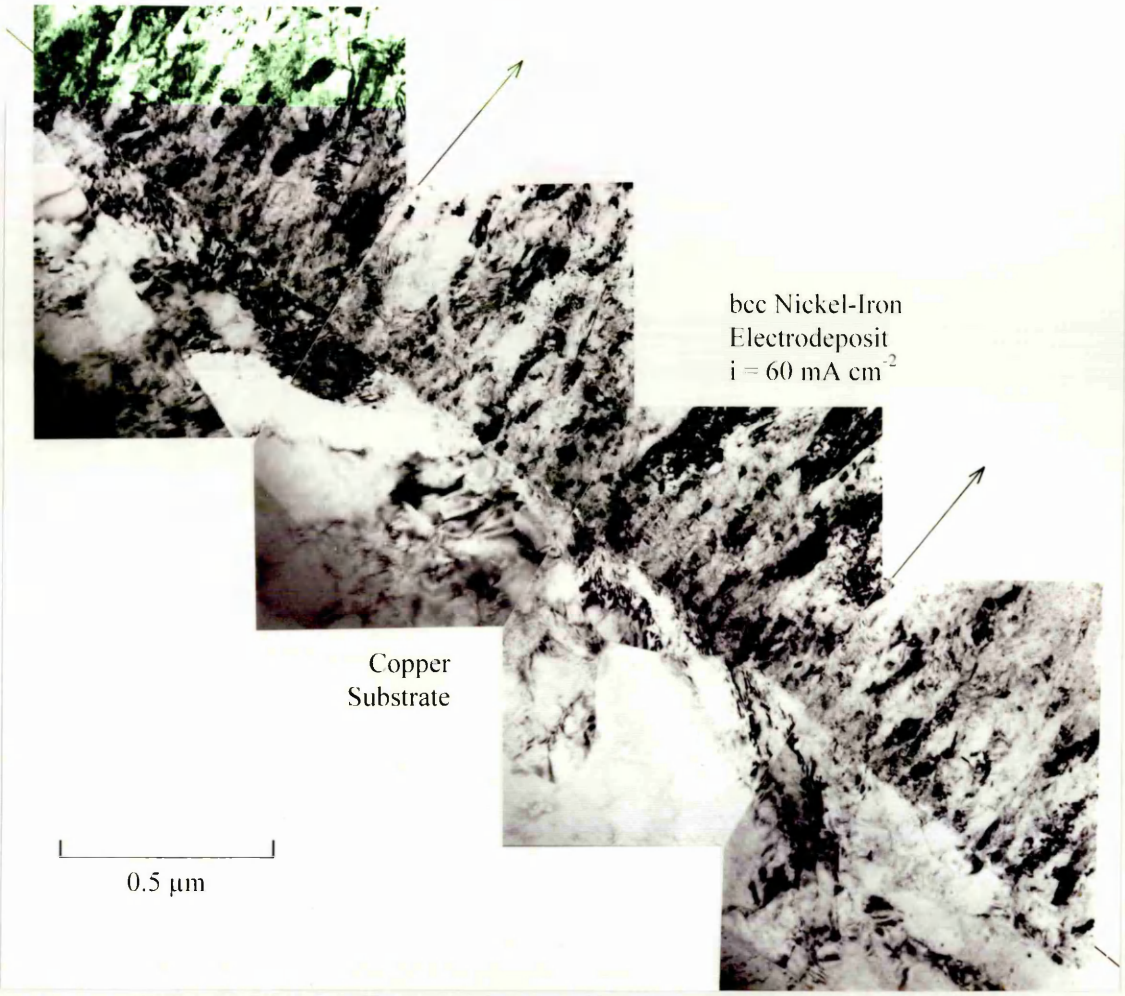

Fig. 4-49: Montage of Bright Field Images Along the Interface Between the bcc Nickel-Iron Electrodeposit and the Copper Substrate.

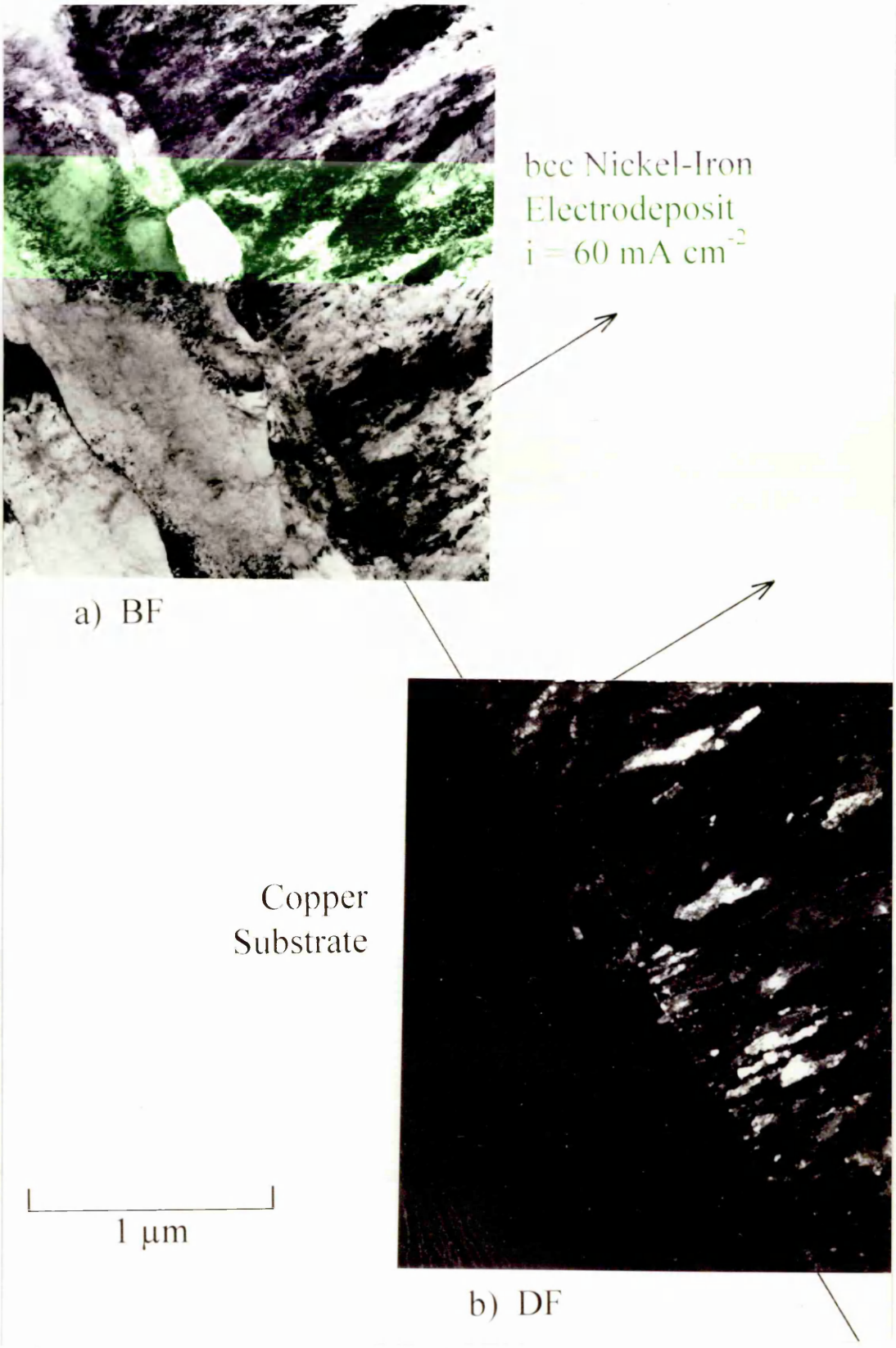

Fig. 4-50: (a) Bright and (b) Dark Field Micrograph of Copper Substrate/bcc Nickel-Iron Electrodeposit Interface.

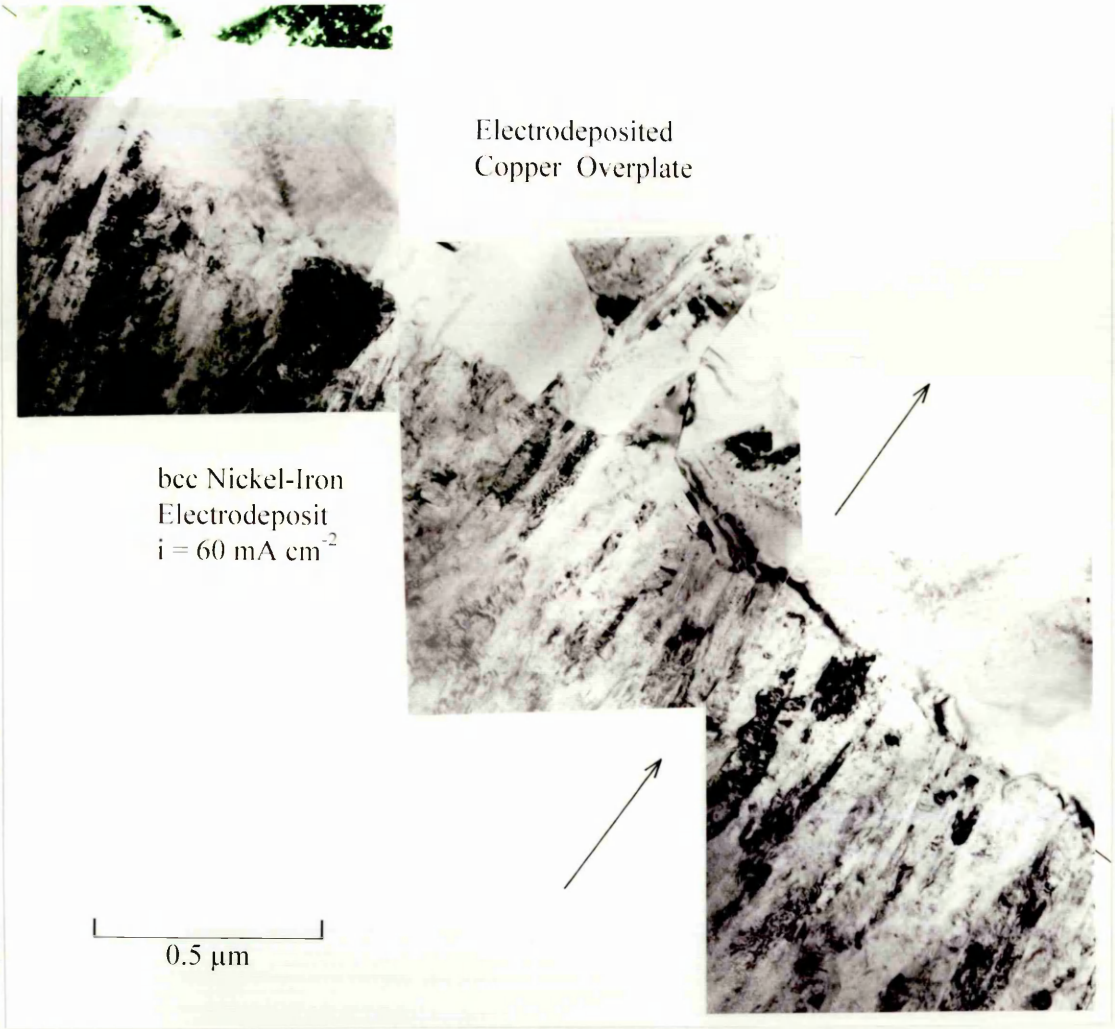

Fig. 4-51: Montage of Bright Field Images Showing the Interface Between the Surface of the Advanced Developed bcc Nickel-Iron Electrodeposit and the Overplated Copper.

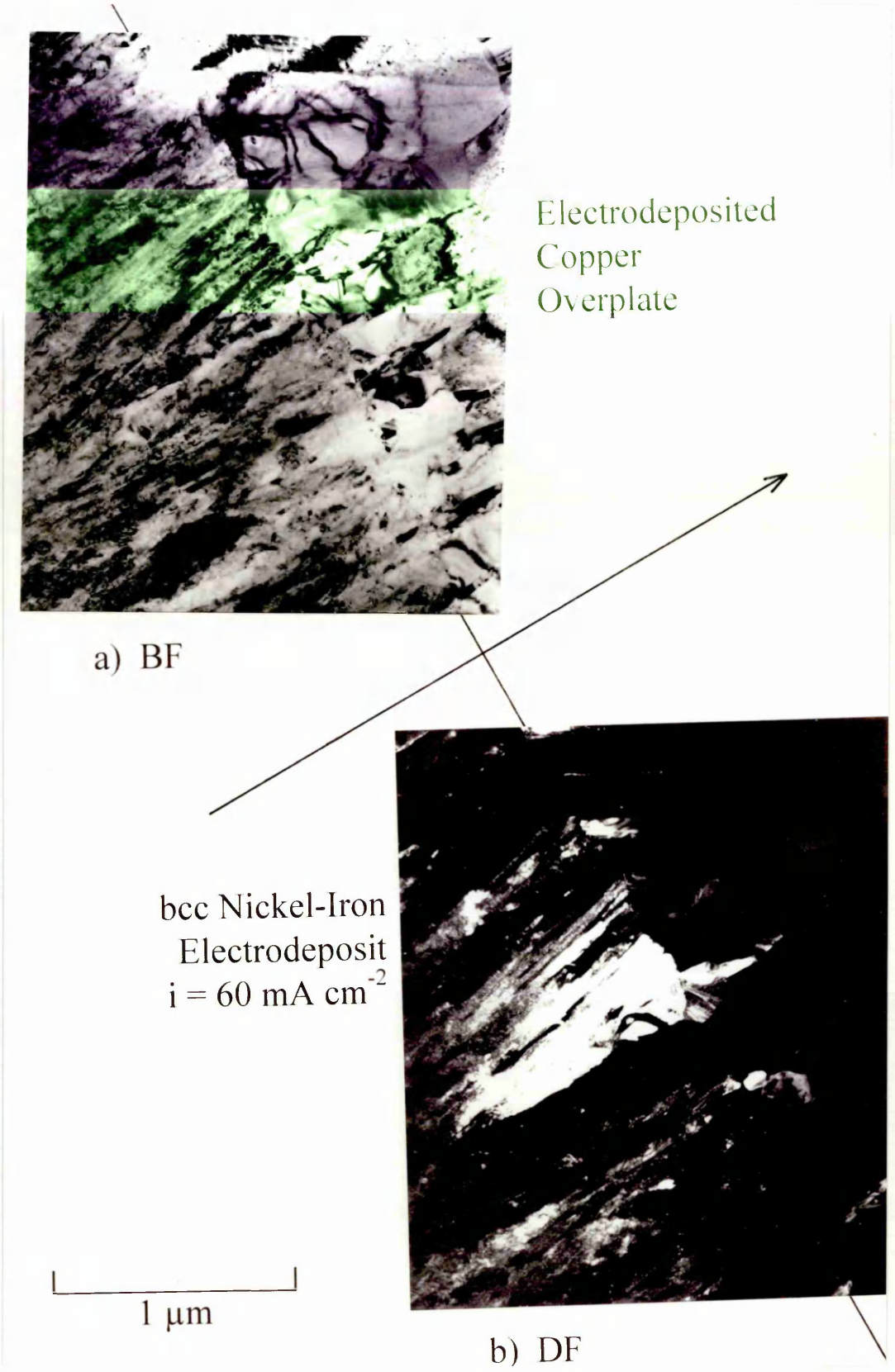

Fig. 4-52: (a) Bright and (b) Dark Field Pair of bcc Nickel-Iron Deposit/Copper Overplate Interface. Bright Grains in (b) Have <211> Growth Direction.

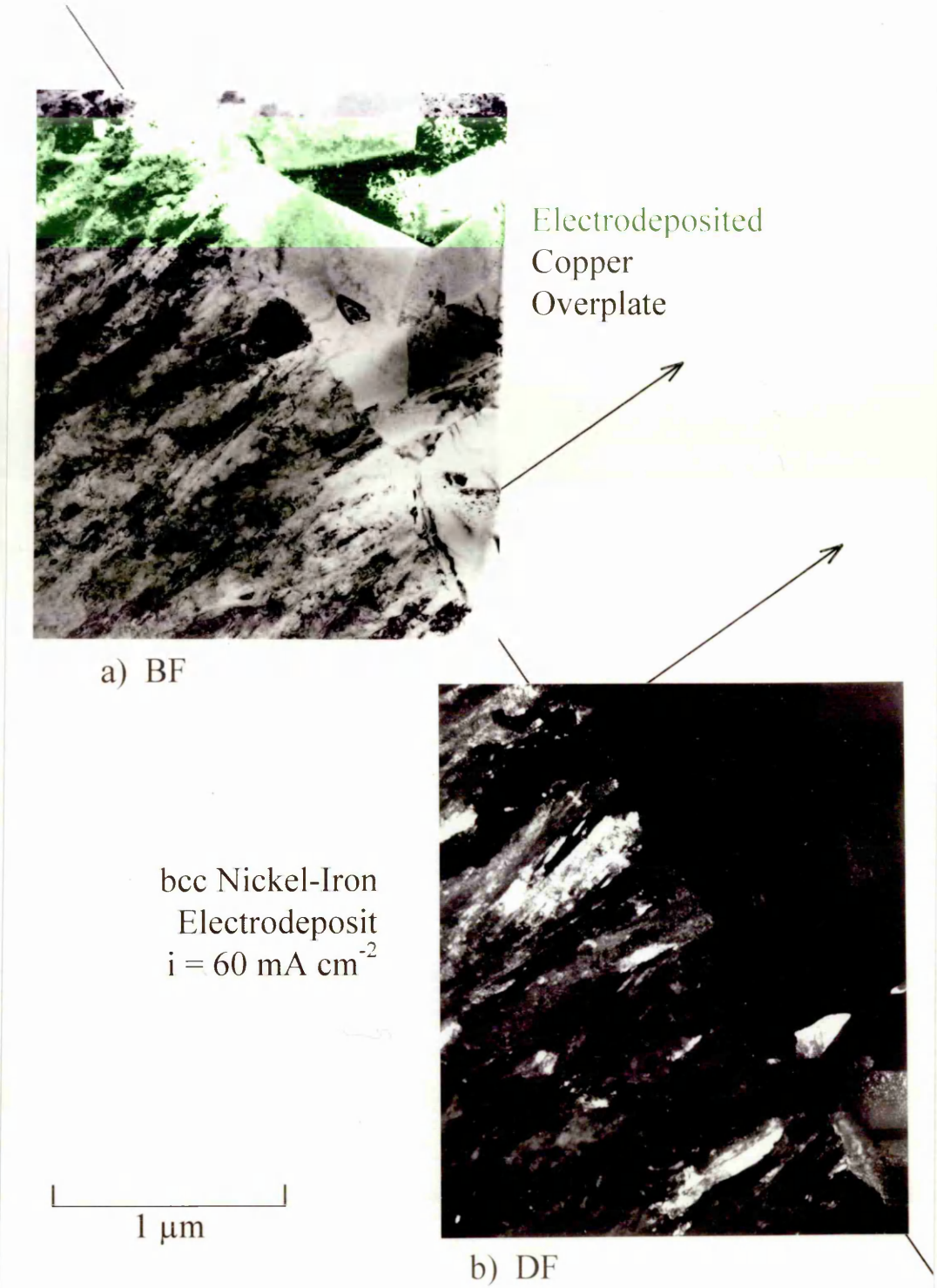

Fig. 4-53: (a) Bright and (b) Dark Field Pair of bcc Nickel-Iron Deposit/Copper Overplate Interface. Bright Grains in (b) Have <211> Growth Direction.

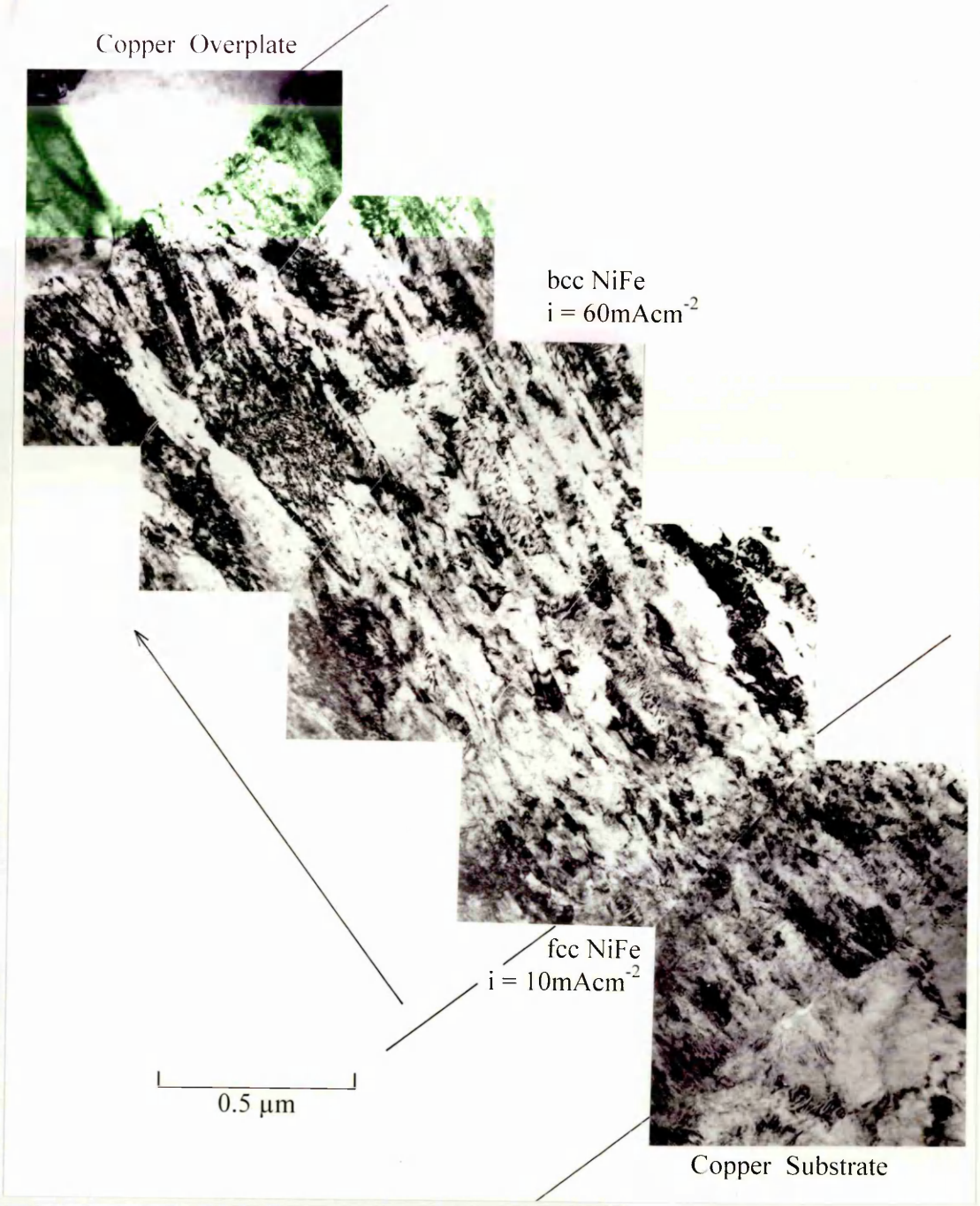

Fig. 4-54a: Montage of Bright Field Images Showing Double Layered 2µm Thick bcc NiFe Nucleated on 0.5µm Thick fcc NiFe Deposit.

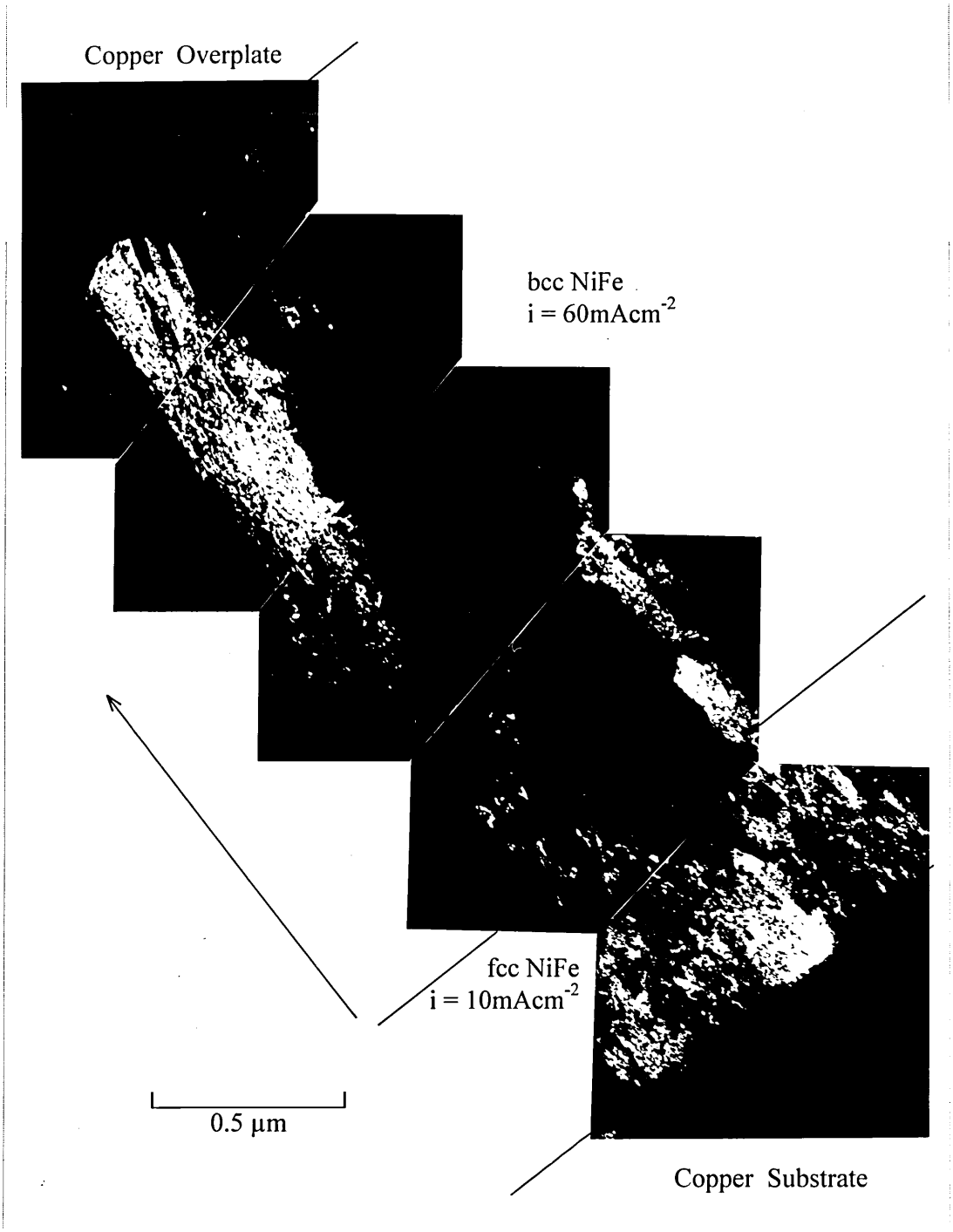

Fig. 4-54b: Montage of Dark Field Images Showing Double Layered 2μm Thick bcc NiFe Nucleated on 0.5μm Thick fcc NiFe Deposit.

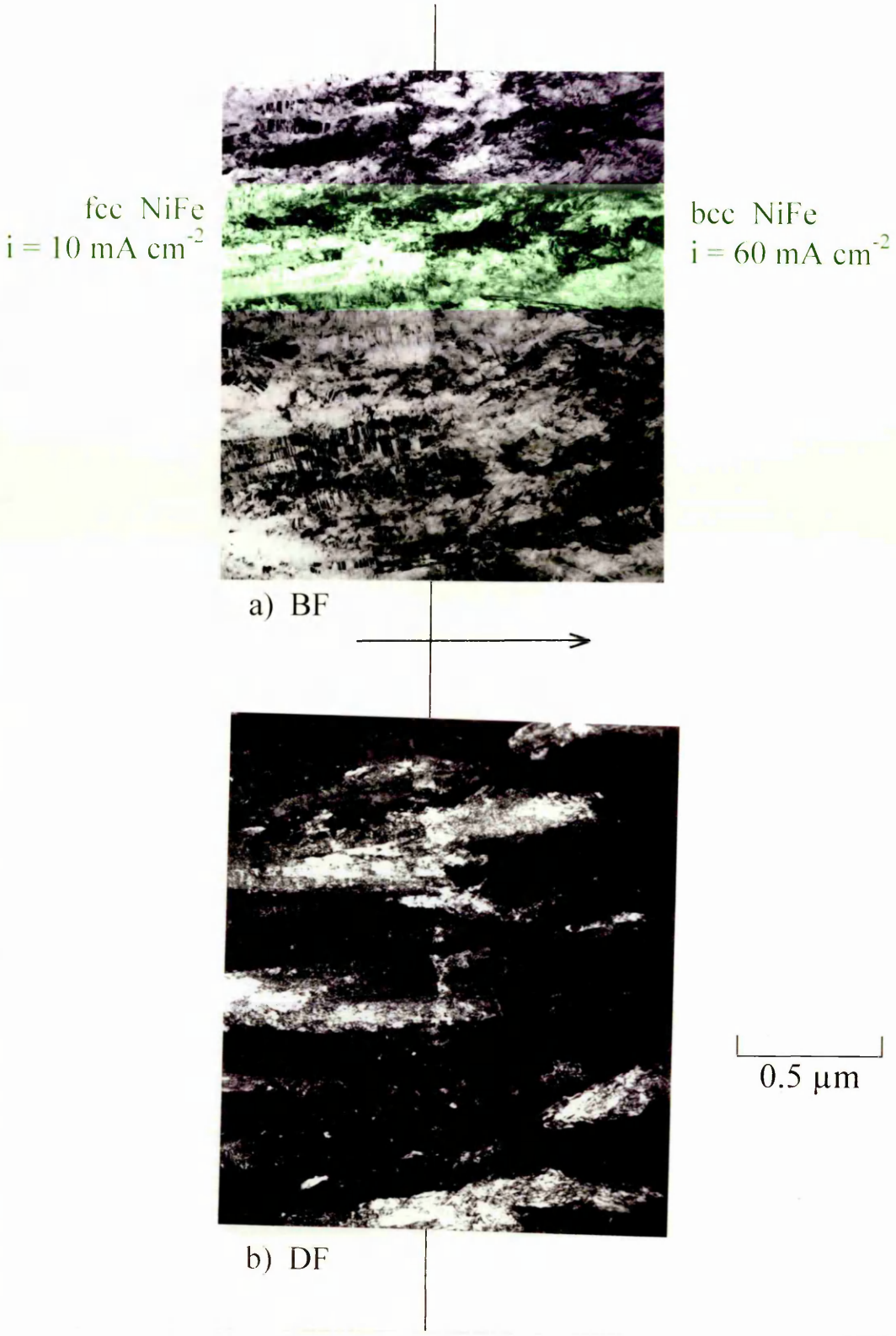

Fig. 4-55: (a) Bright and (b) Dark Field Pair of Interface Between Advanced Developed, 2µm Thick fcc NiFe Deposit and Nucleation Site of bcc NiFe Deposit.

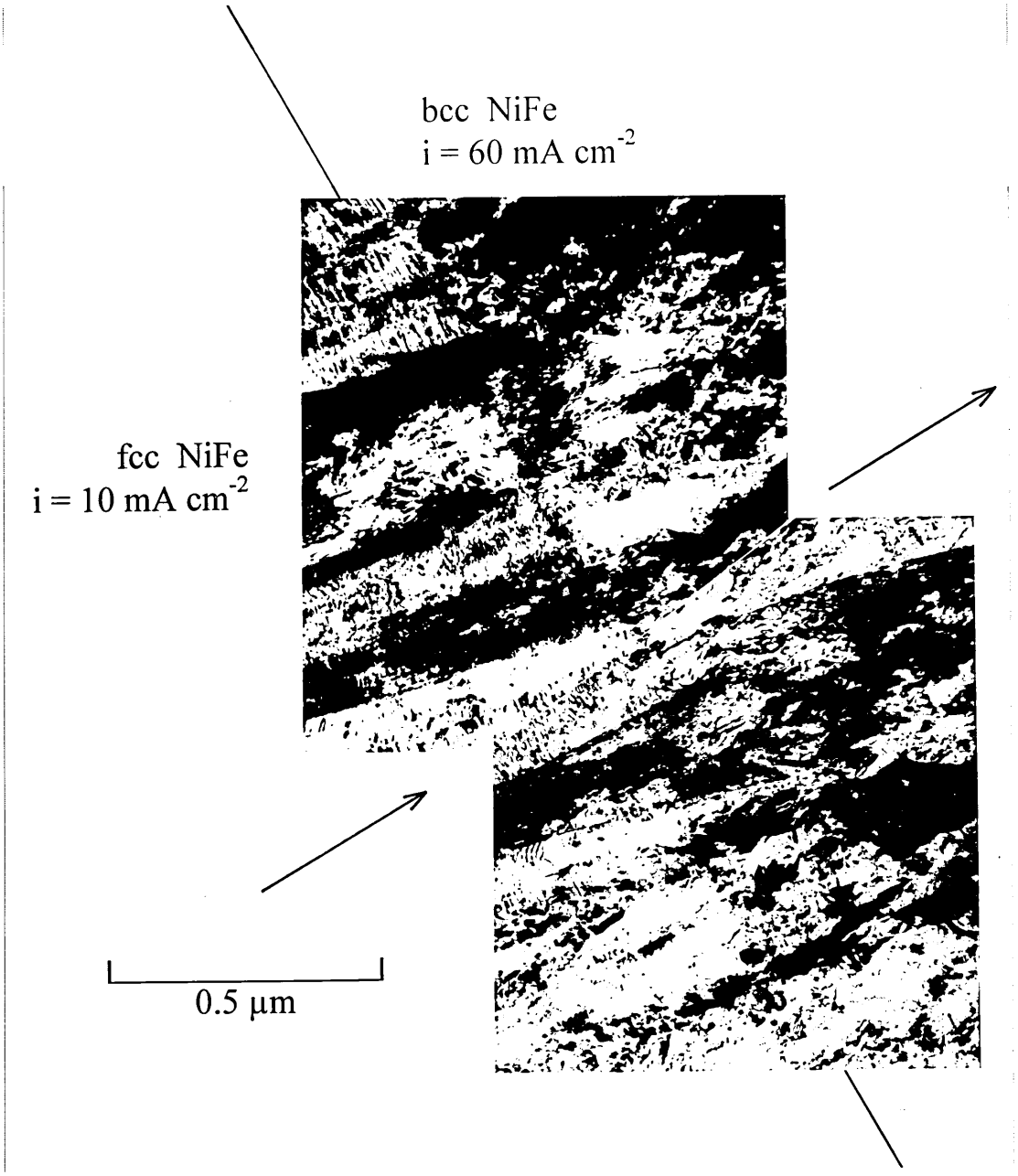

Fig. 4-56: Montage of Bright Field Image Showing Interface Between 2µm Thick, Advanced Developed fcc NiFe Deposit and Nucleation Site of bcc NiFe Deposit.

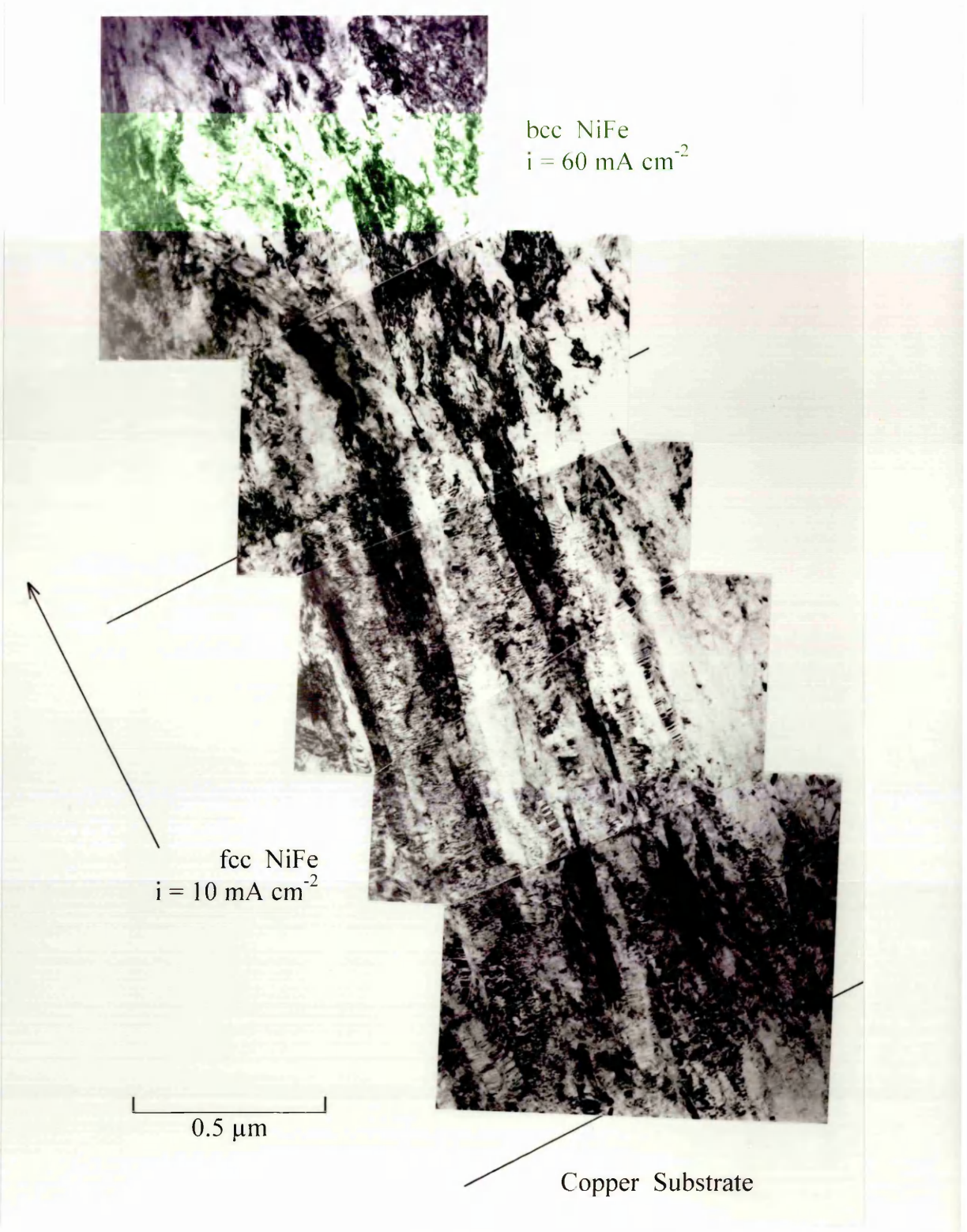

Fig. 4-57a: Bright Field Images of Double Layered 2µm Thick bcc NiFe-Nucleated on 2µm Thick fcc NiFe Deposit.

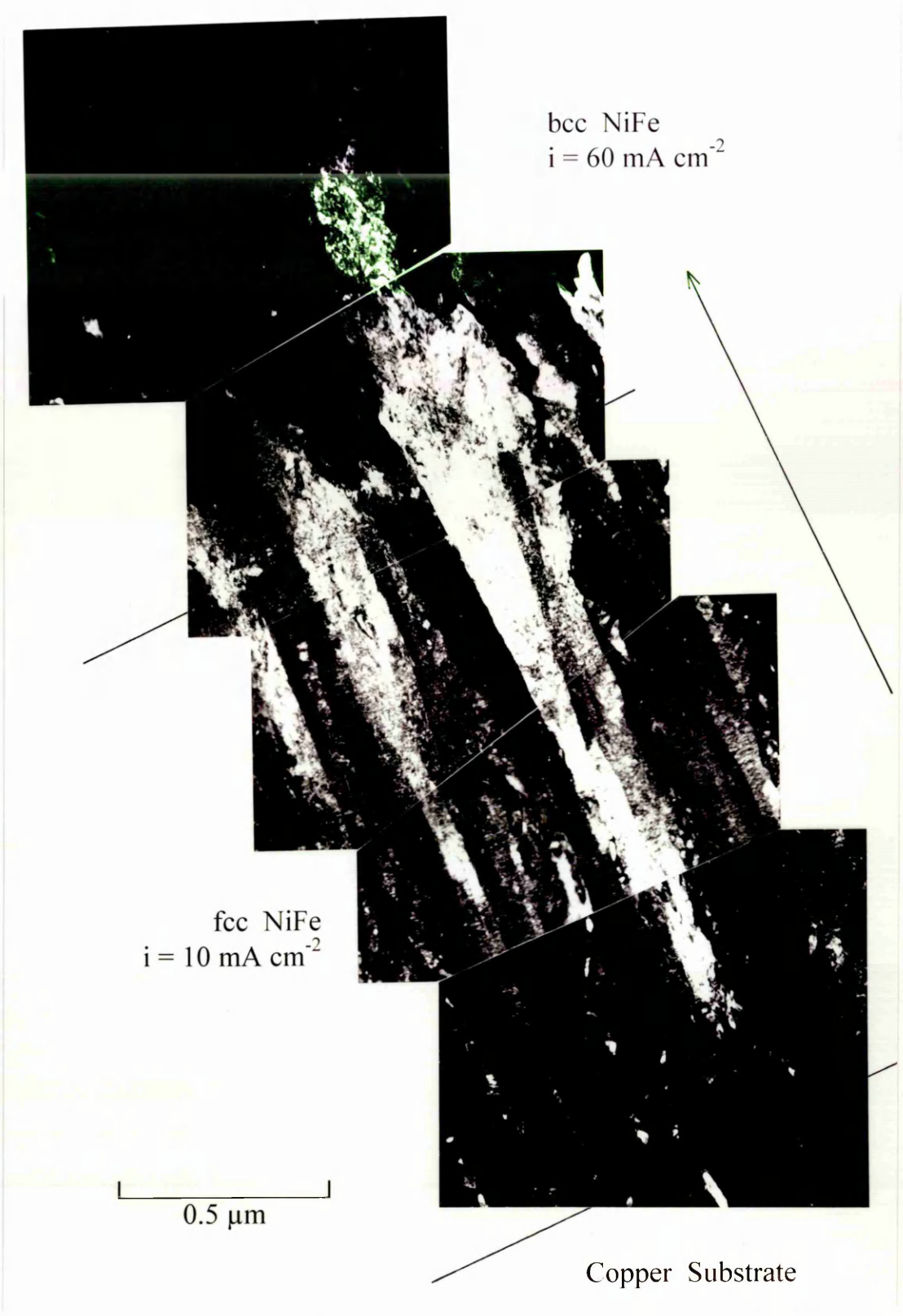

Fig. 4-57b: Dark Field Images of Double Layered 2μm Thick bcc NiFe-Nucleated on 2μm Thick fcc NiFe Deposit.

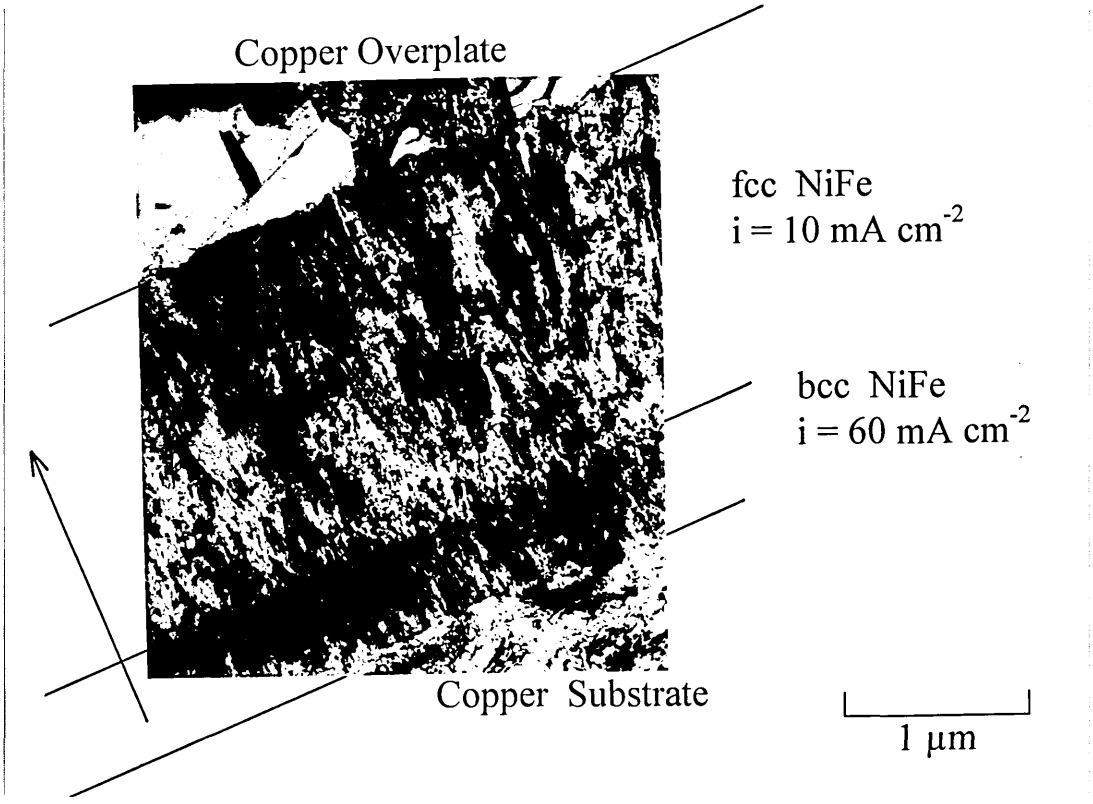

Fig. 4-58: Bright Field Image of Double Layered 2μm Thick fcc NiFe Nucleated on 0.5μm Thick bcc NiFe Deposit.

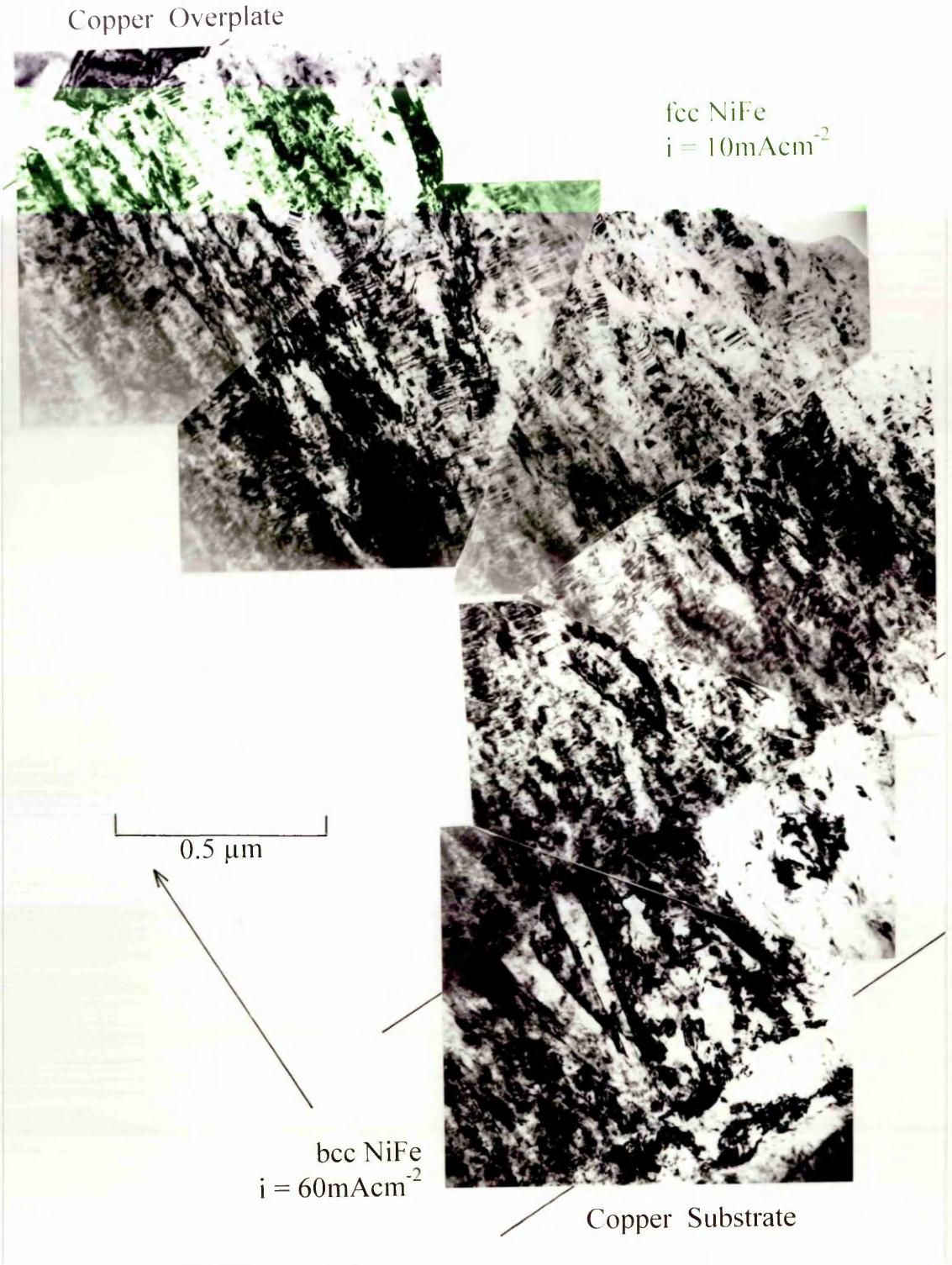

Fig. 4-59: Montage of Bright Field Images of Double Layered 2µm thick fcc NiFe Nucleated on 0.5µm Thick bcc NiFe Deposit.

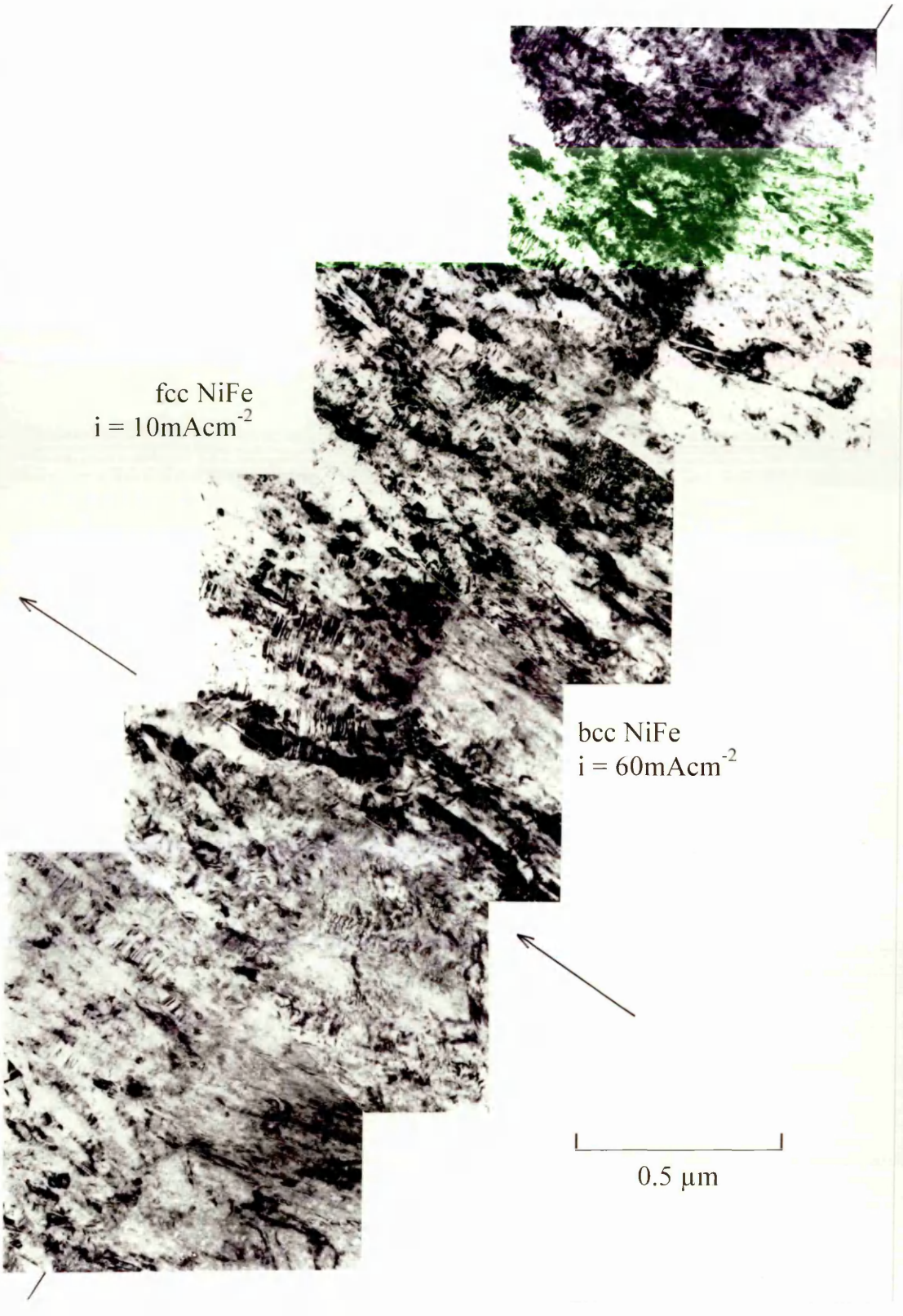

Fig. 4-60a: Montage of Bright Fields Along Interface of Double Layered, 2μm Thick fcc NiFe Deposit Nucleated on 2μm Thick bcc NiFe Deposit.

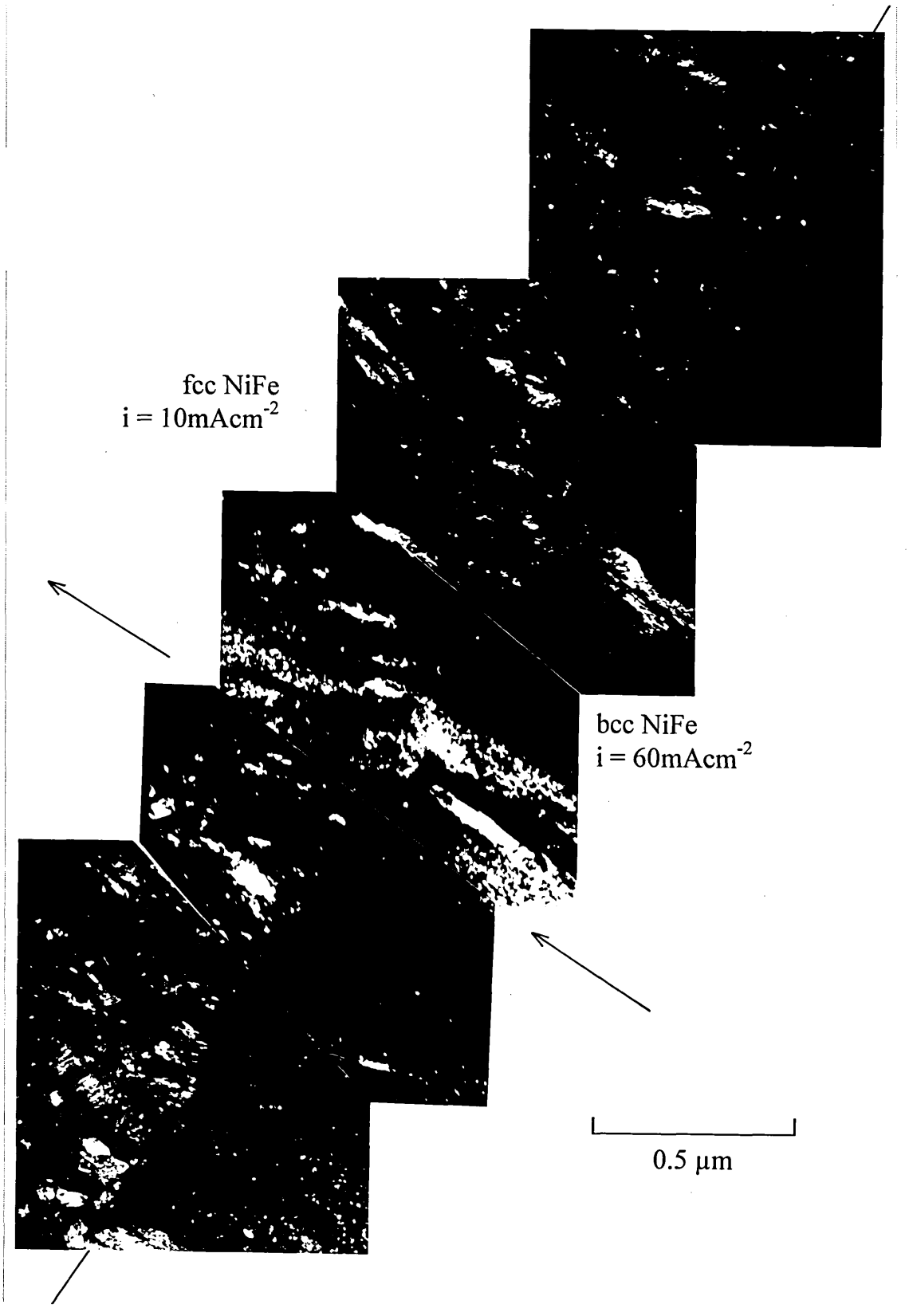

Fig. 4-60b: Montage of Dark Fields Along Interface of Double Layered, 2μm Thick fcc NiFe Deposit Nucleated on 2μm Thick bcc NiFe Deposit.

Fig. 4-61: Montage of Bright Fields Along Interface of Double Layered 2μm Thick fcc NiFe Deposit Nucleated on 2μm Thick bcc NiFe Deposit.

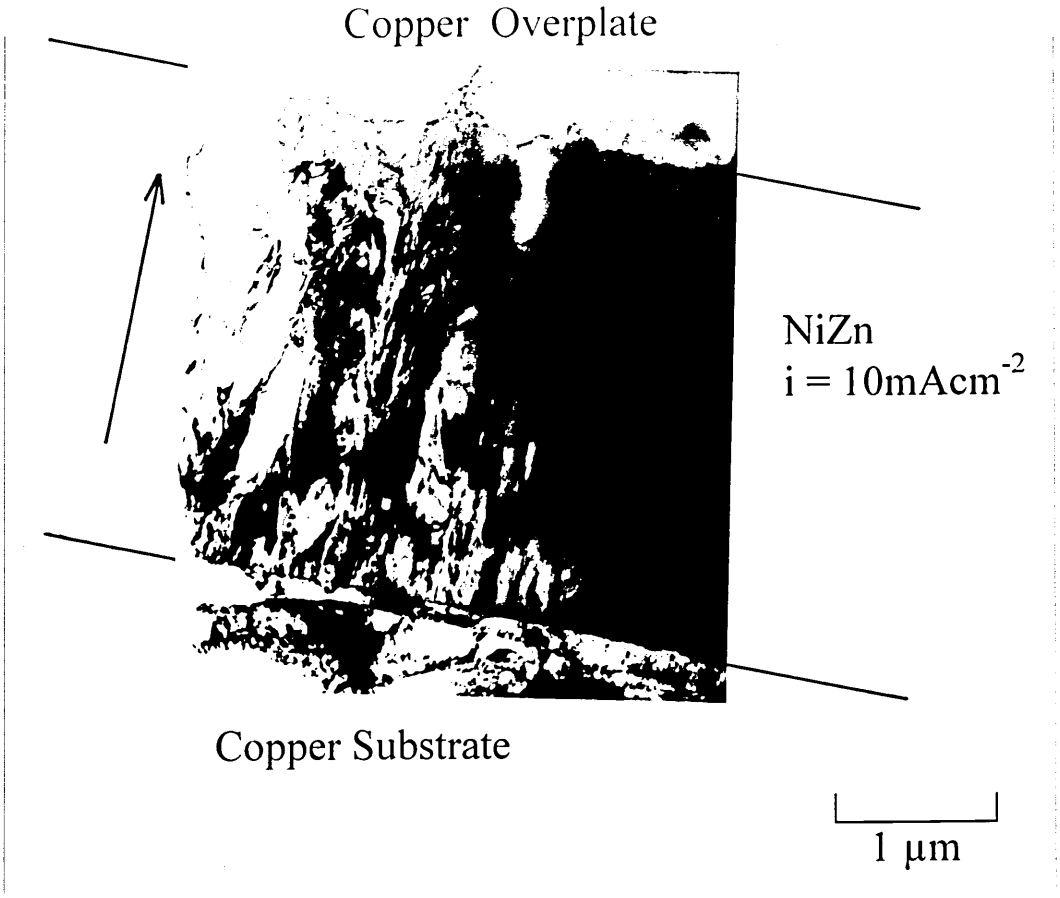

Fig. 4-62: Bright Field Image of NiZn Deposit (i = 10 mA cm^{-2}) on Copper Substrate.

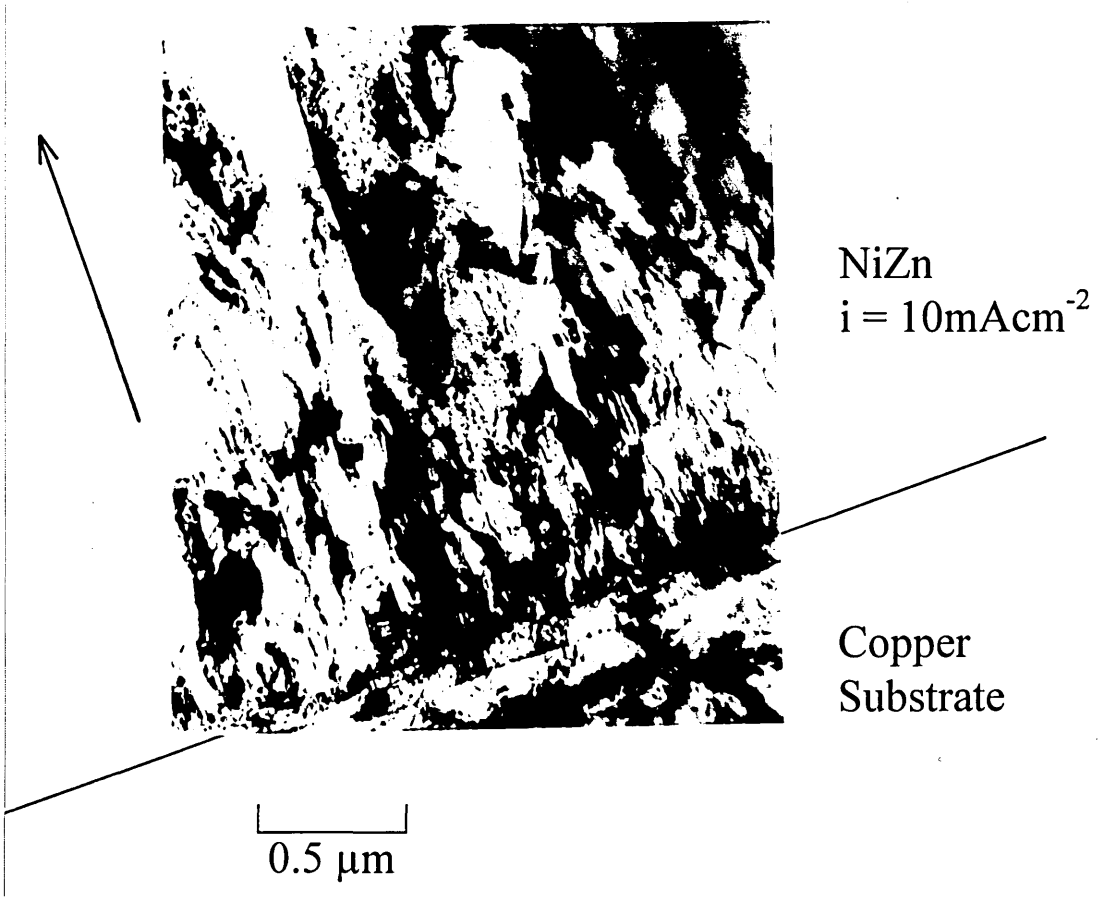

Fig. 4-63: Bright Field Image of Interface between Copper Substrate and Nucleated NiZn Deposit (i = 10 mA cm^{-2}).

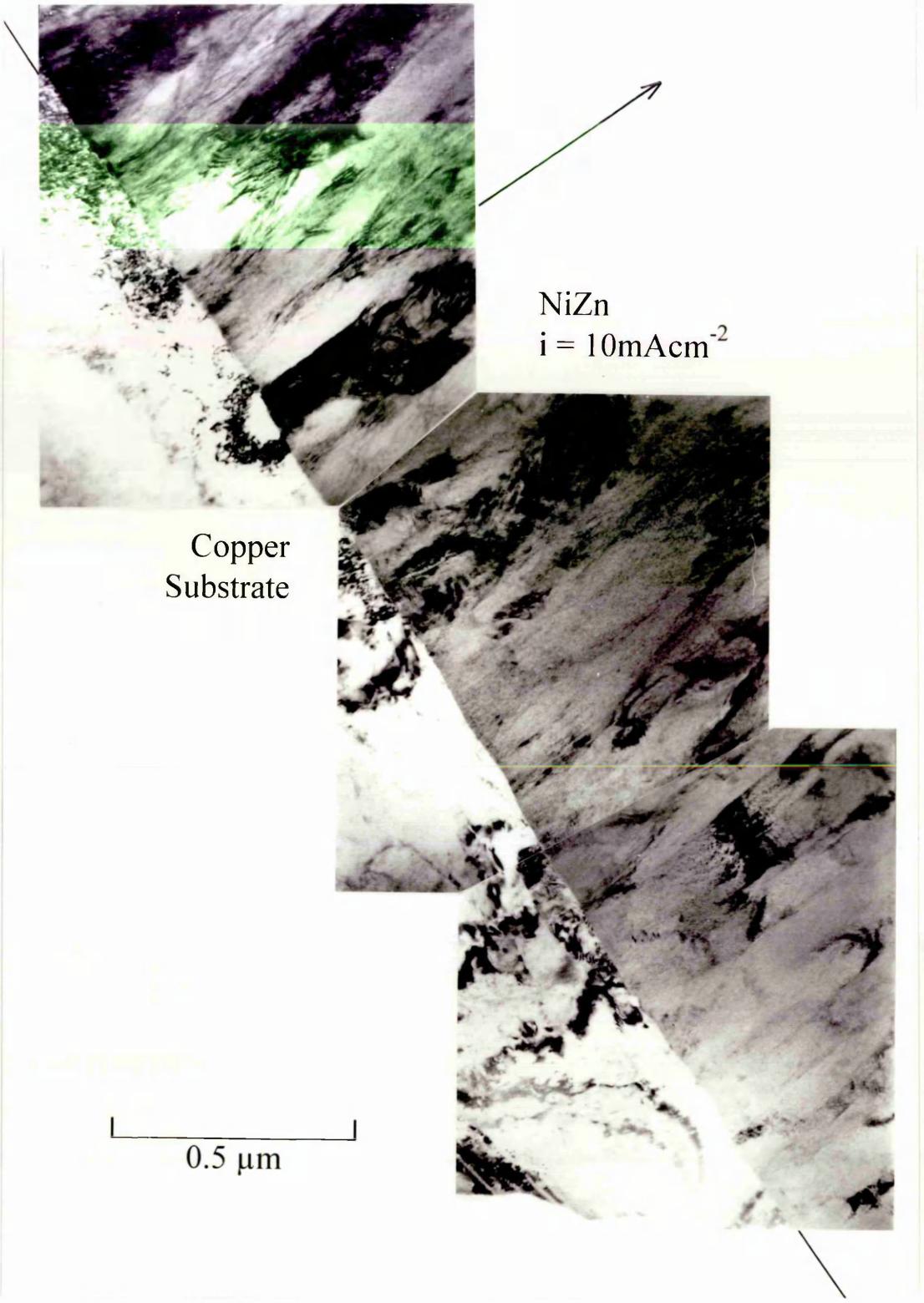

Fig. 4-64: Bright Field Images Along Interface Between Copper Substrate and Nucleated NiZn Deposit (i = 10 mA cm^{-2}).

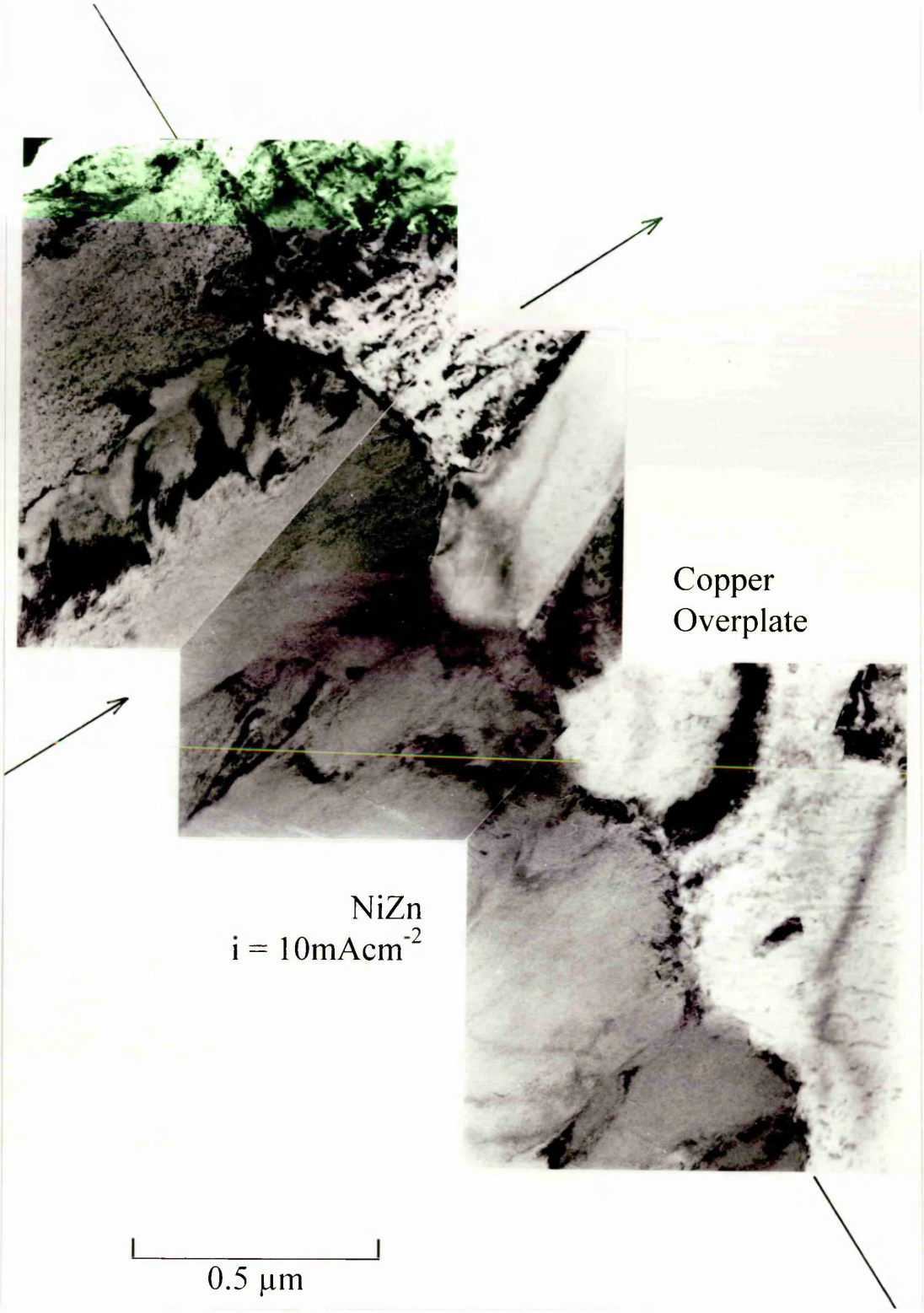

Fig. 4-65: Bright Field Images Along Interface Between Advanced Developed, Approximately 2µm Thick, Coarse Grained NiZn Deposit (i = 10 mA cm^{-2}) and Copper Overplate.

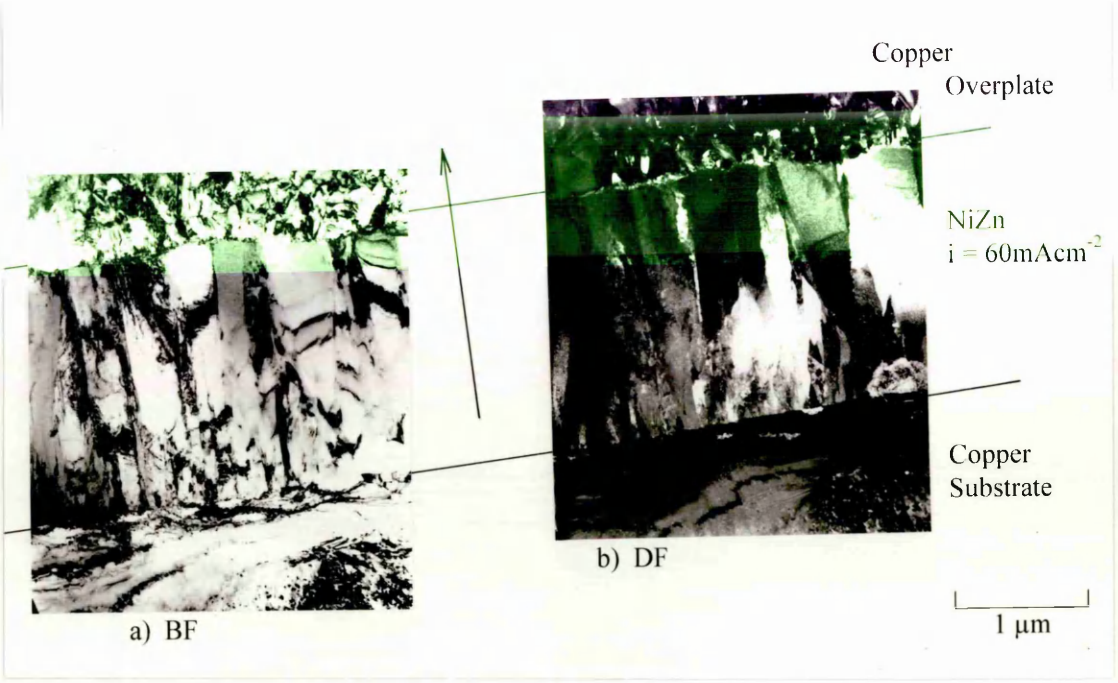

Fig. 4-66: (a) Bright Field and (b) Dark Field Image of Cross-Sectioned NiZn Deposit (i = 60 mA cm^{-2}) Nucleated on Copper.

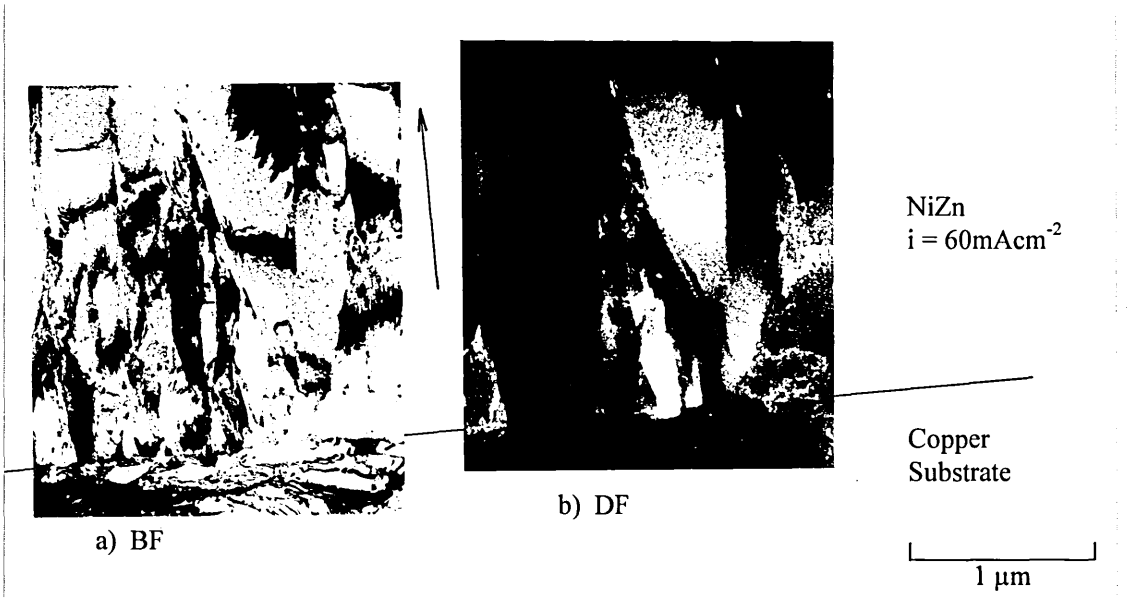

Fig. 4-67: (a) Bright and (b) Dark Field Image of Nucleation Site of NiZn Deposit (i = 60 mA cm^{-2}) on Copper.

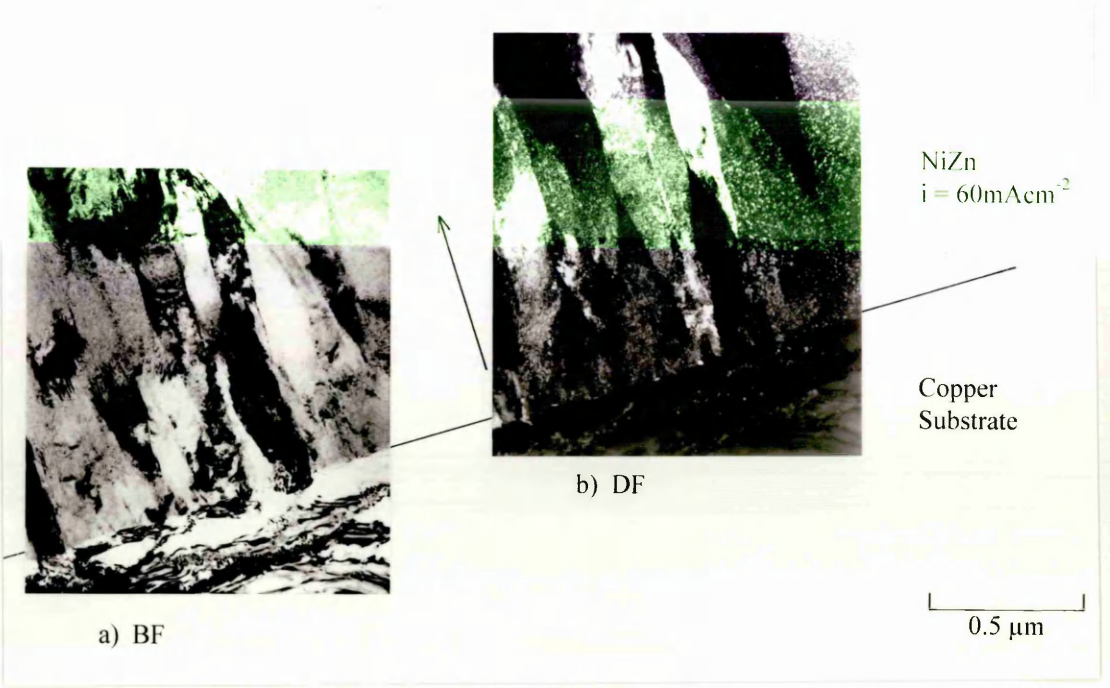

Fig. 4-68: (a) Bright and (b) Dark Field Image of Nucleation Site of NiZn Deposit (i = 60 mA cm^{-2}) on Copper.

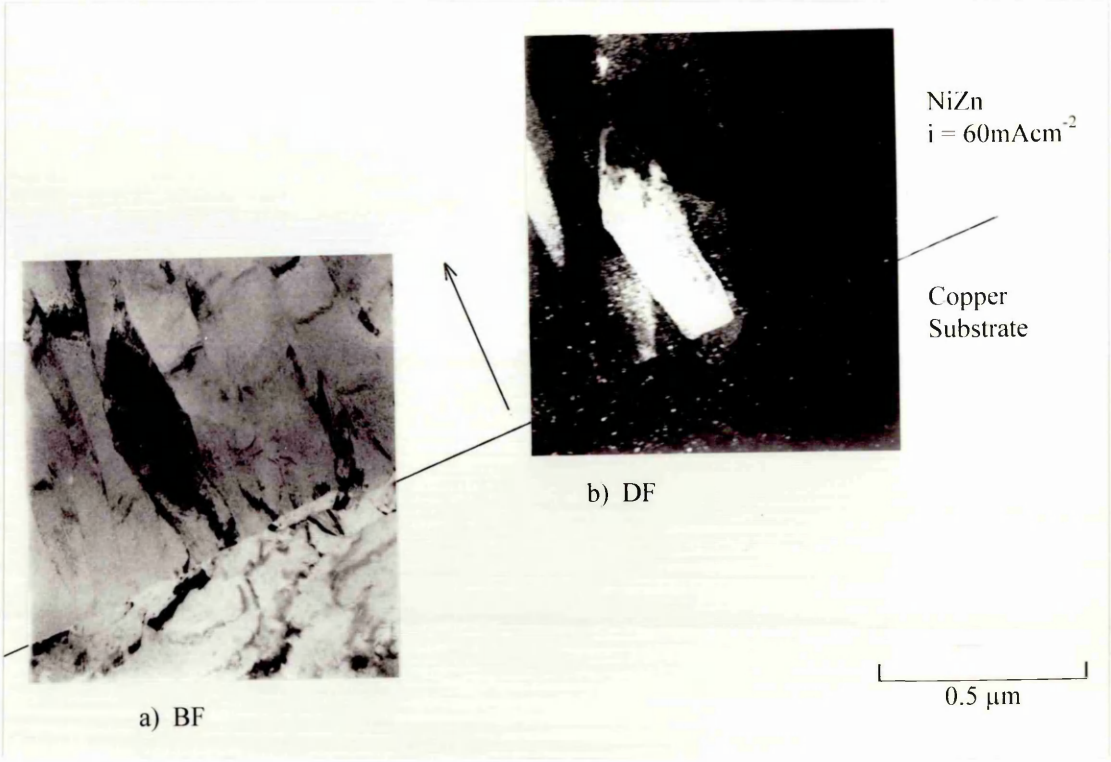

Fig. 4-69: (a) Bright and (b) Dark Field Image of Nucleation Site of NiZn Deposit (i = 60 mA cm^{-2}) on Copper.

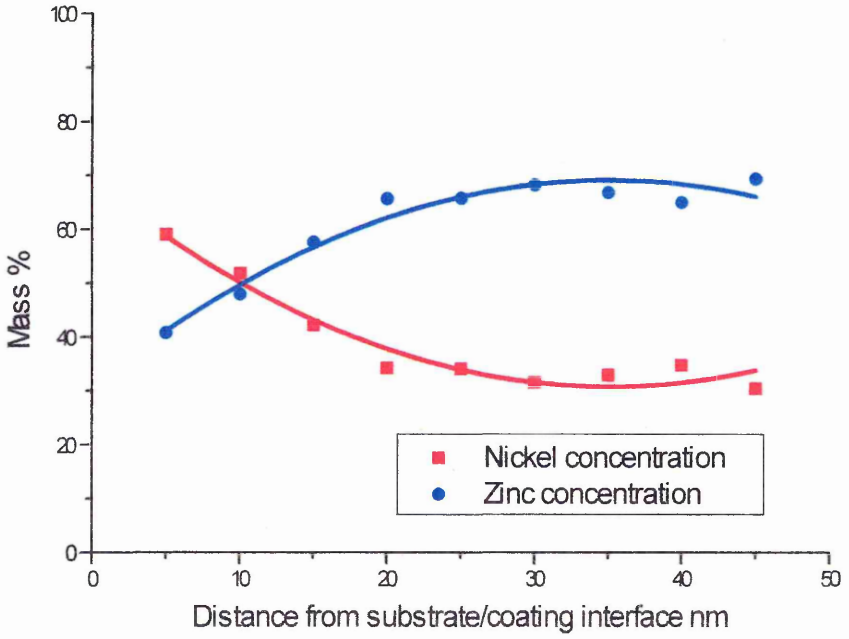

Fig. 4-70: Composition of Nickel Zinc Deposit (i = 10 mA cm^{-2}) versus Distance from Interface Steel Substrate/Nickel Zinc Deposit.

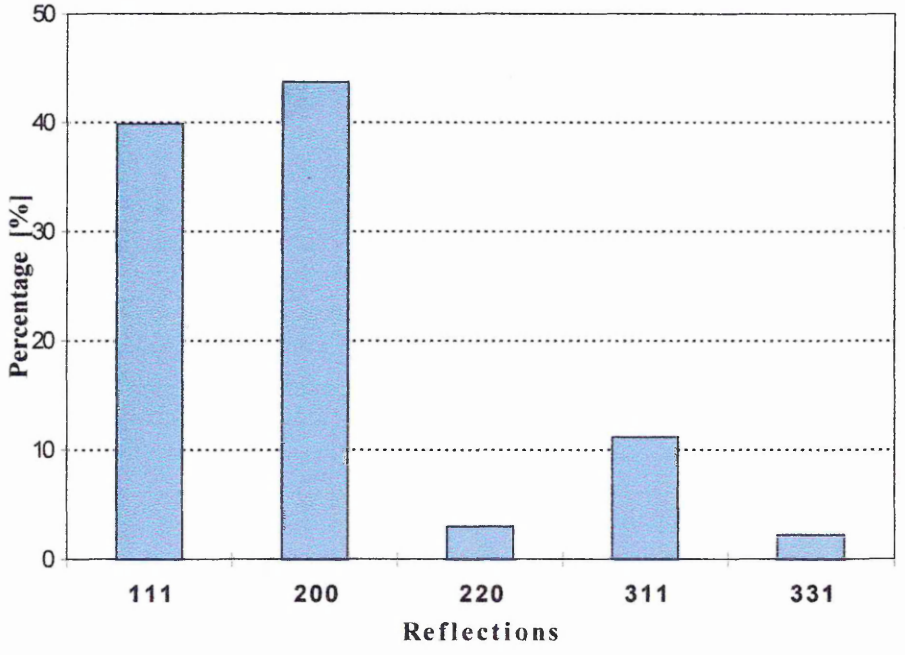

Fig. 4-71: Distribution of Reflections Detected in the Copper Disc Substrate.

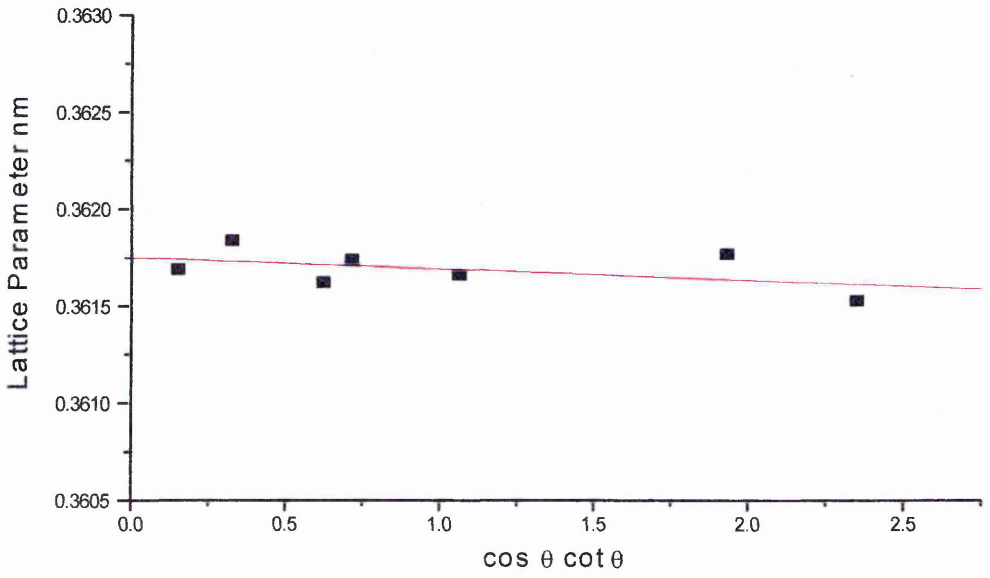

Fig. 4-72: Copper Rod Substrate: Lattice Parameter [nm] Versus cosθ cotθ; Cohen-Wagner Plot for Extrapolation of Lattice Parameter 'a'.

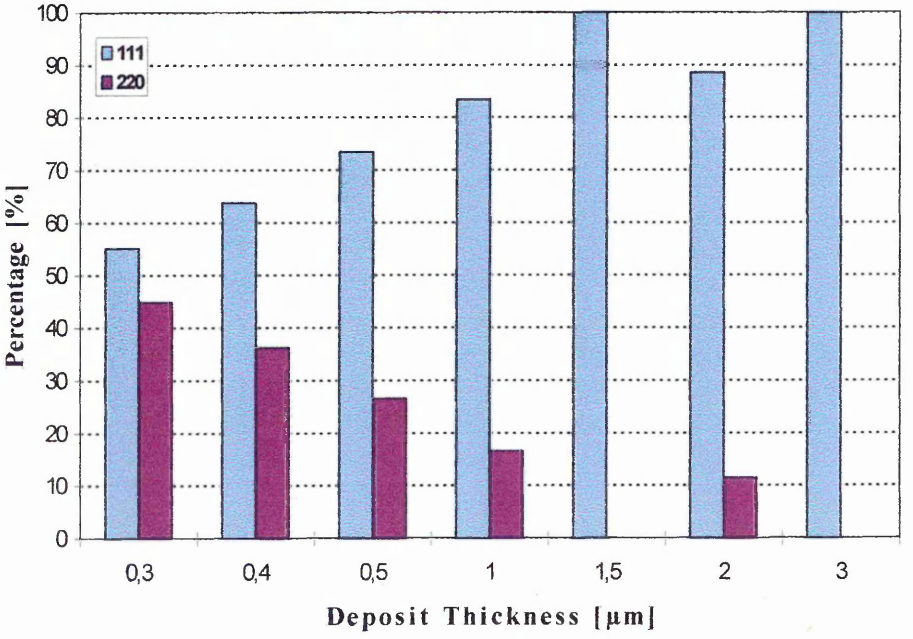

Fig. 4-73: Distribution of Reflections Detected at Various Thicknesses in the fcc NiFe Electrodeposits.

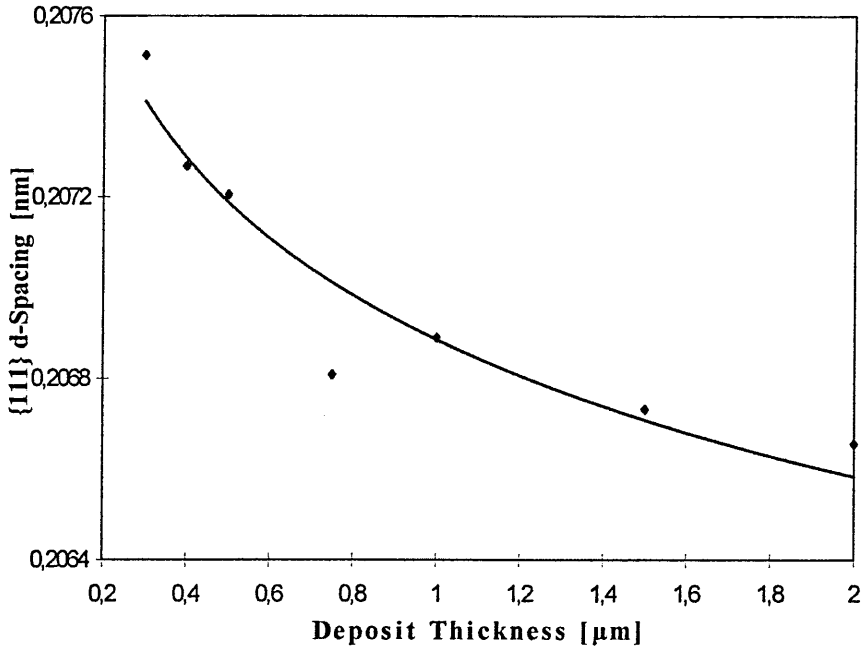

Fig. 4-74: Deposit Thickness Versus {111} Interplanar d-Spacing in fcc NiFe Electrodeposit.

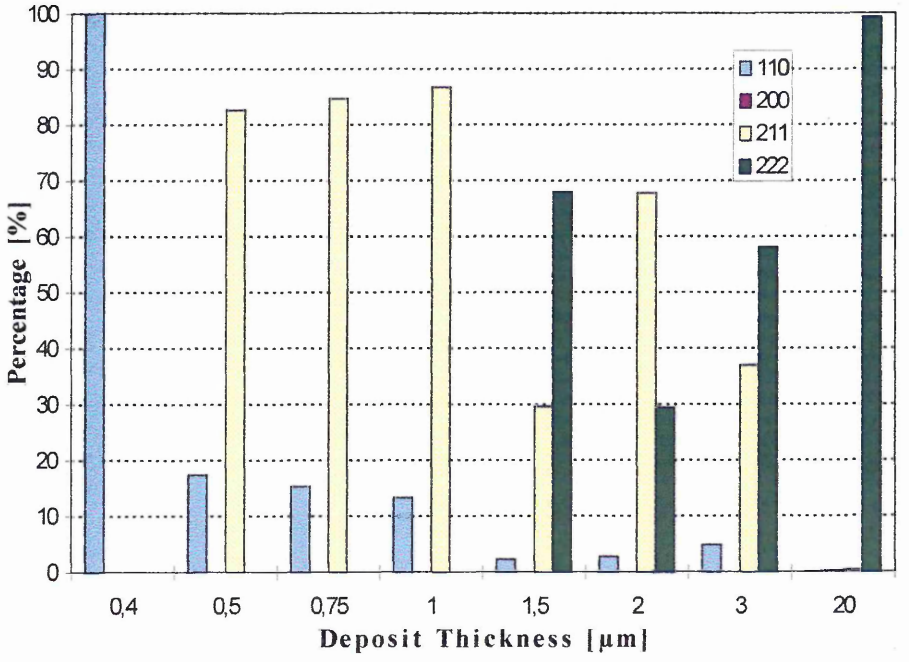

Fig. 4-75: Distribution of Reflections Detected at Various Thicknesses in the bcc NiFe Electrodeposits.

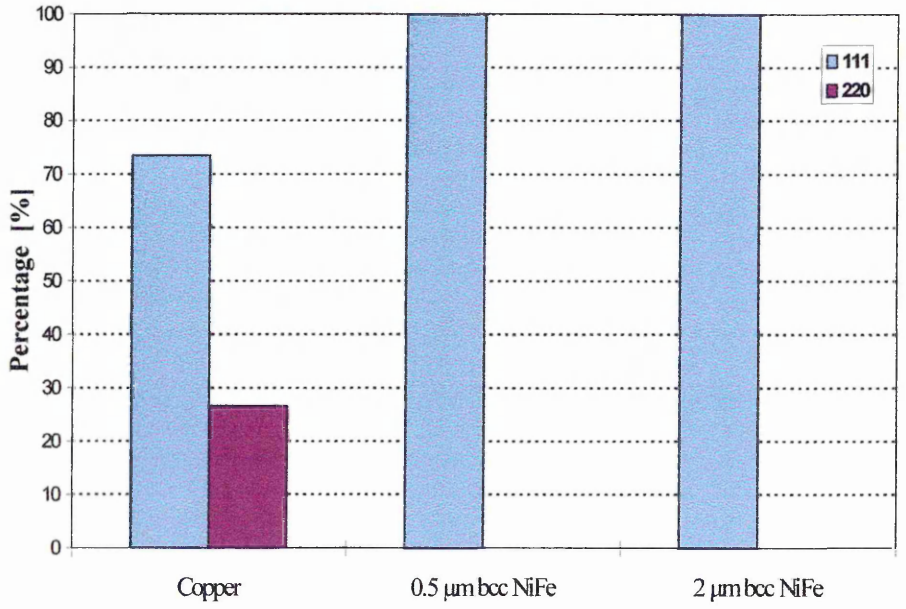

Fig. 4-76: Planar Distribution of 0.5µm Thick fcc NiFe on Copper, 0.5µm bcc NiFe, and 2µm bcc NiFe Electrodeposited Substrates.

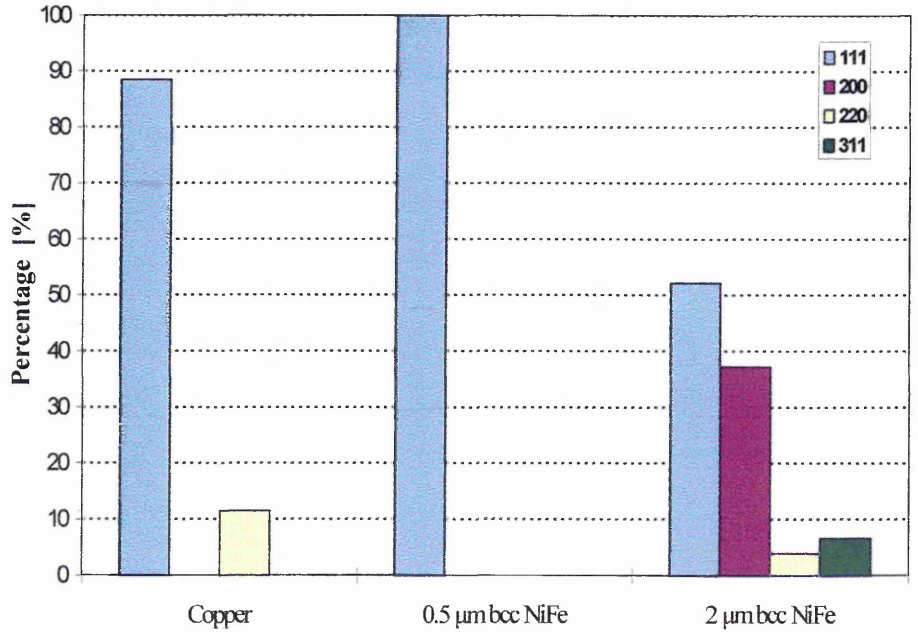

Fig. 4-77: Planar Distribution in per cent of 2µm Thick fcc NiFe Electrodeposits on Copper, 0.5µm bcc NiFe, and 2µm bcc NiFe Electrodeposited Substrates.

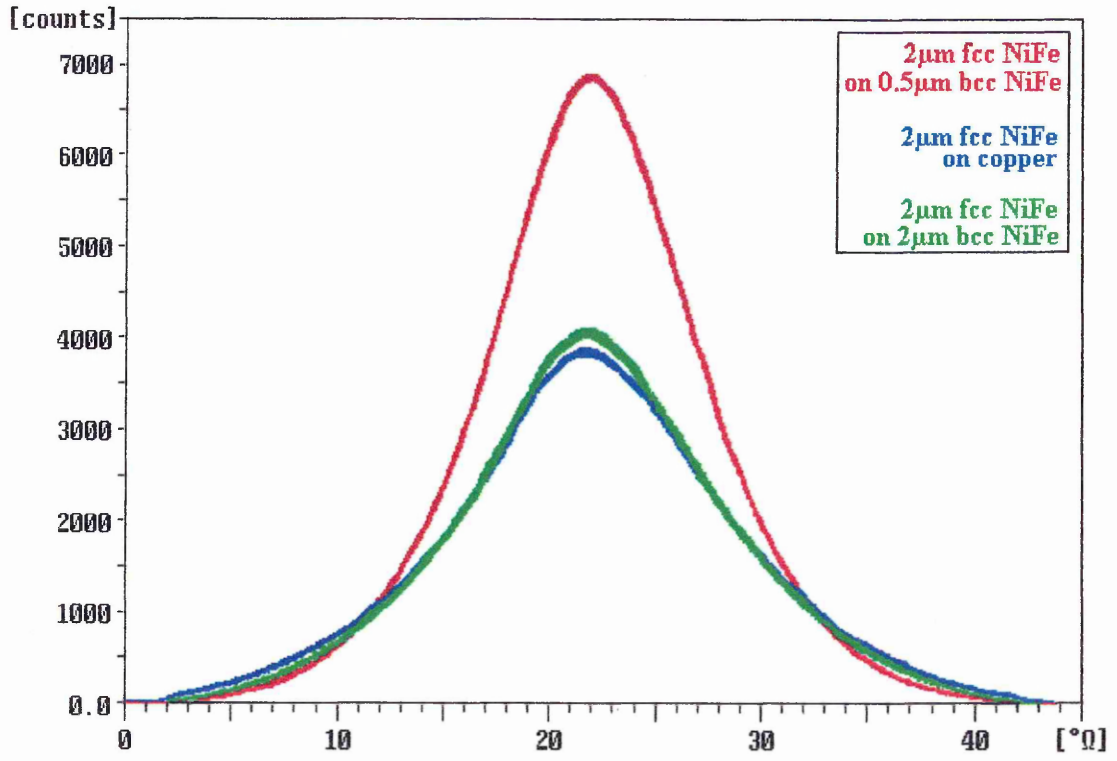

Fig. 4-78: Ω-Scan Spectra of 2µm Thick fcc Structured Nickel-Iron Deposit Electrocrystallized onto Different Substrates, i.e. Copper, 0.5µm bcc NiFe, and 2µm bcc NiFe Electrodeposits.

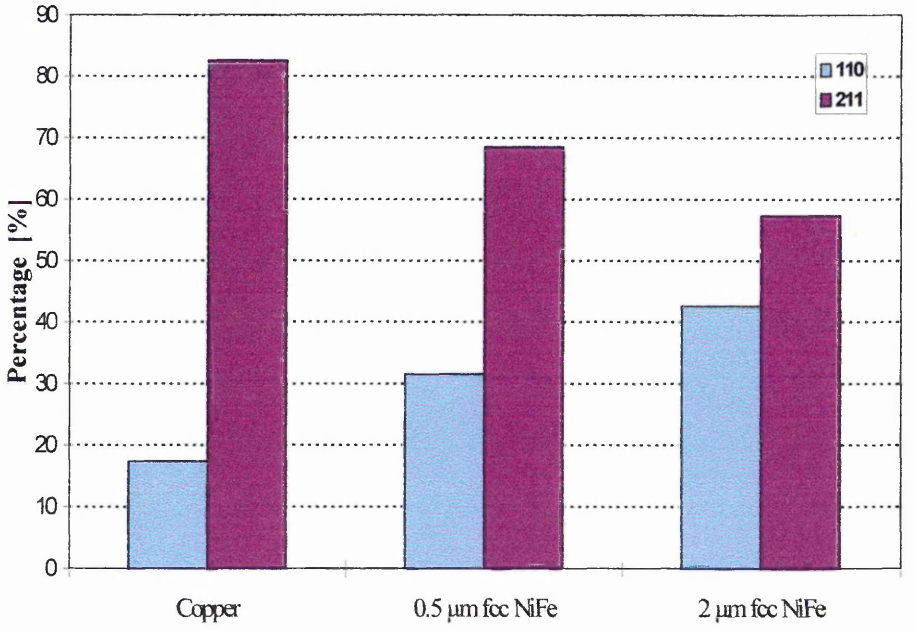

Fig. 4-79: Planar Distribution of 0.5µm Thick bcc NiFe on Copper, 0.5µm fcc NiFe, and 2µm fcc NiFe Electrodeposited Substrates.

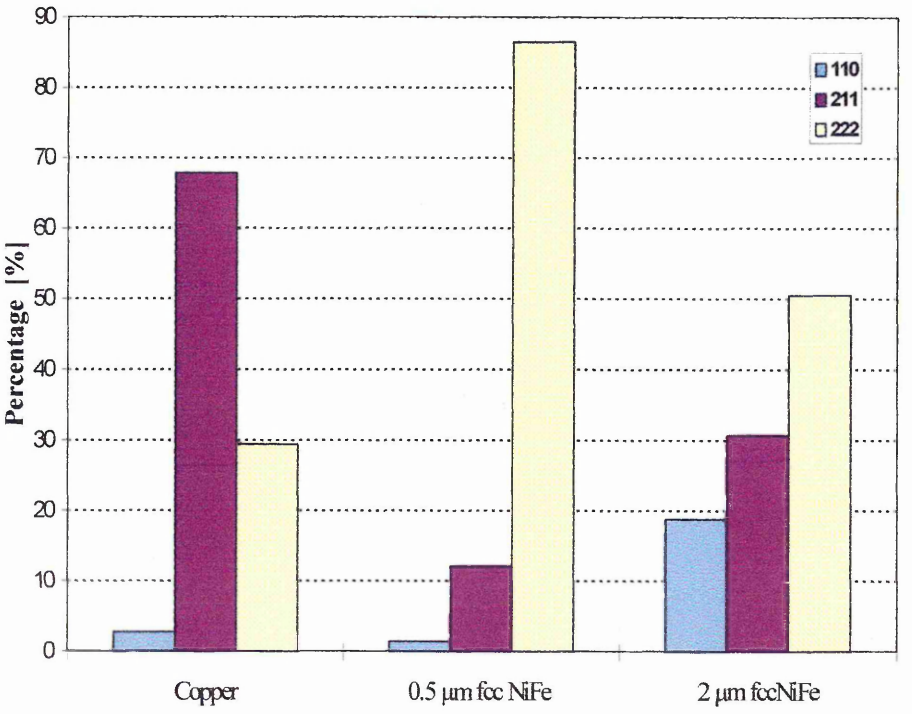

Fig. 4-80: Planar Distribution of 2µm Thick bcc NiFe on Copper, 0.5µm fcc NiFe, and 2µm fcc NiFe Electrodeposited Substrates.

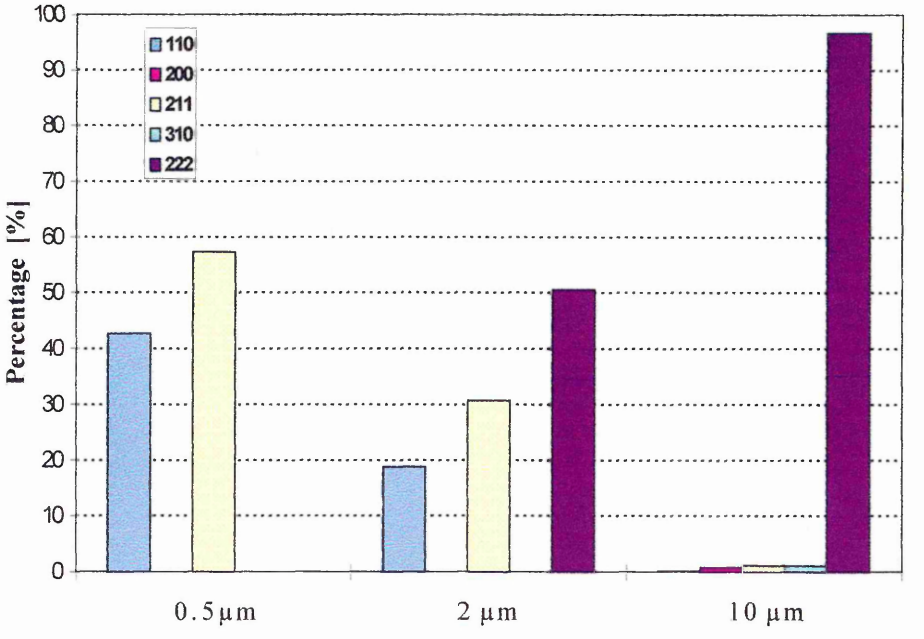

Fig. 4-81: Planar Distribution of 0.5µm, 2µm, and 10µm thick bcc NiFe Electrodeposit on 2µm fcc NiFe Substrate.

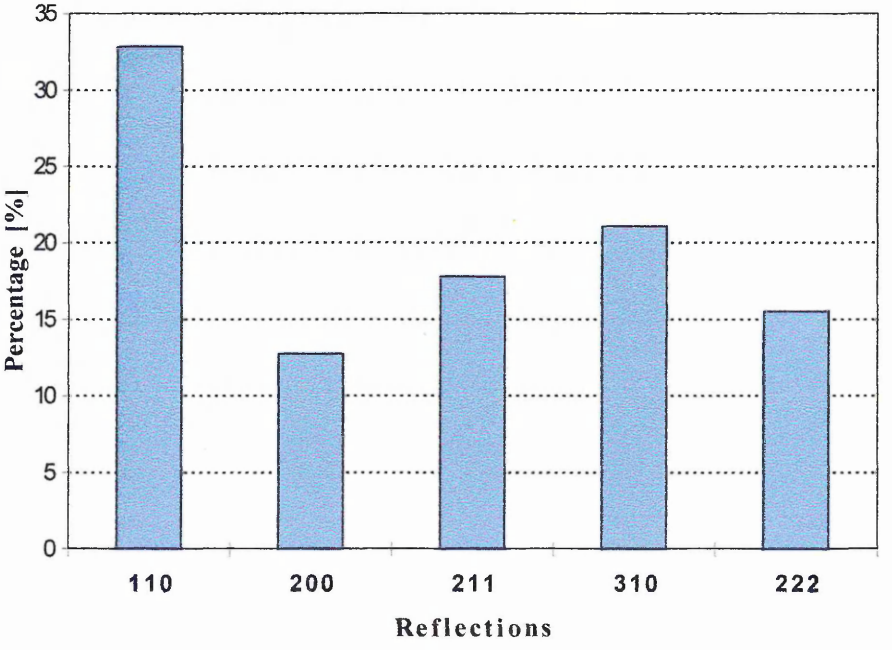

Fig. 4-82: Distribution of Reflections detected in the Mild Steel Disc Substrate.

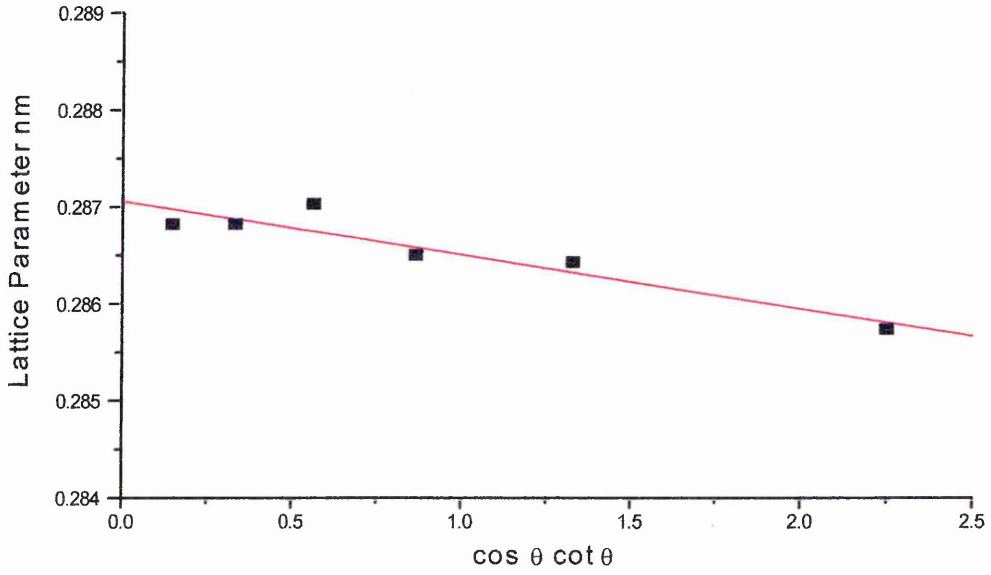

Fig. 4-83: Mild Steel Substrate: Lattice Parameter [nm] Versus cosθ cotθ; Cohen-Wagner Plot for Extrapolation of Lattice Parameter 'a'.

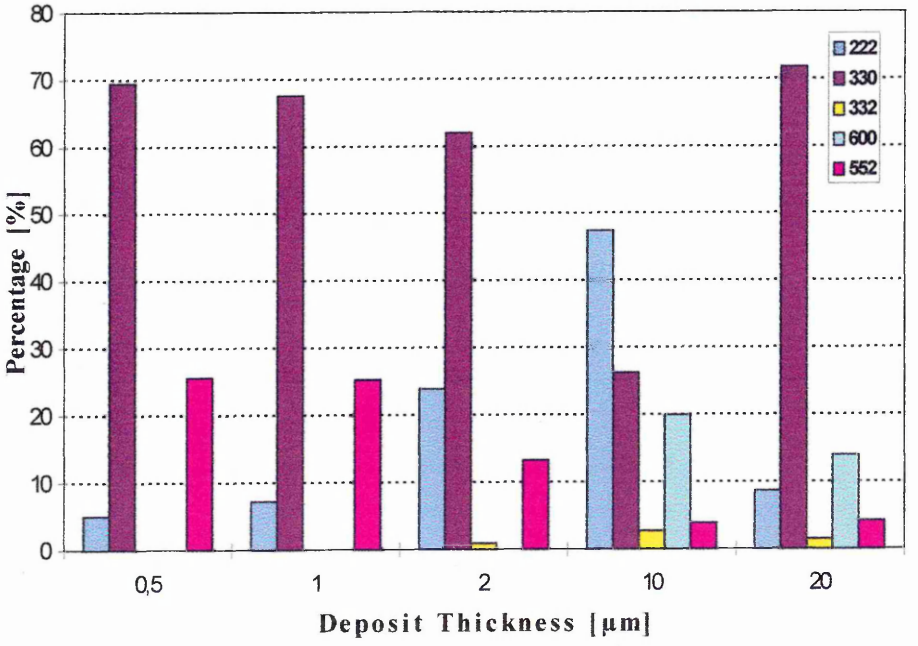

Fig. 4-84: Distribution of Reflections Detected in Nickel-Zinc of Various Thicknesses, Deposited with 10 mA cm^{-2} on Mild Steel Substrates.

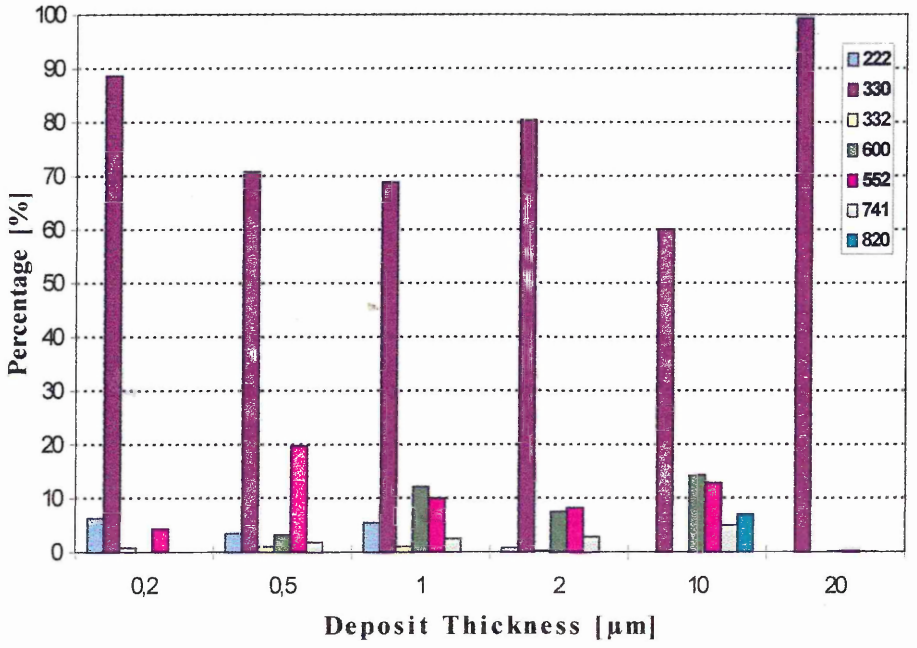

Fig. 4-85: Distribution of Reflections Detected in Nickel-Zinc of Various Thicknesses, Deposited with 60 mA cm^{-2} on Mild Steel Substrates.

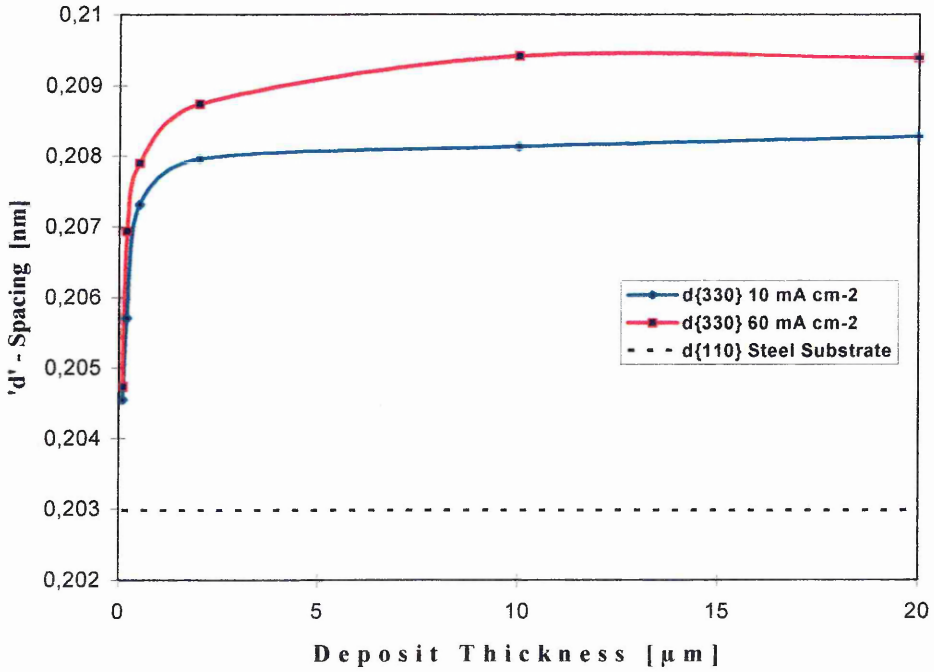

Fig. 4-86: Interplanar {330} d-Spacings of γ-Phase NiZn Deposits Formed at 10 and 60 mA cm^{-2} Versus Deposit Thickness and {110} d-Spacing of Steel Substrate.

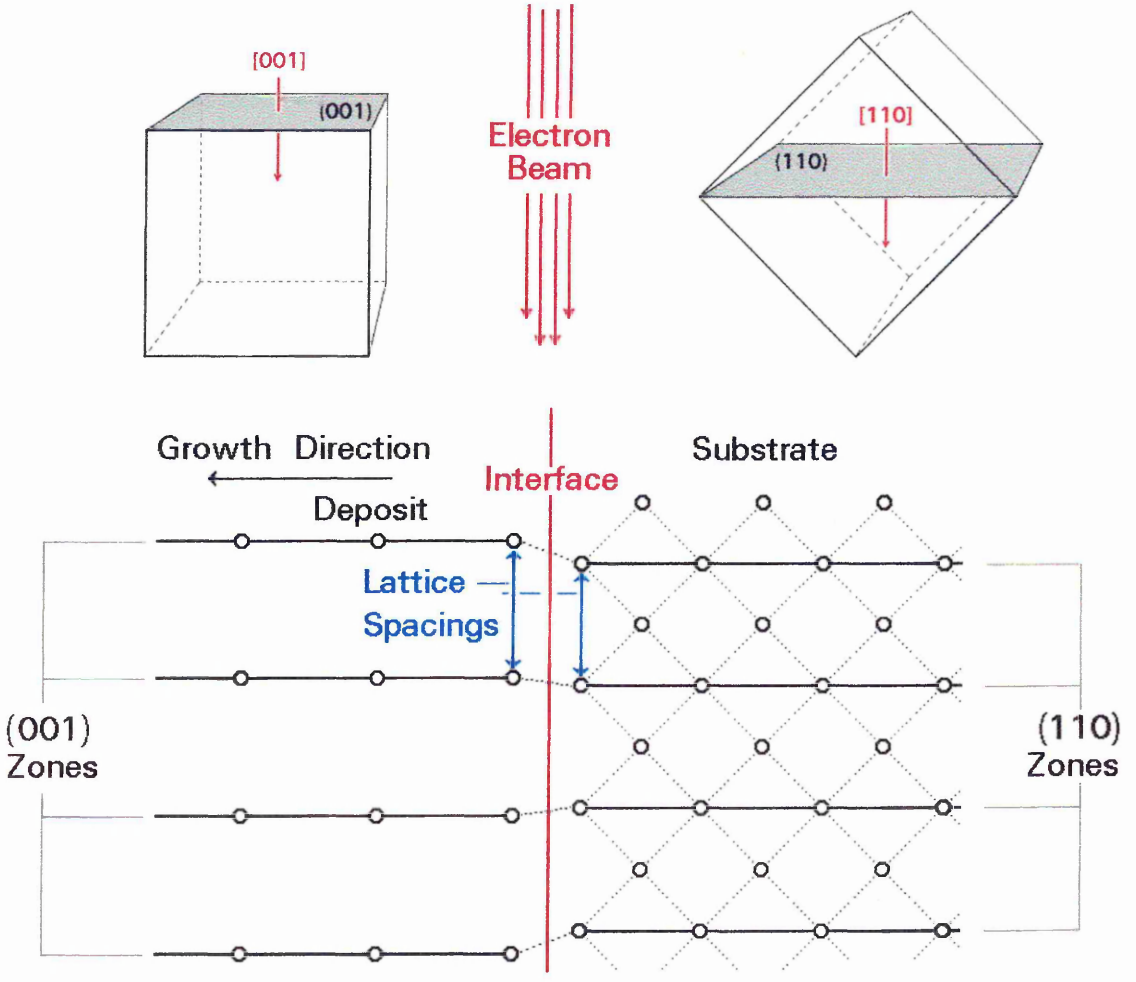

Fig. 5-1: Model of the Electron Beam Interacting with a Cross-Sectioned Specimen, i.e. bcc Nickel-Iron Electrodeposited on a Copper Substrate.

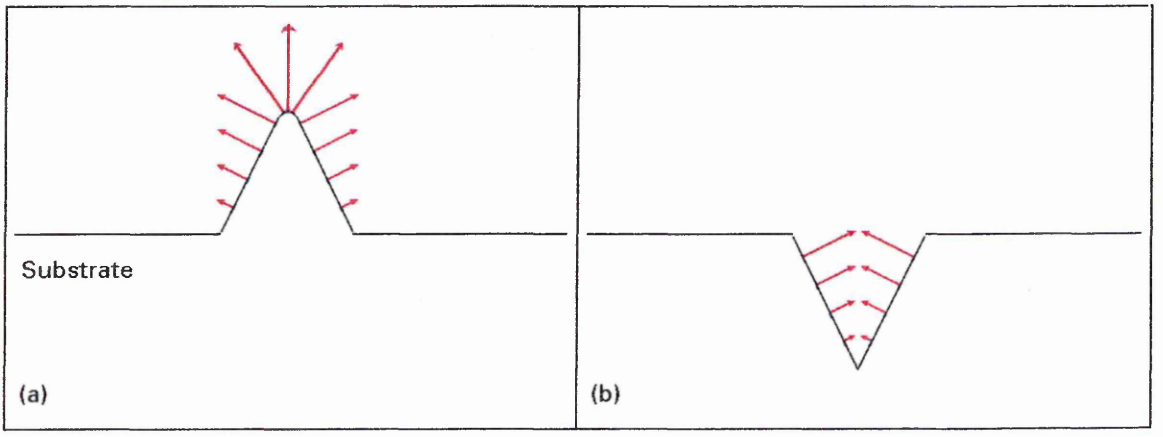

Fig. 5-2: Schematic Representation of Grain Growth (a) at a Protrusion and (b) on a Recessed Area of the Substrate Perpendicular to the Surface.

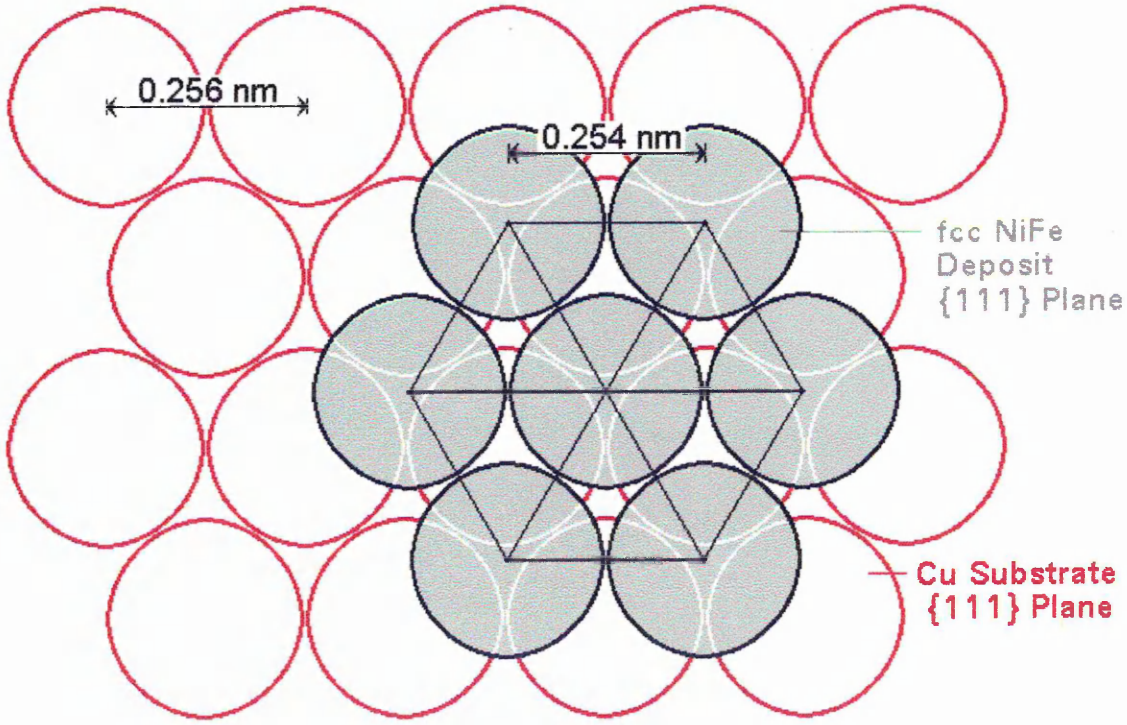

Fig. 5-3: Model of Atoms in {111} Orientated fcc Nickel-Iron Deposit Nucleated onto {111} Textured Copper Substrate (Plan View).

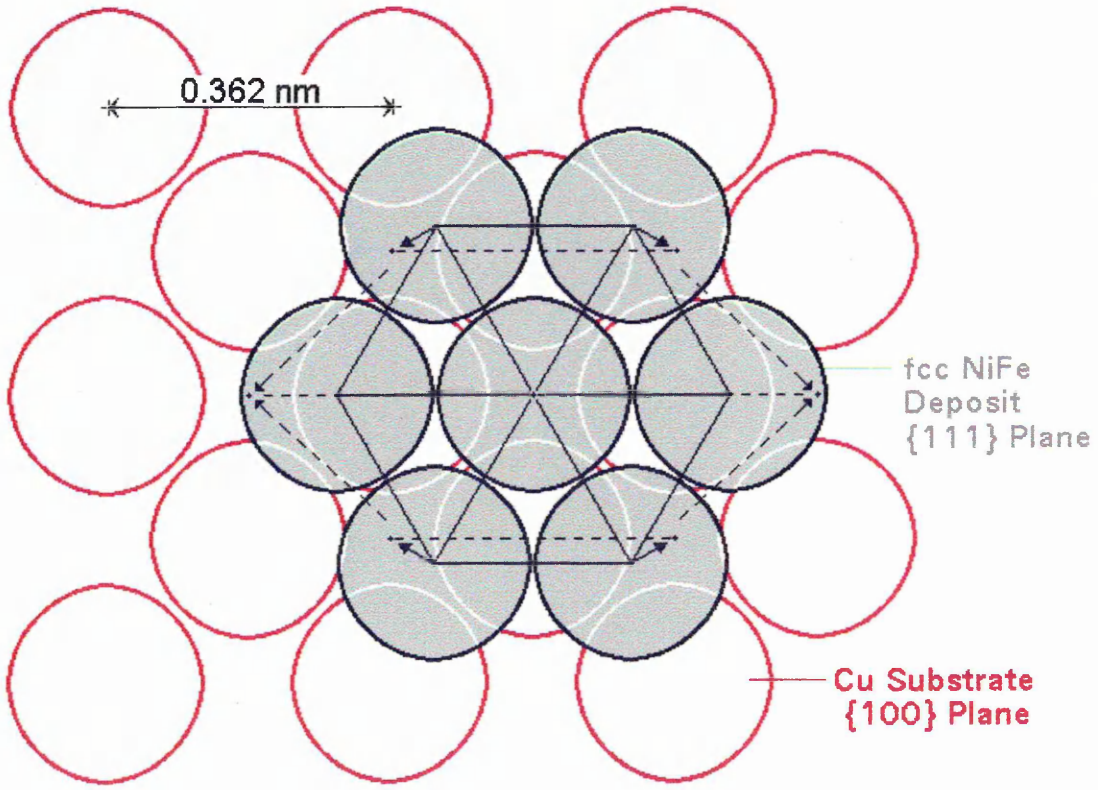

Fig. 5-4: Model of Atoms in {111} Orientated fcc Nickel-Iron Deposit Nucleated onto {100} Textured Copper Substrate (Plan View).

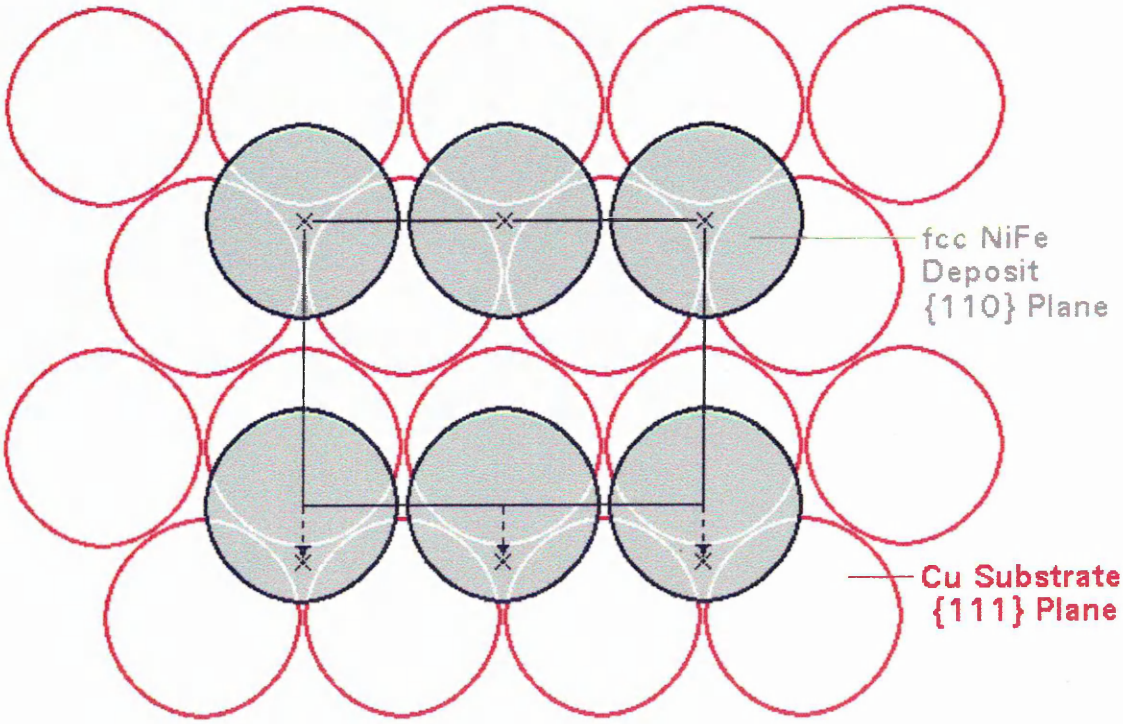

Fig. 5-5: Model of Atoms in {110} Orientated fcc Nickel-Iron Deposit Nucleated onto {111} Textured Copper Substrate (Plan View).

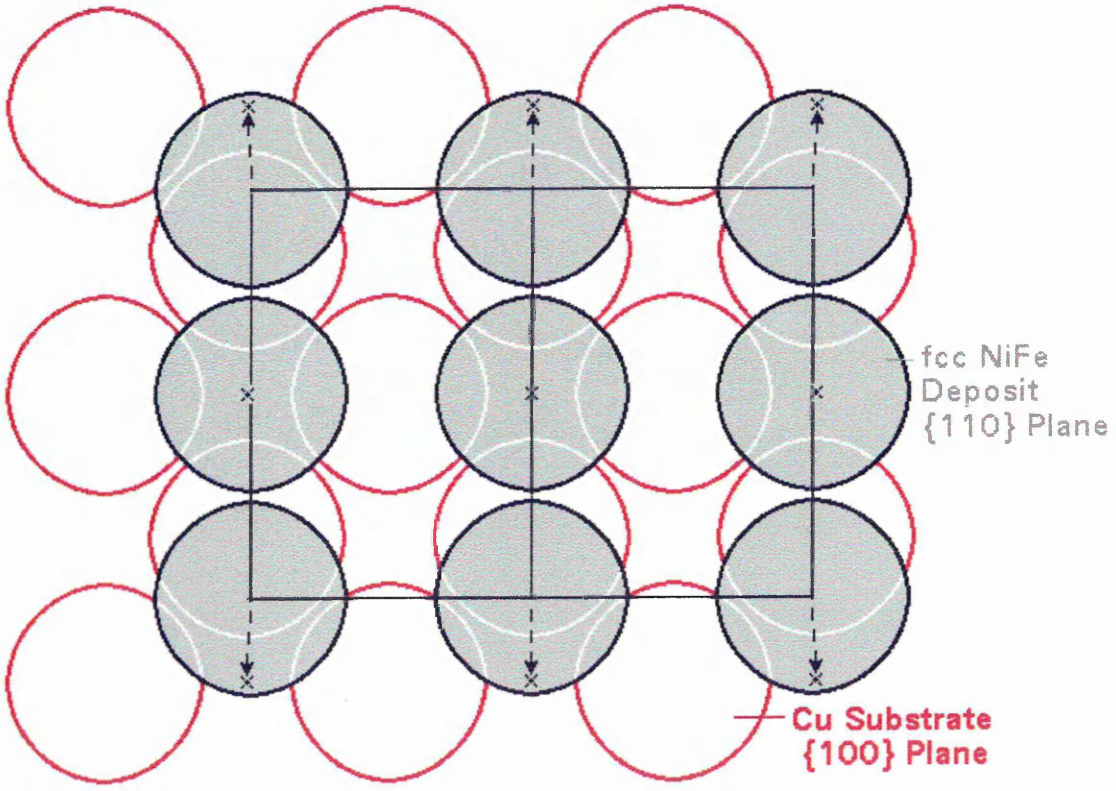

Fig. 5-6: Model of Atoms in {110} Orientated fcc Nickel-Iron Deposit Nucleated onto {100} Textured Copper Substrate (Plan View).

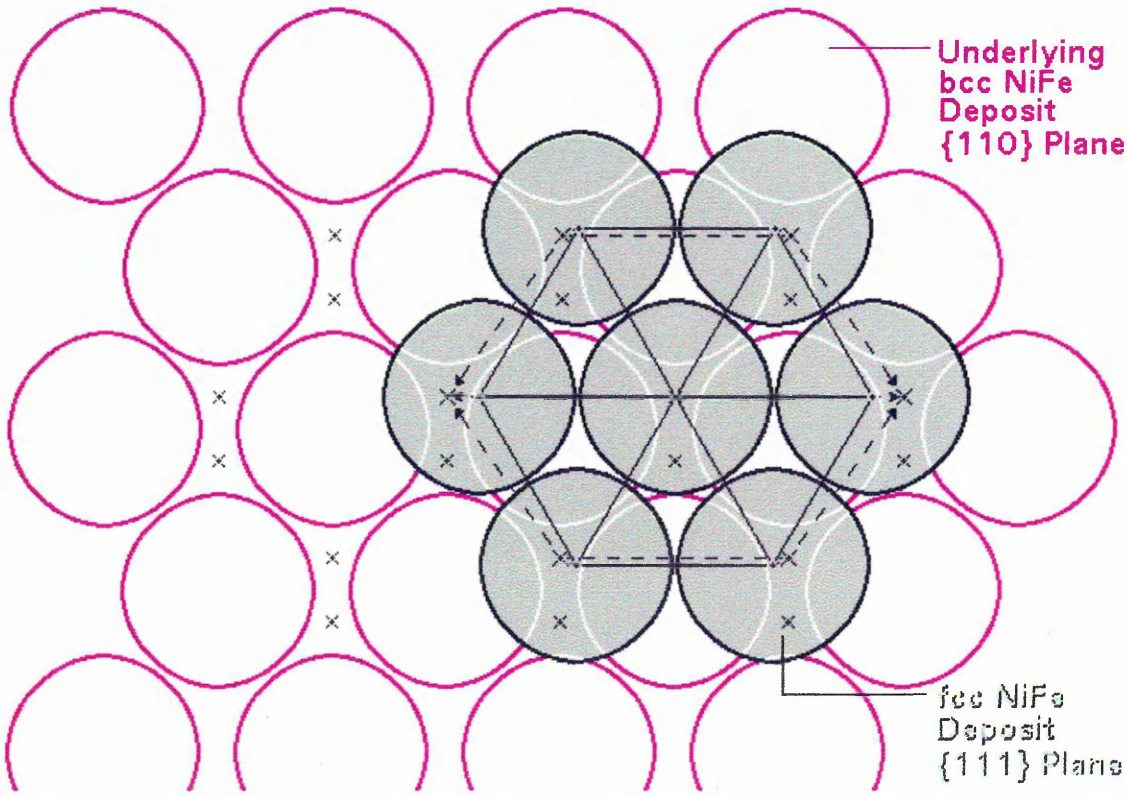

Fig. 5-7: Model of Atoms in {111} Orientated fcc Nickel-Iron Deposit Nucleated onto {110} Textured bcc Structured Nickel-Iron Electrodeposited Substrate (Plan View).

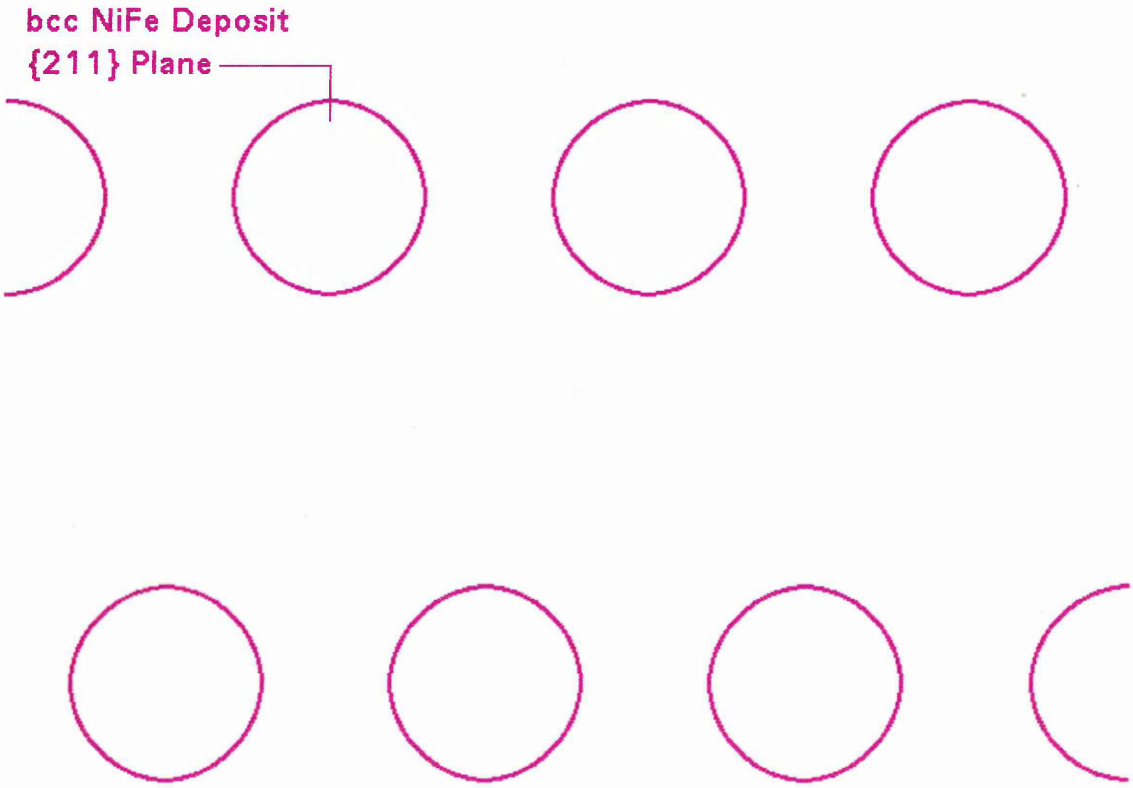

Fig. 5-8a: Model of Atoms in {211} Orientated bcc Nickel-Iron Electrodeposited Substrate (Plan View).

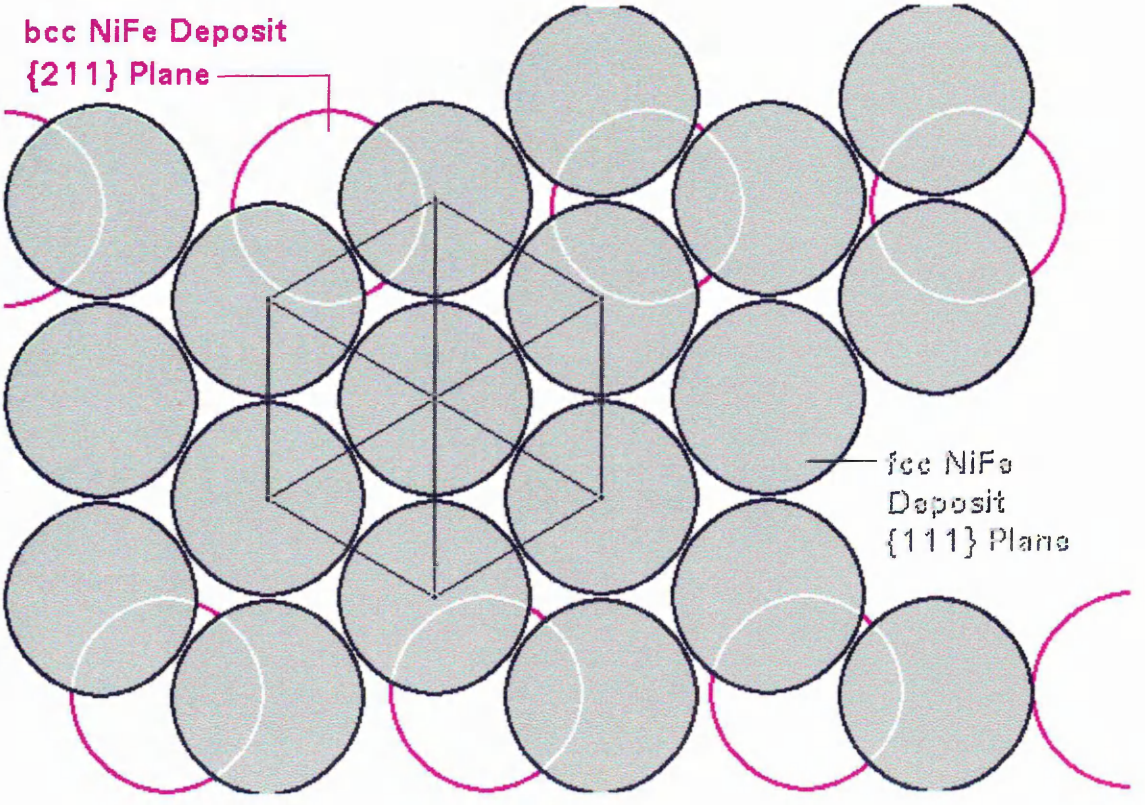

Fig. 5-8b: Model of Atoms in {111} Orientated fcc Nickel-Iron Deposit Nucleated onto {211} Textured bcc Structured Nickel-Iron Electrodeposited Substrate (Plan View).

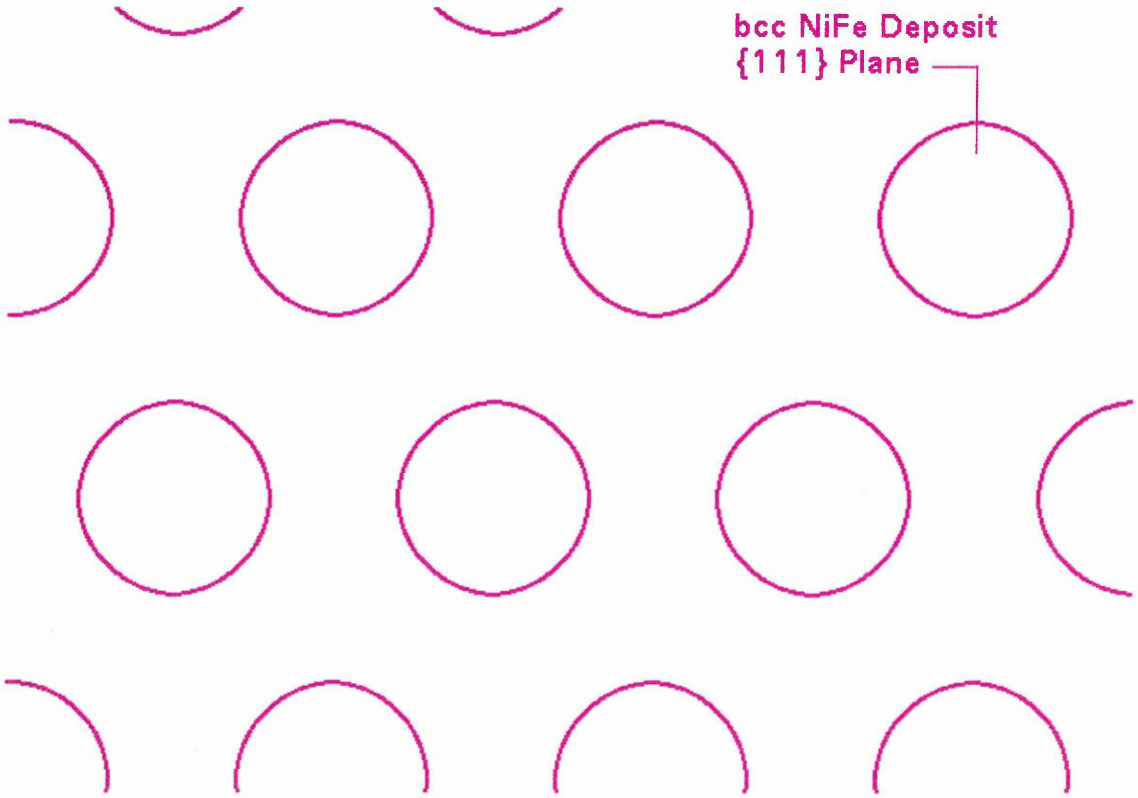

Fig. 5-9a: Model of Atoms in {111} Orientated bcc Nickel-Iron Electrodeposited Substrate (Plan View).

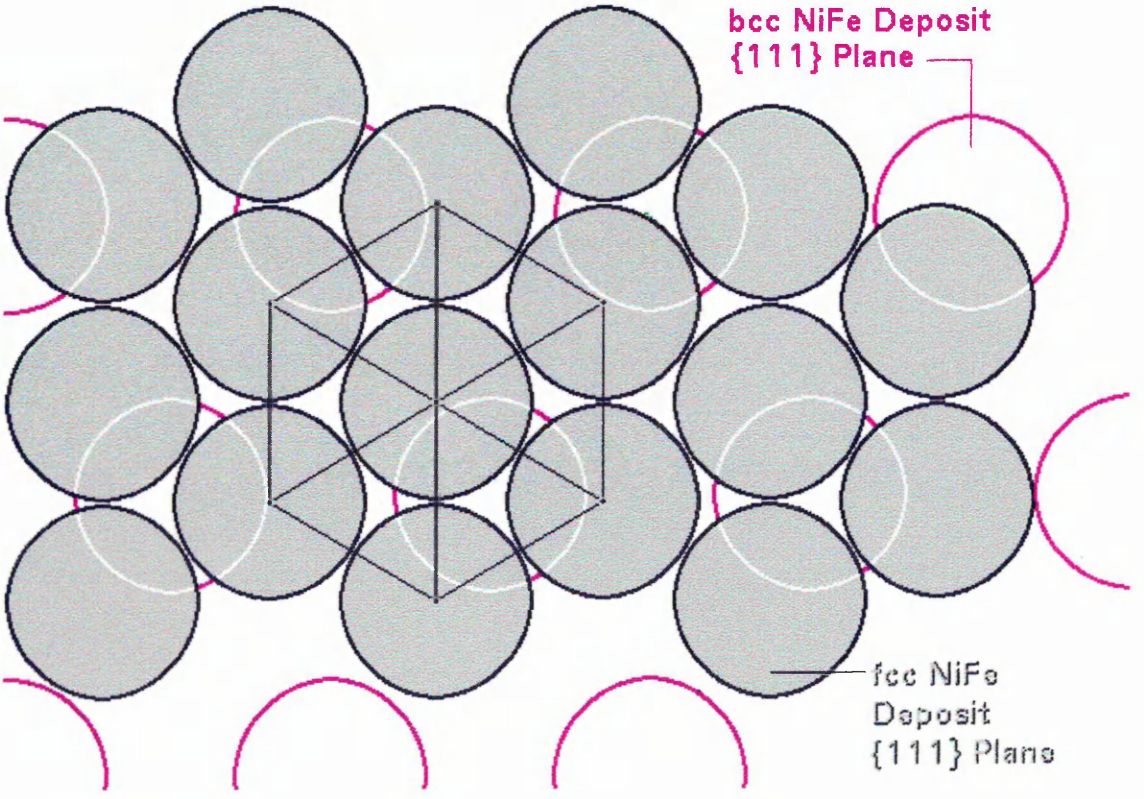

Fig. 5-9b: Model of Atoms in {111} Orientated fcc Nickel-Iron Deposit Nucleated onto {111} Textured bcc Structured Nickel-Iron Electrodeposited Substrate (Plan View).

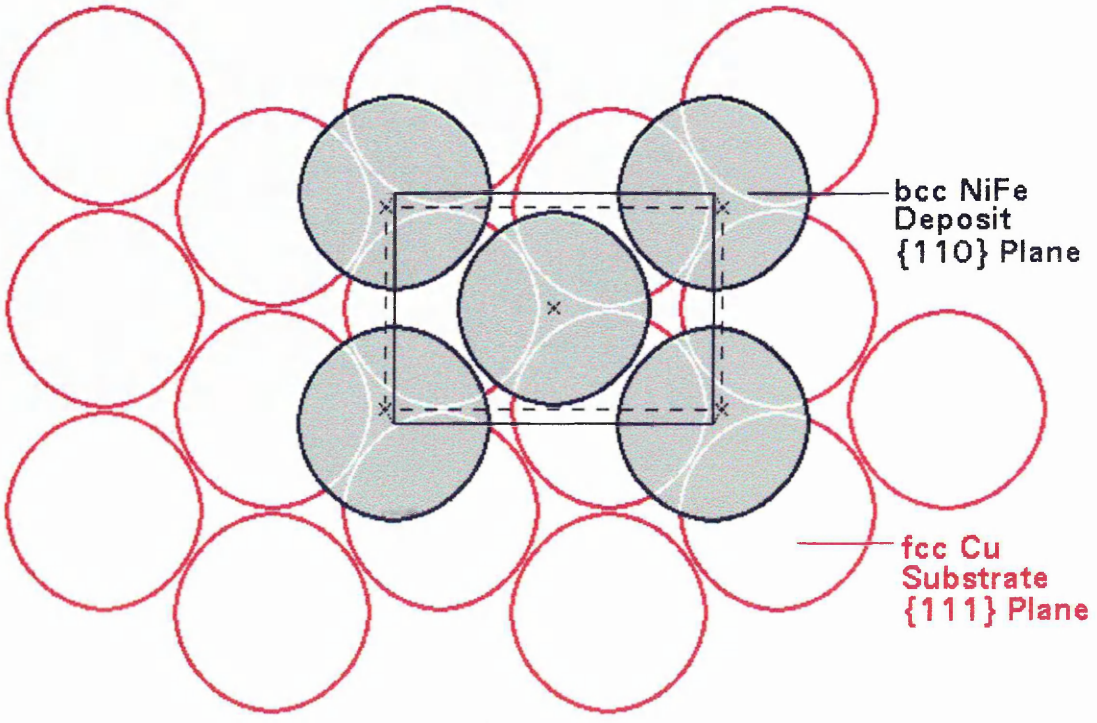

Fig. 5-10: Model of Atoms in {110} Orientated bcc Nickel-Iron Deposit Nucleated onto {111} Textured fcc Copper Substrate (Plan View).

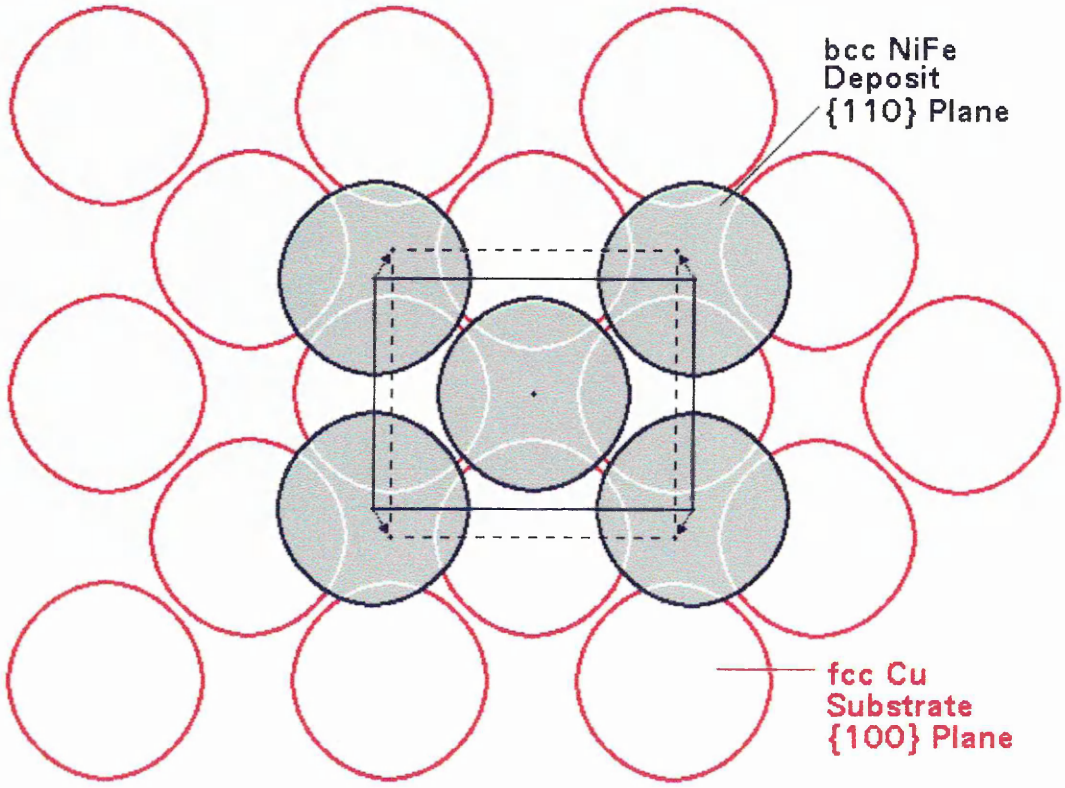

Fig. 5-11: Model of Atoms in {110} Orientated bcc Nickel-Iron Deposit Nucleated onto {100} Textured fcc Copper Substrate (Plan View).

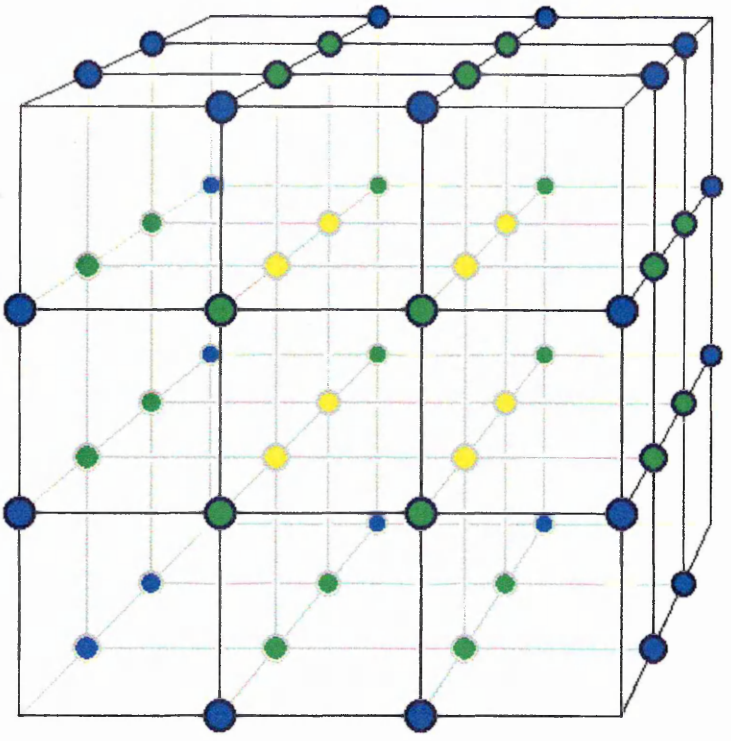

Unit Cell, consisting of 27 Sub Cells, 52 Atoms.

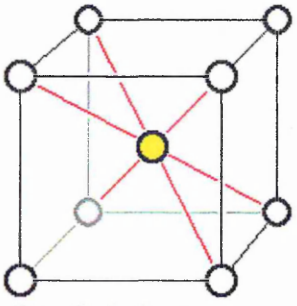

Bcc Sub Cell

● : **Atoms on edges, shared by 4 unit cells.**

$$\frac{24}{4} = 6$$

● : **Atoms on face sides, shared by 2 unit cells.**

$$\frac{24}{2} = 12$$

● : **Atoms inside the unit cell (8 atoms), and accommodated within each sub cell, except the central atom (26 atoms per unit cell), not shared.**

$$8 + 26 = 34$$

Fig. 5-12: Model Depicting the Atomic Arrangement within the Ni_5Zn_{21} Unit Cell, which Consists of 27 Bcc Sub Cells, thus Working out at 52 Atoms per Unit Cell.

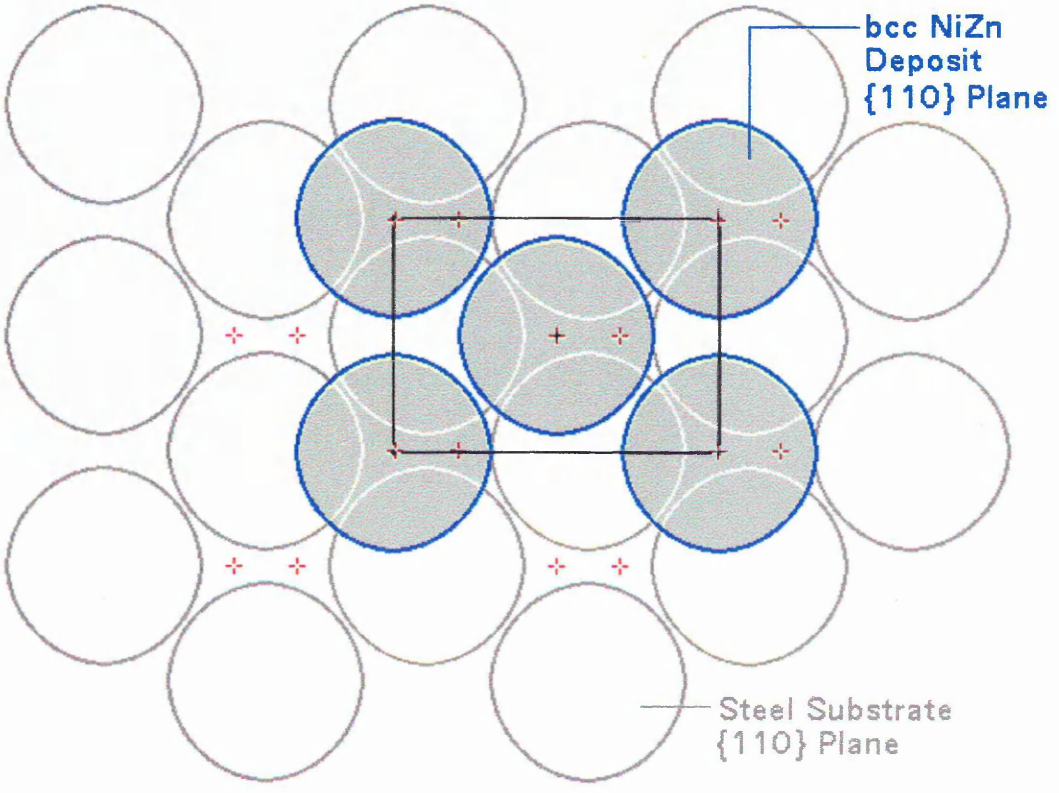

Fig. 5-13: Model of Epitaxial Growth of {110} Orientated bcc γ-Phased Nickel-Zinc Deposit Nucleated onto {110} Textured Steel Substrate (Plan View).

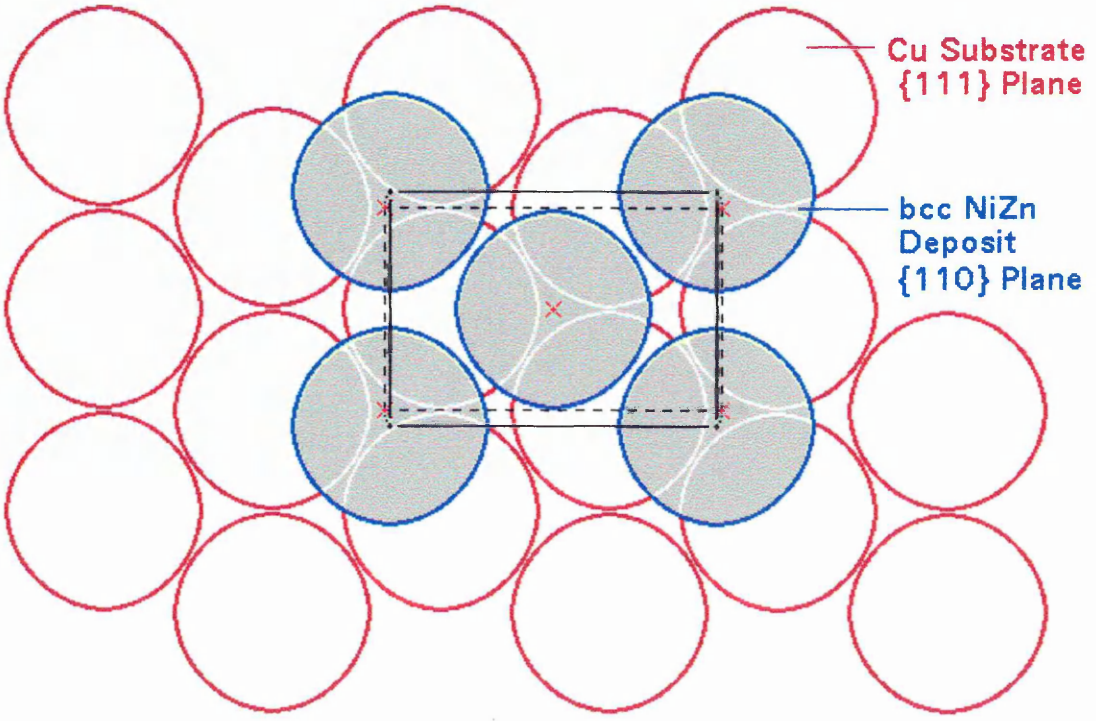

Fig. 5-14: Model of {110} Orientated bcc γ-Phased Nickel-Zinc Deposit Nucleated onto {111} Textured Copper Substrate (Plan View).

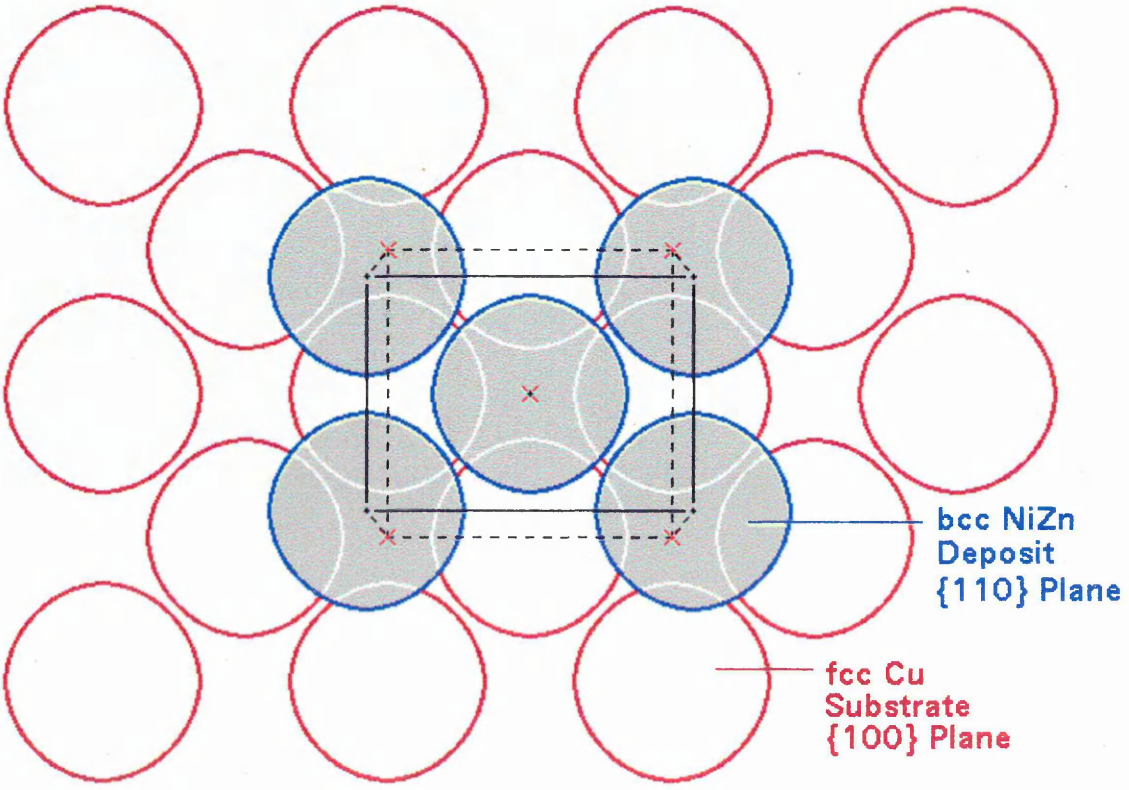

Fig. 5-15: Model of {110} Orientated bcc γ-Phased Nickel-Zinc Deposit Nucleated onto {100} Textured Copper Substrate (Plan View).